Editor QINGBO XU

A HANDBOOK OF MOUSE MODELS OF CARDIOVASCULAR DISEASE

WILEY

A Handbook of Mouse Models of Cardiovascular Disease

A Handbook of Mouse Models of Cardiovascular Disease

Editor

Qingbo Xu

St George's University of London, London, UK

John Wiley & Sons, Ltd

 John Wiley & Sons Ltd, The Atrium, Southern Gate, Chichester,
West Sussex PO19 8SQ, England

Telephone (+44) 1243 779777

Email (for orders and customer service enquiries): cs-books@wiley.co.uk
Visit our Home Page on www.wileyeurope.com or www.wiley.com

Other Wiley Editorial Offices

John Wiley & Sons Inc., 111 River Street, Hoboken, NJ 07030, USA

Jossey-Bass, 989 Market Street, San Francisco, CA 94103-1741, USA

Wiley-VCH Verlag GmbH, Boschstr. 12, D-69469 Weinheim, Germany

John Wiley & Sons Australia Ltd, 42 McDougall Street, Milton, Queensland 4064, Australia

John Wiley & Sons (Asia) Pte Ltd, 2 Clementi Loop #02-01, Jin Xing Distripark, Singapore 129809

John Wiley & Sons Canada Ltd, 6045 Freemont Blvd, Mississauga, ONT, L5R 4J3

Wiley also publishes its books in a variety of electronic formats. Some content that appears in print may not be available in electronic books.

Library of Congress Cataloging-in-Publication Data

(applied for)

British Library Cataloguing in Publication Data

A catalogue record for this book is available from the British Library

ISBN-13 978-0-470-01610-7 ISBN-10 0-470-01610-8

Typeset in 10.5/12.5pt Times by Thomson Digital
Printed and bound in Great Britain by Antony Rowe Ltd, Chippenham, Wiltshire
This book is printed on acid-free paper responsibly manufactured from sustainable forestry
in which at least two trees are planted for each one used for paper production.

Contents

Preface xi

List of Contributors xiii

1 Mice – general information 1
Hermann Dietrich
Historical perspective of house mice as laboratory animals 1
Maintaining and breeding of mice 3
Mouse genetics 5
Blood and bone marrow collection methods 7
Anesthesia and analgesia 7
Euthanasia 14
References 14

2 Naturally occurring variation among mouse strains 19
Weibin Shi and Aldons J. Lusis
Introduction 19
Mapping genes underlying quantitative traits 20
Dissecting QTLs using congenic strains 22
Testing candidate genes in QTL regions 24
Functional tests of candidate genes 26
From mouse to man 28
References 28

3 Transgenic and gene-targeted mice in the study of hyperlipidemia 33
Yadong Huang
Introduction 33
Generation of transgenic mouse models 34
Generation of gene-targeted mouse models 36
Application of transgenic and gene-targeted mouse models in hyperlipidemia research 38
Acknowledgments 39
References 40

4 Bone marrow transplantation: the methodology and its application in atherosclerosis research 43
Menno P.J. de Winther and Marten H Hofker
Introduction 43
Methods 45

Discussion and application 48
Conclusions 50
References 51

5 Hyperlipidemia-induced atherosclerosis 53
Alan Daugherty and Debra L. Rateri
Introduction 53
Induction of hyperlipidemia in mice 54
Mouse strain 56
Environmental factors 57
Gender 57
Analysis of atherosclerotic lesions 57
Determination of lesion composition 62
Statistical analysis 63
Conclusions 64
Acknowledgments 64
References 64

6 Magnetic resonance imaging evaluation of atherosclerotic plaque 67
Martina A. McAteer, Jürgen E. Schneider and Robin P. Choudhury
Introduction 67
Imaging atherosclerosis with MRI 68
Mouse MRI 68
Materials and methods 69
Discussion 75
Application 76
Acknowledgments 76
References 76

7 Plaque rupture 79
Christopher L. Jackson
Introduction 79
Animals 79
Husbandry and welfare 81
Termination 81
Tissue processing 82
Morphological analysis 83
Morphometric analysis 84
Study design considerations 85
Summary 85
Acknowledgment 86
References 86

8 Perivascular cuff-, electronic and chemical injury-induced stenosis 89
Nuno M.M. Pires, Margreet R. de Vries, Abbey Schepers, Daniel Eefting, Jan-Willem H.P. Lardenoye and Paul H.A. Quax
Introduction 89
Materials and methods 92
Discussion 93

Application 94
References 100

9 Flow-induced vascular remodeling 103
Vyacheslav A. Korshunov and Bradford C. Berk
Introduction 103
Materials and methods 104
Discussion 107
Applications 108
References 110
Movie legends 111

10 Vein graft atherosclerosis 113
Yanhua Hu and Qingbo Xu
Introduction 113
Materials and methods 114
Discussion 119
Applications 120
Acknowledgments 122
References 122

11 Angiotensin II-induced aortic aneurysms 125
Yi-Xin Wang, Lisa A. Cassis and Alan Daugherty
Introduction 125
Methods 126
Discussion 133
Acknowledgments 133
References 134

12 Carotidojugular fistula 137
Yves Castier, Alain Tedgui and Stéphanie Lehoux
Introduction 137
Creation of the AVF 138
Hemodynamic and structural data 142
References 144

13 Applications to the study of stroke 147
Jacques Seylaz and Elisabeth Pinard
Introduction 147
Experimental preparation of mice 148
Methods 153
Applications 155
References 157

14 Identifying congenital heart defects in embryos using high-resolution magnetic resonance imaging 159
Jürgen E Schneider and Shoumo Bhattacharya
Introduction 159
Identifying mouse cardiac malformations 160
Magnetic resonance imaging 160

Embryo MRI technique and analysis 161
Discussion 166
Applications 166
Pros and cons of *ex vivo* MRI 169
Acknowledgments 169
References 170

15 Allograft arteriopathy: heterotopic heart transplantation and aortic interposition grafts 173
Koichi Shimizu and Richard N. Mitchell
Introduction 173
Murine models for AA 175
Murine heterotopic cardiac transplantation 177
Murine aortic interposition grafts 183
Translation to clinical investigation 187
References 189

16 Heart preconditioning analysis 193
Guang-Wu Wang, David A Liem, Steven Le and Peipei Ping
Introduction 193
Methods 194
Methodological considerations 198
References 200

17 Myocardial ischemia–reperfusion 203
Bernhard Metzler, Elisabetta Conci and Otmar Pachinger
Myocardial ischemia–reperfusion 203
Ischemia–reperfusion models 206
Measurement of infarction size 210
Electrocardiogram and *in vivo* left ventricular pressure–volume measurements 214
Different mouse types 215
Conclusion 217
References 217

18 Cardiac hypertrophy 221
David J. Grieve, Alison C. Cave and Ajay M. Shah
Introduction 221
Materials and methods 222
Summary 231
Acknowledgments 231
References 231

19 The retrogradely perfused isolated heart model 235
Mihaela M. Mocanu and Derek M. Yellon
Introduction 235
Langendorff system 235
Preparation of hearts for perfusion 237
Experimental protocol 241

Measurement of infarct size 242
Infarct size computation 243
General comments 244
Acknowledgments 244
References 244

20 Measurement of pulse wave velocity 245
Yi-Xin Wang
Introduction 245
Materials and methods 246
Discussion 249
Application 251
References 252

21 Gene transfer to dyslipidemic mice 255
Kazuhiro Oka, Andrew H. Baker and Lawrence Chan
Introduction 255
Mouse models of dyslipidemia 256
ApoB transgenic mice 263
Vectors for liver-directed gene transfer 263
Route or vector delivery 267
Conclusion 268
Acknowledgments 269
References 269

22 Hypertension 273
Daiana Weiss and W. Robert Taylor
Introduction 273
Pharmacological models of hypertension 275
Renal models of hypertension 278
Genetic models of hypertension 279
Measurement of blood pressure in mice 282
Summary 282
References 283

23 Ischemia-induced neovascularisation 287
Ken-ichiro Sasaki, Christopher Heeschen, Alexandra Aicher and Stefanie Dimmeler
Introduction 287
Materials and methods 288
Discussion 296
Application 296
References 297

24 Angiogenesis in biomatrices and artificial materials 299
Pieter Koolwijk and Victor W.M. van Hinsburgh
Introduction 299
Materials and methods 300
Discussion 305

Application 307
Acknowledgments 308
References 308

25 Venous thrombosis 311
Alberto Smith, James Gossage, Matthew Waltham, Bijan Modarai and Julie Humphries
Background 311
Models of thrombosis 313
The St Thomas' model 314
References 319

26 Virus-induced vasculitis 321
Philippe Krebs and Burkhard Ludewig
Introduction 321
Materials and methods 322
Discussion 329
Application 329
References 330

27 Surgically induced chronic heart failure 333
Craig A. Lygate and Stefan Neubauer
Introduction 333
Materials and methods 336
Discussion 340
Applications 346
Conclusions 346
References 347

28 Cardiac electrophysiology 349
Sander Verheule, Toshiaki Sato and Jeffrey E. Olgin
Introduction 349
Anesthesia for adult mice 350
ECG recording and analysis 351
Transesophageal stimulation 352
Open chest epicardial measurements 354
Studies on Langendorff perfused hearts 357
Conclusion 360
References 361

29 Ligation- and wire injury-induced stenosis 363
Volkhard Lindner
Introduction 363
Materials and methods 364
Discussion 367
Acknowledgments 370
References 370

Index 373

Preface

Cardiovascular disease, the principal cause of heart attack, stroke, and gangrene of the extremities, remains a major contributor to morbidity and mortality in the Western World. Many factors, such as genetic polymorphisms, hypercholesterolemia, modified lipoproteins, hypertension, diabetes mellitus, autoimmune responses, infections and smoking have been implicated in the development of cardiovascular diseases. The etiology and pathogenesis of many cardiovascular diseases have not been fully elucidated. Although clinical investigation of these diseases is an important approach for understanding their etiology and therapy, animal models are essential tools for understanding the mechanisms of the pathogenesis as well as of interventions.

Cardiovascular research with animal models, as known today, is nearly 100 years old. The use of animal models in the study of cardiovascular diseases is essential to answer many questions. For instance, evaluation of a risk factor as a single independent variable, with almost complete exclusion of other factors, can best be performed in animals free of intercurrent diseases or abnormalities and with well known genetic characteristics. Furthermore, experiments using animals are the only way to develop and test new diagnostic, preventive, and therapeutic procedures for both ethical and practical reasons. The investigator can choose the time and method, as well as obtain tissue and serum samples and other material needed for measurements under optimal conditions and selective circumstances that are difficult, if not impossible, in studies with human subjects.

Attracted by the availability of well-defined genetic systems of transgenic and knockout mice, a number of investigators have begun to use the mouse as an experimental system for arteriosclerosis research. Hundreds of inbred lines have been established, the genetic map is relatively well defined, and both congenic strains and recombinant strains are available to facilitate genetic experimentation. In just a few years, murine lipoproteins have been characterised, genetic variants of apolipoproteins identified, and genetic variation in susceptibility to atherosclerosis among inbred mouse strains demonstrated. Because inbred strains have low variability, fewer are needed for each experiment, which is also of economic benefit. The mouse is becoming a widely used model for studying all aspects of cardiovascular diseases.

Although the mouse model is widely used by many laboratories, some problems often appear due to insufficient knowledge of the specific animal models, especially technical issues. Many mouse models involve techniques of microsurgery, which cannot be performed without training following specific guidelines. Investigators who are not experienced in using mouse models need to consider several issues before starting their experiments. They need some essential information about experimental

procedures, specific instruments and technical know-how. The present handbook provides a brief background on each individual disease, describes detailed methods and materials used for establishing the mouse model, discusses the problems that may appear in the experiments, and gives some examples for applications of the model. Importantly, the movies on the accompanying CD allow researchers to learn the techniques by directly watching the whole operation. This book covers most, if not all, mouse models of cardiovascular diseases authored by experts in the research field. I believe that this book will be useful for all researchers working with mouse models in cardiovascular research.

Qingbo Xu

List of Contributors

Alexandra Aicher
University of Frankfurt
Frankfurt, Germany

Andrew H. Baker
Cardiovascular Research Centre
Division of Cardiovascular and
Medical Sciences
University of Glasgow
Glasgow, UK

Bradford C. Berk
University of Rochester
Center for Cardiovascular Research
Rochester, NY, USA

Shoumo Bhattacharya
Department of Cardiovascular Medicine
Welcome Trust Centre for Human Genetics
University of Oxford
Oxford, UK

Lisa A. Cassis
Graduate Center for Nutritional Sciences
University of Kentucky
Lexington, KY, USA

Yves Castier
Centre de Recherche Cardiovasculaire
Inserm Lariboisière
Paris, France

Alison C. Cave
Cardiovascular Division
King's College London
London, UK

Lawrence Chan
Departments of Molecular and
Cellular Biology and Medicine
Baylor College of Medicine
Houston, TX, USA

Robin P. Choudhury
Department of Cardiovascular Medicine,
John Radcliffe Hospital
University of Oxford
Oxford, UK

Elisabetta Conci
Department of Cardiology
University Hospital of Internal Medicine
Innsbruck, Austria

Alan Daugherty
Internal Medicine & Physiology, Division
of Cardiovascular Medicine
University of Kentucky
Lexington, KY, USA

Hermann Dietrich
University of Innsbruck Medical School
Innsbruck, Austria

Stephanie Dimmeler
Molecular Cardiology
University of Frankfurt
Frankfurt, Germany

Daniel Eefting
TNO-Quality of Life, Gaubius Laboratory
Leiden, The Netherlands

James Gossage
Academic Dept of Surgery
Cardiovascular Division
King's College London School of Medicine
St Thomas' Hospital, London, UK

David J. Grieve
Cadiovascular Division
King's College London
London, UK

Christopher Heeschen
University of Frankfurt
Frankfurt, Germany

Victor W.M. van Hinsburgh
TNO Quality of Life
Gaubius Laboratory
Leiden, The Netherlands

Marten H. Hofker
Department of Molecular Genetics
Cardiovascular Research Insititute Maastricht
Maastricht, The Netherlands

Yanhua Hu
Department of Cardiac and Vascular Sciences
St George's University of London
London, UK

Yadong Huang
Gladstone Institute of Neurological Disease
University of California
San Francisco, CA, USA

Julia Humphries
Academic Dept of Surgery
Cardiovascular Division
King's College London School of Medicine
St Thomas' Hospital, London, UK

Christopher Jackson
Bristol Heart Insititute
Bristol Royal Infirmary
Bristol, UK

Pieter Koolwijk
TNO Quality of Life
Gaubius Laboratory
Leiden, The Netherlands

Vyacheslav A. Korshunov
Cardiovascular Research Institute and
Department of Medicine
University of Rochester
Rochester, NY, USA

Philippe Krebs
Research Department, Kantonal Hospital
St Gallen
St Gallen, Switzerland

Jan-Willem H.P. Lardenoye
Leiden University Medical Center
Leiden, The Netherlands

Steven Le
Departments of Physiology and
Medicine/Cardiology
David Geffen School of Medicine at UCLA
Los Angeles, CA, USA

Stephanie Lehoux
Centre de Recherche Cardiovasculaire
Inserm Lariboisière
Paris, France

David A Liem
Departments of Physiology and
Medicine/Cardiology
David Geffen School of Medicine at UCLA
Los Angeles, CA, USA

Volkhard Lindner
Center for Molecular Medicine
Maine Medical Center Research Institute
Scarborough, USA

Burkhard Ludewig
Research Department, Kanton Hospital
St Gallen
St Gallen, Switzerland

Aldons Lusis
Department of Medicine, MIMG
and Human Genetics
Center for Health Sciences, UCLA
Los Angeles, CA, USA

Craig A. Lygate
Department of Cardiovascular Medicine,
John Radcliffe Hospital
University of Oxford
Oxford, UK

Martina A. McAteer
Department of Cardiovascular Medicine,
John Radcliffe Hospital
Oxford, UK

Bernhard Metzler
Department of Cardiology
University Hospital of Internal Medicine
Innsbruck, Austria

Richard N. Mitchell
Harvard Medical School
Brigham and Women's Hospital
Boston, MA, USA

Mihaela M Mocanu
The Hatter Cardiovascular Institute
Department of Medicine
University College London, UK

Bijan Moderai
Academic Dept of Surgery
Cardiovascular Division
King's College London School of Medicine
St Thomas' Hospital, London, UK

Stefan Neubauer
Department of Cardiovascular Medicine,
John Radcliffe Hospital
University of Oxford
Oxford, UK

Kazuhiro Oka
Department of Molecular and
Cellular Biology
Baylor College of Medicine
Houston, TX, USA

Jeffrey Olgin
Cardiac Electrophysiology
University of California
San Francisco, CA, USA

Otmar Pachinger
Department of Cardiology
University Hospital of Internal Medicine
Innsbruck, Austria

Elisabeth Pinard
Centre de Recherche Cardiovasculaire
Inserm Lariboisière
Paris, France

Peipei Ping
Departments of Physiology and
Medicine/Cardiology
David Geffen School of Medicine at UCLA
Los Angeles, CA, USA

Nuno M.M. Pires
TNO-Quality of Life, Gaubius Laboratory
Leiden, The Netherlands

Paul H.A. Quax
TNO-Quality of Life, Gaubius Laboratory
Leiden, The Netherlands

Debra L. Rateri
Cardiovascular Research Center
University of Kentucky
Lexington, KY, USA

Ken-ichiro Sasaki
University of Frankfurt
Frankfurt, Germany

Toshiako Sato
Cardio-pulmonary Division
Keio University School of Medicine
Tokyo, Japan

Abbey Schepers
TNO-Quality of Life,
Gaubius Laboratory
Leiden, The Netherlands

Jurgen E. Schneider
Department of Cardiovascular Medicine,
John Radcliffe Hospital
Oxford, UK

Jacques Seylaz
INSERM U 541
UFR-Lariboisière, St. Louis
Paris, France

Ajay M. Shah
Cardiovascular Division
King's College
London, UK

Weibin Shi
University of Virginia
Charlottesville, VA, USA

Koichi Shimizu
Harvard Medical School
Brigham and Women's Hospital
Boston, MA, USA

Alberto Smith
Academic Dept of Surgery
Cardiovascular Division
King's College London School of Medicine
St Thomas' Hospital, London, UK

W. Robert Taylor
Department of Medicine/Division of Cardiology
Emory University
Atlanta, GA, USA

Alain Tedgui
Centre de Recherche Cardiovasculaire
Inserm Lariboisière
Paris, France

Sander Verheule
Department of Physiology, Faculty of Medicine
Maastricht University
Maastricht, The Netherlands

Margreet R. de Vries
TNO-Quality of Life, Gaubius Laboratory
Leiden, The Netherlands

Matthew Waltham
Academic Dept of Surgery
Cardiovascular Division
King's College London School of Medicine
St Thomas' Hospital, London, UK

Guang-Wu Wang
Departments of Physiology and Medicine/Cardiology
David Geffen School of Medicine at UCLA
Los Angeles, CA, USA

Yi-Xin Wang
Department of Pharmacology
Berlex Biosciences
Richmond, CA, USA

Daiana Weiss
Cardiology Division of the Department of Medicine
Emory University School of Medicine
Atlanta, GA, USA

Menno de Winther
Department of Molecular Genetics
Maastricht University
Maastricht, The Netherlands

Qingbo Xu
Department of Cardiac and Vascular Sciences
St George's University of London
London, UK

Derek Yellon
The Hatter Cardiovascular Institute,
Department of Medicine,
University College London, UK

1

Mice – general information

Hermann Dietrich

Central Laboratory Animal Facilities, Innsbruck Medical University, Peter-Mayr-Strasse 4a, A-6020 Innsbruck, Austria

Abstract

The gentle and careful use of laboratory animals requires specific knowledge on the general biology and the characteristic hallmarks of the used animals and the adequate consideration of legal requirements, ethical aspects, and scientific guidelines. In this chapter, important topics of laboratory animal science regarding the mouse as laboratory animal are addressed. Initially, a brief historical overview of the mouse is given and the step from the house mouse to the worldwide actually mostly used laboratory animal species. Moreover, housing conditions of mice, maintaining, and selected genetic principles are described. Commonly used handling techniques are explained in detail. For practical benefit, adequate methods for the sampling of blood and bone marrow cells and the application of substances, in particular, the intravenous injection technique, are described. Finally, useful techniques for anesthesia, analgesia, and euthanasia are emphasized.

Keywords

mice, laboratory animal, housing, breeding, genetics, blood, injection techniques, anesthesia, analgesia, euthanasia

Historical perspective of house mice as laboratory animals

The step of the wild mouse to the worldwide most-used laboratory animal was principally caused by the usefulness of this species for different interests. Historically, mice have been used in biomedical research since the 16th century, when Robert Hooke used mice in England to study the biological consequences of increasing air pressure. Morse[1] reported in 1981 that William Harvey used mice for his fundamental studies on reproduction and blood circulation. In the 19th century several fanciers in

A Handbook of Mouse Models of Cardiovascular Disease Edited by Qinbo Xu

Europe, the United States and Asia were breeding and exchanging in particular pet mice and rats (rarely other rodents like hamsters, guinea pigs, etc.) showing a variety of coat colour or behavioural mutations.

A booming use of mice have been reported since the 20th century in many areas of biomedical research. Mice had played and continue to play an instrumental role in several scientific fields[2], such as genetics, physiology, immunology, metabolism, pathology, oncology, cardiovascular diseases, etc. Several geneticists had created highly standardised mouse strains, whose genetic characteristics were precisely known. To retain those genetic standards, every breeding generation of mice had to be monitored by specific methods.

With a few exceptions, historical records concerning the genealogy of most laboratory inbred mouse strains are well documented and several reviews on this subject are available.[3–5] A chart[6] concerning the genealogy of these strains has been published recently and regularly updated data on the genetics, genomics, and biology of the laboratory mouse[7] are available. One of the worldwide top ranked research institutions and biggest non-profit breeding organisations of laboratory mice is The Jackson Laboratory, which was founded in 1929 in Bar Harbor (Maine, USA) by C.C. Little. The 'Jax-Lab' has played a pivotal role in the promotion of mice[8] as a very useful laboratory animal and still is a unique source of various mouse strains.[9] Several other institutions, like the Oak Ridge National Laboratory in Tennessee (USA) and the MRC Centre at Harwell in the UK have also played an important role in the development of the mouse as a laboratory model for research projects on genetics, oncology and immunology. Recently the European Union has decided to support the establishment of a network of genetic repositories (the so-called European Mouse Mutant Archive or EMMA[10]), with major breeding institutions in Italy (EMMA Headquarters is in Monterotondo, near Roma), in the UK (MRC-Mammalian Genetics Unit, Harwell), in France (CNRS-Centre de Distribution, de Typage et d'Archivage Animal, Orléans-la-Source), in Portugal (FCG-Instituto Gulbenkian de Ciência, Oeiras), and in Germany (GSF-Institute for Experimental Genetics, Munich). Finally, more recently, Japan has established a Bioresource Center at the RIKEN[11] in Tsukuba.

In addition, well established commercial breeding institutions (e.g. Charles River Laboratories, Harlan-Winkelmann, Taconic, etc.) provide laboratory animals worldwide. Those companies also offer special services to scientists, such as cryoconservation, re-derivations of contaminated and infected animals, respectively, health monitoring programs, isolator- and barrier-housing, immunisation protocols for antibody production, and the service of mouse hotels, if limitations of space, technical equipment, adequate hygienic conditions, and trained staff exist in the basic animal house.

Various genetic backgrounds of laboratory mice are available to achieve the envisaged goal of a scientific analysis,[12] e.g. outbred, inbred, hybrid, congenic, etc. In particular, the use of inbred strains of mice has offered investigations at the genomic level, because they can be achieved with a high level of refinement and can be correlated in a very reliable way to the phenotype of the living animal. It can be affirmed that the new types of mouse strains became of expanding interests for the

biomedical research programmes. Scientists predict that mice will be more useful for scientific research that it has been over the last centuries, especially due to the mouse genome project[13] with its contributions worldwide.

In addition, numerous transgenic mouse models were developed to study human diseases, and it is nearly impossible to depict all of them. Animal models are used for numerous diseases of man, e.g. genetic diseases, infectious diseases (parasites, fungi, bacteria, viruses, prion diseases), apoptosis research, oncology, aging, Alzheimer's disease, immunology and xenografting, reproduction research and endocrine disorders, and cardiovascular diseases. Using hereditary, experimentally induced, and transgenic mouse models, specific (patho-)mechanisms and characteristics of diseases can be better understood and reveal a more detailed and mostly superior insight into complex structures and functions, and even allows to define new therapeutic strategies and drugs capable of protecting humans against diseases. Especially transgenic mice are an essential tool to study human diseases, and this methodology is expected to be even more extensively used in the coming decades.

For the understanding of complex correlations in the pathogenesis of cardiovascular diseases, in particular to elucidate pathomechanisms of atherosclerosis, the use of adequate mouse models increased during the past two decades.[14–21] However, some authors had estimated the small size of rodents[22] as impedimentary to be used in cardiovascular research.

Maintaining and breeding of mice

Housing conditions of mice includes several parameters, which can influence growth and development as well as well-being and social behaviour of mice. A well-organised colony management and exactly followed animal care regulations[23] are essential prerequisites for animal experiments of high quality and reproducibility. In general, national and international laws and guidelines for the care and use of laboratory animals exist in line with animal welfare regulations. For details, see relevant textbooks,[24–25] national laws and international conventions. Several recommendations on proper housing conditions of mice[24,26–28] have been published. These guidelines refer to requirements on ventilation, temperature, humidity, light, noise levels, health status, feeding, water supply, animal enclosures, handling and experimentation procedures, including anesthesia, analgesia and euthanasia.

The environmental requirements of mice are summarized in Table 1.1. The standard procedures have to be strictly performed by a specifically educated and well-trained staff.[29] Such standard procedures are (i) daily monitoring of animals for adequate environmental conditions and general health, (ii) food and water control, (iii) regular changes of cages and bedding, (iv) cleaning and sterilisation programs of cages, racks, cage covers, filter hoods, water bottles, and other equipment, and (v) sanitation programmes.

Genetic monitoring of mice is important to analyse mutations and differential fixations of alleles in inbred strains. Phenotypic differences detected among substrains have been shown to be caused by genetic factors. The techniques for

Table 1.1 Environmental requirements of mice

Temperature	20–24°C
Relative humidity	$50 \pm 10\%$
Ventilation (air exchange per h)	8–20 (in IVC cages 30–80)
Photoperiod (light-dark-rhythm)	12/12 or 14/10 hrs
Light intensity	60–400 lx
Noise	$\approx$50 to $\leq$85 dB
Water intake	5–8 ml per day
Food intake	4–8 g per day

See also Fox et al.,[55] GV-SOLAS[26]
From: Hedrich HJ, Mossmann H, Nicklas W. Housing and Maintenance. In: Hedrich HJ, Bullock G, eds. The Handbook of Experimental Animals – The Laboratory Mouse, Amsterdam: Elsevier, 2004:395–408. With permission of Elsevier publishers.

genotyping have to be adjusted to the specific needs of an institution or a group, and may depend on laboratory equipment, maintenance conditions, and the scientific purpose of such analyses. The determination of a genetic profile allows to distinguish among different strains maintained in one animal unit. In general, this genetic profile is composed of monogenetic polymorphic markers which may be further differentiated by biochemical, immunological, morphological, cytogenetic, and DNA markers. Those classic markers have been almost fully replaced in routine applications by the microsatellite marker technique. A huge number of primer pairs is available and can be purchased from companies worldwide.

Laboratory animals have to be housed under specific environmental conditions, which prevent animals from infections by microbial agents, and established the status of 'specific pathogen-free' (SPF) animals. Locks and showers were commonly used for personnel, autoclaving for food, water, materials, and equipment, and mice were maintained in technically adapted (positive pressure, filtered air, etc.) and regularly disinfected animal rooms. During the last decade, filter cabinets, microisolator cages and individually ventilated cage (IVC)-systems have been increasingly used in laboratory animal facilities. Those new cage types offer the advantage of separating small populations from each other and are also frequently used for housing immunocompromised or infected mice. The transmission of infectious agents can be efficiently prevented by such cage systems, which must be considered as self-contained microbiological entities. In IVC systems, every single cage has its individual route for air supply and air exhaust. The rate of ventilation is much more higher in IVCs than in conventional open cages and allows some extension of the cage-changing interval. The major effect of filter cabinets, microisolator cages, and IVCs is to erect an effective hygienic barrier between the animals and their environment, which can provide a better microbiological status of animals used. However, a well-trained staff[29] is needed to run those cage systems effectively. Because of the higher expenditure of time for concomitant work, e.g. using clean benches with laminar flow conditions, manipulation of animal cages under sterile environment, marking of animals, and care and management of animals in breeding procedures, the number of mice per animal technician is

definitely reduced to about 50–70% compared to the hitherto existing open housing systems.

Mouse genetics

The management of breeding colonies of mice requires specific knowledge on the goals of inbred and outbred populations. The objectives for 'outbred' animals are to ensure that the population remains constant in all characteristics for as many generations as possible to maintain the highest level of heterozygosity and to preserve the population's original allelic forms and frequencies as stable as possible over generations. In contrast, for 'inbred' strains efforts are focused on the preservation of isogeneity and a maximum inbreeding coefficient.[4] To achieve the goal of homogenous populations, the main three causes of divergence have to be avoided: genetic contamination, mutations, and residual heterozygosity. Several factors can affect the genetic characteristics of inbred and outbred populations,[30] e.g. the population size, the type of mating scheme, spontaneous mutations, and (positive and negative) selection procedures.

Outbred stocks are characterized by maximum genetic variability (polymorphism) in the population, avoidance of the introduction of new allelic forms, and minimisation of increasing inbreeding from generation to generation by using breeding partners, which are preferably not related to each another. Usually, outbred populations have large numbers of permanent breeding pairs (sometimes more than 200 pairs), no selection criteria (i.e. loss of allelic forms), high interval between generations (to slow down genetic drift), and closed mating populations (no introduction of new breeders).

A different mating scheme is used for inbred strains. Inbred strains are defined as those derived from 20 or more consecutive sister $\times$ brother matings. The main goal of inbreeding is a maximum level of homozygosity at virtually all of the loci, which entails a genetic and phenotypic uniformity. This uniformity reduces the number of mice, which have to be used for experimental approaches, because experimental variability in phenotype is limited to variations in epigenetic, extragenetic, and/or varying uncontrolled environmental factors. However, inbred animals are usually characterised by a lower degree of robustness for infectious agents and environmental factors, a decreased fecundity (fertility rate, litter size, number of weaned pups, etc.), and relatively higher costs than outbred animals. In addition, specific phenotypes can be expressed or even inability to live because of homozygosity for a certain recessive trait[31] and/or lethal gene(s).

The crossing of two inbred strains generates hybrid mice, which are genetically and phenotypically uniform like inbred mice. F_1 hybrids display an overall hybrid vigor, i.e. increased resistance to diseases, better survival under stress situations, greater natural longevity, higher numbers of litter, and are therefore useful as recipients of tissue transplants from mice of either parental strain. Crossings of $F_1 \times F_1$ result in the F_2 progeny, in which alleles of the two parental strains segregate following Mendelian principles of inheritance.

Special breed of inbred lines are recombinant inbred (RI) and congenic strains. RI strains are derived by systematic inbreeding from a cross of two different inbred strains, recombinant congenic (RC) strains are established by backcrossing of F_1 hybrids to mice of one of the parental lines[32,33] (for details see also Chapter 2). Congenic strains are inbred strains carrying a mutant gene or 'foreign' polymorphic allele from a different strain or stock and are expected to be identical at virtually all loci except for the transferred locus ('locus of interest') and a linked segment of the chromosome. A strain is considered congenic after 10 generations of backcrossing to a recipient inbred strain (N_{10}). Using marker-assisted technologies, congenic strains can be established in <10 generations, creating so-called 'speed congenics', from which DNA microsatellite markers are extensively mapped.[7,34]

With regards to cardiovascular research, mice of the C57BL/6J strain are most susceptible for hyperlipidemia-induced atherosclerosis. However, it is known that inbred mice of another inbred strains, for example C3H/HeJ, BALB/cJ and A/J are not sensitive to a cholesterol diet and atherosclerotic lesions cannot be induced by feeding of cholesterol-enriched diets. Concerning the injury models, data indicate that neointimal lesions vary between different strains, but differ from diet-induced atherosclerosis, suggesting that injury-induced neointimal hyperplasia and diet-induced atherosclerosis are controlled by distinct sets of genes; the former appeared to be determined by recessive genes at minimally two loci.[35] Neointimal lesions in vein isografts between C57BL/6J and BALB/c strains revealed no significant difference in either inflammatory responses or the thickness of lesions, suggesting there is less effect of genetics on vein graft models. For transplant arteriosclerosis, different major histocompatibility complex class II antigens between donors and recipients are needed, e.g. between C57BL/6J and BALB/c mice. Thus, careful selection of the model with different genetic background for such experiments is essential for the successful performance of the study.[21]

During the last two decades genetically engineered strains of mice were created by 'transgenesis' and 'targeted mutagenesis'. Transgenic mice have genetic material randomly added to their genome, whereas knockout and knockin mice are produced by the gene targeting technique using mouse embryonic stem (ES) cells. Gene targeting replaces the gene sequence resident in the mouse genome by means of homologous recombination of a related sequence that has been modified in the laboratory to contain a mutation.

Thousands of transgenic mouse strains have been used to study gene function and expression and have resulted[7] in many important disease models. The phenotype of a knockout mouse provides important clues about the gene's normal role. One major application of this technology is the modelling of human diseases caused by loss of gene function. Such knockout mouse models are useful tools to investigate the biochemical and physiological aspects of diseases. Interesting examples of knockout mice for transplant arteriosclerosis research are animals, which lack gene function for interferon-gamma,[36] nitric oxide synthase (NOS),[37] P-selectin,[38] intercellular adhesion molecule-1 (ICAM-1),[17,38] and Apo E.[39]

Blood and bone marrow collection methods

For different analyses in hematology, immunology and similar disciplines, the collection of blood samples[40] is necessary. In this chapter, the scientifically accepted blood collection methods from mice are described. Blood collection techniques should be performed with a minimum of tissue trauma and thus a minimum of pain and suffer to the animals. Methods that enable blood sampling directly from a vessel or plexus are preferred to those that may cause more tissue trauma. The following sites are commonly used for blood collection in mice: orbital sinus, tail vein, heart, aorta, and vena cava.[41] Depending on the site that is used for blood collection, either a terminal procedure (heart, aorta, vena cava, jugular vein) or a survival procedure (orbital sinus, tail vein) is applied. Terminal blood collection procedures must be performed in anesthetised mice only.[12]

Proper handling techniques are necessary for blood sampling from orbital sinus or from the tail vein. After removal from the cage by grasping the animal's tail and, if required, identification of mice, the restraining can be performed either by an immobilisation device or by fixing a skin fold at the rear of the neck with thumb and forefinger. For the collection of blood samples from the orbital sinus an adequate sedation or a brief anesthesia is recommended. For routine hematology, the collected blood should be immediately placed in a tube to let the blood clot for serum extraction. In the case that anticoagulation should be achieved to separate plasma from cell compartments, EDTA (ethylenediamine tetra-acetic acid), heparin, sodium citrate (3.8 per cent) and others are valuable anticoagulants.[41]

For qualitative and quantitative analyses, bone marrow cells are used for smears and counting to evaluate for relative proportions, maturity of precursor cells, storage pools, and other changes. Among the feasible methods used to prepare bone marrow cells are cytospin preparations, paint brush smears and squash preparations.[41] Most commonly, the femur (or other appropriate long bone) is cracked and bone marrow material is either rinsed from the marrow cavity using sterile medium and a 22-gauge $(0.7 \times 30\ \text{mm})$ or 23-gauge needle $(0.6 \times 25\ \text{mm})$, or a slightly moistened paint-brush is introduced into the marrow cavity to pick up a small amount of bone marrow, or bone marrow cells are harvested by centrifugation of the cracked bone in a 0.6 ml centrifugation tube and adequate medium.

Anesthesia and Analgesia

Anesthesia and analgesia protocols require specific knowledge of the mouse physiology and is a real challenge to the mouse anesthetist. The three major 'pillars' of an appropriate anesthesia are adequate analgesia, sedation/hypnosis, and relaxation of skeletal muscles. Hence, an expertly performed anesthesia needs special knowledge and experience. The choice for the used anesthetic regimen is particularly affected by the aim of the scheduled study, the age, sex, and size of the animal species, and the

advantages and disadvantages of various anesthetic drugs. Anesthetics can be administered by injection or by inhalation (and via the route of tank water, if animals are aquatic residents). For major surgery and other long-term procedures a combination of injectable anesthetics with an inhalant anesthetic may be considered.[42]

Several problems can occur in association with the small body size of mice, e.g. the higher surface area relative to body mass, increased sensitivity to blood loss entailing cardiovascular failure, and the lack of intra-anesthetic monitoring. In addition, strain, sex-, and age-dependent variability in the effective dose of some injectable anesthetics may result in inadequate depth of anesthesia or even in a lethal overdose.[42]

For larger animals a fasting period of 12–24 hours is usually emphasized in the preanesthetic phase. In contrast, it is undesirable to withhold food and water before anesthetising mice.[43] For anticholinergic premedication mice should be treated with atropine (0.04 mg/kg, subcutaneously)[44] about 30 minutes prior the induction of anesthesia.

However, anesthetics are usually injected into mice because of easy administration by the subcutaneous (Figure 1.1), intraperitoneal (Figure 1.2), or intramuscular (Figure 1.3) routes. Drug absorption is slow via those routes, and it needs a couple of minutes until the anesthetic drug(s) provide(s) an adequate anesthesia. Rapid

Figure 1.1 Subcutaneous injection. Several locations can be used for subcutaneous application of substances. One example is shown here: After an adequately restraint, the mouse is injected into the skin fold between the knee joint and abdomen. Recommended injection volume is 0.1 to 0.5 ml. *Note*: do not damage one of the dugs (mamma), which can be clearly recognized in the picture. In male mice and sometimes in females the dugs cannot be clearly seen. Another location for subcutaneous injection is the neck region (near or between the fingers of the experimenter, who restraint the mouse) and in the hip region of the mouse. In principle, each location can be used, which is capable for administering substances under the skin. For a color version of this figure, please see the images supplied on the accompanying CD

Figure 1.2 Intraperitoneal injection. Administration of substances into the peritoneal cavity of mice is a frequently used technique. The mouse is properly restraint by grasping the animal's skin in the neck region, and turned the abdominal site upwards. The right injection location can be found as follows: an imaginary line runs between the *processus xyphoideus* (end of the sternum) to the cranial edge of the pubic bone (*os pubis*). This distance is cut in half, and this particular site is used for the i.p. injection. To avoid injuries of the intestine, liver, and of other abdominal organs by the needle, it is important to keep the head of the mouse deeper that the abdominal/pelvic region. The needle is carefully placed at the above described site and inserted in an angle of about 50–60 degree to keep the way through the various skin layers as short as possible (a minimum number of sensitive nerves should be irritated by the needlepoint). The recommended injection volume is 0.1 to 0.5 ml. For a color version of this figure, please see the images supplied on the accompanying CD

absorption, which entails a nearly simultaneous anesthetic effect can be achieved by intravenous application (Figure 1.4).

For the performance of intravenous injections mice are first placed under a heating lamp for about 10 minutes to warm the animals' body. Overheating of mice must be avoided by permanent careful observation. Unless the mice show increasing activity for self-grooming, expressed by distinct wiping movements of the forepaws over face and snout, mice are placed in a restriction device made from plastic or glass. The free movement of the body is restricted, the experimenter has free access to the tail, where the veins can be well seen due to their heat-induced dilatation. On the dorsal site as well as at the left and right lateral site the three tail veins can be observed, if the warming procedure of the mouse has been properly performed (Figure 1.5). At the ventral site of the tail the artery runs along the tail to the tip and should not be used for intravenous applications. One of the three tail veins can be punctured using a 30-gauge needle $(0.3 \times 13\,\text{mm})$. It is emphasized to insert the needle into the vein lumen in an angle of $5–10^{\circ}$, meaning nearly parallel to the surface of the tail skin. The

Figure 1.3 Intramuscular injection. Because of the small muscle mass of mice, the intramuscular application of substances is not a very common technique used in mice. In principle, parts of the *M. glutaeus* are used to be injected. The mouse has to be restraint as described. The appropriate muscles are found between the ischium and the popliteal region. The needle is inserted into the *M. glutaeus* and the injection is performed. The recommended injection volumes should not exceed 0.05 ml for an adult mouse.
Note: take care not to injure the ischiatic and femoralis nerve or the femoralis blood vessels with the needletip. For a color version of this figure, please see the images supplied on the accompanying CD

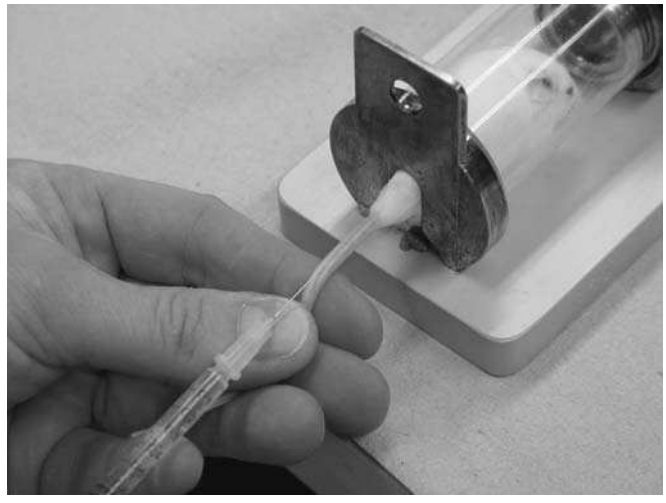

Figure 1.4 Intravenous injection. Before a intravenous injection mice are warmed by a heating lamp for about 10 minutes to warm the animal's body. Tail veins became distinctly visible and can be punctured using a 30-gauge needle. The needle must be inserted into the vein lumen in an angle of 5–10°, nearly parallel to the surface of the tail skin. Because of the application the blood in the vein lumen is displaced and thus indicate the proper placement of the needle in the vessel lumen. Recommended volume for intravenous application into adult mice is 0.05 to 0.15 ml. The intravenous injection technique must be properly educated and trained to ensure successful intravenous injections in mice. For a color version of this figure, please see the images supplied on the accompanying CD

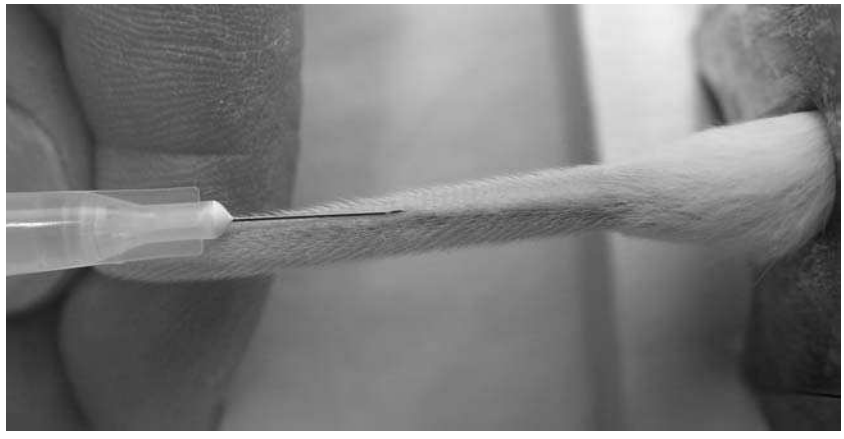

Figure 1.5 'Mouse tail vein'. This picture clearly shows the course of the dorsal tail vein, which can be used for the intravenous injection technique. For a color version of this figure, please see the images supplied on the accompanying CD

application of drugs must be performed slowly and displacement of blood by the injected fluid assure that the injection is properly placed in the vessel lumen. Adequate education and training is required to conduct intravenous injections in mice successfully.

Recommended injection volumes[44–45] range from 0.1 to 0.5 ml for intraperitoneal and subcutaneous applications, from 0.05 to 0.15 ml for intravenous application and should not exceed 0.05 ml for intramuscular injection to an adult mouse. Young mice and animals with a lower body weight should receive reduced injection volumes accordingly.

A recommendable anesthesia can be achieved by intraperitoneal injection of medetomidine (0.5 mg/kg), midazolam (5 mg/kg) and fentanyl (0.05 mg/kg), because those drugs can be neutralized by specific antagonists (atipamezole (2.5 mg/kg), flumazenil 0.5 mg/kg, and naloxone (1.2 mg/kg), subcutaneous application). Optimised and safe intraperitoneal injection anesthesia in mice was analysed by Arras[46] by using combinations of dissociative anesthetics (ketamine, tiletamine), α_2-agonists (xylazine, medetomidine), and/or sedatives (acepromazine, azaperone, zolazepam).

Alternatively, volatile anesthetic drugs, such as enflurane, isoflurane, sevoflurane, etc. are widely used for inhalation anesthesia for mice because of the better controllability on the anesthetic depth. Those volatile agents are applied by a specific device, which vaporises the liquid substances by higher pressure. For the initiation of anesthesia the volatile agent is conducted into a chamber, in which the animal had been placed. Anesthesia is continued by inhalation of the anesthetic vapor via fitting face masks. As an easily manageable system syringes can be used from which the pistols had been removed. For mice, aged >6 weeks, 5 ml-syringes can serve as face masks, for older mice 10 ml-syringes are commonly used. The major advantages of inhalation anesthesia are rapid onset of analgesia, proper sedation, adequate relaxation, and a precise adjustment of the anesthetic depth and period. In larger animal species a tube is inserted into the trachea[45] allowing artificial respiration in case of apnea. Table 1.2 summarizes the use of anesthetics and tranquilizers in mice.

Table 1.2 Anesthetics and tranquilizers used in mice

Drug	Dosage (mg/kg)	Comments	References
α-Chloralose	114 i.p.	5% solution, only in combination with analgetics and/or other anesthetic agents	Windholz[56]
Alphaxolone/alphadolone (Saffan, Althesin)	10–20 i.v.	Unpredictable anesthetic effect following i.p., volume too large for i.m.	Green,[44] Flecknell[43]
Chloral hydrate	60–90 i.p. 370–400 i.p.	Light surgical anesthesia Considerable strain differences	Green[44] Flecknell[43]
Fentanyl/fluanisone (Hypnorm)	0.4 ml/kg i.m.	Muscle rigidity, pronounced respiratory depression, 1:10 dilution	Flecknell[43]
Hypnorm/midazolam	10 ml/kg i.p.	2 parts *water for injection* + 1 part Hypnorm + 1 part midazolam (5 mg/ml)	Flecknell[43]
Fentany/droperidol (Innovar Vet)	0.5 i.m.	Irritant, tissue necrosis, self-trauma following i.m. application	Flecknell[43]
Ketamine	80–100 i.m. 100–200 i.m.	Sedation, muscle	Green[44] Flecknell[43]
Methohexital (Brevital, Brevimytal)	10 i.v. 44 i.p.	Short-term anesthesia	Flecknell[43] Dörr[57]
Medomitate/fentanyl	60/ 0,06 s.c.		Green,[44] Flecknell[43]
Pentobarbital (Nembutal, Vetanarcol)	45 i.p. 50 i.p. 60 i.p.	1:10 dilution, narrow safety margin, marked strain differences in response, severe respiratory depression	Flecknell[43] Erhardt[58] Zeller,[59] Koizumi[60]
Propofol (Rapinovet, Diprivan)	26 i.v. 30 i.v.	Short-term anesthesia, i.v. injection required	Flecknell[43] Koizumi[60]
Thiopental (Penthotal, Trapanal)	30 i.v.	Short-term anesthesia, i.v. injection required, dose dependent hypothermia and respiratory depression	Flecknell[43]
Tiletamine/zolazepam (Telazol)	40 i.p. 80–100 i.p.		Flecknell[43] Silverman[61]
Tribromethanol (Avertin)	125–300 i.p. 240 i.p.	1.2% solution, possible peritonitis, serositis	Flecknell[43] Zeller[59]

i.p., intraperitoneally; i.m., intramuscularly; i.v., intravenously; s.c., subcutaneously.
From: Otto K. Anesthesia, analgesia and euthanasia. In: Hedrich HJ and Bullock G, eds. The Handbook of Experimental Animals–The Laboratory Mouse. Amsterdam: Elsevier, 2004;555–569. With permission of Elsevier publishers.

Monitoring of anesthesia in mice is usually based on the assessment of clinical parameters, such as regular breathing, adequate heart frequency, loss of righting reflex, and analgesia. Unwanted incidents can occur because of hypothermia of animals during anesthesia. To prevent animals becoming hypothermic, various heating equipment can be used, e.g. heating blankets, hot-water bottles, electronic foot-warmers, etc. In addition, during anesthesia sterile saline or an eye ointment

Table 1.3 Analgesics used in mice

Drug	Dosage(mg/kg)	Route	Interval	References
Acetaminophen	300	i.p.		Jenkins[50]
Amitryptiline	5–10	i.p.	24 hourly	Abad[62]
Aspirin	20	s.c.		Flecknell[63]
	120	p.o.	Once	Dobromylskyi[64]
	120–300	p.o.		Jenkins[50]
Buprenorphine	0.01	s.c.		Liles[65]
	0.05	s.c.	8–12 hourly	Flecknell[43]
	0.05–0.10	s.c.	8–12 hourly	Dobromylskyi[64]
	2.0	s.c.		Flecknell[45]
	2.5	i.p.		Harvey[66]
Butorphanol	0.05–5	s.c.		Jenkins[50]
	1–2	i.m., s.c.	4 hourly	Dobromylskyi[64]
	1–5	s.c.	4 hourly	Flecknell[43]
	5.4	s.c.		Harvey[66]
Carprofen	5	s.c., p.o.	Daily	Dobromylskyi[64]
Codeine	20	s.c.	4 hourly	Flecknell,[45] Jenkins[50]
	60–90	p.o.		Flecknell,[45] Jenkins[50]
Diclofenac	8	p.o.	Daily	Dobromylskyi[64]
Fentanyl	0.0125–1.0	i.p.		Thurmon[52]
Flunixin	2.5	s.c.	12–24 hourly	Dobromylskyi[64]
Ibuprofen	7.5	p.o.	Daily	Jenkins[50]
	30	p.o.		Dobromylskyi[64]
Meperidine	20	s.c., i.m.	2–3 hourly	Jenkins[50]
	2.5	i.m., s.c.	2–4 hourly	Flecknell,[43] Dobromylskyi[64]
	10–20	s.c.	2–4 hourly	Flecknell[45,62]
Nalbuphine	1.0	s.c.		Liles[65]
	2–4	i.m.	4 hourly	Dobromylskyi[64]
	4–8	i.p., s.c.		Flecknell[43]
Paracetamol	300	p.o.	4 hourly	Flecknell[63]
Pentazocine	5–10	s.c., i.m.	3–4 hourly	Flecknell,[43] Dobromylskyi[64]
	10	s.c.	3–4 hourly	Flecknell,[62] Jenkins[50]
Pethidine (meperidine)	10–20	s.c., i.m.	2–3 hourly	Flecknell,[43] Dobromylskyi[64]
Phenacetin	200	p.o.	4 hourly	Flecknell[63]
Piroxicam	3	p.o.	daily (?)	Dobromylskyi[64]

i.p., intraperitoneally; i.m., intramuscularly; s.c., subcutaneously; p.o., orally.
From: Otto K. Anesthesia, analgesia and euthanasia. In: Hedrich HJ, Bullock G. The Handbook of Experimental Animals–The Laboratory Mouse. Amsterdam: Elsevier, 2004,566. With permission of Elsevier publishers.

should be applied onto the conjunctivae of the animal's eyes. This moisture prevents the conjunctiva and cornea from desiccation and encumbering lesions.

In concordance with the 3R-principles (reduction–refinement–replacement) of Russel and Burch,[47,48] peri- and postoperative analgesia is strongly emphasized after surgeries and treatments, by which suffering, pain and distress to the animals[49] can be expected. Subcutaneous injections of nonsteroidal antiinflammatory drugs (NSAIDs) and opioids are commonly used, such as carprofene (4 mg/kg), butorphanole 1–5 mg/kg (4 hourly), and buprenorphine (0.05–0.1 mg/kg (8–12 hourly).[47,50–52] An overview of drugs which can be used for adequate analgesia in mice is shown in Table 1.3.

Euthanasia

For euthanasia of animals the used methods must be painless, provide rapid unconsciousness and death, require minimum restraint, avoid excitement, should be appropriate for age, species, and health of the animals, must minimize fear and psychological stress in the animal, must be reliable, reproducible, irreversible, simple to administer and safe for the operator.[53] Death in rodents is indicated by cessation of respiration and heart beat, and absence of reflexes. In addition, death may be confirmed by additional techniques used, such as exsanguination, evisceration, decapitation (e.g. fetuses and newborn mice) or extraction of the heart.

Recommended methods for euthanasia of adult rodents include the use of barbiturates, carbon dioxide, cervical dislocation, decapitation and stunning.[54] Such methods must be taught well to experimenters and co-workers to perform adequate euthanasia of animals.

References

1. Morse HC, III. The laboratory mouse – a histological perspective. In: Foster HL, Small JD, Fox JG, eds. The Mouse in Biomedical Research. New York: Academic Press, 1981: 1–16.
2. Jacoby RO, Fox JG. Biology and diseases of mice. In: Foster HL, Small JD, Fox JG, eds. The Mouse in Biomedical Research, Vol. 1. San Diego, CA: Academic Press, 1981: 31–89.
3. Morse H.C., III. In: Morse HC, III, ed. Origins of inbred mice, Proceedings of a Workshop, Bethesda, MD, February 1978, New York: Academic Press, 1978: 3–21.
4. Festing MF. Inbred Strains in Biomedical Research. Festing MF, ed. London and Basingstoke: The MacMillan Press Ltd. 1979.
5. Rugh R. The Mouse – its reproduction and development. Oxford: Oxford University Press, 1990.
6. Beck JA, Lloyd S, Hafezparast M, Lennon-Pierce M, Eppig JT, Festing MFW, Fisher EMC. Genealogies of mouse inbred strains. *Nat Genet* 2000; **24**: 23–25.
7. Mouse Genome Informatics (MGI), The Jackson Laboratory, Bar Harbor, Maine, (2003) http://www.informatics.jax.org

8. Guénet JL, Bonhomme F. Origin of the laboratory mouse and related subspecies. In: Hedrich HJ, Bullock G, eds. The Handbook of Experimental Animals – The Laboratory Mouse. Amsterdam: Elsevier, 2004: 3–12.
9. Jackson Lab http://www.informatics.jax.org/
10. European Mouse Mutant Archive: http://www.emma.rm.cnr.it/
11. RIKEN Bioresource Center: http://www.brc.riken.jp/en/
12. Wolfensohn S, Lloyd M. Handling of laboratory species. In: Wolfensohn S, Lloyd M, eds. Handbook of Laboratory Animal Management and Welfare. Oxford: Oxford University Press, 1994: 134–135.
13. Waterston RH, Lindblad-Toh K, Birney JF, et al. Initial sequencing and comparative analysis of the mouse genome. *Nature* 2002; **420**: 520–562.
14. Zou Y, Dietrich H, Hu Y, Metzler B, Wick G, Xu, Q. Mouse model of venous bypass graft arteriosclerosis. *Am J Pathol* 1998; **153**(4): 1301–1310.
15. Zou Y, Hu Y, Mayr M, Dietrich H, Wick G, Xu Q. Reduced neointima hyperplasia of vein bypass grafts in intercellular adhesion molecule-1-deficient mice. *Circ Res* 2000; **86**: 434–440.
16. Hu Y, Zou Y, Dietrich H, Wick G, Xu Q. Inhibition of neointima hyperplasia of mouse vein grafts by locally applied suramin. *Circulation* 1999; **100**: 861–868.
17. Dietrich H, Hu Y, Zou, Y, Dirnhofer S, Kleindienst R, Wick G, Xu Q. Mouse model of transplant arteriosclerosis: role of intercellular adhesion molecule-1. *Arterioscler Thromb Vasc Biol* 2000; **20**: 343–352.
18. Dietrich H, Hu Y, Zou Y, et al. Rapid development of vein graft atheroma in ApoE-deficient mice. *Am J Pathol* 2000; **157**: 659–669.
19. Mayr U, Mayr M, Li C, Wernig F, Dietrich H, Hu Y, Xu Q. Loss of p53 accelerates neointimal lesions of vein bypass grafts in mice. *Circ Res* 2002; **90**: 197–204.
20. Henderson B, Tagwerker A, Mayrl C, et al. Progression of arteriovenous bypass restenosis in mice exposed to a 50 Hz magnetic field. *Cell Stress & Chaperones* 2003; **8**: 373–380.
21. Xu Q. Mouse models of arteriosclerosis: From arterial injuries to vascular grafts. *Am J Pathol* 2004; **165**: 1–10.
22. Nevelainen T. Animal models for cardiovascular research. In: Svendsen P, Hau J, eds. Handbook of Laboratory Animal Science, Vol. II, Animal Models. Boca Raton: CRC Press, 1994: 43–47.
23. Hedrich HJ, Mossmann H, Nicklas W. Animal husbandry and production. In: Hedrich HJ, Bullock G, eds. The Handbook of Experimental Animals – The Laboratory Mouse. Amsterdam: Elsevier, 2004: 395–408.
24. ILAR. Guide for the Care and Use of Laboratory Animals. Washington: National Academy Press, 1996.
25. Van Zutphen LFM, Baumans V, Beynen A. Principles of Laboratory Animal Science – A contribution to the humane use and care of animals and to the quality of experimental results. Amsterdam: Elsevier, 2001.
26. GV-SOLAS Publication Nr. 1 (1988). http://www.gv-solas.de/publ/pub.html
27. Jennings M, Batchelor GR, Brain PF, et al. Refining rodent husbandy: the mouse. *Lab Anim* 1998; **32**: 233–259.
28. Weiss J, Maess J, Nebendahl K. Haus- und Versuchstierpflege. In: Weiss J, Maess J, Nebendahl K, eds. Stuttgart: Enke, 2003.
29. FELASA recommendations on the education and training of persons working with laboratory animals: Categories A and C. *Lab Anim* 1995; **29**: 121–131.

30. Lyon M, Rastan S, Brown SDM. Genetic variants and strains of the laboratory mouse, 3rd edn., Vol. 2. Oxford: Oxford University Press, 1996.
31. Threadgill DW, Hunter KW, Williams RW. Genetic dissection of complex and quantitative traits: from fantasy to reality via a community effort. *Mamm Genome* 2002; **13**: 175–178.
32. Darvasi A, Soller M. Advanced intercross lines, an experimental population of fine genetic mapping. *Genetics* 1995; **141**: 1199–1207.
33. Linder CC, Davisson MT. Strains, stocks, and mutant mice. In: Hedrich HJ, Bullock G, eds. The Handbook of Experimental Animals – The Laboratory Mouse. Amsterdam: Elsevier, 2004: 25–46.
34. Wakeland E, Morel L, Achey K, Yui M, Longmate J. Speed congenics: a classical technique in the fast lane (relatively speaking). *Immunol Today* 1997; **18**(10): 472–477.
35. Kuhel DG, Zhu B, Witte DP, Hui DY. Distinction in genetic determinants for injury-induced neointimal hyperplasia and diet-induced atherosclerosis in inbred mice. *Arterioscler Thromb Vasc Biol* 2002; **22**: 955–960.
36. Wessely, R, Hengst L, Jaschke B, et al. A central role of interferon regulatory factor-1 for the limitation of neointimal hyperplasia. *Hum Mol Genet* 2003; **12**: 177–187.
37. Lee JK, Borhani M, Ennis TL, Upchurch Jr. GR, Thompson RW. Experimental abdominal aortic aneurisms in mice lacking expression of inducible nitric oxide synthase. *Arterioscler Thromb Vasc Biol* 2001; **21**: 1393–1401.
38. Manka D, Collins RG, Ley K, Beaudet AL, Sarembock IJ. Absence of P-selectin, but not intercellular adhesion molecule-1, attenuates neointimal growth after arterial injury in Apolipoprotein E-deficient mice. *Circulation* 2001; **103**: 1000–1005.
39. Xu Q, Zhang Z, Davison F, Hu Y. Circulating progenitor cells regenerate endothelium of vein graft atherosclerosis, which is diminished in ApoE-deficient mice. *Circ Res* 2003; **93**: e76–e86.
40. Schnell MA, Hardy C, Hawley M, Propert KJ, Wilson JM. Effect of blood collection technique in mice on clinical pathology parameters. *Hum Gene Ther* 2002; **13**: 155–162.
41. Everds N. Hematology of the mouse. In: Hedrich HJ, Bullock G, eds. The Handbook of Experimental Animals – The Laboratory Mouse. Amsterdam: Elsevier 2004: 271–286.
42. Otto K. Anesthesia, analgesia and euthanasia. In: Hedrich HJ, Bullock G, eds. The Handbook of Experimental Animals – The Laboratory Mouse. Amsterdam: Elsevier 2004: 555–569.
43. Flecknell PA. (1993) Guide to Techniques in Mouse Development. Wasserman PM, De Pamphilis WL, eds. *Methods Enzymol* 1993; **225**: 16–33.
44. Green CJ. Animal Anaesthesia – Laboratory Animal Handbooks 8. In: Green CJ, ed. London: Laboratory Animals Ltd 1979: 147–154.
45. Flecknell PA. Laboratory Animal Anaesthesia. London: Academic Press 1987.
46. Arras M, Autenried P, Rettich A, Spaeni D, Ruelicke T. Optimization of intraperitoneal Injection anesthesia in mice: drugs, dosages, adverse effects, and anesthesia depth. *Compar Med* 2001; **51**: 443–456.
47. Russel WMS, Burch RL. The principles of humane experimental technique. London: Methuen 1959.
48. Russel WMS, Burch RL. The principles of humane experimental technique. *South Mimms: UFAW* 1992.
49. National Research Council. Recognition and Alleviation of Pain and Distress in Laboratory Animals. Washington: National Academic Press 1992.

50. Jenkins WL. Pharmacological aspects of analgesic drugs in animals: An overview. *J Am Vet Med Assoc* 1987; **191**(10): 1231–1240.
51. Tranquilli WJ, Grimm KA. Pharmacology of drugs used for anesthesia and sedation. *Vet Clin North Am Anim Pract* 1996; **12**(3): 501–529.
52. Thurmon JC, Tranquilli WJ, Benson GJ. Anesthesia of wild, exotic and laboratory animals. In: Thurmon JC, Tranquilli WJ, Benson GJ. eds. Lumb & Jones' Veterinary Anesthesia, 3rd edn. Baltimore: Williams & Wilkins 1996: 686–735.
53. Working Party. Recommendations for euthanasia of experimental animals: Part 1. *Lab Anim* 1996; **30**: 293–316.
54. Working Party. Recommendations for euthanasia of experimental animals: Part 2. *Lab Anim* 1997; **31**: 1–32.
55. Fox JG, Cohen BJ, Loew FM. The mouse in biological research. In: Fox JG, Cohen BJ, Loew FM, eds. Laboratory Animal Medicine. Orlando: Academic Press 1984.
56. Windholz M, Budavari S, Blumetti RF, Otterbein ES. The Merck Index. Merck & Co Inc, Rahway (USA) pp 2194; 1983: 2194.
57. Dörr W, Weber-Frisch M. Short-term immobilization of mice by methohexitone. *Lab Anim* 1999; **33**: 35–40.
58. Erhardt W, Hebestedt A, Aschenbrenner G, Pichotka B, Blümel G. A comparative study with various anaesthetics in mice (pentobarbitone, ketamine-xylazine, carfentanyl-etomidate). *Res Exp Med (Berl)* 1984; **184**: 159–169.
59. Zeller W, Meier G, Bürki K, Panoussis B. Adverse effects of tribromoethanol as used in the production of transgenic mice. *Lab Anim* 1998; **32**: 407–413.
60. Koizumi T, Maeda H, Hioki K. Sleep-time variation for ethanol and the hypnotic drugs tribromoethanol, urethane, pentobarbital, and propofol within outbred ICR mice. *Exp Anim* 2002; **51**: 119–124.
61. Silverman J, Huhndorf M, Balk M, Slater G. Evaluation of a combination of tiletamine and zolazepam as an anesthetic for laboratory rodents. *Lab Anim Sci* 1983; **33**: 457–460.
62. Abad F, Feria M, Boada J. Chronic amitriptyline decreases autotomy following dorsal rhizotomy in rats. *Neurosci Lett* 1989; **99**: 187–190.
63. Flecknell PA. The relief of pain in laboratory animals. *Lab Anim* 1984; **18**: 147–160.
64. Dobromylskyi P, Flecknell PA, Lascelles BD, Pascoe PJ, Taylor P, Waterman-Pearson A. Pain Management in Animals, In: Flecknell PA, Waterman-Pearson A., eds. Pain Management in animals. London: W.B. Saunders 2000: 81–145.
65. Liles JH, Flecknell PA. The effects of halothane anaesthesia, surgery and analgesia on body weight and food and water consumption in mice. *J Vet Anaesth* 1993; **20**: 38 (Abstract).
66. Harvey RC, Walberg J. Principles and Practice of Veterinary Anaesthesia. Short CE, ed. Baltimore: Williams & Wilkins 1987: 380–392.

2

Naturally occurring variation among mouse strains

Weibin Shi[1] and **Aldons J. Lusis**[2]

[1]*Department of Radiology and the Cardiovascular Research Center, University of Virginia, Charlottesville, VA, USA and* [2]*Departments of Medicine, Human Genetics, and of Microbiology, Immunology and Molecular Genetics, David Geffen School of Medicine at UCLA, Los Angeles, CA, USA*

Abstract

Mouse genetics is one of the most powerful tools for addressing various questions concerning cardiovascular morphology, physiology, and pathology. Targeted mutagenesis and transgenics are powerful approaches commonly used in mice to examine the role of specific genes in a biological process. Also, inbred mouse strains that display quantitative differences in inherited phenotypes, such as plasma lipid levels and atherosclerotic lesion sizes, have been used to perform quantitative trait locus (QTL) analysis to localize genes that give rise to the traits. Various strategies, including congenic mouse strains can then be used to confirm the QTLs and identify the genes underlying the QTLs.

Keywords

quantitative trait; QTL; mouse genetics; mouse strains; congenic strains

Introduction

Over the past three decades, there has been rapid progress in identifying the genes that are involved in monogenic diseases, such as Tangier disease[1] and homocystinuria.[2] However, progress in identifying genes contributing to common diseases, including atherosclerosis, diabetes, and hypertension, has been slow.[3,4] Studies of the genetic bases of common diseases in humans are difficult, partially due to the involvement on many genes, genetic heterogeneity, and important environmental influence.

A Handbook of Mouse Models of Cardiovascular Disease Edited by Qinbo Xu

The use of mouse models of human diseases overcomes some of the limitations of human genetic studies. Genetic heterogeneity is reduced through the use of inbred strains, and environmental variation can be minimised by using standardised housing conditions and diet. Mice are small (usually <40 g) and can be maintained in breeding colonies comparatively cheaply. They have a short lifespan ($\sim$3 years), a short generation time (sexual maturity is attained by $2 \sim 3$ months), and large litter sizes ($5 \sim 10$ pups). Their short generation time and lifespan means that the effects of transmittable mutations can be monitored easily. Because mice can be bred easily, new strains, including inbred strains, recombinant inbred strains, congenic strains, and comsomic strains, can be generated relatively quickly ($1.5 \sim 4$ years). Over the years a number of strains exhibiting genetic variations in phenotypes of interest have been identified, thus providing valuable resources to identify the critical cells, genes, and pathways underlying the traits (see The Jackson Laboratory website: www.jax.org). Chromosomal regions harboring the relevant genes can be found relatively quickly and inexpensively by crossing strains with phenotypic differences. The loci can then be isolated as congenic strains, thus reducing the complexity of the trait difference. However, it has proved difficult to identify the genes underlying complex traits since, in most cases, individual loci exert a small effect that makes it difficult to distinguish alleles in individual backcross or intercross mice. Fortunately, the completion of human and mouse genome sequences and the advancement of new technologies, such as DNA microarrays, have begun to accelerate and simplify the process of identifying causal genes (see below).

There are two distinct ways to determine the involvement of a particular gene in a biological process. One is called ‘forward genetics’ or ‘phenotype-to-gene’, which uses naturally occurring variation in a phenotype to identify the underlying gene(s) affecting the trait by linkage analysis, followed by testing ‘positional candidates’. If a known gene is suspected of playing a role in a physiologic process, then the ‘candidate gene’ approach is used to look for associations of a particular trait with polymorphic variations of the gene. The other strategy is termed ‘reverse genetics’ or ‘gene-to-phenotype’, which involves the transgenic modification of a known gene, followed by examination of its effect on a physiologic process. Both forward and reverse genetics strategies have been used extensively in mice.

Mapping genes underlying quantitative traits

Quantitative traits are those that show continuous variation from low to high values, such as blood pressure and cholesterol levels. The variation in a quantitative trait is caused by genetic or environmental factors or both. The genetic basis for the continuous variation of a quantitative trait is due to the cumulative effects of multiple genetic loci on the phenotype. A locus that controls a quantitative trait is called a quantitative trait locus (QTL). QTL analysis is the general approach for mapping chromosomal locations of genes that contribute to a polygenetic quantitative trait. QTL mapping begins with construction of a cross between two inbred strains that exhibit variation in the phenotype of interest. Generally, the greater the variation in

the phenotype between two parental strains, the greater the probability of identifying the QTLs for the trait in their crosses. The F_1 hybrids of the two parental strains are crossed back to one of the parental strains (backcross) to create a N_2 population or are themselves mated (intercross) to create a F_2 population. A F_2 cross is more common for QTL analysis, especially when both parental strains have the phenotype differing in magnitude and their F_1 shows an intermediate phenotype. A N_2 cross is more powerful if the trait exhibits recessive inheritance.

The number of animals required for QTL analysis depends on many factors, including QTL effect, the number of QTLs, and the variance of each QTL, but none of them are known at the planning stage of experiments. Darvasi[5] proposes formulas for estimation of the number of progeny to be generated for a F_2 $[65.5/(2d^2 + h^2)]$ or N_2 cross $[60.5/(d + h)^2]$ based on phenotypic differences among two parental strains and their F_1. In the formulas d represents standardized allele effect, which is equal to half of the difference between the means of two homozygous QTL genotypes divided by the within genotype standard deviation, and h stands for dominance effect, which is the difference between the means of the heterozygous QTL genotype and the average of the two homozygous means divided by the within genotype standard deviation. Obviously, the greater the QTL effect the less animals need to be analysed. However, in reality, the goal of the study as well as time and cost considerations often decides the number of animals to be used for QTL analysis. In our experience and in most published studies, a cohort of 200 animals should be sufficient to identify QTLs of major effect on a quantitative trait.[6–9]

Although the F_1 mice from a cross with inbred parental strains are genetically identical (with the exception of the sex chromosomes), the N_2 or F_2 mice are each genetically unique due to independent segregation of chromosomes and crossovers that occur during the F_1 meiotic process. Because the recombinant regions are inherited as relatively large segments of chromosomes, the parental origins of these chromosomal regions can be recognized with polymorphic markers that distinguish the parental strains. The most common method for genotyping is polymerase chain reaction (PCR) assay of simple sequence repeats (SSR) and single nucleotide polymorphism (SNP) genotyping using forms of oligonucleotide hybridization. The most common SSR consists of mono-, di-, tri-, or tetranucleotide repeated sequences, so-called microsatellites. Genotyping by the use of restriction fragment length polymorphisms (RFLP) can also be performed but it is more difficult and time consuming. Each animal in the second generation is genotyped with polymorphic markers covering the entire genome at regular intervals and phenotyped for quantitative trait values. QTL analysis tests whether the measured traits vary significantly across the population on the basis of the parental genotype at any given location in the genome.

Specific software, such as Map Manager QTX, is available for testing the association of a quantitative trait to each genetic marker. Likelihood ratio statistics (LRS) or log of the-odds-ratio (LOD) scores are used to define the significance of the association of a genetic marker with a trait. LOD scores can be calculated by dividing LRS by 4.6. According to the guidelines proposed by Lander and Kruglyak[10], the LOD score required for significant linkage is 4.3 and the P value for a single point is 2×10^{-5} to obtain a genome-wide P value of 0.05 for a F_2 cross (in other words, in an F_2 genome

scan, there is a 5 per cent probability of obtaining a LOD score of 4.3 or greater purely by chance). For suggestive linkage, the LOD score is 2.2 and the *P* value for a single point is 7×10^{-4}. For a backcross experiment, a lower LOD score (3.3) is required for significant linkage). Permutation tests are another method for calculating the threshold of a LOD score that a QTL needs to reach to be statistically significant. This method randomises genotype and phenotype data and estimates an empirical genome-wide probability for observing a given LOD score by chance, using the informative markers and 1000 permuted data sets recommended by Doerge and Churchill.[11] The latest version of QTX allows choosing a trait, a chromosomal region, and other conditions to run a permutation test for establishing suggestive and significant LOD threshold values for interval mapping. The interval mapping method of QTX identifies the presence of a QTL and its position within marker intervals. There will be a particular location along the chromosome where the likelihood of a genetic effect is greatest, referred to as the peak. The position of the peak is the most likely position for the QTL. A region of the chromosome defined by one LOD unit decrease on either side of the peak can be defined, within which there is a 95 per cent statistical likelihood for the QTL location.

Recombinant inbred strains (RI) and advanced intercross lines (AIL) are alternatives to genetic crosses for identification of QTLs contributing to a complex quantitative trait with sufficient strength in the mouse. RI strains are a set of inbred strains derived from two progenitor strains. Breeding pairs are randomly selected from a F_2 population and each pair undergoes 20 generations of strict brother–sister mating to give rise to one new RI strain. As a result, each RI is a unique mixture of the genome of the two parental strains. Thus, analysing a set of RI strains is similar to analysing a F_2 cohort. RI strains for QTL analysis have the advantages of immediate accessibility of the strains and unlimited material for phenotypic assessment. However, RI mapping has low power and precision to detect QTLs, mainly owing to the small number of available strains in each set.[12]

When an F_2 or N_2 population is used for QTL analysis, a limiting factor in QTL detection and localization is the numbers of recombination events that occur. In contrast, an advanced intercross line (AIL) increases recombination frequency in a segregating population. An AIL is produced by first generating a F_2 cohort from two progenitor strains. Breeding pairs are randomly selected from the F_2 population to generate a F_3 population. Similarly, breeding pairs from the F_3 population are randomly selected to produce a F_4 population. This procedure is repeated many times until the F_{10} (or greater) generation is attained. To produce a valuable AIL, a breeding population of more than 100 mice at each generation is required. The final F_{10} (or greater) generation is used for QTL analysis. The accumulation of recombination events in the AIL can lead to several fold reduction in the confidence interval of QTL map location. A similar strategy uses outbred stocks with mixed haplotypes.[13]

Dissecting QTLs using congenic strains

QTL analysis is a statistical approximation of both the presence and the location of genes that influence a quantitative trait. It is therefore likely that QTLs are detected

when there are none (Type 1 error) or QTLs are missed when there are ones (Type 2 error). As a complex quantitative trait is usually controlled by multiple genes, the contribution of each individual locus to the trait is difficult to assess in a genetic cross. Moreover, QTL analysis only yields QTLs that are restricted to chromosomal regions no less than 10 to 30 cM, even in large experimental crosses[14]. A genetic interval of this size corresponds in mice to ~170 to 510 genes, which are too many candidates to evaluate each one individually. One efficient solution to these problems is the construction and analysis of congenic strains. A congenic strain contains a small contiguous portion of the genome of one progenitor strain on the background of the other progenitor.[12] A consomic strain is a special type of congenic strain in which a whole chromosome of one mouse strain is transferred to another. Since in a congenic strain other QTLs have been eliminated, it is possible to assess the contribution of an individual QTL to a complex trait through comparison with the background strain. The use of congenic strains, similar to inbred strains, allows repeat phenotyping of genetically identical individuals. Even more importantly, once a congenic strain is constructed to contain a QTL, it can be used for identification of individual candidate genes in the congenic region.

The construction of congenic strains to move genomic segments between various inbred mouse strains is a classic genetic procedure that was pioneered by Nobel laureate George Snell[15] for dissection of histocompatibility and tumor resistance loci. More recently, the congenic breeding strategies have become the standard procedure for genetically transferring targeted genes or transgenes onto specific genetic backgrounds. The protocol involves serial backcrossing of a gene donor to a recipient strain, accompanied by selection for progeny carrying the desired gene or genomic segment in each backcross generation. This leads to a serial dilution of the donor genome into the recipient genome, with continuous maintenance of the specific gene or genomic segment. By the 10th generation, the genome of the congenic line unlinked to the targeted allele will be about 99.8 per cent of recipient strain origin. It is at this stage that the new strain is considered to be a certified congenic.[12] Linkage will also cause the retention of a significant segment of donor chromosome spanning the selected gene or genomic segment. The expected average length of this donor-derived genomic segment can be calculated as $[200(1 - 2^{-N})/N$, where N is the number of backcross] cM, although the length of the segment may vary considerably due to the random distribution of crossover sites. The strengths of the congenic breeding procedure are that it is relatively simple and is accepted as the standard protocol for the production of a congenic strain. The weaknesses are that it requires 2–3 years to produce a congenic mouse strain and the purity of the congenic strain for recipient genome is based on theoretical calculations.

More recently, the speed congenic approach has been developed to accelerate the introgression of genes or genomic segments between breeds with a marker-assisted selection protocol (MASP).[16] This approach is based on a genome-wide analysis of genetic polymorphisms distinguishing the donor and recipient strains. The optimal breeders are selected with polymorphic markers not only for the presence of the desired donor allele but also for the absence of donor alleles at other parts of the genome. This procedure can lead to creation of a congenic strain with less than

0.5 per cent contaminating donor genome unlinked to the congenic region in a total of four backcrosses.[17] An efficient strategy is to screen 16 to 20 male mice at each backcross generation with markers spaced every 25 cM. The use of larger progeny cohorts and denser markers is of little help in reducing the percentage of contaminating donor genome unlinked to the target region. This approach allows for generation of genetically defined congenic strains within a period of 1.5 years. Also, the purity of the congenic strain for the recipient genome is genetically defined.

Once a congenic strain is constructed to carry a QTL, the next step is to evaluate the phenotypes of interest through comparison with its background strain. If such a congenic strain exhibits the phenotype of interest, then the QTL has been confirmed to be real as defined in the original cross and is subject to further characterisation. Otherwise, the QTL has been eliminated for further consideration.

A congenic strain can be used to reduce the size of the candidate interval once the functional significance of the congenic segment has been confirmed. To achieve this objective, the congenic strain can be backcrossed to the parental strain to produce an F_1 generation that is heterozygous for the congenic segment. These F_1 mice can be brother–sister mated to produce a large F_2 population or backcrossed to the parental strain to produce a large N_2 population. The recombination event that is required for mapping only occurs within the congenic region while the rest of the genome remains homozygous at all locations during the F_1 meiotic process. Therefore, the statistical power of each mouse in the linkage analysis becomes much greater as the interference from rest of the genome that normally reduces sensitivity in a linkage study does not exist.

The second way to narrow the QTL interval using congenic strains is through creation of overlapping subcongenic strains. This involves a backcross between the congenic strain and the parental background strain, followed by two generations of intercross. Mice of the backcross generation become heterozygous on the congenic segment while all the other alleles remain homozygous at all locations. The F_1 mice are brother–sister mated to produce F_2 progeny carrying differing regions of the targeted segment. Male and female mice that are heterozygous for the same region of the targeted segment are then mated to generate mice that are homozygous for the donor parental strain in this region. The narrow region that modifies the trait of interest can then be determined.[18]

Testing candidate genes in QTL regions

Once a QTL for a complex trait is genetically defined by a congenic strain, the next step is to identify QTL genes for the trait. The most direct approach is to sequence the coding regions of candidate genes to search for polymorphisms/mutations of the genes.[14] Most proven QTL genes are identified on the basis of changes in coding sequence because proof for functional significance is relatively easy to obtain.[19] In contrast, the consequences of noncoding sequence variants are difficult to interpret and are still poorly understood.[14] The most common type of genetic variations is a single nucleotide polymorphism (SNP) where a base is replaced by another.

Insertions of additional sequences or deletions are also common genetic variations, which are in the range from one to several thousand base pairs. Polymorphisms/mutations are likely to have functional effects when they result in an amino acid substitution in the gene products or a frameshift in the coding region. Many polymorphisms probably have no functional significance if they have no effect on gene products. There is also a possibility that a polymorphism/mutation directly affects gene transcription, RNA splicing, and mRNA stability and translation.

Candidate gene association is a genetic approach that assesses the association of a candidate gene with a complex trait using an experimental cross. Aitman *et al.*[20] used the CD36 gene as a maker locus in QTL analysis and applied it to defective insulin action in two F_2 crosses and one backcross derived from SHR and WKY rats and found that CD36 was at the peak of linkage to the trait. This approach has also been successfully used in other studies to determine the involvement of candidate genes in control of the polygenic quantitative traits.[21–23] However, significant association of a polymorphism with a disease trait may not ensure that the polymorphism is a primary factor for the disease susceptibility. Thus, the observed association may be due to linkage disequilibrium such that another polymorphism within the gene or in a closely linked gene may actually determine the disease susceptibility. Recent studies have suggested that for many traits, several genes rather than a single gene are responsible for the phenotypic effect of a single QTL.[24–27] This may seem unexpected, but there is selection for such loci in that they may have the strongest effect on the trait. There is therefore a possibility that polymorphisms/mutations occur in several closely linked, interacting genes in one QTL.

Comparative expression profiling of genes in the relevant tissues or cells of a congenic strain and its background strain can be a useful strategy for identification of potential QTL genes. Global expression profiling using microarrays allows genes showing differential expression to be identified on a genome-wide scale and offer an opportunity to prioritize candidate genes for further investigation. When the congenic strain is compared with its background strain, the genes to be expressing differentially should be those in the congenic region or in other regions but affected by gene differences in the congenic region. The commonly used microarray method is a cDNA selection, in which mRNA from the most likely tissues expressing the candidate gene is converted to cDNA, which is then fluorescently or isotopically labeled and hybridised to high density arrays of cDNA clones or of oligonucleotides directly synthesized on glass supports, nylon membranes, or silica wafers. Signals are quantified using phosphorimaging, photomultiplier tubes, or computer-controlled imaging systems and a data set consisting of expression measurements for all of the elements of the array is created. Most microarray experiments consist of either examining changes in gene expression over a temporal or treatment gradient[28] or comparing gene expression between two samples of different genotypes.[29,30]

Microarray assays may also offer new data concerning gene function, regulatory mechanisms, and biochemical pathways.[31–33] Because genes with similar functions tend to cluster together in expression, a gene without known functions can be

tentatively assigned a role in a biological process based on the functions of known genes in the same expression cluster. Importantly, gene expression profiling provides a broad candidate gene approach, which can be powerful when combined with genetically defined linkage regions. By linking information from expression profiling with QTL mapping, recent studies have identified genes contributing to Tangier disease in humans,[34] spontaneous hypertension in rats,[20] and allergic asthma in mice.[35] Recent studies involving a combination of genetic segregation and expression profiling ('genetical genomics') appear to be particularly promising for the identification of positional candidates and causal pathways.[36,37] Nevertheless, there exist limitations to such combined approaches, which include: (1) not all complex trait genes are differentially expressed; (2) environmental factors affect gene expression and may confuse the analysis;[38] and (3) gene expression profiling may not be sufficient in relating gene function to a complex trait.[32]

Functional tests of candidate genes

The final step in QTL gene identification is to prove that the gene identified is the real QTL gene by functional assays. Gene knockout and transgenesis are the most suitable technologies for the verification of QTL genes. The most conclusive evidence is that combination or disruption of a candidate gene results in changes in the phenotype of interest. Due to technical difficulties and the long duration required to generate the animals, these approaches can only be used to test a limited number of genes. RNA interference (RNAi) is a sequence-specific, post-transcriptional gene silencing mechanism initiated by the introduction of double stranded RNA (dsRNA) homologous in sequence to the silenced gene.[39,40] RNAi has significantly advanced our understanding of gene function in the nematode *Caenorhabditis elegans* and more than one third of the nematode genome has already been subjected to functional analysis by RNAi.[41,42] Mammalian cells are only recently amenable to RNAi because the use of long dsRNAs (>30 nt) results in activation of an antiviral response leading to blockage of initiation of protein synthesis and mRNA degradation.[39] However, the introduction of small interfering RNA (siRNA) with 21–22 nucleotides in length does not stimulate the anti-viral response in mammalian cultured cells and can effectively target specific mRNA for gene silencing.[43] The ability of siRNA to silence individual gene expression with a high degree of specificity is also showing promise as a strategy for *in vivo* gene intervention.[44–46] although the potency of siRNA remains limited by intracellular availability and the transient nature of gene silencing. Repeated administration of siRNA overcomes this latter limitation to some extent while plasmid and viral vectors producing siRNA using the polymerase III promoter may offer more efficient siRNA delivery and can theoretically induce stable gene silencing.[47] In addition, with the availability of numerous agonists (activators) and antagonists (inhibitors) to receptors and enzymes, the pharmacological method may serve as a useful tool for functional analysis of signal molecules.

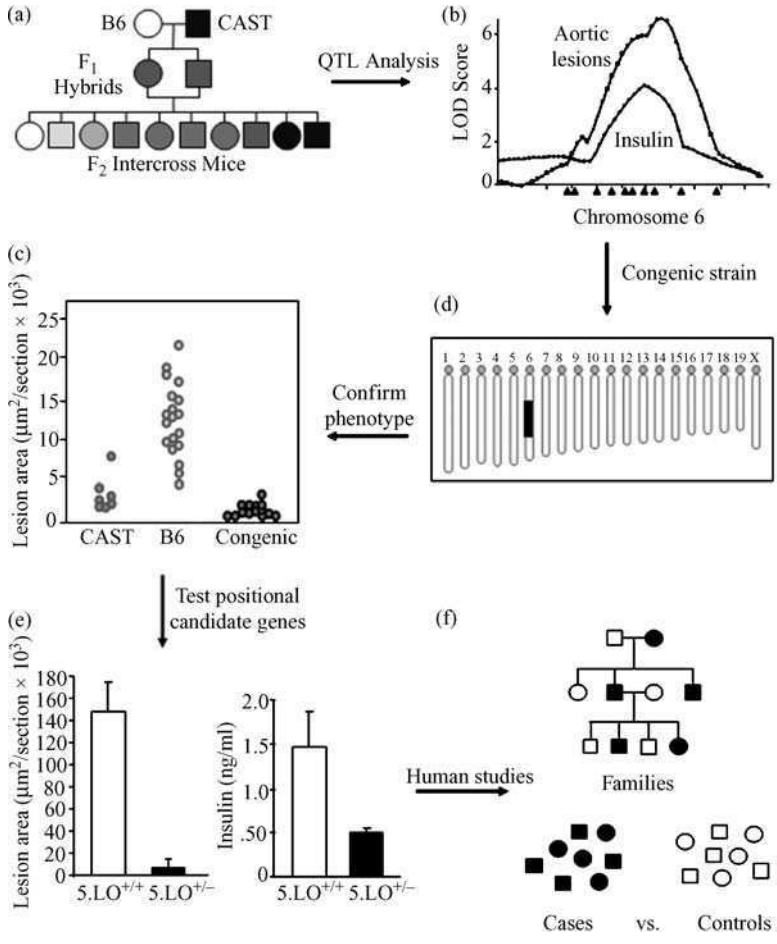

Figure 2.1 Identification of 5–LO as an atherosclerosis susceptibility gene. QTL analysis begins with creation of a cross between inbred strains C57BL/6J [B6] and CAST/Ei [CAST] that differ in their susceptibility to atherosclerosis (a). Statistical analysis of the correlation between phenotypes of F_2 progeny and the genomic regions that they inherited from the parental strains identifies a QTL for aortic lesions and insulin levels on the middle of chromosome 6 (b). This is represented in graphical form by LOD scores, where the highest point of the curve is the most likely location of the underlying gene. Arrows along the x-axis depict genetic markers used to genotype the F_2 animals. A congenic strain is then constructed by sequential backcrossing of an F_1 animal to one of the parental strains (ie, B6), with selection of the chromosomal segment from the other parent (ie, CAST) that encompasses the QTL (c). Phenotyping the congenic strain for the trait(s) originally identified in linkage analysis confirms the locus (d). The underlying gene can be identified by testing positional candidate genes in the locus with either functional studies or transgenic models, in this example, 5–LO–knockout mice (e). The human homolo of the gene (5–LO) is then examined in human populations with family–based or case–control study designs (f). (From Allayee W, Ghazalpoar A, Lusis AJ. Using mice to dissect genetic factors in atherossclerosis. Arterioscler Thromb Vasc Biol 2003;23:1501; with permission from Lippincott Williams & Wilkins). For a color version of this figure, please see the images supplied on the accompanying CD

From mouse to man

The genes that have been identified through the study of mouse models can be used to identify human homologues. This can be pursued to search for mutations associated with disease in human populations and to identify important pathways involved in disease susceptibility that may lead to development of novel diagnostic and therapeutic strategies. Studies of the *Artles* locus on chromosome 6 provide such an example (Figure 2.1). *Artles* is an atherosclerosis susceptibility QTL identified using a F_2 cross between strains C57BL/6J and CAST/Ei.[48] Interestingly, there is coincident linkage of insulin levels with this locus, raising the possibility that the underlying gene has pleiotropic effects on atherosclerosis and other related metabolic traits (Figure 2.1b). Subsequently, a congenic strain was developed to confirm the QTL and used to identify the underlying gene that causes resistance to atherosclerotic lesion formation. Congenic animals carrying the middle region of chromosome 6 derived from CAST/Ei (Figure 2.1c) confirmed the phenotypes of *Artles* because these mice exhibited dramatic resistance to aortic lesion formation and had lower insulin levels compared with the background strain C57BL/6J (Figure 2.1d). Among the candidate genes in the congenic interval is 5-lipoxygenase (5-LO), an enzyme involved in leukotriene production. 5-LO is expressed primarily in leukocytes and bone marrow transplantation experiments have demonstrated the involvement of monocytes/macrophages or other leukocytes in atherosclerosis. To evaluate 5-LO as a candidate gene, Mehrabian et al.[49] created 5-LO and LDLR double knockout mice and fed them a high-fat, high-cholesterol diet. These mice exhibited profound reduction in aortic lesion formation and plasma insulin levels (Figure 2.1e). Conservative amino acid substitutions at the 3′ end of the protein were also identified between CAST/Ei and C57BL/6J.[49] By creating the same substitutions at the conserved positions in the human enzyme, Habenicht and colleagues[50] have tested the function of these amino acid changes and found that the CAST/Ei form of 5-LO has a marked decrease in activity and expression levels. In a human population we have observed variant 5-lipoxygenase genotypes (lacking the common allele), which occur in 6.0 per cent of the population.[51] Interestingly, carotid artery intima media thickness, a parameter of carotid atherosclerosis, was significantly increased among the carriers of two variant alleles as compared with carriers of the wild-type allele. Taken together, these studies provide strong evidence that 5-LO is the gene that underlies *Artles* and demonstrate the power of the QTL approach for identifying genes associated with atherosclerosis.

References

1. Bodzioch M, Orso E, Klucken J, et al. The gene encoding ATP-binding cassette transporter 1 is mutated in Tangier disease. *Nat Genet* 1999; **22**: 347–351.
2. Fowler B, Kraus J, Packman S, Rosenberg LE. Homocystinuria. Evidence for three distinct classes of cystathionine beta-synthase mutants in cultured fibroblasts. *J Clin Invest* 1978; **61**: 645–653.

3. Lusis AJ, Mar R, Pajukanta P. Genetics of atherosclerosis. *Annu Rev Genomics Hum Genet* 2004; **5**: 189–218.
4. Rapp JP. Genetic analysis of inherited hypertension in the rat. Physiol Rev 2000; 80:135–172.
5. Darvasi A. Experimental strategies for the genetic dissection of complex traits in animal models. *Nat Genet* 1998; **18**: 19–24.
6. Dansky HM, Shu P, Donavan M, et al. A phenotype-sensitizing Apoe-deficient genetic background reveals novel atherosclerosis predisposition loci in the mouse. *Genetics* 2002; **160**: 1599–1608.
7. Machleder D, Ivandic B, Welch C, Castellani L, Reue K, Lusis AJ. Complex genetic control of HDL levels in mice in response to an atherogenic diet. Coordinate regulation of HDL levels and bile acid metabolism. *J Clin Invest* 1997; **99**: 1406–1419.
8. Mehrabian M, Wen PZ, Fisler J, Davis RC, Lusis AJ. Genetic loci controlling body fat, lipoprotein metabolism, and insulin levels in a multifactorial mouse model. *J Clin Invest* 1998; **101**: 2485–2496.
9. Welch CL, Bretschger S, Latib N; Localization of atherosclerosis susceptibility loci to chromosomes 4 and 6 using the Ldlr knockout mouse model. *Proc Natl Acad Sci USA* 2001; **98**: 7946–7951.
10. Lander E, Kruglyak L. Genetic dissection of complex traits: guidelines for interpreting and reporting linkage results. *Nat Genet* 1995; **11**: 241–247.
11. Doerge RW, Churchill GA. Permutation tests for multiple loci affecting a quantitative character. *Genetics* 1996; **142**: 285–294.
12. Silver LM. Mouse Genetics: *New York: Oxford University Press*, 1995.
13. Yalcin B, Willis-Owen SA, Fullerton J, et al. Genetic dissection of a behavioral quantitative trait locus shows that Rgs2 modulates anxiety in mice. *Nat Genet* 2004; **36**: 1197–1202.
14. Glazier AM, Nadeau JH, Aitman TJ. Finding genes that underlie complex traits. *Science* 2002; **298**: 2345–2349.
15. Snell GD. Methods for the study of histocompatibility genes. *J. Genet* 1948; **49**: 87–108.
16. Hospital F, Chevalet C, Mulsant P. Using markers in gene introgression breeding programs. *Genetics* 1992; **132**: 1199–1210.
17. Markel P, Shu P, Ebeling C, Carlson GA, Nagle DL, Smutko JS, Moore KJ. Theoretical and empirical issues for marker-assisted breeding of congenic mouse strains. *Nat Genet* 1997; **17**: 280–284.
18. Estrada-Smith D, Castellani LW, Wong H, Wen PZ, Chui A, Lusis AJ, Davis RC. Dissection of multigenic obesity traits in congenic mouse strains. *Mamm Genome* 2004; **15**: 14–22.
19. Korstanje R, Paigen B. From QTL to gene: the harvest begins. *Nat Genet* 2002; **31**: 235–236.
20. Aitman TJ, Glazier AM, Wallace CA, et al. Identification of Cd36 (Fat) as an insulin-resistance gene causing defective fatty acid and glucose metabolism in hypertensive rats. *Nat Genet* 1999; **21**: 76–83.
21. Grisart B, Coppieters W, Farnir F, et al. Positional candidate cloning of a QTL in dairy cattle: identification of a missense mutation in the bovine DGAT1 gene with major effect on milk yield and composition. *Genome Res* 2002; **12**: 222–231.
22. Keightley PD, Morris KH, Ishikawa A, Falconer VM, Oliver F. Test of candidate gene–quantitative trait locus association applied to fatness in mice. *Heredity* 1998; **81**: 630–637.
23. Winter A, Kramer W, Werner FA, et al. Association of a lysine-232/alanine polymorphism in a bovine gene encoding acyl-CoA:diacylglycerol acyltransferase (DGAT1) with variation at a quantitative trait locus for milk fat content. *Proc Natl Acad Sci U S A* 2002; **99**: 9300–9305.

24. Legare ME, Bartlett FS 2nd, Frankel WN. A major effect QTL determined by multiple genes in epileptic EL mice. *Genome Res* 2000; **10**: 42–48.
25. Morel L, Blenman KR, Croker BP, Wakeland EK. The major murine systemic lupus erythematosus susceptibility locus, Sle1, is a cluster of functionally related genes. *Proc Natl Acad Sci U S A* 2001; **98**: 1787–1792.
26. Nadeau JH, Frankel WN. The roads from phenotypic variation to gene discovery: mutagenesis versus QTLs. *Nat Genet* 2000; **25**: 381–384.
27. Podolin PL, Denny P, Armitage N, et al. Localization of two insulin-dependent diabetes (Idd) genes to the Idd10 region on mouse chromosome 3. *Mamm Genome* 1998; **9**: 283–286.
28. DeRisi JL, Iyer VR, Brown PO. Exploring the metabolic and genetic control of gene expression on a genomic scale. *Science* 1997; **278**: 680–686.
29. Arfin SM, Long AD, Ito ET, et al. Global gene expression profiling in Escherichia coli K12. The effects of integration host factor. *J Biol Chem* 2000; **275**: 29672–29684.
30. Schena M, Shalon D, Davis RW, Brown PO. Quantitative monitoring of gene expression patterns with a complementary DNA microarray. *Science* 1995; **270**: 467–470.
31. Bunney WE, Bunney BG, Vawter MP, et al. Microarray technology: a review of new strategies to discover candidate vulnerability genes in psychiatric disorders. *Am J Psychiatry* 2003; **160**: 657–666.
32. Doerge RW. Mapping and analysis of quantitative trait loci in experimental populations. *Nat Rev Genet* 2002; **3**: 43–52.
33. Lockhart DJ, Winzeler EA. Genomics, gene expression and DNA arrays. *Nature* 2000; **405**: 827–836.
34. Lawn RM, Wade DP, Garvin MR, et al. The Tangier disease gene product ABC1 controls the cellular apolipoprotein-mediated lipid removal pathway. *J Clin Invest 1999*; **104**: R25–R31.
35. Karp CL, Grupe A, Schadt E, et al. Identification of complement factor 5 as a susceptibility locus for experimental allergic asthma. *Nat Immunol* 2000; **1**: 221–226.
36. Ghazalpour A, Doss S, Yang X, et al. Thematic review series: The pathogenesis of atherosclerosis toward a biological network for atherosclerosis. *J Lipid Res* 2004; **45**: 1793–1805.
37. Schadt EE, Monks SA, Drake TA, et al. Genetics of gene expression surveyed in maize, mouse and man. *Nature* 2003; **422**: 297–302.
38. Moore KJ, Nagle DL. Complex trait analysis in the mouse: The strengths, the limitations and the promise yet to come. *Annu Rev Genet* 2000; **34**: 653–686.
39. Bass BL. Double-stranded RNA as a template for gene silencing. *Cell* 2000; **101**: 235–238.
40. Hammond SM, Caudy AA, Hannon GJ. Post-transcriptional gene silencing by double-stranded RNA. *Nat Rev Genet* 2001; **2**: 110–119.
41. Fraser AG, Kamath RS, Zipperlen P, Martinez-Campos M, Sohrmann M, Ahringer J. Functional genomic analysis of C-elegans chromosome I by systematic RNA interference. *Nature* 2000; **408**: 325–330.
42. Kim SK. Functional genomics: the worm scores a knockout. *Curr. Biol* 2001; **11**: R85–R87.
43. Elbashir SM, Harborth J, Lendeckel W, Yalcin A, Weber K, Tuschl T. Duplexes of 21-nucleotide RNAs mediate RNA interference in mammalian cell culture. *Nature* 2001; **411**: 494–498.
44. Duxbury MS, Matros E, Ito H, Zinner MJ, Ashley SW, Whang EE. Systemic siRNA–mediated gene silencing: a new approach to targeted therapy of cancer. *Ann Surg* 2004; **240**: 667–674.

45. Song E, Lee SK, Wang J, et al. RNA interference targeting Fas protects mice from fulminant hepatitis. *Nat Med* 2003; **9**: 347–351.
46. Zender L, Hutker S, Liedtke C, et al. Caspase 8 small interfering RNA prevents acute liver failure in mice. *Proc Natl Acad Sci U S A* 2003; **100**: 7797–7802.
47. Brummelkamp TR, Bernards R, Agami R. A system for stable expression of short interfering RNAs in mammalian cells. *Science* 2002; **296**: 550–553.
48. Mehrabian M, Wong J, Wang X, Jiang Z, Shi W, Fogelman AM, Lusis AJ. Genetic locus in mice that blocks development of atherosclerosis despite extreme hyperlipidemia. *Circ Res* 2001; **89**: 125–130.
49. Mehrabian M, Allayee H, Wong J, et al. Identification of 5-lipoxygenase as a major gene contributing to atherosclerosis susceptibility in mice. *Circ Res* 2002; **91**: 120–126.
50. Kuhn H, Anton M, Gerth C, Habenicht A. Amino acid differences in the deduced 5-lipoxygenase sequence of CAST atherosclerosis-resistance mice confer impaired activity when introduced into the human ortholog. *Arterioscler Thromb Vasc Biol* 2003; **23**: 1072–1076.
51. Dwyer JH, Allayee H, Dwyer KM, Fan J, Wu H, Mar R, Lusis AJ, Mehrabian M. Arachidonate 5-lipoxygenase promoter genotype, dietary arachidonic acid, and atherosclerosis. *N Engl J Med* 2004; **350**: 29–37.
52. Thompson JS. Atheromata in an inbred strain of mice. *J Atheroscler Res* 1969; **10**: 113–122.
53. Wang X, Korstanje R, Higgins D, Paigen B. Haplotype analysis in multiple crosses to identify a QTL gene. *Genome Res* 2004; **14**: 1767–1772.

3

Transgenic and gene-targeted mice in the study of hyperlipidemia

Yadong Huang

Gladstone Institute of Cardiovascular Disease and Departments of Pathology and Neurology, University of California, San Francisco, CA, USA

Introduction

Hyperlipidemia, characterized by elevated plasma levels of cholesterol or triglyceride or both, is among the public health problems worldwide. Although the pathogenesis of some types of hyperlipidemia remains poorly understood, it is clearly one of the major risk factors for the development of atherosclerotic heart disease that is the number one killer in many developed countries.[1,2] Epidemiological, clinical, and *in vitro* cell culture studies have identified many candidate genes, proteins, and cellular metabolic pathways that may be involved the pathogenesis of various types of hyperlipidemia. However, only recently have transgenic and gene-targeted mouse models been developed to study *in vivo* the roles of these genes, proteins, and metabolic pathways in the pathogenesis or prevention of hyperlipidemia.

Since mice are resistant to diet-induced hyperlipidemia, transgenic and gene-targeted mouse models are powerful tools for *in vivo* study of various types of hyperlipidemia. Many hypotheses based on the findings of epidemiological, clinical, and *in vitr*o cell culture studies have been proved *in vivo* with the transgenic and gene-targeted mouse models, which have significantly advanced our understanding of the pathogenesis of hyperlipidemia and atherosclerosis. These mouse models have also been useful for screening or testing drugs to treat or prevent hyperlipidemia and atherosclerosis.

A Handbook of Mouse Models of Cardiovascular Disease Edited by Qinbo Xu

Generation of transgenic mouse models

Purpose of using transgenic mice

There are two common uses of transgenic mice in hyperlipidemic research. The first is to study the lipid phenotypic effects of transgene expression in the intact animal. In this case, previously defined promoters are often used to control the expression of the transgene in the desired tissue. The second is to study the control of lipid metabolism-related gene expression in the intact animal. For this purpose, potential control sequence elements (promoter regions) are used to define the specific patterns of the transgene expression in various tissues.

For applications involving the lipid phenotypic effects of transgene expression, transgenic mice expressing the given genes, in general, represent gain-of-function mutations, whereas loss-of-function mutations in many cases can be obtained solely by gene targeting (see below). However, dominant negative mutations can also be obtained through expression of some mutant forms of genes.[3–6] In addition, the expression of transgenes encoding antisense RNA or short interfering RNA successfully inhibited the expression of some endogenous genes in transgenic mice.[7,8]

Most cloned genes introduced into the mouse germ line have shown appropriate tissue-specific and stage-specific patterns of expression despite their integration into apparently random sites in the host genome. Thus, for studies of the control of lipid metabolism-related gene expression, transgenic mice have provided the definitive experimental assay to define the *cis*-acting DNA sequences that control specific patterns of transcription *in vivo*.[9–11]

Procedure of generating conventional transgenic mice

The procedure for generating a conventional transgenic mouse line includes preparing DNA constructs, setting up the mouse colony, microinjecting DNA constructs into the pronuclei of fertilized eggs, characterising transgenic 'founder' mice, and generating transgenic lines from these founder mice.[12]

The quality of the DNA constructs is critical for efficient generation of transgenic founder mice. High purity of the DNA, avoiding the use of ethidium bromide for DNA staining, removing all vector sequences from the cloned genes, and using relative short DNA constructs (<70 kb) usually increase the rate of success (40–60 per cent) of generating founder mice.

The most extensively and successfully used method of gene transfer is microinjection of DNA directly into the pronuclei of fertilized mouse eggs. Infection of embryos with retroviral vectors has also been used. The microinjection method results in the stable chromosomal integration of the foreign DNA in 10–60 per cent of the resulting mice. In most cases, the integration appears to occur at the one-cell stage of the embryos; as a result, the foreign DNA is present in every cell of the transgenic mouse, including all primordial germ cells. In 15–25 per cent of cases, foreign DNA is

integrated at a later stage, resulting in mice that are mosaic for the presence of foreign DNA.

Procedure of generating conditional (inducible) transgenic mice

Sometimes, it is desirable to have transgenes that will be silent until specifically activated by an experimental manipulation, such as the administration of a drug. In early studies, the metallothionein promoter was frequently used to generate inducible transgenic mice, including those for lipid research.[13] The metallothionein promoter drives transgene expression at low basal levels in many tissues; however, feeding the transgenic mice with water containing Zinc can increase the transgene expression up to 100-fold in many tissue, including liver, kidney, and intestine.[13] However, this system lacks tissue specificity.

Recently, the *tet*-operon (Tet-O) system has been used widely to generate conditional (inducible) transgenic mice in a tissue-specific manner.[14,15] In this system, two transgenic mouse lines must be generated: one with the desired transgene under the control of a Tet-O promoter containing a tetracycline-responsive element (TRE) and the other expressing a tetracycline-controlled transactivator (tTA) under the control of a tissue-specific promoter (Figure 3.1). Crossing these two lines will generate transgenic mice carrying both transgenes. When the doubly transgenic mice are fed a diet containing tetracycline, the tetracycline binds to tTA, blocking the binding of the tTA to the TRE of the Tet-O promoter and turning off the transgene expression (Figure 3.1). When the tetracycline is withdrawn, tTA is released and binds to the TRE of the Tet-O promoter, turning on the transgene expression (Figure 3.1).

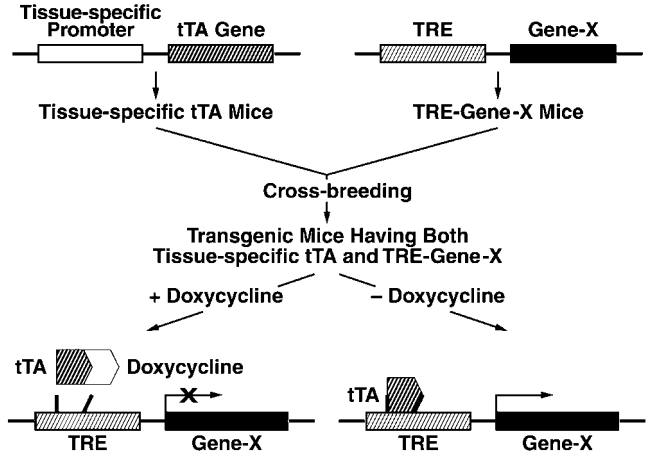

Figure 3.1 Schematic diagram of the tTA-TRE system used to generate inducible transgenic mice. tTA, tetracycline-controlled transactivator; TRE, tetracycline-responsive element

Generation of gene-targeted mouse models

Purpose of using gene-targeted mice

In hyperlipidemic research, gene-targeted mice are animals used to study the physiological functions of a given lipid metabolism-related gene in the intact animal by deleting the gene or functional domain(s) of the gene (knockout) (Figure 3.2a). Gene targeting is also used to generate a 'humanized' mouse – one expressing a given human lipid metabolism-related gene, with or without mutations, under the control of the mouse regulatory elements (knockin) (Figure 3.2b). For both purposes, a sequence replacement vector containing a homologous DNA sequence is used to replace the chromosomal sequence in mice.

Mice generated with a knockout strategy represent loss-of-function mutations, which usually proves whether or not the missing gene is important for lipid metabolism. However, mice generated with a knockin strategy can represent a gain-of-function, either physiological or pathophysiological, if the gene has a normal sequence or dominant negative mutations, respectively.

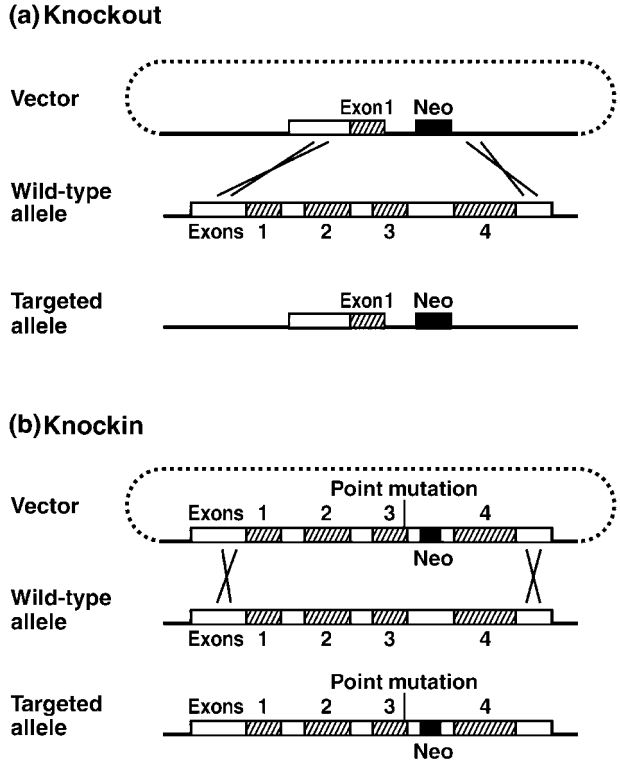

Figure 3.2 Schematic diagram of sequence-replacement, gene-targeting strategy used to generate knock out (a) and knock in (b) mice. Neo, neomycin resistant gene

Procedure of generating conventional gene knockout mice

The procedure for generating a conventional knockout mouse line includes preparing sequence-replacement gene-targeting vector (Figure 3.2a), growing mouse embryonic stem (ES) cells, electroporating the DNA into ES cells, selecting ES cells in which DNA has undergone homologous recombination by PCR and/or Southern blotting, microinjecting the positive ES cells into blastocysts, implantating the injected ES cells into the uterus of pseudopregnant female mice, and characterising the offspring.[16] The most important steps are the design of the sequence-replacement gene-targeting vector and the use of high-quality, well-established ES cells. The gene-targeting vector should contain a selectable marker, usually a neomycin-resistance gene (*neo*), that can be used to screen the positive ES cells (Figure 3.2a). The DNA sequence of the gene of interest in the targeting vector and the ES cells should be from the same strain of mice, if possible. Using unmatched strains of mice can dramatically decrease the chances of getting ES cells with homologous recombination.

Procedure of generating conditional (tissue-specific) gene knockout mice

Sometimes, the gene of interest is so important in mouse development that its absence is lethal to the embryo. Embryonic lethality can be avoided by using a conditional (tissue-specific) gene knockout strategy.[16] For this, two mouse lines must be generated: one gene-targeted line with the desired gene flanked by LoxP sites and the other expressing Cre (Cre-deleter) under the control of a tissue-specific promoter (Figure 3.3). Crossing these two lines introduces Cre into the conditional gene-targeted mice, where Cre expression will delete the DNA sequence between the LoxP sites, leading to a tissue-specific knockout of the gene (Figure 3.3). Sometime, replication-deficient Cre adenovirus can also be used to introduce the Cre into the conditional gene-targeted mice, although the deletion of the targeted gene might not be 100 per cent.

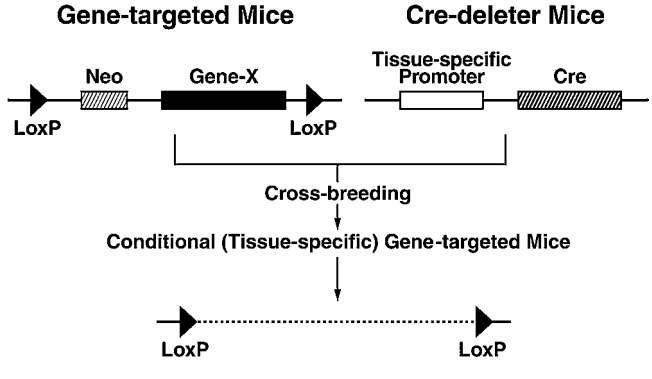

Figure 3.3 Schematic diagram of the Cre-deleting strategy used to generate conditional (tissue-specific) gene targeted mice. Neo, neomycin resistant gene

Procedure of generating gene knockin mice

Mice generated with a knock in strategy are usually used to study the effect of introducing a human lipid metabolism-related gene into mice. The human gene will result in a physiological function if it has a normal sequence or in a pathophysiological function if it has a dominant negative mutation. In knock in mice, the mouse gene is replaced with the homologous human gene, with or without mutations, under the control of the mouse regulatory elements (Figure 3.2B).[16] The advantages of this strategy over the transgenic strategy are that the human lipid-related gene is in the right position in the mouse genome and its expression is controlled by the mouse promoter. Thus, its regulation and its expression pattern are identical to those of the homologous mouse gene, eliminating the potential artificial effects of integration sites and copy numbers sometime observed in transgenic mice. However, the *neo*-selecting gene (usually within an intron of the targeted gene) sometimes reduces the expression of the knockin gene dramatically, generating so-called hypomophic mice.[17] In this case, deletion of the *neo* by crossing the knockin mice with the Cre-deleter mice can usually correct the hypomophic phenotype.[17] Thus, when a sequence replacement gene-targeting vector is designed for a knockin strategy, it is wisely advisable to flank the *neo* gene with LoxP sites.

Application of transgenic and gene-targeted mouse models in hyperlipidemia research

Application of transgenic mouse models

During the past few years, many transgenic mouse lines have been established for hyperlipidemic research.[4,6,18–21] Studies with these mice have provided significant insights into the pathogenesis and potential treatment of hyperlipidemia and atherosclerosis.

The first transgenic hypercholesterolemic mouse model was the one expressing high levels of apoB, which had increased plasma levels of total and low density lipoprotein (LDL) cholesterol and developed severe atherosclerotic lesions in response to high fat diet.[18] Likewise, analysing transgenic mice expressing a dysfunctional apoE variant, apoE(Arg-112, Cys-142), proved for the first time *in vivo* that mutant apoE causes type III hyperlipoproteinemia.[19] Mice expressing high levels (>70 mg/dl) of the dysfunctional apoE had grossly elevated plasma lipids, with cholesterol levels of up to 410 mg/dl and triglyceride levels of up to 1210 mg/dl. In addition, although expression of low levels of apoE (<20 mg/dl) in transgenic mice helped to clear very low density lipoprotein (VLDL) from plasma,[13,20] overexpression of apoE (>30 mg/dl) caused hypertriglyceridemia, with increased hepatic VLDL production and decreased VLDL lipolysis, in transgenic mice, suggesting for the first time the involvement of apoE overproduction in the pathogenesis of hypertriglyceridemia in humans.[20]

Application of gene-targeted mouse models

Studies in gene-targeted mouse models during the past few years have also provided insights into the pathogenesis and the potential treatments of hyperlipidemia and atherosclerosis.

Two widely used hyperlipidemic mouse models are apoE knockout and the LDL receptor knockout mice, both of which develop spontaneous hypercholesterolemia and atherosclerosis, indicating that both apoE and the LDL receptor are very important in maintaining plasma lipid homeostasis.[22–24] Likewise, knockout of lipoprotein lipase (LPL) caused severe hypertriglyceridemia, proving the involvement of LPL in type I hyperlipidemia in humans.[25] In addition, although conditional knockout of the LDL receptor-related protein (LRP) alone did not cause significant hyperlipidemia,[26] double knockout of the LDL receptor and LRP caused more severe hypercholesterolemia than knockout of the LDL receptor alone, suggesting that the LRP, as compared with the LDL receptor, is a backup pathway for clearance of plasma cholesterol.[27]

Application of combined use of transgenic and gene-targeted mouse models

Since some types of hyperlipidemia may be caused by multiple genetic and environmental factors, single transgenic or gene-knockout mouse models might not reflect the complex situation of the lipid disorder. Thus, generation of mouse models in which multiple genes have been manipulated by transgenic and/or gene-targeted approaches helps to understand the importance of interaction of different gene products in the pathogenesis of the polygenetic hyperlipidemia in humans.

For example, familial combined hyperlipidemia (FCHL) is a common inherited lipid disorder, affecting 1 to 2 per cent of the population in Westernised societies. Individuals with FCHL have increased VLDL and LDL and develop premature coronary heart disease. A mouse model displaying some of the features of FCHL was generated by crossing mice carrying the human apolipoprotein C-III transgene with mice deficient in the LDL receptor.[28] A synergistic interaction between the apolipoprotein C-III and the LDL receptor defects produced large quantities of VLDL and LDL and enhanced the development of atherosclerosis. This mouse model provides some clues for better understanding the origin of human FCHL.

Acknowledgments

I thank Dr. John Taylor for his critical reading of the manuscript, John C.W. Carroll and John Hull for assistance with graphics, Gary Howard and Stephen Ordway for editorial assistance, and Karina Fantillo for help with manuscript preparation. This work was supported in part by an NIH grant HL37063.

References

1. Mahley RW, Huang Y. Apolipoprotein E: From atherosclerosis to Alzheimer's disease and beyond. *Curr Opin Lipidol* 1999; **10**: 207–217.
2. Huang Y, Mahley RW (1999). Apolipoprotein E and human disease. In: Barter PJ and Rye K-A, eds. Plasma Lipids and Their Role in Disease. Amsterdam: Harwood Academic Publishers, 1999: **257**–284.
3. Huang Y, Liu XQ, Rall SC, Jr, Mahley RW. Apolipoprotein E2 reduces the low density lipoprotein level in transgenic mice by impairing lipoprotein lipase-mediated lipolysis of triglyceride-rich lipoproteins. *J Biol Chem* 1988; **273**: 17483–17490.
4. Huang Y, Rall SC, J, Mahley RW. Genetic factors precipitating type III hyperlipoproteinemia in hypolipidemic transgenic mice expressing human apolipoprotein E2. *Arterioscler Thromb Vasc Biol* 1997; **17**: 2817–2824.
5. Huang Y, Schwendner SW, Rall SC, Jr, Sanan DA, Mahley RW. Apolipoprotein E2 transgenic rabbits: Modulation of the type III hyperlipoproteinemic phenotype by estrogen and occurrence of spontaneous atherosclerosis. *J Biol Chem* 1997; **272**: 22685–22694.
6. Huang Y, Schwendner SW, Rall SC, Jr, Mahley RW. Hypolipidemic and hyperlipidemic phenotypes in transgenic mice expressing human apolipoprotein E2. *J Biol Chem* 1996; **271**: 29146–29151.
7. Hemann MT, Fridman JS, Zilfou JT, et al. An epi-allelic series of p53 hypomorphs created by stable RNAi produces distinct tumor phenotypes *in vivo*. *Nat Genet* 2003; **33**: 396–400.
8. Rubinson DA, Dillon CP, Kwiatkowski AV, et al. A lentivirus-based system to functionally silence genes in primary mammalian cells, stem cells and transgenic mice by RNA interference. *Nat Genet* 2003; **33**: 401–406.
9. Grehan S, Tse E, Taylor JM. Two distal downstream enhancers direct expression of the human apolipoprotein E gene to astrocytes in the brain. *J Neurosci* 2001; **21**: 812–822.
10. Shih S-J, Allan C, Grehan S, Tse E, Moran C, Taylor JM. Duplicated downstream enhancers control expression of the human apolipoprotein E gene in macrophages and adipose tissue. *J Biol Chem* 2000; **275**: 31567–31572.
11. Allan CM, Taylor S, Taylor JM. Two hepatic enhancers, HCR.1 and HCR.2, coordinate the liver expression of the entire human apolipoprotein E/C-I/C-IV/C-II gene cluster. *J Biol Chem* 1997; **272**: 29113–29119.
12. Nagy A, Gertsenstein M, Vintersten K, Behringer R. In: Nagy A, Gertsenstein M, Vintersten K, Behringer R, eds, Manipulating the Mouse Embryo: A Laboratory Manual. Cold Spring Harbor: Cold Spring Harbor Laboratory Press 2003.
13. Shimano H, Yamada N, Katsuki M, et al. Overexpression of apolipoprotein E in transgenic mice: Marked reduction in plasma lipoproteins except high density lipoprotein and resistance against diet-induced hypercholesterolemia. *Proc Natl Acad Sci U S A* 1992; **89**: 1750–1754.
14. Redfern CH, Degtyarev MY, Kwa AT, et al. Conditional expression of a G_i-coupled receptor causes ventricular conduction delay and a lethal cardiomyopathy. *Proc Natl Acad Sci U S A* 2000; **97**: 4826–4831.
15. Redfern CH, Coward P, Degtyarev MY, et al. Conditional expression and signaling of a specifically designed G_i-coupled receptor in transgenic mice. *Nat Biotechnol* 1999; **17**: 165–169.
16. Joyner AL (ed.) Gene Targeting: A Practical Approach. Oxford: Oxford University Press, 2000.

17. Raffaï RL, Weisgraber KH. Hypomorphic apolipoprotein E mice. A new model of conditional gene repair to examine apolipoprotein E-mediated metabolism. *J Biol Chem* 2002; **277**: 11064–11068.
18. Purcell-Huynh DA, Farese RV, Jr, Johnson DF, et al. Transgenic mice expressing high levels of human apolipoprotein B develop severe atherosclerotic lesions in response to a high-fat diet. *J Clin Invest* 1995; **95**: 2246–2257.
19. Fazio S, Lee Y-L, Ji Z-S, Rall SC, Jr. Type III hyperlipoproteinemic phenotype in transgenic mice expressing dysfunctional apolipoprotein E. *J Clin Invest* 1993; **92**: 1497–1503.
20. Huang Y, Liu XQ, Rall SC, Jr, Taylor JM, von Eckardstein A, Assmann G, Mahley RW. Overexpression and accumulation of apolipoprotein E as a cause of hypertriglyceridemia. *J Biol Chem* 1998; **273**: 26388–26393.
21. de Silva HV, Lauer SJ, Wang J, Simonet WS, Weisgraber KH, Mahley RW, Taylor JM. Overexpression of human apolipoprotein C-III in transgenic mice results in an accumulation of apolipoprotein B48 remnants that is corrected by excess apolipoprotein E. *J Biol Chem* 1994; **269**: 2324–2335.
22. Plump AS, Smith JD, Hayek T, et al. Severe hypercholesterolemia and atherosclerosis in apolipoprotein E–deficient mice created by homologous recombination in ES cells. *Cell* 1992; **71**: 343–353.
23. Zhang SH, Reddick RL, Piedrahita JA, Maeda N. Spontaneous hypercholesterolemia and arterial lesions in mice lacking apolipoprotein E. *Science* 1992; **258**: 468–471.
24. Ishibashi S, Brown MS, Goldstein JL, Gerard RD, Hammer RE, Herz J. Hypercholesterolemia in low density lipoprotein receptor knockout mice and its reversal by adenovirus-mediated gene delivery. *J Clin Invest* 1993; **92**: 883–893.
25. Weinstock PH, Bisgaier CL, Aalto-Setälä K, et al. Severe hypertriglyceridemia, reduced high density lipoprotein, and neonatal death in lipoprotein lipase knockout mice. Mild hypertriglyceridemia with impaired low density lipoprotein clearance in heterozygotes. *J Clin Invest* 1995; **96**: 2555–2568.
26. Rohlmann A, Gotthardt M, Hammer RE, Herz J. Inducible inactivation of hepatic LRP gene by Cre-mediated recombination confirms role of LRP in clearance of chylomicron remnants. *J Clin Invest* 1998; **101**: 689–695.
27. Ishibashi S, Herz J, Maeda N, Goldstein JL, Brown MS. The two-receptor model of lipoprotein clearance: Tests of the hypothesis in 'knockout' mice lacking the low density lipoprotein receptor, apolipoprotein E, or both proteins. *Proc Natl Acad Sci U S A* 1994; **91**: 4431–4435.
28. Masucci-Magoulas L, Goldberg IJ, Bisgaier CL, Serajuddin H, Francone OL, Breslow JL, Tall AR. A mouse model with features of familial combined hyperlipidemia. *Science* 1997; **275**: 391–394.

4

Bone marrow transplantation: the methodology and its application in Atherosclerosis research

Menno P.J. de Winther and **Marten H Hofker**

Dept. of Molecular Genetics, Maastricht University, Maastricht, The Netherlands

Introduction

General

All cellular components of the blood originate from hematopoietic stem cells in the bone marrow. These pluripotent stem cells give rise to two lineages of specialised cells (Figure 4.1), the lymphoid lineage producing mainly B and T cells and the myeloid lineage giving rise to monocytes, erythroblasts (the precursors of erythrocytes) and megakaryocytes (which produce platelets).[1]

Transplantation of the hematopoietic systems offers the unique opportunity to replace genes in cells originating from the bone marrow. Murine recipients can be provided with a complete new permanently functioning hematopoietic system after transplantation with donor bone marrow. The transplantation results in a replacement of the recipient cells by cells from a donor of choice, establishing a new hematopoietic system, including new monocytes and tissue macrophages.

The bone marrow microenvironment is a complex structure where hematopoietic stem cells proliferate, mature, differentiate, migrate into the sinusoidal space and enter the circulation in a strictly regulated fashion. After entering the circulation, bone marrow cells keep their capacity to repopulate the bone marrow. This feature is called 'homing' and is essential for bone marrow transplantation.[2] Upon

A Handbook of Mouse Models of Cardiovascular Disease Edited by Qinbo Xu

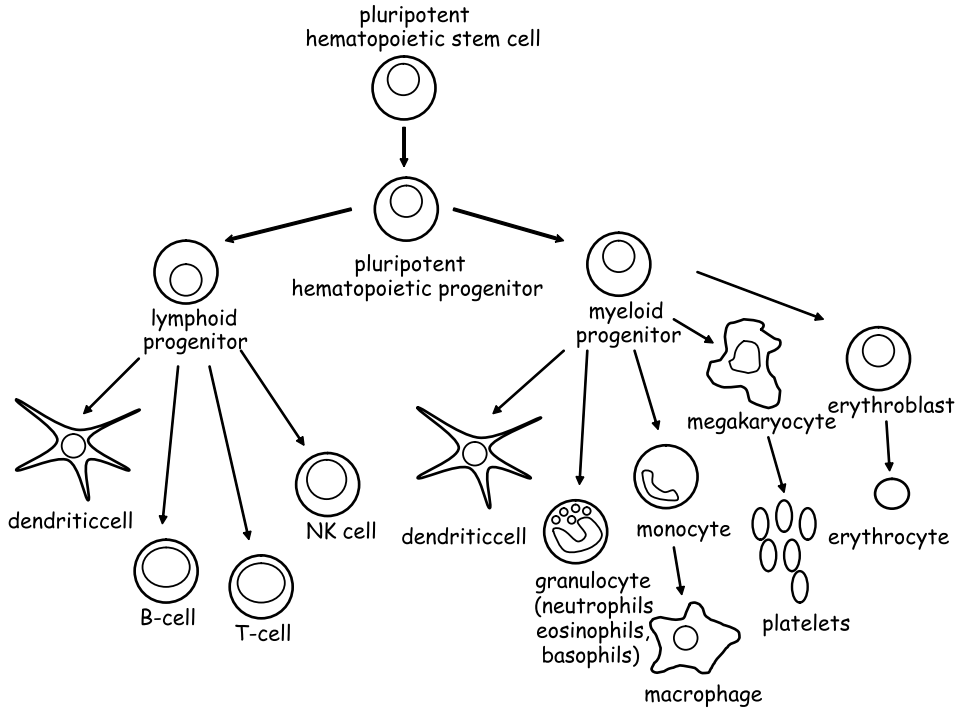

Figure 4.1 The hematopoietic system. Indicated are the lineages that derive from the hematopoietic stem cells and the leukocytes that differentiate from it

transplantation, the stem cells must 'home' themselves to the extravascular compartment of the bone marrow. This can only be achieved if the endogenous stem cells are eradicated, which is usually done by a lethal dose of total body irradiation (TBI) of the recipient. Without donor bone marrow cell transplantation after TBI, the recipient will die within two weeks. Bone marrow aplasia will develop in about 2–3 days and atrophy can be observed in the lymphatic tissues of the lymph nodes, spleen, intestinal tract and the thymus. In two weeks time a strong depression of lymphocytes, granulocytes, thrombocytes, and finally erythrocytes will develop. In the second week after irradiation without transplantation, depletion of the thrombocytes and leukocytes usually results in the death of the mouse due to hemorrhages and septicemia.[3]

However, following administration of donor bone marrow after TBI, repopulation of the marrow will occur and the recipient can survive. Two distinct phases of engraftment can be distinguished. The initial rescue of the hematopoietic system is mediated by committed progenitors, the final long-term recovery owes to the establishment of pluripotent stem cells in the marrow.[4] Four days after administration of the donor cells, repopulation starts through homing of the cells to the marrow cavity. The mechanisms for this homing are not well understood but probably involve integrins.[2] By the 7th day after transplantation, the bone marrow cell population

is completely restored. Peripheral blood cell counts will return to normal levels after 4 weeks, with the number of mononuclear cells being depressed for the longest.

One of the major complications of bone marrow transplantations is graft-versus-host disease (GVHD), in which allogenic bone marrow recognises the tissues of the recipient as foreign, causing a severe inflammatory disease, often resulting in death. These complications are mediated by donor T cells. The easiest way to prevent GVHD is to match the most relevant tissue antigens (major histocompatibility complex; MHC) of the donor with that of the recipient. This is usually established by matching the genetic background of the donor and recipient mice.

Below we will discuss the technique of bone marrow transplantation. This method is especially useful if monocyte or macrophage functions are studied. Conventional bone marrow transplantation will result in replacement of the monocyte/macrophage system in the mice. In addition to the technical procedure of the bone marrow transplantation we will discuss a method to determine the chimerism after transplantation by Taqman analysis of white blood cells and a protocol to examine the leukocytes after transplantation and recovery of the mice is included.

Methods

Bone marrow transplantation

Bone marrow transplantations involve the following steps: preparation of the acceptor mice by semi-sterile housing and antibiotics administrations; irradiation of the acceptor mice to eradicate the original bone marrow cells; isolation and transfer of donor bone marrow cells; engraftment of the donor bone marrow cells and recovery of the animals; execution of the atherosclerosis experiment, as desired. The steps are schematically shown in Figure 4.2 and will be discussed in more detail below.

Preparation of acceptor mice

Seven days before the bone marrow transplantation the acceptor animals are transferred to semi-sterile conditions (e.g. filter-top cages). All subsequent animal handling (i.e. changing of cages, water and food and transplantations) are performed in cross-flow cabinets. The animals are fed regular chow diet that has been irradiated by the supplier to sterilise it. The drinking water of the animals is replaced with autoclaved acidified water (with HCl to pH 2.0) that has been supplemented with neomycin (100 mg/l) and polymyxin B sulfate (60.000 U/l). These antibiotics will eliminate a large part of the gut flora and this has been shown to enhance engraftment and reduce GVHD after transplantation. The animals are kept on the antibiotics until the donor bone marrow has fully engrafted and the mice have recovered from the transplantation, which is normally about 4 weeks after transplantation.

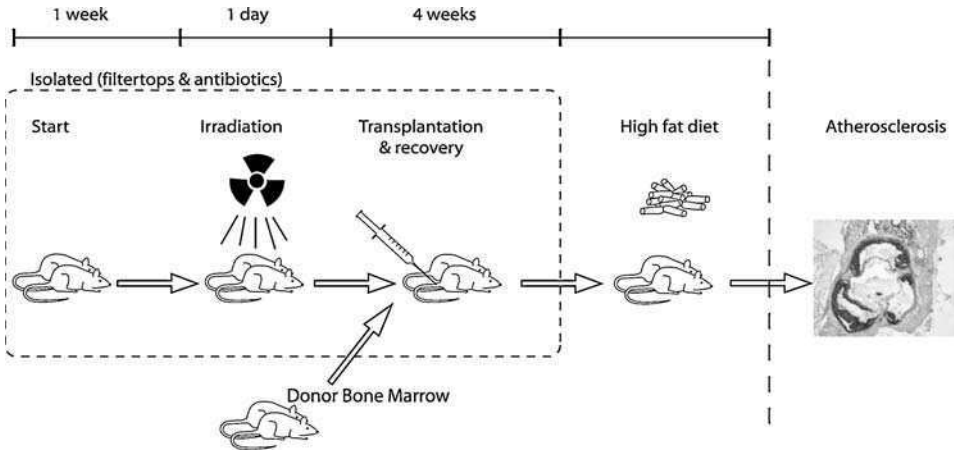

Figure 4.2 Schematic representation of a typical atherosclerosis bone marrow transplantation. Indicated are the different steps through the transplantation. The high fat feeding period to induce atherosclerosis is preceded by a period under isolated circumstances (i.e. in filter-top cages and with antibiotics), during which the actual transplantation and recovery is performed (drawing by S.A.I. Ghesquiere)

Radiation of the acceptor mice

In a cross-flow, the acceptor mice (e.g. $LDLR^{-/-}$ mice) are transferred from their filter-top cages to an irradiation box, which can be a plastic box suitable for five to ten mice. It is important that such a box is completely covered by the field of the X-ray when placed underneath the Röntgen source and that it is so flat that it keeps the mice in a level plane (i.e. the distance from the mice to the source does not change during the irradiation). Then, the mice are subjected to a lethal dose of total body irradiation using a röntgen source. Currently, in our lab we use 10 Gy as the optimal dose but this should be determined empirically. Testing several doses of irradiation followed either by no-transplantation and analysis of survival or by transplantation and analysis of chimerism and circulating leukocytes (see below) after 4 weeks will be essential. After the irradiation, mice are transferred, in the cross flow, back to their filter-top cages.

Isolation of bone marrow cells

On the day of the transplantation (i.e. one day after irradiation) the donor mice are killed by cervical dislocation or CO_2 asphyxiation. After removal of the skin, the hind legs are removed from the animals by cutting into the hip joint, careful not to damage the femur. The femurs and tibia are isolated from the legs by removing as much muscle tissue as possible. The bones are then transferred to ice-cold phosphate-buffered saline (PBS) and taken to a flow cabinet. Next, the bones are sterilised by submerging them for 30 s in

70 per cent ethanol in a Petri dish, after which they are transferred back to new sterile PBS in a Petri dish. The bone marrow is removed from the bones by taking them between forceps, cutting off the ends and flushing them with sterile PBS, using a 10 ml syringe with a 25G needle. The bone marrow is collected in a 50 ml tube. This is repeated for all the bones. Then the cells are made into single cell suspension by first passing them through a 19G needle and transfer to a new tube followed by passage of the cells through a 25G needle and transfer to again a new 50 ml tube. The isolated cells are then counted using a standard hemocytometer. We generally collect 2–4 $\times$ 10^7 cells/donor mouse. Finally, the cells are spun down at 1000 r.p.m. for 5 min at 4 °C, resuspended in RPMI-1640 / 2% FCS / 5 U/ml heparin at a density of 5 $\times$ 10^7 cells/ml and kept on ice.

Transplantation of the bone marrow cells

After isolation of the donor cells the acceptor mice are transplanted with the donor bone marrow. In the cross flow cabinet the mice are injected in the tail vein with 100 µl of donor cell suspension, using a 1 ml syringe with a 27G needle. Hereby, $\sim$5 $\times$ 10^6 cells are transplanted. More easy identification and injection of the tail vein can be accomplished by putting the mice under infrared heat-lamps 5 min before injection. Four weeks after transplantation, the mice may be removed from the filter-top cages, drinking water can be regular again and experiments may start.

Determination of chimerism by taqman analysis

Ideally, complete chimerism is established, meaning that all hematopoietic cells of the recipient mouse are of donor origin. However, sometimes engraftment is incomplete. Therefore, it is important to establish the amount of chimerism in the recipients. This can be done, for example, by transplanting female recipient mice with male donor bone marrow and quantitatively genotyping the bone marrow after transplantation for the presence of Y-markers. Also other genetic differences between donors and recipients can be used to quantify chimerism.

To determine the chimerism in our transplanted mice we take advantage of the fact that the donor bone marrow is wild type for the LDL receptor ($LDLR^{+/+}$) while our recipient mice are $LDLR^{-/-}$. Genomic DNA is isolated using the GFX Genomic DNA Purification Kit (Amersham Pharmacia Biotech.). A standard curve is generated using DNA from $LDLR^{-/-}$ and $LDLR^{+/+}$ bone marrow cells, mixed at different ratios. Chimerism is determined by quantifying the amount of $LDLR^{-/-}$ DNA in samples from 40 µl peripheral blood. To standardise for the amount of input DNA, a non-relevant gene is quantified (nuclear factor (NF)κB1). The samples are assayed in duplicate using the TaqMan Universal PCR Master Mix and the 7700 Sequence Detector (Applied Biosystems) using 300 nM primer and 200 nM probe. The $LDLR^{-/-}$ specific primer/probe set is: forward 5′-GCTGCAACTCATCCA TA TGCA-3′; reverse 5′-GGAGTTGTTGACCTCGACTCTAGAG-3′; probe 5′-6FAM-CCCCAGTCTTTGGGCCTGCGA-TAMRA-3′. The NFκB1 specific primer/probe

set is: forward 5′-AACCTGGGAATACTTCATGTGACTAA-3′; reverse 5′-GCACC AGAAGTCCAGGATTATAGC-3′; probe 5′-TET-TCCGTGCTTCCAGTGTTTCA AATACCTTTTT-TAMRA-3′. The data are analysed using the Sequence Detection Software. A standard curve is generated by plotting the mean delta $C_t(C_{tP50} - C_{tldlr}{}^{-/-})$ of duplicates against the logarithm of the percentage *LDLR*$^{-/-}$ DNA present and calculation of a regression line. Chimerism is calculated from the percentage of *LDLR*$^{-/-}$ DNA in the blood samples (representing the remaining recipient bone marrow), determined by applying the mean delta C_t of the sample to the standard curve.

Analysis of leukocytes after bone marrow transplantation

To characterize the leukocytes after engraftment of the bone marrow, Fluorescence-activated cell sorting (FACS) analysis of the blood is performed. Approximately 50 µl of blood is collected from each mouse in a tube with a drop of heparin. After collection all samples are split in two, sample A and sample B, and transferred to 96-well V-bottom plates and kept on ice for the rest of the procedure. To each well, 150 µl of ice-cold lysis buffer (8.32 g/l NH_4Cl and 0.84 g/l $NaHCO_3$) is added and incubated for 10 min. Spin the plate, for 5 min at 1100 r.p.m. Discard the supernatant and repeat the lysis if red blood cells are still visible. After the final lysis the cells are resuspended in antibody staining solution (5 per cent normal mouse serum plus 2 per cent fetal calf serum (FCS) in ice-cold PBS with the addition of the appropriate antibodies). Sample A of each mouse is stained for monocytes and granulocytes (Mac1-PE, 1 : 300 and Gr1-FITC, 1 : 750) and sample B for B- and T-cells (6B2-PE, 1 : 300 and KT-3-FITC, 1 : 300; all antibodies from BD-Pharmingen). All samples are incubated for 30 min on ice. After the incubation they are washed three times with ice-cold PBS–2 per cent FCS, by resuspending the cells, spinning (5 min, 1100 r.p.m.), discard the supernatant, etc. After the final wash, the cells are resuspended in PBS and analysed by FACS. In sample A monocytes are identified as $Mac1^+$ and $Gr1^-$ cells, while the granulocytes are both $Mac1^+$ and $Gr1^+$. In sample B, B cells are $6B2^+$ and $KT3^-$, while the T-cells are $6B2^-$ and $KT3^+$.

Using this procedure relative numbers (percentages) of the different leukocytes can be obtained. Absolute values can be obtained by the inclusion of TruCount beads (BD biosciences) according to manufacturers' instructions.

Discussion and application

Role of BMT in gene–gene interaction studies

Leukocytes play a very important role in cardiovascular disease, and in particular in atherosclerosis. BMT technology has been pivotal to further understand this role. To study atherosclerosis, susceptible strains are being used as recipients to provide an atherosclerosis sensitive background. In particular the low density lipoprotein receptor (LDLR) knockout mouse has proved itself as a crucial mouse model. Wild type mice are highly resistant to develop atherosclerosis, because their metabolism of atherogenic lipoproteins is very fast. Therefore, most of the cholesterol

in the mouse plasma resides in the anti-atherogenic HDL particles and the levels of proatherogenic low density lipoprotein (LDL) and very low density lipoprotein (VLDL) remnants are extremely low. The LDLR knockout mouse is impaired in the clearance of LDL and VLDL remnant particles. Upon high fat feeding, this mouse model will rapidly develop diet-induced hyperlipidemia and atherosclerosis. On this background strain the role of a host of other processes has been studied, including inflammation, immunity, lipid transport, and apoptosis. The use of the LDLR knockout mouse model as a susceptible strain is often preferred over the apolipoprotein E (ApoE) knockout mouse, which is another widely used mouse model for atherosclerosis. However, the latter mouse requires that the donor cells are deficient for ApoE as well. Interestingly, one of the first applications of BMT in the field of atherosclerosis demonstrated that in the ApoE-deficient mouse wild type bone marrow cells can slow down atherogenesis due to the lowering of plasma lipid levels by macrophage produced ApoE.[5] Eventually this finding led to the discovery that macrophage ApoE protects against the development of foam cell lesions, even in the presence of a hyperlipidemic phenotype. Other, more complex combinations can be made, where the host background and the donor cells can have mutations in other pathways, in addition to the lipid metabolism. Hence, the BMT approach allows excellent opportunities to study gene–gene interactions.

BMT allows efficient use of resources

Technologically, it is possible to perform the experiments described above using transgenic mice whereby the genetic alteration is confined to a specific cell type and specific phase of development. Such models make use of the *Cre–LoxP* system to induce deletions between *LoxP* sites using the *Cre* recombinase expressed in a tissue specific and/or inducible manner. The *Cre–LoxP* system works highly efficiently. However, a drawback of the system is that the breeding costs are sometimes difficult to control, because it requires mice carrying simultaneously five loci, i.e. homozygosity for the *LoxP* mutation and the *LDLR* knockout allele, and one *Cre*-allele. To generate mice with five predetermined alleles often requires several rounds of breeding, which may take more then a year to establish. In contrast, having the gene of choice crossed with a Cre recombinase, followed by BMT to the *LDLR* knockout model is much more cost and time efficient. Only a very small number (we generally use five donor mice for 20 acceptor animals) of *LoxP–Cre* animals are needed for transplantation to *LDLR* mice that can be purchased from most commercial suppliers. Moreover, the BMT technology also helps to confine the genetic alteration within the white blood cells. This is very helpful if a transgenic or knockout model has been engineered where the genetic alteration affects a broad range of cell types. Using BMT, the leukocyte-specific role of such genes in atherosclerosis can be studied.[6] Moreover, BMT also allows studying genetic alterations that compromise mouse development. In this respect, the generation of chimeric mice carrying a homozygous peroxisomal proliferator agonist receptor gamma (PPARγ) gene disruption was possible using the fetal liver as a donor for the white blood cells.[7]

A possible caveat is that some genes of interest may also play a role in the proper development of the white-blood cell compartment. However, despite the wide use of BMT to study a wide range of genes, it has not been identified as an important obstacle. Hence, BMT has proved itself as a robust and highly efficient tool to study the complex etiology of atherogenesis.

Genetic modification of stem cells

A more recent development will stimulate the application of BMT even further. For many years, BMT has been vigorously pursued as a potential route for gene therapy. Similarly, are able to genetically alter the bone marrow before transplantation, rather than using different mouse strains. Although at present this approach is not widely used, there are several reports in the field of atherosclerosis research showing that this is a promising approach. Ishiguro *et al.* made use of a retroviral vector expressing apolipoprotein A1 (ApoA1)[8] to show that promoting cholesterol efflux from the macrophage is anti-atherogenic. More recently, Bot *et al.*[9] was able to knock-down the chemokine receptor CCR2 gene using lentiviral transduction of an RNAi vector to silence gene expression. These recent advances have become possible owing the development novel of approaches that allow targeting the stem cells using efficient tissue culture conditions and advanced retroviral vectors. Eventually, these approaches may even lead to novel therapeutic strategies that specifically target the role of the white blood cells in atherosclerosis.

Tissue macrophages

Upon BMT, also the macrophages that enter specific tissues have been modified and allow investigating the role of macrophages and genes in tissue remodeling other than the vessel wall. Of particular interest is the investigation of the role of macrophages lacking IκB kinase 2 (IKK2) function. It has been shown that in a mouse model for diabetes, the mice are protected when carrying a macrophage specific *IKK2* knockout allele.[10] The decreased susceptibility to develop diabetes is most likely caused by a reduced capacity of the macrophages to participate in tissue remodelling and sustain a low grade inflammatory response. In these experiments an important role for macrophages present in or recruited to the fat tissue is very likely. Additional research to further understand the role of tissue macrophages in metabolic disease is very much helped by the BMT technology.

Conclusions

BMT has proved itself as a robust technology to study the function of leukocytes in cardiovascular diseases. Over the past years, the strong emphasis on genetically pure mice – mostly C57B/6J – has reduced the genetic variation within the experiment.

Similarly, the measures to limit the levels of pathogens within the mouse colonies have been crucial to further improve the quality of animal experiments. Both conditions have improved the reproducibility of these experiments and were also highly beneficial to allow the BMT technology to become the method of choice when studying gene–gene interactions and leukocyte functions in cardiovascular disease. While the various transgene and knockout mouse strains provide a large resource for dissecting the genetic pathways that govern atherosclerosis, new approaches which make use of *in vitro* genetically modified bone marrow stem cells are likely to receive more attention. Particularly BMT in combination with the RNAi gene silencing, which is now a robust strategy,[11] is likely to be a very powerful and versatile technology to study the role of novel leukocyte genes in atherosclerosis.

References

1. Janeway CA, Travers P, Walport M, Capra, DJ (eds) Immunobiology, 4th edn. London/New York: Elsevier Science Ltd/Garland Publishing, 1999.
2. Vermeulen M, Le Pesteur F, Gagnerault MC, Mary JY, Sainteny F, Lepault F. Role of adhesion molecules in the homing and mobilization of murine hematopoietic stem and progenitor cells. *Blood* 1998; **92**: 894–900.
3. Van Bekkum DW, Lowenberg B (eds) Bone marrow transplantation. New York: Marcel Dekker Inc., 1985.
4. Jones RJ, Celano P, Sharkis SJ, Sensenbrenner LL. Two phases of engraftment established by serial bone marrow transplantation in mice. *Blood* 1989; **73**: 397–401.
5. Linto MF, Fazio S. Macrophages, lipoprotein metabolism, and atherosclerosis: insights from murine bone marrow transplantation studies. *Curr Opin Lipidol* 1999; **2**: 97–105.
6. Kanters E, Gijbels MJJ, van der Made I, et al. Hematopoietic NF-κB1 deficiency results in small atherosclerotic lesions with an inflammatory phenotype. *Blood* 2004; **103**: 934–940.
7. Chawla A, Barak Y, Nagy L, Liao D, Tontonoz P, Evans RM. PPAR-gamma dependent and independent effects on macrophage-gene expression in lipid metabolism and inflammation. *Nat Med* 2001; **7**(1): 48–52.
8. Ishiguro H, Yoshida H, Major AS, Zhu T, Babaev VR, Linton MF, Fazio S. Retrovirus-mediated expression of apolipoprotein A-I in the macrophage protects against atherosclerosis *in vivo* J Biol Chem 2001; **276**: 36742–36748.
9. Bot I, Guo J, Van Eck M, et al. Lentiviral shRNA silencing of murine bone marrow cell CCR2 leads to persistent knockdown of CCR2 function *in vivo*. *Blood* 2005; **106**(4): 1147–53.
10. Arkan MC, Hevener AL, Greten FR, Maeda S, Li ZW, Long JM, Wynshaw-Boris A, Poli G, Olefsky J, Karin M. Ikk-beta links inflammation to obesity-induced insulin resistance. *Nat Med* 2005; **11**(2): 191–8.
11. Brummelkamp TR, Bernards R, Agami R. Division A system for stable expression of short interfering RNAs in mammalian cells. *Science* 2002; **296**(5567): 550–3.

5

Hyperlipidemia-induced Atherosclerosis

Alan Daugherty and **Debra L. Rateri**

Cardiovascular Research Center, University of Kentucky, Lexington, KY, USA

Abstract

Hyperlipidemic mice have become the predominant models in atherosclerosis research. Early studies using inbred mice were restricted by the need for severe dietary manipulations that generated diminutive lesions. The use of mice gained wider acceptability following the generation of genetically manipulated mice with enhanced susceptibilities for atherosclerotic lesion formation. The atherosclerotic lesions formed in these mice mimic several facets of the human disease. Mice with deficiencies of either apolipoprotein E or LDL receptors have been the most extensively researched to determine the effects of pharmacological and genetic interventions on lesion size and composition. This chapter will overview issues in the design of experimental studies using these mice. These include discussion of comparisons of the most common mouse models of atherosclerosis, the composition of the dietary stimulus to induce hyperlipidemia, the strain background of mice, the mode of atherosclerotic lesion analysis, methods for characterizing cellular compositions of lesions, and application of appropriate statistical tests. Mouse models have provided considerable insight into mechanisms of atherosclerotic lesion development.

Keywords

mice, cholesterol, atherosclerosis, saturated fat

Introduction

Atherosclerosis is the underlying cause of a majority of cardiovascular diseases, such as acute coronary syndrome and stroke. It is a complex process that develops in specific regions of arteries over protracted intervals. A commonly proposed sequence of atherosclerotic lesion development is as follows:

A Handbook of Mouse Models of Cardiovascular Disease Edited by Qinbo Xu

1. Lipoproteins are deposited in the subendothelial space and become modified to a form that promotes a monocyte chemoattractant response.

2. Monocytes attach to atherosclerosis-prone sites where they subsequently undergo diapedesis through an intact endothelial barrier.

3. Macrophages in the subendothelial space accumulate intracellular lipid. Also T lymphocytes are found in abundance at the site of macrophage recruitment.

4. Smooth muscle cells migrate and proliferate in the subendothelial space.

5. A hypocellular, lipid-rich core evolves as smooth muscle cells form a fibrous cap on the lumen surface of lesions.

6. At later stages, the fibrous cap thins and subsequently fractures to precipitate the development of thrombi. Alternatively, an erosive process can lead to the development of thrombi on the surface of lesions.

While this, and similar schemes, are commonly presented, there are many questions regarding the uniformity of this sequence in humans.[1] This uncertainty is attributable to several issues, including the chronicity and complexity of lesion development, the difficulty of acquiring tissues, and the shortcomings of currently available modalities for noninvasive characterization of arteries.

Given the prevalence of this disease, and its devastating consequences, there is a great need for animal models that recapitulate the human disease. Since the first description of experimental atherosclerosis in rabbits, many species have been models of the disease. Mice are a relatively recent species to be used as models of atherosclerosis. However, they are now the predominantly used species. This increased popularity is partly attributable to the practical and economic benefits of a small animal model, and also the relative ease of manipulating their genetics to define specific pathways in the atherogenic process.

As with most animal models of atherosclerosis, all mouse models require hyperlipidemia to generate lesions.[2] Hyperlipidemia in mice may be induced by diet, genetic manipulation, or a combination of both. The purpose of this chapter will be to discuss the relative merits of the most commonly used mouse models of atherosclerosis and provide an overview for the practical issues of lesion analysis.

Induction of Hyperlipidemia in mice

Diet

High density lipoproteins (HDL) are the only lipoproteins present in plasma of mice fed normal laboratory diets. Atherosclerosis is induced by the presence of cholesterol-delivering lipoprotein fractions such as chylomicron remnants, very low

density lipoproteins (VLDL), and low density lipoproteins (LDL). Early studies used severe dietary manipulations to increase plasma concentrations of cholesterol-delivering lipoproteins and induce atherosclerosis. These diets manipulated three components: saturated fat, cholesterol, and cholate.[3] This approach was designed to increase plasma concentrations of VLDL and LDL by increasing cholesterol absorption and endogenous synthesis, while decreasing cholesterol secretion. Diets that are enriched in saturated fat and cholesterol are still commonly used in contemporary atherosclerosis studies. Most of the diets are enriched in saturated fat to a level of 21 per cent wt/wt (42 per cent of calories). The most common supplier of this diet is Harlan Teklad (Catalog #TD88137). Saturated fat is derived from several sources, the most common from milk, coconut, or lard. The consequences of these different sources of saturated fat have not been systematically evaluated. Finally, cholesterol has been enriched in diets to different extents that usually range from 0.15 to 1.25 per cent wt/wt. Again, systemic studies are lacking on the effects of cholesterol enrichment.

In the era prior to genetic manipulation of mice, the inclusion of cholate was a critical component of hyperlipidemia-induced atherosclerosis. However, the inclusion of cholate has become a contentious issue. Although its presence enhances hypercholesterolemia, there is concern that cholate may directly promote inflammatory responses. Thus, the inclusion of cholate has invoked the criticism for its potential toxic role in inducing lesions by mechanisms that are not relevant to human disease. Clearly, the inclusion of cholate in diets does promote an inflammatory response. However, whether this is a direct effect of cholate or secondary to disturbances in cholesterol metabolism has not been defined. Furthermore, since inflammatory responses are now considered to be important mechanisms of atherosclerosis, the relevance of cholate induced responses cannot easily be dismissed. However, given the concern on the inclusion of cholate, it is preferable to omit it from diets in atherosclerosis studies.

Genetic manipulation

The most commonly used genetic manipulations in mouse atherosclerosis models are those that have increased plasma concentrations of VLDL and LDL. Deletion of apolipoprotein E (ApoE) was one of the initial approaches to induce atherogenic hyperlipidemia.[4,5] ApoE, a ligand present on chylomicron remnants and VLDL, interacts with receptors responsible for removal of these particles from plasma. Thus, ApoE deficiency promotes hypercholesterolemia even when mice are fed a normal laboratory diet. VLDL and LDL account for the majority of particles in the plasma cholesterol distribution in $ApoE^{-/-}$ mice. The composition of these lipoproteins is unusual in regard to both their apolipoprotein and lipid composition. For example, the VLDL fraction from these mice contains an unusual enrichment of ApoA1 and unesterified cholesterol. (Table 5.1)

Another most commonly used mouse model of atherosclerosis is deficiency of the LDL receptor.[6] LDL receptor deficiency is an uncommon human genetic condition

that results in grossly elevated plasma concentrations of LDL cholesterol. In humans afflicted with the homozygous forms of this deficiency, fatal atherosclerosis will developed by the second decade of life. In contrast, mice with LDL receptor deficiency are only modestly hypercholesterolemic. This may be due to the lesser dependency of mice on LDL receptors to removal atherogenic lipoproteins. It should also be noted that the genetic deficiency of the LDL receptor-deficient mice differs from that of humans or Watanabe heritable hyperlipidemic rabbits. In humans or rabbits, there is no functional LDL receptors in patients afflicted with a homozygous form of this deficiency. In the case of mice, the gene was truncated at exon 4. Since the receptor binding region is presumably still synthesised in these mice, this may have a currently uncharacterised effect on plasma lipoproteins. In contrast to LDL receptor deficient humans, atherosclerosis has not been detected in mice lacking this gene when fed normal diet, except in later stages of life.

Mouse strain

Early studies demonstrated that different mouse strains have widely different susceptibilities to the development of atherosclerosis. In non genetically manipulated mice, the C57BL/6 strain is the most susceptible to lesion formation, and consequently, this background is universally used in atherosclerosis studies.

In genetically manipulated mice, it is clear that strain background of the mouse is also a powerful modifier of the extent of atherosclerotic lesion formation. The strain dependent effects are not attributable to changes in plasma lipoprotein concentrations, but instead are due to differences at the level of the aorta. For example, ApoE deficiency in C3H mice have much smaller lesions than in C57BL/6, despite equivalent hypercholesterolemia.[7] Thus, strain background is a critical factor for interpretation of results and comparison between studies. Genetically targeted mice are commonly produced using stem cells from strains such as 129Sv/Ev. As a consequence, studies on recently developed genetically engineered mice have been frequently performed on hybrid mice of different strains. Currently, the ApoE$^{-/-}$ and LDL receptor$^{-/-}$ mice available from the Jackson Laboratory have been backcrossed at least 10 times into a C57BL/6 background.

Although the background strain of atherosclerosis-susceptible mice is now commonly defined, this can be a major issue when compound genetically deficient mice are developed to study a lesion modifier gene. In these studies, the experimental purpose is to define the effects of a single gene difference on atherosclerotic lesion development. Thus, the interpretation of studies will be compromised if the strain background of the single and compound deficient mice are not identical. Knowledge of the strain background of the mice is particularly important when the single and compound deficient mice are maintained as separate colonies. Currently, it is common to accept the equivalence of strains if both the genetically engineered mice used to generate the compound deficient mice have been backcrossed 10 times in a C57BL/6 background. The Jackson Laboratory and other commercial suppliers have genetic screening services that provide an indication of the percentage of genes that are of C57BL/6 origin. However, for practical reasons these services provide a

relatively small number of chromosomal markers. Consequently, these services will not fully validate all chromosomal regions, particularly those in the proximity of the genetically manipulated region. Also, genetic drift may occur in inbred colonies, and thus separate breeding colonies of single and compound deficient mice have the potential to acquire properties that may influence atherosclerosis development, independent of the genetically engineered effect.

The use of littermates circumvents the potential problem of different strain backgrounds imparting effects that may mask or exacerbate a specific genetic manipulation. For this approach to breeding, the common strategy is to maintain parental lines that are homozygous for the atherosclerosis-susceptible genotype (for example, Apoe$^{-/-}$ or LDL receptor$^{-/-}$) and heterozygous for the gene of interest. This approach offers theoretical advantages of identifying the specific effects of a gene manipulation, rather than an effect attributable to variances in strain background. It also provides mice that are wild type, hetero-, and homozygous for the gene of interest to enable determination of gene dosage effects. However, there are some practical compromises. These include large breeding colonies to obtain the required number of wild type and homozygous mice. Also, there is a greater technical burden, since all offspring from this breeding strategy must be genotyped.

Environmental factors

Many animal facilities now house mice under barrier conditions. These sterile environments are obviously important from an institutional perspective in applying infection control to colonies. There are few formal studies that define the effects of sterile environments versus those that are usually termed as 'conventional.' However, there is anecdotal evidence that the extent of atherosclerosis and the mode of responding to an intervention may be altered by the housing environment.

Gender

There is some evidence that, contrary to humans, female mice may develop larger atherosclerotic lesions than males. Despite this premise, an overview of the literature, in which genders have been compared, indicates that there are no consistent gender difference in lesion size in either ApoE$^{-/-}$ or LDL receptor$^{-/-}$ mice. However, there have been many examples of gender-specific responses to interventions. These include administration of PPAR gamma agonists and interferon-gamma deficiency.[8,9] Therefore, we always analyse data on a gender-specific basis. Also, if possible, we include both genders when determining the effects of a specific intervention.

Analysis of Atherosclerotic lesions

There are two common methods of quantifying atherosclerosis in mouse models. Probably the most frequently used method has been to quantify lesion size in the aortic root. This mode of analysis was initially described for mouse atherosclerosis in

the much cited publication from Paigen and colleagues.[10] Another common method is the quantification of lesions on the intimal surface of the aorta, by a process that is frequently referred to as *en face*. A similar form of analysis was commonly used in larger animal models, prior to its introduction into the mouse atherosclerosis field by Palinski and colleagues.[11] There are also less commonly used forms of analysis such as quantification of the innominate artery.[12]

Aortic root lesion quantification

This form of analysis was described initially by Paigen *et al.*[10] to quantify lesion size formed in C57BL/6 mice fed a diet enriched in saturated fat, cholesterol, and cholate. A novel approach to quantifying lesions was needed, since despite these relatively severe dietary manipulations, small lesions form only in the aortic root of these mice. A detailed technical description of this analysis has been published previously.[13] The analysis of this region can be performed on either paraffin-embedded tissues or frozen tissues. The majority of studies that quantify atherosclerotic lesion size in the aortic root are performed on sections that have been cut using a cryostat. This method is preferred because of the greater ease with which the tissue can be orientated, as discussed later. Also, sections that will be stained for neutral lipids need to be frozen sections, since lipids are removed in the process of embedding tissues in paraffin.

Although similar approaches are used in most studies of the aortic root, there are many specific protocol issues for which there is no general agreement. These include:

1. The number of sections in which lesions are quantified.

2. The specific region of the root in which lesions are analysed (for example, sinus versus ascending aorta, or both).

3. The mode of analysis. For example, the analysis of neutral lipid stained regions *versus* tracing of the discernable intimal and medial boundaries of lesions.

The mode of analysis performed by the author's laboratory is illustrated in Figure 5.1. Hearts are dissected from mice that have been perfused with saline to remove blood. For quantitative analysis, it is preferable to perfuse with fixative at arterial blood pressure. The caveat to this approach is that it severely compromises the characterization of lesions, since many antibody epitopes are masked by fixation. The aorta is cut from the excised heart at the region where it emerges from ventricular tissue on the anterior aspect of the heart. The heart is cut to remove approximately two-thirds of the ventricles. The tissue is then placed in embedding media and frozen. The accuracy of this approach relies on sections being cut perpendicular to the aortic axis. Thus, a critical step in this process is to ensure the orientation of the aorta is perpendicular in the embedding mold.

Frozen tissue blocks are placed in the cryostat and cut until the aortic valves become visible. Since the valves are difficult to see without visual aid, it is

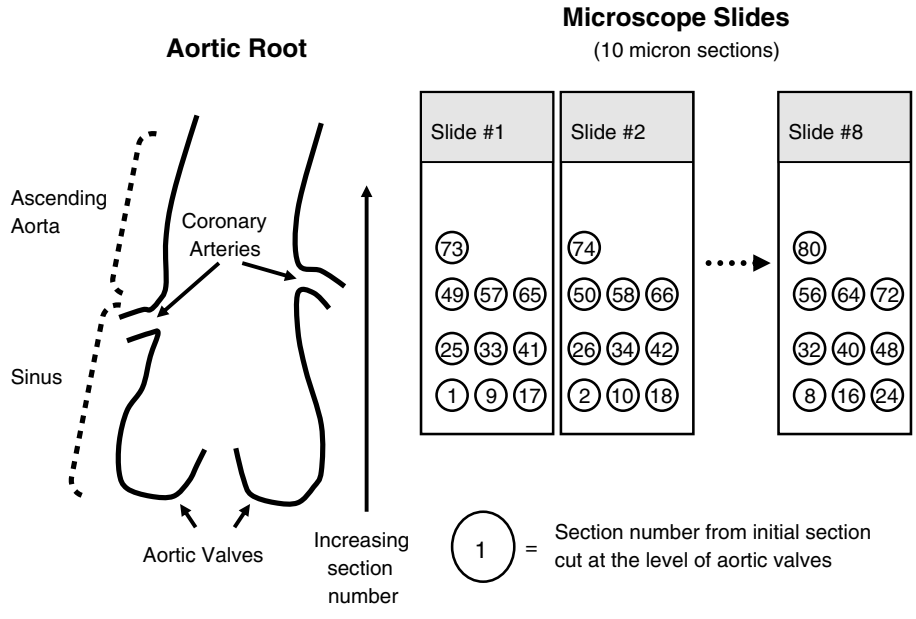

Figure 5.1 Diagrammatic representation of location of aortic root analysis of atherosclerosis and the mode of section layout on slides. For a color version of this figure, please see the images supplied on the accompanying CD

preferable to have a phase microscope in close proximity to permit frequent viewing of sections. Once the aortic valves are present, sections are collected in the manner illustrated in Figure 5.1. Ten micron sections are cut, with the first section being placed in the lower left corner of the first slide, and the second section in this same position on the second slide. This process continues for eight slides. The ninth section is then placed adjacent to the first section of the first slide. This process continues until approximately nine sections are placed on each slide. Upon completion of cutting, each slide has tissue sections at 80 μM intervals throughout the entire aortic root.

Tissue sections can be visualised with standard histological staining. We frequently use just hematoxylin. Sections are occasionally stained with Oil Red O which helps in delineating small lesions in the aortic sinus. For quantification, images of each tissue section on a slide are captured using a standard digital camera. Lesion area measurements on each slide are performed with image analysis software (for example, Image-Pro, Media Cybernetics Inc.) We perform these measurements by manually outlining each lesion as defined by the lumen boundary and the internal elastic lamina. There have been attempts to automate this process, the most common being the determination of the area with Oil Red O staining. This mode can be appropriate if there is uniform neutral lipid staining throughout entire lesions. However, this condition is often not present, especially in more mature lesions that have areas of non-neutral lipid deposition containing unesterified cholesterol and extensive smooth muscle cells.

Following the acquisition of lesion areas on each individual section, we mean the data for sections in the same region. We have found the optimal landmark to normalise the location is the transition point of the aortic sinus and ascending aorta. This is defined as the last section in which aortic valve cusps are visible. This form of analysis permits a graph of the 'topology' of lesions throughout the aortic root. We have found this useful in previous studies since some effects have been limited to the extension of lesions into the ascending aorta. Other interventions may influence the thickness of lesions in the aortic sinus. Subsequent analysis can be performed in which there is a combination of sections to achieve a sum of lesion areas in a defined number of sections. Although there are no publications to date, determination of the lesion area of sequential aortic root sections would permit the determination of lesion volume in this region.

En face lesion quantification

This form of analysis determines lesion area of all, or selected, regions of the aortic intima. For this mode of analysis, we dissect the aorta free from the point that it emerges from the anterior surface of cardiac ventricular tissue through to the ileal bifurcation, as noted above. Aortas are placed in a freshly prepared paraformaldehyde solution (4 per cent wt/wt in phosphate-buffered saline) overnight. Adventitial tissue is removed next day. Complete removal of adventitia can be difficult to achieve, but proficient operators can remove sufficient tissue within 15 min. Aortas are cut as described in Figure 5.2. The initial cut is performed in the lesser aortic curvature and is extended along the length of the vessel to the ileal bifurcation. A second cut is made on the midline of the greater curvature to the level of the subclavian artery. Atherosclerotic lesions in mice can be dislodged from the intimal surface, so care should be taken in the cutting process. The standardisation of these dissection lines is important to maintain a constant region area for lesion analysis.

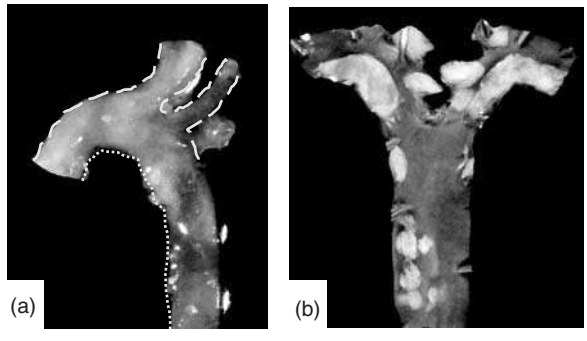

Figure 5.2 En face analysis of atherosclerosis lesions. (a) The dotted and dashed lines indicate the mode of cutting of the aortic arch region. (b) An example of an aorta pinned for image analysis of lesion area. For a color version of this figure, please see the images supplied on the accompanying CD

Aortas are placed on black paper that overlays dental wax. Since there is an interaction between the paper and aorta, a relatively small number of pins (0.2 mm diameter minutien pins, Fine Science Tools, cat #26002-20) will be needed to keep tissues flat. Images are acquired of the intimal surface using a digital camera connected to a dissecting microscope. In our analysis, we routinely acquire photographs of unstained aortas. The staining of neutral lipids, for example using Sudan IV, has the potential to facilitate lesion identification. However, any residual adventitial adipose tissue will be strongly illuminated by neutral lipid staining and will be clearly visible through the translucent mouse aorta. This adventitial staining can confound the identification of lesions. Also, the neutral lipid stain will negate any subsequent analysis of tissue sterols that can be an additional mode of atherosclerotic lesion analysis.

As with the previous mode of analysis, we trace the lesions manually using the grossly discernable margins of lesions. Even with lipid-stained aortas, we have not been able to reliably set a threshold hue to automate lesion area quantification. Since there is some level of subjectivity to the decisions of lesion boundaries, the measurements should be verified by a second operator. In aortas with large atherosclerotic involvement, the distinction of lesion boundaries is clearly defined. Thus, the manual tracing can be completed rapidly and concordance between operators is usually high. In cases in which lesions are small and scattered, the ability to discern lesion boundaries becomes more subjective. In this case, we have two operators independently quantify the area of lesions.

Table 5.1 Comparison of some of the most commonly used mouse models of atherosclerosis when applied to gene manipulations in whole body and bone marrow-derived donor cells

Mouse	Advantages	Disadvantages
C57BL/6	Availability	Requirement for cholate in diet
	Ease of breeding compared to generation of compound deficient mice	Small lesions of simple morphology
$ApoE^{-/-}$	Development of lesions on normal diet	Unusual lipoprotein composition
	Complexity of lesions that can develop containing fibrous caps and necrotic cores	ApoE deficiency may have many confounding effects, for example on immune function
		Limited evidence that ApoE deficiency in humans promotes atherosclerosis
		Use in bone marrow transplantation studies requires donor cells to be $ApoE^{-/-}$
LDL receptor	Rapid development of lesions	Requirement for feeding a modified diet
	Ease of use for bone marrow transplantation studies	Lesions predominantly contain lipid laden macrophages with minimal other components

Data are commonly represented as either absolute lesion area or as a percent of intimal area. Unless there is a change the intimal areas of aortas, in the comparative areas between groups should be the same with both these modes of data representation. During early stages of atherosclerotic development, lesions will be evident mostly in the arch. Thus, quantification of the thoracic and abdominal region may provide rather limited information, except with more advanced disease.

One of the potential shortcomings of this mode of analysis is that area measurements fail to account for any variances in lesion thickness between experimental groups. We have seen in previous studies that large changes in the extent of lesions (defined as thickness or volume) can occur in the absence of any change in coverage of intimal area.[14] Therefore, during image analysis to quantify lesion area, notes should be made regarding lesion appearance, especially in relation to thickness. The evaluation of lesion thickness can be performed using standard histological approaches. However, a systematic evaluation of lesion thickness, even in a restricted area such as the aortic arch, would require the acquisition of many tissue sections and considerable effort. An alternative approach has been to determine the sterol content of the tissue. In unstained paraformaldehyde fixed tissues, sterols can be extracted and quantified using a gas chromatogram or enzymatic technique. In lesions that are predominantly lipid-laden, this provides an index of lesion volume.

Other considerations

Since there are different modes of analyzing atherosclerosis in mice, a question arises as to the relative benefits of measuring lesions in different regions, or if more than one arterial region should be quantified. Since neither the lesions that form in the aortic root or throughout the aortic wall have been implicated in atherosclerosis-induced diseases, it is difficult to rationalise that one area should be prioritised compared to another. Analysis of both areas of the same mouse is plausible, although this increases the workload of an already labor-intensive process. However, if both regions show the same result, this provides greater confidence in the effects of an intervention. In general, effects of interventions on lesions in aortic roots have paralleled those noted by *en face* analysis, although the effects of interventions to reduce atherosclerosis have usually been more profound by *en face* analysis than in the aortic root. There are also a limited number of studies that have noted different effects on atherosclerosis by these two approaches, although this is a minority of publications.

Determination of lesion composition

Atherosclerotic lesions have complex cellular compositions that change at different stages of development. Therefore, in addition to quantifying the size, it is useful to determine the cellular composition of lesions. Table 5.2 provides examples of

Table 5.2 Examples of antibodies used in immunocytochemical studies to characterize cellular composition of atherosclerotic lesions

Cell type	Antigen	Antibody	Source	Reference
Macrophage	Mouse peritoneal macrophages	AIA31240	Accurate Chemical Co	19,20
	CD11b	MAC-1	Serotec	21
	Unknown	MOMA-2	Serotec	17
	CD68	FA-11	Serotec	22
	F4/80	CI:A3-1	Serotec	
T lymphocyte - pan	CD90 (Thy1.2)	F7D5	Serotec	24
CD4	CD4	GK1.5 (L3T4)	Chemicon	24,25
CD8	CD8	YTS105.18	Serotec	24
B lymphocyte	Mouse CD19	1D3	Pharmingen	26
Endothelial	CD31 - PECAM	MEC13.3	BD Pharmingen	26
Smooth muscle	Alpha actin	1A4	Sigma/Dako	17

antibodies used to identify resident cells of the arterial wall (endothelial and smooth muscle) and the most prominent cell types that infiltrate the evolving atherosclerotic lesion (macrophages, T lymphocytes and subclasses, and B lymphocytes). Of the many cell types present in atherosclerosis, perhaps the most difficult to immunodetect in a uniform manner are macrophages, since this cell type is so heterogeneous in lesions. Many of the monoclonal antibodies that react against macrophage antigens are differentiation dependent and therefore react with macrophage subsets. To overcome this, we have used antisera developed in rabbits that have been injected with mouse peritoneal macrophages. The use of a cell as the immunising agent leads to the development of antibodies against many macrophage antigens. This should provide an increased likelihood of detecting all macrophages.

Conventional immunocytochemical procedures are used to detect cells in lesions. However, one issue that should be addressed is the high non-specific background of chromogen development that often occurs within atherosclerotic tissue. This issue amplifies the need for appropriate control experiments. At a minimum, controls should include performing the procedure in the absence of the primary antibody to determine non specific chromogen development through the secondary antibody and detection complex. It is preferable to include a control for the primary antibody that will include non-immune sera for antisera, non-immune antibodies for purified IgG or IgM, and isotype-matched antibodies against irrelevant antigens for monoclonal antibodies.

Statistical analysis

The development of experimental atherosclerosis is usually characterised by inherent variability of lesion size within groups. This may provide some challenges in terms of the number of animals needed to demonstrate an effect. It is also common to acquire

data in which numbers do not conform to equivalence of variance and normality of distribution. Therefore, the basic tenets of statistical analysis apply in that data should be determined for suitability for analysis by parametric or non-parametric tests. Application of the correct statistical test is facilitated by many software packages. In our laboratory, we use SigmaStat which has a user friendly interface and an interactive mode that suggests the optimal test for a specific dataset.

Conclusions

Since the generation of ApoE$^{-/-}$ and LDL receptor$^{-/-}$ mice in the early 1990s, there has been a dramatic increase in the use of the mouse as an atherosclerosis model for studying potential mechanisms of human disease. Despite these many studies, there is a lack of consensus on many facets of atherosclerotic lesion quantification and characterization. An establishment of rigorous standards may reduce the number of studies in which data conflicts. For example, there is conflicting data for the effects of scavenger receptor deficiency on atherosclerotic lesion formation.[15–17]

There is continuing debate on the extent to which lesion development in the mouse mimics human disease. There are specific facets of the early stages of the human disease that are faithfully recapitulated, especially the development of lipid-laden macrophages. Also, some models experience extensive fibrotic components and development of acellular cores containing crystals of unesterified cholesterol. However, lesions in mice infrequently progress to late stages of human disease as defined by American Heart Association class IV and V.[18] As a consequence, mice seldom manifest the diseases that occur so rampantly in humans as a consequence of atherosclerosis. It is likely that future efforts will be directed to devise models in which acute coronary syndromes and strokes will be generated routinely.

Acknowledgments

Studies in the author's laboratory was supported by the National Institutes of Health (HL62846 and HL70239)

References

1. Virmani R, Kolodgie FD, Burke AP, Farb A, Schwartz SM. Lessons from sudden coronary death: A comprehensive morphological classification scheme for atherosclerotic lesions. *Arterioscler Thromb Vasc Biol* 2000; **20**: 1262–1275.
2. Daugherty A. Mouse models of atherosclerosis. *Am J Med Sci* 2002; **323**: 3–10.
3. Paigen B, Mitchell D, Reue K, Morrow A, Lusis AJ, Leboeuf RC. Ath-1, a gene determining atherosclerosis susceptibility and high density lipoprotein levels in mice. *Proc Natl Acad Sci U S A* 1987; **84**: 3763–3767.

4. Zhang SH, Reddick RL, Piedrahita JA, Maeda N. Spontaneous hypercholesterolemia and arterial lesions in mice lacking apolipoprotein E. *Science* 1992; **258**: 468–471.
5. Plump AS, Smith JD, Hayek T, et al. Severe hypercholesterolemia and atherosclerosis in apolipoprotein-E-deficient mice created by homologous recombination in ES cells. *Cell* 1992; **71**: 343–353.
6. Ishibashi S, Goldstein JL, Brown MS, Herz J, Burns DK. Massive xanthomatosis and atherosclerosis in cholesterol-fed low density lipoprotein receptor-negative mice. *J Clin Invest* 1994; **93**: 1885–1893.
7. Shi WB, Haberland ME, Jien ML, Shih DM, Lusis AJ. Endothelial responses to oxidized lipoproteins determine genetic susceptibility to atherosclerosis in mice. *Circulation* 2000; **102**: 75–81.
8. Li AC, Brown KK, Silvestre MJ, Willson TM, Palinski W, Glass CK. Peroxisome proliferator-activate inhibit development of atherosclerosis in LDL receptor-deficient mice. *J Clin Invest* 2000; **106**: 523–531.
9. Whitman SC, Ravisankar P, Daugherty A. IFN-gamma deficiency exerts gender-specific effects on atherogenesis in apolipoprotein $E^{-/-}$ mice. *J Interferon Cytokine Res* 2002; **22**: 661–670.
10. Paigen B, Morrow. A., Holmes P, Mitchell D, Williams R. Quantitative assessment of atherosclerotic lesions in mice. *Atherosclerosis* 1987; **68**: 231–240.
11. Tangirala RK, Rubin EM, Palinski W. Quantitation of atherosclerosis in murine models: Correlation between lesions in the aortic origin and in the entire aorta, and differences in the extent of lesions between sexes in LDL receptor-deficient and apolipoprotein E-deficient mice. *J Lipid Res* 1995; **36**: 2320–2328.
12. Rosenfeld ME, Polinsky P, Virmani R, Kauser K, Rubanyi G, Schwartz SM. Advanced atherosclerotic lesions in the innominate artery of the ApoE knockout mouse. *Arterioscler Thromb Vasc Biol* 2000; **20**: 2587–2592.
13. Daugherty A, Whitman SC. Quantification of atherosclerosis in mice. *Methods Mol Biol* 2003; **209**: 293–309.
14. Daugherty A, Zweifel BS, Schonfeld G. The effects of probucol on the progression of atherosclerosis in mature Watanabe heritable hyperlipidaemic rabbits. *Br J Pharmacol* 1991; **103**: 1013–1018.
15. Daugherty A, Rateri DL, Whitman SC. Class A scavenger receptors: Recent advances in elucidation of structure–function relationships and their role in atherosclerosis. *Curr Opin Cardiovasc Pulm Ren Invest Drugs* 2000; **2**: 223–232.
16. Febbraio M, Podrez EA, Smith JD, et al. Targeted disruption of the class B scavenger receptor CD36 protects against atherosclerotic lesion development in mice. *J Clin Invest* 2000; **105**: 1049–1056.
17. Moore KJ, Kunjathoor VV, Koehn SL, et al. Loss of receptor-mediated lipid uptake via scavenger receptor A or CD36 pathways does not ameliorate atherosclerosis in hyperlipidemic mice. *J Clin Invest* 2005; **115**: 2192–2201.
18. Stary HC, Chandler AB, Dinsmore RE, et al. A definition of advanced types of atherosclerotic lesions and a histological classification of atherosclerosis: A report from the Committee on Vascular Lesions of the Council on Arteriosclerosis, American Heart Association. *Circulation* 1995; **92**: 1355–1374.
19. Daugherty A, Manning MW, Cassis LA. Angiotensin II promotes atherosclerotic lesions and aneurysms in apolipoprotein E-deficient mice. *J Clin Invest* 2000; **105**: 1605–1612.

20. Daugherty A, Rateri DL, Lu H, Inagami T, Cassis LA. Hypercholesterolemia stimulates angiotensin peptide synthesis and contributes to atherosclerosis through the AT1A receptor. *Circulation* 2004; **110**: 3849–3857.
21. Zou Y, Hu Y, Mayr M, Dietrich H, Wick G, Xu Q. Reduced neointima hyperplasia of vein bypass grafts in intercellular adhesion molecule-1-deficient mice. *Circ Res* 2000; **86**: 434–440.
22. Zhao L, Moos MP, Grabner R, et al. The 5-lipoxygenase pathway promotes pathogenesis of hyperlipidemia-dependent aortic aneurysm. *Nat Med* 2004; **10**: 966–973.
23. Napoli C, Ackah E, deNigris F. Chronic treatment with nitric oxide-releasing aspirin reduces plasma low-density lipoprotein oxidation and oxidative stress, arterial oxidation-specific epitopes, and atherogenesis in hypercholesterolemic mice. *Proc Natl Acad Sci U S A* 2002; **99**(19): 12467–12470.
24. Roselaar SE, Kakkanathu PX, Daugherty A. Lymphocyte populations in atherosclerotic lesions of apoE$^{-/-}$ and LDL receptor$^{-/-}$ mice. Decreasing density with disease progression. *Arterioscler Thromb Vasc Biol* 1996; **16**: 1013–1018.
25. Zhou XH, Stemme S, Hansson GK. Evidence for a local immune response in atherosclerosis: CD4(+) T cells infiltrate lesions of apolipoprotein-E-deficient mice. *Am J Pathol* 1996; **149**: 359–366.
26. Saraff K, Babamusta F, Cassis LA, Daugherty A. Aortic dissection precedes formation of aneurysms and atherosclerosis in angiotensin II-infused, apolipoprotein E-deficient mice. *Arterioscler Thromb Vasc Biol* 2003; **23**: 1621–1626.

6

Magnetic resonance imaging evaluation of atherosclerotic plaque

Martina A. McAteer, Jürgen E. Schneider and **Robin P. Choudhury**

Department of Cardiovascular Medicine, John Radcliffe Hospital, Oxford, UK

Keywords

magnetic resonance imaging, mice, atherosclerosis, plaque

Introduction

Deciphering of the mouse genome and advances in molecular biology have led to a rapid expansion of gene knockout and transgenic strategies to study atherosclerosis. Genetically modified mice, such as the apolipoprotein E-knockout ($ApoE^{-/-}$) mouse, are now the animal models of choice for investigating atherosclerotic plaque development.[1,2] Histopathology and immunohistochemistry have provided many insights into mouse lesion morphometry and composition, but do not allow serial evaluation of plaque to enable longitudinal studies, that are particularly appealing for studies of intervention. To address this, the advancement of imaging modalities with the ability to differentiate changes in plaque distribution, size, morphology and, to some extent, composition, at various stages of athero-thrombotic disease have been developed.

High resolution magnetic resonance imaging (MRI) is well suited for *in vivo* characterisation of atherosclerotic plaques as it can provide high resolution images of multiple vascular regions. Since MRI is non-invasive and does not use ionising radiation, it is also suitable for serial *in vivo* monitoring of plaque development over time.[3] Furthermore, MRI is already in widespread clinical use and lessons from mouse imaging studies could potentially be translated into human application.

A Handbook of Mouse Models of Cardiovascular Disease Edited by Qinbo Xu

Imaging Atherosclerosis with MRI

When an imaging subject is placed in a high static magnetic field, MR images can be generated from the emitted radiofrequency (RF) signal following the administration of a RF pulse. The RF signal, usually measured from water protons, varies according to multiple physical and chemical parameters including the concentration of water within the tissues and the relaxation times (T_1 and T_2) of the water protons of the different chemical components of the tissue of interest.[4] Importantly, atherosclerotic plaque components (in particular, lipid-rich, fibrocellular and calcified regions) can be distinguished on the basis of their inherent signal intensities using a combination of multi-contrast sequences (proton density weighted (PDW), T_1- and T_2-weighted (T_{1W}, T_{2W})) with sub-millimeter spatial resolution. In this way, MRI of atherosclerosis has been described in human carotid artery *ex vivo* and in carotid artery and aorta *in vivo*, as well as in larger animal models including rabbits, pigs, and non-human primates (reviewed in Choudhury *et al.*, 2002).[3] A table listing the MR terminology can be found in Chapter 14 (Table 14.1).

Mouse MRI

The greatest challenge for mouse imaging is the extremely small size of the vessels of interest. The aortic root is approximately 1 mm in external diameter, but the normal wall thickness is, perhaps 50 μm. Other sites of interest such as the aortic arch, abdominal aorta and brachiocephalic artery are even smaller. In mice, conventional lesion analysis with histopathology, typically of the aortic root and more recently of the brachiocephalic artery,[5–7] has provided useful information about murine atherosclerotic plaque characteristics. However, since it requires the animal to be killed, it is restricted to 2D analysis of a small number of histological sections at a single time point. Therefore, histopathology can give only limited insight into overall plaque volume and spatial distribution of plaque components within a lesion and cannot be adapted for serial *in vivo* plaque imaging. Examination of sections in isolation or of *en face* specimens also provides very limited information on the 3D distribution of plaques and their components, which may be important in predicting patterns of atherogenesis and its complications.

MRI has been used to quantify murine atherosclerotic plaques *in vivo* in abdominal aorta,[8,9] aortic root,[10] aortic arch[11] and brachiocephalic artery[12] and can measure progression of atherosclerosis in individual mice with time.[13] Serial *in vivo* MRI has also quantified regression of plaque following transplantation of aortic arch segments with advanced atherosclerosis from hypercholesterolemic ApoE$^{-/-}$ mice into normolipidemic wild-type mice.[14] Although MRI is validated for lesion quantification, precise characterisation of plaque composition *in vivo* has proved challenging due to limitations in spatial resolution achievable for *in vivo* MRI of the very small mouse artery wall. We have recently described a very high spatial resolution *ex vivo* MR

microscopy technique at 11.7 Tesla (T) that can be used to quantify lipid-rich/necrotic core and cell-rich cap areas in aortic root and brachiocephalic artery plaques in $ApoE^{-/-}$ mice.[15] The acquisition of images with near-isotropic voxels also enabled 3D reconstruction and examination of the spatial distribution and quantity of plaque and lipid core volumes throughout the brachiocephalic artery, at various stages of atherosclerotic disease.[16] Detailed interrogation of plaque development within the brachiocephalic artery wall is particularly appealing, as the plaques are more advanced, with features suggestive of fibrous cap disruption and intra-plaque haemorrhage.

As availability of high field strength MR systems increases, we aim to provide here a practical guide that explores some of the issues related to MR assessment of murine atherosclerosis both *in vivo* and *ex vivo*.

Materials and methods

Team

Imaging of the type discussed here is not attainable 'off the peg'. Nor, in our experience is any single individual likely to possess all of the skills required for a successful imaging programme. Key to its success is close co-operation between biologists, physiologists, MR physicists and experts in image analysis. As molecular imaging applications expand (see below), chemists, materials scientists and molecular biologists will play an increasingly prominent role.

MR system

Imaging such small vascular structures requires high spatial resolution, but decreasing voxel size reduces the signal to-noise ratio (SNR) and tends to increase imaging time. There is a constant play-off between these factors, which is especially important for *in vivo* imaging, where time constraints are more rigid. In order to achieve optimal images a high field strength magnet (7.0 to 11.7 T) and strong gradient system are required. In addition, RF coils such as birdcage-type coils, optimized in geometry and loading for mice will provide excellent homogeneity of the RF field. Furthermore, birdcage coils can be driven in 'quadrature mode', which further enhances the SNR by up to a factor of $\sqrt{2}$.[17] The inner diameter of a quadrature-driven birdcage coil used for *in vivo* imaging of adult mice (body weight 17–25 g) is 28 mm while for *ex vivo* aortic specimens or *in vivo* imaging of young mice (body weight <17 g), a smaller probe, e.g. 13 mm or 20 mm may be used (see Figure 6.1a). Increased body weight and girth can be an important consideration when imaging mice with metabolic abnormalities and considerations of weight and gender may be important when planning time points for evaluation.

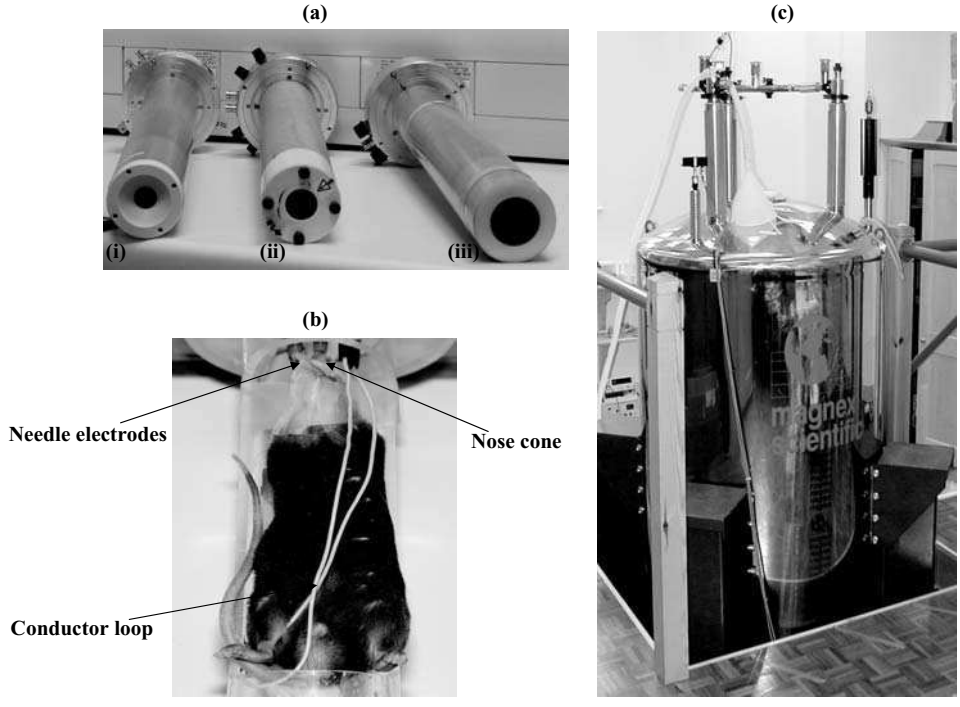

Figure 6.1 MR hardware (a) Quadrature-driven birdcage coils: (i) 20 mm; (ii) 28 mm; (iii) 40 mm. For adult mice (body weight 17–25 g), the internal diameter of the quadrature-driven birdcage coil should be at least 28 mm. For younger mice with body weight $<$17 g or for *ex vivo* aortic specimens, a 20 mm or 13 mm diameter coil may be used. (b) Set-up of mouse in animal cradle. The animal cradle is equipped with a nose cone, needle electrodes for deriving the ECG and a conductor loop for detecting respiratory motion. The mouse is placed on a heating blanket to maintain constant body temperature of 37°C during the MR experiment. (c) 11.7 T vertical magnet as used in our *ex vivo* studies. For a color version of this figure, please see the images supplied on the accompanying CD

Preparation of mouse for *in vivo* imaging

Safe sustainable anesthesia can be obtained using inhaled isofluorane (2 per cent). Ointment should be applied to the eyes in order to keep them moist, due to the suppression of the eye closure reflex during anesthesia. All equipment will need to be MR compatible. The mouse is placed in a dedicated animal cradle, optimised in diameter and length for the mouse (see above). The animal cradle consists of a heating blanket which maintains the core body temperature at 37°C, a nose cone for continuous delivery of the anesthetic and a scavenging line for anesthetic gas recovery. Additional lines can be used if drugs or MR contrast agents need to be administered. Heating blankets may be warmed by air or water, with air having the advantage over water as air does not have an MR signal and thus does not interfere with the RF coil. Needle electrodes ($\sim$25 gauge) are inserted subcutaneously into the forelimbs for deriving the electrocardiogram (ECG) signal that is required for gating

(see below). Respiration may be monitored using pressure pads or conductor loops mounted on top of the chest and the abdomen. The mouse is then secured in the cradle using surgical tape, taking special care not to distort or compress the abdominal or chest cavity regions (see Figure 6.1b). The cradle is then positioned into the RF coil in the magnet.

Gating

One of the principal challenges is to overcome vascular motion due to cardiac and respiratory cycles. The mouse heart rate is typically 300–700 beats per minute. To circumvent this, early studies quantified atherosclerosis in the abdominal aorta, where movement is minimal, but this is not a conventional location for plaque analysis and has the substantial drawback that lesions develop there relatively late.[8] For imaging intrathoracic structures, gating is essential. An electronic cardiac gating device will synchronize the MR cumulative data acquisition to the same point of the cardiac cycle. Respiratory gating, which interrupts MR data acquisition during respiration, is needed at high magnetic field strengths greater than 7 T, where motion artifacts become more pronounced, in order to obtain virtually artifact-free, high-quality images. These devices can be built in-house[18] or are offered by various manufacturers (e.g. SA Instruments Inc).

In vivo MRI

For *in vivo* MRI, the mouse can be reliably maintained under anesthesia in the magnet for up to 60 min. Full recovery without residual ill effect is the rule. Where the goal is lesion quantification, 2D multi-slice ($109 \times 109\,\mu m$ in plane and 0.5 mm slice thickness) MRI (at 9.4 T) with proton density weighted images ($T_E/T_R = 9/2000$ ms) have provided good signal to noise within an acceptable imaging time ($\sim$34 min) (see Figure 6.2).[8] Interval imaging (more than five times) in the same mouse has also quantified changes in lesion size over a period of months.[13]

Ex vivo MRI of aortic specimens

By imaging *ex vivo*, much longer, ungated acquisitions can be obtained using smaller coils on virtually stationary, explanted tissue. These factors greatly enhance the SNR allowing much smaller voxels and consequently greater spatial resolution.

Tissue collection and preparation for *ex vivo* imaging

In order to collect the aorta specimen, the mouse is first anesthetized by inhalation of isofluorane. The chest cavity is then opened to expose the heart and blood is removed

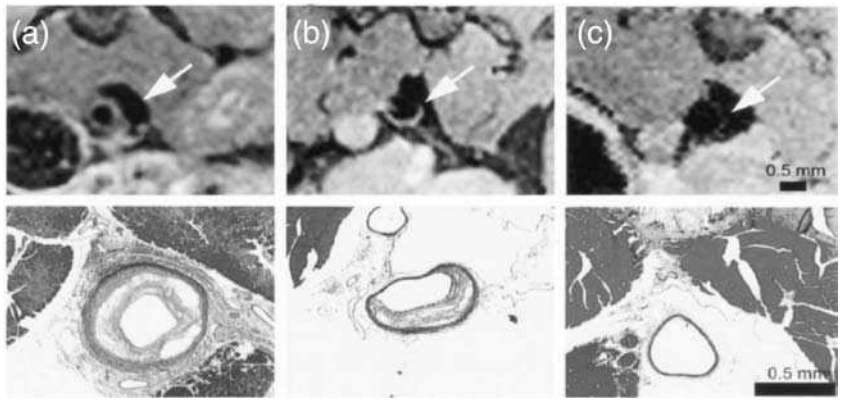

Figure 6.2 *In vivo* MRI of mouse plaques. *In vivo* proton density-weighted MR images ($109 \times 109 \times 500\,\mu m$) of atherosclerosis in the abdominal aorta of ApoE$^{-/-}$ mice and corresponding histological sections (stained with Combined Masson's Trichrome stain) of aorta sections. (a) marked concentric plaque; (b) eccentric thickening apparent on lateral and anterior aspects of aorta; (c) normal, thin walled aorta. For a color version of this figure, please see the images supplied on the accompanying CD

from the right ventricle using a 1 ml syringe and 25 gauge needle. The right atrium is incised to remove blood while the arterial tree is perfusion fixed under physiological pressure via the left ventricle with ~10 ml phosphate-buffered saline (PBS) followed by ~10 ml 4 per cent paraformaldehyde in PBS. The spinal column with the heart and aortic tree attached is then dissected out *en bloc*. Perivascular fat is gently dissected from the ascending aorta, aortic arch and the three branches: brachiocephalic, right carotid and left subclavian. The heart is then instilled with Fomblin (Ausimont, Putney, UK), a liquid hydrocarbon that prevents dehydration, maintains vessel patency, prevents air bubbles from entering the heart and provides an intravascular signal void (and thus excellent contrast with tissues) on MRI. The sample is embedded in an MR tube containing 2 per cent agarose and secured and immobilized with a second layer of 2 per cent agarose.

Ex vivo MRI

For *ex vivo* MRI, we have developed and validated a 3D multi-echo sequence with variable T_{2w} ($T_E/T_R = 7/200$ ms; number of averaged experiments (NAE) = 4; experimental time ~7 h).[15] A matrix size of $256 \times 256 \times 128$ and a field of view (FOV) of $12 \times 12 \times 8$ mm were used to attain a final voxel size of $23 \times 23 \times 31$ μm after zerofilling. This 3D acquistion method improves signal to noise allowing smaller voxels and less partial volume artifact compared to 2D multi-slice techniques. Furthermore the near-isotropic voxels obtained by this method also allowed 3D reconstruction of the artery and lesions in many and arbitrary planes.[16]

Optimising MR images for analysis

For most vascular biological applications, acquiring the 'anatomical image' is not an end itself. It is usually necessary to extract quantitative data on plaque size and composition. Towards this goal, imaging sequences should be optimised to provide images that lend themselves to the analyses required (see above). For instance, atherosclerosis imaging will require excellent delineation of the wall *versus* lumen and wall *versus* perivascular tissue. The former is usually relatively straightforward since the lumen appears dark due to signal loss from flowing blood on spin echo image acquisition. The latter can be facilitated by using a sequence with 'fat suppression' to remove signal from perivascular fat, ideally creating a halo around the artery.

Voxel size in relation to the structure of interest is important. Precise quantification is served by a large number of pixels per imaged structure. Where plaque size is large in relation to pixel size, correlation between MRI and histology is good, but this breaks down where the pixel diameter approaches the size of the structure of interest. It is important to remember, in 2D multi-slice techniques, that while the in-plane resolution maybe small, in order to accomplish this with acceptable signal to noise, it is usually necessary to increase slice thickness, leaving the analysis susceptible to partial volume effects. These occur where the contour of the tissue of interest moves in and out of line of voxel definition as it moves through the depth of a slice. One expects the image value to reflect the average value over the imaged distance. Optimal voxel size will need to be established experimentally for each application.

Automated image analysis

The data sets for imaging [multiple] arteries in mice of several time points are very large. To improve both efficiency and objectivity, it is desirable to use [semi-]automated image analysis software. A relatively large selection of software for morphometry is available. (e.g. NIH image, which is available for free download [http://rsb.info.nih.gov/nih-image/]; or the proprietary Image ProPlus [Media Cybernetics, Silver Spring Maryland]. Where serial MR images are to be compared or MRI *versus* histology findings analysed, it is important to ensure anatomical alignment of the slices or segments under evaluation (see Figure 6.3). It is usual to reference position to fiducial markers such as the origins of side branches or bifurcations. By referencing two markers on either side of the area of interest, it is also possible to address the invariable shrinkage of tissue that occurs during preparation for histological analysis.[8]

We have recently applied a semi-automated, histogram-based, threshold method to the segmentation and quantification of lipid rich necrotic core and cell rich lesion cap in mouse atherosclerosis (see Figure 6.4).[16] For 3D reconstruction and volumetric quantification of brachiocephalic artery plaque, MR image stacks for: (1) the entire brachiocephalic artery; (2) its segmented plaque; and (3) segmented lipid-rich/

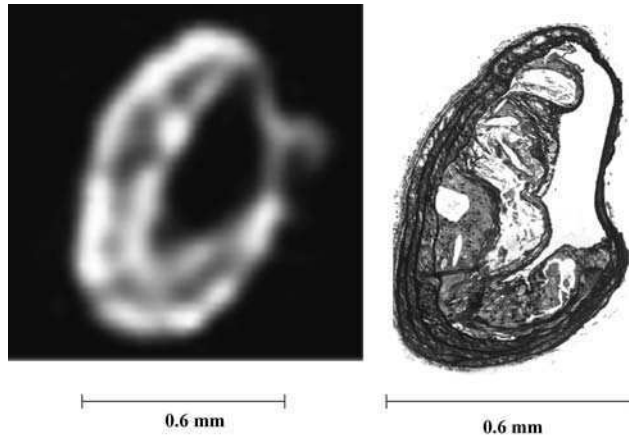

Figure 6.3 *Ex vivo* MRI of mouse brachiocephalic artery plaque. MR image ($23 \times 23 \times 31$ μm) and corresponding histopathology (stained with combined Masson Elastin stain) of a typical brachiocephalic artery of an ApoE$^{-/-}$ mouse fed high fat diet for 20 weeks. By histopathology, white areas within the plaque, representing voids attributable to lipid dissolution during tissue processing, corresponded to black/dark gray regions on the MR image. For a color version of this figure, please see the images supplied on the accompanying CD

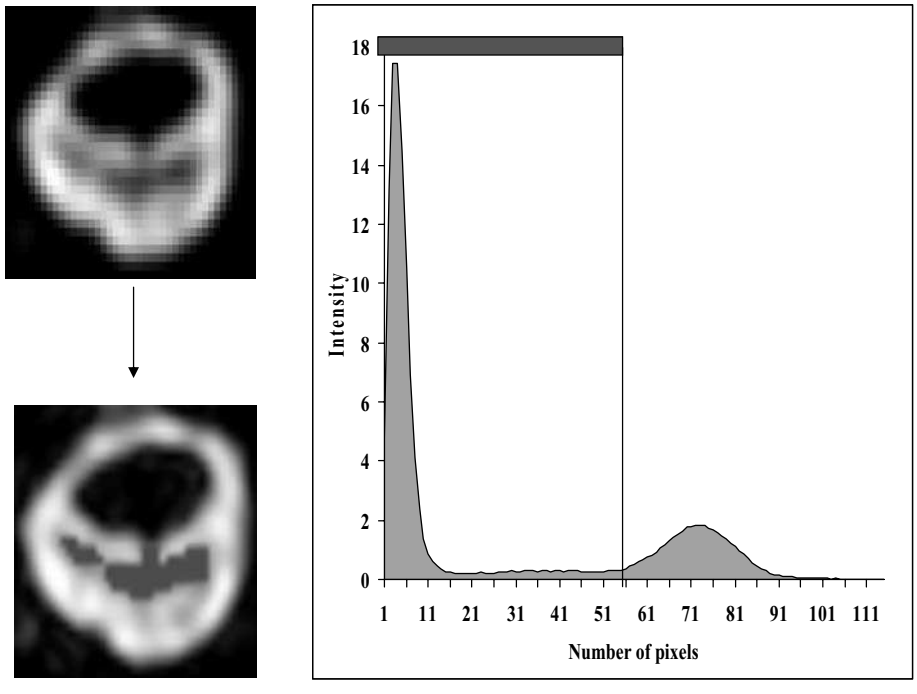

Figure 6.4 Example of automated segmentation of mouse brachiocephalic artery plaque using high resolution *ex vivo* MRI. Black/dark gray regions within the plaque corresponding to lipid-rich necrotic cores are segmented (red overlay) and quantified using the signal intensity histogram generated from gray-scale MR images. For a color version of this figure, please see the images supplied on the accompanying CD

necrotic core 'masks' were assigned to red, blue and green color channels, respectively and reconstructed in 3D using the 3D Constructor plug-in for ImagePro Plus (see Movie 6.1). Isosurfaces for the colour channels corresponding to plaque and lipid-rich/necrotic cores were added (see Movie 6.2) and the enclosed volumes automatically calculated. Itskovich *et al*. (2003) have described a cluster analysis approach to characterise lesions based on integrated information from multi-contrast MRI but such tools have so far not found widespread application.[10]

Discussion

Initial *in vivo* MR studies of atherosclerosis in mice were focused on the measurement of plaque area in the abdominal aorta and common iliac arteries, where the influence of cardiac and respiratory motion is reduced.[9] This was later extended to determine the limits of sensitivity and specificity of *in vivo* MRI to detect plaques in younger mice.[8] Several studies have also reported quantification of lesion size in the aortic root[10] or arch,[11] which are technically more demanding due to substantial cardiac and respiratory motion influence. These *in vivo* studies achieved high resolution in plane ($109 \times 109\,\mu m$) but slice thickness ($500\,\mu m$) led to disabling partial volume effects, precluding characterization of plaque composition. Itskovich *et al*. (2003) first demonstrated the potential of *ex vivo* MRI to identify lipid core and fibrous cap in T_{1W}, T_{2W}, and PDW images of the aortic root of ApoE$^{-/-}$ mice as confirmed by histopathology.[10]

We have recently expanded on this work by developing a very high-resolution *ex vivo* MRI technique that attains very small voxels almost equal in each dimension ($47 \times 47 \times 62.5\,\mu m$ or $23.5 \times 23.5 \times 31.8\,\mu m$ after interpolation) to quantify lipid-rich/necrotic core and fibrous caps in the aortic root and brachiocephalic artery of ApoE$^{-/-}$ mice.[16] The significant improvement in MR spatial resolution was achieved using a 3D rather than a 2D acquisition matrix ($256 \times 256 \times 128$) and although a significantly longer imaging time (7 h) was also required, this was efficiently accommodated by running unsupervised overnight scans.[15] The acquisition of 3D images of near-isotropic voxels also enabled 3D reconstruction and examination of changes in plaque distribution and lipid-rich/necrotic core volume in the brachiocephalic artery over time. Previously, plaque progression in the brachiocephalic artery has been examined only in 2D histological sections, which provide valuable information on plaque morphology, but cannot fully interrogate plaque distribution in relation to the entire artery. *Ex vivo* MRI avoids tissue dehydration and potential size distortion that may be caused during tissue processing for histological examination. The small size of the brachiocephalic artery ($\sim 500\,\mu m$ external diameter) and the technical demands of embedding and sectioning such a small artery for histopathology also introduce a potential risk for disruption of the integrity of the plaque itself. As such, 3D high resolution *ex vivo* MRI is a potentially useful additional tool to accurately and efficiently quantify changes in plaque distribution and composition in mice, without need for histology.

In vivo plaque characterization in mice, that has been achieved by *ex vivo* MRI is ultimately the goal. However, the prolonged imaging protocol time used for *ex vivo* MRI is clearly not feasible *in vivo* due to anesthesia constraints. Furthermore, even with excellent ECG and respiratory gating, relatively small physiological movements, including involuntary movements of skeletal muscle may be sufficient to degrade a very high-resolution image substantially. To overcome these limitations, there is currently considerable interest in developing cellular and molecular imaging tools that will provide structural and functional data that is effectively in the micro- and nanometer range of resolution.[4]

Application

Small animal MR imaging offers exciting prospects for *in vivo* phenotyping to characterize the many small animal models that are contributing to our expanding appreciation of the events of atherogenesis. Over traditional methods, MRI offers *in vivo* evaluation of plaque area and the opportunity for non-tissue-destructive 3D interrogation of its microscopic structure. Three-D reconstruction of *ex vivo* MR images of mouse atherosclerotic plaques have also provided insights into the spatial distribution and pattern of lesion extension in the brachiocephalic artery. Therefore, high resolution *ex vivo* MRI is a potentially useful additional tool for the study of the effects of drug/gene therapies on plaque and lipid distribution and volume over time. Such data will also allow detailed biomechanical modeling of patterns of blood flow, sheer stresses and tension in the arterial wall. In the near future, it is likely that molecular and cellular imaging probes will further extend the utility of small animal MRI. Furthermore, the opportunity to image small arteries and to obtain ready tissue comparisons will advance imaging technologies that may be of clinical use.

However most of the studies that have been discussed here are not available 'off the peg' and require a co-ordinated team. The capital and maintenance costs for the equipment required are clearly an important consideration. These complexities argue that mouse atherosclerosis evaluation with MRI should ideally form part of a larger structured small animal imaging program.

Acknowledgments

Our research has been supported by the Wellcome Trust and by the British Heart Foundation. The contributions of Professor Keith Channon, Professor Stefan Neubauer, and Professor Kieran Clarke are gratefully acknowledged. Dr Zahi Fayad is thanked for much helpful discussion.

References

1. Meir KS, Leitersdorf E. Atherosclerosis in the apolipoprotein-E-deficient mouse: a decade of progress. *Arterioscler Thromb Vasc Biol* 2004; **24**(6): 1006–1014.

2. Breslow JL. Mouse models of atherosclerosis. *Science* 1996; **272**(5262): 685–688.
3. Choudhury RP, Fuster V, Badimon JJ, et al. MRI and characterization of atherosclerotic plaque: emerging applications and molecular imaging. *Arterioscler Thromb Vasc Biol* 2002; **22**(7): 1065–1074.
4. Choudhury RP, Fuster V, Fayad ZA. Molecular, cellular and functional imaging of atherothrombosis. *Nat Rev Drug Discov* 2004; **3**(11): 913–925.
5. Rosenfeld ME, Polinsky P, Virmani R, et al. Advanced atherosclerotic lesions in the innominate artery of the ApoE knockout mouse. *Arterioscler Thromb Vasc Biol* 2000; **20**(12): 2587–2592.
6. Johnson J, Carson K, Williams H, et al. Plaque rupture after short periods of fat feeding in the apolipoprotein E-knockout mouse: model characterization and effects of pravastatin treatment. *Circulation* 2005; **111**(11): 1422–1430.
7. Johnson JL, Jackson CL. Atherosclerotic plaque rupture in the apolipoprotein E knockout mouse. *Atherosclerosis* 2001; **154**(2): 399–406.
8. Choudhury RP, Aguinaldo JG, Rong JX, et al. Atherosclerotic lesions in genetically modified mice quantified in vivo by non-invasive high-resolution magnetic resonance microscopy. *Atherosclerosis* 2002; **162**(2): 315–321.
9. Fayad ZA, Fallon JT, Shinnar M, et al. Noninvasive in vivo high-resolution magnetic resonance imaging of atherosclerotic lesions in genetically engineered mice. *Circulation* 1998; **98**(15): 1541–1547.
10. Itskovich VV, Choudhury RP, Aguinaldo JG, et al. Characterization of aortic root atherosclerosis in ApoE knockout mice: High-resolution in vivo and ex vivo MRM with histological correlation. *Magn Reson Med* 2003; **49**(2): 381–385.
11. Wiesmann F, Szimtenings M, Frydrychowicz A, et al. High-resolution MRI with cardiac and respiratory gating allows for accurate in vivo atherosclerotic plaque visualization in the murine aortic arch. *Magn Reson Med* 2003; **50**(1): 69–74.
12. Hockings PD, Roberts T, Galloway GJ, et al. Repeated three-dimensional magnetic resonance imaging of atherosclerosis development in innominate arteries of low-density lipoprotein receptor-knockout mice. *Circulation* 2002; **106**(13): 1716–1721.
13. Choudhury RP, Fayad ZA, Aguinaldo JG, et al. Serial, noninvasive, in vivo magnetic resonance microscopy detects the development of atherosclerosis in apolipoprotein E-deficient mice and its progression by arterial wall remodeling. *J Magn Reson Imaging* 2003; **17**(2): 184–189.
14. Trogan E, Fayad ZA, Itskovich VV, et al. Serial studies of mouse atherosclerosis by in vivo magnetic resonance imaging detect lesion regression after correction of dyslipidemia. *Arterioscler Thromb Vasc Biol* 2004; **24**(9): 1714–1719.
15. Schneider JE, McAteer MA, Tyler DJ, et al. High-resolution, multicontrast three-dimensional-MRI characterizes atherosclerotic plaque composition in $ApoE^{-/-}$ mice ex vivo. *J Magn Reson Imaging* 2004; **20**(6): 981–989.
16. McAteer MA, Schneider JE, Clarke K, et al. Quantification and 3D reconstruction of atherosclerotic plaque components in apolipoprotein E knockout mice using ex vivo high-resolution MRI. *Arterioscler Thromb Vasc Biol* 2004; **24**(12): 2384–2390.
17. Chen CN, Hoult DI, Sank VJ. Quadrature detection coils: a further (square root of) 2 improvement in sensitivity. *J Magn Reson* 1983; **54**: 324–327.
18. Cassidy PJ, Schneider JE, Grieve SM, et al. Assessment of motion gating strategies for mouse magnetic resonance at high magnetic fields. *J Magn Reson Imaging* 2004; **19**(2): 229–237.

7
Plaque rupture

Christopher L. Jackson

Bristol Heart Institute, University of Bristol, Bristol, UK

Introduction

Investigation into the pathophysiology of atherosclerotic plaque rupture has, in the past, been achieved by study of human post mortem specimens. Much progress has been achieved, but in a very specific direction: understanding of the morphology and anatomy of plaque ruptures that kill. Recently evidence has begun to accumulate to suggest that in fact most plaque ruptures are not fatal.[1–4] This means that a full understanding of the development of instability in plaques requires a system where such lesions can be investigated as soon as a non-fatal rupture occurs, and this in practice means that an animal model is needed. Apolipoprotein E (ApoE) knockout models of plaque rupture began to appear 4 years ago, with the emphasis on the brachiocephalic artery as a site of predilection.[5–7] This chapter aims to summarise the methodologies required for study of plaque instability and rupture at this site in ApoE knockout mice.

Animals

Ruptured atherosclerotic plaques have been observed in homozygous apolipoprotein E null (ApoE knockout) mice and, anecdotally, in ApoE/low-density lipoprotein receptor double knockout mice. The bulk of the published data derive from the former, but of these there are two types. Commercially available ApoE knockouts have usually been back-crossed onto the C57BL/6 strain background, and generally derive originally from animals with a null mutation to the ApoE gene created in the

A Handbook of Mouse Models of Cardiovascular Disease Edited by Qinbo Xu

laboratory of Dr Nobuyo Maeda.[8] The mice used in our laboratories in Bristol have not been backcrossed and are on a mixed strain background that is approximately 70 per cent C57BL/6 and 30 per cent 129: they derive originally from null mutated mice created in Dr Jan Breslow's laboratory at Rockefeller University.[9] These animals are not commercially available but academic institutions can obtain breeding pairs by contacting the author; commercial institutions should also contact the author in the first instance, who will pass the enquiry on to Rockefeller University.

The genotype of the animals is checked by polymerase chain reaction (PCR) analysis of tail-tip DNA, according to the following protocol:

1. Make up primers to 200 μmol/L stock in TE buffer.

2. Dilute this 200 μmol/l stock to 2 μmol/L in water for everyday use.

3. Make up dNTP mix from individual nucleotides each at 2 μmol/L.

4. Defrost 10 × buffer, 2 μmol/L primers, dNTPs and DNA samples and keep on ice.

5. Pipette 1 μL of DNA into a PCR tube.

6. Add 29 μL of the correct premix (Table 7.1) to each 1 μL of DNA, making sure the solutions mix thoroughly.

7. PCR reaction:

    a. 95°C for 5 min

    b. 94°C for 1 min

    c. 64°C for 1 min

    d. 72°C for 3 min

    e. Repeat steps b, c, d 30 times

    f. 72°C for 10 min

    g. 4°C indefinitely.

8. Identification of genotype from the gel:

    a. 1 band at 350bp signifies homozygote knockout

    b. 1 band at 600bp signifies homozygote wild-type

    c. 2 bands at 600bp and 350bp signifies heterozygote.

Table 7.1 Premix compositions

Premix	μL per sample
10 × PCR buffer	3.0
1753	3.0
1754	3.0
901	3.0
dNTPs	3.0
Taq	0.5
Water	13.5

9. Primers:

   a. 1753 (2nd exon sense):
   CTC TGT GGG CCG TGC TGT TGG TCA CAT TGC TGA CA

   b. 1754 (3rd exon antisense):
   CTC GAG CTG ATC TGT CAC CTC CGG CTC TCC C

   c. 901 (neo gene sense):
   CGC CGC TCC CGA TTC GCA GCG CAT CGC

   d. Knockout uses 901 + 1754; wild-type uses 1753 + 1754

Husbandry and welfare

Animals are housed under normal conditions. Breeding and nurturing are normal, and the animals are weaned at approximately 3 weeks of age. Normal mouse diet is given *ad libitum* for 6 weeks, and then at the start of the experimental phase this is switched to a high-fat diet that contains 21 per cent pork lard and 0.15 per cent cholesterol (Diet 821424: Special Diets Services, Witham, UK). In the short term there are no adverse health effects associated with receiving the high-fat diet despite the extreme hypercholesterolemia that results. After about 3 months of high-fat feeding some animals develop cutaneous xanthomas that the mouse may scratch, breaking the skin. Such animals are killed. Periods of feeding beyond about 6 or 7 months produce quite a high incidence of xanthomatosis and should be avoided.

Some animals suffer sudden death, the reasons for which are not clear but may berelated to myocardial ischemia and infarction.[10] Sudden deaths are relatively infrequent in the first 3 months of high-fat feeding, but by 9 months there will be few (if any) survivors.

Termination

Animals should be perfusion fixed at constant physiological pressure while the brachiocephalic artery is still *in situ*. The simplest way to achieve this is to induce

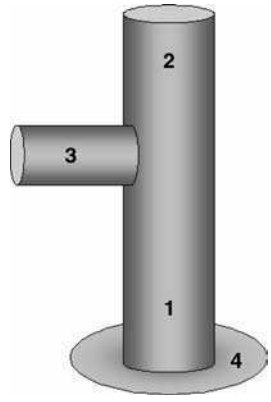

Figure 7.1 Representative diagram of the brachiocephalic artery after dissection, ready for embedding for histology. 1 = Brachiocephalic artery. 2 = Right common carotid artery. 3 = Right subclavian artery. 4 = 'Skirt' of outer curvature of the aortic arch

deep surgical anesthesia by intraperitoneal injection of sodium pentobarbitone, then to exsanguinate the animal by arterial perfusion at a constant pressure of 100 mmHg via the abdominal aorta or left ventricle with phosphate-buffered saline (PBS). Outflow of blood and perfusate is via the incised external jugular veins. This is followed by constant pressure perfusion with the fixative of choice: 10 per cent formalin in PBS works well for general histology and most immunostaining.

There are several ways of achieving constant pressure perfusion. The simplest is to position the fluid reservoir at the appropriate height above the animal: 1.36 m equates to 100 mmHg.

Dissection proceeds as shown in the accompanying video. The general approach is to locate the right common carotid artery and to use this to lift the brachiocephalic artery while it is freed from the underlying tissues. The brachiocephalic artery is removed together with a piece of the right common carotid artery, the stump of the right subclavian artery, and a 'skirt' of aortic arch (Figure 7.1). These landmarks aid orientation of the tissue during embedding for histological processing.

Tissue processing

For paraffin wax processing, brachiocephalic arteries should first be pre-embedded in molten 1.5 per cent agar in PBS. This allows manipulation of the tissue as the agar sets, to ensure that the vessel is exactly perpendicular. After paraffin wax embedding using standard procedures, 3 μm sections are cut starting at the proximal (aortic arch) end. Sections are cut and discarded until the most proximal part of the brachiocephalic artery is reached. This can be monitored by inspecting the surface of the paraffin wax block and looking for gradual diminution of the size of the ring of aortic arch tissue. When the ring stops diminishing, the brachiocephalic artery has been

reached. A good system for surveying the proximal portion of the brachiocephalic artery is to cut 3 μm sections at 30 μm intervals, out to 150 μm.

The most useful histological stain is an elastin stain, such as Miller's/van Gieson, because this allows delineation of the fibrous cap and shows breaches in it very clearly. Other stains (such as haematoxylin and eosin, or trichrome stains) are useful for identifying specific features of the plaque such the lipid pool, fibrin, collagen etc.

Miller's/van Gieson method for elastin staining:

1. Paraffin wax sections are deparaffinised then rehydrated.
2. Immerse section in 32 mmol/L potassium permanganate for 10 min.
3. Immerse section in 70 mmol/L oxalic acid for 5 min.
4. Rinse in 70 per cent ethanol.
5. Incubated in Miller's elastin stain (BDH Laboratory Supplies, Poole, UK) for 3 h.
6. Rinse in 70 per cent ethanol.
7. Incubate in van Gieson solution (50 per cent saturated picric acid solution, 0.09 per cent acid fuchsin) for 5 min.
8. Blot section dry then dehydrate, clear and mount.

Morphological analysis

Assessment of the features of plaque stability is always made on elastin-stained sections. These features are buried fibrous caps, representing previous healed plaque ruptures, and a break in the fibrous cap, representing an acute plaque rupture that has not yet healed. In the latter case, in order to exclude fibrous cap breaks caused during dissection or processing, we also require to see formed blood elements within the plaque at the site of cap breakage. These are usually erythrocytes.

Recognition of the features of plaque instability is not straightforward and requires practise. Buried fibrous caps appear as linear arrangements of bundled elastin fibres, usually overlain by foam cells, and when there are multiple buried fibrous caps they are usually offset from one another (we presume that this is because most ruptures occur at the shoulder of the plaque, so that the secondary overlying lesion then grows over that part of the earlier lesion). Acute, unhealed plaque ruptures can be very difficult to discern. The best approach is to scan the surface of the fibrous cap at high magnification looking for any discontinuities: where one is seen, the underlying plaque tissue needs to be examined very carefully for the presence of erythrocytes, betraying a rupture. An example of a plaque containing buried fibrous caps and an acute plaque rupture is shown in Figure 7.2.

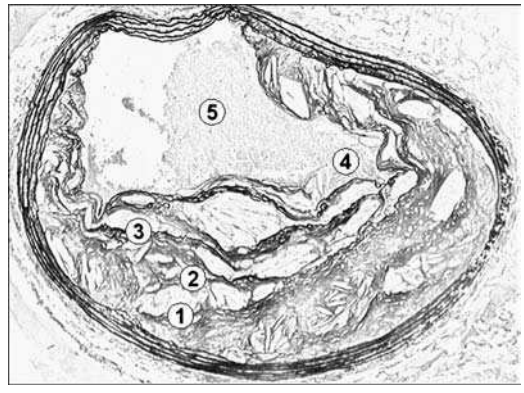

Figure 7.2 Plaque in a proximal brachiocephalic artery. 1,2,3 = Buried fibrous caps representing previous healed ruptures. 4 = Acute plaque rupture. 5 = Thrombus. For a color version of this figure, please see the images supplied on the accompanying CD

Morphometric analysis

The morphometric analysis scheme is outlined in Figure 7.3. Computerised morphometry is used to determine the following parameters:

1. The length of the outer elastic lamina ('OEL')

2. The length of the inner elastic lamina ('IEL')

3. The area of the plaque ('P')

The various aspects of vessel morphometry are then calculated according to the following formulae:

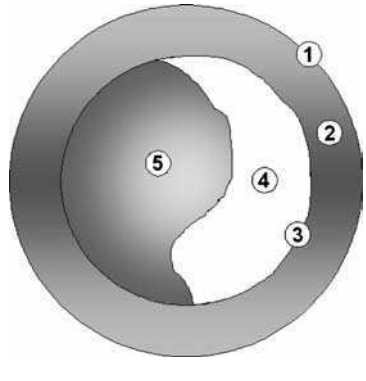

Figure 7.3 Diagrammatic representation of a lesioned artery. 1 = Outer elastic lamina. 2 = Media. 3 = Inner elastic lamina. 4 = Lumen. 5 = Plaque

Total vessel area $= \mathrm{OEL}^2/4\pi$

Media area $= (\mathrm{OEL}^2\text{-}\mathrm{IEL}^2)/4\pi$

Plaque area $= \mathrm{P}$

Lumen area $= (\mathrm{IEL}^2/4\pi) - \mathrm{P}$

These calculations assume that the vessel is perfectly circular in life, and that it has been sectioned at exactly 90° to its long axis. The latter assumption can be tested by inspection of the elastic laminae in the media: if they appear thickened at two regions that are 180° apart, the vessel is on a slant and needs to be re-embedded and re-sectioned.

It is also possible to measure fibrous cap thickness and the plaque content of lipid, collagen and elastin. The maximum fibrous cap thickness is determined from elastin-stained sections. For plaque fractional volumes of the component of interest, the simplest method is to use computerised morphometry and colour segmentation to select the component of interest. The area occupied by that component can be expressed as a percentage of total plaque area.

Study design considerations

We have shown that the first plaque ruptures occur after as little as 2 months of high-fat feeding.[11] This means that intervention studies can be carried out over this relatively short time period. Longer-term studies can be carried out over about 6 months, although the loss of animals to sudden death becomes an increasing problem as the time course is extended. The third protocol we use is 'late intervention': animals are fed high-fat diet for 16 weeks before the intervention is introduced, and treatment is continued for about 2 months.

Group sizes are of course dependent on the magnitude of the effect that is required to be found significant, which is a matter for the individual researcher. They are also dependent on the variability of the response being measured, and the responses (such as plaque area, incidence of acute plaque rupture, plaque lipid content, etc) vary widely in variability. Table 7.2 provides a guide to choosing group sizes for mouse plaque rupture studies.

Summary

The mouse model described herein is technologically simple and studies can be carried out over a reasonably short time frame. It should facilitate the discovery and preclinical development of interventions that may inhibit rupture, and also enable deeper investigation of the pathophysiology of this process. To what extent findings

Table 7.2 Animal group size used in plaque rupture studies

	Change from control		
Variable	25%	50%	75%
Media area	25	7	3
Plaque area	175	50	20
Lumen area	35	9	5
Total vessel area	25	7	4
Plaque lipid	60	17	9
Fibrous cap thickness	135	38	17
Buried fibrous caps	>300	100	45
Acute plaque ruptures	>300	165	70
Total plaque ruptures	200	55	25

Group sizes to detect as statistically significant ($P < 0.05$), with 80% power, the specified changes from control values of a range of parameters. Values have been calculated from a database of 446 male and female apolipoprotein E knockout mice fed high-fat diet for up to 48 weeks.

from the mouse can be applied to human plaques is still open to question: the positive action of pravastatin in this regard is a very encouraging sign,[11] but clearly more studies are still needed.

Acknowledgment

The author would like to thank Dr Helen Williams, Dr Jason Johnson, Dr Kevin Carson and Dr Ray Bush for their indispensable scientific input into the development of the mouse model of plaque rupture.

References

1. Mann J, Davies MJ. Mechanisms of progression in native coronary artery disease: role of healed plaque disruption. *Heart* 1999; **82**: 265–268.
2. Burke AP, Kolodgie FD, Farb A, Weber DK, Malcom GT, Smialek J, Virmani R. Healed plaque ruptures and sudden coronary death: evidence that subclinical rupture has a role in plaque progression. *Circulation* 2001; **103**: 934–940.
3. Takano M, Inami S, Ishibashi F, et al. Angioscopic follow-up study of coronary ruptured plaques in nonculprit lesions. *J Am Coll Cardiol* 2005; **45**: 652–658.
4. Ambrose JA, D'Agate DJ. Plaque rupture and intracoronary thrombus in nonculprit vessels: an eyewitness account. *J Am Coll Cardiol* 2005; **45**: 659–660.
5. Johnson JL, Jackson CL. Atherosclerotic plaque rupture in the apolipoprotein E knockout mouse. *Atherosclerosis* 2001; **154**: 399–406.
6. Rosenfeld ME, Polinsky P, Virmani R, Kauser K, Rubanyi G, Schwartz SM. Advanced atherosclerotic lesions in the innominate artery of the ApoE knockout mouse. *Arterioscler Thromb Vasc Biol* 2000; **20**: 2587–2592.

7. Calara F, Silvestre M, Casanada F, Yuan N, Napoli C, Palinski W. Spontaneous plaque rupture and secondary thrombosis in apolipoprotein E-deficient and LDL receptor-deficient mice. *J Patho* 2001; **195**: 257–263.
8. Piedrahita JA, Zhang SH, Hagaman JR, Oliver PM, Maeda N. Generation of mice carrying a mutant apolipoprotein E gene inactivated by gene targeting in embryonic stem cells. *Proc Natl Acad Sci USA* 1992; **89**: 4471–4775.
9. Plump AS, Smith JD, Hayek T, et al. Severe hypercholesterolemia and atherosclerosis in apolipoprotein E-deficient mice created by homologous recombination in ES cells Cell 1992; **71**: 343–353.
10. Williams H, Johnson JL, Carson KG, Jackson CL. Characteristics of intact and ruptured atherosclerotic plaques in brachiocephalic arteries of apolipoprotein E knockout mice. *Arterioscler Thromb Vasc Biol* 2002; **22**: 788–792.
11. Johnson J, Carson K, Williams H, et al. Plaque rupture after short periods of fat feeding in the apolipoprotein E-knockout mouse: model characterization and effects of pravastatin treatment. *Circulation* 2005; **111**: 1422–1430.

8

Perivascular cuff-, electronic and chemical injury-induced stenosis

Nuno M.M. Pires,[1,2] Margreet R. de Vries,[1] Abbey Schepers,[1,2] Daniel Eefting,[1,2] Jan-Willem H.P. Lardenoye[2] and Paul H.A. Quax[1,2]

[1]TNO-Quality of Life, Gaubius Laboratory, Leiden, The Netherlands and [2]Leiden University Medical Center, Leiden, The Netherlands

Abstract

Mice models for restenosis are based on infliction of vascular injury either via an intravascular (aimed at de-reendothelisation) or via a perivascular treatment. In the current chapter the mice restenosis models based on perivascular injury are described. Special emphasis is given to the perivascular cuff-induced neointima formation in the femoral artery.

All technical details for the procedure are given, the possible mechanism of action is described, and several applications of the cuff-model, either in combination with transgenic/atherosclerotic mice, with gene therapeutic approaches or in combination with drug-eluting cuffs, are illustrated.

Keywords

restenosis, neointima formation, perivascular injury, cuff, atherosclerosis, inflammation, smooth-muscle cell

Introduction

Mouse models for studying restenosis are of interest taking into account the availability of many transgenic mice, including those with an atherosclerotic phenotype, such as the apolipoprotein (Apo) E knockout mouse[1] ($Apoe^{-/-}$), the low-density lipoprotein (LDL) receptor knockout mouse[2] ($LDLR^{-/-}$) and the diet-dependent hyperlipidemic Apoe*3-Leiden transgenic mouse.[3]

A Handbook of Mouse Models of Cardiovascular Disease Edited by Qinbo Xu

Intravascular injury models to mimic the injury that is inflicted to the vessel wall during percutaneous coronary angioplasty are available, as described elsewhere in this book, but are technically complicated and the reproducibility is not that good, e.g. due to the lack of balloon catheters of appropriately small sizes. As an alternative, models based on perivascular injury are developed to study neointima formation in mouse models.

External perivascular arterial injury for vascular stenosis

A number of mouse models for neointima formation and vascular (re)stenosis have been extensively used based on the perivascular injury of the vessel wall. All these models have in common that formation of a vascular stenosis is induced through the perivascular injury of the blood vessel. This injury can be inflicted in several different ways. In the present chapter we describe some of these models of perivascular injury-induced neointima formation and discuss in further detail one of the most commonly used models; the mouse femoral artery perivascular cuff injury-induced stenosis.

Electronic injury-induced stenosis mouse model

In 1997, Carmeliet and colleagues described an injury model in which femoral arteries in mice were injured perivascularly via a single delivery of an electric current.[4] After surgical exposure of the femoral artery, a single current pulse of two seconds (160 μA) causes a complete loss of all medial smooth muscle cells (SMC) in the affected vessel over a length of 2–3 mm. In addition, by this treatment the arterial segment is denuded of intact endothelium and mural (non-occlusive) platelet-rich thrombosis is present within 2 h after injury. Via a vascular wound-healing response the mural thrombus degrades, transient infiltration of the vessel wall by inflammatory cells appears, and the necrotic debris diminishes progressively several days after the intervention. Simultaneously, SMC originating from the borders of the injured segment migrate towards the necrotic centre, ultimately leading to SMC accumulation. Within three weeks after injury, SMC migration and proliferation results in neointima formation containing a maximum of 12 layers of SMC. Although, the electric injury model is little comparable to human clinical pathology, this model is useful as a model of vascular wound healing.

Chemical injury-induced stenosis mouse model

Two mouse models of chemical injury-induced neointima formation, both adapted from thrombosis models, have been described in the past years.

Kikuchi *et al*. adapted a (photo)chemical model of thrombosis to a model of neointima formation in the mouse femoral artery.[5] In this model, endothelial injury is inflicted by photochemical reaction by a transluminal green light and intravenous administration of rose Bengal solution. An approximately 2 mm long segment of the

intact femoral artery is irradiated until blood flow completely stops due to a platelet- and fibrin-rich thrombus. Twenty-four hours later, spontaneous reflow is seen with denudation of the endothelium and medial SMC loss. Within 7 days neointima formation starts and reaches a maximum after 21 days, mainly consisting of SMC. In this (photo)chemical injury-induced stenosis, the outcome can be affected by the duration of the photo-irradiation, rose Bengal concentration, green light intensity and thickness of the vessel wall. These factors may seriously influence the reproducibility of the procedure.

Zhu *et al*. adapted a thrombosis model developed by Farrehi and colleagues[6] to a vascular injury model.[7] In this model, the carotid artery is carefully exposed and a filter paper saturated with a 10 per cent ferric chloride solution is placed on the adventitia for 3 min. This oxidative vascular injury leads to the formation of a transiently occlusive platelet-rich thrombus with endothelial cell loss and medial cell necrosis. After four weeks, intimal and medial hyperplasia is present in hyperlipidemic mice mainly consisting of SMC and foam cells. No or only minimal neointima formation is seen in normocholesterolemic mice. These results indicate that both abnormal lipid metabolism and arterial injury are necessary to induce significant neointima formation in this model.

Perivascular cuff injury-induced stenosis mouse model

In 1989, Booth and colleagues established a model for accelerated formation of atherosclerotic-like lesions in the carotid arteries of rabbits.[8,9] This model is based on placement of a plastic perivascular collar in the rabbit common carotid artery which results in the development of an intimal lesion containing foam cells and SMC in the cuffed segment. Based on the success of this model, in the mid 1990s, this model was downscaled to mice and modified using both non-constrictive and constricting tubes. These murine models are widely used to study both accelerated atherosclerosis phenomena and the process of restenosis.

Von der Thüsen *et al*. defined a mouse model in which a constricting silastic collar is placed around the common carotid artery of hypercholesterolemic mice.[10] The development of collar-induced lesions is found to occur predominantly in the area proximal to the collar and to be dependent on a high-cholesterol diet. Atherosclerotic-like lesions are evident after three and six weeks in $Apoe^{-/-}$ mice and $LDLR^{-/-}$ mice, respectively. Lumen stenosis reaches 85 per cent in $Apoe^{-/-}$ mice and 61 per cent in $LDLR^{-/-}$ mice 6 weeks after collar insertion. Presumably due to changes in shear stress, plaque formation is seen in the vessel segment proximal to the collar, whereas the intra-collar segment remains unaffected. Lesions initially consist of monocyte-derived foam cells and as maturation progresses plaques become increasingly heterogeneous with the development of a necrotic core and a fibrous caps with typical shoulder regions. Interestingly the model is dependent of a hypercholesterolemic environment, since no neointimal response emerges in normocholesterolemic mice. For the reasons mentioned above, this model is proposed to be a model for accelerated atherosclerosis rather than vascular stenosis.

Moroi *et al*. were the first to describe a model for inducing neointima formation in the femoral artery of mice.[11] The murine femoral artery is isolated and loosely sheathed with a non-occlusive polyethylene cuff. In this model, the endothelial cells are not directly manipulated or removed, oppositely to what occurs in other intravascular injury models for induction of neointima formation. Placement of the cuff results in highly reproducible neointima formation within the cuffed vessel segment in a 2- to 3-week period and mainly consists of SMC on top of the internal elastic lamina underneath an endothelial monolayer. Remarkably, arteries dissected from surrounding tissues (sham-operated) but where a cuff is not placed, do not develop a neointima. The presence of the cuff seems to be essential for inducing the neointima formation after the initial perivascular injury inflicted during surgery. Moreover, if in a similar way a cuff is placed around the carotid artery in the mouse, no neointima formation is observed in the cuffed vessel segment. The reason for this most likely is the anatomic difference between the femoral artery and the carotid artery in the mouse.

A more specific evaluation of the practicability, applications and mechanism of intimal formation of this widely used murine model of vascular stenosis is assessed in detail next.

Materials and methods

At the time of surgery, mice are anesthetized with an intraperitoneal injection of a 5 mg/kg Dormicum (Roche, Basel, Switzerland, contact: www.roche.com), 0.5 mg/kg Domitor (Orion, Helsinki, Finland, contact: www.orion.fi) and 0.05 mg/kg Fentanyl (Janssen, Geel, Belgium, contact: www.janssenpharmaceutica.be). This cocktail of anesthetics gives complete narcosis for at least 1 h and can be quickly antagonized with Antisedan 2.5 mg/kg (Orion) and Anexate 0.5 mg/kg (Roche).

A microscope with 10–15 × total magnification is necessary for the microsurgery (e.g. Olympus SZX9 microscope, contact: www.olympus-europa.com).

Basic instruments needed to perform the microsurgery are: (1) a blunt microforceps (length: 10.5 cm, height: 0.3 mm, Medicon Instruments, Tuttlingen, Germany, contact: www.medicon.de); (2) a sharp microforceps (length: 10.5 cm, height: 0.3 mm, Medicon Instruments); (3) a microscissor (length: 12.5 cm, height: 10 mm, Medicon Instruments); (4) a microneedle holder (length: 18.5 cm, Medicon Instruments).

A longitudinal 1–2 cm incision is made in the internal side of the leg and the femoral artery is dissected for 3 mm length from the femoral nerve and femoral vein. The femoral artery is looped with a ligature (USP: 6/0, Metric: 0.7., Silkam natural silk, B. Braun, Melsungen, Germany, contact: www.bbraun.com) and a non-constrictive fine bore polyethylene tubing (0.40 mm inner diameter, 0.80 mm outer diameter, Portex, Kent, UK, contact: www.portex.com) is cut to 2.0 mm length and longitudinally opened and sleeved loosely around the femoral artery. The cuff is closed up with two 6/0 ligature knots in the extremities of the cuff (Figure 8.1). Finally, the skin incision is closed with a running suture (USP: 6/0, Metric: 0.7.,

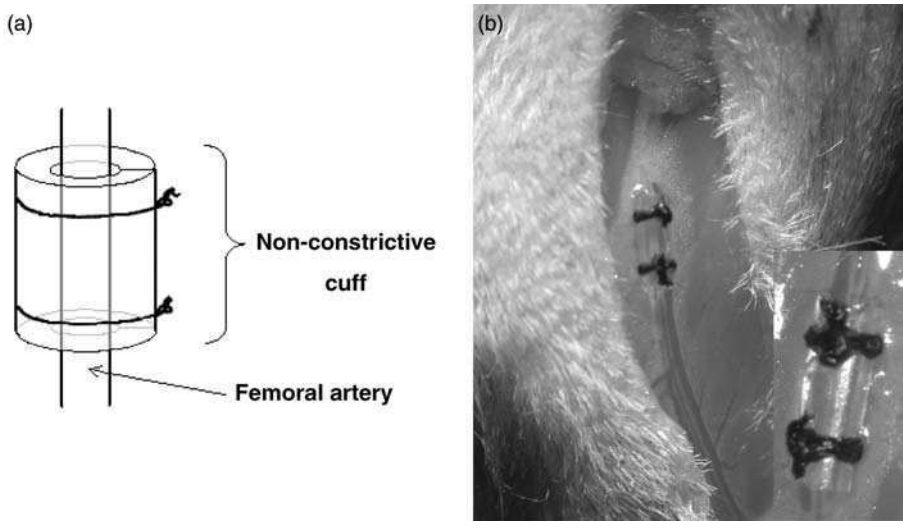

Figure 8.1 Schematic representation (a) and microphotograph (b) of femoral artery cuff positioning. For a color version of this figure, please see the images supplied on the accompanying CD

Silkam silk). The whole procedure takes about 20 to 30 min for a skilled operator and can also be repeated in the contralateral femoral artery. After surgery, animals are placed in a clean cage on top of a heating pad for a few hours.

For histological analysis, animals are typically killed 2–3 weeks after cuff placement. After anesthesia, the thorax is opened and a mild pressure-perfusion (100 mmHg) with 4 per cent formaldehyde in 0.9 per cent NaCl (v/v) is performed for 5 min by cardiac puncture. After perfusion, a longitudinal 2 cm incision is made in the internal side of the leg and the cuffed femoral artery is harvested as a whole and fixed overnight in 4 per cent formaldehyde.

Discussion

The cuff model extensively described in this chapter is one of the most often used models to mimick the process of post-angioplasty restenosis. Its popularity has several reasons. One of the main advantages is its feasibility; the model is easy to learn and can be performed in a limited amount of time. Complications during surgery hardly ever occur and thrombosis of the femoral artery due to the procedure is a rarity. The most important pitfall during surgery is femoral nerve injury. This can occur during the dissection of the femoral artery and results in clinical symptoms of paralysis of the lower extremity. Another advantage of this model is reproducibility. Inter-surgeon variability is small when performed in similar inbred mice strains. However, when a highly skilled surgeon performs the microsurgery, in some cases no neointima formation occurs. This phenomenon was experienced in our laboratory and

also reported by others. It is believed that because of the reduced tissue damage made by a skilled operator during the procedure, a 'threshold' of minimal tissue damage is not exceeded. We were able to overcome this problem with the introduction of a 'standardized mechanical injury' during surgery. This injury consists of gently squeezing the femoral artery with the blunt microforceps before the cuff is sleeved over the artery.

The exact mechanism underlying the induction of neointima formation in this mouse model is not fully understood. We believe that several factors are involved in the induction of neointima formation. First, the mild perivascular injury inflicted during the surgical procedure is of importance, as suggested by the low success rate of the highly skilled operators. In response to this injury expression of the extra domain A of fibronectin (EDA fibronectin) and its receptor Toll-like receptor 4 (Tlr4) is induced. Cuff placement subsequently triggers the influx of granulation cells in the perivascular space, which induces a perivascular inflammatory response. Together with the activation of Tlr4 by its endogenous ligand EDA fibronectin, this results in the induction of expression of various inflammatory cytokines (unpublished data), such as monocyte chemoattractant protein 1 (MCP-1), tumor necrosis factor-α (TNFα), regulated on activation, normal T cell expressed and secreted (RANTES), and macrophage inflammatory protein 1-α (MIP1-α). The importance of this reaction is underscored by the fact that sham operated arteries do not develop a neointima, although initially the expression of Tlr4 and EDA fibronectin is also induced in these sham-operated vessel segment. Only in cuffed vessel segments Tlr4 expression remains elevated during at least 7 days (unpublished data). The causal role of the Tlr4 pathway in cuff induced neointima formation is demonstrated by the reduced neointima formation in Tlr4-deficient mice[12] and stimulation of neointima formation by local lipopolysaccharide application.[13] The fact that cuff-induced neointima formation is strongly inhibited by local application of dexamethasone underscores an important role of inflammatory activation in this model.[14]

Subsequently, SMC in the media become activated and SMC migration and proliferation occurs (Figure 8.2).[11,15,16] Recently, it was demonstrated that the generation of reactive oxygen species also plays an important role in the regulation of cuff induced neointima formation.[17]

Application

In the femoral artery perivascular cuff model, the primary endpoint is neointima formation. Cuff placement around the femoral artery results in a profound neointima formation in 2–3 weeks, consisting of four to six layers of SMC. The cuff-induced neointima consists primarily of SMC on top of the internal elastic lamina, beneath a layer of platelet-endothelial cell adhesion molecule (PECAM)-positive endothelial cells (Figure 8.3, left column). Contrary to other vascular restenosis models in the mouse, the endothelial monolayer is not directly manipulated or removed allowing to study of the effect of individual endothelial factors (e.g. endothelium-derived NO) on neointima formation. Therefore, this cuff model is believed to be complementary to

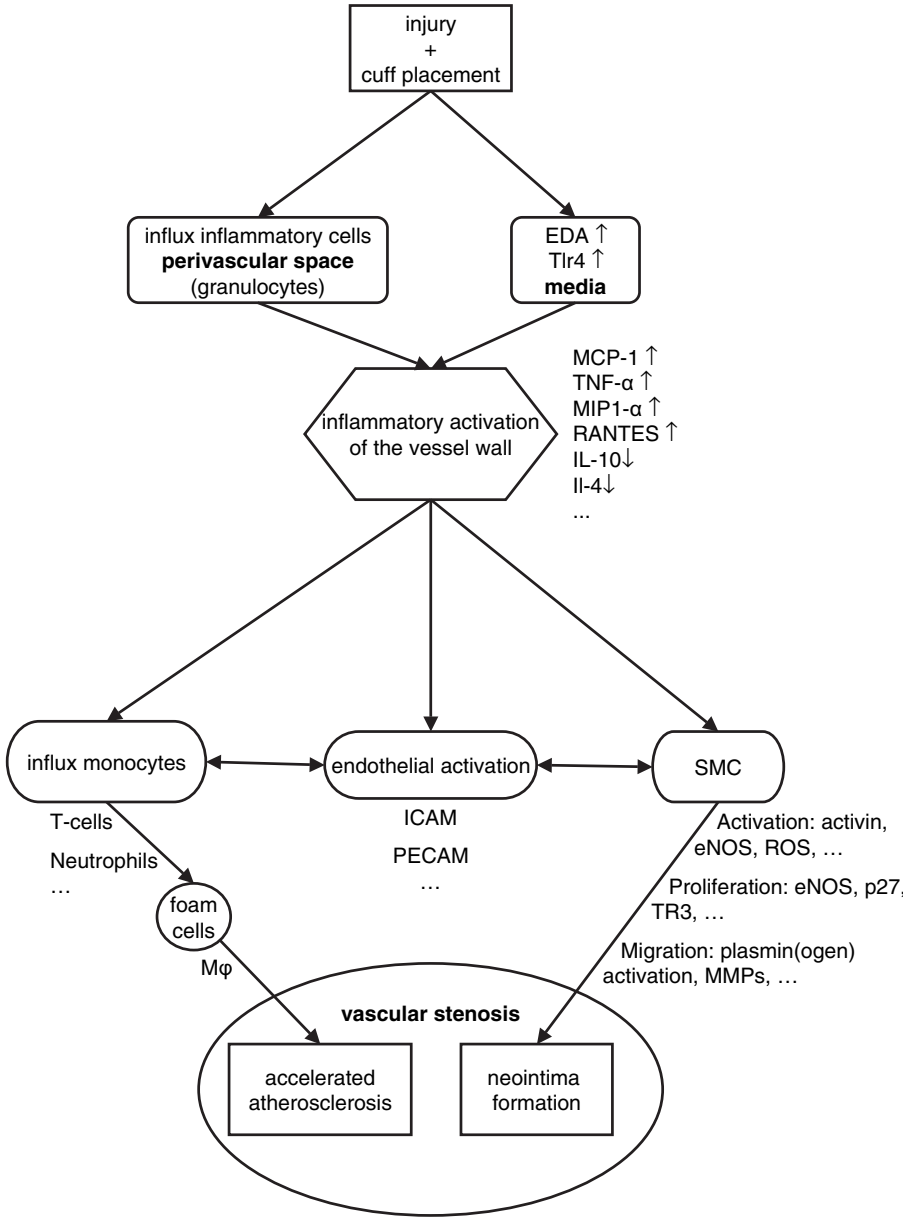

Figure 8.2 Proposed mechanism underlying the induction of neointima formation of the mouse femoral artery perivascular cuff model

other models of neointima formation by offering the capability to examine vessel responses to injury that are relevant to vascular remodeling.

This elegant mouse model has been proven to be reproducible, easily quantifiable, and lends itself well to analysis of individual gene products that can be manipulated by transgenic approaches and targeted gene disruption.

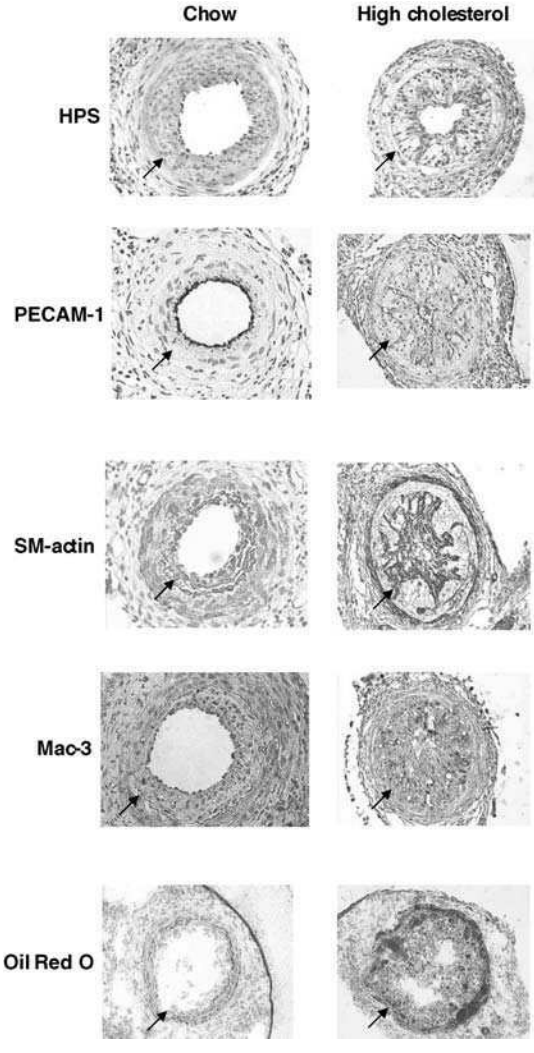

Figure 8.3 Cross-section of the murine femoral artery 14 days after placement of cuff in mice on a chow and a high cholesterol diet. Hematoxylin–phloxine–saffron (HPS) staining. In mice on a chow diet, a multiple cell layer-thick intimal hyperplasia is observed. In mice on a high cholesterol diet, significant increase in intimal hyperplasia is observed; PECAM-1 staining for endothelial cells. In both mice on a chow and on a high cholesterol diet, endothelial cells are present at the luminal side of the intimal lesion; α-SMC actin staining. Intimal hyperplasia in mice on a chow diet predominantly consists of α-SMC actin-positive cells. In mice fed a high cholesterol diet, SMC occur mainly on the luminal side of the foam cell accumulation; Mac-3 staining for macrophages. Intimal lesions of mice on a high cholesterol diet predominantly consist of lipid-loaded foam cell macrophages. Macrophages are also present in granulation tissue within the cuff of both mice on a chow diet, as in mice on a high cholesterol diet; Oil red O lipid staining. Abundant lipid deposition in foam cells in mice on a high cholesterol diet, both in the intimal lesion as well as in the media. Arrows indicate inner elastic lamina; Magnification 100$\times$. For a color version of this figure, please see the images supplied on the accompanying CD

Hyperlipidemia

Moroi and colleagues showed, for the first time, that this mouse model for neointima formation was responsive to strain and gender variations.[11]

In the past, we have assessed the effect of diet-induced hypercholesterolemia on neointima formation in diet-dependent hyperlipidemic mice.[18] Femoral artery cuff-induced neointima formation was induced in ApoE*3-Leiden transgenic mice fed a chow diet or a high cholesterol diet. In mice fed a chow diet (mean plasma-cholesterol level, 2.3 mmol/l), a two- to four-cell layers thick intima, predominantly consisting of α-SMC actin-positive cells, was observed after 14 days. A high cholesterol diet (mean plasma-cholesterol level, 28.6 mmol/l) resulted in a 7.8-fold increase of total intimal area. In the high-cholesterol group, the intima consisted predominantly of lipid-loaded foam cells and α-SMC actin-positive cells (Figure 8.3). The development of the atherosclerotic-like lesions started directly after the placement of the cuff as demonstrated by monocyte adhesion, which was already present after 1 day. The first deposition of lipid-filled foam cells on the luminal side of the inner elastic lamina was observed as early as 3 days after the placement of the cuff, resulting in a near-total occlusion of the lumen after 14 days (Figure 8.4). Hypercholesterolemia resulted in a rapid, cholesterol-dependent induction of foam cell-rich neointima in cuffed femoral arteries of diet-driven hyperlipidemic ApoE*3-Leiden transgenic mice. This accelerated diet-dependent induction of atherosclerotic-like lesions is of value in studying the mechanisms of accelerated atherosclerosis.

Genetic modified factors

Over the past years, numerous research groups made use of this sensitive mouse model to study and modulate the role of several factors on neointima formation. Through the use of knockout and transgenic mice strains, as well the use of viral vectors approaches, the role of several factors have been addressed in combination with this mouse model to unravel in more detail the molecular and cellular key players in the process of (re)stenosis. The majority of these studies address the role of inflammation-promoting factors, SMC proliferation and migration features and lipid metabolism.

An accumulating body of evidence recognises a pivotal role for inflammation in the development and progression of vascular stenosis. Several inflammatory factors, like MCP-1 and its receptor (CCR2) or Tlr2 and -4 have been knocked down or overexpressed to address the role of such elements on neointima formation.[12,19,20]

Likewise, SMC migration and proliferation is known to play a major role in restenosis. Once again, the involvement of numerous factors like adrenomedullin deficiency or overexpression, osteopontin absence, TR3 orphan receptor overexpression and plasmin activity inhibition directly at the cell surface via an adenovirus vector (Ad.CMV.mATF.BPTI) have been addressed in combination with this mouse model of neointima formation (Figure 8.5).[15,21–24]

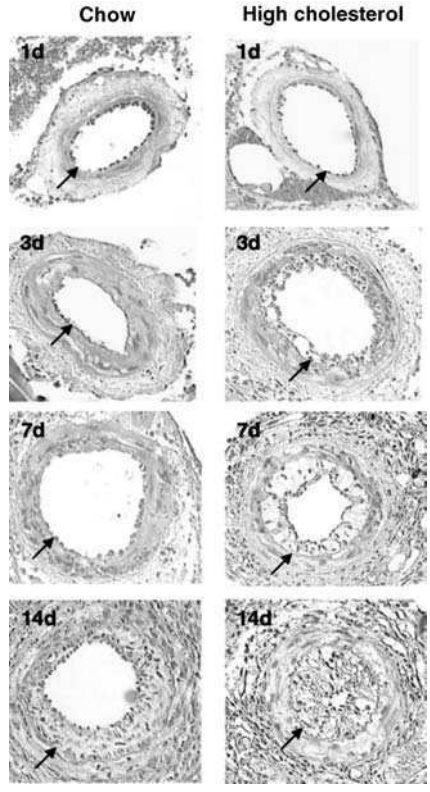

Figure 8.4 Cross-section of murine femoral artery on several time points after cuff placement in mice on a chow and a high cholesterol diet. In mice on a chow diet, the first signs of neointima formation are observed 7 days after placement of the cuff. After 14 days, intimal hyperplasia is two to four cell layers thick. In mice on a high cholesterol diet, however, cell adhesion is observed on the luminal side of the inner elastic lamina one day after cuff placement. After three days, foam cell deposition on the inner elastic lamina is detectable in mice on a high cholesterol diet. Seven days after cuff placement in mice on a high cholesterol diet, foam cell accumulation in the intimal lesion progressed and foam cells are observed in the media. Foam cell accumulation progressed in time until near-total occlusion of the lumen 14 days after cuff placement in mice on a high cholesterol diet. HPS staining. Arrows indicate inner elastic lamina. Magnification 100×. For a color version of this figure, please see the images supplied on the accompanying CD

Moreover, the involvement of the lipid metabolism and metabolic syndrome (e.g. insulin receptor substrate-1 and -2 and the very low density lipoprotein receptor) and the contribution of bone marrow derived cells in neointima formation have also been assessed in concert with this mouse model.[25–27]

Mimicking drug-eluting stents

Our laboratory has recently showed that the use of drug-eluting stents (DES) can be mimicked in the mouse by using a drug-eluting perivascular cuff constructed from a

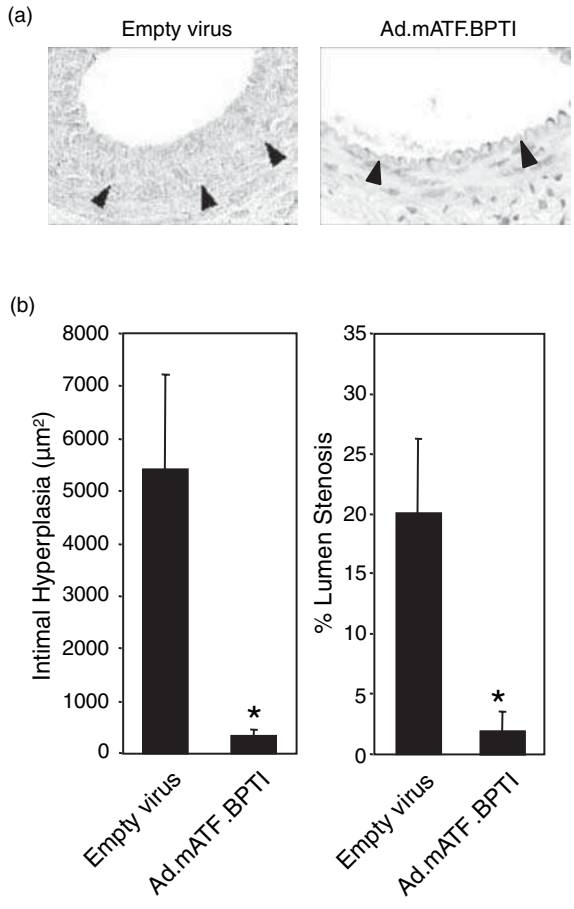

Figure 8.5 Directly after cuff placement, mice were infected intravenously with Ad.mATF.BPTI. Mice were killed after 19 days and neointima formation was analysed. Representative histological sections are shown (a). HPS staining. Arrowheads indicate inner elastic lamina. Magnification $400\times$. (b) Neointima and percentage of lumen stenosis in cuffed arteries were quantified in multiple cross-sections of segments in Ad.Control- and Ad.mATF.BPTI-infected mice (mean $\pm$ SEM, $n = 6$, $^*P < 0.001$). For a color version of this figure, please see the images supplied on the accompanying CD

poly(ε-caprolactone) (PCL) polymeric formulation suitable for controlled drug delivery.[28] This novel drug-eluting cuff simultaneously induces reproducible neointima formation in the mouse femoral artery similarly to the established polyethylene cuff and can easily be loaded with anti-restenotic compounds, i.e. paclitaxel and rapamycin, to give an *in vitro* sustained and dose-dependent release for at least 3 weeks, allowing locally confined delivery of anti-restenotic compounds to the cuffed vessel segment (Figure 8.6). This new approach gives the possibility to evaluate the effects of the anti-restenotic pharmacological strategies to be used in combination with DES technologies on neointima formation, vessel wall pathology and potential side effects. A relative shortcoming is that this model delivers the tested compounds

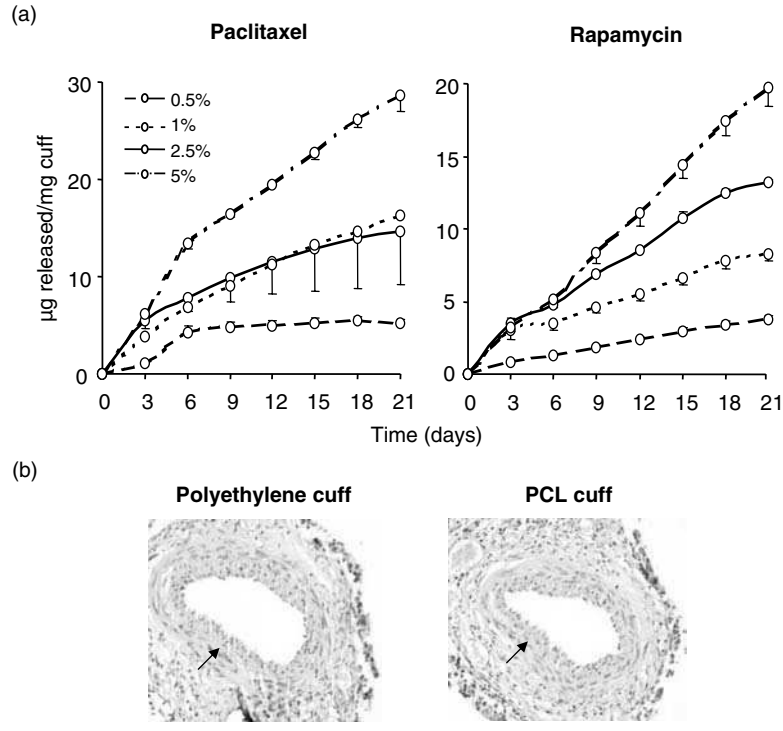

Figure 8.6 *In vitro* release profiles of poly(ε-caprolactone) (PCL) cuffs loaded with increasing percentages of anti-restenotic drugs for a 21-day period (a). Cross-section of cuffed murine femoral artery 21 days after placement of either a polyethylene or a PCL cuff (b); a comparable multiple cell layer thick intimal hyperplasia is observed in both cuff types. HPS staining. Arrows indicate inner elastic lamina. Magnification 100 ×. For a color version of this figure, please see the images supplied on the accompanying CD

periadventitialy rather then intraluminarly as it occurs in the clinical setting. Nevertheless, the mouse femoral artery is only a few cells layers thick and compounds can easily cross the vessel wall and be present at high concentration at the luminal side.

References

1. Zhang SH, Reddick RL, Piedrahita JA, Maeda N. Spontaneous hypercholesterolemia and arterial lesions in mice lacking apolipoprotein E. *Science* 1992; **258**: 468–471.
2. Ishibashi S, Brown MS, Goldstein JL, Gerard RD, Hammer RE, Herz J. Hypercholesterolemia in low density lipoprotein receptor knockout mice and its reversal by adenovirus-mediated gene delivery. *J Clin Invest* 1993; **92**: 883–893.
3. van den Maagdenberg AM, Hofker MH, Krimpenfort PJ, et al. Transgenic mice carrying the apolipoprotein E3-Leiden gene exhibit hyperlipoproteinemia. *J Biol Chem* 1993; **268**: 10540–10545.

4. Carmeliet P, Moons L, Stassen JM, et al. Vascular wound healing and neointima formation induced by perivascular electric injury in mice. *Am J Pathol* 1997; **150**: 761–776.
5. Kikuchi S, Umemura K, Kondo K, Saniabadi AR, Nakashima M. Photochemically induced endothelial injury in the mouse as a screening model for inhibitors of vascular intimal thickening. *Arterioscler Thromb Vasc Biol* 1998; **18**: 1069–1078.
6. Farrehi PM, Ozaki CK, Carmeliet P, Fay WP. Regulation of arterial thrombolysis by plasminogen activator inhibitor-1 in mice. *Circulation* 1998; **97**: 1002–1008.
7. Zhu Y, Farrehi PM, Fay WP. Plasminogen activator inhibitor type 1 enhances neointima formation after oxidative vascular injury in atherosclerosis-prone mice. *Circulation* 2001; **103**: 3105–3110.
8. Booth RF, Martin JF, Honey AC, Hassall DG, Beesley JE, Moncada S. Rapid development of atherosclerotic lesions in the rabbit carotid artery induced by perivascular manipulation. *Atherosclerosis* 1989; **76**: 257–268.
9. Kockx MM, De Meyer GR, Jacob WA, Bult H, Herman AG. Triphasic sequence of neointimal formation in the cuffed carotid artery of the rabbit. *Arterioscler Thromb* 1992; **12**: 1447–1457.
10. von der Thusen JH, van Berkel TJ, Biessen EA. Induction of rapid atherogenesis by perivascular carotid collar placement in apolipoprotein E-deficient and low-density lipoprotein receptor-deficient mice. *Circulation* 2001; **103**: 1164–1170.
11. Moroi M, Zhang L, Yasuda T, et al. Interaction of genetic deficiency of endothelial nitric oxide, gender, and pregnancy in vascular response to injury in mice. *J Clin Invest* 1998; **101**: 1225–1232.
12. Vink A, Schoneveld AH, van der Meer JJ, et al. In vivo evidence for a role of toll-like receptor 4 in the development of intimal lesions. *Circulation* 2002; **106**: 1985–1990.
13. Hollestelle SC, De Vries MR, Van Keulen JK, et al. Toll-like receptor 4 is involved in outward arterial remodeling. *Circulation* 2004; **109**: 393–398.
14. Pires NM, Schepers A, van der Hoeven BL, et al. Histopathologic alterations following local delivery of dexamethasone to inhibit restenosis in murine arteries. *Cardiovasc Res* 2005; **68**: 415–424.
15. Quax PH, Lamfers ML, Lardenoye JH, et al. Adenoviral expression of a urokinase receptor-targeted protease inhibitor inhibits neointima formation in murine and human blood vessels. *Circulation* 2001; **103**: 562–569.
16. Engelse MA, Lardenoye JH, Neele JM, et al. Adenoviral activin a expression prevents intimal hyperplasia in human and murine blood vessels by maintaining the contractile smooth muscle cell phenotype. *Circ Res* 2002; **90**: 1128–1134.
17. Ozumi K, Tasaki H, Takatsu H, et al. Extracellular superoxide dismutase overexpression reduces cuff-induced arterial neointimal formation. *Atherosclerosis* 2005; **181**: 55–62.
18. Lardenoye JH, Delsing DJ, de Vries MR, et al. Accelerated atherosclerosis by placement of a perivascular cuff and a cholesterol-rich diet in ApoE*3Leiden transgenic mice. *Circ Res* 2000; **87**: 248–253.
19. Egashira K, Zhao Q, Kataoka C, et al. Importance of monocyte chemoattractant protein-1 pathway in neointimal hyperplasia after periarterial injury in mice and monkeys. *Circ Res* 2002; **90**: 1167–1172.
20. Schoneveld AH, Oude Nijhuis MM, van Middelaar B, Laman JD, de Kleijn DP, Pasterkamp G. Toll-like receptor 2 stimulation induces intimal hyperplasia and atherosclerotic lesion development. *Cardiovasc Res* 2005; **66**: 162–169
21. Kawai J, Ando K, Tojo A, et al. Endogenous adrenomedullin protects against vascular response to injury in mice. *Circulation* 2004; **109**: 1147–1153.

22. Imai Y, Shindo T, Maemura K, et al. Resistance to neointimal hyperplasia and fatty streak formation in mice with adrenomedullin overexpression. *Arterioscler Thromb Vasc Biol* 2002; **22**: 1310–1315.
23. Isoda K, Nishikawa K, Kamezawa Y, et al. Osteopontin plays an important role in the development of medial thickening and neointimal formation. *Circ Res* 2002; **91**: 77–82.
24. Engelse MA, Arkenbout EK, Pannekoek H, de Vries CJ. Activin and TR3 orphan receptor: two 'atheroprotective' genes as evidenced in dedicated mouse models. *Clin Exp Pharmacol Physiol* 2003; **30**: 894–899.
25. Kubota T, Kubota N, Moroi M, et al. Lack of insulin receptor substrate-2 causes progressive neointima formation in response to vessel injury. *Circulation* 2003; **107**: 3073–3080.
26. Tacken PJ, Delsing DJ, Gijbels MJ, et al. VLDL receptor deficiency enhances intimal thickening after vascular injury but does not affect atherosclerotic lesion area. *Atherosclerosis* 2002; **162**: 103–110.
27. Tanaka K, Sata M, Hirata Y, Nagai R. Diverse contribution of bone marrow cells to neointimal hyperplasia after mechanical vascular injuries. *Circ Res* 2003; **93**: 783–790.
28. Pires NM, van der Hoeven BL, de Vries MR, et al. Local perivascular delivery of anti-restenotic agents from a drug-eluting poly(epsilon-caprolactone) stent cuff. *Biomaterials* 2005; **26**: 5386–5394.

9

Flow-induced vascular remodeling

Vyacheslav A. Korshunov and **Bradford C. Berk**

Cardiovascular Research Institute and Department of Medicine, University of Rochester, Rochester, NY, USA

Introduction

Recent clinical data demonstrate that regions of low shear stress develop progressive atherosclerosis measured by increased intima-media thickening (IMT) and outward remodeling of coronary arteries.[1,2] More importantly, IMT is associated with an increased risk of heart disease and stroke[3] and has a strong genetic correlation.[4]

In many situations changes in vessel size will be driven by changes in lumen diameter, which serve to normalise wall shear stress.[5] In particular, maintenance of wall shear stress at physiologic values (10–20 dyne) appears to be an important mechanism for remodeling.[6-8] Several animal models of partial carotid ligation have been developed by our laboratory and others for rabbit,[9] mouse[7] and rat.[10] We showed that significant remodeling occurred in rats when the internal and external left carotid arteries were ligated, reducing left common carotid blood flow by 90 per cent to that of the patent occipital artery. There was a small decrease in the 'low flow' left common carotid diameter and a substantial increase in 'high flow' right common carotid diameter with normalisation of shear stress. A potential disadvantage of the partial ligation technique in rats and rabbits is the lack of a neointima in the low flow vessels. In contrast in the mouse, after complete carotid ligation with blood flow cessation[11] there is substantial neointima formation. However, the physiologic relevance of this model to study the effects of chronic 'low flow' is diminished by the absence of flow (zero flow) and the presence of occlusive thrombus.

A Handbook of Mouse Models of Cardiovascular Disease Edited by Qinbo Xu

Materials and methods

Animals

Male (~22 g) and female (~19 g) inbred mice were used at 9 weeks (Jackson Laboratories, Bar Harbor, ME, USA). All procedures were approved by the University of Rochester Animal Care Committee in accordance with the guidelines of the National Institutes of Health for the *Care and Use of Laboratory Animals*.

Surgery

Mice were anesthetised with an intraperitoneal injection (26G1/2 needle, BD) of ketamine (130 mg/kg) and xylazine (8.8 mg/kg) in saline (10 ml/kg). The neck was shaved, but for better results commercially available hair removal cream (Nair brand) was used for 1 minute. Operation field was cleaned by a sponge (5 × 5 cm), an iodine solution applied, followed by 70 per cent alcohol. The mouse was restrained and maintained at 37 °C on a heating pad under aseptic conditions. Prior to incision, two sterile 6-0 silk ligatures (2 cm long each) were precut. The procedure is as follows. Begin with a midline incision of skin only. Next using two pairs of forceps (FST, Dumont) dissect away the *submaxillary glands* to expose the muscles and the trachea. Then move 20–40 mm caudally and to the right, which is between the *masseter* and *sternohyoid muscles*. Dissect connective tissues along the *masseter muscle* to expose the carotid bifurcation, which is covered by the *caudal belly of the digastric muscle* and the *left vagus nerve*. For better exposure of the carotid bifurcation, gently dissect and reposition the nerve to your right and, if needed, the *caudal belly* also. Next expose the *external carotid artery* by gently dissecting away the *left occipital artery*, which goes over the *external carotid* and down to the *left vagus nerve*. Holding closed your right hand non-sharp forceps (#S&T JFA-5b) make a 'scoop' move (move forceps at 90 ° to *external carotid artery*, when pass forceps laterally from the right to the left) to hold only *external carotid artery* on the forceps. Gently open your forceps reach for the ligature and pass the ligature from the left to the right (try to avoid twisting the vessel). Leave the ligature in place and dissect the *internal carotid artery.* Dissect from the left side and expose the *superior thyroid artery.* Make the same move of your right-hand forceps to pass a ligature around the *internal carotid artery.* Put simple untied knots on both branches. Ligate the carotids in the following order: the *external carotid* and *internal carotid* by one tie as shown in Figure 9.1. Cover the incision with warm sterile saline (keep in a 1 ml syringe) and using sterile cotton buds retract the *submaxillary glands*. Remove excess saline and close the neck incision by interrupted sutures using 6-0 Vicryl coated suture. For the controls use a sham-operation in which the branches of the *left carotid artery* are exposed as described above but not ligated. The animals are allowed to recover and housed individually under specific pathogen-free conditions with 12 light/12 hour dark cycle. Based on our studies 14 days after the surgery is the optimal time to study intima formation.[12–14]

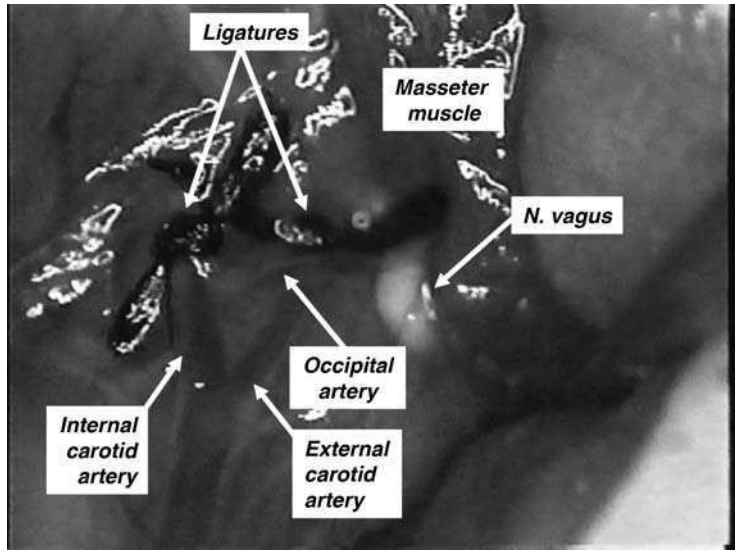

Figure 9.1 Microphotograph of the ligated *external carotid* and *internal carotid arteries*. After ligation flow was maintained only through the *occipital artery*. Magnification is 3x. For a color version of this figure, please see the images supplied on the accompanying CD

We have found that the reduction of blood flow and shear stress was similar among five inbred mice strains as shown in Table 9.1.[13]

Perfusion fixation and tissue processing

At the time of termination, animals are anesthetised and perfused with saline at a pressure of 100 mmHg through the left ventricle for 4 min followed by 3 min perfusion with 10 per cent paraformaldehyde in sodium phosphate buffer (pH 7.0). The left and right common carotid arteries as well as the thoracic aorta are harvested, and placed in perfusion solution overnight. Bifurcation sites of *carotids* are marked

Table 9.1 Changes of blood flow and shear stress after ligation among inbred mice strains

	ΔBlood flow (%)		ΔShear stress (%)	
	Left carotid	Right carotid	Left carotid	Right carotid
C3H	-82 ± 1	64 ± 22	-65 ± 1	90 ± 25
DBA	-75 ± 2	62 ± 7	-86 ± 1	$25 \pm 5^{*}$
C57	-90 ± 2	74 ± 8	-87 ± 3	$38 \pm 6^{*}$
SJL	-82 ± 10	34 ± 14	-73 ± 15	$9 \pm 12^{*}$
FVB	-77 ± 7	48 ± 11	-87 ± 4	$-2 \pm 8^{*}$

All data presented as mean ± SEM.
$^{*}L < 0.05$ compared with C3H (ANOVA).
Adapted from Korshunov and Berk, 2004.[13]

with two different colors of tissue marking dye (TBS, USA; e.g., red, Cat #TMD-R – for the *right carotid*, green, Cat #TMD-G – for the *left carotid*) when put into the multi-chamber cassette (Cat # M503-2, Stat Lab Medical Products) prior to processing and later, embedded in parallel in a paraffin block. A series of cross-sections (4 μm) are made from the bifurcation every 200 μm through 2 mm length of *carotid artery* (usually, 14 divisions of sections) as described.[12,14]

Histology

Cross-sections are stained with hematoxylin and eosin, and analysed using MCID image software (MCID Elite 6.0 software from Imaging Research Inc.). The circumference of the lumen, the length of the internal elastic lamina (IEL) and external elastic lamina (EEL) are determined by tracing along the luminal surface. The circumference of the lumen is used to calculate the lumen area. The intimal area is determined as the area defined by luminal surface and IEL. The medial area is defined by the IEL and EEL. The adventitia area is defined by EEL and vessel surface. Quantitative morphometry is facilitated since the external elastic lamina is easy to identify in hematoxylin and eosin stained cross-sections.

Data analysis

To improve reproducibility we based our morphometric analysis using the *carotid* bifurcation as a landmark. The initial point for measurements is determined by vessel appearance as described (Figure 9.2a). Initially we analysed the morphometry along the entire length of the carotid as shown (Figure 9.2b). We observed no significant differences in the intima+media area along the length of the *carotid*. However, there was greater variability in the measurements in the more proximal portions (near the aorta) of the *carotid*. This variability may reflect changes in accuracy of measurements further from the bifurcation or may be due to more variable hemodynamics near the origin of the *carotid*. For this reason we chose to analyse a series of 4 μm cross-sections every 200 μm over a 2 mm length of *carotid artery* beginning at the origin defined by bifurcation morphology. Two or three sections were analysed and the mean for each of 10 divisions was calculated for both arteries for every animal. To obtain more accurate data we developed an approach for evaluating remodeling over 2 mm *carotid* length:

$$\text{Volume} = \sum_{i=8} (\text{Area}_i \times 200)\mu\text{m}$$

Volume is the area volume on 1600 μm length of *carotid*; Area_i is area at one division; *i* is the number of divisions; 200 is the length between divisions is μm. We used division numbers 2–9 for calculating *Volume* from 10 initial divisions, because area variability occurred next to the bifurcation due to enlargement of arteries.

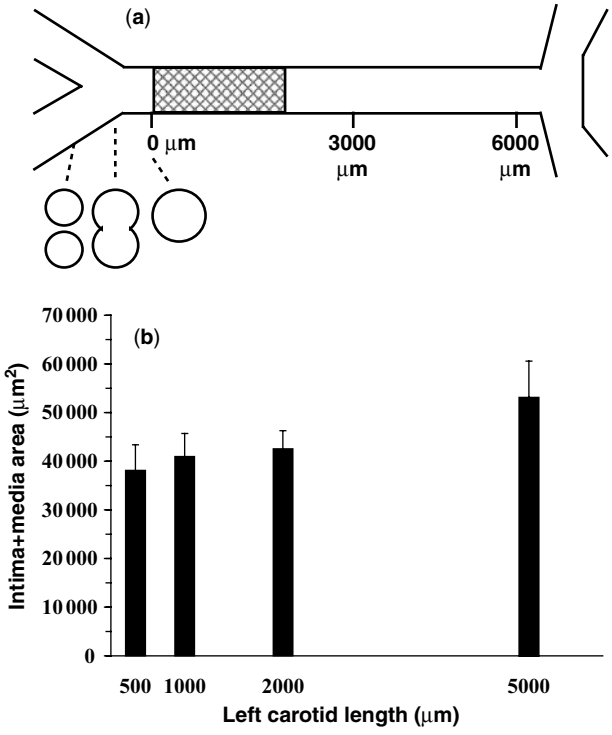

Figure 9.2 The media + intima area over length of the left carotid 2 weeks after ligation. (a) Scheme of left carotid artery (LCA). Note the distance = 0 mm is defined as the beginning of a single vessel without the 'figure 8' appearance of the bifurcation. (b) Ligation increases intima + media areas in LCA. There were no significant differences in intima + media area after ligation over the length from 0 to 5000 μm. Data are the average of three sections from three animals. Values are mean ±SEM

Discussion

The present model of flow-dependent vascular remodeling in the mouse is a simple and reproducible model that recapitulates several aspects of human cardiovascular disease. We encourage usage of both genders since there was no sex-difference in vascular remodeling noted for the five inbred strains of mice we studied (Table 9.2).[13] A possible difficulty that may be encountered while learning this technique could be anatomical variations among mice in dissection of the *external carotid artery*. These problems may be avoided by defining the mouse neck anatomy prior to starting experiments. It is critical while operating on arteries to be gentle and avoid any overstretch. Importantly, some genetically altered mice may exhibit reduced vessel wall elasticity making the vessels more prone to damage. In addition, since the incision on the neck of the mouse may make chewing difficult, we usually put a couple pieces of chow soaked with water into the cage for feeding by mice during recovery. As survival surgery, other severe conditions (e.g. irradiation prior

Table 9.2 Comparison of vessel compartments between genders among inbred-mice strains

		Lumen volume	Intima + media volume	Adventitia volume
C3H	Males	63 ± 1	30 ± 4	28 ± 3
	Females	67 ± 6	26 ± 3	28 ± 3
DBA	Males	62 ± 10	31 ± 2	24 ± 2
	Females	67 ± 6	39 ± 4	30 ± 4
C57	Males	57 ± 5	38 ± 8	26 ± 2
	Females	51 ± 5	38 ± 6	27 ± 4
SJL	Males	39 ± 6	65 ± 7	33 ± 2
	Females	37 ± 3	59 ± 10	26 ± 3
FVB	Males	95 ± 13	85 ± 10	31 ± 3
	Females	91 ± 6	78 ± 9	31 ± 1

For each strain ~six males and six females were studied. All data are mean ± SEM. There were no significant sex-differences in all strains.

bone marrow implantation) should be used with caution, and should likely include with immunosuppressive treatment as reported for flow cessation model.[15]

Another important factor for remodeling we discovered is the blood flow measurements. The blood flow in the *common carotid artery* was measured using an ultrasonic transit-time volume flowmeter (Transonic Systems, Inc), while the vessels were covered with saline and acoustic gel to achieve acoustic contact. The blood flow signal was recorded and analysed by a computerised PowerLab System using Chart 1.3 software for Macintosh. Zero flow on the flowmeter was checked at the beginning of the experiments by temporarily occluding the vessel with aseptic silk 6-0 suture. However, at the time of ligation, manipulations associated with flow measurements in *common carotid artery* decreased vascular remodeling (Figure 9.3). Thus, we strongly emphasise that blood flow should be measured directly only at the time of termination.

We also found that inflammation plays an important role in flow-induced vascular remodeling.[12,14] However, there were no morphologic differences between sham *carotids* and *carotids* that underwent surgery and placement of a suture without ligature for either intima+media area (Figure 9.4a) or adventitia area (Figure 9.4b) along a 2 mm length of the *carotid artery.*[12] There was no intima formation in either sham or untied ligature animals. Thus, placement of suture material by itself did not cause vessel remodeling in our experiments.

Applications

The model described here offers many novel approaches to study physiological vascular remodeling in response to alterations in blood flow in the mouse. This model has several unique features. First, it involves a dramatic reduction in flow in the left carotid (~90 per cent decrease) with maintenance of an intact endothelium and no thrombosis, in contrast to the complete flow cessation model of Kumar and Lindner.[11] Second, this is the first partial ligation model to exhibit intima formation

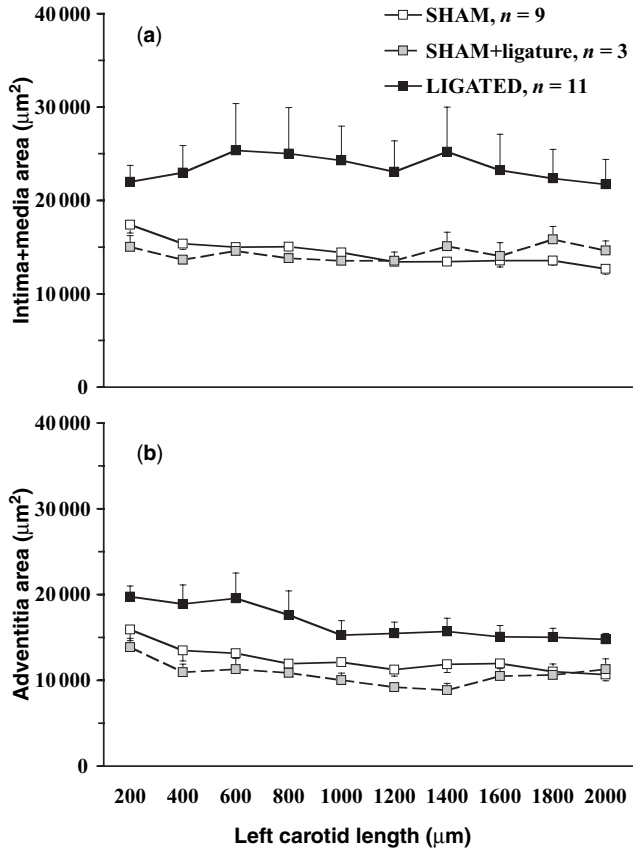

Figure 9.3 Effect of untied ligature on the remodeling in the left carotid of C57Bl1/6J mice 2 weeks after ligation. (a) Intima + media area. (b) Adventitia area. There were no morphologic differences between sham carotids and carotids that underwent surgery and placement of a suture without ligature for either intima + media area or adventitia area along a 2 mm length of the carotid artery. There was no intima formation in either sham or untied ligature animals. In contrast, ligation induced a significant increase in intima + media and adventitia areas in the LCA. Thus placement of suture material by itself did not cause vessel remodeling in our experiments. Values are mean ± SEM

in the low flow vessel. Finally, the present model provides access in one animal to two vessels responding to opposing changes in blood flow: increased in the *right carotid* (high-flow associated with increased lumen area) and decreased in the *left carotid*.

This model should be very useful to study candidate genes that influence important processes such as vascular remodeling and development of IMT as well as new treatments. We have already utilized this low flow model to study genetic aspects of the 'Glagov phenomenon' among five inbred strains of mice.[13] We also characterized the role of the two major matrix degrading systems: plasminogen activators and matrix metalloproteinases in ligated carotids from C57Bl/6J and FVB/NJ mice.[14]

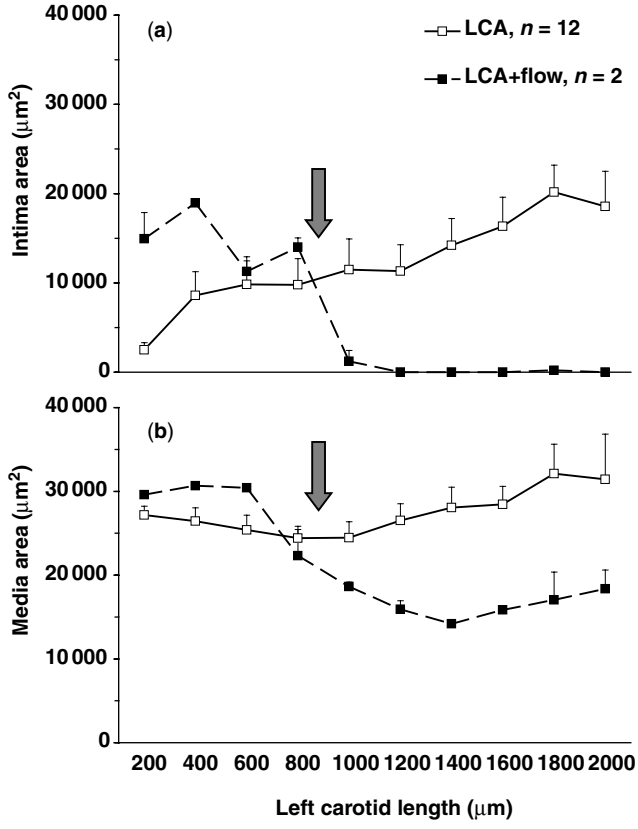

Figure 9.4 Effect of blood flow measurements at the time of ligation on remodeling in the left carotid (LCA) of FVB/NJ mice 4 weeks after ligation. (a) Intima area. (b) Media area. Gray arrows point on the site application of the flow-probe. There was a significant reduction in vascular remodeling after flow probe application at the time of ligation. Similar data were observed at the earlier time-points (1 and 2 weeks after ligation). Values are mean ± SEM

Recently, we characterized the role of Axl, a receptor tyrosine kinase, in flow-induced vascular remodeling by using a knockout mouse.[16]

References

1. Stone PH, Coskun AU, Kinlay S, et al. Effect of endothelial shear stress on the progression of coronary artery disease, vascular remodeling, and in-stent restenosis in humans. In vivo 6-month follow-up study. *Circulation* 2003; **108**: 438–444.
2. Wentzel JJ, Janssen E, Vos J, et al. Extension of increased atherosclerotic wall thickness into high shear stress regions is associated with loss of compensatory remodeling. *Circulation* 2003; **108**: 17–23.
3. O'Leary DH, Polak JF, Kronmal RA, Manolio TA, Burke GL, Wolfson SK Jr. Carotid-artery intima and media thickness as a risk factor for myocardial infarction and stroke in

older adults. Cardiovascular Health Study Collaborative Research Group. *N Engl J Med* 1999; **340**: 14–22.
4. Fox CS, Polak JF, Chazaro I, Cupples A, Wolf PA, D'Agostino RA, O'Donnell CJ. Genetic and environmental contributions to atherosclerosis phenotypes in men and women: heritability of carotid intima-media thickness in the framingham heart study. *Stroke* 2003; **34**: 397–401.
5. Tronc F, Wassef M, Esposito B, Henrion D, Glagov S, Tedgui A. Role of NO in flow-induced remodeling of the rabbit common carotid artery. *Arterioscler Thromb Vasc Biol* 1996; **16**: 1256–1262.
6. Langille BL, O'Donnell F. Reductions in arterial diameter produced by chronic decreases in blood flow are endothelium-dependent. *Science* 1986; **231**: 405–407.
7. Rudic RD, Shesely EG, Maeda N, Smithies O, Segal SS, Sessa WC. Direct evidence for the importance of endothelium-derived nitric oxide in vascular remodeling. *J Clin Invest* 1998; **101**: 731–736.
8. Ueno H, Kanellakis P, Agrotis A, Bobik A. Blood flow regulates the development of vascular hypertrophy, smooth muscle cell proliferation, and endothelial cell nitric oxide synthase in hypertension. *Hypertension* 2000; **36**: 89–96.
9. Langille BL, Bendeck MP, Keeley FW. Adaptations of carotid arteries of young and mature rabbits to reduced carotid blood flow. *Am J Physiol* 1989; **256**: H931–939.
10. Miyashiro JK, Poppa V, Berk BC. Flow-induced vascular remodeling in the rat carotid diminishes with age. *Circ Res* 1997; **81**: 311–319.
11. Kumar A, Lindner V. Remodeling with neointima formation in the mouse carotid artery after cessation of blood flow. *Arterioscler Thromb Vasc Biol* 1997; **17**: 2238–2244.
12. Korshunov VA, Berk BC. Flow-induced vascular remodeling in the mouse: a model for carotid intima-media thickening. *Arterioscler Thromb Vasc Biol* 2003; **23**: 2185–2191.
13. Korshunov VA, Berk BC. Strain-dependent vascular remodeling: the 'Glagov phenomenon' is genetically determined. *Circulation* 2004; **110**: 220–226.
14. Korshunov VA, Solomatina MA, Plekhanova OS, Parfyonova YV, Tkachuk VA, Berk BC. Plasminogen activator expression correlates with genetic differences in vascular remodeling. *J Vasc Res* 2004; **41**: 481–490.
15. Lessner SM, Prado HL, Waller EK, Galis ZS. Atherosclerotic lesions grow through recruitment and proliferation of circulating monocytes in a murine model. *Am J Pathol* 2002; **160**: 2145–2155.
16. Korshunov VA, Mohan A, Berk BC. Axl is a novel mediator of flow-induced vascular remodeling. *Arterioscler Thromb Vasc Biol* 2005; **25**: e47.

Movie legends

Starting from a mouse chin, camera is following to the middle part of the mouse neck. Following with a midline incision of the skin only. Next to expose the muscles and the trachea two pairs of forceps dissecting away the *submaxillary glands*. Then move 20–40 mm caudally and to the right, which is between the *masseter* and *sternohyoid muscles* to expose the *carotid* bifurcation, which is covered by the *caudal belly of the digastric muscle* and the *left vagus nerve*. For a better exposure of the vasculature a higher magnification (3x) next applied. The *carotid* bifurcation is now in greater detail. The *external carotid artery* is gently dissecting away the *left occipital artery*,

which goes across and down to the *left vagus nerve*. A right hand non-sharp forceps moving at 90 ° to *external carotid artery* when pass forceps laterally from the right to the left to hold only *external carotid artery* on the forceps. Gently opened forceps reaching for the ligature and pass it from the left to the right. Leave the ligature in place and dissect the *internal carotid artery*. Dissect from the left side and expose the *superior thyroid artery*. Make the same move of your right-hand forceps to pass ligature around the *internal carotid artery*. Simple untied knots are on both branches of the carotid artery now. Ligate carotids in the following order the *external carotid* and *internal carotid* by one tie as shown in Figure 9.1. Cover the incision with warm sterile saline and using sterile Q-tips retract the *submaxillary glands*. Remove excess saline and close the neck incision by interrupted sutures using 6-0 vicryl coated suture.

10

Vein graft atherosclerosis

Yanhua Hu and **Qingbo Xu**

Department of Cardiac and Vascular Sciences, St George's University of London, London, UK

Introduction

Autologous veins are the most widely used arterial conduit for the treatment of occlusive coronary and peripheral vascular disease.[1] However, the formation of atherosclerotic-like lesions in the intima of the grafted vein conduit often leads to the occlusion of the vessel, which limited the patency rate of the grafts. It is believed that 15 per cent of venous grafts becoming occluded during the first year after bypass surgery. The percentage of occlusion increase every year, and by 10 years after surgery only 60 per cent of vein grafts are patent.[2] The pathogenic mechanism of this disease remains elusive and controversial, and there is still no effective therapy available to prevent this event.

Several animal models manifesting lesions resembling human vein graft arteriosclerosis have been developed and have helped address specific interventional issues,[3–5] but they have not helped to clarify the underlying mechanism of the disease. Because of the relatively well-defined genetic map from the mouse and the availability of hundreds of inbred lines, congenic strains and recombinant strains, a number of investigators have begun to use mouse as an experimental system for atherosclerosis research.[6,7] We have established the first mouse model of vein bypass graft atherosclerosis,[8] that allows us to take advantage of transgenic, knockout, or mutant animals to study the molecular mechanism of atherosclerosis at the genetic level and to dissect the role of a single protein or gene in the development of atherosclerosis and gene transfer to evaluate the effect of certain genes on suppression of lesion formation in animal models. This mouse model is also useful for investigation of effects of locally applied agents, e.g. drug- or cell-based approaches on graft disease.

A Handbook of Mouse Models of Cardiovascular Disease Edited by Qinbo Xu

Materials and methods

Reagents and surgical instruments

- Sodium pentobarbital
- Atropine sulfate
- 0.9% NaCl saline
- Ringer-lactate
- Heparin: Sigma, to be diluted in saline to 100 unit/ml
- 4% phosphate-buffered formaldehyde.
- Forceps and scissors:

  For skin: gross forceps: Martin, 12-172-15
  standard scissors

  For soft tissue: microdissecting forceps: S&T, JFX-7

  For vessel: Microforceps: S&T, JFL-3dZ, and D-5aZ
  spring scissors: Roboz, RS-5675

- Microhemostat clips: for 1 mm diameter vessels, aesculap, REF: FE720K
- Mini-applier for micro hemostats clips: AESCULAP, FE572K
- Needle holder: Roboz
- Surgical sutures:

  Black virgin silk suture: 8-0, ETHICON

  VICRYL resorbable surgical suture, 6-0, ETHICON, V489,
  Johnson & Johnson

- Nylon tubing & cuff: autoclavable, with a 0.65 mm outside diameter and 0.5 mm inside (Portex LTD, London, UK). The cuff, in length of 1 mm and with a 1 mm handle, is prepared by cutting first with scalpel and then cutting handle with scissors.
- Syringes: 1 ml, 2 ml, 5 ml

- Scalpel: ordinary
- Electrocoagulator: model SN 54.131, with bipolar micro hemostat forceps, 80-91-12-04, Martin
- Dissection microscope: with up to 15× magnification
- Others: plaster, cotton buds, gauze compress, oxygen inhalation system, hair shaver.

Mouse anesthesia

The mice used are about 12 weeks old and weighing 25–30 g. Animals in good health are preferable to be able to withstand the operation procedure and any possible bleeding or other tissue damage. The mouse is anesthetised by intraperitoneal injection of sodium pentobarbital (50 mg/kg body weight). At same time atropine sulfate is also administrated at a dose of 1.7 mg/kg body weight to keep the respiratory tract clear by reducing salivary secretion. The sodium pentobarbital is usually pre-diluted with saline and given with 1 ml syringe in a volume of 0.25 to 0.35 ml. Atropine is given combined with pentobarbital. Allow a 10-min interval between the injection and operation to make sure the muscle tension is in a relaxed condition.

Fixation and incision

The mouse is shaved in the neck area of the ventral side and then fixed in a supine position with a strip of 3M Transpore™ adhesive plaster over each leg and stuck to a board to let the legs moderately stretched. The neck is extended by stretching the head with a strip of plaster over the incisors. The tongue is pulled to one side to make sure the respiratory tract is not blocked. The skin is disinfected with 70 per cent alcohol. A midline incision is made from the lower aspect of the mandible to the sternum (1–1.5 cm) with scissors.

Preparation of carotid artery

A dissecting microscope with magnification from 5× to 15× is needed for the following steps. Microdissecting forceps with curved tips are highly suggested for the procedures. First the skin is disconnected from underneath connective tissue by blunt dissection. To expose the right common carotid artery the right salivary glands are separated from the left on the central line and laid over the right ear. The cleidomastoid muscle is first coaggulated with an electrocoagulator (model SN54.131; Martin) at both ends, between which the muscle is then dissected at the places where burnt. It is confirmed that the dissection of cleidomastoid muscle does

not influence mouse health and movement. The right common carotid artery is carefully freed from surrounding connective tissues from the bifurcation at its distal end toward the proximal end as far as possible by blunt dissection. Any direct grasp at the carotid artery should be avoided.

Preparation of vein graft conduits

The isogenic vena cava is harvested from a donor mouse anesthetised with sodium pentobarbital (50 mg/kg body weight). An incision is made at the midline of abdomen. After dissection of skin and muscle layers the intestines are pulled to one side to expose the spine. Saline solution (0.3 ml) containing heparin (100 unit/ml) is injected into the inferior vena cava. After 3 min, the anterior thoracic cage is opened from the level of the diaphragm and incised laterally to the internal mammary vessels. Connective tissues surrounding vena cava are carefully removed and openings in the superior vena cava are made to flush the vena cava with 5 ml cold Ringer lactic solution containing 100 unit/ml heparin by a puncture under the diaphragm. A 1-cm segment of the intrathoracic vena cava between the diaphragm and atrium is finally dissected with scissors and removed, and then kept in cold Ringer-lactic solution.

For autologous or isogenic external jugular vein preparation, the mouse is fixed in a supine position, and neck well extended with plaster strips over the teeth. A midline incision in the neck area is made and right external jugular vein is exposed carefully. Three branches are ligated with an electrocoaggulator. Both proximal and distal ends are ligated with the 8-0 silk suture. A 1-cm vein segment between the two knots is harvested and kept in cold Ringer-Lactic solution.

Preparation of arterial conduits

If a mouse model for arterial isograft or allograft is used, similar techniques for harvesting aortas and carotid arteries could be used.[9] For thoracic artery preparation, the anterior thoracic cage is opened from the level of the diaphragm and incised laterally to the internal mammary vessels. Lungs and esophagus are carefully removed. The connective tissues surrounding spinal column are removed to expose the aorta without damaging it. The aorta is cut at the upper part of the descending aorta and held with forceps to help separation from the surrounding tissues. Each pair of intercostal arteries is ligated with microhemostat clamps and dissected. A puncture from the distal end under the diaphragm is made to flush the aorta with 5 ml cold Ringer lactic containing 10 U/ml heparin. A 1-cm segment of the thoracic aorta is dissected with scissors and kept in cold Ringer-lactic solution.

For common carotid artery preparation, a midline incision from abdomen through to neck area is made. Common carotid artery (left or right) is exposed from the proximal end and up to the distal end of the bifurcation. The thoracic cage is opened to expose the heart and aortic arch. A puncture is made at the brachiocephalic artery

or left common carotid artery to flush with 5 ml cold Ringer lactic containing 100 U/ml heparin. A 1-cm common carotid artery segment from the bifurcation to the proximal end is cut and kept in cold Ringer-Lactic solution.

Cuff application

The common carotid artery is ligated twice in the middle with 8-0 silk sutures, which are about 1.5 cm in length is order to make knotting easier. The distance between these two ties in about 1 mm and dissection is made in the middle. The proximal and distal portions of the carotid artery are passed through cuffs prepared prior to the operation. The vessel, together with the handle, is fixed with microhemostat clamps (4 mm in length; Martin, Tuttlingen, Germany), with the handle behind the vessel. After removing the suture at the end of the artery, rinse the vessel's open end immediately with heparin-saline to get rid of the blood clot. A segment of the artery is everted over the cuff body with fine tweezers, and immediately fixed to the cuff with an 8-0 silk suture. To avoid stripping the back of the vessel a suture prepared before operation in a form of a loop is laid beside the cuff so that a knot can be made as fast as possible. A smooth cutting edge of cuff is essential for each eversion of the arterial wall. After a double knot is made, cut the suture as short as possible and rinse the cuff well with heparin-saline. Another portion of the artery is similarly prepared (Figure 10.1). Cotton buds are used here to dry off the saline, but it should be done under a microscope to avoid any direct touch to the everted endothelial tissue over the cuffs.

End-to-end anastomosis

The vein (artery) segment is sleeved over to the distal cuff and ligated together with 8-0 suture. Similarly, another end is pulled over the proximal cuff and ligated. After vascular clamps are removed, pulsations should be visible in both the grafted and native vessels. If there are no pulsations or the pulsations diminish within a few minutes of restoration of blood flow, clot formation or occlusion of output may be assumed and the procedure should be considered to be a surgical failure. If there are vigorous pulsations in the grafted vessel, the salivary gland should be put back to the original position. Vicryl resorbable sutures of 6-0 with needle are used to close the wound; after the first knot a continuous suturing is used. The plaster is detached and the mouse laid on its side.

Postoperative care

The mouse is subcutaneously administered with 2 ml of 0.9 per cent saline immediately after the operation. The recovery time is variable, from 30 min to 2 h. Warm blanket and oxygen inhalation may be applied, but is not essential. In our opinion analgesics and antibiotics are not necessary.

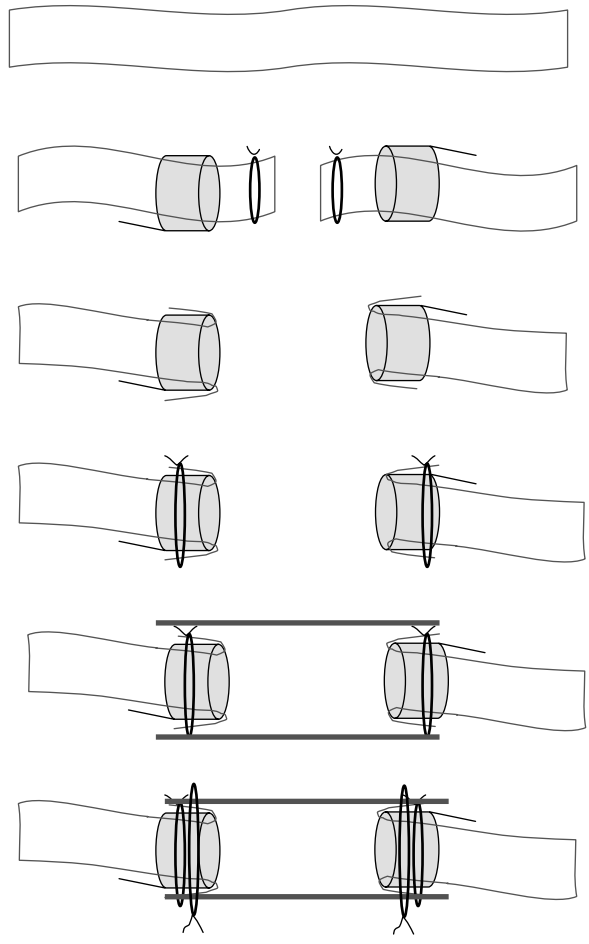

Figure 10.1 Schematic representation of vein bypass graft. The right common carotid artery is ligated with 8-0 silk suture, dissected between the two ties and passed through cuffs, respectively. The vessel, together with the cuff handle are fixed with microhemostat clamps, the suture at the end of the artery is removed and a segment of the artery turned inside out with fine tweezers to cover the cuff body, which is fixed to the cuff with a 8-0 silk suture. The right external jugular or vena cava vein segment (1 cm) is harvested and grafted between the two ends of the carotid artery by sleeving the ends of the vein over the artery-cuff and suturing them together with an 8-0 suture ligation. The vascular clamps are removed; pulsations are seen in the grafted vein. For a color version of this figure, please see the images supplied on the accompanying CD

Harvesting vessel grafts

After different time intervals, i.e. 1, 2, 3, 5 days and 1, 2, 4, 8, 16 weeks postoperatively, the mice are anesthetised with sodium pentobarbital (50 mg/kg body weight, intraperitoneally). The mice are fixed in a supine position and the neck extended with a plaster strip over the teeth. A midline incision from neck to

abdomen is made. The graft is carefully exposed free from connective tissues without directly grasping it. For histological analysis, the thoracic cage is opened and the aortic arch and left carotid artery exposed. Perfusion with 0.9 per cent saline and subsequently with 4 per cent phosphate-buffered formaldehyde (pH 7.2) through a puncture at the low end of right common artery or left ventricle for 2 to 5 min (preferably at 100 mmHg) is carried out. The graft is removed by cutting the transplanted segments from the native vessels at the cuff end and keeping them in 4 per cent formaldehyde at 4°C for 24 hrs before histological processing. For immunohistochemical analysis the vein graft is removed and immediately frozen in liquid nitrogen.

Discussion

To choose a strain of mice, we suggest that C57BL/6J mice could be used as donors and recipients for vein grafts, because these mice are susceptible to atherosclerosis when a cholesterol-enriched diet is administered.[10] Additionally, many mutant, transgenic and knockout mice are available with this genetic background. However, there is no evidence of a strain-related difference in the success rate of surgery. We did not find the difference in terms of neointimal lesion size between C57BL/6J and Balb/c mice. Importantly, the health condition and body weight (over 20 g) are more important for a successful surgical procedure.

For many new investigators who perform the surgical procedure for vein grafting, a major problem is that the mouse dies after or during recovery from anesthesia. This is mostly due to the formation of thrombus. A change of respiratory rhythm or decrease of respiratory extent immediately after the vascular clamps' release or later indicates a probable thrombus/embolus following clot formation, which is responsible for most death after grafting. To solve this problem, we suggest that the donor mice should be treated with a higher dose of heparin (100 units) before the vena cava or vessel is harvested. After heparin injection, the mouse must be kept in for more than 10 minutes to allow good heparin distribution in the donor mouse vessel before the vessel is harvested. After the vessel is harvested, it should be flushed with and kept in heparin solution until grafting. Such a treatment could result in less than 5 per cent failure. In the recipient mouse, any visible clots are carefully flushed away during and after cuffs are prepared. Higher doses of heparin or other medication may be even harmful to the recipient mouse by increasing bleeding risk. Therefore, use of heparin to the recipient is not recommended.

Endothelium is a barrier between blood and subendothelial matrix proteins, which is essential for preventing thrombus formation and subsequent neointimal lesion development in vein grafting. A great effort must be made to avoid any surgical damage to the vessel. We suggest that you may neither directly grasp the vein conduit nor contact recipient vessel endothelium in the area exposed to blood flow with forceps and cotton buds or other materials. There should be no suture left exposed to the circulating blood. The necessary grasp on the cuff should be kept to a minimum.

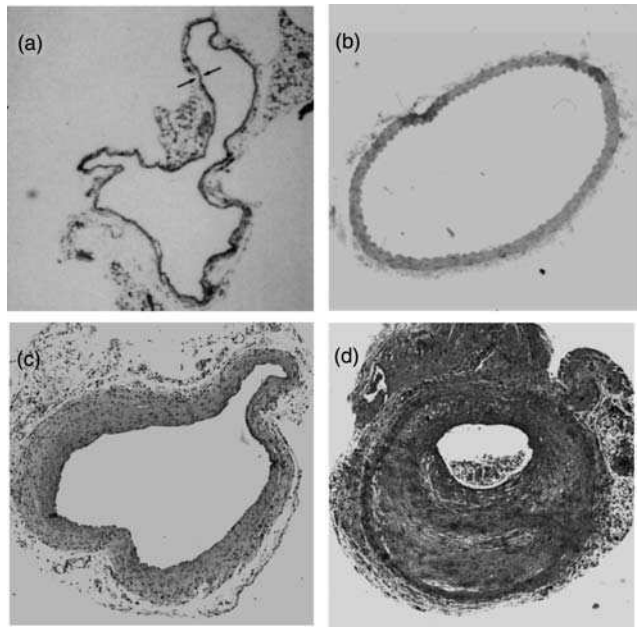

Figure 10.2 HE-stained sections of mouse vein grafts. Under anesthesia, vena cava veins of wildtype (a) or ApoE$^{-/-}$ mice are removed and isografted into carotid arteries of wildtype (c) or ApoE$^{-/-}$ (d), respectively. (b) Is a picture of cross-section from mouse artery. Animals are killed 8 weeks after surgery, and the grafted tissue fragments fixed in 4 per cent phosphate-buffered (pH 7.2) formaldehyde, embedded in paraffin, sectioned, and stained with hematoxylin–eosin (HE), original magnification 40×. For a color version of this figure, please see the images supplied on the accompanying CD

As shown in Figure 10.2(a), the media of vein wall is composed of two to three layers of cells. It is difficult to find the border between neointima and media in vein graft, especially in early stage of grafts. To solve this problem, we usually measure the neointimal areas just excluding the adventitia (Figure 10.2c). It is easier to find the border in atherosclerotic lesions of vein grafts in ApoE-deficient mice, as indicated in Figure 10.2(d), since the lesions are big and detached from the media.[11–13]

Applications

Study the pathogenesis of vein graft atherosclerosis

The vein conduit grafted to carotid artery is exposed to increased blood pressure or biomechanical stress, which is believed to play an important role in atherosclerosis.[14,15] The arteriosclerotic lesion is characterised by smooth muscle cell (SMC) hyperplasia or hypertrophy and matrix protein accumulations in the intima and/or media resulting in thickening and stiffness of the arterial wall. With the help of this model, we have studied the cellular and molecular mechanisms of vein graft

atherosclerosis and found that cell death or apoptosis is the earliest event in the development of vein graft atherosclerosis.[16] After cell death, massive mononuclear cell infiltration into the vessel wall and smooth muscle cell proliferation occurs.

Based on the observations on the mouse model and on our understanding the process of the pathogenesis, we hypothesise that any protein or molecule influencing apoptosis, inflammation or proliferation could enhance or inhibit neointimal lesion formation in vein grafts. For instance, the transcription factor p53 is essentially involved in regulation of cell death and proliferation, and p53-deficient mouse smooth muscle has decreased apoptosis and a higher rate of proliferation and migration. We demonstrated accelerated neointima formation in $p53^{-/-}$ knock-out mice.[17] Furthermore, a member of the protein kinase C family, PKCdelta, signals cells to undergo proliferation, differentiation and apoptosis, and shown that the intimal lesions of vein grafts in $PKCdelta^{-/-}$ mice are markedly increased in comparison to their wildtype littermates, which indicated the pivotal role of PKCdelta-mediated signalling to cell apoptosis in the pathogenesis of arteriosclerosis.[18] Similarly, knockouts of intercellular adhesion molecule-1 (ICAM-1), an important factor in cell adhesion and inflammation, significantly reduced neointimal hyperplasia of vein grafts suggesting the crucial role of inflammatory response, e.g. mononuclear/macrophage accumulation in the early stage of vein graft atherosclerosis.[19]

Drug and gene therapies for vein graft atherosclerosis

Since the mouse vein cava wall is very thin, it allows a local application of drugs solved in pluronic-127 gel around the graft for up to 4 weeks. Drug may penetrate the vessel wall and work on the cells without systemic side effects. For example, suramin, a growth factor receptor antagonist that inhibits cell proliferation, inhibited SMC migration and proliferation *in vivo* and *in vitro* by blocking platelet-derived growth factor (PDGF) initiated PDGF receptor activation and mitogen-activated protein kinase-AP-1 signalling, and is also effective in inhibition of neointima hyperplasia in mouse venous bypass grafts after local application.[20] In addition, locally applied aspirin did not only reduce the thrombus formation, but also significantly reduced neointimal lesion. With this model a local gene transfer of tissue inhibitor of metalloproteinase-2 is carried out, which resulted in a reduction of vein graft diameter, or vascular remodeling. These results indicate that the mouse vein graft model can also be used for inventing or evaluating drug and gene therapies for atherosclerosis.[21–24]

Cell origins in vein graft atherosclerosis and contribution of progenitor cells

Endothelial denudation in the early stage and regeneration, and SMC accumulation in the intima occur in vein graft. The origin of these cells is a controversial issue. The traditional concept, believing that denuded endothelium can be replaced by the

remaining cells in the vicinity and SMCs migrate from media, is challenged by recent data showing the role of stem cells in repairing the damaged vessel. Using transgenic mice expressing the LacZ gene in endothelial cell or SMC only,[25,26] we provided the evidence that the regenerated endothelial cells of vein grafts originated from recipient circulating blood, one-third of those regenerated cells are from bone marrow stem cells. Smooth muscle cells in vein graft atherosclerosis lesion have heterogeneous origin, i.e. ~22 per cent derived from recipients and 69 per cent from grafted vessels. These findings are crucial for understanding the pathogenesis of vein graft atherosclerosis, and for establishing a new therapeutic intervention for the disease.

The vascular adventitia is increasingly considered as a highly active segment of vascular tissue that contributes to a variety of disease pathologies, including atherosclerosis and restenosis. We have provided the evidence that stem cells exist in the adventitia of vessel walls and these cells can differentiate into SMC *in vitro*.[27] When stem cell marker-positive cells isolated from transgenic mice expressing LacZ gene in SMC only are transferred to the adventitial side of vein graft in ApoE-deficient mice, there are beta-gal^{+} cells found in atherosclerotic lesions of the intima. These data confirm that adventitial progenitor cells differentiated to SMC *in vivo* and contributed to vein graft atherosclerosis, and indicate an important issue that *ex vivo* expansion of progenitor cells may have implications for cellular, genetic and tissue engineering approaches to vascular diseases.

In summary, the mouse model of vein bypass graft atherosclerosis develops neointimal and atherosclerotic lesions, which share many similarities to the lesions observed in humans. By using this model, we demonstrated the cellular process of the disease, i.e. apoptosis, inflammation and smooth muscle proliferation. If any process of those is interrupted, the lesion formation is either enhanced or inhibited. In addition, this model is also proven to be useful for studying therapeutic intervention for the disease by locally applied drugs, genes or stem cells.[28]

Acknowledgments

This work was supported by grants from the British Heart Foundation and Oak Foundation.

References

1. Mehta D, Izzat MB, Bryan AJ, Angelini GD. Towards the prevention of vein graft failure. *Int J Cardiol* 1997; **62**(Suppl1): S55–63.
2. Motwani JG, Topol EJ. Aortocoronary saphenous vein graft disease: pathogenesis, predisposition, and prevention. *Circulation* 1998; **97**: 916–931.
3. Landymore RW, Kinley CE, Cameron CA. Intimal hyperplasia in autogenous vein grafts used for arterial bypass: a canine model. *Cardiovasc Res* 1985; **19**: 589–592.
4. Boerboom LE, Olinger GN, Liu TZ, Rodriguez ER, Ferrans VJ, Kissebah AH. Histologic, morphometric, and biochemical evolution of vein bypass grafts in a nonhuman primate

model. III. Long-term changes and their modification by platelet inhibition with aspirin and dipyridamole. *J Thorac Cardiovasc Surg* 1990; **99**: 426–432.
5. Norman PE, House AK. The influence of nifedipine on microvascular vein graft intimal thickening. *Aust N Z J Surg* 1993; **63**: 294–298.
6. Paigen B, Morrow A, Brandon C, Mitchell D, Holmes P. Variation in susceptibility to atherosclerosis among inbred strains of mice. *Atherosclerosi*s 1985; **57**: 65–73.
7. Zhang SH, Reddick RL, Piedrahita JA, Maeda N. Spontaneous hypercholesterolemia and arterial lesions in mice lacking apolipoprotein *E. Science* 1992; **258**: 468–471.
8. Zou Y, Dietrich H, Hu Y, Metzler B, Wick G, Xu Q. Mouse model of venous bypass graft arteriosclerosis. *Am J Pathol* 1998; **153**: 1301–1310.
9. Dietrich H, Hu Y, Zou Y, et al. Mouse model of transplant arteriosclerosis: role of intercellular adhesion molecule-1. *Arterioscler Thromb Vasc Biol* 2000; **20**: 343–352.
10. Lusis AJ, Taylor BA, Wangenstein RW, LeBoeuf RC. Genetic control of lipid transport in mice. II. Genes controlling structure of high density lipoproteins. *J Biol Chem* 1983; **258**: 5071–5078.
11. Dietrich H, Hu Y, Zou Y, et al. Rapid development of vein graft atheroma in ApoE-deficient mice. *Am J Pathol* 2000; **157**: 659–669.
12. Lardenoye JH, De Vries MR, Grimbergen JM, et al. Inhibition of accelerated atherosclerosis in vein grafts by placement of external stent in apoE*3-Leiden transgenic mice. *Arterioscler Thromb Vasc Biol* 2002; **22**: 1433–1438.
13. Lardenoye JH, de Vries MR, Lowik CW, et al. Accelerated atherosclerosis and calcification in vein grafts: a study in APOE*3 Leiden transgenic mice. *Circ Res* 2002; **91**: 577–584.
14. Wernig F, Xu Q. Mechanical stress-induced apoptosis in the cardiovascular system. *Prog Biophys Mol Biol* 2002; **78**: 105–137.
15. Xu Q. Biomechanical-stress-induced signaling and gene expression in the development of arteriosclerosis. *Trends Cardiovasc Med* 2000; **10**: 35–41.
16. Mayr M, Li C, Zou Y, Huemer U, Hu Y, Xu Q. Biomechanical stress-induced apoptosis in vein grafts involves p38 mitogen-activated protein kinases. *FASEB J* 2000; **14**: 261–270.
17. Mayr U, Mayr M, Li C, et al. Loss of p53 accelerates neointimal lesions of vein bypass grafts in mice. *Circ Res* 2002; **90**: 197–204.
18. Leitges M, Mayr M, Braun U, et al. Exacerbated vein graft arteriosclerosis in protein kinase Cdelta-null mice. *J Clin Invest* 2001; **108**: 1505–1512.
19. Zou Y, Hu Y, Mayr M, Dietrich H, Wick G, Xu Q. Reduced neointima hyperplasia of vein bypass grafts in intercellular adhesion molecule-1-deficient mice. *Circ Res* 2000; **86**: 434–440.
20. Hu Y, Zou Y, Dietrich H, Wick G, Xu Q. Inhibition of neointima hyperplasia of mouse vein grafts by locally applied suramin. *Circulation* 1999; **100**: 861–868.
21. Torsney E, Mayr U, Zou Y, Thompson WD, Hu Y, Xu Q. Thrombosis and neointima formation in vein grafts are inhibited by locally applied aspirin through endothelial protection. *Circ Res* 2004; **94**: 1466–1473.
22. Schachner T, Zou Y, Oberhuber A, et al. Local application of rapamycin inhibits neointimal hyperplasia in experimental vein grafts. *Ann Thorac Surg* 2004; **77**: 1580–1585.
23. Schachner T, Zou Y, Oberhuber A, et al. Perivascular application of C-type natriuretic peptide attenuates neointimal hyperplasia in experimental vein grafts. *Eur J Cardiothorac Surg* 2004; **25**: 585–590.

24. Li X, Chyu KY, Neto JR, et al. Differential effects of apolipoprotein A-I-mimetic peptide on evolving and established atherosclerosis in apolipoprotein E-null mice. *Circulation* 2004; **110**: 1701–1705.
25. Xu Q, Zhang Z, Davison F, Hu Y. Circulating progenitor cells regenerate endothelium of vein graft atherosclerosis, which is diminished in ApoE-deficient mice. *Circ Res* 2003; **93**: e76–86.
26. Hu Y, Mayr M, Metzler B, Erdel M, Davison F, Xu Q. Both donor and recipient origins of smooth muscle cells in vein graft atherosclerotic lesions. *Circ Res* 2002; **91**: e13–20.
27. Hu Y, Zhang Z, Torsney E, et al. Abundant progenitor cells in the adventitia contribute to atherosclerosis of vein grafts in ApoE-deficient mice. *J Clin Invest* 2004; **113**: 1258–1265.
28. Xu Q. Mouse models of arteriosclerosis: From arterial injuries to vascular grafts. *Am J Pathol* 2004; **165**: 1–10.

11

Angiotensin II-induced aortic aneurysms

Yi-Xin Wang,[1] **Lisa A. Cassis**[2] and **Alan Daugherty**[3]

[1]*Berlex Biosciences, Richmond, CA, USA,* [2]*Graduate Center for Nutritional Sciences, University of Kentucky, Lexington, KY, USA and* [3]*Cardiovascular Research Center, University of Kentucky, Lexington, KY, USA*

Abstract

Abdominal aortic aneurysms (AAAs) are permanent dilations of the aorta that pose a significant health problem. These dilations are relatively asymptomatic, but insidious, as rupture of an AAA is associated with a high degree of mortality due to excessive blood loss. The prevalence of AAAs increases with advancing age in both males and females, but is greater in males compared to females at all ages. Despite the common occurrence of this disease, we have limited understanding of the sequential biochemical and cellular events of AAA initiation and progression. In part, the lack of knowledge is due to the practical difficulties of studying this asymptomatic disease in humans. Recently, several mice models of AAAs have been developed that have provided novel insights into mechanism of AAA formation. The most widely used model of AAAs induces the disease during chronic subcutaneous infusion of angiotensin II. The purpose of this chapter is to introduce the background of this model, provide experimental details of its implementation, and discuss its relevance to the human disease.

Introduction

Studies on the chronic subcutaneous infusion of angiotensin II (AngII) into hyperlipidemic mice were initiated as an attempt to develop a model of hypertension-induced atherosclerosis.[1–3] These initial studies demonstrated that AngII infusion was a profound stimulus in the development of atherosclerosis. However, contrary to the original hypothesis of the studies, this marked atherogenic effect was due to direct inflammatory effects rather than elevations in blood pressure.[3] During the processing

A Handbook of Mouse Models of Cardiovascular Disease Edited by Qinbo Xu

of the aortas from AngII-infused mice, the presence of large abdominal aortic aneurysms (AAAs) were noted in the suprarenal aorta.[2] The ability of AngII infusion to promote the development of AAAs in mice has now been duplicated by many laboratories.[4–11]

The development of AngII-induced AAAs is a complex pathology that involves multiple cell types that initiate mechanisms at specific stages of AAA formation. Within days of AngII infusion, macrophages accumulate in the media of the AAA-prone region.[12] This leukocyte accumulation is associated with breaks in elastin fibers. Medial dissection, occurring early in the process, leads to aortic dilation with the integrity of the lumen being maintained by the adventitia. The medial dissection results in formation of an intramural thrombus. There is a profound infiltration of macrophages that presumably occurs in response to thrombus formation. The dissected region enters a phase in which leukocytes of the innate and acquired immune system infiltrate while the vessel remodels. The leukocytes that have been detected in AngII-induced aneurysm tissue include macrophages, T and B lymphocytes. The dissected region forms a 'neomedia' that becomes completely relined with endothelial cells. Prominent atherosclerotic regions form in the remodeled region at later stages in the progression of AAAs.[12]

This chapter will describe experimental design, methodology with discussion of the potential pitfalls of the AngII-induced model of AAA formation.

Methods

Mouse selection

The majority of published studies on AngII-induced AAAs have used mice that are hyperlipidemic either as a consequence of deficiency of either apolipoprotein E (ApoE) or low density lipoprotein (LDL) receptors. Studies using ApoE$^{-/-}$ mice were either fed a normal diet or one supplemented with saturated fat.[2,4] All the studies using LDL receptor$^{-/-}$ mice have fed a diet enriched in saturated fat and cholesterol.[1,13] No overt differences have been noted in the incidence, severity, or characteristics of AngII-infused AAAs between these two genetically targeted mice. To date, all the publications on AngII-induced AAAs in these genetically engineered hyperlipidemic backgrounds have used mice that have been backcrossed in a C57BL/6 background. Wild type C57BL/6 mice also develop AngII-induced AAAs, albeit at a much lower incidence.[6] Interestingly, the low incidence of AAA formation did not increase when C57BL/6 mice were fed a high cholesterol diet that doubled serum cholesterol.[14] Thus, at present it is unclear whether hyperlipidemia or pre-existing atherosclerosis accelerate AngII-induced AAA formation in genetically targeted mice.

There have been no studies that have demonstrated clearly an effect of age on the development of AngII-induced AAAs. Studies have used mice that range in age from 2.5 to 11 months of age at the initiation of AngII-infusion, with the typical start of AngII infusion at 10 weeks of age. Across this varied age range, the incidence of AngII-induced AAAs in published studies is fairly consistent (70–90 per cent

incidence in hyperlipidemic mice). One of the practical limits of using younger mice is related to their size. Implantation of the Alzet pump model most commonly used in these studies requires that the body weight of mice be at least 20 g to achieve effective drug delivery.

Gender plays a prominent role in the development of AngII-AAAs. As in the development of AAAs in humans, male mice are more prone to developing AngII-induced AAAs.[15] Ovarian hormones influence the development of AngII-induced AAAs, as demonstrated by the attenuation of AAAs in male $ApoE^{-/-}$ mice administered with 17beta estradiol.[7] However, the reduction of endogenous estrogen by ovariectomy of female mice did not affect the incidence or severity of AAAs.[15] In contrast, the reduction of male hormones by orchidectomy deceased the incidence and severity of AAAs to a level that was indistinguishable from females.[15] Thus, although exogenous estrogen administration lessens AngII-induced AAA formation, it appears that androgens are the endogenous sex hormones that are responsible for the enhanced susceptibility of males. The mechanism underlying the androgen induced susceptibility for AngII-induced AAAs is undefined.

Preparation and implantation of Alzet pumps

All published studies on AngII-induced AAAs have used Alzet pumps to administer the octapeptide. Alzet pumps have a flexible reservoir that is surrounded by a salt sleeve and encased by a semi-permeable membrane. The salt sleeve promotes the flux of fluids across the membrane that compresses the drug-containing reservoir and displaces fluids at a highly controlled rate that is regulated by a flow moderator. Most studies have used the 2004 model which delivers fluids at a rate of approximately 2.5 μl/h for 28 days. The flow rates vary with lot numbers and have sufficiently wide variance that the flow rate of a specific batch needs to be known in order to calculate peptide delivery rates.

Infusion rates of AngII that have generated AAAs have ranged from 500 to 2500 ng/kg/min.[2,4,8] Most studies have used a rate of 1000 ng/kg/min that generates greater than 80 per cent AAAs in hyperlipidemic male mice. The calculation of the dose of AngII to be given to the mouse is determined by the required infusion rate and the weight of the mouse, taking into consideration the weight of the mouse over the duration of the 28-day infusion. Calculation of the AngII dose based on the body weight at the start of the study will lead to lower doses being administered at later stages of the infusion. Some investigators calculate the infusion rate based on the anticipated weight of the mice at the mid point of the infusion period. This calculation requires previous experience, since weight gain over the 28-day period can be altered by several variables including strain of mouse, diet, and gender. An additional consideration when calculating the infusion rate at study mid point is the effect of AngII infusion to decrease body weight, which has been observed under certain conditions (i.e. high fat-fed mice).

Thus, the infusion rate of AngII is based on the daily dose, weight of the mice, and the infusion rate of the specific batch of Alzet pumps. The first step in preparing the pumps is

the dissolution of AngII. AngII is commonly supplied as a lyophilised powder in glass bottles. However, AngII in solution has a high affinity for glass. Thus, AngII solutions must be dissolved in plastic vessels. Alzet pumps are filled as per the manufacturer's instructions. The 2004 model of Alzet pump requires a priming period of 40 hours prior to it extruding the solution from the reservoir. If an experimental design requires that peptide infusion starts immediately on implantation, the filled pumps will need to be incubated in sterile saline at 37°C prior to placement.

Most of the studies implant the pumps in the subcutaneous space. This is achieved by making a small cut in the skin in the back of the neck, using blunt dissection to form a pouch on the flank, placing the Alzet pump into the subcutaneous space, and closing the incision point with surgical glue or staples. The incision site should be monitored to ensure it retains its closure. Because female mice groom more extensively than males, they have a greater propensity to open the incision site.

Monitoring during AngII infusion

Mice should be visually inspected daily during the infusion of AngII. The majority of mice will have no overt adverse effects during the infusion of AngII. A small percentage of the mice will develop partial hind limb paralysis. Some mice will die during infusion due to ruptured AAAs. The incidence of mortality is based on several variables including the strain of mouse, gender, and dose. Necropsy should be performed on mice to determine the cause of death. The vast majority of the mice will have a large blood clot in the peritoneal cavity in the vicinity of the left kidney. A few mice will have clots in the upper thorax in the region of the ascending aorta.

During the infusion period, we acquire body weights on a weekly basis. As described above, the higher doses of AngII may lead to attenuation of body weight gain, or even loss. Blood pressure is also commonly monitored at intervals during the infusion of AngII. Systolic blood pressure is most commonly acquired using a computerized system in which blood flow is monitored during the inflation of a cuff on the tail.

Acquisition of AAAs

Most of the published studies have terminated mice after 28 days of AngII infusion. However, the incidence of AngII-induced AAAs is similar at 14 days of infusion.[16] Infusions of AngII beyond 28 days can be achieved by replacing the Alzet pumps. The limited published studies show differing characteristics of AAAs with more protracted intervals of AngII infusion, although these have not been extensively characterised.[12]

At termination of studies, mice are perfused with saline to remove blood. The aorta can be dissected free either with, or without, perfusion with a fixative such as paraformaldehyde. Perfusion of the mouse with fixative at physiological pressures can better preserve the tissue. However, fixation ablates the immunoreactivity of

many antibodies. Thus, the decision of whether to use fixatives is based on the tissue characterization that will be performed.

An alternative mode to not fixing the tissue, but maintaining its patency, is to perfuse at a constant pressure of 100 mmHg through the heart with phosphate-buffered saline followed by warm (37°C) agarose (SeaPlaque GTG Agarose, low-melt, FMC BioProducts, Rockland, ME, USA) diluted in saline (3 per cent wt/vol) and colored with a green tissue dye. After the agarose solidifies, the abdominal aorta can be dissected free from the surrounding connective tissue.

Quantification of AAAs

The size and heterogeneity of AAAs provides some hurdles to the quantification of AAAs. There are three common approaches to the quantification of experimental AAAs, which are: (1) percentage incidence; (2) severity based on arbitrary comparisons; (3) measurements of the physical dimensions.

In addition to the quantification of AAAs following excision of the tissue, there are methods recently available for the detection and quantification of AAAs using noninvasive techniques in living animals. The only methodology that has been fully validated as an approach to date is the use of ultrasound.[17] This is discussed later in this chapter.

Incidence of aneurysm formation

There is a lack of agreement as to what constitutes an AAA in humans. The criterions are based either on an absolute measurement of aortic width or one that is relative to a 'normal' segment.[18] Similarly, there is also no uniform standard for the definition of an AAA in mouse models of the disease. However, all the initial studies on AngII-induced AAA have included the percent incidence as a quantitative parameter. The mean outer diameter of the suprarenal aortic region of male mice is approximately 0.9 mm. We have used the criterion of an expansion that is 50 per cent greater than normal as a definition of AAAs. This is based on absolute measurements since the involvement of AAA in the suprarenal region can be extensive and negate the ability to make comparisons with a 'normal' area.

Based on the acceptance of this specific criterion, the use of percentage incidence provides an easily defined mode of quantification. However, the use of a dichotomous variable is a relatively insensitive mode of statistical analysis. Therefore, unless a specific intervention produces dramatic differences on the development of AAA, large group sizes will be needed to achieve results with appropriate statistical power.

Severity indexes

We originally proposed a scheme for classifying the severity of aneurysm pathology based on the appearance of AAAs.[7] This initial classification took into account the

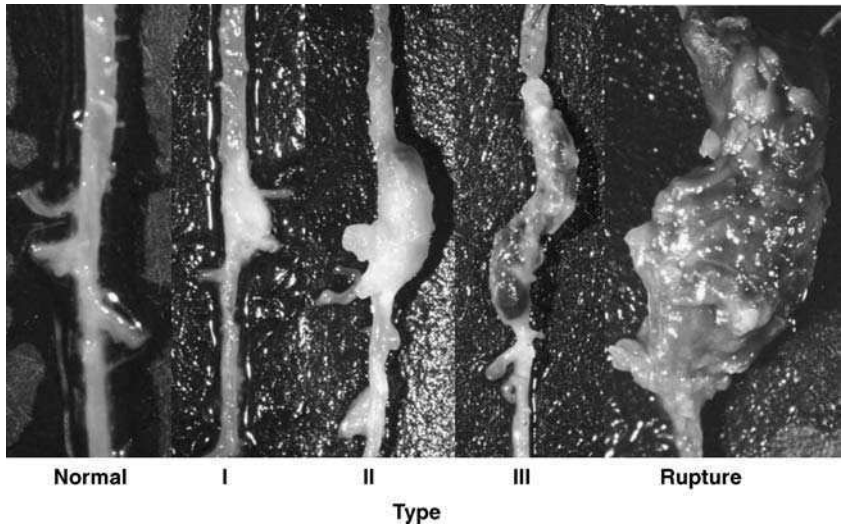

Figure 11.1 A suggested scale for quantification of the severity of AAAs that develop following infusion of AngII. Further description of these classes is provided in the text. For a color version of this figure, please see the images supplied on the accompanying CD

presence of thrombus.[13,16] However, now that we have defined characteristics of AAAs at multiple stages following AngII infusion, we have realised that the presence of thrombus is more a function of time of AAA formation rather than severity. With several years of experience in assessing AngII-induced AAAs, we have modified this scheme. The descriptors of these types are:

- Type I: A discernable dilation that is 1.5 to 2 times the diameter of a normal abdominal aorta.
- Type II: A single large dilation that is more than 2 times the diameter of a normal abdominal aorta.
- Type III: Multiple dilations generally extending proximal to the suprarenal region.
- Rupture: The ultimate dire consequence of AAA formation. Ruptured AAAs are clearly evident by the appearance of clots in the retroperitonium and death.

Examples of each type of AAA are provided in Figure 11.1.

Measurements of physical dimensions of AAAs

Unlike the dichotomous mode of defining AAA by incidence, continuous traits are a more powerful mode of generating statistical significance. Thus, there are a number of modes in which physical measurements can be performed to permit the use of

statistical analysis of continuous traits. There are several ways in which the physical dimensions of AAAs can be quantitated as described below.

Abdominal aortic weight

Abdominal aorta (defined as the region between the diaphragm and the ileal bifurcation) can be blotted and weighed. This has been used to determine the severity of AAA formation.[15] While potentially useful, it should be noted that AAAs that have uniformly thinned walls may not have an increase in weight.

External aortic diameter

This is a common measurement in other mouse models of disease that involve elastase infusion or adventitial calcium chloride exposure.[19,20] This is achieved by computer-assisted morphometric analysis of digital pictures of the aorta. These measurements are usually performed in dissected tissues. Although these measurements can be performed *in vivo*, the difficulty in defining the boundary between the adventitia and the surrounding tissue brings some subjectivity into the process.

Cross-sectional measurement

This is optimally performed on fixed aortas. Cross-sections of the aorta (2.5 μm in thickness) are made between the superior mesenteric and right renal arteries. A small portion of the right renal artery is left attached to the samples to facilitate orientation of the specimen. The tissue is dehydrated through a graded ethanol series, cleared with xylene, infiltrated with warm paraffin, embedded in paraffin blocks, cut at 5 μm thickness, and stained with hematoxylin & eosin. The lumen and adventitial circumferences at the maximal expanded portion of the suprarenal aorta are quantified by CSimple Imaging Systems (Compix, Mars, PA, USA), which are then used to calculate the luminal and outer diameters of the vessel. The wall thickness is calculated from the difference between the luminal and outer diameters.

Non-invasive ultrasound method

Recently, ultrasound machines have been developed that have the capabilities to detect blood vessels in mice. This advance permits the non-invasive detection of AAAs in mice.[17] Thus, a single mouse can now be followed on a sequential basis.

At any interval during the infusion of AngII, each mouse is anesthetised using 1.5 per cent isoflurane and laid supine on a platform with all legs taped to electrocardiogram electrodes for heart rate monitoring. Body temperature is monitored via a rectal thermometer and maintained at ~37°C using a heating pad and lamp. All hair is removed from the abdomen using a chemical hair remover (Nair; Carter-Horner, Mississauga, Ontario, Canada) to minimize ultrasound signal attenuation. To provide a coupling medium for the transducer, a pre-warmed ultrasound gel (Aquasonic 100; Parker Laboratories, Orange, NJ, USA) is spread over the abdominal wall. Imaging starts after waiting 1–2 min for the mouse to stabilise. The complete examination for each mouse lasts for about 5 min.

A newly developed ultrasound biomicroscope with built in software analysis (Vevo 660; VisualSonics, Toronto, Ontario, Canada) can be used. The single-crystal mechanical transducer has a central frequency of 40 MHz, a focal length of 6 mm, and a frame rate of 30 Hz. The maximum field of view of two-dimensional imaging is obtained in a 20 × 20 μm area of focal plane with spatial resolution of 68 μm (lateral) by 39 mm (axial). A longitudinal image of the abdominal aorta between the diaphragm and ~3 mm below the level of the left renal artery is acquired. In addition, transversal images of the suprarenal aorta, at the level of the suprarenal gland, and the infrarenal aorta, ~1 mm below the left renal artery, are taken. Doppler signals measuring the cardiac cycle obtained from the position in the middle of the assumed vessel are used to validate that the concerned image is the abdominal aorta. The obtained images are stored digitally on a built in hard drive for off-line analysis. The abdominal aortic measurements are taken off-line with a built in software from both the longitudinal and transversal images.

Characterisation of AAAs

The cellular and chemical composition of AngII-induced AAAs are complex and heterogeneous. These can be characterised by techniques such as histology, immunocytochemistry and *in situ* hybridisation. Using these techniques, some of the most prominent features can be described including integrity of extracellular matrix, cellular composition, and expression of protein involved in the disease process. Although these are largely routine techniques, the application of immunocytochemical techniques can provide some challenges in non-specific staining, presumably due to the high abundance of extracelluar matrix elements.

Since extracellular proteases are thought to be involved in the development of AAAs, their characterisation is common, particularly for the matrix metalloproteinases (MMP). This is commonly performed on extracts of aortic tissues that are subjected to gel zymography.[4,8,10] This process requires the electrophoresis of the tissue extract in polyacrylamide gels that are impregnated with a MMP substrate. The most common substrate is gelatin, that is acted on by MMP-2 and -9. This process permits detection of these specific MMPs and relative presence of latent versus activated enzyme.

Discussion

AngII-induced AAAs have been used in many studies to define mechanisms of the disease. The extrapolation of findings require that the model is recapitulating the human disease. The extent to which AngII-induced AAAs in mice mimick the human disease is largely unknown. This is primarily due to a dearth of information on the mechanisms of the human disease. One similarity in the mouse model is the increased proclivity of males to develop the disease as in humans. Some pathological characteristics of the human disease are reproduced in this mouse model. These include fragmentation of elastic fibers, proteolytic destruction of medial connective tissue, regions of intact media, inflammation, and atherosclerosis.[21] All these characteristics have been described in AngII-induced AAAs.[12] However, the location of the AAAs is an overt difference between the human and mouse disease. In humans, AAAs occur in the infrarenal area; while in AngII-infused mice, they have been uniformly localized to the suprarenal aortic region. This may represent a difference in the stress patterns in the aorta of the biped human versus the quadruped mouse. Interestingly, this location is also where AAAs occur in mice that are hyperlipidemic, endothelial nitric oxide synthase deficient, or smooth muscle specific deficient in LDL receptor-related protein.[22–25]

The early publications on this model used aged hyperlipidemic mice that had extensive atherosclerotic lesions. However, many of the recent studies have used younger mice in which atherosclerotic lesions are sparse, especially at the site of AAA formation. The lack of a required role of atherosclerosis in this process can be gleaned from studies that show AngII-induced AAAs can occur in normolipidemic mice.[6] However, the incidence of AAAs is much less in normolipidemic mice. Feeding wild type mice a high cholesterol diet did not affect the incidence of AngII-induced AAAs.[14] However, cholesterol supplementation of diets produces only minor increases in plasma cholesterol concentrations. Thus, hypercholesterolemia may facilitate the development of AngII-induced AAAs through promotion of atherosclerosis or vascular inflammation. Hypercholesterolemia may also enhance the development of AngII-induced AAAs through enhancing the cellular responses to AngII. For example, smooth muscle cells are presumed to be pivotal to the development of AAAs and AT1 receptor expression in this cell type is enhanced by increasing cellular cholesterol.[26]

Overall, the infusion of AngII into hyperlipidemic mice is a highly reproducible model for the production of AAAs. Although the model does not recapitulate all aspects of the human disease, many facets are present in both human and mouse aneurysmal tissue. Therefore, it provides a mode of defining mechanisms involved in the initiation and propagation of AAAs.

Acknowledgments

Work in the Cassis and Daugherty laboratories is supported by the National Institutes of Health (HL,62846, HL73085 and HL70239). We appreciate the editorial assistance of Debra Rateri.

References

1. Daugherty A, Cassis L. Chronic angiotensin II infusion promotes atherogenesis in low density lipoprotein receptor$^{-/-}$ mice. *Ann NY Acad Sci* 1999; **892**: 108–118.
2. Daugherty A, Manning MW, Cassis LA. Angiotensin II promotes atherosclerotic lesions and aneurysms in apolipoprotein E-deficient mice. *J Clin Invest* 2000; **105**: 1605–1612.
3. Weiss D, Kools JJ, Taylor WR. Angiotensin II-induced hypertension accelerates the development of atherosclerosis in ApoE-deficient mice. *Circulation* 2001; **103**: 448–454.
4. Wang YX, Martin McNulty B, Freay AD, et al. Angiotensin II increases urokinase-type plasminogen activator expression and induces aneurysm in the abdominal aorta of apolipoprotein E-deficient mice. *Am J Pathol* 2001; **159**: 1455–1464.
5. Tham DM, Martin McNulty B, Wang YX, et al. Angiotensin II is associated with activation of NF-kappa B-mediated genes and downregulation of PPARs. *Physiol Genom* 2002; **11**: 21–30.
6. Deng GG, Martin-McNulty B, Sukovich DA, et al. Urokinase-type plasminogen activator plays a critical role in angiotensin II-induced abdominal aortic aneurysm. *Circ Res* 2003; **92**: 510–517.
7. Martin McNulty B, Tham DM, daCunha V, et al. 17 beta-estradiol attenuates development of angiotensin II induced aortic abdominal aneurysm in apolipoprotein E deficient mice. *Arterioscler Thromb Vasc Biol* 2003; **23**: 1627–1632.
8. Bruemmer D, Collins AR, Noh G, et al. Angiotensin II-accelerated atherosclerosis and aneurysm formation is attenuated in osteopontin-deficient mice. *J Clin Invest* 2003; **112**: 1318–1331.
9. Ishibashi M, Egashira K, Zhao Q, et al. Bone marrow-derived monocyte chemoattractant protein-1 receptor CCR2 is critical in angiotensin II-induced acceleration of atherosclerosis and aneurysm formation in hypercholesterolemic mice. *Arterioscler Thromb Vasc Biol* 2004; **24**: e174–178.
10. Wang YX, Martin-McNulty B, da Cunha V, et al. Fasudil, a Rho-kinase inhibitor, attenuates angiotensin II-induced abdominal aortic aneurysm in apolipoprotein E-deficient mice by inhibiting apoptosis and proteolysis. *Circulation* 2005; **111**: 2219–2226.
11. Gavrila D, Li WG, McCormick ML, et al. Vitamin E Inhibits abdominal aortic aneurysm formation in angiotensin II-infused, apolipoprotein E-deficient mice. *Arterioscler Thromb Vasc Biol* 2005; **25**: 1671–1677.
12. Saraff K, Babamusta F, Cassis LA, Daugherty A. Aortic dissection precedes formation of aneurysms and atherosclerosis in angiotensin II-infused, apolipoprotein E-deficient mice. *Arterioscler Thromb Vasc Biol* 2003; **23**: 1621–1626.
13. Manning MW, Cassis LA, Daugherty A. Differential effects of doxycycline, a broad-spectrum matrix metalloproteinase inhibitor, on angiotensin II-induced atherosclerosis and abdominal aortic aneurysms. *Arterioscler Thromb Vasc Biol* 2003; **23**: 483–488.
14. Wang YX. Cardiovascular functional phenotypes and pharmacological responses in apolipoprotein E deficient mice. *Neurobiol Aging* 2005; **26**: 309–316.
15. Henriques TA, Huang J, D'Souza SS, Daugherty A, Cassis LA. Orchiectomy, but not ovariectomy, regulates angiotensin II-Induced vascular diseases in apolipoprotein E deficient mice. *Endocrinology* 2004; **145**: 3866–3872.
16. Manning MW, Cassis LA, Huang J, Szilvassy SJ, Daugherty A. Abdominal aortic aneurysms: fresh insights from a novel animal model of the disease. *Vasc Med* 2002; **7**: 45–54.

17. Martin-McNulty B, Vincelette J, Vergona R, Sullivan ME, Wang YX. Noninvasive measurement of abdominal aortic aneurysms in intact mice by a high frequency ultrasound imaging system. *Ultrasound Med Biol* 2005; **31**: 746–749.
18. Daugherty A, Cassis LA. Mechanisms of abdominal aortic aneurysm formation. *Curr Atheroscler Rep* 2002; **4**: 222–227.
19. Pyo R, Lee JK, Shipley JM, et al. Targeted gene disruption of matrix metalloproteinase-9 (gelatinase B) suppresses development of experimental abdominal aortic aneurysms. *J Clin Invest* 2000; **105**: 1641–1649.
20. Longo GM, Xiong W, Greiner TC, Zhao Y, Fiotti N, Baxter BT. Matrix metalloproteinases 2 and 9 work in concert to produce aortic aneurysms. *J Clin Invest* 2002; **110**: 625–632.
21. Powell JT, Brady AR. Detection, management, and prospects for the medical treatment of small abdominal aortic aneurysms. *Arterioscler Thromb Vasc Biol* 2004; **24**: 241–145.
22. Tangirala RK, Rubin EM, Palinski W. Quantitation of atherosclerosis in murine models: Correlation between lesions in the aortic origin and in the entire aorta, and differences in the extent of lesions between sexes in LDL receptor-deficient and apolipoprotein E-deficient mice. *J Lipid Res* 1995; **36**: 2320–2328.
23. Daugherty A, Cassis LA. Mouse models of abdominal aortic aneurysms. *Arterioscler Thromb Vasc Biol* 2004; **24**: 429–434.
24. Kuhlencordt PJ, Gyurko R, Han F, Scherrer Crosbie M, Aretz TH, Hajjar R, Picard MH, Huang PL. Accelerated atherosclerosis, aortic aneurysm formation, and ischemic heart disease in apolipoprotein E/endothelial nitric oxide synthase double-knockout mice. *Circulation* 2001; **104**: 448–454.
25. Boucher P, Gotthardt M, Li WP, Anderson RGW, Herz J. LRP: Role in vascular wall integrity and protection from atherosclerosis. *Science* 2003; **300**: 329–332.
26. Nickenig G, Jung O, Strehlow K, Zolk O, Linz W, Scholkens BA, Bohm M. Hypercholesterolemia is associated with enhanced angiotensin AT1-receptor expression. *Am J Physiol* 1997; **272**: H2701–2707.

12

Carotidojugular fistula

Yves Castier, Alain Tedgui and **Stéphanie Lehoux**

Centre de Recherche Cardiovasculaire Inserm Lariboisière, Paris, France

Introduction

Hemodynamic conditions play a key role in the pathogenesis of atherogenesis, restenosis after angioplasty, and aortic aneurysms. Clinical findings and experimental studies indicate that chronic changes in blood flow lead to vascular remodeling, due to compensatory responses induced in the vascular wall to normalize wall shear stress.[1] In the case of persistent increases in flow, adaptive remodeling of the vessel involves the reorganisation of cellular and extracellular components, leading to vessel enlargement. This is best exemplified in models of arteriovenous fistula (AVF), where steep increases in flow result in the most spectacular illustration of adaptative outward vascular remodeling. Because the molecular mechanisms of this process remain largely unknown, we considered that a reliable model of arteriovenous fistula in the mouse would be a valuable tool, taking into account the number of transgenic animals and different strains of this species available. The AVF would also be useful to investigate endothelial responses to high shear stress, which hereto have been studied predominantly *in vitro*.[2,3] Understanding these processes could help explain how changes in blood vessel wall structure occur in pathological conditions.

One model of AVF already exists in the mouse: the central aortocaval fistula. However, this procedure incurs important hemodynamic modifications leading to volume overload in the heart, and it is in fact widely used in rats or in mice to study cardiac failure.[4] Because we wanted to investigate endothelial cell responses to high shear stress *in vivo* and shear stress-induced vascular remodeling independently of

A Handbook of Mouse Models of Cardiovascular Disease Edited by Qinbo Xu

such systemic effects, we developed a mouse model of peripheral arteriovenous fistula, connecting the common carotid artery with the jugular vein, which does not modify the blood pressure.

Creation of the AVF

Anesthesia and mouse preparation

Adult mice aged at least 12 weeks (25 g minimum) are used. Mice are weighed, then they are anesthetised by intraperitoneal injection of a mixture of ketamine hydrochloride (0.20 mg/g) and xylazine (0.02 mg/g).

After 10 min, the neck and thorax area is carefully shaved, and the neck skin is swabbed with 70 per cent ethanol and 10 per cent betadine. The mouse is fixed in a supine position with its neck extended, the tongue gently pulled out, and placed so that the operator is on the right side of the animal (Figure 12.1). Each animal receives of an intraperitoneal injection of heparin (1 U/g) at the onset of the procedure.

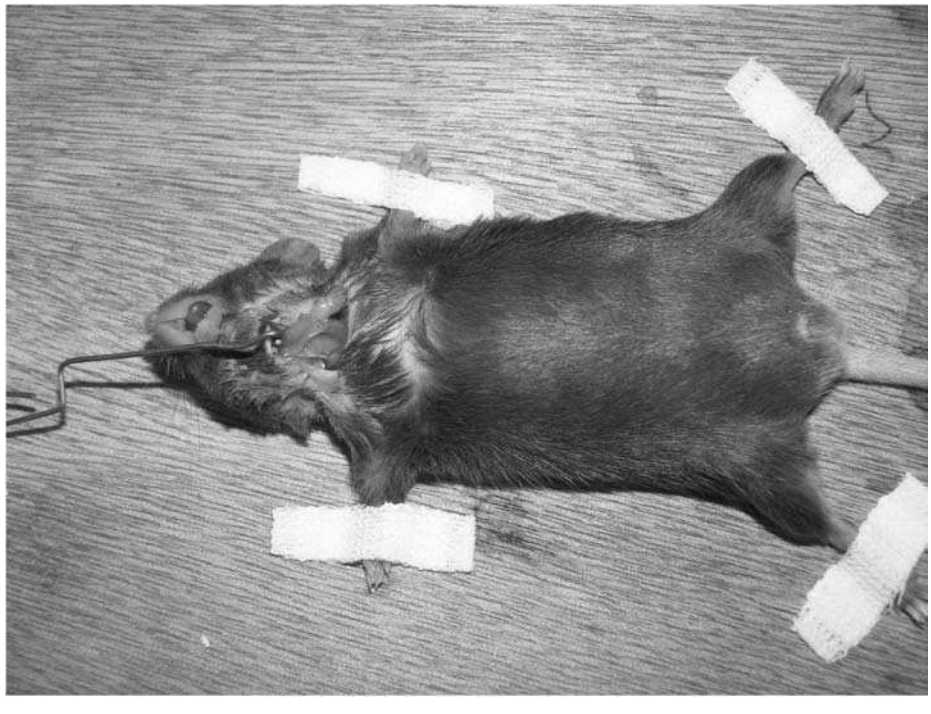

Figure 12.1 A mouse is fixed in a supine position with its neck extended, a transverse incision of the neck is made just above the sternum, and the salivary glands are pulled back upwards. For a color version of this figure, please see the images supplied on the accompanying CD

Microsurgical tools and sutures

The operation is performed under a dissecting microscope (Nikon SMZ 1000). The magnifications used for the procedure are $\times 17$ for dissection and ligation of the vessels, and $\times 30$ for anastomosis construction.

Microsurgical tools:

- Two microvascular forceps, Moria, straight, extra delicate, 13 cm long (Moria, ref 9980);
- One scissor, Dowell, straight sharp blades (Moria, ref 9926);
- One miniature scissor, Vannas-Moria, straight and pointed blades 5×0.5 mm (Moria, ref 9600);
- One needle holder, Ikuta, straight extra delicate jaws 0.8 mm (Moria, ref 9990);
- One irrigating cannula, olive tip, 3 cm long (Moria, ref 13221);
- Three micro clamps, straight, pressure 15 g (Moria, ref 201);
- Microsurgical sutures (Ethicon, Johnson & Johnson Intl): Polypropylene 8/0 (ref F1836), Polyamide 10/0 (ref FG2880), Polyamide 11/0 (ref NS2881).

Surgical procedure

During the entire procedure, the operative field and the vessel lumens are irrigated with a physiological saline solution containing 100 U/ml of heparin. A transversal skin incision is made in the neck just above the sternum (shoulder to shoulder line). The salivary glands are driven back upwards with a retractor (Figure 12.1). The right jugular vein (RJV) is dissected and exposed. All side branches of the RJV are ligated with 10-0 suture and cleaved, leaving an appropriate length ($\sim$3-4 mm) of vein totally free of any collateral vessels. The right sternocleidomastoid muscle is ligated with 8-0 thread and resected. The right common carotid artery (RCCA) is dissected and exposed. To avoid vagus nerve traumatism during dissection of the artery, we raise the RCCA gently with forceps and cut away the surrounding tissue, taking care to never touch the nerve. The RCCA must be dissected free from the clamping area, as close to the sternum as possible, upto the carotid bifurcation. The RCCA is clamped proximally, then ligated just below the carotid bifurcation with an 8-0 ethilon and cleaved immediately upstream of the ligature (Figure 12.2a). The lumen of the RCCA is irrigated to flush out any remaining blood. The RJV is clamped proximally and distally, such that the area between the clamps is that devoid of collateral branches described above, and a venotomy is performed in its middle part (Figure 12.2b). The

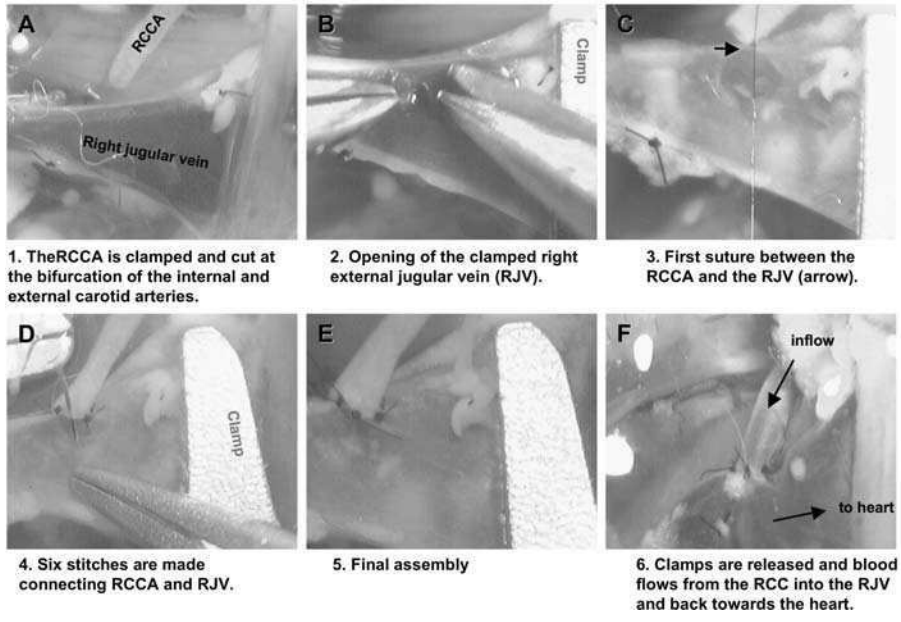

Figure 12.2 Photos showing six consecutive steps of the surgical procedure. (a) The right common carotid artery (RCCA) is clamped and cut at the bifurcation of the internal and external carotid arteries. (b) Opening of the clamped right external jugular vein (RJV). (c) First suture between the RCCA and the RJV (arrow). (d) Six stitches are made connecting RCCA and RJV. (e) Final assembly. (f) Clamps are released and blood flows from the RCC into the RJV and back towards the heart (arrows). For a color version of this figure, please see the images supplied on the accompanying CD

lumen of the RJV is irrigated. The size of the venotomy must be exactly identical to the that of the RCCA.

Using 11/0 suture, an end-to-side RCCA/RJV anastomosis is completed. The anastomosis is performed with six stitches (interrupted sutures). The three first stitches are placed opposite to the operator as shown in Figures 12.2c and 12.3a. The construction of the anastomosis is certainly the most critical step of the whole procedure. The most important features are: (i) to ensure equidistance between each stitch; (ii) to minimise the overlap between artery and vein, making sutures as close to the edges as possible; (iii) not to over-tighten the knots. Any major technical error will lead to immediate thrombosis of the fistula when the clamps are removed.

After completion of the anastomosis (Figures 12.2d and 12.2e), the jugular clamps are removed followed by the carotid clamp, and fistula patency is verified (Figures 12.2f and 12.3b). The operative field is irrigated with warm physiological saline solution and the skin is closed with continuous sutures using 6-0 vicryl. Two ml of saline solution is injected subcutaneously between the shoulders at the end of the procedure. Operative time averages 80 min, and animals are kept warm until complete recovery under a heating lamp.

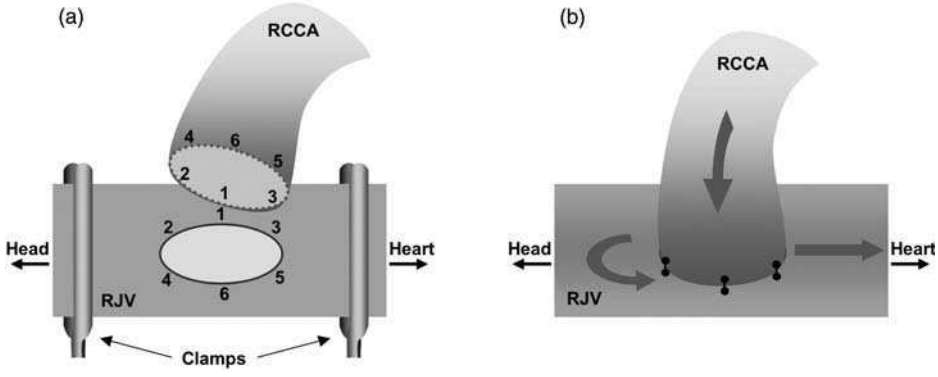

Figure 12.3 Schematic representation of the technical aspect for the construction of the anastomosis with the placement of the six stitches. (a) The three first stitches are placed opposite to the operator (1,2,3). (b) Arrows represent direction of blood flow in the RCCA (right common carotid artery) and RJV (right jugular vein) after release of the clamps. For a color version of this figure, please see the images supplied on the accompanying CD

Arterial blood pressure measurement

Arterial blood pressure is measured in operated and control mice. To measure arterial blood pressure in awake mice, animals are placed on a heating platform at 37°C and allowed to adapt to the environment for 5 min. Systolic arterial blood pressure is measured using the tail-cuff method (BP-2000, Blood pressure analysis system, Visitech Systems, USA).

To measure arterial blood pressure under anesthesia, mice are anesthetised as indicated above. The right leg is shaved and swabbed with 70 per cent ethanol. An inguinal incision is made, the skin is retracted and the femoral artery exposed. A polyethylene catheter (30G) with a beveled edge is flushed with physiological saline solution. The femoral artery is clamped, and the catheter is inserted via arteriotomy. Pressure is measured using a Gould transducer.

Hemodynamic measurements at the carotid level

Mice are anesthetised as indicated above, and both carotid arteries are exposed, the left CCA serving as a non-operated internal control. The dissection of the fistula is often difficult, especially in the first week after its creation. The arteries are photographed *in situ*, alongside a 460 µm wide scale placed parallel to the vessel, using a camera (Logitech) attached to the surgical microscope. Precise arterial diameters are measured with the help of image analysis software (Histolab). Blood flow velocity is measured by using a 20 MHz pulsed Doppler system (Milar) connected to a voltmeter system (Hewlett Packard). The pen probe position is adjusted to obtain a 30° angle with the vessel axis. Blood flow is measured 5 mm

upstream of the AVF in the RCCA and at the equivalent location in the left CCA. Velocities (V, cm/s) are obtained from the measured Doppler frequency shifts and volume flow Q is calculated by multiplying the mean velocity by the cross-sectional area of the vessel lumen, using the formula Q (cm^3/s) $= \pi r^2 V$, where r is the radius in cm. Wall shear stress is calculated using the Poiseuille formula $\tau = 4\mu\ Q/\pi r^3$. In this formula, μ is the viscosity of blood (taken to be 0.035 poise).

Immediately after AVF construction, RCCA blood flow increases approximately six-fold (blood flow in the left CCA is about 0.6 ml/min) and the calculated wall shear stress reaches a mean value of 2400 to 2800 $\mu N/cm^2$ (versus 340 to 400 $\mu N/cm^2$ before the intervention).

Tissue harvesting

At the end of the experiment, mice are anesthetised as indicated above, and both carotid arteries are exposed. Thereafter animals are killed by overdose of sodium pentobarbital (0.5 mg/ml). The abdomen is opened longitudinally and mice are perfused with physiological NaCl solution via a catheter (24G) inserted in the abdominal aorta, to eliminate any residual blood in the CCAs. For frozen preparations, arteries are harvested, immediately frozen in liquid nitrogen, and stored at −80°C. For histological analysis, arteries are perfused at 80 mmHg with 4 per cent phosphate-buffered formaldehyde (pH 7.2) for 20 min before harvesting. Fixation is completed by placing vessels overnight in the formaldehyde solution at 4°C.

Hemodynamic and structural data

We have recently demonstrated[5] that the creation of an AVF between the RCCA and jugular vein in the mouse produced an abrupt increase in arterial blood flow, reaching more than six-fold from the onset, as calculated on day 1 (Figure 12.4). Flow in the carotid artery remained consistently high during the following 3 weeks. In comparison, shear stress peaked on the first day, inducing signal transduction pathways that stimulate arterial enlargement. As the weeks progressed, the arterial diameter gradually increased, such that shear stress values returned towards baseline levels (Figure 12.4). Given that arterial remodeling is driven by wall shear stress, it was not entirely surprising to see that the most acute change in diameter (22 per cent) was observed within the first 7 days after AVF construction, when shear stress was greatest. The RCCA enlarged more gradually (3–4 per cent per week) during the subsequent weeks. Despite the marked increases in vessel diameter, no changes in artery thickness were observed in the RCCA. Moreover, blood pressure and heart rate were unaffected by the procedure, and no changes in blood flow or vessel diameter were observed in the contralateral artery.

One of the striking characteristics of the arterial wall proximal to an AVF is extensive tearing and fragmentation of the internal elastic lamina (IEL)[6,7] which

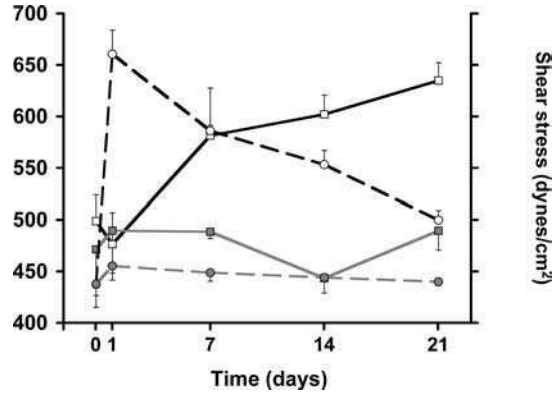

Figure 12.4 Characterization of the remodeling reponse in mouse carotid arteries before (day 0) and after AVF creation. Shear stress (black dotted line) in the carotid artery peaks immediately (day 1) after AVF creation, then decreased with time, as carotid diameter (black solid line) gradually increases. Shear stress and diameter do not vary in the contralateral artery (gray lines)

augments arterial distensibility, leading to enhanced vessel diameter. Matrix metalloproteinases (MMPs) are likely instigators of IEL degradation in the vessel wall. MMP-2 and MMP-9 are upregulated shortly after AVF construction, and heightened activity of these enzymes persists until shear stress is normalised.[8,9] Furthermore, several studies have reported that MMP inhibition diminishes flow-mediated arterial enlargement in rat[8,10] and rabbit[9] AVF models, and prevents elastin degradation associated with AVF-inducd arterial enlargement.[9] The contribution of nitric oxide (NO) in flow-induced vascular remodeling has been well established by our group[7,9] and others.[11] After effective long-term blockade of NO synthesis with L-NAME, artery enlargement and the corresponding wall tissue growth expected in response to increased blood flow are dampered, and the wall shear stress in flow-loaded common carotid arteries increases proportionately to blood flow.

We recently used our mouse model of AVF to determine the role of reactive oxygen species (ROS) in high flow-induced vascular remodeling, and to specify whether reduced nicotinamide adenine dinucleotide phosphate(NADPH) oxidase, one of the many enzymes able to generate ROS in the vasculature, contributes to this process. We found[5] that ROS production is enhanced in arteries exposed to chronic high flow and that NADPH oxidase comprising the p47phox subunit is the major generator of shear stress-induced ROS in the vascular wall; gp91phox, in comparison, played a negligible role in this process. Our observations made in $p47phox^{-/-}$ mice and endothelial nitric oxide synthase $(eNOS)^{-/-}$ mice provided direct evidence that endogenous ROS and NO modulate not only the activity of MMPs, but also their production, in arteries exposed to elevated blood flow. This allowed us to conclude that together with NO derived from eNOS activation, ROS produces peroxynitrite, which is probably the major activator of MMPs in this setting. This is the first study using a mouse carotid fistula model to investigate

the molecular mechanisms behind long term structural adaptation to altered blood flow.

Perhaps one limitation of the mouse carotid fistula model is that mice develop stenosis at the site of anastomosis, such that vessel patency is reduced in many animals after 28 days. Hence, complete remodeling is not achieved, since at 3 weeks shear stress has not yet returned to physiological baseline values.[12] This might appear surprising, given that fistulated rabbit carotid arteries remodel entirely 15 days after AVF.[9] However, the adaptive response to great stresses appears to require a longer period of time, as shown using the monkey iliac artery, where restoring shear stress to a baseline value after a 10-fold increase in flow required 6 months.[13] Nonetheless, mouse carotid enlargement does allow for a compensatory reduction in shear stress from over seven-fold of upon fistula opening to less than two-fold at 3 weeks, and would probably have progressed until shear stress returned to normal levels had not fistula permeability become compromised beyond that time point. On the positive side, the stenosis faithfully reproduces what occurs in arteriovenous fistulas practised on hemodialysis patients, which are often plagued by complications due to thrombosis at the sites of stenosis, leading to fistula failure. The mouse AVF model may therefore be used to investigate how this process occurs.

References

1. Lehoux S, Tronc F, Tedgui A. Mechanisms of blood flow-induced vascular enlargement. *Biorheology* 2002; **39**: 319–324.
2. Davies PF. Overview: temporal and spatial relationships in shear stress-mediated endothelial signalling. *J Vasc Res* 1997; **34**: 208–211.
3. Resnick N, Yahav H, Shay-Salit A, Shushy M, Schubert S, Zilberman LC, Wofovitz E. Fluid shear stress and the vascular endothelium: for better and for worse. *Prog Biophys Mol Biol* 2003; **81**: 177–199.
4. Hatt PY, Rakusan K, Gastineau P, Laplace M, Cluzeaud F. Aorto-caval fistula in the rat. An experimental model of heart volume overloading. *Basic Res Cardiol* 1980; **75**: 105–108.
5. Castier Y, Brandes RP, Leseche G, Tedgui A, Lehoux S. p47phox-Dependent NADPH Oxidase Regulates Flow-Induced Vascular Remodeling. *Circ Res* 2005; **97**: 553–540.
6. Greenhill NS, Stehbens WE. Scanning electron microscopic investigation of the afferent arteries of experimental femoral arteriovenous fistulae in rabbits. *Pathology* 1987; **19**: 22–27.
7. Tronc F, Wassef M, Esposito B, Henrion D, Glagov S, Tedgui A. Role of NO in flow-induced remodeling of the rabbit common carotid artery. *Arterioscler Thromb Vasc Biol* 1996; **16**: 1256–1262.
8. Karwowski JK, Markezich A, Whitson J, Abbruzzese TA, Zarins CK, Dalman RL. Dose-dependent limitation of arterial enlargement by the matrix metalloproteinase inhibitor RS-113,456. *J Surg Res* 1999; **87**: 122–129.
9. Tronc F, Mallat Z, Lehoux S, Wassef M, Esposito B, Tedgui A. Role of matrix metalloproteinases in blood flow-induced arterial enlargement. *Arterioscler Thromb Vasc Biol* 2000; **20**: e120–e126.

10. Abbruzzese TA, Guzman RJ, Martin RL, Yee C, Zarins CK, Dalman RL. Matrix metalloproteinase inhibition limits arterial enlargements in a rodent arteriovenous fistula model. *Surgery* 1998; **124**: 328–334.
11. Guzman RJ, Abe K, Zarins CK. Flow-induced arterial enlargement is inhibited by suppression of nitric oxide synthase activity in vivo. *Surgery* 1997; **122**: 273–279.
12. Kamiya A, Togawa T. Adaptive regulation of wall shear stress to flow change in the canine carotid artery. *Am J Physiol* 1980; **239**: H14–H21.
13. Zarins CK, Zatina MA, Giddens DP, Ku DN, Glagov S. Shear stress regulation of artery lumen diameter in experimental atherogenosis. *J Vasc Surg* 1987; **5**: 413–420.

13

Applications to the study of stroke

Jacques Seylaz and **Elisabeth Pinard**

Cardiovascular Research Centre Lariboisière, Inserm U 689, Paris, France

Keywords

mice, brain, microcirculation, confocal microscopy, dynamic imaging

Introduction

The brain is critically dependent on its blood supply, since it has no energy reserves. However, the brain microcirculation has been poorly explored *in vivo* due to the major obstacle of the skull. The protection of brain tissue is ensured by the cranial bone and by meninges, including the dura mater, arachnoid and pia mater. The cerebrospinal fluid (CSF) flows in the meninges, bathing all pial vessels (i.e. superficial vessels), and fills the perivascular spaces of penetrating arteries.

This chapter describes the surgical procedure for implanting a closed cranial window that can be used repeatedly for at least 1 month to monitor in real-time the microcirculation at the surface of the mouse brain. We also explain how to label red blood cells with a fluorescent marker for investigating the dynamics of capillary blood flow in living mice using laser-scanning confocal fluorescence microscopy, and how to perform these experiments. Finally, we describe the methods used to occlude focally an artery through the window, producing a small ischemic infarct, and we indicate the possibility to study vessel remodeling, angiogenesis, and changes in the blood–brain barrier permeability in the peri-ischemic area over time. Lastly, we show another application of *in vivo* confocal microscopy, with an example of the long-term monitoring of exogenous fluorescent adult stem cells transplanted through the window into the ischemic surrounding.

A Handbook of Mouse Models of Cardiovascular Disease Edited by Qinbo Xu

Experimental preparation of mice

Anesthesia

All surgery is performed under isoflurane anesthesia. First, the mouse is placed in an appropriate box and made to inhale 2 per cent isoflurane in a mixture of 25 per cent oxygen and 75 per cent nitrous oxide for about 5 min to induce anesthesia. The isoflurane inhalation is then reduced to 1.4–1.8 per cent for surgery, and adapted to each animal. The advantage of isoflurane is that, first, only a minute quantity (0.17 per cent) is metabolised, thus minimising hepatotoxicity and nephrotoxicity, making it relatively safe for the investigator, and second, the animal wakes up very rapidly when the inhalation stops. In addition, mice undergoing repeated prolonged experiments stay in good physiological conditions, as checked by measuring their arterial blood pressure, blood gases and pH.

Implanting the closed cranial window

The general protocol was reported by Tomita *et al.*[1] and is described here in detail. The window itself is prepared from a 140-µm thick quartz coverslip of the type generally used for histology. The coverslip is cut with a diamond to obtain a round window, whose diameter is 3 to 3.5 mm (Figure 13.1), depending on the size of the hole in the cranium.

Any strain of mouse can be used and a body weight of 20–25 g is ideal. The age of the mouse must correspond to the stereotaxic atlas of the mouse brain (for instance Franklin and Paxinos, 1997[2]) if the study deals with specific areas or requires intracerebral injections.

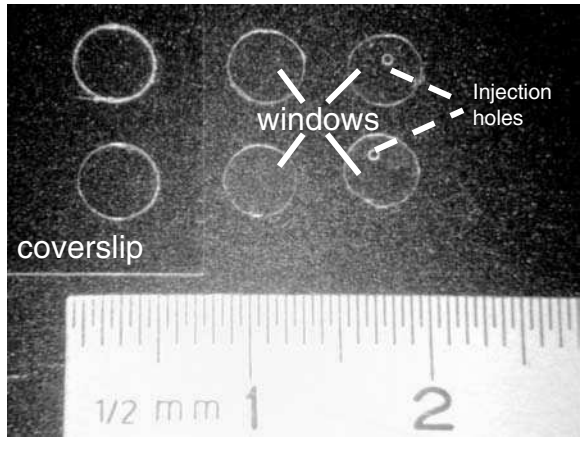

Figure 13.1 Left: portion of a quartz coverslip used to make windows. Right: four cranial windows, two of them with an injection hole

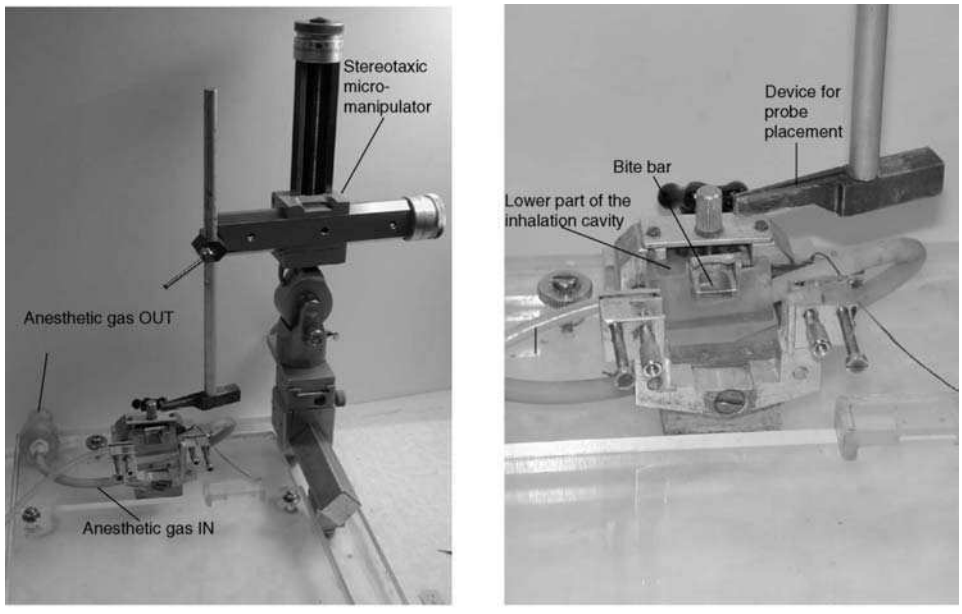

Figure 13.2 (a) General view of the custom-built plexiglass contention system, including a stereotaxic micromanipulator; (b) Magnified view of the system receiving the mouse head, maintaining its teeth and delivering the anesthetic gas. The device on the right is connected to the stereotaxic micromanipulator and used to place a laser-Doppler probe, a thermoprobe or an injection micropipette. Note that part of the system is detachable and can be secured to the microscope stage. For a color version of this figure, please see the images supplied on the accompanying CD

The cranial window is implanted using a special custom-built system equipped for delivering anesthetic gas (Figure 13.2a). This system secures the mouse head during cranial surgery (Figure 13.2b), enables a stereotaxic device to be used to support a laser-Doppler probe for blood flow measurement, a thermoprobe for temperature measurement, or a micropipette for intracerebral injection, and stabilizes the whole system under a confocal microscope. We can thus place the mouse in the same position for all investigations and rapidly change experimental tools. The rectal temperature is kept at 37 °C using a feedback-controlled homeothermic blanket. This is important, since temperature significantly influences most events of the cerebral ischemic cascade (see for review Dietrich *et al*., 1996[3]).

The protocol is similar to that used in the rat,[4] but the size and location of the cranial window are different, and the dura mater is kept intact.

The mouse is placed in a prone position. All surgery is performed under an operating micoscope at high magnification. Hair is carefully shaved off and the skin painted with disinfectant. The skin is incised longitudinally and reflected. All connective tissue is removed from the visible part of the bone using a scraper (Figure 13.3a). A thin layer of dental cement (Palavit 55VS, Kulzer, Germany) is

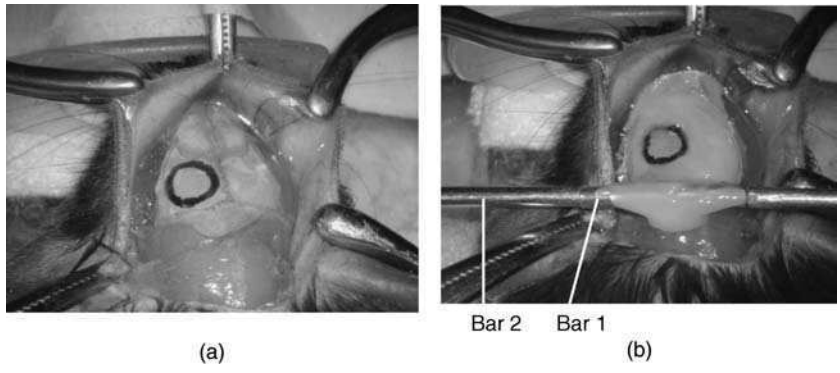

Figure 13.3 (a) A mouse head, focusing on the cranial bone, after reflection of conjonctive tissue. The black circle grossly indicates the place where the window has to be placed; (b) the cranial bone after the spread of dental cement and the placement of the chronically-glued bar (Bar 1) glued to the bone by dental cement. The detachable bar (Bar 2) is inserted into Bar 1 to secure the mouse head to the contention system. For a color version of this figure, please see the images supplied on the accompanying CD

applied all over the bone to facilitate anchoring the window to the bone. Remember that dental cement adheres only to perfectly dry bone. Also, take care to keep the dental cement from contacting the skin or membranes as it is toxic to tissues. Then, the mouse head is secured in the stereotaxic frame by inserting the teeth in the bite bar and then gluing a steel bar (1.8 mm OD, 1.3 mm ID) to the very posterior part of the skull with dental cement (Luxaflow, DMG, Germany). This bar will maintain the head in the selected position by inserting inside it a longer bar that can be secured to the frame at each experimental time (Figure 13.3b). As the device includes a rotary system, the whole frame can be inclined so that the place on the skull where the window will be implanted is horizontal.

The area to be explored is delineated and a 3-mm diameter hole is drilled above the left parietal–occipital cortex, 2.5 mm posterior to the bregma and 2.5 mm lateral to the midline,[2] as shown in Figure 13.4a. The area under the window defined using these stereotaxic coordinates is a distal region of the middle cerebral artery (MCA). This artery corresponds to the Sylvian artery in humans. It is relatively often the site of thrombosis that causes cerebral ischemia.

Other window sizes and locations can be used, depending on the aim of the study. The main restrictions are space, the round edges of the horizontal part of the bone and the vascular sutures. A small dental drill is used to remove bone circularly (Figure 13.5a), while cooling the preparation with water to avoid warming the brain. The whole remaining disk of bone is removed by inserting an ultra-thin needle in the drilled area and using it as a lever arm.

A suitable 140-μm thick round quartz coverslip is then selected by trial and error. The window is then sealed to the bone with dental cement (Ionosit, DMG, Germany), making the preparation waterproof (Figure 13.5b).

We use one of three different dental cements, depending on their specific properties: adhesion strength, drying time, and toxicity. Only mice whose cranial window

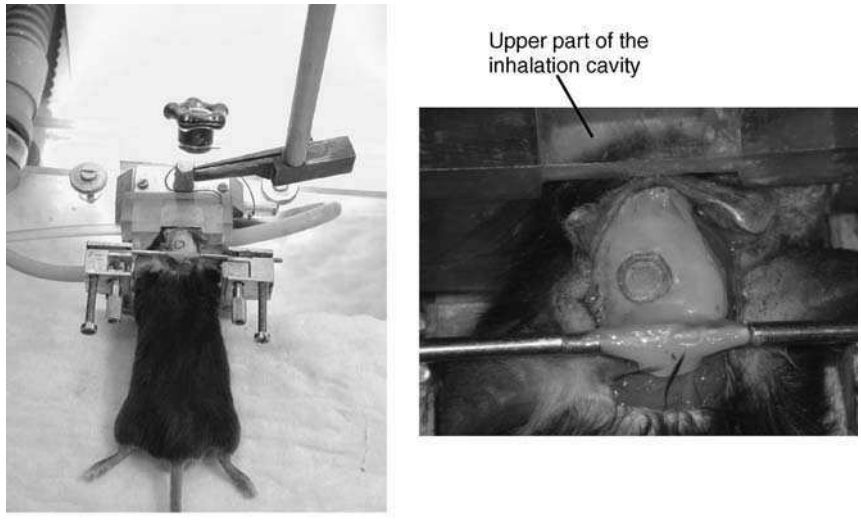

Figure 13.4 (a) General view of an anesthetised mouse placed in the contention system and maintained by the bars. (b) Magnified view of the head with the nose inserted into the cavity in which anesthetic gas is delivered. For a color version of this figure, please see the images supplied on the accompanying CD

shows no bleeding or inflammation can be used to successfully visualise vessels through the window over the long term. This is usually about 75 per cent of implanted mice. Experiments should not be started until several days after implanting the window, to allow for the resorption of any inflammation. In all cases, mice equipped with a cranial window exhibit a normal behavior as shown in Figure 13.6.

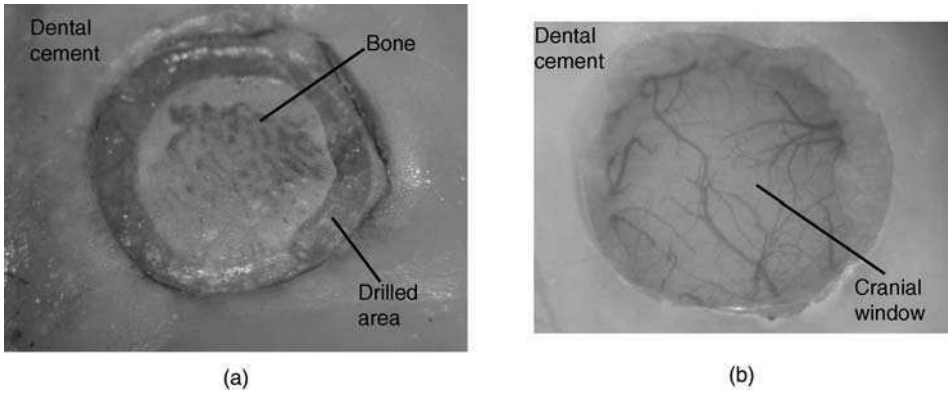

Figure 13.5 (a) Ring of thin cranial bone drilled at the periphery of the window; note that an ultra-thin needle is placed in this ring to remove cautiously the internal disc of bone; (b) a completed closed cranial window. For a color version of this figure, please see the images supplied on the accompanying CD

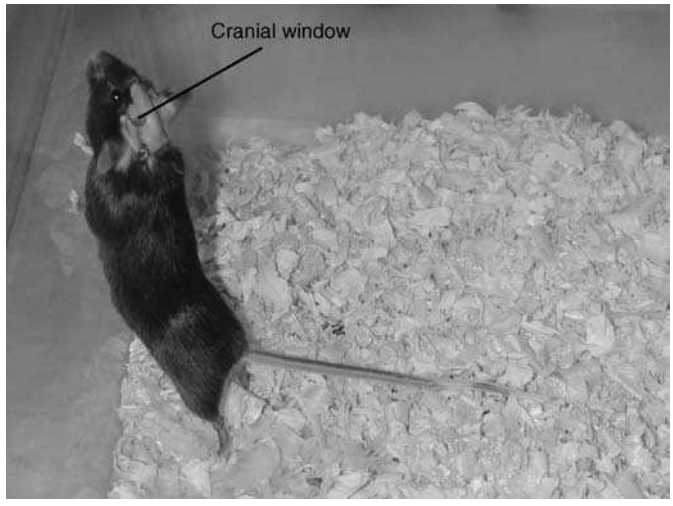

Figure 13.6 A mouse awakening from window implantation. For a color version of this figure, please see the images supplied on the accompanying CD

Fluorescent labeling of red blood cells

Studies on the microcirculation under the cranial window, especially the capillary circulation, use red blood cells that have been labeled *ex vivo* following the protocol of Seylaz *et al*.,[4] derived from that of Sarelius and Duling.[5] An aliquot (1 ml) of arterial blood is taken from a donor animal using a catheter placed upstream. Blood is placed in an heparinized Eppendorf tube, and centrifuged at 2000 r.p.m. for 7 minutes at 20 °C. The supernatant is removed and the tube is filled to within 1 cm of the top with phosphate-buffered saline–ethylene diamine tetra-acetic acid (PBS-EDTA) (pH 7.4). This procedure is repeated three times.

Fluorescein isothiocyanate (10 mg; FITC Isomer 1, Sigma, France) is dissolved in 1 ml PBS-EDTA (pH 8), and placed in the Eppendorf tube. It is incubated with the red blood cells for 2 h at ambient temperature, with agitation and protection against light. The tube is then centrifuged at 2000 r.p.m. for 7 min at 20 °C, the supernatant removed and the pellet of red blood cells rinsed four times with PBS-EDTA (pH 7.4). Fluorescent-labeled erythrocytes should be used on the day they are prepared, but they can be kept refrigerated for several days if covered with aluminium foil to protect them from light.

The fluorescently labeled red blood cells should be checked before starting the blood flow experiment. Place one drop of RBC suspension on a slide and cover it with a coverslip. Examine the cells using a fluorescence microscope. If there are large amounts of unbound fluorescence, the cells should be rinsed again.

Catheterisation of the tail vein

Tracers (fluorescent red blood cells or fluorescent dextran) are injected via a catheter inserted into a tail vein at each experimental time. The mouse is placed in a prone

position and the hind legs turned laterally on either side so that the tail also turns by about 30°; this ensures that one caudal vein is uppermost. The tail is kept in this position using adhesive tape. Under an operating microscope, a longitudinal 2–3-mm long incision is made in the tail skin to reveal the underlying vein. A small incision is then made in the vein and a polyethylene tube (OD 700 μm, ID 300 μm; Biotrol, France) that has been warmed and stretched to a convenient size is inserted into the vein with the tip towards the heart. Both the catheter and tail are kept in place with a suture around the tail.

The venous catheter remains permeable for several hours. Venous electrocoagulation is topically achieved at the catheter withdrawal. Thus it is possible to insert a venous catheter several times over a long period, each time more proximally than the last.

Methods

Laser-Doppler flowmetry

Tissue blood flow in the parieto-occipital cortex just below the window is measured using a laser-Doppler flowmeter (MBF 3D, Moor Instruments, Axminster, UK). Under the surgical microscope, the laser probe is positioned over the cranial window using the micromanipulator, away from large pial vessels. Blood flow is measured before and after arterial occlusion to check whether ischemia occurs. Blood flow is measured in arbitrary units.

Dynamic laser-scanning confocal fluorescence microscopy (Video)

The local microcirculation can be repeatedly monitored through the closed cranial window using a Viewscan DVC-250 confocal laser-scanning unit (BioRad, UK) attached to an Optiphot-2 fluorescence microscope (Nikon, Japan). This method was developed in rats[4] and currently used for studies on this species.[6–8] The light source is an argon/krypton laser whose wavelengths are 488, 568 and 647 nm. Various objectives can be used: a Nikon dry lens (×10), or a Nikon water immersion lens (×20 and ×40). The numerical apertures are 0.40 (working distance: 1.8 mm) and 0.55 (working distance: 2.0 mm). This microscope has a linear pinhole, allowing the rapid acquisition of 2D images. The mouse is placed under the microscope by securing the plexiglass system to the microscope stage so as to place the window below the objective (Figure 13.7 top). Fluorescent tracers are injected via a tail vein. A tracer dose (50 μl) of rhodamin B isothiocyanate-dextran (RITC-Dextran, Sigma, France; molecular weight = 70 000; 2 mg/ml) or of fluorescein isothiocyanate-dextran (FITC-Dextran, Sigma, France; molecular weight = 77 000; 2.5 mg/ml) in 0.9 per cent NaCl is used to label the microvascular network. Fluorescent erythrocytes (50 μl) are then injected to show all microvessels in the cortex to a depth of about 200 μm. Appropriate filters must be used. Parenchymal capillaries are focused manually. Images in a single plane are recorded at video speed (50 frames per second)

with an SIT camera (C-2400, Hamamatsu Photonics, Japan) and a digital videorecorder (DSR-25 DVCAM, Sony, Japan). The images can be stored on a PC using a suitable software. The video shows fluorescent red blood cells circulating in mouse cerebral microvessels at increasing magnifications.

Static laser-scanning confocal fluorescence microscopy

Both superficial vessels and transplanted stem cells can be repeatedly visualised at high definition using a classical laser-scanning confocal fluorescence microscope (for instance MRC 600, BioRad) whose characteristics are similar to those of the dynamic confocal microscope, except that it has a pinhole diaphragm instead of a slot. Unlike the Viewscan confocal microscope, several planes can be summed when using a classic single-photon confocal microscope, which makes it possible to visualise the superficial layers of the cortex. The quality of static images is higher than that of dynamic images for several reasons: the pinhole diaphragm; image sampling is much slower (2 seconds per frame instead of 50 frames/second); and the same image can be acquired several times and then summed.

Blood vessels can be labeled by an intravenous injection of rhodamine-dextran and visualised at 568 nm (Figure 13.7a,b), while cells from transgenic mice overexpressing the green fluorescent protein (GFP) fluoresce at 488 nm, as shown below. The properties of the confocal microscope enable brain tissue and microvessels to be explored to a depth of 200 μm below the brain surface, while the presence of the cranial window ensures that they can be explored repeatedly over the long term.

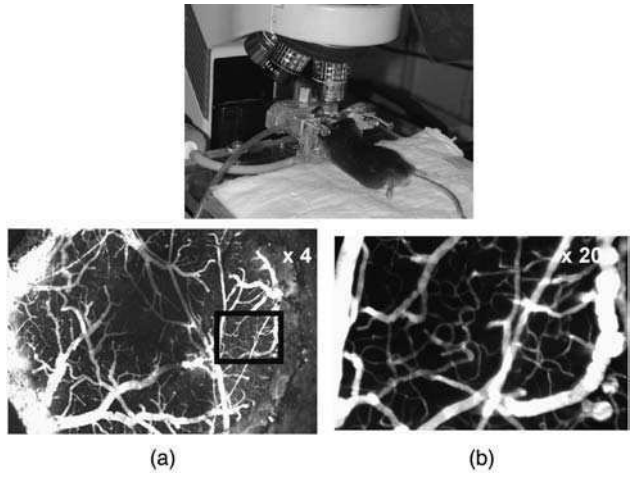

Figure 13.7 Top: an anesthetised mouse maintained in the contention system and placed under a confocal microscope. Bottom: (a) a vascular network filled with Rhodamine-dextran and visualised by confocal microscopy across the cranial window; (b) a capillary network at high magnification. For a color version of this figure, please see the images supplied on the accompanying CD

Repeated *in vivo* imaging of pial and cortical microvessels in an ischemic area of the mouse brain using laser-scanning confocal microscopy may also be useful for directly exploring possible vascular remodeling or angiogenesis.

The permeability of the blood–brain barrier (BBB) to various sizes of fluorescent molecules can also be evaluated quantitatively over time, as described in rats by Mayhan and Heistad.[9]

Applications

Stroke model

Focal ischemia can be induced one week after window implantation under the same experimental conditions.[1] The mouse is anesthetised with isoflurane and its head is secured in the stereotaxic frame. The frame is inclined so that the window is horizontal. The whole superficial vascular network under the window can be seen under the operating microscope (Figure 13.8a). Usually, two distal branches of the left MCA are visible in the upper left part of the window. Topical cauterization of these branches for 2 s through the cranial window produces immediate arterial thrombosis followed by ischemia in the underlying cortical tissue, as indicated by the whitening of the area (Figure 13.8b). The decrease in tissue blood flow after the arterial occlusion can be checked by laser-Doppler flowmetry. A decrease in tissue blood flow of about 80 per cent close to the occluded arteries, and of about 50 per cent in the periphery is a sure indication of stroke induction. These reductions in tissue blood flow correspond to the core of the infarction and its penumbra. This procedure for producing stroke causes a 2 °C increase in tissue temperature for 20 s, which is far from deleterious. Spontaneous reperfusion of the occluded arteries can occur in the days following occlusion.

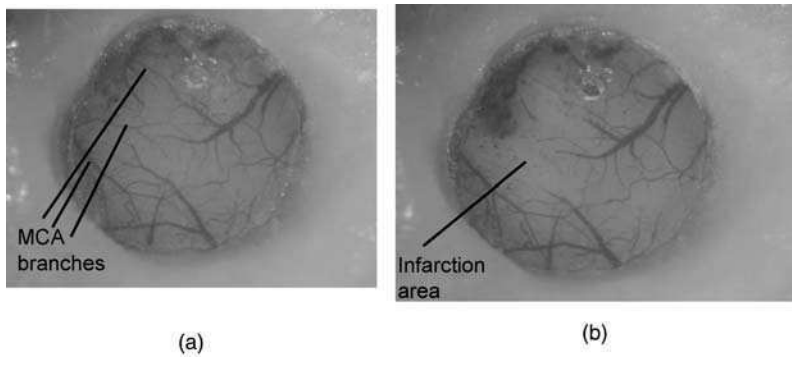

Figure 13.8 (a) Pial vessels under the window, with branches of the middle cerebral artery (MCA) on the left; (b) same pial vessels just after the occlusion of the two upper MCA branches. For a color version of this figure, please see the images supplied on the accompanying CD

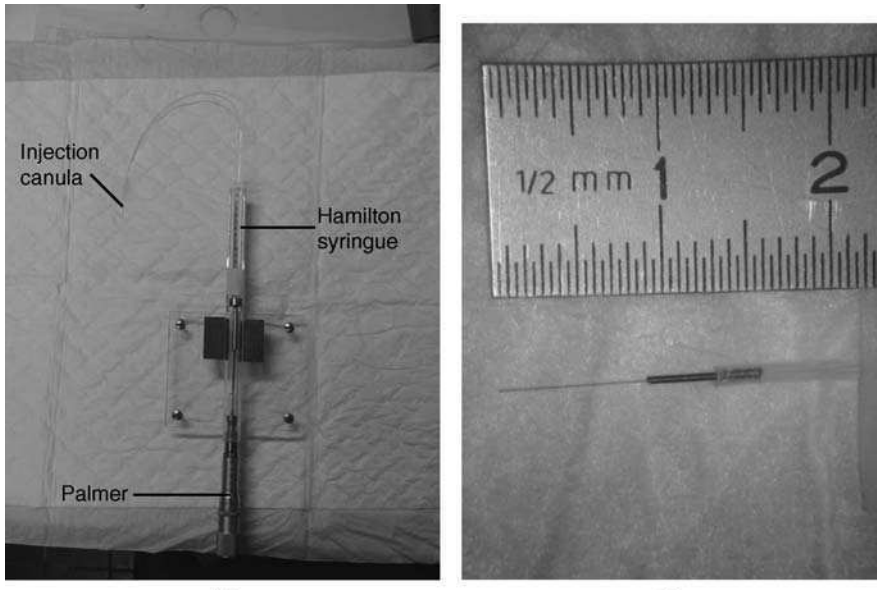

Figure 13.9 (a) The injection system; (b) the canula for intracerebral injections (OD 120 μm, ID 40 μm). For a color version of this figure, please see the images supplied on the accompanying CD

Tracking transplanted fluorescent stem cells

In vivo confocal microscopy can also be used to evaluate the therapeutic potential of cell therapy in the brain. Cells harvested from transgenic mice overexpressing the green fluorescent protein (GFP) (with or without culture) are suspended in PBS and stereotaxically injected using a 10 μl Hamilton syringe and a custom-built cannula (OD 120 μm, ID 40 μm) (Figure 13.9a,b). Intracerebral injection is done through a small hole drilled in the cranial window (Figures 13.1 and 13.8). A total volume of 0.5 μl is slowly injected, and the needle is left in place for about 5 min to prevent any reflux. The quantity of cells per microliter varies according to the cell size. Fluorescent cells are immediately visualised in the injection hole by confocal microscopy to be sure that the injection has been successful.

Fluorescent stem cells can be tracked for at least 1 month to determine whether they survive, migrate, proliferate or change their morphology.[10] Figure 13.10 shows an example of GFP-expressing marrow stromal cells transplanted into the mouse brain and monitored *in vivo* by confocal microscopy at various times after their transplantation.

Thus, *in vivo* confocal fluorescence microscopy is a useful tool for monitoring the microcirculation or tracking transplanted cells in the mouse brain through a closed cranial window that can be used for an extended period. The recently developed two-photon confocal microscope provides improved quality of dynamic imaging and increases the depth inside the brain that can be studied, as shown in studies on

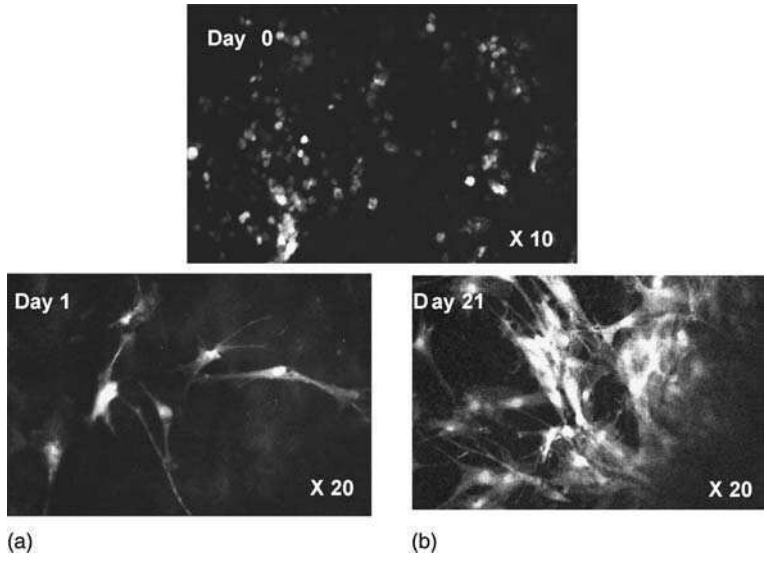

Figure 13.10 Top: bone marrow stromal cells overexpressing GFP visualised by confocal microscopy across a cranial window, immediately after injection; Bottom: (a) same cells in the same mouse 1 day later, at higher magnification; (b) same cells in the same mouse 3 weeks later, at higher magnification. Note the changes in morphology of the cells, and the persistent quality of images

capillary blood flow in the olfactory bulb glomeruli[11] and on resting microglial cells[12] for example. More generally, *in vivo* imaging opens the way to long-term pathophysiological and pharmacological studies of stroke in mice with certain genes knocked out, as it provides direct visualization of events through the window.

References

1. Tomita Y, Kubis N, Calando Y, Tran Dinh A, Meric P, Seylaz J, Pinard E. Chronic *in vivo* investigation of mouse cerebral microcirculation by fluorescence confocal microscopy in the area of focal ischemia. *J Cereb Blood Flow Metab* 2005; **25**: 858–867.
2. Franklin KBJ, Paxinos G. The Mouse Brain in Stereotaxic Coordinates. San Diego: Academic Press Harcourt Brace & Company, 1997.
3. Dietrich WD, Busto R, Globus MY, Ginsberg MD. Brain damage and temperature: cellular and molecular mechanisms. *Adv Neurol* 1996; **71**: 177–197.
4. Seylaz J, Charbonné R, Nanri K, et al. Dynamic *in vivo* measurement of erythrocyte velocity and flow in capillaries and of microvessel diameter in the rat brain by confocal laser microscopy. *J Cereb Blood Flow Metab* 1999; **19**: 863–870.
5. Sarelius IH, Duling BR. Direct measurement of microvessel hematocrit, red cell flux, velocity and transit time. *Am J Physiol* 1982; 243 (suppl):H1018–H1026.
6. Pinard E, Engrand N, Seylaz J. Dynamic cerebral microcirculatory changes in transient forebrain ischemia in rats: involvement of nitric oxide from neurons. *J Cereb Blood Flow Metab* 2000; **20**: 1648–1658.

7. Pinard E, Nallet H, Mac Kenzie ET, Seylaz J, Roussel S. Penumbral microcirculatory changes associated with periinfarct depolarizations in the rat. *Stroke*, 2002; **33**: 606–612.
8. Belayev L, Pinard E, Nallet H, et al. Albumin therapy of transient focal cerebral ischemia: *in vivo* analysis of dynamic microvascular responses. *Stroke* 2002; **33**: 1077–1084.
9. Mayhan WG, Heistad DD. Permeability of blood–brain barrier to various sized molecules. *Am J Physiol* 1985; **248**: H712–718.
10. Tran Dinh A, Kubis N, Tomita Y, Karaszewski B, Calando Y, Oudina K, Petite H, Seylaz J, **Pinard E**. *In vivo* imaging with cellular resolution of bone marrow cells transplanted into the ischemic brain of a mouse. *NeuroImage*, sous presse 2006.
11. Chaigneau E, Oheim M, Audinat E, Charpak S. Two-photon imaging of capillary blood flow in olfactory bulb glomeruli. *Proc Natl Acad Sci USA* 2003; **100**: 13081–13086.
12. Nimmerjahn A, Kirchhoff F, Helmchen F. Resting microglial cells are highly dynamic surveillants of brain parenchyma *in vivo*. *Science* 2005; **308**: 1314–1318.

14

Identifying congenital heart defects in embryos using high-resolution magnetic resonance imaging

Jürgen E Schneider and **Shoumo Bhattacharya**

Department of Cardiovascular Medicine, University of Oxford, Wellcome Trust Centre for Human Genetics, Oxford, UK

Introduction

Of the genetically tractable organisms used in studying development, the mouse is anatomically and phylogenetically closest to the human. Of particular importance for human congenital malformations are the unique mammalian features – in the cardiovascular and respiratory systems – that have evolved as specific adaptations for life on land. Like the human, the mouse has a four-chambered heart with a septated outflow tract, and left-sided great arteries.[1] Thus it is a good anatomical model for common cardiac malformations, such as ventricular and atrial septal defects, outflow tract malformations, and aortic arch malformations, which cannot be identified in other organisms such as the fruitfly or zebrafish. While the cardiovascular and respiratory systems of mammals and birds are superficially similar, phylogenetic evidence indicates that they have undergone considerable evolutionary divergence. For instance, birds have right-sided aortic arches, lack the major mammalian respiratory muscle – the diaphragm, and have lungs with air capillaries rather than alveoli.[2] At a more fundamental level, birds have mechanistically distinct pathways that establish laterality – necessary for the establishment of left–right

A Handbook of Mouse Models of Cardiovascular Disease Edited by Qinbo Xu

asymmetry in cardiovascular development.[3] Theoretical considerations notwithstanding, empirical observations indicate the power of mouse models. Thus, several mouse mutations, e.g. in *Cbp*,[4,5] *Tfap2*,[6,7] *Tbx5*,[8–10] *Tbx1*[11–13] and *Zic3*,[14,15] generated using transgenic technology recapitulate the cardiac malformations observed in patients with mutations in these genes. Most importantly, the identification of certain human coronary heart disease (CHD) genes (e.g. *NKX2.5*,[16] *GATA4*,[17] *CRYPTIC*,[18] *LEFTY2*,[19] and *ACVR2B*[20]) has resulted directly from an understanding of their function in mice. These observations indicate that the mouse is the model organism of choice to help us understand the genetic basis of human cardiopulmonary and other developmental malformations.

Identifying mouse cardiac malformations

A genetic change or environmental insult that results in early gestational death is unlikely to be an important factor in causing developmental malformations in children. Understanding the mechanisms underlying common developmental malformations using mouse models therefore requires identifying embryos with malformations in late gestation. Many cardiac malformations (e.g. atrial septal defect, ventricular septal defect, outflow tract defects) can only be confidently identified after 14.5 days post coitum (dpc), when cardiac and outflow tract septation are completed in normal embryos.[21] The mouse embryo, unlike that of the zebrafish, is unfortunately opaque at these late gestational stages. The identification of malformations in late gestation embryos typically relies on histological sectioning, which is labor intensive, results in the irretrievable loss of 3D information – which is essential for the interpretation of complex cardiovascular malformations – and is not amenable to high-throughput approaches. Approaches for embryonal analysis that capture 3D information include techniques such as episcopic fluorescence image capture (EFIC),[22] and optical projection tomography.[23] EFIC involves wax embedding and sectioning of embryos at 2 μm intervals, and photographing the wax block face using autofluorescence. Although the resolution obtained here is very high, a 12 mm embryo would require ~6000 sections, making this approach unsuitable for high-throughput studies. Optical projection tomography has been used to image mouse embryos up to 13.5 dpc,[23] but its use for later stage embryos that are more opaque has not yet been demonstrated.

Magnetic resonance imaging

Unlike histology and optical techniques, magnetic resonance imaging (MRI) is non-destructive, and is not limited by the optical properties of the tissue. The application of MRI for embryo imaging essentially derives from the pioneering work of Bradley Smith and colleagues at Duke University.[24–28] High contrast and resolution of cardiac structures with spin-echo MRI is obtained by cannulating the umbilical vessels, and

perfusing the embryo with a paramagnetic contrast agent.[26] This is, however, technically difficult, and requires significant operator skill and time per embryo. More recently, spin-echo MRI techniques[29] have been used on parformaldehyde fixed embryos (without cannulating the umbilical vein) to identify a number of embryonic structures including the heart, lungs, brain, spinal cord and vertebral bodies. These studies typically take up to 36 h for single embryos, rendering them impractical for high-throughput phenotyping.

We have developed a high-resolution 3D MRI approach that provided sufficient anatomic detail to visualise normal and abnormal cardiovascular anatomy (the major interest of our laboratories). The emphasis was on achieving high throughput, without relying on a difficult embryo preparation technique. In contrast to previous studies we used a fast gradient echo magnetic resonance imaging approach on paraformaldehyde fixed single mouse embryos with an experimental resolution of up to $21 \times 21 \times 20\,\mu$/voxel in unattended overnight runs, that allows us to visualise normal organs, and cardiac and visceral malformations in mutant mouse embryos with high accuracy.[30–33]

Embryo MRI technique and analysis

Embryos

Embryos are dissected out at 15.5 dpc and fixed in 4 per cent paraformaldehyde made up in phosphate buffered saline (pH 7.4) containing 2 mM gadolinium- diethylenetriamine penta-acetic acid (Gd-DTPA) (Magnevist, Schering) for 1–2 days or longer. We have imaged younger and older embryos as well but we chose the 15.5 dpc time point for analysis as this represents the earliest at which the anatomical development of most organs (especially the heart) resembles that of the adult. This time point also maximises the recovery of live mutant embryos, before they die and are resorbed. Embryos are embedded in 1 per cent agarose spiked with 2 mM of paramagnetic Gd-DTPA in nuclear magnetic resonance (NMR) tubes (Figure 14.1a, b) either singly, with the anteroposterior axis in the long axis of the tube (preparation time ~10 min), or in layers of four embryos each (eight layers in total, preparation time ~120 min). The left front limb of each embryo is removed to aid identification of the left side during image analysis. Each embryo in a given layer is uniquely identified by also removing either the left or right hind limbs or the tail. The agarose immobilises the embryos in the tube and is prepared by microwaving 1 g agarose in 100 ml distilled water. The volume of the dissolved agarose is remeasured and topped up to 100 ml if required. 400 µl Gd-DTPA is added to the agarose solution while it is being stirred using a magnet on a hotplate. The stirring removes air bubbles trapped in the agarose, which must be avoided as they cause local loss of signal and resolution. We use NMR tubes for single embryo MR (SE MRI) with inner diameters of 13 mm, and for multi embryo MR (ME MRI) with inner diameters of 28 mm, respectively. A custom-made Teflon disk screwed onto a nylon rod in the centre of the tube facilitates the removal of the embryos after MRI.

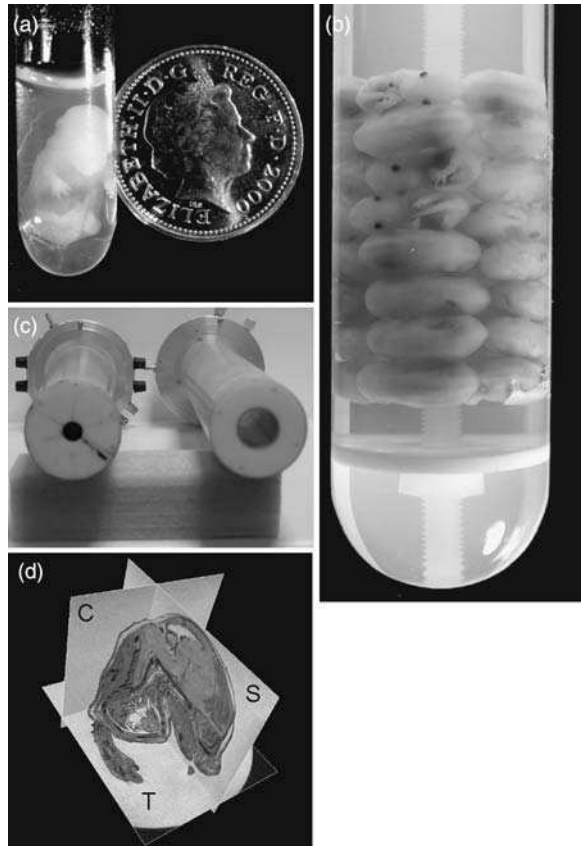

Figure 14.1 Magnetic resonance imaging set-up. (a), A single mouse embryo (15.5 dpc), in a 13 mm NMR tube. The embryo is immobilised in agarose. (b), Stack of 32 embryos embedded in a 28 mm NMR tube. (c), Radiofrequency (RF) coils used in embryonic imaging for transmitting the B_1 field into the sample and detecting the resulting signal. (left: 13 mm, right: 28 mm birdcage probe). (d), The 3D dataset (written as a stack of 2D TIFF files) can be analysed in any user-defined orientation using the software program Amira. Here it is sectioned in transverse (T), coronal (C), and sagittal planes. For a color version of this figure, please see the images supplied on the accompanying CD

MRI

A glossary of terms used in MRI is presented in Table 14.1. We image embryos using a purpose-built quadrature driven birdcage coil (id: 13 mm and 28 mm; Rapid Biomedical Würzburg, Germany – Figure 14.1c) on a vertical ultra-high field magnet (11.7 T, Magnex Scientific, Oxford, UK), equipped with a shielded gradient system (maximal gradient strength of 548 mT/m, risetime 160 µs (Magnex Scientific). Gradient-induced heating is minimised by using compressed air (flow: 2000 l/h) at room temperature. Tuning and matching the probe, global shimming and flip-angle calibration are performed manually prior to each experiment. For high-resolution embryonic imaging,

Table 14.1 A glossary of magnetic resonance terminology

MRI	Magnetic resonance imaging
B_0-field	Static magnetic field that is generated by a superconducting magnet. Clinical MR scanners have a magnetic field strength of typically 1.5 –3 T, experimental MR system up to 11.7 T and more (for comparison: natural magnetic field of earth: 25–65 μT).
Magnetic field gradients	Pulsed magnetic field gradients are used to obtain spatial information from the sample. The gradient fields are generated by separate coils, which are switched rapidly during the experiment. Spatial information can be obtained by (a) slice-selection, (b) frequency encoding and (c) phase encoding. Slice selection and frequency encoding is achieved in one scan, which has to be repeated *N*-times with varying strength of the phase encoding gradient to obtain spatial information in the 2nd dimension (*N*: number of points in 2nd dimension).
RF coil	RF-coils are used for transmitting the B_1-field into the region of interest and detecting the NMR signal. Typical designs are solenoid-shaped coils or birdcage coils. Some coils such as birdcage coils can be designed that they detect both components of the transverse magnetization simultaneously, referred to as 'quadrature driven' coils. This results in a signal-to-noise improvement of up to a factor of $\sqrt{2}$.
Flip angle	Angle which magnetisation is tilted out of the equilibrium after the application of a RF-pulse.
T_1-Relaxation time	Longitudinal or spin-lattice relaxation time – time constant, which describes the return of the z-component of the magnetisation to its equilibrium value M_0. This process involves energy exchange between the spin system and their nuclear frame-work. Different tissue types can have different longitudinal relaxation times, which facilitates tissue identification.
T_2-Relaxation time	Transverse or spin–spin relaxation time – time constant that describes the decay of the transverse magnetisation (excluding magnetic field inhomogeneities). This process involves interaction between neighboring spins. Different tissue types can have different spin–spin relaxation times, which also facilitates tissue identification.
Spin echo sequence (SE)	Pulse sequence consisting of two RF-pulses: A 90° excitation pulse is followed by a 180° refocusing pulse after a period of τ_1. A spin echo can be observed after second period τ_2, if $\tau_1 = \tau_2$. The time $TE = \tau_1 + \tau_2$ defines the echo time of the sequence, the repetition time of the sequence is the period between two 90° excitation pulses. T_2-contrast in the MR images can be obtained by longer TEs, and T_1-contrast by shorter repetition times.

(*continued on next page*)

Table 14.1 (*continued*)

Gradient echo sequence (GE)	A RF-pulse followed by a gradient pulse to dephase the spins before rephasing them by applying an equal but opposite gradient. The gradient echo appears when the areas under the positive and the negative gradients are equal. The echo-time of a gradient echo sequence is defined as the period between the centre of the RF-pulse and the appearance of the gradient echo. The repetition time of the sequence is the period between two successive RF-pulses. Gradient echo sequences are inherently faster than spin echo sequences and provide different contrast compared to SE images. Strong T_1-contrast in the MR images can be obtained by high flip angles (i.e. 90 °) and short TR's.
Field-of-view (FOV)	Size of MR image. The image consists of discrete voxels. The experimental resolution is given as the FOV divided by the number points in this dimension.
Zero-filling	Interpolation technique to visualise image information that is already present in the original data. This process requires the application of filters (Butterworth filter) to avoid artifacts caused by the interpolation.

we use a 3D spoiled gradient echo sequence with an echo time of $T_E = 10$ ms. A 90 ° excitation pulse (rectangular pulse shape, 90 ° = 100 μs), with a short repetition time (30 ms) resulting in strong T_1 contrast. We apply 608 × 608 phase encoding steps with either 1024 (SE MRI) or 1408 (ME MRI) points in frequency encoding direction (i.e. long axis of the NMR tube) at a field of view of 13 × 13 × 20 mm (SE MRI) or 26 × 26 × 50 mm (ME MRI), yielding an experimental resolution of 21 × 21 × 20 μm or 43 × 43 × 36 μm, respectively. The total imaging time is approximately 12 h, with each phase encoding step being averaged four times. The total 'hands-on' operator time involved is under 1 h.

Reconstruction

Data reconstruction requires sufficient computational power, computer memory (RAM preferably >2Gb), hard disk space and dedicated graphic cards. Reconstruction of the raw MRI data sets (with a size of up to 4 Gb) was performed using a purpose-written C-software on RedHat Linux. Specifically, we apply zero-filling (SE MRI: factor of 2 in each dimension; ME MRI: interpolation to 1024 × 1024 × 2048 points) and a modified third order Butterworth filter[34] function before Fourier transformation. This results in 2048 transverse axial 16-bit resolution per pixel 2D TIFF format images. Zero-filling yields a final voxel size of 12.7 × 12.7 × 9.8 μm (SE MRI) and 25.4 × 25.4 × 24.4 μm (ME MRI). Typical images obtained from an ME MRI scan are shown in Figure 14.2.

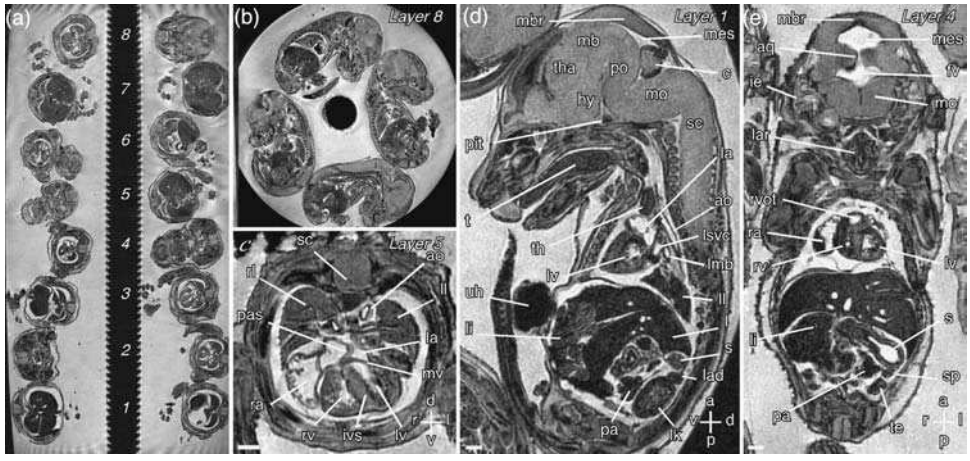

Figure 14.2 Multi-embryo MRI. (a) Section through the long axis of the NMR tube showing embryos in eight layers. (b) Sagittal section through layer 8 showing the four embryos in this layer. (c-e) Transverse, sagittal, and coronal sections through individual embryos in layers 5, 1 and 4 respectively. The voxel size is 25.4 × 25.4 × 24.4 μm. Structures indicated are the spinal cord (sc), the right and left lungs, atria and ventricles (rl, ll, ra, la, rv, lv), primary atrial and interventricular septa (pas, ivs), mitral valve (mv), midbrain roof (mbr), midbrain (mb), mesencephalic vesicle (mes), thalamus (tha), hypothalamus (hy), pons (po), cerebellum (c), medulla oblongata (mo), pituitary (pit), tongue (t), thymus (th), left superior vena cava and main bronchus (lsvc, lmb), aorta (ao), liver (li), stomach (s), left adrenal and kidney (lad, lk), pancreas (pa), intestines (i), umbilical hernia (uh), aqueduct of Sylvius (aq), fourth ventricle (fv), inner ear (ie), larynx (lar), right ventricular outflow tract (rvot), spleen (sp), and testes (te). Scale bars = 500 μm; axes: d - dorsal; v - ventral; r - right; l - left; a - anterior, p - posterior. From Schneider et al., 2004[33]. Reproduced by permission of Biomed central ltd

Analysis

The datasets are analysed using a Dell Precision workstation with a Xeon processor (2.4 GHz), 3 GB RAM, and a Wildcat 3 graphics card, running Amira 3.0 (TGS Europe, Merignac Cedex France) on Microsoft Windows XP or on RedHat Linux. A limitation of Windows is that entire datasets (which are $\geq$4 GB each) cannot be loaded at once, and so we typically use a dual-boot PC that runs both Windows and Linux. Datasets are typically analysed using the Orthoslice and Obliqueslice functions, which allow virtual resectioning of the dataset in any orientation (Figure 14.1d). This typically takes about 30 min per embryo to exclude major internal malformations. 3D reconstructions are made in a semi-automated fashion using the 'Image Segmentation Editor' in Amira followed by the 'SurfaceGen' module. We have found the 'magic-wand', 'paintbrush', and 'interpolation' tools particularly useful for segmenting our datasets. 3D reconstructions of the heart and great vessels typically take between 1 and 2 h for an experienced user. Tissue or organ volumes can be accurately measured after segmentation using the 'Measure Tissue Statistics' tool in Amira – this is a powerful method for identifying and quantifying organ hypoplasia, which can then be corrected for embryo size.

Discussion

The most powerful use of MRI in our hands has been the analysis of cardiac malformations.[32] We have shown that it is possible to visualise normal cardiac structures such as the atria and ventricles, the atrial and ventricular septa, valves, and great arteries and veins (Figure 14.3). We can also accurately identify atrial and ventricular septal defects, atrial isomerism, outflow tract defects (e.g. double outlet right ventricle), malformations of the great arteries (e.g. aberrant aortic arches and aortic vascular rings) (Figure 14.4). These studies were originally done in *Cited2* and *Pitx2c* knockout embryos,[35,36] to validate the MRI technique. Subsequently we have used SE MRI to identify unexpected cardiac malformations in *cyclinE*-deficient embryos,[37] left–right patterning defects of the heart in *Cited2*-deficient embryos.[38] We have used our ME MRI technique to identify cardiac malformations in *Ptdsr* knockout embryos.[33] As both normal and malformed hearts are complex 3D structures, the ability to use segmentation analysis to reconstruct the heart in 3D vastly enhances our ability to understand fetal heart topography, and to accurately quantify malformations.

Applications

We see the applications of embryo MRI in three major areas: investigating genetically modified mice, in high throughput mutagenesis screens, and in investigating teratogens and environmental effects on development.

Investigating genetically modified mice

Many mouse gene knockouts display late gestational lethality, but incomplete analysis and loss of 3D information consequent to histological sectioning, results in major developmental malformations being frequently missed. For instance, cardiac defects in *Tfap2a*$^{-/-}$, *Isl1*$^{-/-}$, and *splotch* homozygous mice were unrecognised until very recently,[7,39,40] and adrenal agenesis, a highly penetrant phenotype in *Cited2*$^{-/-}$ mice,[31,35] was not recognised in independent descriptions of these mice.[22,41,42] It is also becoming increasingly important to examine the same mutation in different genetic backgrounds as genetic modifiers play a major role in determining the final phenotype. Moreover, it is particularly important to characterise heterozygotes, as many human defects are a result of haploinsufficiency. Typically the penetrance in heterozygotes is low, requiring the analysis of large numbers of embryos. These large studies are possible with MRI.

High-throughput genetic screens

A typical ENU recessive screen (e.g. 100 first generation mutants per year) would require the analysis of ~2400 embryos per year.[43] This is possible with multi-embryo

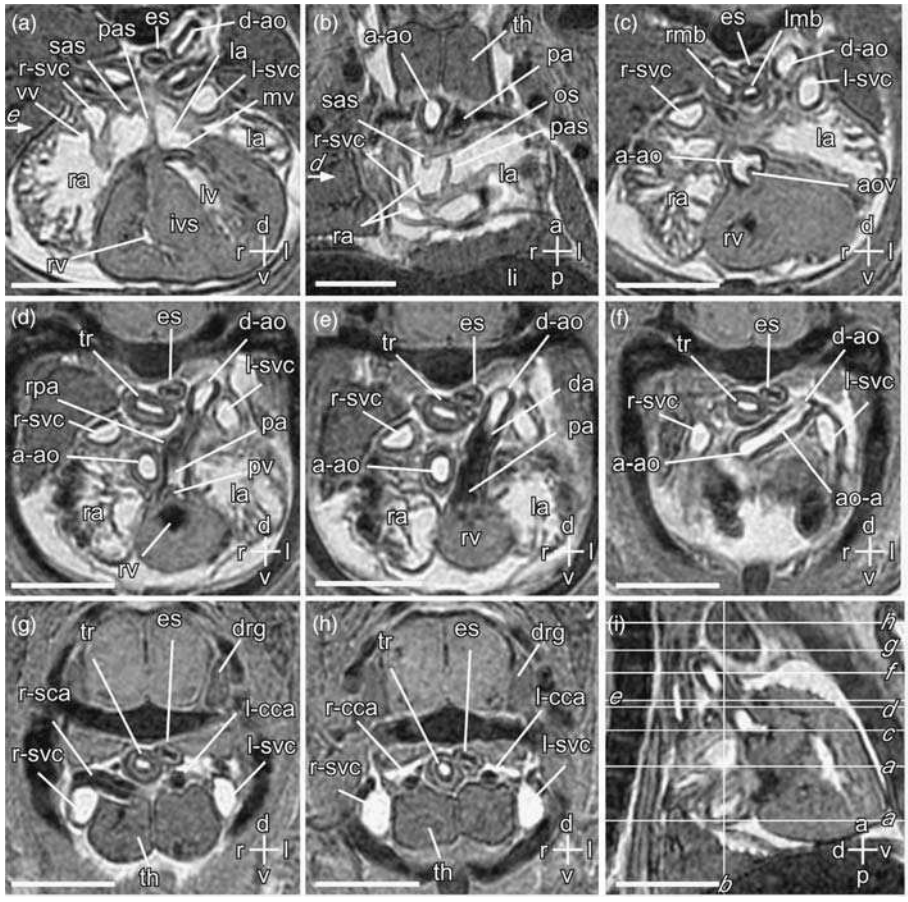

Figure 14.3 Normal cardiac anatomy. All images are from a wild-type embryo at 15.5 dpc. The section planes indicated (i), which shows a sagittal section. (a), The right and left ventricles (rv and lv), are separated by the interventricular septum (ivs). The left atrium (la) opens into the left ventricle via the mitral valve (mv), and is separated from the right atrium (ra) by the primary atrial septum (pas). The right superior vena cava (r-svc) opens into the right atrium and the venous valve (v) is clearly seen. The left superior vena cava (l-svc) is also seen, as is the descending aorta (d-ao), esophagus (es), and the posterior edge of the secondary atrial septum (sas). (b), Coronal section through the primary and secondary atrial septa (pas and sas2). The ostium secundum (os) at the upper edge of the primary atrial septum is seen, and the image was chosen to show its maximum size. The primary atrial septum overlaps the second to form the valve of the oval foramen. The ascending aorta (a-ao), pulmonary artery (pa), and the thymus (thym) are also seen. (c), The origin of the ascending aorta (a-ao) and part of the aortic valve (aov) are seen. (d), The pulmonary artery and valve (pa, pv), the origin of the right pulmonary artery (rpa) are seen. The right ventricle (rv) appears dark as it contains blood. (e) The pulmonary artery (containing blood) continues on as the ductus arteriosus (da) which joins the descending aorta. (f), The aortic arch (ao-a) connecting the ascending aorta (a-ao) to the descending aorta (d-ao) is seen. (g, h), The branches of the aorta (right subclavian artery (r-sca), and right and left common carotid arteries (rcca, lcca) are seen. Note also the dorsal root ganglion (drg). Scale bars = 1 mm; axes: d- dorsal; v – ventral; r – right; l– left; a – anterior, p – posterior

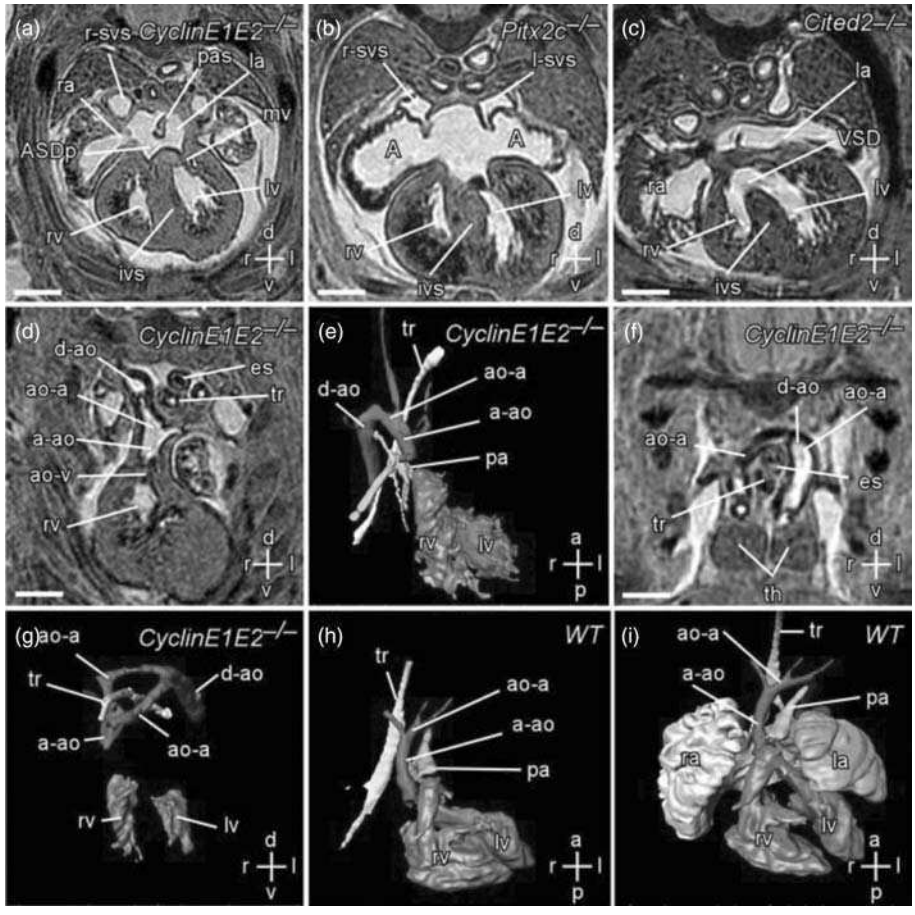

Figure 14.4 Cardiac malformations identified by MRI (a), Atrial septal defect primum. Transverse section showing left and right atria and ventricles (la, ra, lv, rv). An ostium primum type of atrial septal defect (ASD-P) is present at the ventral margin of the primary atrial septum (pas). (b) Right atrial isomerism. Transverse section showing a large atrial septal defect resulting in common atrium (A), with bilateral systemic venous sinuses (l-svs, r-svs) into which drain the left and right superior vena cava. (c), Ventricular septal defect. Section showing a ventricular septal defect (VSD) in the interventricular septum (ivs) in a Cited2 null embryo[35]. (d, e) Right aortic arch. Transverse section and 3D reconstruction (right ventral oblique view) respectively, showing a right-sided aortic arch (ao-a) passing to the right of the trachea (tr) and the esophagus (es) before continuing as the descending aorta (d-ao). The ascending aorta (a-ao) arises from the right ventricle (rv) as does the pulmonary artery (pa), i.e. double outlet right ventricle. (f, g) Aortic vascular ring. Transverse section and 3D reconstruction (anterior view) respectively, showing bilateral aortic arches (ao-a) forming a vascular ring around the trachea (tr) and the esophagus (es). Also indicated is the thymus (th). (h, i), 3D reconstructions of a wild type embryo showing right ventral oblique and ventral views respectively. Note the aortic arch and pulmonary artery on the left of the trachea. Scale bars = 500 μm; axes: d – dorsal; v – ventral; r – right; l – left. For a color version of this figure, please see the images supplied on the accompanying CD

MRI, where we image up to 32 embryos simultaneously – a potential throughput of over 10 000 embryos a year. This allows us to identify cardiac and other malformations with high sensitivity and specificity. Multi-embryo MRI is therefore highly suited to high-throughput ENU mutagenesis screens. Such screens performed at late gestation would be expected to identify genes that affect later aspects of development, and hypomorphic or haploinsufficient alleles of genes that affect earlier steps of development.

Investigating teratogens and environmental effects on development

Environmental factors increasing the risk of congenital heart disease include maternal rubella and diabetes, drugs such as phenytoin, thalidomide, trimethadione, retinoic acid, ethanol, ecstasy, and cocaine, and environmental toxins such as trichloroethylene metabolites.[44–47] The extent to which genetic and environmental factors interact to affect the risk of congenital heart disease is unclear, but has important public health implications. MRI could potentially be useful in these investigations, which would typically require a large throughput.

Pros and cons of *ex vivo* MRI

A major disadvantage of MRI is the relatively high equipment cost – >£1 million for a 11.7 T magnet. Nevertheless, equivalent MR equipment is available in many academic centres in the UK and in the US. Importantly, embryonal anatomical imaging at night maximises the use of an expensive MR facility. Another disadvantage of *ex vivo* MRI is that it gives us no clue to embryo physiology, and does not allow one to follow the same embryo through development. Thus *ex vivo* MRI needs to be complemented with techniques such as *in vivo* high-frequency ultrasound.[48,49] This would be particularly important for identifying mutations that affect cardiac physiology (e.g. blood flow, heart rate) rather than structure. A major advantage of *ex vivo* MRI however is the ability to easily transfer paraformaldehyde fixed embryos from referring laboratories by courier. This minimises the expense of animal relocation, rederivation, and breeding required to generate the embryos, and significantly reduces animal experimentation. Finally, the experimental resolution of *ex vivo* MRI using our current approach is ~25μ. While this is sufficient for identifying most cardiac and other organ malformations, it does not allow the identification of smaller structures such as the coronary arteries or the cytoarchitecture of different organs. Here it is likely that MRI can be usefully complemented with techniques such as EFIC, and in younger embryos, by OPT.

Acknowledgments

The embryo MRI techniques were developed in collaboration with Stefan Neubauer and Kieran Clarke (University of Oxford). These studies were funded by the

Wellcome Trust and the British Heart Foundation. S.B. is a Wellcome Trust Senior Fellow in Clinical Science. This chapter and Figures 14.1, 14.3 and 14.4, and Table 14.1, are substantially based on a review previously published by the authors.[50] Figure 14.2 is from Schneider *et al.* (2004).[33]

References

1. Kent GC, Carr RK. Circulatory system. In Comparative anatomy of the vertebrates (McGraw Hill, Boston, 2001).
2. Liem KF, Bemis WE, Walker WF, Grande L. Functional anatomy of the vertebrates: an evolutionary perspective. Fort Worth, *Harcourt College Publishers*, 2000.
3. Kathiriya IS, Srivastava D. Left-right asymmetry and cardiac looping: implications for cardiac development and congenital heart disease. *Am J Med Genet* 2000; **97**: 271–279.
4. Petrij F. et al. Rubinstein-Taybi syndrome caused by mutations in the transcriptional co-activator CBP. *Nature* 1995; **376**: 348–351.
5. Oike Y, et al. Truncated CBP protein leads to classical Rubinstein–Taybi syndrome phenotypes in mice: implications for a dominant-negative mechanism. *Hum Mol Genet* 1999; **8**: 387–396.
6. Satoda M. et al. Mutations in TFAP2B cause Char syndrome, a familial form of patent ductus arteriosus. *Nat Genet* 2000; **25**: 42–46.
7. Brewer S, Jiang X, Donaldson S, Williams T, Sucov HM. Requirement for AP-2alpha in cardiac outflow tract morphogenesis. *Mech Dev* 2002; **110**: 139–49.
8. Basson CT. et al. Mutations in human TBX5 cause limb and cardiac malformation in Holt–Oram syndrome. *Nat Genet* 1997; **15**: 30–35.
9. Li QY. et al. Holt–Oram syndrome is caused by mutations in TBX5, a member of the Brachyury (T) gene family. *Nat Genet* 1997; **15**: 21–29.
10. Bruneau BG et al. A murine model of Holt–Oram syndrome defines roles of the T-box transcription factor Tbx5 in cardiogenesis and disease. *Cell* 2001; **106**, 709–721.
11. Lindsay, EA, et al. Tbx1 haploinsufficieny in the DiGeorge syndrome region causes aortic arch defects in mice. *Nature* 2001; **410**: 97–101.
12. Merscher S, et al. TBX1 is responsible for cardiovascular defects in velo-cardio- facial/ DiGeorge syndrome. *Cell* 2001; **104**: 619–629.
13. Jerome LA, Papaioannou VE. DiGeorge syndrome phenotype in mice mutant for the T-box gene, Tbx1. *Nat Genet* 2001; **27**: 286–291.
14. Gebbia M. et al. X-linked situs abnormalities result from mutations in ZIC3. *Nat Genet* 1997; **17**: 305–308.
15. Purandare SM, et al. A complex syndrome of left-right axis, central nervous system and axial skeleton defects in Zic3 mutant mice. *Development* 2002; **129**: 2293-2302.
16. Schott JJ et al. Congenital heart disease caused by mutations in the transcription factor NKX2-5. *Science* 1998; **281**: 108–111.
17. Garg V, et al. GATA4 mutations cause human congenital heart defects and reveal an interaction with TBX5. *Nature* 2003; **424**: 443–447.
18. Bamford RN, et al. Loss-of-function mutations in the EGF-CFC gene CFC1 are associated with human left-right laterality defects. *Nat Genet* 2000; **26**: 365–369.
19. Kosaki K, et al. Characterization and mutation analysis of human LEFTY A and LEFTY B, homologues of murine genes implicated in left–right axis development. *Am J Hum Genet* 1999; **64**: 712–721.

20. Kosaki R, et al. Left–right axis malformations associated with mutations in ACVR2B, the gene for human activin receptor type IIB. *Am J Med Genet* 1999; **82**: 70–76.
21. Kaufman MH. The Atlas of Mouse Development. Academic Press, London: 1994.
22. Weninger WJ, Mohun T. Phenotyping transgenic embryos: a rapid 3-D screening method based on episcopic fluorescence image capturing. *Nat Genet* 2002; **30**: 59–65.
23. Sharpe J, et al. Optical projection tomography as a tool for 3D microscopy and gene expression studies. *Science* 2002; **296**: 541–554.
24. Smith BR, Johnson GA, Groman EV, Linney E. Magnetic resonance microscopy of mouse embryos. *Proc Natl Acad Sci U S A* 1994; **91**: 3530–3353.
25. Smith BR, Linney E, Huff DS, Johnson GA. Magnetic resonance microscopy of embryos. Comput Med Imaging Graph 1996; **20**: 483–490.
26. Smith BR. Magnetic resonance microscopy in cardiac development. *Microsc Res Tech* 2001; **52**: 323–330.
27. Smith BR. Magnetic resonance imaging analysis of embryos. In Tuan R, Lo CW, eds. Developmental Biology Protocols, Vol. 1. Totawa, NJ: Humana Press Inc., 2000): 211–216.
28. Smith BR, Huff DS, Johnson GA. Magnetic resonance imaging of embryos: an Internet resource for the study of embryonic development. Comput Med Imaging Graph 1999; **23**: 33–40.
29. Dhenain M, Ruffins SW, Jacobs RE. Three-dimensional digital mouse atlas using high-resolution MRI. *Dev Biol* 2001; **232**: 458–470.
30. Schneider JE, et al. High-resolution, high-throughput magnetic resonance imaging of mouse embryonic anatomy using a fast gradient-echo sequence. *Magma* 2003; **16**: 43–51.
31. Schneider JE, et al. High-resolution imaging of normal anatomy, and neural and adrenal malformations in mouse embryos using magnetic resonance microscopy. *J Anat* 2003; **202**: 239–247.
32. Schneider JE, et al. Rapid identification and 3D reconstruction of complex cardiac malformations in transgenic mouse embryos using fast gradient echo sequence magnetic resonance imaging. *J Mol Cell Cardiol* 2003; **35**: 217–222.
33. Schneider JE, et al. Identification of cardiac malformations in mice lacking Ptdsr using a novel high-throughput magnetic resonance imaging technique. *BMC Dev Biol* 2004; **4**: 16.
34. Gonzalez RC, Wintz P. Digital Image Processing. Reading, MA Addison-Wesley Publishing Company, 1983.
35. Bamforth SD, et al. Cardiac malformations, adrenal agenesis, neural crest defects and exencephaly in mice lacking Cited2, a new Tfap2 co-activator. *Nat Genet* 2001; **29**: 469–474.
36. Liu C, et al. Pitx2c patterns anterior myocardium and aortic arch vessels and is required for local cell movement into atrioventricular cushions. *Development* 2002; **129**: 5081–5091.
37. Geng Y, et al. Cyclin E ablation in the mouse. *Cell* 2003; **114**: 431–443.
38. Bamforth SD, et al. Cited2 controls left-right patterning and heart development through a Nodal-Pitx2c pathway. *Nat Genet* 2004; **36**: 1189–1196.
39. Cai CL, et al. Isl1 identifies a cardiac progenitor population that proliferates prior to differentiation and contributes a majority of cells to the heart. *Dev Cell* 2003; **5**: 877–889.
40. Conway SJ, Henderson DJ, Kirby ML, Anderson RH, Copp AJ. Development of a lethal congenital heart defect in the splotch (Pax3) mutant mouse. *Cardiovasc Res* 1997; **36**: 163–173.

41. Barbera JP, et al. Folic acid prevents exencephaly in Cited2 deficient mice. *Hum Mol Genet* 2002; **11**: 283–293.
42. Yin Z, et al. The essential role of Cited2, a negative regulator for HIF-1{alpha}, in heart development and neurulation. *Proc Natl Acad Sci U S A* 2002; **99**: 10488–10493.
43. Herron BJ, et al. Efficient generation and mapping of recessive developmental mutations using ENU mutagenesis. *Nat Genet* 2002; **30**: 185–189.
44. Burn J, Goodship J. Congenital heart disease. In Rimoin DL, Connor JM, Pyeritz RE, Korf BR, eds. Principles and Practice of Medical Genetics. London: Churchill Livingstone, 2002.
45. Johnson PD, Dawson BV, Goldberg SJ. Cardiac teratogenicity of trichloroethylene metabolites. *J Am Coll Cardiol* 1998; **32**: 540–554.
46. Dawson BV, Johnson PD, Goldberg SJ, Ulreich JB. Cardiac teratogenesis of halogenated hydrocarbon-contaminated drinking water. *J Am Coll Cardiol* 1993; **21**: 1466–1472.
47. Kuehl KS, Loffredo C. Risk factors for heart disease associated with abnormal sidedness. *Teratology* 2002; **66**: 242–248.
48. Zhou YQ, et al. Applications for multifrequency ultrasound biomicroscopy in mice from implantation to adulthood. *Physiol Genomics* 2002; **10**: 113–126.
49. Foster FS, et al. A new ultrasound instrument for in vivo microimaging of mice. *Ultrasound Med Biol* 2002; **28**: 1165–1172.
50. Schneider JE, Bhattacharya S. Making the mouse embryo transparent: identifying developmental malformations using magnetic resonance imaging. *Birth Defects Res Part C Embryo Today* 2004; **72**: 241–249.

15

Allograft arteriopathy: heterotopic heart transplantation and aortic interposition grafts

Koichi Shimizu and **Richard N. Mitchell**

Harvard Medical School, Brigham and Women's Hospital, Boston, MA, USA

Introduction

In the current era of immunosuppression, graft failure due to acute rejection occurs relatively infrequently, and one-year graft survival for most solid organs exceeds 90%. However, long-term allograft survival has not markedly improved in the last 10 to 20 years, with graft half-lives (the timepoint at which 50 per cent of grafts fail) still largely fixed at 7–9 years for kidney transplantation,[1] and with comparable half-life statistics for other solid organs. The major failure mode for solid organs is allograft arteriopathy (AA); with continual improvements in reducing opportunistic infections and neoplasia related to immunosuppression, AA has become the most important limitation to successful long-term transplantation.

In AA, allograft arteries develop severe, diffuse intimal hyperplastic lesions leading eventually to lumenal stenoses and to ischemic graft failure. These intimal lesions are called a variety of different things in the literature: chronic rejection, transplant associated arteriosclerosis, transplant vasculopathy, graft vascular sclerosis, graft arterial disease, or allograft arteriopathy. They result from an initial alloimmune response directed against vascular wall cells, although the subsequent pathogenic pathways remain incompletely described.[2,3] Of note, although it occurs in all vascularised grafts, AA is most prominent in cardiac transplants;[4–6] clinically, patients develop congestive heart failure due to progressive loss of functioning

A Handbook of Mouse Models of Cardiovascular Disease Edited by Qinbo Xu

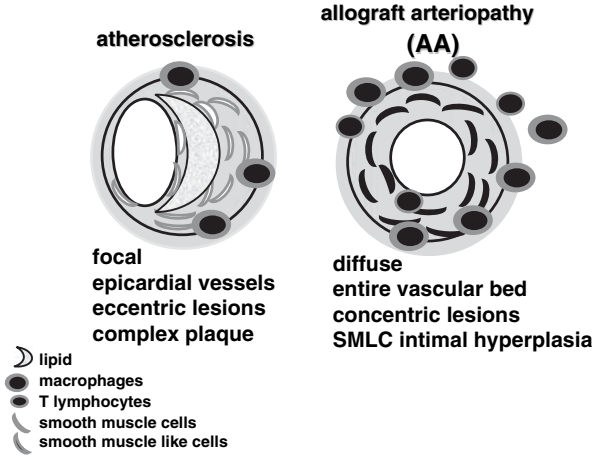

Figure 15.1 Schematic comparing typical atherosclerosis and allograft arteriopathy (modified from Shah and Mitchell, 2005[58]). Note that the cells that comprise the intimal hyperplastic lesions in allograft arteriopathy (AA) are identified as smooth muscle-*like* cells. This highlights the fact that although they express many established smooth muscle cell markers, they have a different synthetic, proliferative, and contractile phenotype than typical medial smooth muscle cells.[49] AA lesions have variable amounts of extracellular matrix and cells, although lipid deposition is not typical unless there is pre-existing atherosclerosis in the coronaries of a transplanted heart; the cellularity is composed of smooth muscle cells, fibroblasts, macrophages, and T lymphocytes (used with permission from Elsevier)

myocardium, or may have a sudden cardiac death due to a lethal arrhythmia or large infarct.[7] AA differs from conventional atherosclerosis in that it forms concentric, lipid-poor, and longitudinally diffuse lesions, usually extending from epicardial vessels into intramyocardial arterioles (Figure 15.1). It is also worth emphasizing that AA is quite likely a stereotypical response to vascular injury; in the case of AA, the inciting vascular injury is immunologic rejection. Thus, despite some differences in appearance, AA almost certainly shares a number of fundamental pathogenic similarities with intimal lesions formed in the setting of the inflammation that contributes to atherosclerosis and restenosis injury.

Since AA typically affects such an extensive length of the coronary anatomy, affected hearts are not usually amenable to conventional bypass surgery or angioplasty. The only therapeutic recourse for most patients is re-transplant. Distressingly, AA lesions occur even in the setting of immunosuppression regimens adequate to block most acute parenchymal rejection, and do not strictly correlate with episodes or severity of allograft rejection.[8] To date, there has been only partial success in attenuating AA by pharmacologic means; HMG-CoA reductase inhibitors,[9,10] antioxidant therapies,[11] and alternate immunosuppressive regimens – especially those involving rapamycin (Sirolimus)[12,13] – are promising but imperfect.

Clearly, a better understanding of the pathogenic mechanisms underlying AA is necessary. Unresolved issues concern the roles of antibodies versus cells in the pathogenesis, the contribution of alloantigen non-specific mediators such as

macrophages and/or cytokine networks, the effects of ischemia and thrombosis, and the pathways by which the intimal smooth muscle cells are recruited. AA is also a process that cannot be readily modeled *ex vivo*. Multiple cell types participate in the initial immune response or subsequent AA development (vascular wall cells, innate and adaptive immune cells, smooth muscle cell precursors); indeed it is becoming apparent that the smooth muscle cells that populate the intimal lesions do not derive from the original donor media but instead are recruited from circulating precursors (see below).[14,15] Moreover, the interactions of multiple mediators both circulating (complement, antibodies) and locally produced (cytokines, and chemokines) argue for the use of *in vivo* models to accurately recapitulate the disease process.

Murine models for AA

Two major and complementary murine models for AA have been developed, each with certain advantages and drawbacks. These are abdominal heterotopic cardiac transplantation[16,17] and aortic interposition grafts.[14,18] One of the most important distinctions between the two models is that aortic interposition transplantation does not require any immunosuppression for long-term maintenance of allografts; consequently, there is severe medial smooth muscle cell rejection and apoptosis that is not usually seen in cardiac allografts (see below).[14,18–20] Although the increased immune-mediated injury in the aortic allografts conceivably influences the intimal cell populations, cardiac and aortic transplant models yield similar results, and may be used to focus on different aspects of AA without substantive concern for discrepant outcomes.

Although technically challenging and requiring the development of surgical expertise, mouse transplant models have a number of theoretical and practical benefits both for understanding the mechanisms of AA, as well as for developing therapeutic interventions. The histology and composition of the vascular lesions in both models accurately recapitulate those seen in humans (Figure 15.2).[14,17,19] Moreover, the murine models reproducibly develop AA lesions within 8–12 weeks of transplantation (as against months to years in humans), making them practical and affordable to use in the laboratory setting. Since the transplanted tissues can be removed at any intermediary timepoint after surgery, potentially relevant mediators can be assessed at each step along the way, rather than having to infer from an endpoint what may have driven the process.

In addition, one of the major benefits of mouse models (as against relying on human transplant databases) is the availability of large numbers of inbred mouse strains with defined major histocompatibility complex (MHC) and non-MHC differences. We have focused on a rather restricted number of mouse strains (Table 15.1), in part due to the well-defined MHC I, MHC II, total MHC, and non-MHC mismatches in this collection of animals. In addition, the majority of congenitally deficient ('knockout') and transgenic mice (see below) are initially derived in the 129 strain, with subsequent back-breeding onto the C57BL/6 background; by having

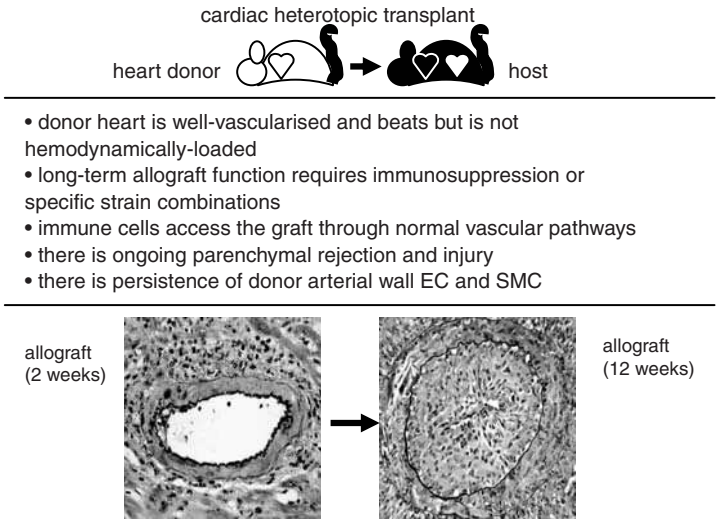

Figure 15.2 Heterotopic cardiac transplant (modified from Shah and Mitchell, 2005[58]). To permit the long-term engraftment necessary for the grafts to develop AA (8–12 weeks), immunosuppression or specific strain combinations must be used; otherwise the grafts fail earlier due to severe acute parenchymal rejection. In these combinations, there is ongoing rejection and low-grade injury, but donor endothelial and smooth muscle cells persist.[31] Due to the primary vascularisation, immune cells enter the graft via normal post-capillary venule pathways. Histology (elastic van Gieson) shows a representative example of a coronary artery in this preparation at two weeks (left panel) and at twelve weeks (right panel); the intimal hyperplasia nearly completely occludes the lumen (courtesy of Dr. Jun-ichi Suzuki) (used with permission from Elsevier). For a color version of this figure, please see the images supplied on the accompanying CD

extensive experience with 129 and C57BL/6 donors and recipients, we can take immediate advantage of newly generated mouse knockouts.

The broad availability of several congenic and transgenic strains that express distinct markers (e.g., Thy-1 isoforms, green fluorescent protein, or β-galactosidase) also permits unambiguous identification of host *vs* donor cell origin; this is particularly helpful with experiments involving the adoptive transfer of bone marrow or other cell populations. Besides the different mouse strains, there are well-characterised and commercially available murine reagents including purified cytokines and monoclonal antibodies directed against virtually every relevant mediator; the latter may be used both for blocking experiments as well as *ex vivo* analysis. Although drugs may have different effects in mice versus humans (see below), the animal models nevertheless permit a reasonably inexpensive and rapid assessment of therapeutic efficacy. Finally, and perhaps most appealingly, the murine research community has generated an extraordinary menagerie of congenitally deficient ('knockout') or transgenic mice expressing unique repertoires of cytokines, chemokines, receptor molecules, and even entire cell populations. Thus, animals lacking interferon-γ[19,21] or the interferon-γ receptor[22] have been used to evaluate the role of this cytokine in both acute rejection and AA. Allografts have also been transplanted into immunodeficient mice lacking T and B lymphocytes (e.g., severe combined

Table 15.I Mouse strain combinations and immunosuppression regimens

Mismatch	Graft survival without immunosuppression	Immunosuppression required for long-term graft survival
Isograft (no mismatch) e.g. C57BL/6 ($H2^b$)→C57BL/6 ($H2^b$)	>12 weeks	None
MHC I mismatch e.g. bm1 ($H2^{bm1}$)→C57BL/6 ($H2^b$)	>12 weeks	None
MHC II mismatch e.g. bm12 ($H2^{bm12}$)→C57BL/6 ($H2^b$)	8–12 weeks	None or anti-CD4/anti-CD8 pre-transplant only, or 15 mg/kg QD ciclosporin A, or 1 mg/kg QOD rapamycin
Non-MHC mismatch e.g. 129 ($H2^b$)→C57BL/6 ($H2^b$)	8–12 weeks	None or Anti-CD4/anti-CD8 pre-transplant only, or 15 mg/kg QD ciclosporin A, or 1 mg/kg QOD rapamycin
Total mismatch (non-MHC, MHC I, MHC II) e.g. BALB/c ($H2^d$)→C57BL/6 ($H2^b$)	7–10 days	Anti-CD4/anti-CD8 pre- and/or post-transplant, *or* 1 mg/kg QOD rapamycin

Other strain combinations have been used, particularly across complete MHC mismatches. Long-term immunosuppression in total allomismatches has been achieved using various regimens of CD4 and CD8 monoclonal antibodies, anti-adhesion molecule antibodies, or by anti-CD40 ligand antibodies. We have focused on the combinations outlined above in part due to the defined MHC I, MHC II, or non-MHC mismatches. In addition, the majority of knockout mice are initially generated in 129 embryonic stem cell lines and thus in 129 mice ($H2^b$), with most being backbred onto the C57BL/6 ($H2^b$) background. Consequently, transplant combinations with C57BL/6 mice are most amenable to rapid translation into engineered strains.

immunodeficient (SCID) or recombinase-deficient mice). In these animals, grafts survive indefinitely without developing pathology. However, the host animals may then be manipulated by the adoptive transfer of defined cytokine,[23] antibody,[24,25] or purified cell preparations[26] to test their capacity for inducing AA.

Murine heterotopic cardiac transplantation

Murine heterotopic cardiac transplantation is a technique developed in the early 1970s;[16] since then it has been widely used by multiple groups to examine diverse aspects of AA. Not only do the vascular AA lesions recapitulate the human disease (Figure 15.2), the histology and composition of the myocardial parenchymal rejection is also similar to that seen in clinical transplantation.[17,19]

Technical aspects

The procedure was originally described by Corry *et al.*,[16] and is schematically drawn in Figure 15.3. It is also demonstrated on the video clip accompanying this chapter.

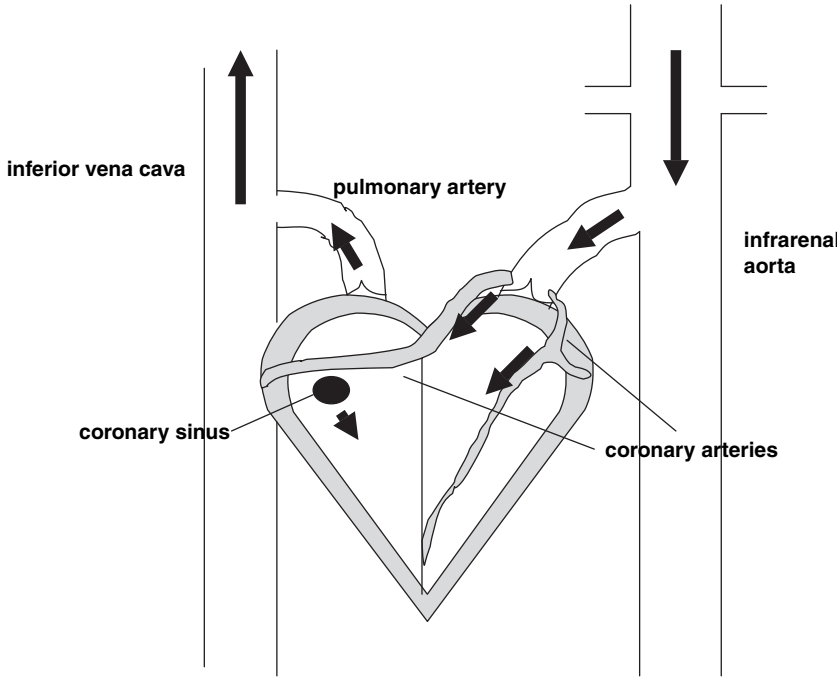

Figure 15.3 Heterotopic cardiac transplant. Schematic illustrating how donor hearts are anastomosed aorta to host infra-renal aorta, and pulmonary artery to host inferior vena cava.[16] The grafts are primarily vascularised and beat, but are not hemodynamically loaded; the host does not rely on the transplant to survive. The donor heart pulmonary veins and superior and inferior vena cava are ligated. Blood flows into the donor aorta and out the coronary arteries to perfuse the heart. Cardiac venous blood returns via the coronary sinus to the right side of the heart and is then ejected out the pulmonary artery into the host inferior vena cava. When the aortic valve becomes incompetent, blood enters the left ventricle and eventually becomes an organised thrombus. For a color version of this figure, please see the images supplied on the accompanying CD

Donor and recipient mice are usually 8–12-week-old male mice (25–30 g); younger mice are too difficult to perform surgery on due to their smaller size and tissue fragility, while older animals tend to accrue too much adipose tissue, making dissection difficult. Male mice are routinely used as both recipients and donors to avoid potential confounding H-Y antigen mismatches. We find that certain mouse strains (e.g. C57BL/6) tolerate the procedure extremely well as graft recipients, while others (e.g. BALB/c) are not as robust. Nevertheless, with practice, we have been able to use a wide variety of strains.

Mice may be anesthetised by methoxyfluorane, or isofluorane inhalation. Methoxyfluorane (Metofan; Pittman-Moore, Mundelein, IL, USA) is preferable due to its slower and more easily regulated anesthesia; we have also found lesser strain variation in dosing. Donor hearts are perfused with chilled, heparinised 0.9 per cent saline or heparinised Stanford solution[27] via the inferior vena cava, and are harvested after ligation of the vena cavae and pulmonary veins with 5-0 silk. The aorta and pulmonary artery of the donor heart are anastomosed to the infrarenal

abdominal aorta and the inferior vena cava of the recipient mouse, respectively using microsurgical techniques and 10-0 Ethilon (Ethicon, Somerville, NJ, USA). Typically, the aortic anastomosis is performed first using two separate running sutures each of four to six throws. The pulmonic anastomosis is performed second with one continuous suture and eight to ten throws. Surgical loupes do not provide adequate magnification, and we find that a dissecting microscope with 2.5–4 × magnification is required.

Ischemic time during the procedure is routinely 30 mins, with greater than 90 per cent initial graft and recipient survival; grafts resume spontaneous beating prior to closure. The accompanying video clip shows the gross appearance of the heterotopic transplant in the abdomen. Grafts that do not resume spontaneous beating are deemed surgical failures, and are not used for analysis.

Even untrained personnel can typically achieve viable grafts by the fifth to tenth attempt, and develop routine success by the 25–30th transplant. Surgically adept individuals can master the technique much sooner. New trainees are encouraged to practice initially only with isografts; their surgical abilities are evaluated by histologically assessing the extent of ischemic injury one week post-transplant. When only mild ischemic injury (less than 10 per cent cross-sectional area) is routinely obtained, more challenging strains and allograft combinations are undertaken.

Because the aortic valve is initially competent, there is no retrograde flow into the left ventricular lumen; rather, blood flows into the coronary arteries at aortic pressures, perfusing the myocardium. Venous blood flow returns to the right atrium via the coronary sinus. Flow patterns (if not blood volumes) are thus normal through the tricuspid and pulmonic valves, with blood exiting into the inferior vena cava anastomosis. To date, no successful orthotopic (i.e. donor heart replacing the recipient heart) murine cardiac transplantation has been reported. The fact that the grafts in this model are heterotopic and are therefore not necessary for host survival also permits the development of severe graft rejection that could not be sustained if the recipient depended on graft function.

Allograft function is assessed by daily palpation of the heterotopic graft. Typically, grafts beat less vigorously and at a slower rate as rejection proceeds, until all activity ceases. Palpation for heartbeat requires practice, and observer skill influences whether weak heartbeats are appreciated; loss of heartbeat is defined as the date of rejection. It is particularly difficult to distinguish heartbeats from respirations; transient gentle squeezing will suppress breathing for the period of time necessary to palpate heartbeat. Although cardiac ultrasound can be used, animals must be anesthetised to get accurate readings, and the technique requires equipment not typically available to most laboratories. Since echocardiography roughly correlates with manual palpation (M. Russell, personal communication), we use palpable heartbeat as our only clinical criterion for graft function. Nevertheless, it must be emphasised that graft function should *always* be correlated with graft histology (see below). Survival data based exclusively on palpable beat is highly subjective, and is not by itself a reliable end-point. Moreover, the histology frequently suggests the pathways by which the graft failure occurred (e.g. parenchymal rejection versus vasculitis with thrombosis).

Allograft evaluation

Grafts can be explanted at the time of beat cessation, or, to evaluate any intermediary pathology, at any other timepoint. It is critical that grafts without heartbeat be expeditiously recovered; even a 24-h delay in removing failed allografts will result in necrosis that makes the specimen useless for analysis. Parenchymal rejection begins 3–4 days after transplant in total mismatched combinations and will cause graft failure by 7–10 days.[20] (Table 15.1; well-developed AA lesions are present only after 8–12 weeks[17,19]).

We routinely evaluate grafts by a variety of modalities. Explanted allografts are sectioned transversely into thirds; the most basal third, with larger diameter coronary vessels, is fixed in phosphate-buffered 10 per cent formalin, embedded in paraffin, and serial 5–6 μm sections are stained by routine histologic techniques. Hematoxylin and eosin are used for grading rejection, and van Gieson elastic fiber stain is used to identify the internal elastic lamina of arteries for assessing the extent of AA.

Parenchymal rejection is graded using a scale modified from the International Society for Heart and Lung Transplantation: 0, no rejection; 1, focal mononuclear cell infiltrates without necrosis; 2, focal mononuclear cell infiltrates with necrosis; 3, multifocal infiltrates with necrosis; 4, widespread infiltrate with hemorrhage and/or vasculitis.[19,28] The AA score is calculated from the number and severity of involved vessels: 0, vascular occlusion <10 per cent; 1, 10–25 per cent occlusion; 2, 25–50 per cent occlusion; 3, 50–75 per cent occlusion; 4, <75 per cent occlusion. Typically, 10 or more vessels are scored for each heart, and the degree of vascular occlusion for each is averaged. Scores for each specimen uniformly fall within a range of one grade for two to three blinded observers, and are averaged.[19] As noted above, mature AA lesions are typically present by 8-12 weeks post-transplant; at earlier time points (e.g. 2–4 weeks), vessels primarily exhibit a dense perivascular mononuclear inflammatory cell infiltrate. It is worth emphasising that these early lesions are *not* the intimal hyperplastic lesions of AA containing smooth muscle cells and increased extracellular matrix. While probably representing AA precursor lesions, they should not be scored as AA.[19]

An important caveat for the histologic evaluation is the recognition of injury attributable to perioperative ischemia. Such damage is usually distinguishable from rejection due to the presence of increased acute inflammatory cells as well as interstitial edema; rejection (other than fulminant) is more associated with mononuclear cell inflammatory infiltrates without significant interstitial edema (although perivascular edema may be present. In cases where greater than 50 per cent of the graft cross-section exhibits principally ischemic injury, interpretation of either acute rejection or AA findings is problematic. In particular, ischemic injury alone can lead to the development of AA-like lesions, even in isografts.[29,30] In addition, in long-term grafts, mesenteric adipose tissue, loops of bowel, and/or pancreas will frequently be attached to the epicardial surface by post-surgical adhesions; we have found no evidence that these influence parenchymal rejection or AA.

The middle third of each heart is frozen in OCT compound (Ames Co., Division of Miles Laboratories, Elkhart, IN, USA) and stored at –80°C for immunohistochem-

istry. Staining can be performed for a variety of markers, including adhesion molecules (e.g. vascular cell adhesion molecule-1 (VCAM-1), intercellular adhesion molecule-1 (ICAM-1)), costimulatory molecules (e.g. CD40, B7), inflammatory cell subsets (e.g. CD4 or CD8 T cells, B cells, and macrophages), cytokines, and MHC molecules.[17,19,20,24,31]

The most apical third is either collagenase digested to recover infiltrating inflammatory cells for flow cytometric analysis,[32] or solubilised in TRIzol (Gibco BRL/Life Technologies, Grand Island, NY, USA) per the manufacturer's recommendations for extracting RNA for polymerase chain reaction or RNase protection assay analysis of cytokine message production.[32]

Immunosuppression

Isografts typically function for long periods of time without immunosuppression. Likewise, non-MHC-mismatched grafts (e.g. 129 grafts into C57BL/6 recipients), MHC I-disparate grafts (e.g. bm1 into C57BL/6 hosts) and MHC II-mismatched grafts (e.g. bm12 into C57BL/6 hosts) usually function for at least 8–12 weeks without treatment. For most routine experiments we use the MHC class II mismatch, as it does not require daily immunosuppression or other manipulations (see below). In comparison, total allogeneic mismatched grafts (e.g. BALB/c hearts into C57BL/6 hosts, with MHC I, MHC II, and non-MHC antigen differences) cease functioning within 7–10 days of transplantation[20] (Table 15.1). Consequently, to yield long-term functioning grafts across such total mismatched combinations (i.e. long enough to develop AA lesions at 8–12 weeks), some form of immunosuppression is usually required.

For such strain combinations, we have extended the antibody depletion protocol originally developed by Russell *et al.*[17] involving intraperitoneal administration of anti-CD4 (derived from rat hybridoma GK1.5) and anti-CD8 (derived from rat hybridoma 2.43). After a single injection of these monoclonal antibodies, peripheral $CD4^+$ and $CD8^+$ T-cell depletion is 98 per cent at 1 week and approximately 88 per cent at 2 weeks. After three injections (days 6, 3 and 1 pretransplant), peripheral blood T-cell depletion is >98 per cent at 2 weeks, and approximately 87 per cent at 4 weeks [20]. The antibody approach also allows selective depletion of $CD4^+$ helper or $CD8^+$ cytolytic T cells.

With the three-dose pretransplant immunosuppression protocol, total allomismatched grafts typically fail by 4–5 weeks, coincident with the recovery of peripheral $CD4^+$ and $CD8^+$ T cells. Additional weekly antibody administration post-transplant (in addition to the three doses pretransplant) yields long-term allograft survival, but no parenchymal rejection or AA.[20] Thus, to achieve a satisfactory model for AA in total allomismatched combinations, grafts are transplanted without prior immunosuppression and are allowed to reject for four days. At that point, weekly anti-CD4 and anti-CD8 antibody administration is begun, completely abolishing any further T-cell-mediated responses. In addition to reliably inducing AA in total allomismatched strain combinations, this protocol also highlights the observation that a single episode

of rejection is sufficient to recruit and activate secondary effectors that can eventually result in AA.[20]

We have also developed alternate, more 'human-like' immunosuppression protocols (Hasegawa *et al.*, unpublished data) as models for evaluating the mechanisms of AA. Ciclosporin A alone, even at 30 mg/kg per day, does not permit long-term survival of total allomismatched hearts (grafts cease beating at 3–4 weeks).[33,34] However, rapamycin alone (1 mg/kg every other day) yields long-term survival of total allomismatched grafts, and allows AA formation. Interestingly, combination therapy with ciclosporin A (15 mg/kg per day) and rapamycin (1 mg/kg every other day) prevented both parenchymal rejection and AA in total allomismatched strain combinations (Hasegawa *et al.*, unpublished data).

Advantages of heterotopic cardiac transplantation relative to other murine AA models

Although technically more demanding, the vascularised heterotopic model is preferable to non-vascularised grafts implanted on the neck or ear pinna.[35] In the neck or ear pinna model, allografts are not primarily anastomosed to arteries and veins but instead become secondarily vascularised as host vessels grow in after days to weeks; at that time, the grafts typically resume normal beating. However, in the neck or ear pinna model, allografts invariably exhibit extensive ischemic injury; this early ischemia significantly confounds the analysis of events driven by antigen-specific alloreactivity. Moreover, graft survival and/or subsequent immune responsiveness is largely a function of neovascularisation and not necessarily representative of processes that occur in human solid organ transplants.

The heterotopic cardiac transplant model also has an advantage over carotid or aortic interposition vascular grafts[36,37] in that the role of parenchymal rejection pathways in AA development can be assessed (Figure 15.2). Indeed, we have demonstrated that parenchymal rejection precedes AA; inflammatory cells initially localize to the myocardium, presumably as effector cells egress into the allograft using adhesion molecules and chemokines expressed in the post-capillary venules. Inflammatory cells subsequently coalesce around arterial walls (again presumably driven by specific adhesion molecule and chemokine stimuli) and attack vascular wall cells from the ablumenal aspect.[19] With interposition grafts, there is no intact post-capillary circulation and inflammatory cells putatively attach and initiate injury directly beginning at the lumenal aspect of the vessel wall or by migrating in from the adventitial surface.

Disadvantages of the heterotopic transplant model

The allograft must function and have an intact vasculature for at least 8 weeks after transplantation. Shorter duration survival renders the graft unusable for AA analysis, although it may be appropriate for examining mechanisms related to acute parenchymal

rejection. Another hypothetical drawback to the model is the absence of left ventricular hemodynamic loading (Figures 15.2 and 15.3). While the effects of myocardial pressure and volume loading on allograft rejection have not been formally investigated, the reduction of left ventricular work could conceivably affect the metabolic demands placed on the myocardium and result in less ischemic injury despite advancing AA. An additional artifact of the heart allograft model is the formation of a thrombus in the left ventricle occurring as the graft aortic root dilates and the aortic valve becomes incompetent. This is an important consideration primarily in graft analysis; inflammation associated with the organising thrombus should not be interpreted as rejection.

Murine aortic interposition grafts

Aortic interposition grafting is a technique originally developed in rats,[18] and only recently adapted to the mouse;[14] carotid interposition grafts have also been done in the mouse,[36,38] and human internal mammary artery grafts have been implanted in the infrarenal aorta in SCID mice to examine pathways potentially unique to human tissues.[23] As with heart allograft AA, aortic AA lesions recapitulate human disease (Figure 15.4).[14]

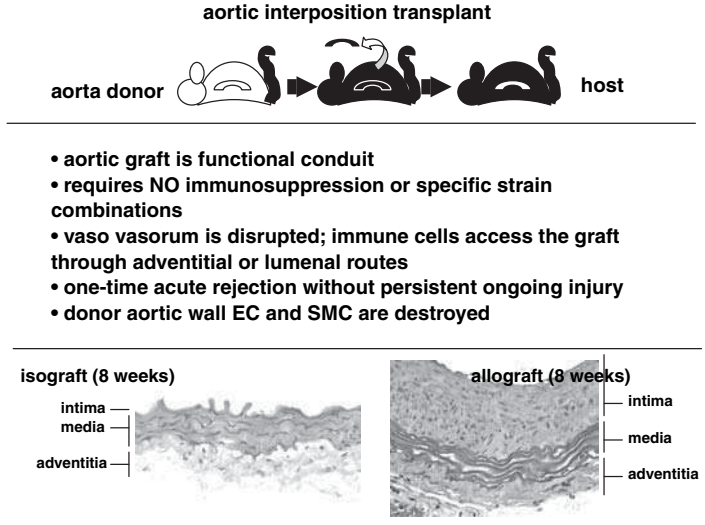

Figure 15.4 Aortic interposition transplant (modified from Shah and Mitchell, 2005[58]). There is an early (1–2 weeks) acute rejection that leads to loss of donor endothelial and smooth muscle cells, but host inflammatory cells do not persist in the grafts at the time of AA development (8–12 weeks).[14] Immune cells access the graft either by infiltration from the adventitial side of the graft or by adhesion to the lumenal face. Histology (H&E) demonstrates that long-term isografts (left panel) are viable and do not develop AA lesions; allogeneic grafts (at eight weeks) show virtually complete medial smooth muscle cell loss with intimal hyperplastic lesions composed primarily of SMLC and extracellular matrix[14] (used with permission from Elsevier). For a color version of this figure, please see the images supplied on the accompanying CD

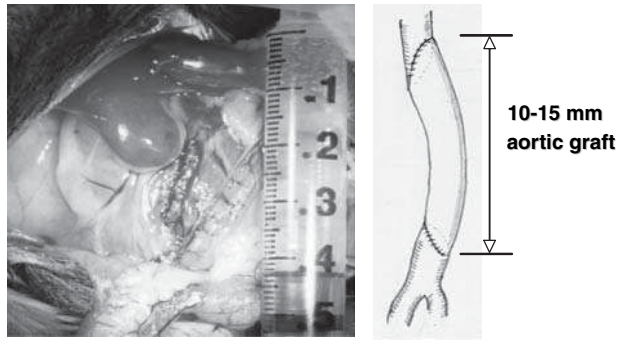

Figure 15.5 Aortic interposition transplant. Host infrarenal aortic segments are excised and replaced with donor aortic segments from the descending thoracic aorta.[14] The grafts are functional, but do not require immunosuppression or specific strain combinations to maintain long-term patency. For a color version of this figure, please see the images supplied on the accompanying CD

Technical aspects

The procedure is pictorially and schematically represented in Figure 15.5, and the accompanying video clip to this chapter shows the steps in the procedure and the gross appearance of the aortic transplant in the abdomen. Donor and recipient mice are usually 8–12-week-old males (25–30 g); again, male mice are routinely used as both recipients and donors to avoid potential confounding H-Y antigen mismatches.

Mice are anesthetised as for heart transplantation. A 10–15 mm segment of donor descending thoracic aorta is used to replace an excised segment of host infrarenal aorta. The graft is sutured in place end-to-end using 11-0 monofilament nylon sutures (Ethicon) with magnification provided by an operative microscope. The complete grafting procedure requires 50–70 min to perform. Graft patency is evaluated at surgery as described by Acland,[39] including grossly observable pulsatility, and graft engorgement. Graft patency is also inferred postoperatively in that thrombosis frequently results in loss of lower limb mobility. Finally, graft patency is assessed by direct inspection at the time of removal for histologic evaluation. Grafts that occlude within the first 10 days are considered technical failures and are excluded from analysis. This procedure is more technically demanding than the heart transplant procedure. With expertise accrued over 100 transplants, the long-term success rate of aortic interposition grafts is more than 90 per cent.

Allograft evaluation

Allograft function is followed by gross observation of the host animal; absence of lower limb paralysis is strongly indicative of graft patency. Although ultrasonography has been used to examine aortic patency and dimensions (especially in models of

aneurysmal disease[40]), animals must be anesthetised to get accurate readings, and the technique requires equipment not available to most laboratories.

Isografts function indefinitely and show no intimal hyperplasia; despite the absence of an intact vaso vasorum, these aortic segments show no evidence of ischemic injury and presumably function by diffusion of oxygen and nutrients directly from the vessel lumen.

Patency is the principal criterion for successful transplantation in this model. However, as opposed to the cardiac transplant model, immunosuppression is not required to maintain such long-term aortic graft function. Consequently, in the absence of immunosuppression, aortic allografts undergo a severe profound rejection with $CD4^+$, $CD8^+$ and macrophage-rich infiltrates that peak in the first 1–2 weeks.[14] During this time, virtually all of the donor endothelial cells and medial smooth muscle cells are killed, leaving behind only extracellular matrix. Nevertheless, in standard strain combinations where the dominant response results in Th1 cytokine elaboration (e.g. interferon-γ), the residual matrix is sufficient to preserve normal aortic hemodynamic parameters and aneurysms do not develop.[40] Following the early severe rejection, the vast majority of the host inflammatory cells either undergoes apoptosis or migrates away, and in long-term grafts, host inflammatory cells are rare.

We routinely evaluate grafts by a variety of modalities. Thus, freshly explanted allografts are sectioned transversely unless it is desirable to examine the anastomoses; in that case, longitudinal sections are taken. Hematoxylin and eosin are routinely used, as is elastic van Gieson staining to identify elastic lamellae. AA is quantified by the surface area occupied by intimal lesions on aortic cross-sections; the internal elastic lamina demarcates the intimal and medial boundary. Additional sections can be frozen in OCT compound (Ames Co.) and stored at –80°C for immunohistochemistry. Staining can be performed for a variety of markers including cell type, adhesion molecules, cytokines, metalloproteinases, and histocompatibility molecules.[14,40] In addition, segments can be solubilised in TRIzol (Gibco BRL/Life Technologies) or other media to extract RNA, infiltrating cells, or proteins to assess e.g. enzymatic activity.[40] As opposed to the heart transplant model where the bulk of cells (protein and mRNA) at any time derive from myocardium, late aortic grafts are largely composed of the smooth muscle-like cells that comprise the intimal AA lesions. Transplanted aortic segments typically yield only 1–5 μg of mRNA, whereas apical myocardium specimens yield at least 30-fold greater quantities.

Immunosuppression

As opposed to the cardiac transplant model, no immunosuppression is required for aortic grafts to maintain normal function (i.e. patency) for the 8–12 weeks required to generate AA lesions. As a consequence, the aortic grafts undergo a more profound acute rejection and the vast majority of donor cells are killed. Nevertheless, even in the absence of ongoing immune responsiveness to the graft, these vessels develop robust AA lesions.

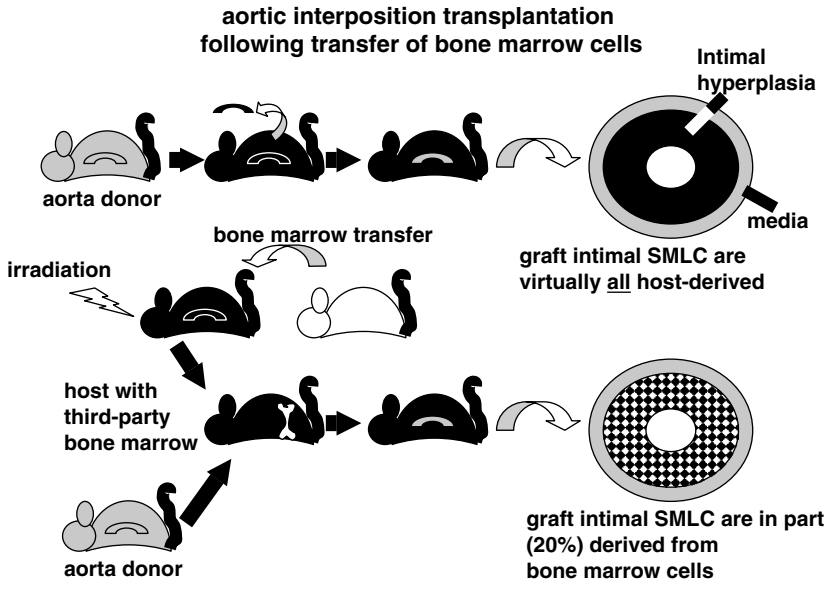

Figure 15.6 Experimental schematic to identify the source of intimal SMLC in AA (modified from Shah and Mitchell, 2005[58]). Various markers such as histocompatibility molecules, transgenes expressed in host cells only (e.g. β-galactosidase or green fluorescent protein), or Y chromosome (e.g. female graft in male host) can be used to identify whether intimal SMLC are host- or donor-derived. In the top part of the figure, a 'gray' aorta is transplanted into a 'black' mouse; the resulting AA SMLC are virtually all 'black' indicating their origin from the host.[14] In the lower part of the figure, the host mouse is lethally irradiated and has its bone marrow reconstituted with third-party 'white' cells. When a subsequent 'gray' aortic graft is transplanted, the resulting AA lesion is composed of up to 20 per cent 'white' SMLC demonstrating that at least some of the cells originate from bone marrow precursors.[14] Similar results are obtained using either the aortic or heart transplant models[14](used with permission from Elsevier)

Advantages of aortic interposition grafts relative to other murine transplant arteriopathy models

Bigger surface area and intimal thickness means that one can more easily identify the source of the intimal cells (Figure 15.6). Indeed, studies from our own laboratory used aortic transplants of wild-type aortas into β-galactosidase (β-gal) expressing ROSA26 mice.[14] At 8 weeks post-transplant, donor medial smooth muscle cells were largely absent. However, in β-gal hosts, virtually all the intimal smooth muscle-like cells (SMLC) were β-gal-positive (we make the distinction between medial smooth muscle cells and intimal smooth muscle-*like* cells because the two populations have distinct proliferative and synthetic phenotypes). Furthermore, if wild type hosts were irradiated and administered ROSA26 bone marrow cells prior to transplantation with allomismatched aortas, the aortic graft intima contained up to 20 per cent β-gal$^+$, α-actin$^+$ SMLC.[14] The results indicate that bone marrow-derived precursors are in part responsible for intimal SMLC in AA lesions. Evaluation of graft–host anastomoses

confirmed that intimal SMLC did not arise by migration from adjacent host medial smooth muscle cells. Similar results were subsequently seen in heart transplant models, and additional work by others confirm the host origin of intimal SMLC in murine allotransplants, and even in conventional atherosclerosis in mice[41,42] (see also below).

Disadvantages of the heterotopic transplant model

A hypothetical drawback to the model is the complete elimination of donor cells, and the entry of inflammatory cells into grafts through unusual pathways (i.e. not via post-capillary venules). The fact that the results thus far are entirely comparable between the aorta and heart models suggest that these concerns are more theoretical than real.

Translation to clinical investigation

The murine transplant model permits experimental approaches to questions not readily amenable to investigation in human transplant recipients. Given the caveat that drug metabolism in experimental animals may not necessarily reflect that seen in humans, the effects of particular therapeutics and interventions on both parenchymal rejection and AA can also be tested.

Examples of specific questions that can be addressed using the murine transplant models:

- Hearts or aortas can be transplanted across well-defined MHC incompatibilities, with selective depletion of particular inflammatory cell subsets (using either monoclonal antibodies or knockout strains) to identify the relative importance of T-cell subsets, B cells, and natural killer cells in particular MHC combinations.

- Hearts can be explanted at intermediate time points to assess the pathologies that ultimately give rise to vascular lesions. In this manner we showed that parenchymal rejection predominates at early time points (days to 4 weeks), progressing to a coalescence of inflammation around arteries, with a lesser component of intraluminal inflammation.[19] As time progresses (8–12 weeks), parenchymal and perivascular inflammation recedes, while vessel intima are expanded by SMLC and matrix.[19] Thus, by only examining the end-point of AA pathology, intermediate states potentially amenable to intervention may be overlooked. This point is also important in that the inflammatory cells and mediators present at later time points may not be at all indicative of the cells and effectors that initiated or drove the development of AA.

- The number and severity of rejection episodes can be controlled experimentally. Thus, a single early episode of rejection is sufficient to induce the cascade of events that culminate in AA.[20] The result agrees with experiments using a rabbit heterotopic transplant model, where transient interruption of CsA

immunosuppression led to more severe AA lesions.[43] The results also imply that aggressive immunosuppression (limited by risk of infection or malignancy) could conceivably reduce the incidence and/or severity of AA.

- The effects of prolonged perioperative ischemia on AA development can also be examined critically. Thus, 4-h cold ischemia (comparable to the upper limit of cold ischemia allowable for human cardiac transplants) can induce very mild AA in isografts; however, the contribution of the alloresponse to AA far overwhelms any cold ischemia effect.[29] We conclude that any transient responses induced by ischemia alone are unlikely to significantly affect AA development.

- Using the available strains and highly specific antibodies, we (and others) demonstrated that the majority of endothelial and medial smooth muscle cells in AA lesions in long-term cardiac allografts are donor-derived.[15,31] The identity of vascular wall cells in cardiac allografts is significant in that donor cell persistence can conceivably drive an alloresponse that culminates in AA.

- Although host smooth muscle cells were identified in some arterial allograft models,[18] it was generally assumed that the majority of intimal SMLC in AA lesions originated by ingrowth of donor smooth muscle cells from the media of engrafted vessels.[44] It was subsequently shown that intimal SMLC in vascular grafts are virtually all host-derived;[14,15,41,45] in particular, we demonstrated that a proportion of these could originate from host bone-marrow-derived cells.[14] This result is consistent with the observation that bone-marrow stem cells are capable of developing into multiple mesenchymal lineages,[46] and that peripheral blood contains $CD34^+$, $flt1^+$, and $flk1^+$ precursors capable of smooth muscle cell differentiation.[47] The findings also provide a rationale for the long-standing observations concerning the significant phenotypic differences between medial smooth muscle cells and intimal SMLC.[48–54]

- Allograft transplanted into congenitally immunodeficient recipients (e.g. SCID or recombinase-deficient hosts) will survive indefinitely without immunosuppression; purified allospecific T cells, antiserum, or even cytokine mediators[23,24,26] can then be added back ('adoptive transfer') to identify relevant contributors to rejection or AA pathways. Thus, allospecific antiserum induced AA in the absence of host cellular responses, suggesting that humoral immunity can play a role in the disease process.[24,25] Conversely, adoptive transfer of T cells also induced AA lesions in grafts in $Rag^{-/-}$ hosts, in the complete absence of B cells;[26] the apparently contradictory results really indicate that multiple different forms of vascular injury can result in the same pathologic outcome. Finally, Tellides *et al.* demonstrated that interferon-γ administration alone (even in the absence of other inflammatory cells) is sufficient to induce AA lesions.[23]

- Transplantation experiments that take advantage of the multiple knockout and transgenic mouse strains can directly test the contribution of selected cytokines,

costimulatory molecules, and cell populations. For example, the necessary role of interferon-γ in AA pathogenesis was demonstrated by transplantation into hosts congenitally lacking interferon-γ; allograft hearts in this setting do not develop AA.[19,20,55] The same effect can be seen when blocking antibodies to interferon-γ are administered at weekly intervals, confirming that the result in the knockout strain is not attributable to some developmental anomaly.[19,56] Although the mechanism(s) underlying the requirement for interferon-γ are not known, the transplant model has been helpful in sorting out many of the possibilities; cardiac allografts in interferon-γ-deficient recipients exhibited diminished MHC II, CD40, VCAM-1, and ICAM-1 expression relative to control recipients.[19] Interestingly, although interferon-γ strongly induces vascular production of CXC chemokines that regulate inflammatory cell recruitment, allografts in interferon-γ-deficient hosts showed similar (or even increased) numbers of mononuclear inflammatory cells.

- Therapeutic efficacy of various drugs in humans can be preliminarily assessed using the mouse transplant models; new immunosuppressive regimens, anti-tumor necrosis factor therapy, and PPAR agonists have all been evaluated for effectiveness. Moreover, peculiarities of murine metabolism can be used to better define mechanisms of action. For example, statins (HMG-coA reductase inhibitors) have long been a part of the medical management of transplant recipients, putatively by attenuating some of the lipid abnormalities associated with immunosuppression regimens.[10] Mice, however, are normocholesterolemic and statins have no additional effect on their cholesterol levels. Nevertheless, therapeutic doses of statin agents lead to attenuation of AA in mice; the mechanism involves reduction in chemokine synthesis with reduced inflammatory cell and smooth muscle cell recruitment.[57]

References

1. Meier-Kriesche H, Schold J, Kaplan B. Long-term renal allograft survival: have we made significant progress or is it time to rethink our analytic and therapeutic strategies? *Am J Transpl* 2004; **4**: 1289–95.
2. Libby P, Salomon R, Payne D, et al. Functions of vascular wall cells related to the development of transplant-associated coronary arteriosclerosis. *Transplant Proc* 1989; **21**: 3677–3684.
3. Libby P, Pober J. Chronic rejection. *Immunity* 2001; **14**: 387–397.
4. Costanzo M, Naftel D, Pritzker M, et al. Heart transplant coronary artery disease detected by coronary angiography: A multi-institutional study of preoperative donor and recipient risk factors. *J Heart Lung Transplant* 1998; **17**: 744–753.
5. Hosenpud JD, Bennett LE, Keck BM, et al. The Registry of the International Society for Heart and Lung Transplantation: eighteenth Official Report - 2001. *J Heart Lung Transplant* 2001; **20**: 805–815.
6. Trulock E, Edwards L, Taylor D, et al. The Registry of the International Society for Heart and Lung Transplantation: twenty-first official adult heart transplant report - 2004. *J Heart Lung Transplant* 2004; **23**: 804–815.

7. Schoen F, Libby P. Cardiac transplant graft arteriosclerosis. *Trends Cardiovasc Med* 1991; **1**: 216–223.
8. Hauptman P, Nakagawa T, Tanaka H, et al. Acute rejection: culprit or coincidence in the pathogenesis of cardiac graft vascular disease? *J Heart Lung Transplant* 1995; **14**: S173–S180.
9. Kobashigawa J, Katznelson S, Laks H, et al. Effect of pravastatin on outcomes after cardiac transplantation. *N Engl J Med* 1995; **333**: 621–627.
10. Kobashigawa J. Statins and cardiac allograft vasculopathy after heart transplantation. *Semin Vasc Med* 2004; **4**: 401–406.
11. Liu L Meydani M. Combined vitamin C and E supplementation retards early progression of arteriosclerosis in heart transplant patients. *Nutr Rev* 2002; **60**: 368–371.
12. Häyry P, Aavik E, Sarwal M, et al. Chronic rejection: prospects for therapeutic intervention in fibroproliferative vascular disease. *Exp Clin Transplant* 2003; **1**: 35–38.
13. Reichenspurner H. Overview of tacrolimus-based immunosuppression after heart or lung transplantation. *J Heart Lung Transplant* **24**:119–130.
14. Shimizu K, Sugiyama S, Aikawa M, et al. Host bone-marrow cells are a source of donor intimal smooth muscle-like cells in murine aortic transplant arteriopathy. *Nat Med* 2001; **7**: 738–741.
15. Hillebrands J, Klatter F, Hurk Bvd, et al. Origin of neointimal endothelium and alpha-actin-positive smooth muscle cells in transplant arteriosclerosis. *J Clin Invest* 2001; **107**: 1411–1422.
16. Corry R, Winn H Russell P. Primary vascularised allografts of hearts in mice. *Transplant* 1973; **16**: 343–350.
17. Russell P, Chase C, Win H, et al. Coronary atherosclerosis in transplanted mouse hearts. I. Time course and immunogenetic and immunopathological considerations. *Am J Pathol* 1994; **144**: 260–274.
18. Plissonier D, Nochy D, Poncet P, et al. Sequential immunological targeting of chronic experimental arterial allograft. *Transplant* 1995; **60**: 414–424.
19. Nagano H, Mitchell R, Taylor M, et al. Interferon-γ deficiency prevents coronary arteriosclerosis but not myocardial rejection in transplanted mouse hearts. *J Clin Invest* 1997; **100**: 550–557.
20. Nagano H, Libby P, Taylor M, et al. Coronary arteriosclerosis after T-cell-mediated injury in transplanted mouse hearts. Role of Interferon-γ. *Am J Pathol* 1998; **152**: 1187–1197.
21. Dalton D, Pitts-Meek S, Keshav S, et al. Multiple defects of immune cell function in mice with disrupted interferon-gamma genes. *Science* 1993; **259**: 1739–1742.
22. Halloran P, Afrouzian M, Ramassar V, et al. Interferon-γ acts directly on rejecting renal allografts to prevent graft necrosis. *Am J Pathol* 2001; **158**: 215–226.
23. Tellides G, Tereb D, Kirkiles-Smith N, et al. Interferon-gamma elicits arteriosclerosis in the absence of leukocytes. *Nature* 2000; **403**: 207–211.
24. Russell P, Chase C, Winn H, et al. Coronary atherosclerosis in transplanted mouse hearts. II. Importance of humoral immunity. *J Immunol* 1994; **152**: 5135–5141.
25. Hancock W, Buelow R, Sayegh M, et al. Antibody-induced transplant arteriosclerosis is prevented by graft expression of anti-oxidant and anti-apoptotic genes. *Nat Med* 1998; **4**: 1392–1396.
26. Furukawa Y, Cole S, Shah R, et al. Wild-type but not interferon-gamma-deficient T cells induce graft arterial disease in the absence of B cells. *Cardiovasc Res* 2004; **63**: 347–356.

27. Drinkwater D, Rudis E, Laks H, et al. University of Wisconsin solution versus Stanford cardioplegic solution and the development of cardiac allograft vasculopathy. *J Heart Lung Transplant* 1995; **14**: 891–896.
28. Billingham M, Cary N, Hammond M, et al. A working formulation for the standardisation of nomenclature in the diagnosis of heart and lung rejection: Heart Rejection Study Group. The international Society for Heart Transplantation. *J Heart Transplant* 1990; **9**: 587–593.
29. Furukawa Y, Libby P, Stinn J, et al. Cold ischemia enhances cytokine/cell adhesion molecule expression and induces graft arterial diseas in isografts, but does not accentuate alloimmune responses of non-immunosuppressed hosts. *Am J Pathol* 2002; **160**: 1077–1087.
30. Tilney N, Guttmann R. Effects of initial ischemia/reperfusion injury on the transplanted kidney. *Transplant* 1997; **64**: 945–947.
31. Hasegawa S, Becker G, Nagano H, et al. Pattern of graft- and host-specific MHC class II expression in long-term murine cardiac allografts. Origin of inflammatory and vascular wall cells. *Am J Pathol* 1998; **153**: 1–11.
32. Stinn J, Taylor M, Becker G, et al. Interferon-γ-secreting T-cell populations in rejecting murine cardiac allografts: Assessment by flow cytometry. *Am J Pathol* 1998; **153**: 1383–1392.
33. Morris R, Wu J, Shorthouse R. A study of the contrasting effects of ciclosparine, FK-506, and rapamycin on the suppression of allograft rejection. *Transplant Proc* 1990; **22**: 1638–1641.
34. Mollison K, Fey T, Krause R, et al. Comparison of FK-506, rapamycin, ascomycin, and ciclosparine in mouse models of host-versus-graft disease and heterotopic heart transplantation. *Ann NY Acad Sci* 1993; **685**: 55–57.
35. Judd K, Trentin J. Cardiac transplantation in mice. I. Factors influencing the take and survival of heterotopic grafts. *Transplant* 1971; **11**: 298–302.
36. Shi C, Russell M, Bianchi C, et al. A murine model of accelerated transplant arteriosclerosis. *Circ Res* 1994; **75**: 199–207.
37. Chow L, Huh S, Jiang J, et al. Intimal thickening develops without humoral immunity in a mouse aortic allograft model of chronic vascular rejection. *Circ* 1996; **94**: 3079–3082.
38. Shi C, Lee W, He Q, et al. Immunologic basis of transplant associated arteriosclerosis. *Proc Natl Acad Sci U S A* 1996; **93**: 4051–4056.
39. Acland R. Signs of patency in small vessel anastomosis. *Surgery* 1972; **72**: 744–748.
40. Shimizu K, Shichiri M, Libby P, et al. Th2-predominant inflammation and blockade of IFN-gamma signaling induce aneurysms in allografted aortas. *J Clin Invest* 2004; **114**: 300–308.
41. Li J, Han X, Jiang J, et al. Vascular smooth muscle cells of recipient origin mediate intimal expansion after aortic allotransplantation in mice. *Am J Pathol* 2001; **158**: 1943–1947.
42. Sata M, Saiura A, Kunisato A, et al. Hematopoietic stem cells differentiate into vascular cells that participate in the pathogenesis of atherosclerosis. *Nat Med* 2002; **8**: 403–409.
43. Nakagawa T, Sukhova G, Rabkin E, et al. Acute rejection accelerates graft coronary disease in transplanted rabbit hearts. *Circulation* 1995; **92**: 987–993.
44. Kennedy L, Weissman I. Dual origin of intimal cells in cardiac-allograft arteriosclerosis. *N Engl J Med* 1971; **285**: 884–887.
45. Saiura A, Sata M, Hirata Y, et al. Circulating smooth muscle progenitor cells contribute to atherosclerosis. *Nat Med* 2001; **7**: 382–383.

46. Pittenger M, Mackay A, Beck S, et al. Multilineage potential of adult human mesenchymal stem cells. *Science* 1999; **284**: 143–147.
47. Simper D, Stalboerger P, Panetta C, et al. Smooth muscle progenitor cells in human blood. *Circulation* 2002; **106**: 1199–1204.
48. Majesky M, Giachelli C, Reidy M, et al. Rat carotid neointimal smooth muscle cells reexpress a developmentally regulated mRNA phenotype during repair of arterial injury. *Circ Res* 1992; **71**: 759–768.
49. Owens G. Regulation of differentiation of vascular smooth muscle cells. *Physiol Rev* 1995; **75**: 487–517.
50. Schwartz S, Campbell G Campbell J. Replication of smooth muscle cells in vascular disease. *Circ Res* 1986; **58**: 427–444.
51. Campbell G, Chamley-Campbell J. Invited review: the cellular pathobiology of atherosclerosis. *Pathology* 1981; **13**: 423–440.
52. Ross R, Glomset J. The pathogenesis of atherosclerosis (second of two parts). *N Engl J Med* 1976; **295**: 369–377.
53. Ross R. The pathogenesis of atherosclerosis: A perspective for the 1990s. *Nature* 1993; **362**: 801–809.
54. Ross R. Atherosclerosis - an inflammatory disease. *N Engl J Med* 1999; **340**: 115–126.
55. Raisanen-Sokolowski A, Glysing-Jensen T, Koglin J, et al. Reduced transplant arteriosclerosis in murine cardiac allografts placed in interferon-gamma knockout recipients. *Am J Pathol* 1998; **152**: 359–365.
56. Russell P, Chase C, Winn H, et al. Coronary atherosclerosis in transplanted mouse hearts. III. Effects of recipient treatment with a monoclonal antibody to interferon-gamma. *Transplant* 1994; **57**: 1367–1371.
57. Shimizu K, Aikawa M, Takayama K, et al. Cerivastatin has immunomodulatory effects on donor endothelial cells and host inflammatory cells and attenuates allograft arteriopathy. *Circulation* 2001; **104**: II212–II113.
58. Shah R, Mitchell R. The role of stem cells in the response to myocardial and vascular wall injury. *Cardiovasc Pathol* 2005; **14**: 225–231.

16

Heart preconditioning analysis

Guang-Wu Wang, David A Liem, Steven Le and **Peipei Ping**

Departments of Physiology and Medicine/Cardiology
David Geffen School of Medicine at UCLA, Los Angeles, CA, USA

Introduction

Coronary artery disease is currently the leading cause of mortality and morbidity in the western world. The serious and often fatal consequence of coronary artery disease is an acute myocardial infarction, which results from the acute occlusion of one of the major coronary arteries. In this scenario, the best hope of limiting the size of the myocardial infarction is the timely restoration of coronary blood flow, by either thrombolysis or primary percutaneous coronary artery angioplasty. Despite these current reperfusion strategies, the morbidity and mortality associated with an acute myocardial infarction remains significant, necessitating the development of novel cardioprotective strategies, which can be used as adjunctive therapy to the current reperfusion strategies.

One of the most powerful mechanisms for protecting the myocardium before the acute coronary artery occlusion occurs is to ischemically precondition the myocardium, a powerful cardioprotective phenomenon first described in 1986 by Murry *et al.*[1] in which transient non-lethal episodes of myocardial ischemia confer protection against the myocardial infarction induced by a subsequent sustained episode of lethal myocardial ischemia. The time course of ischemic preconditioning (PC) is characterised by an immediate but short-lived wave of protection (early phase of PC)[2–6] followed, 12–24 h later, by a second, sustained window of protection that lasts at least 72 h (late phase of PC).[7–13] Because of its remarkable efficacy, there is considerable interest in exploiting ischemic PC to develop therapeutic strategies that can enhance the tolerance of the heart to ischemic injury in patients with coronary artery

A Handbook of Mouse Models of Cardiovascular Disease Edited by Qinbo Xu

disease.[4,6,14–19] Clinical application of ischemic PC, however, will require a detailed understanding of the molecular and cellular mechanisms underlying this endogenous adaptive phenomenon. By overexpression or targeted disruption of specific genes, the mouse model present a unique approach to study ischemic heart diseases. Accordingly, the mouse model of ischemic PC should be a useful tool to unravel the molecular mechanism of PC.

Methods

Use of mouse strains

In general, we prefer to use adult male mice (8–13 weeks old), such as ICR (outbred), C57BL/6J (inbred), and B6129F2/J (hybrid). These strains have good reproductive performance and also preconditionable.[20–22] Recently, several studies have shown that the genetic strain is an important determinant of the susceptibility of mice to myocardial infarction and ischemic preconditioning.[20] Specifically, FVB/N mice have much smaller infarcts after a 30 min coronary occlusion than do the ICR, C57BL/6J, and B6/129SF2/J mice, and that 129SvEv mice do not develop late preconditioning.[20] Thus, when using gene targeted or transgenic mice, controls should consist of mice with a genetic background as close as possible to that of the gene targeted or transgenic mice (littermates are the best controls, if they are available). Please note that data obtained in one strain of mice cannot be extrapolated to another strain of mice.

Anesthetic medication

Mice are given intraperitoneal injection of pentobarbital sodium (50 mg/kg). Additional doses of pentobarbital are given during the protocol as needed to maintain anesthesia.[22,23]

Open-chest procedure

The animals are placed in a supine position with the paws taped to the operating table. Surface leads are placed subcutaneously to obtain the electrocardiogram (ECG), which is recorded throughout the experiments on a thermal array chart recorder. After a midline cervical skin incision, the trachea is visualised and the endotracheal tube is inserted into the trachea followed by positive pressure ventilation with a rodent ventilator (Harvard apparatus, South Natick, MA, USA) at a rate of 105 breaths/min with a tidal volume of 2.5 ml with oxygen-enriched room air. These values in the mouse have previously been shown to maintain optimal arterial values of PO_2 and PCO_2 and pH. To maintain temperature within physiological range, the animals are

positioned on a heating path. Rectal temperature is continuously measured and maintained at 36.5–37.5°C. After the animal is rotated on its right site, the chest is opened under a dissecting microscope through a left thoracotomy in the third intercostal space between ribs three and four.[22,23]

Myocardial infarction procedure

With the aid of a dissecting microscope and a microcoagulator, the pericardium is teared open and a silk 8-0 nylon suture is looped under the left anterior descending coronary artery (LAD) 1–3 mm from the tip of the normally positioned left atrium. A clear vision of the LAD can be attained by reflection of light on the myocardium under the dissecting microscope. Sketches of the mouse left coronary anatomies are illustrated in Figure 16.1. Please note that the LAD follows two major anatomical patterns. One is that LAD courses to the apex as a single major vessel with branches of variable size appearing in many cases horizontal to the main axis. The second pattern illustrates the LAD bifurcating into two major vessels as it courses to the apex.[23] Coronary occlusion is induced by ligation of the suture. Before occlusion, a 1 to 2 mm section of PE-10 tubing (A-M Systems, inc) is placed between the suture and the artery to prevent damage to the vessel (Figure 16.2). After 30 min of LAD occlusion, the suture is removed to allow coronary reperfusion, and then followed by chest wall closure by a 5-0 polyester suture. Coronary artery reperfusion can be verified by one of the following three methods: (1) visual inspection, (2) changes in ventricular function, or (3) histopathological changes. The chest wall is then closed by approximating ribs three and four with a 5-0 ticron blue polyester suture. Next, the superficial muscle layer is approximated in one layer, and finally the skin is closed. A

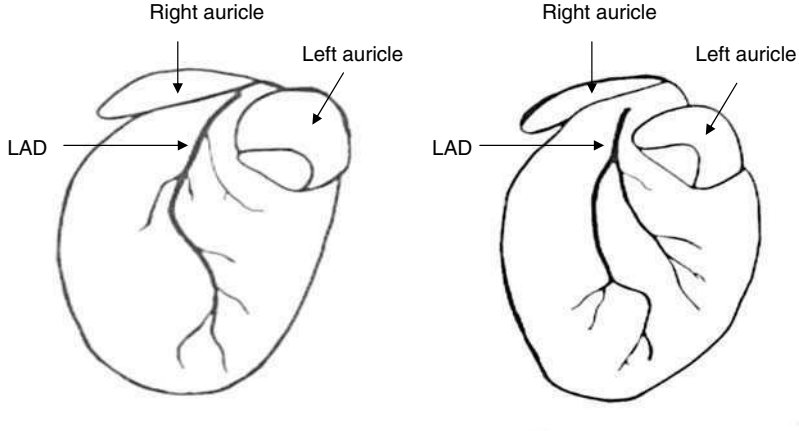

Figure 16.1 Schematic line drawings of left coronary arterial anatomy of mouse hearts. Left: a common pattern where there is a major singular LAD; right: another common pattern with major bifurcating of LAD. For a color version of this figure, please see the images supplied on the accompanying CD

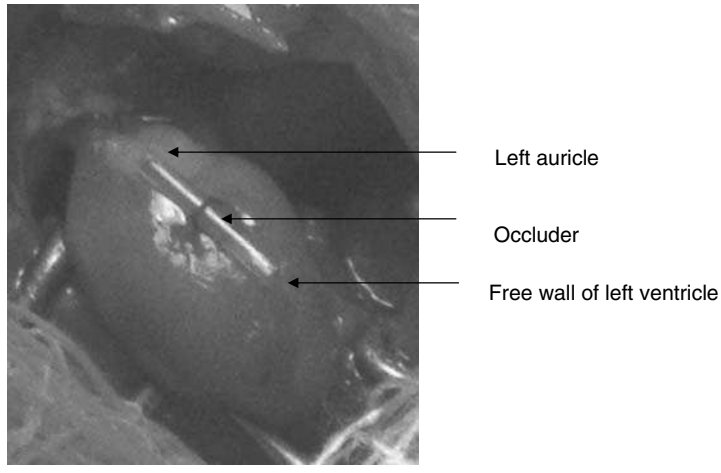

Figure 16.2 Photograph of open-chest mouse with an occluder on left anterior descending coronary artery to induce myocardial infarction. For a color version of this figure, please see the images supplied on the accompanying CD

small catheter is left in the thorax for 10–20 min to evacuate air and fluids. After approximately 1 h, the animal is removed from the respirator and the endotracheal tube is withdrawn. While the animal is allowed to recover, it is kept warm with a heating pad, given fluids (1.0–1.5 ml of 5 per cent dextrose in water intraperitoneally), and allowed 100 per cent oxygen via nasal cone.

PC procedure

Ischemic PC

By using a balloon occluder, ischemic PC is produced with a sequence of six cycles of 4 min coronary occlusion separated by 4 min reperfusion. With the aid of a dissecting microscope and a microcoagulator, an 8-0 nylon suture is passed with a tapered needle under the LAD 2–3 mm from the tip of the left auricle, and a nontraumatic balloon occluder is applied on the artery. Coronary artery occlusion is induced by inflating the balloon occluder. Successful performance of coronary occlusion and reperfusion can be verified by visual inspection (i.e. by noting the development of a pale color in the distal myocardium on inflation of the balloon and the return of a bright red color due to hyperemia after deflation) and by observing S-T segment elevation and widening of the QRS on the ECG during ischemia and their resolution after reperfusion. After completion of the ischemic PC protocol, the chest is closed in layers. Twenty-four h later, the animals from both groups are subjected to ischemic injury by 30 min occlusion of the LAD followed by 24 h reperfusion.[22]

Pharmacological preconditioning

Pharmacological preconditioning (i.e. nitric oxide donor-induced PC) is produced by four bolus injections of diethylenetriamine/nitric oxide (DETA/NO; 4×0.1 mg/kg i.v.) each separated by 25 min. The control groups are given the DETA/NO solvent phosphate-buffered saline (PBS). Twenty-four h later, the animals from both groups are subjected to ischemic injury by 30 min occlusion of the LAD followed by 24 h reperfusion.[24,25]

Postmortem analysis

After 24 h of coronary artery reperfusion, the chest is reopened, the heart is excised and postmortem perfused as previously described.[22,24] In order to start this procedure the mice are given heparin intraperitoneally (1 U/g) followed by anesthesia with pentobarbital sodium (50 mg/kg body wt). After a laparoscopy, the inferior caval vein is dissected to induce euthanasia with an intravenous bolus of KCl (15 per cent, $\sim$2 ml). Next, the aorta is cannulated with a 23G Luer stub, and phosphate buffer is perfused into the aorta and coronary arteries for distribution throughout the whole heart to flush postmortem waste products. To distinguish infarcted myocardium from viable myocardium, the heart is then perfused with 3 ml of a 1 per cent solution of 2,3,5-triphenyltetrazolium chloride (TTC) in phosphate buffer at a pressure of approximately 60 mmHg over 3 min. The use of tetrazolium stains such as TTC is well established to identify and quantify infarcted tissue in different species.[20] Cells from viable myocardial tissue reduce tetrazolium salts to formazan-insoluble colored precipitates (red pigments by use of TTC) by dehydrogenases using the reduced form of nicotinamideadenine dinucleotide (NADH) as electron donors. Thus, after staining with TTC, viable myocardial tissue stains red while the infarcted tissue remains pale. To delineate the ischemic-reperfused coronary vascular area (i.e. the area at risk), the coronary artery is tied again at the site of the previous occlusion. Subsequently, the aortic root is perfused with a 5 per cent solution of Evans Blue Dye in phosphate buffer. The portion of normally perfused area stains blue whereas the area at risk region remains unstained. Next, the atrial and right ventricle tissues are separated from the heart and the remaining left ventricle is frozen at -20°C for 1 h. The left ventricle is sliced transversely into five slices from apex to base which are each fixed in 4 per cent paraformaldehyde for 24 h. Each side of every slice is imaged, and the area of infarction for each slice is defined by computerised planimetry using an NIH image analysis software program (NIHImages). Myocardial infarction is defined as a percentage of total area at risk which is determined by the following equation: $(AR1 \times WT1) + (AR2 \times WT2) + (AR3 \times WT3) + (AR4 \times WT4) + (AR5 \times WT5)$, where AR is the percent area of infarction by planimetry from subscribed numbers 1–5 representing sections, and WT is weight of the same numbered sections. The area

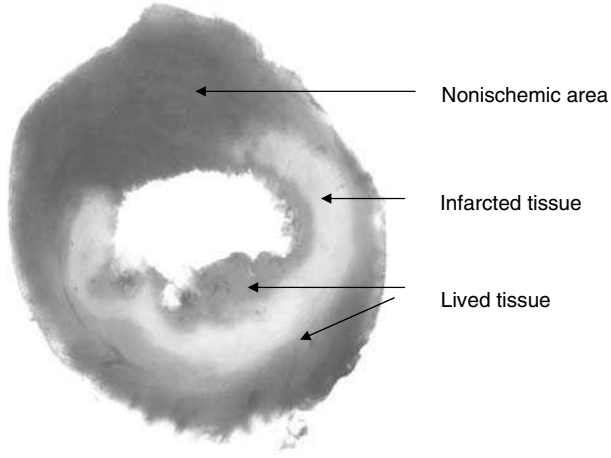

Figure 16.3 Representative example of a heart slice from the mouse subjected to a 30min coronary occlusion and 24 h of reperfusion. The infarcted area is delineated by perfusing the aortic root with 2,3,5-triphenyltetrazolium chloride; the area at risk is delineated by perfusing the aortic root with Evans blue after tying the previously occluded artery. As a result of this procedure, the non-ischemic portion of the left ventricle was stained dark blue and viable tissue within the area at risk was stained bright red, whereas infarcted tissue was white. For a color version of this figure, please see the images supplied on the accompanying CD

at risk as percentage of left ventricle is calculated by (WT of left ventricle − WT of left ventricle that stained blue, i.e. the area of left ventricle that is continuesly perfused) (Figure 16.3).

Methodological considerations

Because temperature is a major determinant of infarct size,[26–28] this variable is tightly controlled about 37°C throughout the experiment by using heating pads while continuously monitoring rectal temperature. Hypoxemia, acidosis, and alkalosis may also have a major influence upon animal survival, infarct size, and/or ischemic preconditioning. With a ventilatory rate of 105/min and an average tidal volume of 2.2 ml, all parameters such as arterial pH, PO_2, PCO_2 were within the physiologic range for the mouse;[22] in particular, arterial pH is kept at ∼7.40 and adequate oxygenation is maintained throughout the open-chest state.[22] Careful control of blood gases is important in the mouse, since small variations in ventilatory rate result in marked variations in arterial blood gases.[22]

Heart rate and arterial pressure are important indices of normal cardiovascular homeostasis and are also important determinants of the severity of myocardial ischemia. Clearly outside of the physiological range, which in the pilot studies in conscious mice was found to be 490 to 760 bpm (average, 688 ± 31 bpm).[22] With pentobarbital anesthesia, the heart rates were reasonably close to those measured in

conscious mice in the pilot studies.[22] The blood volume of a 25 g mouse has been estimated to range between 1.5 and 2.3 ml.[22] To avoid hypotension, surgery is performed with a microcoagulator, and every effort made to minimise blood losses. Pilot studies, however, showed that opening the chest caused a significant drop in arterial blood pressure, so that the mice became severely hypotensive despite the administration of 13.3 ml/kg (~0.4 ml) of blood.[22] Besides causing mortality, severe hypotension could lead to myocardial hypoperfusion and, possibly, induce preconditioning as a result of myocardial ischemia and/or reflex adrenergic activation.[22]

The use of vital stains such as TTC, to measure myocardial infarct size following coronary artery occlusion and reperfusion in experimental animals is[22,24,29,30] widely accepted technique. The size of myocardial infarction measured by the detection of tetrazolium staining depends on the duration of coronary occlusion and the duration of reperfusion. The detection of tetrazolium staining after myocardial ischemia–reperfusion also depends on species differences. In the rabbit a minimum of 30 min or 45 min of coronary artery occlusion is used,[31] whereas in canine and porcine 45 min or 60 min of occlusion are more common.[32] In the rat, most studies use 30 minutes[33] or 60 minutes[34] of total occlusion. In the mouse, most studies use 30 min of coronary occlusion.[22–24] In addition, different occlusion or reperfusion periods in the same species might result in different infarct sizes. Moreover, there has been some controversy about the optimal duration time of the reperfusion necessary to accurately measure tetrazolium staining and thus the extent of myocardial cell death.[30] After a relatively short reperfusion period, the TTC staining can underestimate the myocardial infarct area. Furthermore, the infarcted area as assessed with TTC staining increases with a prolonged reperfusion period. Accordingly, to estimate the maximal infarcted area by TTC staining requires a minimum reperfusion period which also seems to depend on the species differences.[30] In the rat model, it has been suggested that a minimum of 60 min of reperfusion is optimum to visualize a homogeneous infarct and that longer reperfusion periods do not contribute to a better demarcation of myocardial infarction or result in a larger infarct.[30] However, in larger animal models such as the rabbit it has been shown that a minimum of 3 h of reperfusion following coronary occlusion is required to obtain a clear contrast between viable and non-viable myocardial tissue.[35] Since metabolic rates are higher in smaller animals such as rodents, it may be that the development of cell death during ischemia occurs faster compared to larger animals such as the rabbit and that a shorter duration of reperfusion is necessary. Mice are the smallest animals used for myocardial ischemia–reperfusion studies; it can therefore be assumed that the minimal reperfusion period is no shorter than 60 minutes. Nevertheless, in our previous studies we applied either 4 h[36] or 24 h of reperfusion,[24] which is significantly longer than the minimal reperfusion period in the rat. Mice in which 30 minutes of LAD coronary artery occlusion was followed by 4 h of reperfusion showed similar infarct size compared to mice that were followed with 24 h of reperfusion.[22] This suggests that in the mouse model of ischemia–reperfusion, a 4 h period of reperfusion should be sufficiently enough to express the final extent of myocardial cell death.

References

1. Murry CE, Jennings RB, Reimer KA. Preconditioning with ischemia: a delay of lethal cell injury in ischemic myocardium. *Circulation* 1986; **74**: 1124–1136.
2. Auchampach JA, Gross GJ. Adenosine A_1 receptors, K_{ATP} channels, and ischemic preconditioning in dogs. *Am J Physiol* 1993; **264**: H1327–H1336.
3. Burckhartt B, Yang XM, Tsuchida A, Mullane KM, Downey JM, Cohen MV. Acadesine extends the window of protection afforded by ischemic preconditioning in conscious rabbits. *Cardiovasc Res* 1995; **29**: 653–657.
4. Cohen MV, Downey JM. Preconditioning during ischemia. *Cardiol Rev* 1995; **3**: 137–149.
5. Cohen MV, Yang XM, Downey JM. Conscious rabbits become tolerant to multiple episodes of ischemic preconditioning. *Circ Res* 1994; **74**: 998–1004.
6. Downey JM. Tschemic preconditioning: nature's own cardioprotective intervention. *Trends Cardiovasc Med* 1992; **2**: 170–176.
7. Baxter GF, Goma FM, Yellon DM. Involvement of protein kinase C in the delayed cytoprotection following sublethal ischaemia in rabbit myocardium. *Br J Pharmacol* 1995; **115**: 222–224.
8. Baxter GF, Goma FM, Yellon DM. Characterisation of the infarct-limiting effect of delayed preconditioning: time course and dose-dependency studies in rabbit myocardium. *Basic Res Cardiol* 1997; **92**: 159–167.
9. Baxter GF, Marber MS, Patel VC, Yellon DM. Adenosine receptor involvement in a delayed phase of myocardial protection 24 hours after ischemic preconditioning. *Circulation* 1994; **90**: 2993–3000.
10. Baxter GF, Mocanu MM, Yellon DM. Attenuation of myocardial ischaemic injury 24 h after diacylglycerol treatment in vivo. *J Mol Cell Cardiol* 1997; **29**: 1967–1975.
11. Stein AB, Tang XL, Guo Y, Xuan YT, Dawn B, Bolli R. Delayed adaptation of the heart to stress: late preconditioning. *Stroke* 2004; **35**(11 Suppl 1): 2676–2679.
12. Ren X, Wang Y, Jones WK. TNF-alpha is required for late ischemic preconditioning but not for remote preconditioning of trauma. *J Surg Res* 2004; **121**: 120–129.
13. Piper HM, Abdallah Y, Schafer C. The first minutes of reperfusion: a window of opportunity for cardioprotection. *Cardiovasc Res* 2004; **61**: 365–371.
14. Bolli R. The early and late phases of preconditioning against myocardial stunning and the essential role of oxyradicals in the late phase: an overview. *Basic Res Cardiol* 1996; **91**: 57–63.
15. Marber MS, Yellon DM. Myocardial adaptation, stress proteins, and the second window of protection. *Ann N Y Acad Sci* 1996; **793**: 123–141.
16. Hausenloy DJ, Tsang A, Yellon DM. The reperfusion injury salvage kinase pathway: a common target for both ischemic preconditioning and postconditioning. *Trends Cardiovasc Med* 2005; **15**: 69–75.
17. Pasupathy S, Homer-Vanniasinkam S. Surgical implications of ischemic preconditioning. *Arch Surg* 2005; **140**: 405–410.
18. Sanada S, Kitakaze M. Ischemic preconditioning: emerging evidence, controversy, and translational trials. *Int J Cardiol* 2004; **97**: 263–276.
19. Kloner RA, Rezkalla SH. Cardiac protection during acute myocardial infarction: where do we stand in 2004? *J Am Coll Cardiol* 2004; **44**: 276–286.
20. Bao W, Guo Y, Tang XL, Wu WJ, Bolli R. Variability in susceptibility to ischemia among different strains of mice. *J Mol Cell Cardiol* 2000; **32**: A21.

21. Guo Y, Jones WK, Xuan YT, *et al.* The late phase of ischemic preconditioning is abrogated by targeted disruption of the inducible NO synthase gene. *Proc Natl Acad Sci U S A* 1999; **96**: 11507–11512.
22. Guo Y, Wu WJ, Qiu Y, Tang XL, Yang Z, Bolli R. Demonstration of an early and a late phase of ischemic preconditioning in mice. *Am J Physiol* 1998; **275**: H1375–H1387.
23. Michael LH, Entman ML, Hartley CJ, *et al.* Myocardial ischemia and reperfusion: a murine model. *Am J Physiol* 1995; **269**: H2147–H2154.
24. Wang G, Liem DA, Vondriska TM, *et al.* Nitric oxide donors protect murine myocardium against infarction via modulation of mitochondrial permeability transition. *Am J Physiol* 2005; **288**: H1290–H1205.
25. Qiu Y, Rizvi A, Tang XL, *et al.* Nitric oxide triggers late preconditioning against myocardial infarction in conscious rabbits. *Am J Physiol* 1997; **273**: H2931–H2936.
26. Duncker DJ, Klassen CL, Ishibashi Y, Herrlinger SH, Pavek TJ, Bache RJ. Effect of temperature on myocardial infarction in swine. *Am J Physiol* 1996; **270**: H1189–H1199.
27. Hale SL, Kloner RA. Myocardial temperature in acute myocardial infarction: protection with mild regional hypothermia. *Am J Physiol* 1997; **273**: H220–H227.
28. Schwartz LM, Verbinski SG, Vander Heide RS, Reimer KA. Epicardial temperature is a major predictor of myocardial infarct size in dogs. *J Mol Cell Cardiol* 1997; **29**: 1577–1583.
29. Klein HH, Puschmann S, Schaper J, Schaper W. The mechanism of the tetrazolium reaction in identifying experimental myocardial infarction. *Virchows Arch* 1981; **393**: 287–297.
30. Schwarz ER, Somoano Y, Hale SL, Kloner RA. What is the required reperfusion period for assessment of myocardial infarct size using triphenyltetrazolium chloride staining in the rat? *J Thromb Thrombolysis* 2000; **10**: 181–187.
31. Goto M, Tsuchida A, Liu Y, Cohen MV, Downey JM. Transient inhibition of glucose uptake mimics ischemic preconditioning by salvaging ischemic myocardium in the rabbit heart. *J Mol Cell Cardiol* 1995; **27**: 1883–1894.
32. Sack S, Mohri M, Arras M, Schwarz ER, Schaper W. Ischaemic preconditioning – time course of renewal in the pig. *Cardiovasc Res* 1993; **27**: 551–555.
33. Schultz JE, Rose E, Yao Z, Gross GJ. Evidence for involvement of opioid receptors in ischemic preconditioning in rat hearts. *Am J Physiol* 1995; **268**: H2157–H2161.
34. Gho BC, Schoemaker RG, van den Doel MA, Duncker DJ, Verdouw PD. Myocardial protection by brief ischemia in noncardiac tissue. *Circulation* 1996; **94(9)**: 2193–2200.
35. Birnbaum Y, Hale SL, Kloner RA. Differences in reperfusion length following 30 minutes of ischemia in the rabbit influence infarct size, as measured by triphenyltetrazolium chloride staining. *J Mol Cell Cardiol* 1997; **29**: 657–666.
36. Baines CP, Song CX, Zheng YT, *et al.* Protein kinase Cepsilon interacts with and inhibits the permeability transition pore in cardiac mitochondria. *Circ Res* 2003; **92**: 873–880.

17

Myocardial ischemia–reperfusion

Bernhard Metzler, Elisabetta Conci and **Otmar Pachinger**

Department of Cardiology, University Hospital of Internal Medicine, Innsbruck, Austria

Abstract

The past few years have witnessed a remarkable advance in our understanding of the pathophysiology of coronary atherosclerosis. Myocardial ischemia usually occurs on the basis of coronary atherosclerosis. Although the functional consequences of depriving the myocardium of its blood supply have been appreciated for many years, the coronary heart disease is still the leading cause of morbidity and mortality in the western world. This has focused the attention of physicians on restoring blood flow to the ischemic region in order to prevent tissue necrosis and regain organ function. Reperfusion of ischemic tissues is often associated with microvascular dysfunction that is manifested as impaired endothelial-dependent dilatation in arterioles and leukocyte plugging in capillaries. The availability of a broad variety of knockout mice provides important clues about the progression of the ischemia/reperfusion (I/R) injury. Therefore mouse models for I/R are of great importance for the development of new therapeutic strategies for humans.

Key words

ischemia/reperfusion, heart, mice model

Myocardial ischemia–reperfusion

Acute coronary syndromes resulting from occlusion of one of the coronary arteries expose the heart to ischemic conditions. Brief periods of ischemia (<20 min) are reversible if followed by reperfusion. They are not associated with development of necrosis but often result in the phenomenon of stunning. If duration of coronary occlusion is prolonged beyond this point, a wave front of necrosis propagates from subendocardium to subepicardium. Myocardial ischemia–reperfusion injury involves activation of multiple cell types, including leukocytes and endothelial cells. Reperfusion

A Handbook of Mouse Models of Cardiovascular Disease Edited by Qinbo Xu

beyond a few hours does not reduce myocardial infarct size. Myocardial ischemia–reperfusion induces a profound inflammatory condition in the myocardium that results in tissue destruction and impaired ventricular function, which may lead to hypokinesis, akinesis or dyskinesis.[1] Some of the known risk factors for cardiovascular disease (hypercholesterolemia, diabetes and hypertension) appear to exaggerate many of the microvascular alterations elicited by ischemia and reperfusion.

Within seconds of cessation of blood flow, energy metabolism shifts from mitochondrial respiration to anaerobic glycolysis. Simultaneously, effective contractions diminish and then cease. Lactate and protons accumulate in cardiomyocytes, inducing acidosis and osmotic load and then cell oedema. In addition, intracellular Ca^{2+} rises probably due to the combined action of the Na^{+}/H^{+} and Na^{+}/Ca^{2+} exchangers activated by cellular acidosis. If prolonged, this will eventually lead to cell necrosis.[2]

Restoration of arterial flow is necessary to restore aerobic metabolism and save the ischemic myocytes. It, however, induces by itself further damage: this process has been termed 'reperfusion injury' (Figure 17.1). A form of reperfusion injury is myocardial stunning, which was described by Braunwald and Kloner as 'prolonged, postischemic dysfunction of viable tissue salvaged by reperfusion,' i.e. myocardium

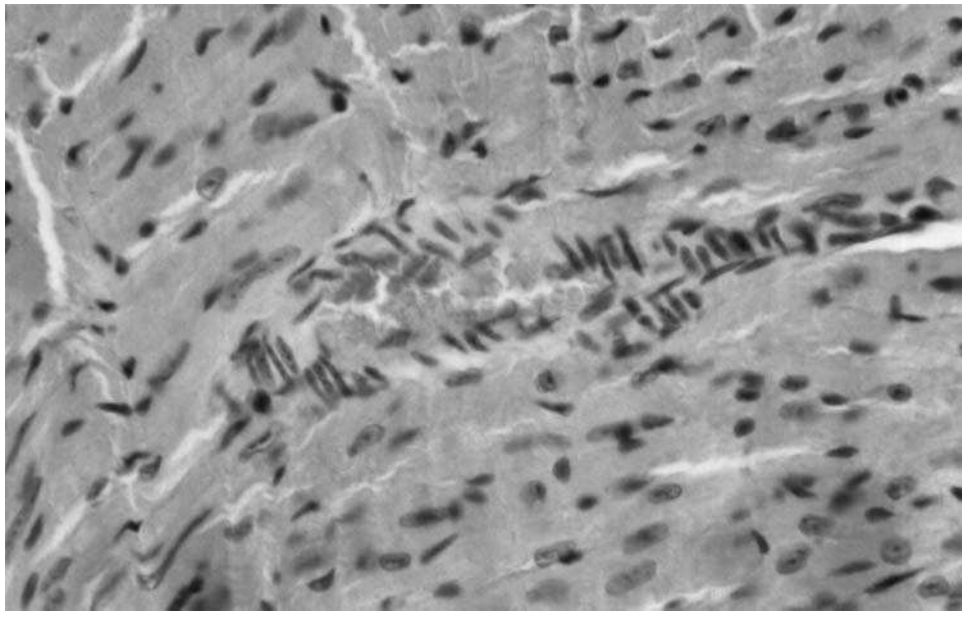

Figure 17.1 Typical photomicrograph of ischemia–reperfused mouse myocardium. The trafficking of leukocytes in a postcapillary venule is demonstrated. The endothelial dysfunction in postcapillary venules accounts for most of the inflammatory responses that are associated with ischemia–reperfusion. Leukocyte–endothelial cell adhesion and subsequent transendothelial leukocyte migration are characteristic features of the venular response to ischemia–reperfusion. For a color version of this figure, please see the images supplied on the accompanying CD

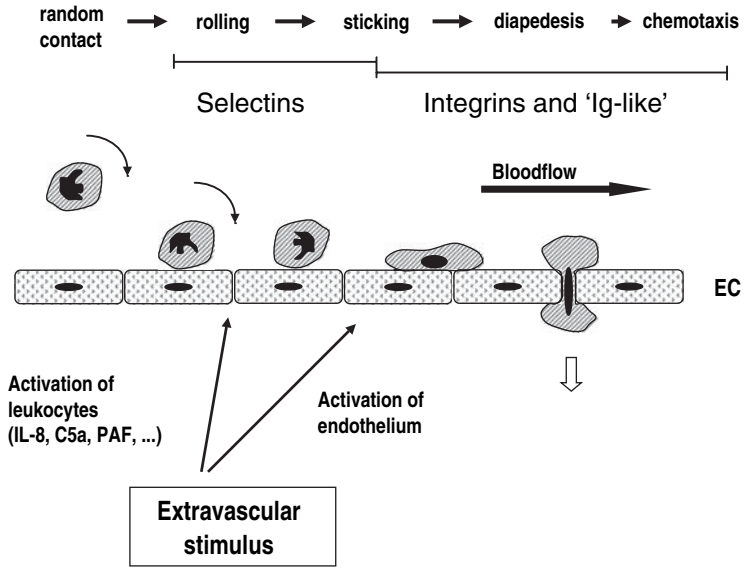

Figure 17.2 Scheme of involvement of the adhesion molecules in ischemia–reperfusion Under normal conditions, there are virtually no interactions between the endothelium and neutrophils. After coronary ischemia–reperfusion, the blood vessel's ability to form NO is severely reduced. With decreased supplies of NO, the coronary vessel may constrict. Additional, adhesion molecules were expressed on the endothelium and polymorphonuclear leukocytes (PMNs) begin with rolling as the first step in PMN sequestration. As the PMN slows, tighter interactions between CD18 (on PMN) and intercellular adhesion molecule-1 (on endothelium) cause the second phase of the PMN-EC interaction called sticking. The final step, the diapedesis involves the coordination of many factors

exhibits temporary contractile failure even though it is alive and aerobic.[3] Much of the inflammatory response results from intensified leukocyte–endothelial cell interactions via enhanced expression of adhesion molecules. A burst of reactive oxygen species liberated during the first few minutes of reperfusion is probably the cause of this contractile failure (Figure 17.2). Alterations in Ca^{2+} homeostasis rather than alteration of the contractile apparatus are probably the consequence of reactive oxygen species generation and the origin of this dysfunction.[4]

Although much experimental evidence exists in support of the reperfusion component of injury, ischemia without following reperfusion will cause the destruction of most of the ischemic myocardium. This leads to an obvious paradox: the need for re-establishing blood flow at the expense of a profound inflammatory response.[3]

In the present review, we will describe the different mouse models for myocardial ischemia–reperfusion. With the help of the big variety of genetically manipulated mice the pathophysiological effects of the targeted genes can be assessed and should bring some new insights about ischemia–reperfusion.

Ischemia–reperfusion models

Open chest ischemia–reperfusion model

In 1995 Michael *et al*.[5] first described the open chest *in vivo* mouse model. Mice were anesthetised with phenobarbital (50 mg/kg, i.p.), fixed in the supine position by taping the extremities and the upper jaw. The midline skin incision from the xiphoid process to the submentum was made. After separating the salivary glands, the muscles overlying the trachea were retracted, and a tracheotomy was performed. A polyethylene tube (No. 90) was carefully inserted into the trachea (about 5 mm from the larynx), taped in place to prevent dislodgement, and connected via a loose junction to a rodent ventilator (model 687; Harvard Apparatus). After ventilation (tidal volume 1.2 ml/min, rate 110 strokes/min) was started by supplementation of 100 per cent oxygen, the chest was opened by a lateral cut along the left side of the sternum. An adequate tidal volume resulted in an adequate inflation of the lungs without overexpression. The whole procedure was aided by a microscope (Olympus SZH 10). With an electrocoagulator, intercostal blood vessels were coagulated. The chest walls were then retracted by use of 6-0 silk suture for better visualisation of the heart. After removing the pericardial sac and slightly retracting the left auricle, the left descending artery (LAD) became clearly visible. A 1 mm section of a PE-10 tubing was placed on top of the LAD to secure the ligation of the LAD without damaging the artery. The LAD ligation was done with a 8-0 silk and was evident by discoloration of the left ventricle (Figure 17.3). The retraction sutures were removed, and the chest wall was approximated. To prevent desiccation the chest was covered with a small moist swab. To avoid cooling of the animal, it is of great importance to use a heating pad placed under the mouse.

After a defined time of LAD occlusion, the ligature can be removed by cutting the knot on top of this PE-10 tube and reperfusion can visually be confirmed.

Minimal invasive ischemia–reperfusion model

A few years after the description of the open chest heart ischemia–reperfusion model the same group published an *in vivo* model with an implantable device for occlusion of the left anterior descending coronary artery.[6] The aim of this model was to overcome the high level of background inflammation due to the surgical trauma associated with the open chest model. The background levels of the different cytokines and other mediators of the inflammatory process often were indistinguishable from those of the ischemia–reperfusion of the myocardium. This led to the development of a chronic model of ischemia–reperfusion which allowed to dissipate the trauma and the inflammation that occurs in the acute phase of surgical manipulation, permitting a more predictable and interpretable response.

The surgical preparation of the animal was performed as follows. After that the thoracotomy was performed as described above in the ‘open chest’ model. The pericardium was dissected and an 8-0 Surgipro monofilament polypropylene suture

Figure 17.3 Open mouse chest with occluded left descending coronary artery. Photograph of open-chest mouse with occluded left descending coronary artery by the help of a PE-10 plastic tubing. The LAD ligation was done with an 8-0 silk and was evident by discoloration of the left ventricle. Arrows indicate the area at risk. For a color version of this figure, please see the images supplied on the accompanying CD

with the U-shaped tapered needle was passed under the LAD. The needle was then cut from the suture, and the two ends of the 8-0 suture were then threaded through a 0.5 mm piece of PE-10 tubing, forming a loose snare around the LAD. The PE-10 tubing had been previously soaked for 24 h in 100 per cent ethanol. Each end of the suture was then threaded through the end of a size 3 Kalt suture needle (Fine Science Tools) and exteriorized through each side of the chest wall. The chest was closed with four interrupted stitches utilising 6-0 sutures, with care taken to avoid pneumothorax. The ends of the exteriorised 8-0 suture were then tucked under the skin, which was then also closed with 6-0 sutures. The animal was removed from the respirator, the endotracheal tube was withdrawn and kept warm with a heat lamp, and the animal was allowed to breathe 100 per cent O_2 via a nasal cone until full recovery of consciousness.

Ischemia without reperfusion

Similar to the *in vivo* open chest model for myocardial ischemia–reperfusion the thorax of the mice is opened and prepared in this model. Because reperfusion is not demanded, the LAD ligation was done with an 8-0 silk and was evident by discoloration of the corresponding regions of the left ventricle.[7] Afterwards, the retraction sutures were removed and the chest wall and skin were closed with sutures, and the animals were allowed to recover. According to the experimental protocol they can be killed after induction of a transmural myocardial infarction with any desired time of ischemia. This protocol seems to be important for heart failure studies.

Ischemia–reperfusion with ischemic preconditioning

Among the first who demonstrated the early phase of ischemic preconditioning in the myocardium in the *in vivo* mouse model were Miller *et al*.[8] We also used this protocol and showed its highly effectiveness in inducing a significant limitation of the myocardial damage.[9] After dissecting the pericardium an 8-0 silk suture with a U-shaped needle was passed under the LAD. After cutting the needle from the suture the LAD ligation was done with an 8-0 silk and was evident by discoloration of the left ventricle. For the preconditioning protocol the knot on top of the 1 mm plastic tube was tighten carefully and loosen after the given time. Great attention should be paid to avoid damage of the LAD. The use of fine surgical instruments is essential for all procedures (Figure 17.4). For preconditioning, mice underwent three cycles of 5 min artery occlusion/5 min reperfusion, respectively. Ten minutes later, the animals underwent 30 min of coronary occlusion of the artery, followed by 2 h of reperfusion. With this protocol it is possible to demonstrate a reduction of the infarction of about 50 per cent. The mechanism leading to that reduction of the infarction is still not fully elucidated. A number of possible mechanisms and various signaling pathways that may contribute were published. Among the most important

Figure 17.4 Surgical instruments for performing the open-chest mouse model. The normal surgical scissors is used for opening the skin and the chest wall. With help of an electrocoagulator the intercostal blood vessels were coagulated before opening with the scissors. The small pair of tweezers is used for preparing the small parts such as bring into position the 1-mm section of a PE-10 tubing on top of the LAD to secure the ligation of the blood vessel. Also the small scissors is used for the wispy parts such as opening the pericardial sac and cutting the thin silk after ligation. For a color version of this figure, please see the images supplied on the accompanying CD

were reactive oxygen species, isoforms of the protein kinase C (PKC), and adenosine.

Langendorf model (*ex vivo*)

Animals are usually injected with heparin (1000 U/kg, i.p.) 20 min prior to the experimental protocol. To anesthetise the animal, ketamine/xylazine has been the drug of choice in mice (0.1 ml/100 g, i.p.) since it has little direct cardiac toxicity. Once the animal is anesthetised, a surgical incision is made posterior to the xiphoid process. Cut superiorly until reaching the xiphoid process and make another incision running down the chest cavity. Continue cutting through the sternum until the diaphragm is evident. Cut down along the diaphragm to avoid damaging the heart. The rib cage may be dissected and removed. To remove the heart, pick the organ

up between the index finger and thumb and cut the aorta below. Place the heart in a weigh bath with some of the Ca^{2+}-containing buffer and weigh the organ. While the heart is in the buffer, carefully remove all remnant tissue around the organ, specifically exposing the aorta. Make sure that there is enough aortic tissue to allow adequate perfusion superiorly to the carotid bifurcation. Holding the aorta with two forceps, lift the heart from the buffer and place on the perfusion cannula, that should have buffer running through at a slow rate. Clamp the aorta to the perfusion needle and tie it (below the branches) with a piece of surgical thread. Increase the buffer flow rate until the drops fall between 5 and 10 times per minute. If the procedure is performed successfully, the carotid arteries will fill with buffer and become clear, the heart will begin to beat rhythmically and the drops will become clear.

Once the heart is successfully hung, it is perfused (at 37°C) with Krebs–Henseleit bicarbonate (KHB) buffer containing (in mM): 118 NaCl, 4.7 KCl, 1.25 $CaCl_2$, 1.2 $MgSO_4$, 1.2 KH_2PO_4, 25 $NaHCO_3$, 10 *N*-[2-hydro-ethyl]-piperazine-*N*′-[2-ethanesulfonic acid] (HEPES) and 11.1 glucose, equilibrated with 5%CO_2–95% O_2.[10]

Measurement of infarction size

Scoring of the reperfused myocardium

For quantitative estimation of tissue damage the previously published scoring system by Zingarelli *et al.*[11] can be used. For that purpose the hearts were harvested and cut into two portions 1 mm below the ligation suture. Tissues were fixed in 4 per cent paraformaldehyde at 4°C overnight and embedded in paraffin. Sections of 5 μm were cut from the cross area and stained with hematoxylin and eosin (HE) for histological evaluation of tissue damage. According to the score from Zingarelli,[11] the following criteria were considered: score 0, no damage; score 1 (mild), interstitial edema and focal necrosis; score 2 (moderate), diffuse myocardial cell swelling and necrosis; score 3 (severe), necrosis with the presence of contraction bands and neutrophil infiltrate; and score 4 (highly severe), widespread necrosis with the presence of contraction bands, neutrophil infiltrate, and haemorrhage. Usually about 10 animals per group should be used for doing the statistical analysis.

Assessment of area at risk and infarction size with Evans blue and TTC-staining

The aorta was cannulated with a 22G Luer stub, and 1 per cent Evans blue was perfused into the aorta and coronary arteries with distribution throughout the ventricular wall proximal to the coronary artery ligature. The left ventricle of each heart was excised and weighed. After this procedure, the heart was sectioned transversely into five sections with one section being made at the site of the ligature, and the sections were weighed. Sections of the ventricle above the site of ligature

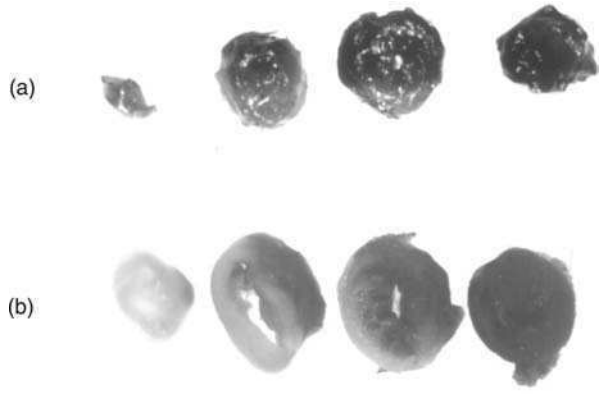

Figure 17.5 Cross-sections of the stained heart. (a) Areas at risk are delineated by Evans blue dye in a representative heart with occlusion of the left descending coronary artery. All areas that stain blue were therefore not at risk. (b) Areas that appear pale white are infarcted. Areas that remain red were not infarcted but were within the area at risk. Transverse sections are from the apex to the base (from left to right side). For a color version of this figure, please see the images supplied on the accompanying CD

were uniformly completely blue. Sections of the ventricle from the level of the ligature to the apex, which have areas that are not blue (the area at risk) are then incubated in 1.5% triphenyltetrazoliumchloride (TTC). After TTC staining, viable myocardium stains brick red and the infarct appears pale white (Figure 17.5). The apical side of each slice was imaged, and the area of infarction for each slice was determined by computerized planimetry using an image analysis software program (OPTIMAS, Bioscan, Redmond, WA, USA). The colour camera system (TEC-470, Optronics Engineering, Goleta, CA, USA) has frame-grabbed support via an ALR 486/66 MHz PC and both are connected to a Leitz Diaplan microscope. Images were acquired by OPTIMAS via the frame grabber and stored for later analysis. Colour enhancement was used to accentuate the differences between areas that are stained blue, red or which remain pale. The size of infarction was determined by the following equations: weight of infarction $= (A_1 \times WT_1) + (A_2 \times WT_2) + (A_3 \times WT_3) + \ldots$, where A is the percent area of infarction by planimetry from subscribed numbers 1–4 representing sections, and WT is weight of the same numbered sections. Percentage of infarcted LV is (WT of infarction/WT of LV) $\times$ 100. Area at risk as percentage of LV was calculated by (WT of LV – WT of LV stained blue)/WT of LV. The weight of LV stained blue was calculated in a similar fashion sum of products of the percent area of each slice $\times$ the weight of the representative slice.[5]

Measurement of the infarction area with transmission microscope

After reperfusion, the hearts were harvested and cut into two portions 1 mm below the ligation suture. Tissues were fixed in 4 per cent paraformaldehyde at 4°C overnight

and embedded in paraffin. Sections of 5 μm were cut from the cross area and stained with HE for histological evaluation of tissue damage.

The measurement of the infarct or the scar area was done by reviewing the sections with a B×60 microscope (Zeiss, Jena, Germany) equipped with a Sony 3CCD camera and television monitor. A transmission scanning microscope (Bio-Rad), equipped with a 488 nm argon ion laser and Plan Neofluar 10 × 0.3 oculars connected with the program START LSM 510 was used to scan the images. The scar was defined as the region between the living myocytes and the cardiac membrane. Areas were measured and recorded in square micrometers.[12]

Despite the fact, that the extension of a myocardial infarction is a three-dimensional one, this two-dimensional approach has some practical advantages. The first one is that the above mentioned technique with 1 per cent Evans blue and 1.5 per cent TTC shows good results after at least a few hours of ischemia. For doing ischemia–reperfusion studies this time frame usually is too long, so that other techniques are desirable. The second one is that due to the small size of a murine heart the measurement of the infarction area after staining with Evans blue is relatively inaccurate. This is mainly caused by the unintentional diffusion of the staining colour into the area at risk. The Evans blue staining therefore seems to be much more suitable for bigger animal hearts like those of a pig or a dog. The third one is that the technique by use of a transmission scanning microscope is quite easy to perform, and is less time consuming than the Evans blue staining.

Measurement of the cardiac enzymes

The measurement of blood concentrations of cardiac enzymes can be used as an index of cardiac cellular damage. We and others demonstrated a very good correlation between the markers for cardiac damage and the size of myocardial infarction.[7]

Heparin-blood can be collected when the mice were sacrificed. Usually the blood is taken by puncture of the inferior vena cava. Blood concentrations of troponin T were measured as an index of cardiac cellular damage by using the quantitative rapid assay kit (Roche Diagnostics, Mannheim, Germany). A 10 ml volume of plasma was used, and each test strip was rechecked visually.

Creatine kinase and lactate dehydrogenase isoenzyme 1 (LDH-1) were electrophoretically analysed using commercially available kits (Paragon, Fullerton, CA, USA). The gels were scanned with a densitometer and the relative activity of each isoenzyme fraction was calculated against total enzyme activities.

Echocardiography (transthoracic and transesophageal)

Transthoracic echocardiography was performed using a Sonos 5500 ultrasound machine (Hewlett Packard Co.) with a 12 MHz phased array transducer and a

frame rate of 41/s. The transducer was covered with a surgical latex glove finger filled by ultrasound transmission gel to provide a standoff of 0.5∼0.7 cm. The transducer was used at a depth setting of 2 cm to optimise resolution. Mice were anesthetised with a half dose of the anesthetic mixture used for open-chest surgery to maintain light anesthesia and spontaneous breath. The chest was shaved. Mice were placed on a heating pad in a shallow left lateral position and a standard lead II electrocardiogram was recorded for heart rate measurement. After a two-dimensional (2D) image was obtained in parasternal short axis view at the level close to papillary muscles, a 2D guided M-mode trace crossing the anterior and posterior wall of the LV was recorded at a sweep speed of 100 mm/s. Caution was given not to apply excessive pressure over the chest, which could cause bradycardia and deformation of the heart. The following parameters were measured digitally on the M-mode tracings and averaged from three cardiac cycles: LV internal end-systolic and end-diastolic diameters (LVESd, LVEDd), external LV diastolic diameter (ExLVDd), anterior and posterior wall thickness of systole and diastole (Aws th, Awd th, Pws th and Pwd th). The measurements were made using the leading edge method of the American Society of Echocardiography.[13] Particular attention was given to acquire the largest LVEDd from the 2D image in infarcted mice to avoid underestimation of LV dilatation due to asymmetric alterations in the LV cavity. LV fractional shortening (FS) was calculated as $FS\% = [(LVEDd - LVESd)/LVEDd] \times 100$. LV mass was calculated following an uncorrected cube formula: $LV\ mass = [(LVEDd + Awd\ th + Pwd\ th)^3 - LVEDd^3] \times 1.055$, where 1.055 is the gravity of myocardium.[14,15] Scherrer-Crosbie et al described a three-dimensional echocardiographic assessment of left ventricular wall motion abnormalities after infarction in the mouse heart.[16] Also a transesophageal echocardiographic approach is described for assessment of the left ventricular function in mice after a myocardial infarction.[17]

Magnetic resonance imaging (MRI) assessment of murine cardiac function

The group around Weiss described an *in vivo* MRI assessment technique of the murine heart.[18] Therefore high-resolution images were obtained to confirm position, define the regions of metabolic interest, or quantify ventricular function. After the cradle containing the mouse was positioned in the magnet, and the position of the spectroscopy coil relative to the heart ascertained by fast scout images, an ECG-gated, spin-echo transverse image for correlation with spectroscopic data was obtained [echo time (TE) = 11 ms, recycle time (TR) = ∼500 ms, slice thickness (ST) = 1.6 mm, field of view (FOV) = 32 mm, matrix size = 256 × 128 (zero-filled to 256 × 256), numerical aperture = 2–8, total acquisition time = 2–8 min]. Diffusion gradients were applied symmetrically on both sides of the refocusing pulse to crush the blood signal and minimize flow artifacts. In some mice, a complete set of multislice short-axis images (ST = 1.2 mm, no gap between slices) for end diastole and end systole was acquired. Each slice was acquired exactly at the same time point

in the R-R interval by waiting one R-R interval between slices. Left ventricular volumes at end diastole and end systole were determined using the software package NIH Image version 1.52 for a Macintosh computer from these multislice images (matrix size 256×256). The left ventricular ejection fraction was calculated from the relative difference in end-diastolic and end-systolic cavity volumes. For further details please see the above cited paper from Chacko *et al*.[18]

Single photon emission computed tomography (SPECT)

Early pinhole SPECT studies of cardiac function in a rat model of myocardial infarct gave good agreement between *in vivo* imaging data and postmortem autoradiographic and staining studies.[19] The importance of myocardial imaging in small animals has led to the development of SPECT systems designed specifically for this application.[20] Phantom measurements of a simulated mouse left ventricle indicated that myocardial perfusion defects could be detected with very high accuracy on SPECT images, which correlated with the true size of the defect. This has important implications for the study of cardiac function in mice, and may be useful in phenotyping transgenic mouse models of heart disease.

Electrocardiogram and *in vivo* left ventricular pressure–volume measurements

Electrocardiographic measurements

Continuous ECG recordings can be made with a two-lead ECG Hemodynamic Data Acquisition System apparatus (Instrument Services, Maastricht, The Netherlands) to detect arrhythmias. The first lead was positioned in the left lower leg, the second lead in the right upper leg. The recordings were made in trend save mode (every 5 s) with a sample interval of 1 ms and were started at the beginning of the surgical procedure.[21]

In vivo left ventricular pressure–volume measurements

Left ventricular function can be assessed by simultaneous measurement of left ventricular pressure and volume. This can be done with a Sigma SA (CDLeycom, Zoetermeer, The Netherlands) single segment data acquisition module. The system operated on a constant excitation current of 30 μA to prevent interaction with the murine cardiac conduction system. The time-varying ventricular volume $V(t)$ was estimated from $V(t) = \rho L^2\ [G(t) - G^P]$ where ρ (rho) is the mouse specific blood resistance, L indicates the distance between the sensing electrodes and $G(t)$ the instantaneous conductance. Parallel conductance G^P was determined by hypertonic saline injection and substrate offline. CONDUCT 2000 software (CDL-eycom) was used for data acquisition and Cirlab software (LUMC, Leiden, The Netherlands)

was used for offline data analysis. A 1.4 Fr Millar pressure-conductance catheter (SPR-719, Millar Instruments, Houston, TX, USA) was used for the LV pressure–volume measurements. The pressure signal was calibrated with a mercury manometer at the beginning of each experiment. Baseline zero reference was obtained by placing the sensor in 37°C normal saline before insertion. Acquired resistance was converted to relative volume units (RVU) by the Sigma SA acquisition module. The correction for electric field inhomogenity α was calculated by conductance and echocardiographic measurements of end-diastolic volume. The specific resistance of murine blood (ρ) was determined by using a Rho-cuvette (CDLeyom). The murine specific Rho-cuvette has a content of 150 µl.[21]

Different mouse types

Beside the use of conventional laboratory mice the availability of a broad variety of genetically altered mice in the last years lead to a rise in interest for these mice.

Knockout mice

Knockout mice are produced by a technique called gene targeting. This is the replacement of one gene sequence, the sequence resident in the mouse genome, with a related sequence that has been modified in the laboratory to contain a mutation. The replacement occurs by a process called homologous recombination, where two very similar DNA sequences line up next to each other and exchange parts. Gene targeting is carried out in mouse embryonic stem cells (ES cells). These cells are derived from a very early (usually male) mouse embryo and can therefore differentiate into all types of cell when introduced into another embryo. The aim is to get the modified ES cells to contribute to the germ line, which gives rise to sperm. Some sperm are produced that carry the desired mutation, and if these fertilise a normal egg, mice develop with one copy of the mutated gene in every cell. Interbreeding such mice will produce some homozygous individuals in the next generation – mice inheriting the mutation from both parents and therefore carrying two copies of the mutant gene. These are knockout mice. Although knockout mice are extremely useful in studying gene function, producing custom knockout mice is very expensive. There are now hundreds of knockout mice commercially available. These can be purchased from a variety of companies, one being The Jackson Laboratory in Bar Harbor, ME, USA. Also double knockout mice are now available to investigate more complex questions. It is also important to consider the cost of care for genetically altered animals, as they require special transgenetic core facilities where staff can assist researchers with housing and taking proper measures to keep these knockout animals at optimal conditions for research purposes. Other limitations of the knockout mice were the developmental defects, so that many knockout mice die while they are still embryos. Even if a mouse survives, several mouse models have somewhat different physical and physiological (or phenotypic) traits than their human counterparts. The goal of

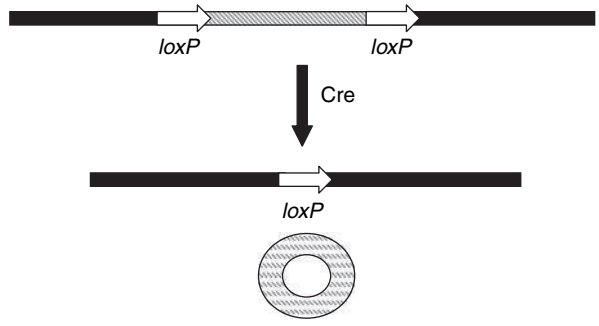

Figure 17.6 *Cre/LoxP* site-specific recombination. *Cre* recombinase recognizes a consensus sequence (*LoxP* site) and catalyses recombination between two *LoxP* sites. If the sites are placed on the same DNA strand in the same orientation the recombination results in a deletion of the intervening sequence

conventional knockout technology is to knock out both alleles so that the gene is entirely absent from all cells. The purpose of the more advanced types of knockouts, the so called conditional knockouts, in contrast, is to delete a gene in a particular organ, cell type, or stage of development.

Conditional knockout mice

The latest wave of mouse models has advanced beyond generalised gene knockouts to develop new strategies for the precision engineering of endogenous genes within specific cell types. The most successful approach has been based on the generation of mice that harbour floxed alleles, which contain *LoxP* recognition sequences that flank a critical exon that is required for the expression or function of the gene of interest.[22] These mice are generated by homologous recombination of targeting vectors in embryonic stem cells that bring in the *LoxP* sites into the germ line (Figure 17.6). The floxed allele mice express the normal gene product, because the *LoxP* sites are located within the intron sequences that are spliced out during RNA processing. However, the intervening sequences between the *LoxP* sites can be excised by the expression of *Cre* recombinase, which is brought into the genetic background of the floxed allele mice via interbreeding. By controlling the expression of *Cre* recombinase to a specific tissue, for example to the ventricular chamber, it is possible to generate mice that harbour a ventricular-restricted mutation in a gene that is widely expressed, thereby allowing a direct examination of the role of a given gene within cardiac muscle.[23]

Transgenic mice

A transgenic mouse contains additional, artificially-introduced genetic material in every cell. This often confers a gain of function, for example the mouse may produce

a new protein, but a loss of function may occur if the integrated DNA interrupts another gene. A transgenic mouse is a very useful system for studying mammalian gene function and regulation because analysis is carried out on the whole organism. DNA can be integrated by injecting it into the pronucleus of a fertilized ovum. The DNA can integrate anywhere in the genome, and multiple copies often integrate in a head-to-tail fashion. There is no need for homology between the injected DNA and the host genome.

Conclusion

Due to the fact that coronary heart disease is still the number one killer in the western world, scientists and doctors are encouraged to find new therapeutic strategies. Due to ethical considerations experimental ischemia–reperfusion studies almost exclusively can be performed in laboratory animals. The availability of a broad variety of genetically altered mice in the last years led to a remarkable rise in the interest for experimental mouse models.

This review describes the different mouse ischemia–reperfusion models and the techniques for quantification of ischemia–reperfusion damage. Beside the conventional *in vivo* mouse model for ischemia–reperfusion, the open chest mouse model, also newer ones, such as the closed chest ischemia–reperfusion model are described. Further, the novel quantification of ischemia–reperfusion damage by help of a transmission microscope is explained. Also known techniques established in clinical practice in humans, such as echocardiography and MRI, are described for mice. The advantages and disadvantages of the different approaches also were discussed. The given company names for the different technical devices should serve just as a proposal. We know that there are a number of equal technical devices manufactured by different companies. This review should help the interested scientists to choose the most suitable mouse ischemia–reperfusion model to clarify their specific questions.

With new insights gained in ischemia–reperfusion damage by the use of mouse models new pathways will be revealed. This findings could generate new hypotheses that can be tested in human subjects and may lead to the development of new therapeutic strategies in future.

References

1. Pfeffer MA, Braunwald E. Ventricular remodeling after myocardial infarction. *Circulation* 1990; **81**: 1161–1172.
2. Kloner RA, Jennings RB. Consequences of brief ischemia: stunning, preconditioning, and their clinical implications: part 1. *Circulation* 2001; **104**: 2981–2989.
3. Braunwald E, Kloner RA. The stunned myocardium: prolonged, postischemic ventricular dysfunction. *Circulation* 1982; **66**: 1146–1149.

4. Bolli R, Jeroudi MO, Patel BS, DuBose CM, Lai EK, Roberts R, McCay PB. Direct evidence that oxygen–derived free radicals contribute to postischemic myocardial dysfunction in the intact dog. *Proc Natl Acad Sci* U S A 1999; **86**: 4695–4699.
5. Michael LH, Entman ML, Hartley CJ, et al. Myocardial ischemia and reperfusion: a murine model. *Am J Physiol* 1995; **269**: H2147–H2154.
6. Nossuli TO, Lakshminarayana V, Baumgarten G, Taffet GE, Ballantyne CM, Michael LH, Entman ML. A chronic mouse model of myokardial ischemia–reperfusion: essential in cytokine studies. *Am J Physiol Heart Circ Physiol* 2000; **278**: H1049–H1055.
7. Metzler B, Lercher-Hammerer A, Dietrich H, Jehle J, Pachinger O, Mair J. Plasma cardiac troponin T closely correlates with infarct size in a mouse model of acute myocardial infarction. *Clinica Chimica Acta* 2002; **325**: 87–90.
8. Miller DL, Van Winkle DM. Ischemic preconditioning limits infarct size following regional ischemia–reperfusion in in-situ mouse hearts. *Cardiovasc Res* 1994; **42**: 680–684.
9. Mayr M, Metzler B, Chung Y, et al. Ischemic preconditioning exaggerates cardiac damage in PKC-δ null mice. *Am J Physiology* 2004; **287**: H946–H956.
10. Ren J, Wold LE. Measirement of cardiac mechanical function in isolated ventricular myocytes from rats and mice by coputerized video-based imaging. *Biol Proc Online* 2001; **3**: 43–53.
11. Zingarelli B, Salzman AL, Szabo C. Genetic disruption of poly (ADP-ribose) synthetase inhibits the expression of P-selectin and intercellular adhesion molecule-1 in myocardial ischemia/reperfusion injury. *Circ Res* 1998; **83**: 85–94.
12. Metzler B, Mair J, Lercher A, Schaber C, Hintringer F, Pachinger O, Xu Q. Mouse model of myocardial remodeling after ischemia: role of intercellular adhesion molecule-1. *Cardivasc Res* 2001; **49**: 399–407.
13. Sahn DJ, DeMaria A, Kisslo J, Weyman A. Recommendations regarding quantitation in M-mode echocardiography: results of a survey of echocardiographic measurements. *Circulation* 1978; **58**: 1072–1083.
14. Tanaka N, Dalton N, Mao L, et al. Transthoracic echocardiography in models of cardiac disease in the mouse. *Circulation* 1996; **94**: 1109–1117.
15. Pombo JF, Troy BL, Russell RO. Left ventricular volumes and ejection fraction by echocardiography. *Circulation* 1971; **43**: 480–490.
16. Scherrer–Crosbie M, Steudel W, Hunziker PR, Liel-Cohen N, Ullrich R, Zapol WM, Picard MH. Three-dimensional echocardiographic assessment of left ventricular wall motion abnormalities in mouse myocardial infarction. *J Am Soc Echocardiogr* 1999; **12**: 834–840.
17. Ramani R, Mathier M, Dawson J, McTiernan CF, Feldman AM. Assessment of infarct size and myocardial function in mice using transesophageal echocardiography. *J Am Soc Echocardiogr* 2004; **17**: 649–653.
18. Chacko VP, Aresta F, Chacko SM, Weiss RG. MRI/MRS assessment of in vivo murine cardiac metabolism, morphology, and function at physiological heart rates. *Am J Physiol* 2000; **279**: H2218–2224.
19. Yukihiro M, Inoue T, Iwasaki T, Tomiyoshi K, Erlandsson K, Endo K. Myocardial infarction in rats: high resolution single photon emission tomography imaging with a pinhole collimator. *Eur J Nucl Med* 1996; **23**: 896–900.
20. Wu MC, HasegawacBH, Dae MW. Performance evaluation of a pinhole SPECT system for myocardial perfusion imaging of mice. *Med Phys* 2002; **29**: 2830–2839.

21. Lips DJ, van der Nagel T, Steendijk P, et al. Left ventricular pressure–volume measurements in mice: comparison of closed-chest versus open-chest approach. *Basic Res Cardiol* 2004; **99**: 351–359.
22. RajewskY K, Gu H, Kühn R, Betz UA, Müller W, Roes J, Schwenk F. Conditional gene targeting. *J Clin Invest* 1996; **98**: 600–603.
23. Chien KR. To cre or not to cre. The next generation of mouse models of human cardiac disease. *Circ Res* 2001; **88**: 546–549.

18

Cardiac hypertrophy

David J. Grieve, Alison C. Cave and **Ajay M Shah**

Cardiovascular Division, King's College London, London, UK

Introduction

The heart responds to a sustained increase in cardiac work, commonly secondary to hypertension, by the process of left ventricular hypertrophy (LVH).[1] The most obvious feature of LVH is a thickening of the LV wall, which tends to normalise increased wall stress. However, the underlying mechanisms of LVH are complex and involve a series of alterations in cardiac myocyte, extracellular matrix, coronary vessel and chamber structure and function that are driven largely by changes in gene expression. Sustained pressure overload and chronic LVH eventually leads to contractile dysfunction, ventricular dilatation and ultimately heart failure. The occurrence of chronic heart failure is accompanied by substantial morbidity and mortality.[2] Pathological LVH as described above differs from physiological hypertrophy (e.g. in response to chronic exercise), where the heart appears to be well adapted to the increased workload and there is no progression to heart failure.

The mechanisms responsible for the development of LVH and the subsequent progression or transition to chronic heart failure remain poorly defined and are the subject of intense investigation.[3] Animal models that mimic the initiation and progression of the human condition have significantly advanced the study of these mechanisms. In particular, the availability of numerous specific gene-modified animals has made the mouse one of the most informative animal models to study in the field of LVH and heart failure. On the other hand, the small size of mice poses significant technical challenges with regard to the study of *in vivo* LVH models. Here, we provide detailed descriptions of three commonly used experimental models of murine cardiac hypertrophy as well as a brief description of the detailed

A Handbook of Mouse Models of Cardiovascular Disease Edited by Qinbo Xu

characterization of cardiovascular hemodynamics in such a model, in order to able to relate changes in molecular mechanisms to alterations in cardiac phenotype and function.

Materials and methods

Animals

The ensuing methods are optimal for adult male C57BL6/J mice, this being the most common background strain for most genetically modified mice used in cardiovascular studies. The use of other strains would most likely require at least minor modifications in the protocols described. All the surgical procedures performed in our laboratory are undertaken in strict accordance with the Guidance on the Operation of the Animals (Scientific Procedures) Act 1986 (Her Majesty's Stationery Office, London, UK) and institutional guidelines.

Anesthesia

The type of anesthetic and the depth of anesthesia can cause profound alterations in myocardial contractility and hemodynamics.[4] Therefore it is important to use an anesthetic regime that has minimal cardiovascular effects. Although many different anesthetic agents are used in the study of murine cardiovascular physiology in the literature, agents such as urethane, sodium pentobarbital and ketamine/xylazine can cause profound systemic hemodynamic depression.[5] It is therefore advisable to avoid such agents when studying cardiovascular (patho)physiology. In our experience, the preferred agent is the inhalational anesthetic, isofluorane, which has been shown to have minimal cardiovascular effects.[5] Isofluorane is also relatively short acting so that experimental animals are able to recover rapidly after completion of surgery, in contrast to injectable anesthetics such as sodium pentobarbital, where recovery can take 2–3 h. In addition, it is usually not necessary to withhold food or water from the mice prior to surgery in our experience. The procedures described below are relatively short and no significant anesthetic-related adverse effects have been observed.

Pressure overload-induced LVH

Aortic constriction is one of the most commonly used methods to induce LVH. There are two main variations of the method, one involving constriction at the aortic arch (known as transverse aortic constriction; TAC) and the other at the suprarenal abdominal aorta.

Transverse aortic constriction

This method was initially established in mice mainly by Rockman and colleagues,[6] and has since become widely used.[7–10] TAC results in a rapid development of LVH, with a 40 per cent increase in LV/body weight ratio within 7 days, and carries a relatively low perioperative mortality of approximately 15 per cent in experienced hands.[6]

Adult male mice of varying ages (8–26 weeks) can be used.[6,9] Anesthesia has typically been achieved with a mixture of ketamine (100 mg/kg, i.p.), xylazine (5 mg/kg, i.p.) and morphine (2.5 mg/kg, i.p.), but other agents such as isofluorane can also be used (see later). Essentially the same regime may be used for coronary ligation surgery. Appropriate analgesia (e.g. buprenorphine, 0.05 mg/kg, i.m.) is administered at this time. The animal should then be placed on its back and the neck and chest shaved with an animal hair clipper (VetTech Solutions, PO001). Mice may be intubated either by tracheotomy or non-invasively,[11] although it is much easier if the trachea can be visualised during intubation. In order to do this, a midline cervical incision of approximately 1 cm is made and the salivary glands are separated by blunt dissection using a probe (John Weiss, 0105072) to expose the trachea and carotid arteries.[6] The mouse is then intubated by holding the tongue with small forceps and introducing an 18G intubation tube (supplied with MiniVent, Harvard Apparatus) with the other hand. The intubation tube is advanced into the trachea (taking care not to enter the esophagus) and taped in position to avoid it being sucked too far into the lungs. Once in place, the intubation tube is connected to a ventilator (MiniVent, Harvard Apparatus) and the mouse ventilated with room air. For a 25–30 g mouse, we typically use a stroke volume of 250 µl at a rate of 150 strokes/min, although these can be adjusted for animal weight.

Once the mouse has been successfully intubated and ventilated, the chest cavity is entered at the level of the second left intercostal space.[6] First, a transverse cut of approximately 5 mm is made in the skin about 2 mm from the left upper sternal border. Then, both layers of pectoral muscle are cut with sharp scissors, taking care to avoid the mammary vessels, thus exposing the semitransparent chest wall, through which the ribs and lungs are clearly visible. The chest cavity is then opened with scissors along the second left intercostal space, avoiding the internal mammary artery that runs along the sternal border on the inner surface of the chest wall. The second and third ribs are spread to a distance of about 5 mm using a self-retaining retractor (Fine Science Tools, 17002-02), taking care not to damage the lungs (which may be protected by a damp swab). The pericardium is then removed with small dissection scissors (World Precision Instruments, 501234) before the aortic arch is isolated with the blunt-ended probe (Figure 18.1). A 7/0 nylon suture is then passed around the transverse aorta between the right subclavian and left carotid artery using a curved suture holder (Aesculap, BM801R), before being tied down onto a blunted 27G needle (for 18–22 g mice; needle gauge can be adjusted for body weight). The needle is then quickly removed resulting in an approximate 70 per cent constriction of the aorta.

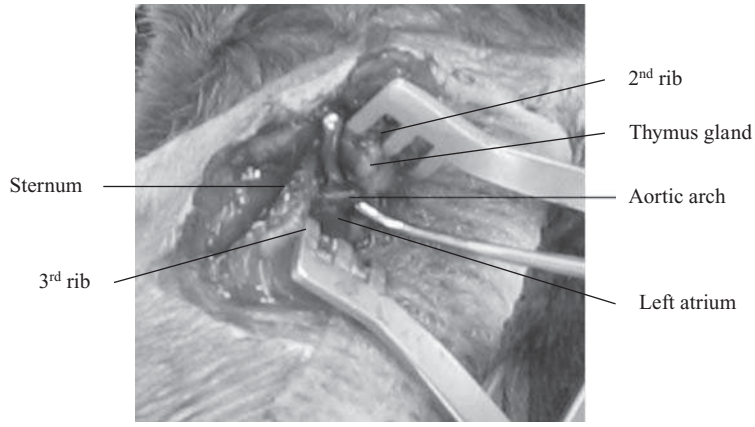

Figure 18.1 Photograph of the surgical preparation for transverse aortic constriction. The second and third ribs are spread with a retractor and the aortic arch isolated using a blunt-ended probe. For a color version of this figure, please see the images supplied on the accompanying CD

After TAC, the retractor is carefully removed and the pneumothorax evacuated by occluding the ventilator outflow for 1 s before each suture is tied. Typically, three interrupted 5/0 vicryl sutures tied around the second and third ribs are required to achieve complete chest closure. With each tie slight pressure is applied on the chest with the needle holder in order to extrude free air within the chest cavity. The skin layer is then closed in a similar fashion before the intubation tube is removed. Animals are then allowed to recover in a heated recovery chamber at 30 °C for 24 h.

In acute studies, it is possible to measure the pressure gradient across the aortic constriction either during or after surgery.[6,9] This is done by cannulating both the right and left carotid arteries with flame-stretched PE50 tubing connected to fluid-filled pressure transducers. Studies have shown that under ketamine/xylazine anesthesia, the pressure gradient across the carotid arteries after TAC is 45–50 mmHg and is reproducible.[6,9]

As a control for TAC, it is important to undertake sham operations which involve an identical procedure apart from aortic constriction.

Suprarenal abdominal aortic constriction

The method of suprarenal abdominal aortic constriction is a simpler alternative to TAC and has been the preferred method in our laboratory. With this method, there is no need for thoracotomy or intubation/ventilation and the perioperative mortality is approximately 10 per cent or less. It is a much faster and less traumatic procedure than TAC. However, since the constriction is more distal than in TAC and there are more branch vessels (left carotid, spinal, celiac arteries, etc.) between the stenosis and the heart, the degree of pressure overload can be more variable so that this method requires more precise surgical criteria to ensure the successful development of LVH. In addition, suprarenal abdominal constriction results in a greater degree of activation

of the renin–angiotensin system than TAC,[12] which may be an important consideration in some studies.

We typically use young adult male mice weighing 15–18 g (5–6 weeks old) in which the growth of the animal (which is linear at that age) into the aortic band contributes to an increased pressure overload. Constriction with a blunted 29G needle between the celiac and superior mesenteric arteries leads to progressive development of LVH, which is significant by 1 week and reaches approximately 40 per cent by 2 weeks post-surgery.[13] The development of morphological LVH beyond 2 weeks post-surgery is accompanied by readily detectable cardiac contractile dysfunction (eg, by LV pressure-based indices or echocardiography).[14] By 8 weeks post-surgery, LV/body weight increases by 60–70 per cent, with marked LV depression although there are usually minimal clinical signs of heart failure (similar to TAC).

For abdominal aortic constriction, adult male mice (15–18 g) are first anesthetised in an induction chamber using a 2 per cent isofluorane/oxygen mixture. They are then transferred to an anesthetic mask and laid on their right side on a warming pad (VetTech Solutions, HE006) before being shaved with an animal hair clipper (VetTech Solutions, PO001). After generous application of antiseptic iodine solution, a 2 cm lateral incision is made in the skin just below the rib cage and the muscle wall is opened along the same line using scissors, taking care not to perforate the intestines. Two retractors are then inserted into the abdomen, one to move the intestines, liver and spleen to the left (John Weiss, 0107012) and the other to move the kidney to the right (Aesculap, OA310). They should be adjusted until a good field of view is obtained in which the abdominal aorta can be clearly visualised (Figure 18.2a). Once positioned, the retractors can either be held in place by metal pins or manually by an assistant (which is probably easier). A blunt-ended probe (John Weiss, 0105072) is now used to clear the surrounding fascia and connective tissue

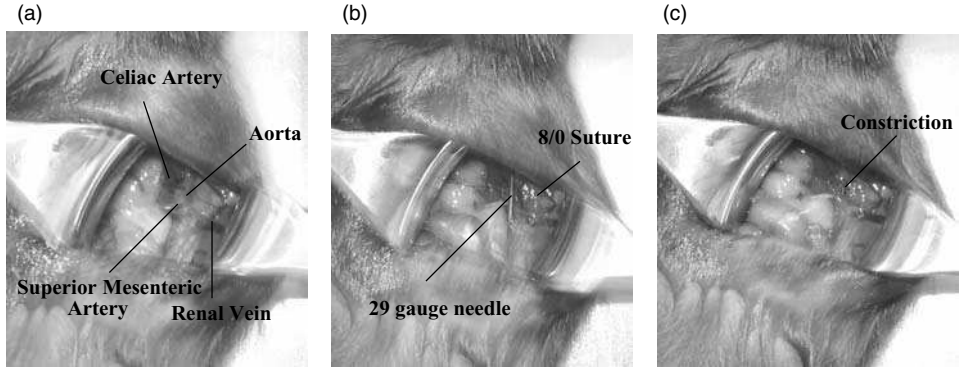

Figure 18.2 Photographs of the surgical preparation for induction of pressure overload by abdominal aortic constriction. A lateral incision is made just below the diaphragm and the abdominal aorta exposed (a). The vessel is then cleared of any adherent fascia and connective tissue before a length of suture is passed around the aorta (b). A blunted 29G needle is then laid beside the vessel and double tied. Finally, the needle is removed, resulting in an approximate 70 per cent constriction (c). For a color version of this figure, please see the images supplied on the accompanying CD

from the section of aorta between the celiac and superior mesenteric arteries. This is best achieved by using the probe in combination with a cotton bud in the other hand, which provides a slightly abrasive surface against which to move the probe. Great care should be taken when clearing the vessel as it is relatively easy to puncture the aorta. It is of paramount importance that the aorta is completely clean as any residual connective tissue may lead to a variable degree of constriction. Once the aorta is satisfactorily cleared, a length of 8/0 nylon suture is passed around the vessel between the celiac and superior mesenteric arteries, using a curved suture holder (Aesculap, BM801R). A short length of blunted 29G needle is then laid along side the aorta (Figure 18.2b) before the suture is double-tied firmly around it and the vessel. The needle is then removed resulting in an approximate 70 per cent constriction (Figure 18.2c). Assessment of invasively measured systolic blood pressure under isofluorane anesthesia indicated that aortic constriction at the abdominal site results in significant reproducible pressure overload of approximately 45 mmHg.[13] Before stitching up, 1 ml of warmed saline is added to the abdominal cavity in order to compensate for fluid loss during surgery. The muscle and skin layers are then closed separately with 5/0 vicryl using a continuous and interrupted suture, respectively. Animals are then administered buprenorphine analgesia (0.05 mg/kg, i.p.) and allowed to recover in a heated recovery chamber at 30 °C for 1 h before being returned to their cage.

As with TAC, sham operations that involve an identical procedure with the exception of aortic constriction, are performed as a control.

Pharmacologically induced hypertrophy

While pressure overload induced by aortic constriction is a clinically relevant method of inducing LVH, it involves a complex set of inducing stimuli (both mechanical and neurohumoral). Complementary models of LVH involve the infusion of specific cardioactive or vasoactive agents, e.g. angiotensin II, norepinephrine (noradrenaline), isoproterenol, typically using an osmotic infusion minipump (Alzet, Palo Alto, CA, USA) set for subcutaneous infusion. Here, we describe the use of angiotensin II infusion in this way.[13,15]

The infusion pumps continuously deliver drugs at controlled rates via osmotic displacement. They contain an empty reservoir within their core that is filled with the drug solution to be delivered. The drug reservoir is surrounded by a chamber containing a high concentration of salt, which causes water to been drawn into the pump through its semipermeable external layer. This in turn causes compression of the flexible drug reservoir and subsequent delivery of the drug solution via a flow moderator. Osmotic infusion pumps are available in several sizes and infusion rates, the selection of which depends on the animal and duration of study. For a mouse, we typically use model 1002, which is relatively small (1.5 × 0.6 cm, 0.4 g) and allows continuous infusion for up to 14 days at a rate of 0.25 µl/h. For longer durations of infusion, the pump has to be replaced. Although larger pumps capable of infusion for up to 28 days are available (model 2004), these are rather big (3.0 × 0.7 cm, 1.1 g) for

a mouse. The concentration of drug to be added to the osmotic pump must be calculated for the final desired dose and animal weight and be diluted in saline or appropriate vehicle. Agents such as angiotensin II may be infused at either a subpressor dose (up to 0.3 mg/kg/per day for C57Bl6/J mice) or a pressor dose (1.1 mg/kg/per day or greater) depending upon the experimental protocol. A subpressor infusion allows the direct effects on the heart to be potentially distinguished from effects secondary to increased blood pressure but will usually result in less hypertrophy. Subpressor or pressor angiotensin II infusion will result in readily detectable hypertrophy of about 20 per cent after 14 and 6 days, respectively.[13,15]

Surgery for implantation of osmotic infusion pumps is straightforward. The pump is filled just before surgery according to the supplier's instructions. Animals are anesthetised in an induction chamber using a 2 per cent isofluorane/oxygen mixture. They are then transferred to an anesthetic mask and laid on their front on a warming pad (VetTech Solutions, HE006). The back of the neck is shaved with an animal hair clipper (VetTech Solutions, PO001). After application of antiseptic iodine solution, a 5–10 mm vertical incision is made in the skin in the subscapular region. A large subcutaneous pocket is then made by blunt dissection using a small pair of scissors (John Weiss, 0103159) which are advanced down the back of the mouse, separating the skin away from the underlying muscle. The pump is then inserted as far as possible into the pocket with the flow moderator facing away from the incision. It is important to ensure that the subcutaneous pocket is as large as possible and that the pump is well positioned to avoid it subsequently eroding through the skin. The skin is closed with 5/0 vicryl suture using two or three interrupted stitches and buprenorphine analgesia (0.05 mg/kg, i.p.) is administered before the animals are returned to their cage. Sham operations involve an identical procedure except that the animals receive vehicle-filled instead of drug-filled osmotic pumps.

In vivo assessment of hemodynamics by pressure/microconductance

A precise characterization of cardiovascular dynamics is usually essential in order to relate molecular changes to alterations in cardiac phenotype and function. Methods that may be employed in the intact animal include echocardiography and magnetic resonance imaging (both of which are modalities that assess volume-based indices of function) while *ex vivo* assessment includes the study of isolated hearts and isolated cardiomyocytes. Optimal *in vivo* assessment is generally accepted to require the simultaneous measurement of both pressure and volume, and in larger animals (including humans) has been undertaken for many years using the analysis of LV pressure–volume relations. One of the most specific and reliable methods of undertaking this is the LV conductance technique coupled with measurement of high fidelity LV pressure.[16–18] Recent technological advances have allowed the application of this technique in mice using a commercially available 1.4 F microconductance catheter/pressure transducer (SPR-839, Millar Instruments).[19–21] The catheter consists of a high-fidelity pressure transducer flanked by four platinum electrodes. The two outermost excitation electrodes are each separated from a sensing electrode by a

distance of 0.5 mm, with a standard spacing between the two inner sensing electrodes of 4.5 mm. A constant current is applied to the excitation electrodes and the instantaneous voltage signal is then measured by the sensing electrodes, thus allowing the calculation of volume (Aria^{TM} 1 pressure–volume conductance system, Millar Instruments). Pressure data is simultaneously sampled at 1 kHz via a PowerLab module (ADInstruments). For a detailed description of the basis for volume calculations, the interested reader is referred to excellent published articles.[16,17,22]

As this technology is widely accepted as the 'gold standard' method for *in vivo* assessment of cardiac contractile function,[23] we provide a description of its use. The conductance catheter may be introduced into the LV by two routes, either by direct puncture through the LV apex or via cannulation of the right carotid artery and subsequent retrograde passage through the aortic valve.[19,24] The former method requires an open-chest preparation with intubation and ventilation while the latter may be more physiological due to the intact chest and free breathing. We usually prefer to use the carotid route in our laboratory.

Several important methodological considerations need to be addressed. The importance of anesthetic regimes that causes minimal cardiovascular effects has already been discussed. We first induce anesthesia in a chamber with a 2 per cent isofluorane/oxygen mixture. Mice are then transferred to a low-profile anesthetic mask (VetTech Solutions) and laid on their back on a warming pad (Harvard Apparatus). Maintenance of animal body temperature is essential, with changes having profound effects on heart rate. A rectal probe is inserted to allow feedback control to ensure that body temperature is maintained at 37 °C. An operating microscope with at least 10× magnification is required for carotid cannulation and catheter introduction. First, a midline cervical incision of approximately 1 cm is made in the neck and the salivary glands are separated using a blunt-ended probe (John Weiss, 0105072) in order to expose the right carotid artery. A length of 5/0 nylon suture is then tied around the distal end of the artery and taped to the anesthetic mask in order to apply a small amount of tension to the exposed vessel. The carotid artery is then carefully cleared of any adherent fat or connective tissue using sharp curved forceps (World Precision Instruments, 14097). Another length of 5/0 nylon suture is then passed around the proximal portion of the vessel (that closest to the aorta) and is looped over once, but not tied. The cut ends of the suture are then held by a needle holder (Aesculap, BM200R) which is draped over the animal's abdomen in order to create further tension on the vessel, thereby occluding blood flow to the cleared section.

Before introduction, the microconductance catheter should be soaked (for at least 30 min) in a saline-filled syringe positioned on the warming pad beside the mouse, to ensure a stable baseline, and then zeroed. A small incision is made in the artery using extra fine spring scissors (Fine Science Tools, 15000-08). The catheter is then inserted using special cannulation forceps (Fine Science Tools, 00608-11), whilst grasping the upper margin of the incision with fine forceps (Fine Science Tools, 11251-35), and advanced into the vessel until the proximal electrodes are just past the looped suture. This suture is then tied to avoid blood loss and the catheter advanced into the heart. The passage of the catheter is greatly assisted if the neck area is submerged in saline

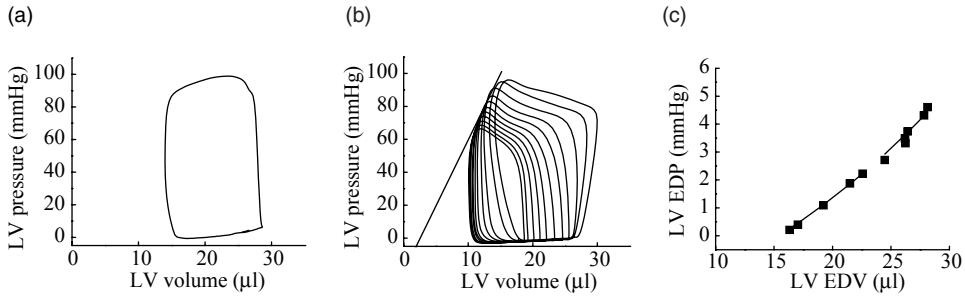

Figure 18.3 Representative examples of pressure volume data obtained from a wild type mouse. (a) steady state pressure volume loop; (b) end-systolic pressure volume relationship (ESPVR); (c) end-diastolic pressure volume relationship (EDPVR)

after the initial cannulation. The catheter usually finds its own way into the heart, although resistance may be encountered at the aortic valve; if this occurs, the catheter is gently moved back and forth until it slides into the LV. It can then be correctly oriented in the LV by gentle manipulation, using the pressure–volume trace on the computer as a reference, and taped in position. The use of echocardiography can facilitate positioning although this is not essential.

After 15–20 min equilibration time, steady state data are recorded. A representative example of a baseline pressure volume loop is shown in Figure 18.3a; typical mean steady state data are shown in Table 18.1. The inferior vena cava (IVC) is then isolated in order to study LV function under variable loading conditions, allowing analysis of both the end-systolic and end-diastolic pressure–volume relations (ESPVR and EDPVR, respectively). A small lateral incision is made just below the diaphragm and the section of IVC between it and the liver is isolated using the blunt-ended probe. The IVC is then transiently occluded for 2–3 s by applying downward pressure using a cotton bud, taking care not to perturb the heart. This results in a beat-to-beat reduction in LV filling pressure and a consequent change in the pressure–volume relation, from which the ESPVR and EDPVR can be calculated. The ESPVR is generally acknowledged to be the best load-independent measure of 'contractility'; its slope is related to the intrinsic inotropic state of the myocardium.[16,25] The slope of the EDPVR, which is exponential in shape, relates to chamber stiffness and is thought to be one of the best measures of diastolic function.[26,27] Representative examples of both the ESPVR and EDPVR are shown in Figure 18.3b and c, respectively.

In order to acquire meaningful data, the volume signal requires calibration. A detailed explanation of the underlying principles can be found in published papers.[16,17,22] Briefly, before catheter introduction, the relative volume settings on the Aria^{TM} system need to be adjusted. In order to allow for *in situ* alterations in conductance, which occur in the animal, relative volume measurements need to be converted to absolute volumes. First, the conductance catheter is submerged in a series of cylindrical holes of known diameter housed within a Plexiglas block, which are filled with blood taken from the animal at the end of the experiment. This method

Table 18.1 Hemodynamic parameters derived from pressure-volume relations in wild type mice

	Heart rate (bpm)	LVESP (mmHg)	LVEDP (mmHg)	$LVdP/dt_{max}$ (mmHg/s)	$LVdP/dt_{min}$ (mmHg/s)	τ (ms)	LVESV (µl)	LVEDV (µl)	SV (µl)	SW (mmHg µl/g)	EF (%)	E_a (mmHg/µl)
Mean	611	94.4	4.2	10475	−9167	4.9	16.4	26.8	14.5	13640	51.1	6.9
SEM	±33	±2.3	±0.6	±680	±706	±0.5	±2.4	±3.6	±1.5	±1890	±2.0	±0.5

Values were calculated from eight individual experiments.
LVESP, LV end-systolic pressure; LVEDP, LV end-diastolic pressure; $LVdP/dt_{max}$ and $LVdP/dt_{min}$, maximum and minimum first derivative of LV pressure with respect to time; τ, time constant of fall in LV pressure; LVESV, LV end-systolic volume; LVEDV, LV end-diastolic volume; SV, stroke volume; SW, stroke work; EF, ejection fraction; E_a, arterial elastance.

ensures that both blood resistivity and catheter electrode spacing are accounted for in the volume calibration. Second, in order to allow for differences in the density of the electrical field within Plexiglas and heart tissue, absolute volume measurements need to be divided by α, which is defined as the ratio of the actual stroke volume to the stroke volume measured by conductance.[21] The 'real' stroke volume may be measured using either an ultrasonic flow probe placed around the ascending aorta or conveniently by echocardiographic estimation of cardiac output and therefore stroke volume from the aortic outflow trace. Finally, the measured volume signal includes an offset term, due to parallel conductance of the myocardium and surrounding structures, which is caused by extension of the electric current beyond the LV cavity.[17] Parallel conductance is therefore estimated by the saline dilution method,[17,20] which involves injecting a 1 µl bolus of hypertonic (5 N) saline into the right jugular vein, causing a transient change in the conductivity of the blood in the LV. The offset term is calculated by plotting the linear relation between maximum and minimum volume from each loop and is based on the assumption that when the conductivity of the blood is zero, all current is conducted through surrounding structures. At the end of the experiment the animal is sacrificed and the heart dissected and weighed, so that functional data can be expressed per LV mass.

Summary

Over recent years, the mouse has become an essential experimental model for the investigation of cardiovascular pathophysiology. The experimental models of cardiac hypertrophy described in this chapter can be applied to the study of many different aspects of the pathogenesis and pathophysiology of LVH and heart failure as well as to investigate potential therapeutic strategies.[13,28–32] It is often necessary to relate pathophysiological mechanisms to *in vivo* hemodynamic function and the analysis of pressure–volume relations provides the optimal method with which to undertake this.

Acknowledgments

The authors' work is supported by the British Heart Foundation. AMS holds the BHF Chair of Cardiology at King's College London.

References

1. Swynghedauw B. Molecular mechanisms of myocardial remodeling. *Physiol Rev* 1999; **79**: 215–262.
2. The SOLVD investigators. Effect of enalapril on survival in patients with reduced left ventricular ejection fractions and congestive heart failure. *N Engl J Med* 1991; **325**: 293–302.

3. Hunter JJ, Chien KR. Signaling pathways for cardiac hypertrophy and failure. *N Engl J Med* 1999; **341**: 1276–1283.
4. Shimosato S, Etsten BE. Effect of anesthetic drugs on the heart: a critical review of myocardial contractility and its relationship to hemodynamics. *Clin Anesth* 1969; **3**: 17–72.
5. Janssen BJA, De Celle T, Debets JJM, et al. Effects of anesthetics on systemic hemodynamics in mice. *Am J Physiol Heart Circ Physiol* 2004; **287**: H1618–H1624.
6. Rockman HA, Ross RS, Harris AN, et al. Segregation of atrial-specific and inducible expression of an atrial natriuretic factor transgene in an in vivo murine model of cardiac hypertrophy. *Proc Natl Acad Sci U S A* 1991; **88**: 8277–8281.
7. Date M, Morita T, Yamashita N, et al. The antioxidant *N*-2-mercaptopropionyl glycine attenuates left ventricular hypertrophy in in vivo murine pressure-overload model. *J Am Coll Cardiol* 2002; **39**: 907–912.
8. Rockman HA, Wachhorst SP, Mao L, Ross J, Jr. ANG II receptor blockade prevents ventricular hypertrophy and ANF gene expression with pressure overload in mice. *Am J Physiol Heart Circ Physiol* 1994; **266**: H2468–H2475.
9. Dorn GW, Robbins J, Ball N, Walsh RA. Myosin heavy chain regulation and myocyte contractile depression after LV hypertrophy in aortic-banded mice. *Am J Physiol Heart Circ Physiol* 1994; **267**: H400–H405.
10. Akhter SA, Luttrell LM, Rockman HA, et al. Targeting the receptor-Gq interface to inhibit in vivo pressure overload myocardial hypertrophy. *Science* 1998; **280**: 574–577.
11. Brown RH, Walters DM, Greenberg RS, Mitzner W. A method of endotracheal intubation and pulmonary functional assessment for repeated studies in mice. *J Appl Physiol* 1999; **87**: 2362–2365.
12. Freeman RH, Davis JO, Spielman WS. Renin–angiotensin system and aldosterone secretion during aortic constriction in the rat. *Am J Physiol Renal Physiol* 1977; **232**: F434–F437.
13. Byrne JA, Grieve DJ, Bendall JK, et al. Contrasting roles of NADPH oxidase isoforms in pressure-overload versus angiotensin II-Induced cardiac hypertrophy. *Circ Res* 2003; **93**: 802–805.
14. Grieve DJ, Cave AC, Byrne JA, Layland J, Shah AM. Analysis of ex vivo left ventricular pressure-volume relations in the isolated murine ejecting heart. *Exp Physiol* 2004; **89**: 573–582.
15. Bendall JK, Cave AC, Heymes C, Gall N, Shah AM. Pivotal role of a gp91phox-containing NADPH oxidase in angiotensin II-induced cardiac hypertrophy in mice. *Circulation* 2002; **105**: 293–296.
16. Kass DA, Yamazaki T, Burkhoff D, Maughan WL, Sagawa K. Determination of left ventricular end-systolic presure-volume relationships by the conductance (volume) catheter technique. *Circulation* 1986; **73**: 586–595.
17. Baan J, Van der Velde T, De Bruin HG, et al. Continuous measurement of left ventricular volume in animals and humans by conductance catheter. *Circulation* 1984; **70**: 812–823.
18. Ito H, Takaki M, Yamaguchi H, Tachibana H, Suga H. Left ventricular volumetric conductance catheter for rats. *Am J Physiol Heart Circ Physiol* 1996; **270**: H1509–H1514.
19. Georgakopoulos D, Mitzner WA, Chen C-H, et al. In vivo murine left ventricular pressure-volume relations by miniaturized conductance micromanometry. *Am J Physiol Heart Circ Physiol* 1998; **274**: H1416–H1422.
20. Yang B, Larson DF, Watson R. Age-related left ventricular function in the mouse: analysis based on in vivo pressure–volume relationships. *Am J Physiol Heart Circ Physiol* 1999; **277**: H1906–H1913.

21. Reyes M, Freeman GL, Escobedo D et al. Enhancement of contractility with sustained afterload in the intact murine heart. Blunting of length-dependent activation. *Circulation* 2003; **107**: 2962–2968.
22. Georgakopoulos D, Kass DA. Estimation of parallel conductance by dual-frequency conductance catheter in mice. *Am J Physiol Heart Circ Physiol* 2000; **279**: H443–H450.
23. Kass DA, Maughan WL. From E_{max} to pressure–volume relations: a broader view. *Circulation* 1988; **77**: 1203–1212.
24. Kohout TA, Takaoka H, McDonald PH, et al. Augmentation of cardiac contractility mediated by the human {beta}3-adrenergic receptor overexpressed in the hearts of transgenic mice. *Circulation* 2001; **104**: 2485–2491.
25. Baan J, Van der Velde T, Steendijk P. Ventricular pressure-volume relations in vivo. *Eur Heart J* 1992; **13** (Suppl. E): 2–6.
26. Little WC, Downes TR. Clinical evaluation of left ventricular diastolic performance. *Prog Cardiovasc Dis* 1990; **32**: 273–290.
27. Mirsky I, Tajimi T, Peterson KL. The development of the entire end-systolic pressure-volume and ejection fraction-afterload relations: a new concept of systolic myocardial stiffness. *Circulation* 1987; **76**: 343–356.
28. Ichinose F, Bloch KD, Wu JC, et al. Pressure overload-induced LV hypertrophy and dysfunction in mice are exacerbated by congenital NOS3 deficiency. *Am J Physiol Heart Circ Physiol* 2004; **286**: H1070–H1075.
29. Shibata R, Ouchi N, Ito M, et al. Adiponectin-mediated modulation of hypertrophic signals in the heart. *Nat Med* 2004; **10**: 1384–1389.
30. Takimoto E, Champion HC, Li M, et al. Chronic inhibition of cyclic GMP phosphodiesterase 5A prevents and reverses cardiac hypertrophy. *Nat Med* 2005; **11**: 214–222.
31. Tachibana H, Naga Prasad SV, Lefkowitz RJ, Koch WJ, Rockman HA. Level of {beta}-adrenergic receptor kinase 1 inhibition determines degree of cardiac dysfunction after chronic pressure overload-induced heart failure. *Circulation* 2005; **111**: 591–597.
32. Marano G, Vergari A, Catalano L, et al. $Na^+//H^+$ exchange inhibition attenuates left ventricular remodeling and preserves systolic function in pressure-overloaded hearts. *Br J Pharmacol* 2004; **141**: 526–532.

19

The retrogradely perfused isolated heart model

Mihaela M. Mocanu and **Derek M. Yellon**

The Hatter Cardiovascular Institute, Department of Medicine, University, College London, UK

Introduction

The mouse is probably the best animal model for biomedical investigations. It does not require much space or a complicated diet and has an outstanding speed of reproduction. Recent advances in elucidating the mouse genome and the development of techniques for its manipulation have created unique opportunities for exploring the influence of single gene alterations on complex physiological mechanisms, making this model highly regarded and more and more used in all fields of biological/medical research.

With regard to cardiac investigations, the isolated mouse heart model facilitates the assessment of the direct effect upon myocardium of various pharmacologic agents and procedures that may possess therapeutic properties.

However, it is important to underline that the use of the isolated murine heart is also associated with difficulties particularly that related to its small size. Typically a mouse heart weights about 150 mg, with variations according to age, sex and strain, and spontaneously contracts at a rate of 400–600 beats per minute.

Langendorff system

Principle of the method

The isolated perfused heart has been recognised for over a century as a suitable experimental model for studying myocardial function, the regulation of coronary

A Handbook of Mouse Models of Cardiovascular Disease Edited by Qinbo Xu

blood flow and cardiac metabolism.[1] The principle of the method involves the cannulation of the aorta above the sinus of Valsalva, and subjecting the heart to retrograde perfusion. Thus the aortic valve is forced shut by the pressure of the perfusate which then enters the coronary system, eventually leaving the heart via the cut ends of the pulmonary arteries. Throughout this procedure, the chambers of the heart remain essentially empty. By adjusting the perfusion equipment the investigator can choose to perfuse in a constant flow or a constant pressure mode (Figure 19.1), described below in more details on p.00).

Langendorff system: technical data

Both constant flow and constant pressure systems (Figure 19.1) need: a reservoir in which the buffer is aerated with carbogen (95 per cent CO_2 and 5 per cent O_2) and the pH can be checked and adjusted to 7.45–7.50 by modulating the gas output; a

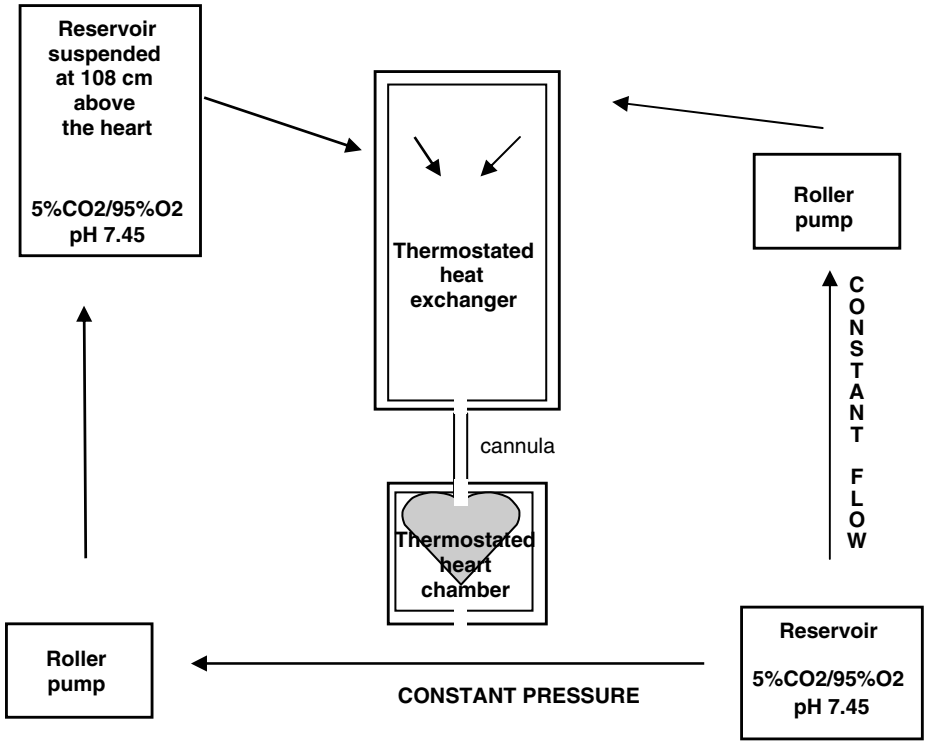

Figure 19.1 Simplified scheme of a Langendorff system. Both models (constant pressure and constant flow) are represented. In constant pressure the roller pump supplies the oxygenated perfusate to an open-to-air reservoir situated above the heart, higher enough to provide the desired pressure (usually 102 cm which are the equivalent of 80 mmHg). In constant flow the roller pump supplies the oxygenated buffer to the heart with a constant flow rate through a closed-to-air circuit

thermostated heat exchanger in which the buffer is warmed up to 37°C, and a thermostated heart chamber in which the buffer is delivered to the heart. The exchanger and the chamber are double jacket glassware connected to a thermostated water pump.

A roller pump is also required for both systems: in the constant pressure system it keeps the level of the buffer in the reservoir at 108 mm water column (about 80 mmHg); in the constant flow system it drives the buffer from the reservoir into the heat exchanger at a speed sufficient to give the desired constant flow. For more details see Doring.[1] This system can be built using individually purchased components.

Electronic transducers are necessary for monitoring heart function and controlling and regulating the functionality of the Langendorff system. The most commonly used transducer is the pressure transducer connected to an isovolumic balloon inserted into the left ventricle. The balloon is inflated to a maximum pressure of 10 mmHg and gives data about the heart rate and the developed pressure. From these raw data other functional parameters can be calculated (e.g. rate pressure product, dp/dt). Other transducers available commercially can measure coronary flow, perfusion pressure, whilst more complex equipment for measuring the left ventricular transversal diameter or to register the ECG are also available.

A pacing electrode can also be used in the Langendorff heart preparation. Pacing counterbalances the decrease in heart rate that is associated with this model. However, pacing should not be used if the aim of the study is to investigate drugs which affect arrhythmogenesis and/or the heart rate. If pacing is not used, many investigators choose to calculate rate pressure product (heart rate × left ventricular developed pressure) instead of reporting these values separately.

For ready made systems we recommend searching the Internet for different suppliers. There are providers (e.g. http://www.adinstruments.com or http://www.hugo-sachs.de) who offer the glassware, the transducers used to register heart parameters, the appropriate electronic equipment necessary to maintain experimental conditions (e.g. constant pressure/constant flow and temperature) and to register all these data. Sometimes assembling your own glassware and purchasing only the electronics required for the system can prove to be a much more economical option than buying a complete system 'off-the-shelf'.

Usually Tyrode, Locke or Krebs–Henseleit buffers are used. They need to be filtered because even the purest chemicals may contain insoluble particles which will obstruct the small coronary vessels. We use a modified Krebs–Henseleit buffer (Table 19.1) bubbled with carbogen, with a pH between 7.4 and 7.5.

Preparation of hearts for perfusion

Anesthesia and anticoagulation

All animals are weighed prior to experimentation. Heparin 100 IU, is administered via intraperitoneal (i.p.) injection for prophylaxis against the formation of thrombus

Table 19.1 Modified Krebs–Henseleit buffer

Compound	Concentration (mM)
NaCl	118.0
$NaHCO_3$	25.0
KCl	4.7
KH_2PO_4	1.21
$MgSO_4 \cdot 7H_2O$	1.22
Glucose	11.0
$CaCl_2 \cdot H_2O$	1.84

The perfusion buffer we normally use is the modified Krebs–Henseleit buffer originally recommended for the mouse heart. However Krebs–Henseleit buffer with slightly different compositions may be employed. The debates about calcium concentration and calcium chelators in this buffer need to be taken into account.[8,9]

within the coronary vasculature or ventricular chambers. After 5 min (time allowed to activated partial thromboplastin time (APTT), to increase), the animals should be killed either by an anesthetic overdose (e.g. sodium pentobarbital 60 mg/kg i.p.) or by rapid cervical dislocation. The animal is then transferred to a dissection block and the limbs secured with adhesive tape.

Dissection

A skin incision is performed at the xyphoid sternum and continued to the lateral ends of the left and right costal margins. The incision is then continued through the ribs at the left and right anterior axillary lines to create a clam-shell thoracotomy. The anterior chest wall is deflected upwards providing an optimal operating field (Figure 19.2). The heart is removed by transecting the descending aorta and inferior vena cava, followed by the ascending aorta and superior vena cava and transferred to a dissection dish containing ice cold Krebs–Henseleit buffer (Table 19.1). It is expected that in the initial experiments the thoracic organs will be removed *en bloc*. However, with time, the investigator will gain experience and the heart will be removed with less extra cardiac tissue. In this stage of the experiment the priority is to transfer the heart into the cold buffer as quickly as possible to avoid any detrimental effects of hypoxia.

Cannulation of the aorta and transfer of the heart to the Langendorff apparatus

The excess of extra cardiac tissues such as lungs, vessels, thymus is trimmed off and the ascending aorta is exposed and cannulated with a primed 21G stainless steel murine cannula under Krebs solution to avoid air embolisation of the coronaries (Figure 19.3a). This technically difficult step is presented on the CD that accompanies

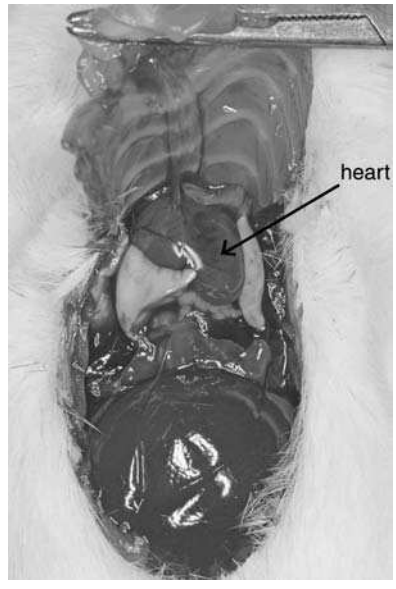

Figure 19.2 The general view of the opened thorax before the removal of the heart. For a color version of this figure, please see the images supplied on the accompanying CD

this book. In summary the cannula is inserted into the aorta by manoeuvring the heart with as little trauma as possible. This is achieved using two small forceps which hold the atrial appendages. It should be noted that care should be taken *not* to insert the cannula too deep into the aorta to avoid forcing the aortic valve open and reaching into the left ventricle. This situation is not redeemable by rapid withdrawal of the cannula as the aortic valve is invariable irreversibly damaged, resulting in a reduced coronary perfusion (buffer will be lost via left ventricle) and the heart will not perform as expected. The opposite situation, i.e. not inserting the cannula deep enough, may have the same result; if the cannula is tightly secured above the aortic branches (e.g. brachiocephalic trunk) some buffer will be lost through them. Consequently, the perfusion flow entering into the coronary system will be diminished. Therefore it is essential that insertion of the cannula deeper than the point where the aorta leaves the base of the heart should be avoided. The aorta is secured to the cannula using a 5-0 suture, and transferred to the Langendorff perfusion apparatus. The buffer should run slowly through the system prior to mounting the cannula, so that the heart will receive nutrients and oxygen as soon as it is placed in the system. Once securely attached to the perfusion apparatus, retrograde perfusion at a constant pressure or constant flow must be started. The time taken from the moment of the opening of the thorax until the heart is mounted and perfused on the Langendorff system needs to be under 3 min, in order to avoid the potential effect of ischemic preconditioning due to delayed perfusion.[2,3]

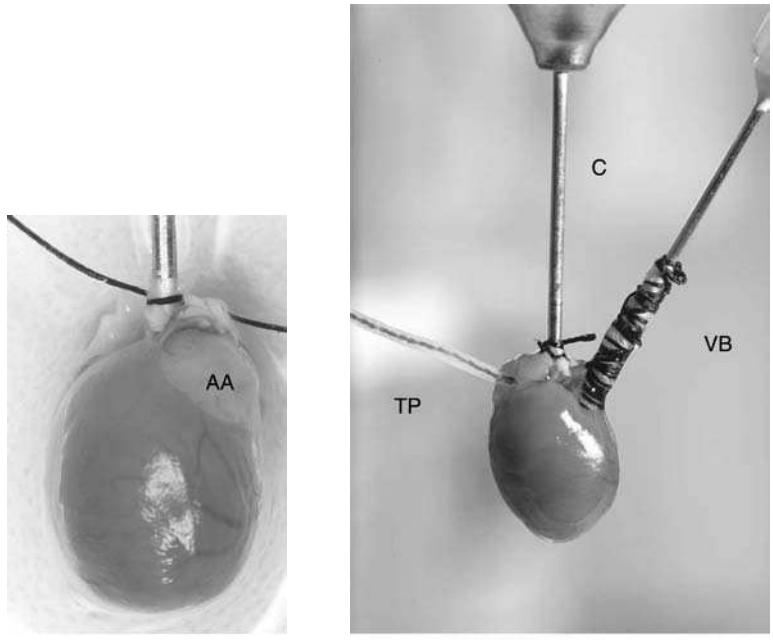

Figure 19.3 (a) Heart mounted on the cannula. AA, atrial appendage. (b) Heart mounted in the Langendorff system. A ventricular balloon (VB) is inserted in the left ventricle; a thermoprobe (TP) is inserted via the pulmonary artery; C, cannula. For a color version of this figure, please see the images supplied on the accompanying CD

Instrumenting the heart after mounting on the Langendorff system

A small incision is made in the pulmonary outflow tract to allow free drainage of coronary effluent. Through this orifice a fine microthermocouple can be retrogradely passed into the right ventricle and attached to a digital thermometer to permanently monitor the temperature inside the heart (Figure 19.3b).

Heart rate and the left ventricular developed pressure are measured using an intraventricular balloon. This balloon needs to be pliant but non-elastic. We recommend it to be hand-made from a little piece of tempered cellophane tightly knotted with suture on a 21G stainless steel tube and completely filled with fluid (deionised water). Latex ready-made balloons are available commercially (Hugo Sacks) but in our experience they are found not to be sensitive enough to obtain a proper signal. The balloon is connected to a pressure transducer using a non-pliable line also filled with deionised water. It is very important that all these components filled with water (the balloon, the non-pliable line and the internal space of the transducer) to be free of any air bubbles, because air, in contrast to water, is compressible and will reduce the strength of the signal. The deflated balloon should be inserted gently into the heart either via the left atrium, after removing the atrial appendage (Figure 19.3b), or via the pulmonary veins. Once positioned into the heart,

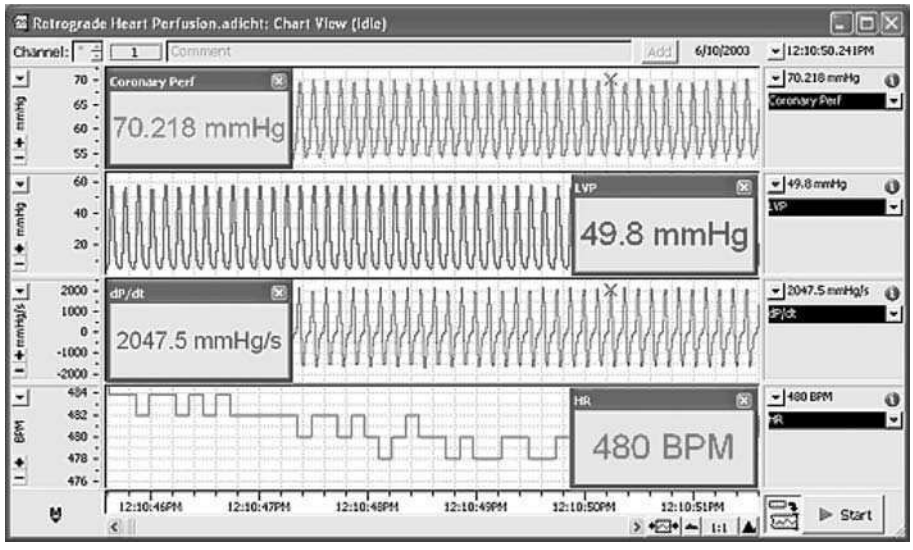

Figure 19.4 Chart visualising and recording the functional parameters of the Langendorff heart. For a color version of this figure, please see the images supplied on the accompanying CD

the balloon is inflated to 5–10 mmHg in order to obtain a good signal (Figure 19.4). The size of the balloon in relation to that of the heart is an important factor in obtaining a good signal. The coronary flow rate, the temperature and the pressure signals can be monitored, displayed and recorded. We use an AD Instruments complete Langendorff system (hardware and software) and record the values on a Power Macintosh personal computer.

Experimental protocol

We describe below the protocol we use in investigating myocardial infarction following global normothermic ischemia–reperfusion injury.

After commencing retrograde aortic perfusion hearts are allowed to stabilise for 30 min. During this period hearts must meet certain functional requirements. The following exclusion criteria are used: prolonged time to perfusion (>3 min), abnormal coronary flow rate (<1.5 ml/min or >6.0 ml/min) arrhythmia in stabilisation (>3 min), low heart rate at the end of stabilisation (<300 beats/min) and low left ventriclular developed pressure at the end of stabilisation (<60 mmHg).

Ischemia can be induced either by stopping the coronary flow (completely in global ischemia or partially in low flow ischemia) or by temporarily obstructing the left descending coronary artery (regional ischemia). We will refer here only to the no flow global normothermic ischemia. It is essential to determine the duration of the ischemia injury in relation to the end point of the study. A short period of ischemia may induce stunning but no infarction, whilst a prolonged period of ischemia may be so detrimental that any cardioprotective mechanism will not be able to reduce the infarct size. We

normally use an injury of 30 min no flow normothermic global ischemia which, in our experience, is associated with approximately 50 per cent infarction of the left ventricle. Maintaining normothermia of the heart during this stage of the protocol is very important because it has been demonstrated that ischemia in the hypothermic setting is associated with reduced injury.[4] However, maintaining normothermia in these small hearts is very difficult especially during global ischemia. Usually the thermostated heart chamber is filled with warm buffer and the heart is immersed in the fluid for the duration of ischemia. The investigator should keep the system under close observation as overheating may occur.

Reperfusion is commenced by restoring the flow. This is another experimental moment when temperature may shift dramatically, and overheating the heart may occur. Emptying the suspension chamber and reducing the temperature of the oxygenated buffer are two remedial options that may be considered. With regard to the duration of reperfusion, this varies between laboratories. However the recovery of function depends greatly upon the duration of ischaemic insult.[5] Different groups recommend different durations of reperfusion in order to obtain clear infarct data. The time allowed for reperfusion before staining with tetrazolium is 30 min in our model. Although this period may appear inadequate for effective washout of dehydrogenase enzymes from infarcted tissue, the mouse heart has a high coronary flow rate per gram, and there is adequate enzyme washout in this short time period. However, in order to verify this we have carried out experiments in which hearts have been subjected to 2 h reperfusion before infarct measurement. The infarct size in this hearts was not found to be different form hearts which had been reperfused for only 30 min.[6]

End points

The Langendorff perfused heart model can be use for the investigation of various end points. Thus, the measurement of infarct size at the end of reperfusion or collecting tissue samples at various time points for molecular biology investigation (e.g. Western blotting), collecting coronary effluent for biochemical measurements (e.g. lactate dehydrogenase and creatine kinase release, or high pressure liquid chromatography), investigating the occurrence and duration of arrhythmias or to measure changes in heart function (coronary flow, heart rate, left ventricular developed pressure, etc.) may also be considered. We use infarct size determination as our main end point.

Measurement of infarct size

Infarct size staining

At the end of the reperfusion period 1 per cent 2,3,5 triphenyltetrazolium chloride (TTC, 1% in phosphate buffer, pH 7.4) is injected down the side arm of the aortic

cannula and infused into the coronary circulation. The heart is then detached from the cannula and placed in TTC at 37°C for 10 min. Staining with TTC delineates viable myocardium from infarcted myocardial tissue.[7] TTC stain crosses the cell membrane, and binds to intracellular dehydrogenase enzymes. Viable cells with reducing potential (preserved reduced necotinamide adenine dinucleotide phosphate) are colored dark red whilst non-viable cells, with ruptured sarcolemmal membranes, appear pale. Once the hearts have been stained dark red they are removed, blotted dry and weighed. They are then frozen and stored at −20°C. Within 24 h the hearts are sliced into 1 mm sections parallel to the atrioventricular groove after which the slices are left overnight in 10 per cent formaldehyde (obtained by diluting the commercially available 40 per cent formaldehide with an appropriate volume of 0.9 per cent NaCl solution) for a clearer delineation between the viable and non-viable tissues. It is recommended that the heart slices should not be kept in formaldehyde longer than 24 h before infarct size computation to avoid the discoloration that may affect the infarct size measurement.

Infarct size computation

The feasibility of measuring infarct size by tetrazolium staining in such a small heart has now been established. A magnified video image can be digitalised by a computer video card allowing accurate planimetry using appropriate software.

After 24 h in formaldehyde the heart slices are arranged from apex to base and compressed between two Plexiglas plates mounted 0.57 mm apart and photographed using a mega pixel video camera with a high resolution lens (Figure 19.5). A 'My TV 2 Go MAC USB-TV Tuner' (Gainward Co. Ltd) is used to transfer the images to an i-Mac personal computer. Each digital heart slice image is then saved as a single frame and analysed by 'drag-and-drop' into an open window of the National Institute of Health free share image analysis programme, NIH Image (version 1.63; downloaded from http://rsb.info.nih.gov/nih-image/). Graph paper (1 mm squares) is used to calibrate the image areas, which are then multiplied by the slice thickness (0.57 mm) to generate the planimetered volume. The result is expressed as infarct developed in the risk zone (I/R%).

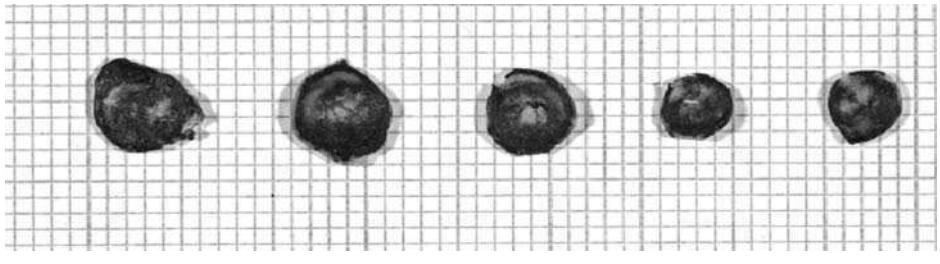

Figure 19.5 Mouse heart slices in which viable tissue is stained dark red (dark) and the infarction pale white. For a color version of this figure, please see the images supplied on the accompanying CD

General comments

The retrogradely perfused (Langendorff) mouse heart model is largely used in cardiovascular investigations because it offers many advantages, the most important of which results from the use of genetically modified myocardium. It should be noted that the method as described is not restrictive and many slight differences will occur across different groups. These differences will reflect minor variances in details of the equipment construction, the duration of ischemia–reperfusion, the use of constant pressure or constant flow or the buffer composition. Therefore consistency within the group is the primary aim to ensure reproducibility across groups.

Acknowledgments

Our thanks to Drs Christopher C.T. Smith and James C. Simpkin for their assistance in the preparation of this chapter.

References

1. Doring HJ. The isolated perfused heart according to Langendorff technique – function – application. *Physiol Bohemoslov* 1990; **39**: 481–504.
2. Awan MM, Taunyane C, Aitchison KA, et al. Normothermic transfer times up to 3 min will not precondition the isolated rat heart. *J Mol Cell Cardiol* 1999; **31**: 503–511.
3. Minhaz U, Koide S, Shohtsu A, et al. Perfusion delay causes unintentional ischemic preconditioning in isolated heart preparation. *Basic Res Cardiol* 1995; **90**: 418–423.
4. Hale SL, Kloner RA. Myocardial hypothermia: a potential therapeutic technique for acute regional myocardial ischemia. *J Cardiovasc Electrophysiol* 1999; **10**: 405–413.
5. Headrick JP, Peart J, Hack B, et al. Functional properties and responses to ischemia–reperfusion in Langendorff perfused mouse heart. *Exp Physiol* 2001; **86**: 703–716.
6. Sumeray MS, Yellon DM. Characterisation and validation of a murine model of global ischemia–reperfusion injury. *Mol Cell Biochem* 1998; **186**: 61–68.
7. Fishbein MC, Meerbaum S, Rit J, et al. Early phase acute myocardial infarct size quantification: validation of the triphenyl tetrazolium chloride tissue enzyme staining technique. *Am Heart J* 1981; **101**: 593–600.
8. Sutherland FJ, Shattock MJ, Baker KE, et al. Mouse isolated perfused heart: characteristics and cautions. *Clin Exp Pharmacol Physiol* 2003; **30**: 867–878.
9. Patton C, Thompson S, Epel D. Some precaustions in using chelators to buffer metals in biological solutions. *Cell Calcium* 2004; **35**: 427–431.

20

Measurement of pulse wave velocity

Yi-Xin Wang

Berlex Biosciences, Richmond, CA, USA

Introduction

A common consequence of atherosclerosis is an increase in the stiffness of the aorta and major arteries,[1,2] resulting in decreased vascular elasticity and compliance, which has been seen in humans,[3–5] non-human primates,[6,7] dogs,[8] pigs[9] and rabbits.[10,11] Many methodologies, both invasive and noninvasive, have been used to assess arterial elasticity *in vivo* (see review[12]). Dating back to the early part of the last century, Nachev *et al*. measured the velocity of arterial wave propagation as an index of vascular stiffness and vascular health.[13] Pulse wave velocity (PWV) is defined by the Moens–Korteweg equation, PWV $= \sqrt{(Eh/2\rho R)}$, where E is Young's modulus of the arterial wall, h is wall thickness, R is radius at the end of diastole, and "ρ" is blood density. The stiffer the vessel and the greater the Young's modulus, the faster a pulsatile wave moves.[8] Thus, PWV has been used widely to estimate the stiffness of conduit vessels in human,[3–5] non-human primates,[6,7] dogs,[8] pigs[9] and rabbits[10,11] as a surrogate marker for vascular diseases, including atherosclerosis.[5,14]

Due to small size of rodents, technically it has been very difficult to measure PWV *in vivo*, especially in mice, until resent development of high fidelity physiological sensors as well as fast and powerful data acquisition systems made it feasible. More recently, Hartley *et al.* developed a non-invasive Doppler method to measure PWV, which greatly facilitated research in phenotyping cardiovascular functions under a physiological condition in genetically altered mice.[15-17]

A Handbook of Mouse Models of Cardiovascular Disease Edited by Qinbo Xu

Materials and methods

Invasive method

Surgical procedure

Mice are anesthetised with an intramuscular injection of a mixture of 120 mg/kg Ketamine (Ketaset; Fort Dodge Laboratories, Inc., Fort Dodge, IA, USA) and 7 mg/kg xylazine (Rompun; Bayer Corporation, Shawnee Mission, KS, USA) and placed on a heating board at 37°C to maintain body temperature. Spontaneous breathing is facilitated via a tracheal intubation through a midline incision. The left carotid artery is isolated, cleared from surrounding tissue, and inserted with an 1.4 Fr. Mikro-tip pressure transducer (Millar Instruments, Houston, TX, USA) with the tip being reached to the aortic arch for measuring intravascular arterial blood pressure (proximal pressure wave). The abdominal aorta is exposed through a suprapubic incision, and inserted with another Millar catheter (1.8-Fr) with the tip being reached to the abdominal aorta at a site just passing iliac bifurcation for recording distal pressure waveform. In order to simplify surgical procedure and minimise interruption of normal physiological condition, the distal pulsatile waveform can also be obtained by placing a Millar catheter (1.8-Fr) underneath the abdominal aorta at a site just above the iliac bifurcation to record an extravascular tonometric pressure waveform. The best signals can be obtained by orienting the catheter tip at right angles to the vessel axis and the side-mounted sensor flat against the vessel. The catheter is lifted slightly to maintain contact and to applanate the vessel against the sensor. By simultaneously measuring intravascular pressure and extravascular tonometric waveform at the same site, Hartley *et al.* validated that the timing of the upstrokes of both waveforms is identical and not affected by change of blood pressure and heart rate.[16] When the surgery is completed, all wounds are closed to minimise evaporative fluid loss.

Experimental procedure

When blood pressure and heart rate stabilise for approximately 30 min, both the proximal (aortic arch) and distal (abdominal aorta) waveforms are recorded simultaneously. The signals are digitised and stored using a data acquisition system (Powerlab 16/s, ADI, Australia). The sampling rate of data acquisition is 10 kHz. Since the Millar pressure transducer has a response frequency ranging from flat to 10 kHz, it is able to provide high-fidelity signals of the pressure waveforms in mice with heart rate up to 600 beats per min.

Data analysis

Systolic, diastolic, pulse and mean arterial blood pressure and heart rate are calculated by the data acquisition system from the proximal pressure wave. As

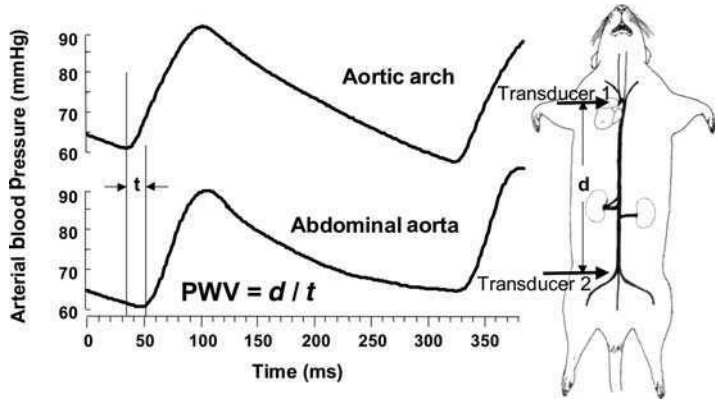

Figure 20.1 Illustration of the measurement of aortic stiffness by pulse wave velocity (PWV). Transducer 1 is inserted into the aortic arch via the carotid artery for measuring the proximal pressure waveform. Transducer 2 is inserted into the abdominal aorta at bifurcation via the femoral artery for measuring the distal pressure waveform. (Adapted from reference [21].). For a color version of this figure, please see the images supplied on the accompanying CD

illustrated in Figure 20.1, the propagation time (t) for a pulse wave moving from the aortic arch to the abdominal aorta is measured by the time delay between the upstrokes (foot) of each pressure wave front. At least 10 normal consecutive cardiac cycles are used to average each measurement. At the end of the experiment after animal is killed, the distance between two measurement sites is measured using a damp cotton thread stuck onto the aorta between the tips of the two pressure transducers and marked. The thread is then removed and laid straight for measurement of the distance (l) between the two marks. PWV is calculated by dividing the distance by the pulse wave propagation time (l/t) in units of m/s.

Non-invasive method

Animal preparation

Light anesthesia is used to immobilise the animal during the experiment. The animal is placed in a closed chamber of an anesthesia machine (IMPAC 6, VetEquip, Pleasanton, CA, USA) ventilated with 1.5 per cent isoflurane for 3–5 min. After induction, light anesthesia is maintained by placing a coaxial tubing set from the anesthesia machine over the face of the mouse, which is taped supine to electrocardiogram (ECG) electrodes incorporated into a temperature-controled circuit board, which includes four ECG electrodes under the four limbs, and an array of 50 surface-mounted heat-generating resistors positioned under the body of the mouse. A temperature sensor (Physitemp, Clifton, NJ, USA) is inserted into the rectum of the mouse for monitoring and controling the board temperature between 35 and 40°C so that the body temperature can be maintained at 36°C throughout the study. The ECG electrodes are connected to a high-fidelity ECG amplifier with a 0.1 kHz

bandwidth set to record lead II ECG. The ECG board, amplifier, and temperature controller, along with the Doppler transducers and signal processing, specifically for use with mice are developed by Dr Craig Hartley from Baylor College of Medicine.

Doppler data acquisition system

The Doppler probes are connected to a modular pulsed Doppler system designed by Hartley originally for use with implantable probes in animals.[18] The Doppler audio output is connected to a data acquisition and signal processing system integrated into a personal computer (Indus Instruments Inc., Houston, TX, USA). Briefly, the quadrature audio Doppler signals from the 20 MHz pulsed Doppler modules and the amplified ECG signal are sampled and digitised at 125 kHz. A complex fast Fourier transform is calculated and displayed in real-time on a computer monitor along with the ECG for use by the operator in optimising and adjusting the probe position. When the desired signals are obtained, a button is pressed on a remote keypad to save the last two second unprocessed signals to a data file.

Experimental procedure

A 20 MHz Doppler probe with a focal distance of 4 mm is placed just left of the sternum at a 90° angle to the sternum to record flow velocity in the aortic arch moving toward the probe at a depth of 2–4 mm. A mark is made on the chest at the aortic arch measurement site and a second mark is made 40 mm distal on the abdomen; another measurement is then taken with the probe angled toward the heart to record flow velocity in the abdominal aorta moving toward the probe at a depth of 2–3 mm (Figure 20.2).

Signal processing and calculation of pulse wave velocity

Digitised quadrature Doppler and ECG signals are processed off-line. The 2 s data file from each location on each mouse, consisting of 10–20 cardiac cycles, is played back and displayed using an adjustable 64- to 1024-point fast Fourier transform. A semiautomated program is used to outline the upper edge of the Doppler spectrum. We typically use a 256-point (2–4 ms) spectral window that is advanced through the data set at 0.1 ms intervals, resulting in a temporal resolution of 0.1 ms and a frequency resolution of 250–500 Hz depending on the sampling rate. The analyser can be adjusted to optimise temporal resolution for PWV. Aortic pulse-wave velocity is calculated by dividing the separation distance by the difference in arrival times of the velocity pulse timed with respect to the ECG (Figure 20.2).

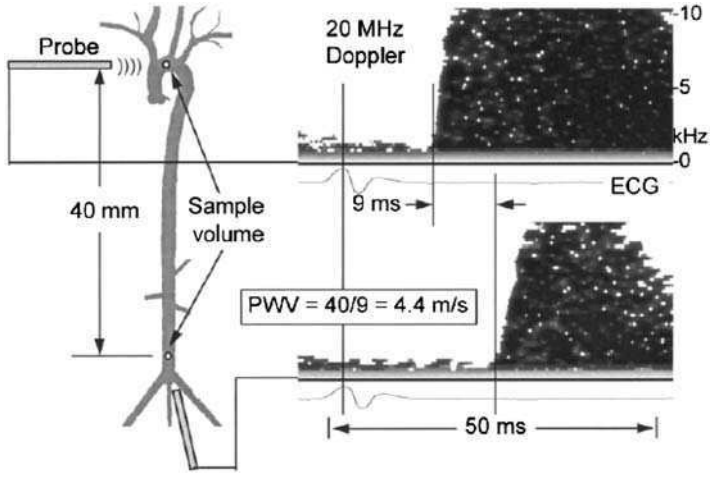

Figure 20.2 Diagram and Doppler waveforms and electrocardiogram (ECG) displayed with expanded time and amplitude scales for determination of aortic pulse wave velocity (PWV) in mice. Velocity measurements are made at the aortic arch and at the descending aorta 40 mm distal. PWV is calculated by dividing the separation distance (40 mm) by the difference in velocity pulse arrival times (9 ms in this example). (Adapted from reference [15].)

Discussion

Factors affect *in vivo* measurement of pulse wave velocity

Effect of blood pressure

It has been known that blood pressure, especially diastolic pressure can directly affect *in vivo* measurement of PWV in intact animals.[11,19,30] Indeed, we have observed that when blood pressure was increased by administration of phenylephrine, PWV was also increased correspondingly.[21] Therefore, to avoid a direct impact of blood pressure on *in vivo* measurement of PWV, it is important to compare PWV among different experimental groups at an equal level of blood pressure. Alternatively, β-index ($2.11 \times \text{PWV}^2$/diastolic pressure) can be used to normalise the difference in diastolic pressure for comparison of PWV among different experimental groups when blood pressure may not be at a similar level.[11,19–21]

Sampling rate of data acquisition

Due to the fast heart rate (up to 600 beats per min) in mice, a slow data acquisition sampling rate can distort the waveform, thus, compromising accuracy of exact time localization on waveform. Therefore, at least 100 samples per cardiac cycle are

needed for recording a high fidelity waveform. Furthermore, since the length of a mouse aorta is short (only about 40 mm), the time for a pulse wave moving from proximal to distal measurement point is only about 10 ms. Thus, a temporal resolution of 0.1 ms can be reached with a sampling rate of 10 kHz.

Land-markers on the waveforms for measurement

Although there are multiple land-markers, such as systolic or diastolic peak, etc., on the waveforms for the determination of propagation time, we chose to use the starting point at the upstroke of the wave front,[15,16,21,22] because it has been shown to be less affected by distortion than other parts of cardiac cycle.[23] We have also validated that the central location of diastolic phase is another reliable land-marker,[21] because it has also been shown to be less affected by distortion than the systolic phase of cardiac cycle.[8] With simple programming, we were able to make real-time (cycle by cycle) computer automated measurement of propagation time, which greatly facilitated data processing and enhanced accuracy and reproducibility.[21]

Physiologic and pathophysiologic impact of vascular stiffness

An elastic conduit aorta constitutes a hydraulic buffer converting intermittent cardiac output into steady flow, which not only reduces cardiac workload during systole and conserves energy expenditure for the heart, but also alleviates pulsatile stress and improves diastolic blood supply to the perfused organs. A stiffening conduit artery increases pulsatile component, exerting detrimental hemodynamic load on the heart, limiting coronary perfusion, impairing ventricular performance, and eventually exacerbating the development of congestive heart failure. Accumulating evidence suggests that abnormalities in pulsatile characteristics of the arteries occur early in disease processes associated with increased cardiovascular risk, and can be favorably modified by therapeutic interventions. Changes in mechanical behavior of blood vessels can also influence growth and remodeling of all sections of the arterial vasculature, and potentially influence development and progression of arterial disease. Emerging results support the concept that cardioprotective actions of drug interventions may, at least in part, be dependent on favorably influencing these processes in blood vessels and not simply changing arterial blood pressure. The importance of assessing arterial wall mechanics has been highlighted by studies demonstrating that impaired pulsatile arterial function is an independent predictor of risk for cardiovascular events with aging and various disease states, including coronary heart disease, left ventricular hypertrophy, congestive heart failure, hypertension and diabetes mellitus, thus, providing important prognostic and therapeutic information beyond that provided by traditional blood pressure measurements.[24–28]

Application

Apolipoprotein-E knockout (ApoE-KO) mice spontaneously develop hyperlipidemia and atherosclerotic lesions as they age, detectable predominantly in the aortic arch and carotid arteries. Thus, apoE-KO mice have been used widely in the vascular biology research as an animal model of hyperlipidemia and atherosclerosis. By using both invasive[22] and noninvasive[15,16] methods, we have shown age-dependent increases in aortic stiffness measured by PWV in apoE-KO mice fed with a normal diet.[29,30] Although there was a moderate aortic atherosclerotic lesion development in apoE-KO mice of 4 months old, PWV was not significantly different from that in age-matched C57 black/6J wild type controls until 13 months old when PWV significantly increased in apoE-KO compared to wildtype mice. Our data also demonstrated that the PWV measured by different methods, invasively[23] and noninvasively,[15,16] is consistent. However, the noninvasive method has multiple advantages, such as ''higher throughput'' (about 5 min per measurement), non-terminal procedure (enabling repeated measurements over time without sacrificing animal), and under more physiological condition with no surgical intervention, etc.

Using the noninvasive Doppler method, we also detected a further increase in PWV in apoE-KO mice treated with angiotensin II (Ang II), which is not only a vasoconstrictor, but also has been implicated in vascular inflammation, progression of atherosclerosis and other cardiovascular diseases.[31] The *in vivo* PWV measurement in this study was consistent with the *in vitro* measurement by elastigraphy as well as associated with morphological (breaks in the internal elastic lamina and inflammatory cell infiltration) and biochemical (increase in collagen and decrease in elastin content) changes in the aortic wall.[31] Molecular mechanisms for Ang II-induced vascular injury involve activation of NF-κB dependent proinflammatory mediators, such as IL-6, ICAM-1, VCAM-1, E-selectin, MCP-1, M-CSF, COX-2, etc., and downregulation of anti-inflammatory molecules, such as peroxisome proliferator-activated receptors (PPARs), members of the nuclear receptor super family of transcription factors that control the expression of a large array of genes, in the aortic wall.[31-33] Activation of proinflammatory mediators promotes monocyte/macrophage infiltration into the vascular wall. These inflammatory cells are a major source of urokinase-type plasminogen activator (uPA) as well as other proteolytic enzymes, such as matrix metalloproteinases (MMPs). uPA hydrolyzes plasminogen to form plasmin, a trypsin-like proteolytic enzyme capable of directly degrading components of the extracellular matrix, and activating MMPs.[34] Indeed, the expression of uPA and MMP 2 and 9 was significantly up-regulated in the aortas from the mice treated with Ang II.[35] These proteolytic enzymes degrade components of the extracellular matrix,[34] including elastin in the aortic wall, thus contributing to aortic stiffening.

Nitric oxide (NO) is capable of modulating vascular stiffness.[36] Administration of a NO donor has been shown to reduce stiffness in dog aorta[37] and human brachial artery.[38] Using acetylcholine to stimulate endogenous NO release in sheep dose-dependently decreases hindlimb vascular stiffness, which can be reversed by a NO synthase (NOS) inhibitor, N^G-monomethyl-L-arginine (L-NMMA).[39] Consistent with

this report, we also demonstrated in rats that acute administration of a NOS inhibitor, N^{ω}-nitro-L-arginine methyl ester (L-NAME), significantly increased PWV independent of blood pressure increase.[21] Chronic administration of L-NAME for 3 weeks further increased PWV. These results provide the evidence that endogenous NO modulates vascular stiffness. Arterial compliance is also determined by functional factors, such as vasoactive neurohormones, and structural factors, such as collagen and elastin. Thus, the acute change of vascular stiffness by NO could be attributed to modulation of vascular tone. Chronic increase in vascular stiffness due to NO deficiency presumably resulted from vascular remodeling, since it has been reported that chronic treatment with L-NAME caused perivascular fibrosis, medial thickening and increased ratios of intima/media or wall/lumen in the mesenteric microvascular beds, arterioles, coronary arteries, and aorta.[40-44]

Furthermore, we have recently demonstrated that inhibition of NO production by L-NAME synergistically facilitated Ang II-induced vascular stiffness.[45] In this study, we chronically treated C57 black/6J mice with a sub-threshold dose of Ang II or L-NAME that each individual treatment did not cause vascular stiffening measured non-invasively by PWV as well as by *in vitro* elatigraph. However, combination of both treatments significantly increased vascular stiffness, accompanied by an increase in the ratio of collagen/elastin contents in the aortic wall without significantly increase in blood pressure. Thus, NO may play a role in attenuation of Ang II-induced vascular stiffening by reducing collagen production and preserving elastin in the vascular wall.

References

1. Makita Z, Yanagisawa K, Kuwajima S, Bucala R, Vlassara H, Koike T. The role of advanced glycosylation end-products in the pathogenesis of atherosclerosis. *Nephrol Dial Transplant* 1996; **11**(Suppl 5): 31–33.
2. Vlassara H. Advanced glycation end-products and atherosclerosis. *Ann Med* 1996; **28**(5): 419–426.
3. Asmar R, Benetos A, Topouchian J, et al. Assessment of arterial distensibility by automatic pulse wave velocity measurement. Validation and clinical application studies. *Hypertension* 1995; **26**(3): 485–490.
4. Hirai T, Sasayama S, Kawasaki T, Yagi S. Stiffness of systemic arteries in patients with myocardial infarction. A noninvasive method to predict severity of coronary atherosclerosis [published erratum appears in Circulation 1989 Dec; **80**(6): 1946]. Circulation 1989;80(1):78–86.
5. Lehmann ED, Hopkins KD, Jones RL, Rudd AG, Gosling RG. Aortic distensibility in patients with cerebrovascular disease. Clin Sci (Colch) 1995;89(3):247–253.
6. Farrar DJ, Bond MG, Riley WA, Sawyer JK. Anatomic correlates of aortic pulse wave velocity and carotid artery elasticity during atherosclerosis progression and regression in monkeys. *Circulation* 1991; **83**(5): 1754–1763.
7. Farrar DJ, Bond MG, Sawyer JK, Green HD. Pulse wave velocity and morphological changes associated with early atherosclerosis progression in the aortas of cynomolgus monkeys. *Cardiovasc Res* 1984; **18**(2): 107–118.

8. Nichols W, O'Rourke MF. McDonald's Blood Flow in Arteries. Theoretical, Experimental and Clinical Principles. London: Arnold, 1998.
9. Wang YX, Fitch R, Li W, et al. Reduction of cardiac functional reserve and elevation of aortic stiffness in hyperlipidemic Yucatan minipigs with systemic and coronary atherosclerosis. *Vascul Pharmacol* 2002; **39**(1-2): 69–76.
10. Fitch R, Da Cunha V, Kauser K, et al. Increased nitric oxide accounts for decreased basal vascular tone and responsiveness in the resistance vessels of high-cholesterol-fed rabbits. *Pharmacology* 2001; **63**(4): 220–227.
11. Sato M, Katsuki Y, Kanehiro H, Iimura M, Akada Y, Mizota M, Kunihiro Y. Effects of ethyl all-*cis*-5,8,11,14,17-icosapentaenoate on the physical properties of arterial walls in high cholesterol diet-fed rabbits. *J Cardiovasc Pharmacol* 1993; **22**(1): 1–9.
12. Oliver JJ, Webb DJ. Noninvasive assessment of arterial stiffness and risk of atherosclerotic events. *Arterioscler Thromb Vasc Biol* 2003; **23**(4): 554–566.
13. Nachev C, O'Brien E, Rosenfeld J, et al. The velocity of the pulse wave in man. *Proc R Soc Lond B Biol Sci* 1922; **93**: 298–306.
14. Maldonado J, Galhano E, Almeida L, et al. [Pulse wave velocity as initial marker of atherosclerosis]. *Rev Port Cardiol* 1994; **13**(11): 845–851, 08.
15. Hartley CJ, Reddy AK, Madala S, et al. Hemodynamic changes in apolipoprotein E-knockout mice. *Am J Physiol Heart Circ Physiol* 2000; **279**(5): H2326–2334.
16. Hartley CJ, Taffet GE, Michael LH, Pham TT, Entman ML. Noninvasive determination of pulse-wave velocity in mice. *Am J Physiol* 1997; **273**(1 Pt 2): H494–500.
17. Hartley CJ, Taffet GE, Reddy AK, Entman ML, Michael LH. Noninvasive cardiovascular phenotyping in mice. *Ilar J* 2002; **43**(3): 147–158.
18. Hartley CJ, Cole JS. An ultrasonic pulsed Doppler system for measuring blood flow in small vessels. *J Appl Physiol* 1974; **37**(4): 626–629.
19. Kawasaki T, Sasayama S, Yagi S, Asakawa T, Hirai T. Non-invasive assessment of the age related changes in stiffness of major branches of the human arteries. *Cardiovasc Res* 1987; **21**(9): 678–687.
20. Sato M, Katsuki Y, Kanehiro H, Kawano H, Mizota M. [Effects of ethyl all-*cis*-5,8,11,14,17-icosapentaenoate (EPA-E) on elasticity and endothelium-dependent relaxation of the aorta in high cholesterol diet-fed rabbits]. *Nippon Yakurigaku Zasshi* 1994; **104**(1): 31–38.
21. Fitch RM, Vergona R, Sullivan ME, Wang YX. Nitric oxide synthase inhibition increases aortic stiffness measured by pulse wave velocity in rats. *Cardiovasc Res* 2001; **51**(2): 351–358.
22. Wang YX, Halks-Miller M, Vergona R, et al. Increased aortic stiffness assessed by pulse wave velocity in apolipoprotein E-deficient mice. *Am J Physiol Heart Circ Physiol* 2000; **278**(2): H428–434.
23. Mitchell GF, Pfeffer MA, Finn PV, Pfeffer JM. Comparison of techniques for measuring pulse-wave velocity in the rat. *J Appl Physiol* 1997; **82**(1): 203–210.
24. Benetos A, Rudnichi A, Safar M, Guize L. Pulse pressure and cardiovascular mortality in normotensive and hypertensive subjects. *Hypertension* 1998; **32**(3): 560–564.
25. Chae CU, Pfeffer MA, Glynn RJ, Mitchell GF, Taylor JO, Hennekens CH. Increased pulse pressure and risk of heart failure in the elderly. *JAMA* 1999; **281**(7): 634–639.
26. Cohn JN. Vascular wall function as a risk marker for cardiovascular disease. *J Hypertens* 1999; **17**(Suppl 5): S41–44.
27. Franklin SS, Khan SA, Wong ND, Larson MG, Levy D. Is pulse pressure useful in predicting risk for coronary heart disease? The Framingham heart study. *Circulation* 1999; **100**(4): 354–360.

28. Vaccarino V, Holford TR, Krumholz HM. Pulse pressure and risk for myocardial infarction and heart failure in the elderly. *J Am Coll Cardiol* 2000; **36**(1): 130–138.
29. Wang YX. Cardiovascular functional phenotypes and pharmacological responses in apolipoprotein E deficient mice. *Neurobiol Aging* 2005; **26**(3): 309–316.
30. Wang YX, Fitch RM. Vascular stiffness: measurements, mechanisms and implications. *Curr Vasc Pharmacol* 2004; **2**(4): 379–384.
31. Tham DM, Martin-McNulty B, Wang YX, et al. Angiotensin II injures the arterial wall causing increased aortic stiffening in apolipoprotein E-deficient mice. *Am J Physiol Regul Integr Comp Physiol* 2002; **283**(6): R1442–1449.
32. Tham DM, Martin-McNulty B, Wang YX, et al. Angiotensin II is associated with activation of NF-kappaB-mediated genes and downregulation of PPARs. *Physiol Genom* 2002; **11**(1): 21–30.
33. Tham DM, Wang YX, Rutledge JC. Modulation of vascular inflammation by PPARs. *Drug News Perspect* 2003; **16**(2): 109–116.
34. Carmeliet P, Moons L, Lijnen R, et al. Urokinase-generated plasmin activates matrix metalloproteinases during aneurysm formation. *Nat Genet* 1997; **17**(4): 439–444.
35. Wang YX, Martin-McNulty B, Freay AD, et al. Angiotensin II increases urokinase-type plasminogen activator expression and induces aneurysm in the abdominal aorta of apolipoprotein E-deficient mice. *Am J Pathol* 2001; **159**(4): 1455–1464.
36. Kinlay S, Creager MA, Fukumoto M, Hikita H, Fang JC, Selwyn AP, Ganz P. Endothelium-derived nitric oxide regulates arterial elasticity in human arteries in vivo. *Hypertension* 2001; **38**(5): 1049–1053.
37. Bank AJ, Kaiser DR, Rajala S, Cheng A. In vivo human brachial artery elastic mechanics: effects of smooth muscle relaxation. *Circulation* 1999; **100**(1): 41–47.
38. Latson TW, Hunter WC, Katoh N, Sagawa K. Effect of nitroglycerin on aortic impedance, diameter, and pulse-wave velocity. *Circ Res* 1988;**62**(5): 884–890.
39. Wilkinson IB, Qasem A, McEniery CM, Webb DJ, Avolio AP, Cockcroft JR. Nitric oxide regulates local arterial distensibility in vivo. *Circulation* 2002; **105**(2): 213–217.
40. Ito A, Egashira K, Kadokami T, et al. Chronic inhibition of endothelium-derived nitric oxide synthesis causes coronary microvascular structural changes and hyperreactivity to serotonin in pigs. *Circulation* 1995; **92**(9): 2636–2644.
41. Numaguchi K, Egashira K, Takemoto M, Kadokami T, Shimokawa H, Sueishi K, Takeshita A. Chronic inhibition of nitric oxide synthesis causes coronary microvascular remodeling in rats. *Hypertension* 1995; **26**(6 Pt 1): 957–962.
42. Takemoto M, Egashira K, Tomita H, et al. Chronic angiotensin-converting enzyme inhibition and angiotensin II type 1 receptor blockade: effects on cardiovascular remodeling in rats induced by the long-term blockade of nitric oxide synthesis. *Hypertension* 1997; **30**(6): 1621–1627.
43. Takemoto M, Egashira K, Tsutsui Y, Shimokawa H, Takeshita A, Sueishi K. [Vascular remodeling and nitric oxide]. *Rinsho Byori* 1997; Suppl(**104**): 216–223.
44. Takemoto M, Egashira K, Usui M, et al. Important role of tissue angiotensin-converting enzyme activity in the pathogenesis of coronary vascular and myocardial structural changes induced by long-term blockade of nitric oxide synthesis in rats. *J Clin Invest* 1997; **99**(2): 278–287.
45. Fitch R, Rutledge JC, Wang Y-X, Powers AF, Tseng JL, Clary T, Rubanyi GM. Synergistic effect of nitric oxide synthase inhibitor and angiotensin II in increasing aortic stiffness in mice. *Am J Physiol 2006; 290: H1190–H1198.*

21

Gene transfer to Dyslipidemic mice

Kazuhiro Oka,[1] **Andrew H. Baker**[2] and **Lawrence Chan**[1]

[1]*Departments of Molecular and Cellular Biology, and Medicine, Baylor College of Medicine, Houston, TX USA and* [2]*Cardiovascular Research Center, Division of Cardiovascular and Medical Sciences, University of Glasgow, Glasgow, UK*

Abstract

Gene-targeted and transgenic mice have been crucial in investigating the genetic and environmental factors affecting lipoprotein metabolism. Moreover, these models have contributed to the progress in our understanding of the pathogenesis of atherosclerosis associated with dyslipidemia. The development of efficient viral and nonviral gene delivery systems has transformed the experimental approach to studying the roles of genes under genetically defined conditions. This article describes the progress in mouse models of dyslipidemia and reviews the recent progress in liver-directed gene transfer systems.

Introduction

Coronary artery disease is the major cause of morbidity and mortality in industrial countries. Atherosclerosis accounts for this major complication. Atherosclerosis is a complex process in which many genes and environmental factors are involved. Over the past decade the mouse has emerged as the model of dyslipidemia because of its rapid reproduction, the extensive knowledge of its genetics, the ability to manipulate its gene expression, the relatively rapid lesion formation in genetically modified mice, and the relative ease of lesion analysis. However, as a species, the mouse is resistant to atherosclerosis, which is in part due to substantial differences in lipoprotein physiology. In an attempt to replicate human atherosclerotic conditions, mouse models of dyslipidemia have been developed through induced mutations or transgenic technology. The development of mouse models of diet-induced atherosclerosis was initiated by Paigen *et al.*'s works to identify a susceptible locus, Ath-1. Ath-1 is a

A Handbook of Mouse Models of Cardiovascular Disease Edited by Qinbo Xu

phenotype in which mice have increased fatty streaks at the aortic root and reduced high-density-lipoprotein (HDL) cholesterol in response to an atherogenic diet containing high fat, high cholesterol, and cholic acid.[1] In their studies, they identified important inbred strains which are susceptible (C57BL/6J) and resistant (C3H/HeJ) to an atherogenic diet. It should be noted that the C57BL/6 strain is exclusively used as a mouse model of atherosclerosis since this is the only strain which develops substantial atherosclerosis. Most of the useful mouse models are available through The Jackson Laboratory on a C57BL/6 strain. In this article, we will discuss mouse models of dyslipidemia, viral vectors used for gene transfer, and the route of vector administration.

Mouse models of Dyslipidemia

The most critical development for studying atherosclerosis caused by lipid disorders has been the generation of two popular mouse models, apolipoprotein E (ApoE) deficient ($Apoe^{-/-}$)[2,3] and low-density-lipoprotein (LDL) receptor-deficient ($Ldlr^{-/-}$) mice.[4] Intermediate-density-lipoprotein (IDL)/LDL cholesterol in $Ldlr^{-/-}$ mice is higher than wild type mice, and total plasma cholesterol is only 200–250 mg/dl but is increased to 350–450 mg/dl on a high-cholesterol diet.[4] In contrast, plasma cholesterol levels of $Apoe^{-/-}$ mice are 450–500 mg/dl and increased to 1500–2000 mg/dl in response to high cholesterol feeding.[3] The lipoprotein phenotypes observed in these two types of knockout mice are in sharp contrast to those in the corresponding genetic deficiencies in humans. Patients with homozygous familial hypercholesterolemia have much higher plasma cholesterol than those with an ApoE deficiency. This species-dependent phenotypic difference is in part caused by the differences in lipoprotein physiology. In humans, all ApoB generated in the liver is ApoB100, while about 70 per cent of the ApoB mRNA is edited in the liver of mice. This results in very-low-density lipoprotein (VLDL) containing ApoB48 which is more rapidly cleared through an ApoE ligand. Another major difference is the lack of cholesteryl ester transfer protein (CETP) in mice. These differences in lipoprotein metabolism are highlighted in Figure 21.1. Various genetic mouse models have been created to shed light on the pathogenesis of lipid abnormalities found in humans. Although gain-of-function transgenic mice have proven to be useful models, gene inactivation is the most widely used approach to study the function of specific proteins involved in lipoprotein metabolism and atherosclerosis. Below we review some of the most commonly used mouse models of dyslipidemia.

Abca1$^{-/-}$ mice

Tangier disease is an autosomal recessive lipid disorder. Affected individuals present enlarged orange tonsils, decreased total plasma cholesterol, LDL and HDL levels, decreased apolipoprotein A-I (Apoa-I) and A-II, but increased plasma triglyceride

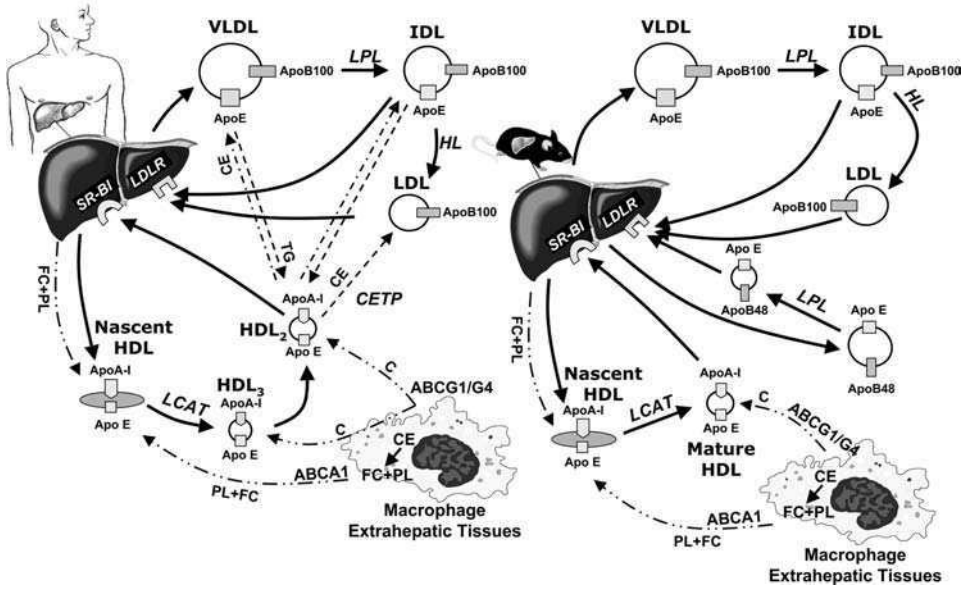

Figure 21.1 Overview of liver-secreted lipoprotein metabolism in humans and mice. Humans: ApoB100 containing TG-rich VLDL is secreted from the liver. TGs on VLDL are hydrolyzed to free fatty acids and glycerol by lipoprotein lipase (LPL). This process remodels VLDL to a smaller, denser IDL, which is taken up by the LDL receptor (LDLR) or other ApoE receptors through ApoE ligand, and are further remodeled by hepatic lipase (HL). ApoB100 is the sole apolipoprotein (apo) in LDL particles which are taken up by LDLR. Lipid-free or lipid-poor ApoA-I is secreted from the liver and serve as an acceptor for ABC transporter A1 (ABCA1)-mediated lipid efflux from hepatocytes as well as macrophages in extrahepatic tissues. ABCA1-mediated efflux of free cholesterol (FC) and phospholipids (PL) to ApoA-I forms nascent or pre β-high-density-lipoprotein (HDL) that are further modified by lecithin-cholesterol acyltransferase (LCAT).[13] The resulting large, less dense HDL_2 and smaller, more dense HDL_3 can serve as acceptors for ABCG1/ABCG4-mediated cholesterol (C) efflux. Cholesteryl ester (CE) from HDL can be transferred to apoB containing lipoproteins by the action of CETP in exchange for TG. HDL cholesterol is taken up by the liver and secreted into the bile for disposal through scavenger receptor BI (SR-BI). Mice: In mice, liver-secreted VLDL contains both ApoB100 and ApoB48 due to the presence of ApoB mRNA editing activity. TGs on ApoB48-VLDL are hydrolysed by LPL and remodeled to smaller, denser ApoB48-VLDL remnants. These particles are taken up by ApoE receptors including LDLR. The CETP activity is absent in mice, which results in large, ApoE-rich HDL_1 in addition to α-migrating regular HDL. However, HDL_1 overlaps substantially with apoB-containing remnant particles in both size and density. Broken arrows denote CE movement; double broken arrows denote TG movement; and triple broken arrows denote C, FC, and PL movement. Note: HDL_1 is not indicated

(TG); they also display an accumulation of cholesterol in tissues and macrophages as well as moderately accelerated atherosclerosis. The genetic mutations in patients have been identified in the gene for ATP-binding cassette transporter A1 (ABCA1). ABCA1 transporter facilitates the efflux of cellular phospholipids and cholesterol to apolipoprotein acceptors such as ApoA-I and ApoE during the formation of nascent or pre-β HDL. Increased ABCA1 activity has been reported to protect against

atherosclerosis. However, in the absence of ApoE, overexpression of ABCA1 increases atherosclerosis which suggests an important role of macrophage ApoE in ABCA1-mediated cholesterol efflux.[5]

The mouse *Abca1*$^{-/-}$ phenotype confirms the relationship between Tangier disease and ABCA1's function. HDL cholesterol is virtually absent in *Abca1*$^{-/-}$ mice with a reduced total plasma cholesterol and the presence of lipid deposition. In addition, the placenta is malformed, resulting in retardation of embryonic growth and fetal and neonatal loss. Altered steroidogenesis due to the lack of HDL cholesterol may be the primary cause. By 6 months of age, mice lacking ABCA1 develop autoimmune glomerulonephritis caused by an accumulation of immunocomplexes, and subsequent cardiomegaly with ventricular dilatation and hypertrophy, ultimately leading to congestive heart failure.[6] Nevertheless, hepatic cholesterol and phospholipid contents in these mice are not different from those in wild-type mice whether they are on either a normal chow or a high-fat, high-cholesterol diet. This suggests that HDL levels and ABCA1 activity do not control net cholesterol transport from the peripheral tissues via the liver into the bile.[7] The importance of ABCA1 in macrophages has been studied by Aiello et al. using double knockout mice and bone marrow transplantation.[8] The absence of ABCA1 reduces plasma cholesterol in both *Apoe*$^{-/-}$ and *Ldlr*$^{-/-}$ mice with concomitant skin xanthomatosis characterised by cholesteryl ester (CE) accumulation and the presence of foamy macrophages. However, global ABCA1 deficiency did not affect the development, progression, or composition of atherosclerotic lesions in these two models of hypercholesterolemia. In contrast, the selective inactivation of ABCA1 in macrophages markedly increased atherosclerosis in *Apoe*$^{-/-}$ mice. Therefore, the complete ABCA1 deficiency leads to an anti-atherogenic lipoprotein profile with macrophage ABCA1 having the anti-atherogenic properties independent of plasma lipids and HDL levels.

Apoa1$^{-/-}$ mice

ApoA-I is the main protein component of HDL. HDL deficiency constitutes the most common lipid abnormality in patients with coronary artery disease. The inverse correlation between HDL levels and coronary heart disease in humans suggests that HDL is protective against atherosclerosis development. This is supported by an ApoA-I transgenic mice or induced overexpression of ApoA-I in mouse models of hypercholesterolemia. Epidemiological studies have indicated that ApoA-I is a better marker of cardiovascular protection than HDL cholesterol. In patients with an ApoA-I deficiency, HDL levels are extremely low, and these patients are predisposed to atherosclerosis. Contrary to what might be expected, ApoA-I deficiency in mice does not induce atherosclerosis despite a marked reduction of HDL cholesterol, probably because the atherogenic lipoproteins are also low in these mice. The lack of ApoA-I in HDL is partly compensated for by ApoE.[9] However, HDL deficiency *per se* in *Apoa1*$^{-/-}$ mice does not lead to the development of atherosclerosis but does increase atherosclerosis susceptibility in combination with other risk factors such as elevated LDL, as in ApoB transgenic *Apoa1*$^{-/-}$ mice.[10]

Apobec-1$^{-/-}$ mice

ApoB mRNA editing is a posttranscriptional process by which ApoB100 mRNA is converted to ApoB48 mRNA. The reaction is mediated by an editing complex of which ApoB mRNA editing catalytic subunit-1 (APOBEC-1) is an essential catalytic component. Humanised mice can be created by liver-specific inactivation of APOBEC-1. Unexpectedly, *Apobec-1*$^{-/-}$mice have an essentially normal lipoprotein phenotype.[11] As mentioned above, there are important differences in lipoprotein metabolism between human and mouse species. Therefore, inactivation of APOBEC-1 has profound phenotypic effects when combined with other models of dyslipidemia.[12] CETP transfers CE from HDL to ApoB-containing lipoproteins such as VLDL and LDL in exchange for TG in humans.[13] CETP activity is absent in mice, which accounts in part for the low VLDL, IDL and the high HDL in this species. Transgenic CETP expression in *Apobec-1*$^{-/-}$ mice increases plasma ApoB100 levels and causes a shift of plasma cholesterol from the HDL to the IDL/LDL fraction without a significant effect on total plasma cholesterol. Feeding of a Western diet further increases this trend.[12] As expected, double knockout for APOBEC-1 and LDLR increases plasma ApoB100 and apoE levels with a concomitant increase of total plasma cholesterol in non-HDL fractions. The hypercholesterolemia in these mice is further exaggerated by feeding a Western-type diet. In contrast, mice deficient for both APOBEC-1 and ApoE have lower total plasma cholesterol levels than mice deficient for apoE only. This was due to the reduction of VLDL + IDL fractions in the double knockout mice. However, the difference in lipoprotein patterns is abolished by feeding a Western-type diet which further increases the total plasma cholesterol concentration. Therefore, in the absence of hepatic APOBEC-1, the severity of LDLR- and ApoE-deficient phenotypes are reversed, resulting in humanised mouse models.

Apoe$^{-/-}$ mice

ApoE is a plasma glycoprotein synthesised mainly in the liver and the brain, but also in low amounts in other tissues; it is a component of all lipoproteins except LDL. ApoE is a ligand for multiple lipoprotein receptors and plays an important role in cholesterol homeostasis. It is also synthesised by macrophages and is involved in inflammatory reactions in the vascular wall during atherosclerosis development. *Apoe*$^{-/-}$ mice have a total plasma cholesterol concentration of 450–500 mg/dl while on a normal chow diet, mostly distributed in the VLDL and chylomicron remnant fractions. They spontaneously develop atherosclerosis[3,14] and are the most popular model to study atherosclerosis.[15] Fatty streaks, indicative of early stage atherosclerosis with fat-laden macrophages and activated T cells, start to develop in the proximal aorta in *Apoe*$^{-/-}$ mice fed a normal chow at 3 months of age. A Western-type diet accelerates the process. After feeding a Western diet for 6 months, the lesions advanced to a complex phenotype including calcification and a thin fibrous cap, which provides a useful model to study remodeling of advanced lesions.

Development of atherosclerotic lesions reproducibly affects sites of the vascular tree that are associated with areas of low shear stress, oscillatory flow, or turbulent flow.[16] It should be noted that there are significant differences between humans and mice in relation to lipid homeostasis and atherosclerosis. In addition to differences in lipoprotein metabolism, there are also significant differences in atherosclerotic plaque pathology in the two species; plaque ruptures are rare in mice, whereas these are common clinical events in humans. Furthermore, the aortic sinus or root, an area frequently used for analysis in mice, is not a frequent site of clinically significant lesions in humans. The coronary arteries are the most important sites for development of clinically significant atherosclerosis in humans, whereas in mice, the coronary vessels normally consist of only a single layer of cells and are not generally used as an endpoint for morphological analysis of mouse lesions. Despite these limitations, *Apoe*$^{-/-}$ and *Ldlr*$^{-/-}$ mice have become powerful models for studying the pathogenesis of atherosclerosis as well as for developing therapeutic interventions. Furthermore, both models have been reported to develop spontaneous plaque rupture and secondary thrombosis albeit at low frequency.[17]

There are two methods to measure lesions. The first measures cross-sectional lesion thickness in slices taken at the level of the aortic sinus, which is useful for mild or early stage lesions. The second method called *en face* analysis involves morphometric quantitation of lesion areas of the entire aorta. Due to the selective, site-specific modulation of atherosclerosis, many laboratories study multiple affected sites or combine multiple methods of analysis.

Hl$^{-/-}$ mice

Hepatic lipase (HL) hydrolyses TG and phospholipids in chylomicron remnants, IDL, and HDL. It is a determinant of HDL levels by converting the phospholipid (PL)-rich HDL_2 to HDL_3. Like lipoprotein lipase, a non-catalytic function of HL has been reported, which includes enhancement of the binding or uptake of lipoproteins by interacting with cell surface receptors.[18] Patients with an HL deficiency have premature atherosclerosis and elevated plasma cholesterol, TG, VLDL, IDL, chylomicron remnants, TG-rich LDL and HDL subfractions, which are very similar to those in patients with type III hyperlipoproteinemia. *Hl*$^{-/-}$ mice have mildly (about 30 per cent) elevated plasma cholesterol, PL, and HDL cholesterol. The less dense, large HDL_1 is increased in these mice, demonstrating the importance of HL in HDL metabolism.[19] Overexpression of HL results in an anti-atherogenic lipid profile and reduces the aortic cholesterol content in cholesterol-fed transgenic mice.[20] However, HL deficiency in *Apoe*$^{-/-}$ mice reduces atherosclerosis despite an increase of total plasma cholesterol.[21] Similarly, HL deficiency in lecithin cholesterol acyltransferase (LCAT) transgenic mice reduces atherosclerosis in the presence of increased pro-atherogenic ApoB-containing lipoproteins.[22]

Lcat1$^{-/-}$ mice

Lecithin cholesterol acyltransferase (LCAT) is a plasma enzyme that mediates the transfer of fatty acids from phosphatidyl choline to free cholesterol (FC), forming CE and lysophosphatidyl choline. LCAT is synthesised mainly in the liver and circulates in plasma primarily by binding to HDL. It mediates the conversion of discoidal, nascent HDL particles into mature, spherical HDL.[13] Complete LCAT deficiency and Fish-eye disease (partial LCAT deficiency) are associated with markedly decreased levels of HDL cholesterol without an increase in atherosclerosis risk.[23] The markedly increased catabolism of ApoA-II and ApoA-II-containing HDL and containing and modestly increased catabolism of HDL particles containing ApoA-I may explain why patients with LCAT deficiency are not at an increased risk for premature atherosclerosis despite the presence of markedly decreased levels of HDL cholesterol.[23] Total plasma cholesterol, HDL cholesterol, and ApoA-I are markedly reduced in *Lcat1*$^{-/-}$ mice; they are modestly reduced in *Lcat1*$^{+/-}$ mice. In addition, plasma TG levels were higher in male, but remained normal in female *Lcat1*$^{-/-}$ mice. These mice also exhibit heterogeneous pre-β-migrating HDL and TG-rich VLDL.[24] The role of LCAT in atherosclerosis has been studied by crossing *Lcat1*$^{-/-}$ mice to *Ldlr*$^{-/-}$, *Apoe*$^{-/-}$ or CETP transgenic mice. Despite the presence of reduced HDL, atherosclerosis was significantly reduced in all mouse models with an LCAT deficiency.[25]

Ldlr$^{-/-}$ mice

Familial hypercholesterolemia (FH) is a common autosomal dominant disorder that affects approximately one in 500 individuals in the heterozygous form. FH is characterized clinically by elevated LDL cholesterol and deposition of cholesterol in tendons and skin (xanthomas) and in arteries (atheromas). Homozygous FH patients frequently die of myocardial infarction secondary to severe atherosclerosis by the second decade. The primary defect in FH is a mutation in the LDLR gene. The exact phenotype of *Ldlr*$^{-/-}$ mice was difficult to predict due to a major difference in LDL metabolism between humans and mice. In 1993, Ishibashi *et al*. reported the production of *Ldlr*$^{-/-}$ mice. These mice have plasma cholesterol levels of 200–250 mg/dl compared with levels of 90–125 mg/dl in wild type mice. A gene dosage effect is also evident. Total plasma cholesterol elevation involves mainly the IDL/LDL fractions. The HDL-cholesterol was also mildly elevated ($\sim$1.3-fold) in *Ldlr*$^{-/-}$ mice. The plasma cholesterol in *Ldlr*$^{-/-}$ mice increased to 350–450 mg/dl with little change in HDL cholesterol when these mice are put on a diet supplemented with 0.2 per cent cholesterol/10 per cent coconut oil.[4] *Apoe*$^{-/-}$/*Ldlr*$^{-/-}$ mice have a lipoprotein cholesterol pattern similar to that of *Apoe*$^{-/-}$ mice, with the total plasma cholesterol level of 620 ± 43 mg/dl compared to that of 579 ± 41 mg/dl in *Apoe*$^{-/-}$ mice on a normal chow diet. However, *Apoe*$^{-/-}$ mice have a marked elevation in ApoB48 but not in ApoB100, whilst *Ldlr*$^{-/-}$ mice have marked elevations in both

ApoB48 and ApoB100. An LDLR deficiency on an *Apoe*$^{-/-}$ background does not increase hypercholesterolemia beyond that seen with an ApoE deficiency alone even when the mice are fed a high cholesterol diet.[26] Although feeding *Ldlr*$^{-/-}$ mice with normal chow for 7 months did not induce significant atherosclerosis, feeding them with a diet containing 1.25 per cent cholesterol, 7.5 per cent cocoa butter, 7.5 per cent casein, and 0.5 per cent cholic acid increases plasma cholesterol levels to >1500 mg/dl and induces extensive atherosclerosis.[27] Both *Apoe*$^{-/-}$ and *Ldlr*$^{-/-}$ mice develop atherosclerosis throughout the aorta. However, *Ldlr*$^{-/-}$ mice are the preferred models for bone marrow transplantation experiments. Bone marrow cell reconstitution studies using donor cells from genetically modified mice other than those on an *Apoe*$^{-/-}$ background reduces plasma cholesterol levels in *Apoe*$^{-/-}$ mice, which leads to indirect effects of cholesterol lowering on atherosclerosis.[28] In contrast, transplants using *Ldlr*$^{+/+}$ donor bone marrow cells do not affect plasma cholesterol in *Ldlr*$^{-/-}$ mice.

Lpl$^{-/-}$ mice

Lipoprotein lipase (LPL) is a key enzyme that hydrolyses TG in circulating lipoproteins such as VLDL and chylomicrons. LPL also has non-catalytic functions by anchoring atherogenic lipoproteins to matrix molecules within the arterial wall and plays a role in the selective uptake of lipoprotein CE. This non-catalytic action of LPL may play an important role in modulating atherosclerosis development.[29] The importance of the catalytic function of LPL on lipoprotein metabolism is well documented in patients with an LPL deficiency (also known as type I hyperlipoproteinemia), a rare autosomal recessive disorder characterised by high TG and low HDL. The low HDL is caused by an insufficient transfer of surface components from VLDL to HDL. Type I hyperlipoproteinemia can also be caused by a deficiency of ApoC-II, a cofactor of LPL. Heterozygous LPL mutations are common and could lead to a familial combined hyperlipidemia phenotype. When these mutations are compounded by other risk factors, a significant increased risk of cardiovascular disease has been observed.[29] A homozygous LPL deficiency is lethal shortly after birth in mice. At birth, *Lpl*$^{-/-}$ mice have elevated TG and VLDL cholesterol levels. When permitted to suckle, *Lpl*$^{-/-}$ mice become pale, then cyanotic, and finally die with severe hypertriglyceridemia (15 087 mg/dl versus 188 mg/dl in controls). Heterozygotes had higher TG than wild type mice. Muscle-specific expression of LPL rescues *Lpl*$^{-/-}$ mice.[30]

Srb1$^{-/-}$ mice

Scavenger receptor class B type I (SR-BI) mediates the transfer of a variety of lipids between cells and lipoproteins. Unlike the interaction of other lipoproteins with lipoprotein receptors, the binding of HDL to SR-BI does not lead to its lysosomal degradation. Instead, SR-BI mediates selective lipid uptake from lipoproteins and

participates in cholesterol efflux. Overexpression of SR-BI in transgenic mice or by adenovirus-mediated hepatic gene transfer results in a disappearance of plasma HDL, whereas $Srb1^{-/-}$ mice have increased HDL cholesterol.[31] $Ldlr^{-/-}/Srb1^{-/-}$ mice show increased LDL cholesterol and ApoB levels. Atherosclerotic lesion size is significantly increased in males compared to $Ldlr^{-/-}$ mice.[32] When $Apoe^{-/-}/Srb1^{-/-}$ mice are maintained on a normal chow, they exhibit increased plasma cholesterol levels, mainly in the VLDL size fraction.[33] They also have large HDL-like lipoproteins. Atherosclerosis is markedly accelerated in these double knockout mice.

ApoB transgenic mice

In humans, the major cholesterol-carrying lipoprotein fraction is ApoB100-containing LDL, while it is HDL in mice. Apart from the generation of $Apobec\text{-}1^{-/-}$ mice described earlier, two other approaches have be used to increase the LDL fraction in mice: overexpresion of ApoB100 (transgenic) and making ApoB100 only mice by knocking in an artificial ApoB construct that contains a stop codon at the normal ApoB48 termination codon (ApoB48-only) or an ApoB construct that is resistant to ApoB mRNA editing (ApoB100-only). ApoB100-only mice crossed to $Apoe^{-/-}$ or $Ldlr^{-/-}$ mice reveal that the apoB100-only allele ameliorates the hypercholesterolemia in $Apoe^{-/-}$ mice, but aggravates the condition in $Ldlr^{-/-}$ mice. Interestingly, total plasma cholesterol levels are very similar in these two double transgenic mice (275–325 mg/dl). However, the prominent cholesterol peak is in the VLDL fraction in $Apoe^{-/-}/ApoB^{100/100}$ mice, while it is in the LDL fraction in $Ldlr^{-/-}/ApoB^{100/100}$ mice. *En face* analysis revealed that $Ldlr^{-/-}/ApoB^{100/100}$ mice have more atherosclerotic lesions than $Apoe^{-/-}/ApoB^{100/100}$ mice. This confirms that the smaller LDL particles (mean size of 24 nm) are more atherogenic than the larger VLDL particles (mean size 63 nm).[34] Sanan *et al*. used ApoB100 transgenic mice and found severe atherosclerosis in $Ldlr^{-/-}/ApoB^{100}$ transgenic mice, in which both ApoB48 and ApoB100 are synthesised in the liver.[35]

Vectors for liver-directed gene transfer

The liver is the only organ which has the machinery for cholesterol disposal into bile acids. Therefore, many gene transfer studies for dyslipidemia have targeted the liver. Despite much progress in non-viral vectors, viral vectors remain the major gene transfer vehicles.[36] Although naked or liposome-complexed plasmid DNA have not been a preferred gene delivery vector due to poor hepatocyte transduction and short lived transgene expression, nonviral plasmid DNA should not be written off due to the development of a hydrodynamic injection method as described in a later section. The recent setback in a gene therapy clinical trial for X-linked severe combined immunodeficiency using an integrating retroviral vector raised an old concern on

the potential complication of malignancy following gene transfer using integrating viral vectors such as retrovirus and lentivirus. In any case, these vectors are not the first choice for liver-directed gene transfer since they do not efficiently transduce hepatocytes. To date, adeno-associated virus (AAV) and adenovirus (Ad) remain the most useful vectors for *in vivo* gene transfer into the liver.

Adeno-associated virus (AAV)

AAV is a single-stranded DNA virus which was first described as a contaminant of tissue culture-grown simian adenovirus. AAV is a member of the Parvoviridae family and has a capsid with icosahedral symmetry approximately 20 nm in diameter.[37] At least 11 serotypes have been adopted for use as gene delivery vectors to date. However, more serotypes have been identified, expanding the AAV repertoire rapidly. The relatively poor transduction efficiency in liver in mice has been a limitation to the use of AAV serotype 2 (AAV2), the best characterised AAV vector. Several AAV, receptors and co-receptors have been identified, which include heparan sulphate proteoglycan, $\alpha_V\beta_5$ integrins, fibroblast growth factor receptor-1, platelet-derived growth factor receptor and sialic acid.[38] The presence of these receptors or co-receptors in tissues determines cell type- or tissue-specific transduction, which must be considered for targeting tissues. Therefore, one should be vigilant for the most recent development for AAV serotypes. AAV8, a recently isolated AAV, has been reported to be highly efficient in hepatic transduction. Unlike AAV2, AAV8 effectively transduces hepatocytes following intravenous administration.[39]

One disadvantage of an AAV vector has been its cloning capacity, which is about 4.7 kb. However, this size limitation can be overcome by an intermolecular joining method using two AAV vectors. Chao *et al*. used this approach to transfer the 7 kb Factor VIII gene by intraportal injection of two split AAV vectors.[40] Compared with an Ad vector, an AAV vector has a relatively long latent period between vector delivery and initiation of transgene expression. This lag period occurs because AAV vectors package a single-stranded genome and require host cell synthesis of the complementary strand for transduction. This problem can be overcome by a self-complementary AAV vector system in which the genome with half wild-type size can be packaged into either two copies or dimeric inverted repeat DNA molecules.[41] Serotypes 2, 5, and 8 capsid proteins mediate transduction of mouse liver. However, an AAV vector pseudotyped with serotype 8 expresses transgene at much higher levels than those with serotype 2 or 5. Interestingly this is due to a more rapid conversion of the single-stranded genome into a transcriptionally active, stable DNA duplex.[42]

Large-scale vector production of AAV is relatively demanding. The most popular production protocols require a three plasmid cotransfection of cells such as 293 or 293T cells with an AAV vector plasmid, helper plasmid which contains Ad E2A and E4, and AAV serotype-specific helper constructs encoding a *cap* as well as *rep* genes. In order to overcome this laborious protocol, a helper plasmid encoding

both Ad and AAV helper functions has been developed. In combination with iodixanol density centrifugation, the production of AAV vectors has become more affordable.[43]

Although AAV is considered a non-pathogenic virus, there has been a report of a potential role of AAV2 in hepatocellular carcinoma in mice. However, in a large-scale study in mice using AAV with serotypes 1, 2, 5, 7, 8 and 9 capsids, there was no increased incidence of tumorigenesis.[44] During latency in humans, AAV2 preferentially integrates at a site on chromosome 19q13.3-qtr, the so-called 'AAVS1' site, by targeting a sequence composed of a *rep* binding element and a terminal resolution site identical to the viral terminal repeats. Similar sites have been identified in CV-1 cells isolated from the African Green Monkey [45] and on mouse chromosome 7.[46] Upon infection with a helper virus such as Ad or herpes simplex virus, AAV enters the lytic cycle and undergoes replication and productive infection. Although most recombinant AAV vectors do not contain *rep* gene and will not integrate, the potential for mutation and oncogenesis may exist. In the absence of *rep* gene, the AAV genome has been shown to integrate randomly into the mouse genome with propensity towards gene regulatory sequences albeit at low frequency.[47] Despite some limitations, AAV has become a popular viral gene delivery system. For example, AAV2, AAV7 and AAV8 have been used to transfer LDLR gene into $Ldlr^{-/-}$ mice. AAV8 was the most effective in inhibiting atherosclerotic lesion progression.[48]

Adenoviral vector

Adenovirus (Ad) is a nonenveloped, double-stranded DNA virus approximately 70–100 nm in diameter and has an icosahedral protein shell surrounding a protein core that contains the linear viral genome of ~35 kb. Ad infects cells independent of the cell cycle. The primary attachment site of the fiber protein of Ad subgroup C to cell surface receptors is coxackievirus and adenovirus receptor (CAR). The internalization of Ad vector is mediated by interaction of the penton base protein with integrin $\alpha_V\beta_3$ or $\alpha_V\beta_5$ as the secondary internalisation receptors.[49] Heparan sulfate proteoglycans and LDLR-related protein have also been reported as cellular attachment sites for this subgroup of Ads.[50] In contrast, subgroup B such as serotype 11 and 35 uses CD46 as the entry site.[51] Of the over 50 different Ad serotypes, subgroup B, serotype 2 and 5 are the most characterized. First generation Ad vectors (FGAd) are based on these serotypes. FGAds contain all essential Ad genome except E1A, which encodes the key regulators of early gene expression. FGAd vectors are produced in E1A complementing cell lines such as HEK 293 cells. FGAd is replication defective; however, leaky viral gene expression occurs in the absence of the E1A element, which accounts for some of the toxicity resulting from FGAd vector-mediated gene transfer *in vivo*. In addition to its toxicity and immunogenecity, transgene expression mediated by FGAd is short-lived. In order to further attenuate its toxicity, the second and third generation Ad vectors have been developed. Overall improvement in the *in vivo* toxicity or duration of transgene expression of these vectors was marginal. Nevertheless, these early

generation Ad vectors have provided important information on the role of gene products involved in the pathogenesis of atherosclerosis.

Despite substantial efforts directed at improving the safety profile and prolonging transgene expression of early generation Ad vectors, the toxicity and immunogenecity of these vectors preclude their use for liver-directed gene therapy. Helper-dependent adenoviral vector (HDAd) is the latest Ad vector which has an improved safety profile with sustained transgene expression *in vivo*.[52] The HDAd vector lacks all viral coding genes with the exceptions of the inverted terminal repeats (ITR) for replication and the packaging signal. Helper virus, a FGAd, provides the necessary viral proteins *in trans* for packaging in culture. Chronic hepatotoxicity has been eliminated from HDAd vectors. However, the minimal acute toxicity exists. The innate immune response to HDAd vectors may be the underlining cause of the toxicity, which is the result from the direct interaction of viral particles with innate immune effector cells upon systemic vector administration, an ideal route for global hepatocyte transduction. Transient depletion of Kuppfer cells has been found effective to reduce toxicity as well as to increase hepatic transduction.[53] HDAd vector has a natural tropism to the liver, and it is our preferred gene delivery vector in liver-directed experimental gene therapy in small animals. Another advantage is its large cloning capacity, accommodating an insert of up to 37kb. Despite a greatly improved safety profile and long-term *in vivo* transgene expression, large-scale production of HDAd vectors has been a practical problem. However, a new protocol and the introduction of a suspension cell culture system have addressed this problem.[54]

Hybrid vector

Hybrid vectors are the newest improvement in gene delivery as they take advantage of the high infectivity of Ad vectors and the gene integration capabilities of other viral systems. The vectors can be categorised based on whether integration of vector genome is random (AAV ITR, *Sleeping Beauty* transposon) or site-specific (AAV-ITR combined with the expression of *rep* gene). Hybrid HDAd vectors reported include HDAd/retrovirus vector, HDAd/lentiviral vector, HDAd/AAV vector, HDAd/retrotransposon vector and HDAd/Epstein–Barr vector.[55] Integration of these hybrid vectors is random. For example, HDAd vectors in which the transgene is flanked by AAV-ITR have intergration at random sites on the host chromosome. An advantage of this hybrid is to expand the packaging limit of the AAV vector while allowing integration. Site-specific integration of AAV-ITR flanked transgene into mice carrying the human AAVS1 site has been reported by Recchia *et al*.[56] Hybrid vectors with the ability to integrate often require additional genes that have no role for the therapeutic outcome. For example, Rep protein is necessary for site-specific integration for a HDAd/AAV hybrid vector. However, Rep protein has negative effects on viral replication and is toxic to the cell. This problem has been addressed by using a tetracycline-regulated Rep expression system so that the protein is only produced in the presence of the antibiotic.

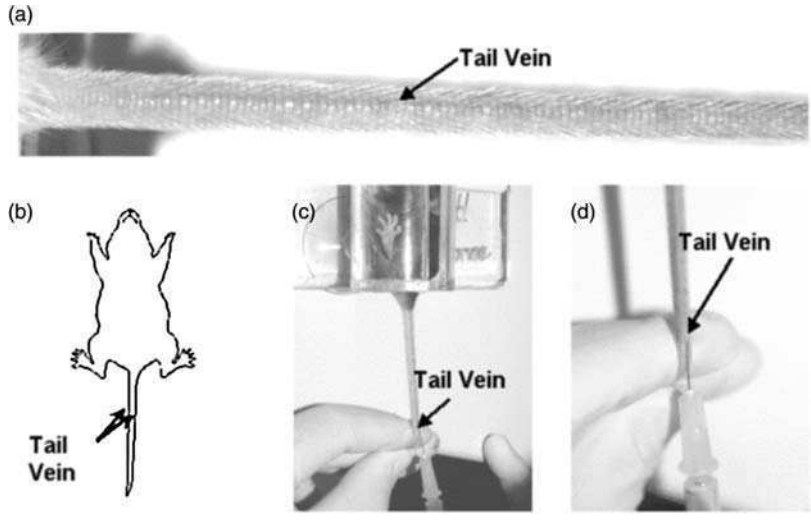

Figure 21.2 Illustration of tail vein injection. Mouse tail vein extends throughout the entire mouse tail length. (a) The wall of the mouse tail vein is thin and just underneath the tail skin, which can be visualised. (b) Two veins, which can be used for injection are located on the right and left lateral sides of the tail. (c) To administer a tail vein injection, the mouse is confined in a strainer in the left or right lateral position. Hold the end of the tail to extend it and to position the vein. (d) Using a one milliliter syringe with a 30G1/2 needle attachment, position the needle at 10–15° from the vein surface to insert the needle into the tail vein. For a color version of this figure, please see the images supplied on the accompanying CD

Route of vector delivery

Regular intravenous injection

The most popular gene delivery into the liver is through tail vein injection. This procedure requires some practice, especially for C57BL/6 mice because of the small vein size in this strain as shown in Figure 21.2. Representative mouse hepatocyte transduction by Ad vectors is shown in Figure 21.3. Alternative injection routes are intraportal infusion or injection through the jugular vein.

Hydrodynamic systemic injection

The use of naked plasmid DNA has obvious advantages including preparation of DNA and storage. It can be handled as a chemical instead of a biological item. The major limitation for transfection of the liver by naked DNA is poor transfection efficiency by systemic administration. It requires local administration or a surgical procedure. To overcome this problem, a hydrodynamics-based transfection method has been developed. The procedure includes rapid injection of a large volume of approximately 8–12 per cent of the body weight within 5–8 s. The liver is the major

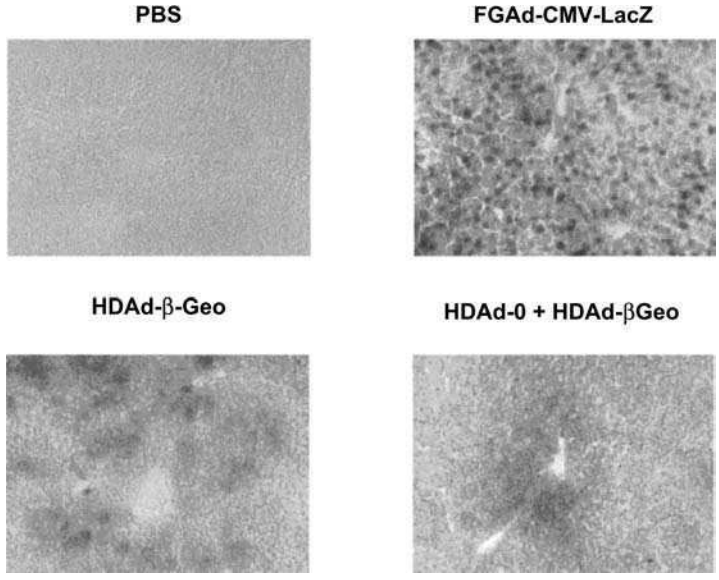

Figure 21.3 Hepatocyte transduction following intravenous injection of Ad vectors. C57BL/6 mice were injected via tail vein with 0.2 ml of phosphate-buffered saline (PBS) or PBS containing 1×10^{11} vector particles (vp) of FGAd-CMV-LacZ or HDAd-βgeo. One group of mice (HDAd-0 + HDAd-βgeo) was injected with 0.8×10^{11} vp of HDAd-0 (empty vector) followed by the second injection with 0.2×10^{11} vp of HDAd-βgeo 4 h later. PBS- and FGAd-CMV-LacZ-treated mice were killed 4 days after vector injection and HDAd vector-treated mice were killed 14 days after vector injection. For a color version of this figure, please see the images supplied on the accompanying CD

site for transduction, which has more than 1000-fold higher transgene expression than that of other organs. A single tail vein injection of 5 μg of plasmid DNA resulted in approximately 40 per cent of hepatocyte transduction. Furthermore, repeated injection can be made.[57] By combining this injection method and nonviral integrating vector systems such as retrotransposase and phage C31 integrase, naked plasmid DNA may serve an alternative gene delivery method to the liver in mice.[58]

Conclusion

The development of *Apoe*$^{-/-}$ and *Ldlr*$^{-/-}$ mice has been the most important progress in mouse models of dyslipidemia. Despite major differences in cholesterol metabolism between humans and mice, these models have offered a unique opportunity to investigate the genetic and environmental factors affecting the atherosclerotic process. The combination of mouse models and the application of gene transfer have further enhanced the utility of mouse models. However, certain limitations exist. The species differences in lipoprotein physiology, cardiovascular physiology, and plaque pathology must be taken into consideration before the results obtained in mouse models are extrapolated to human conditions.

Acknowledgments

We thank Dr. H. Chao and S. Cormier for their assistance in manuscript preparation. This work was supported in part by US Institutes of Health Grants HL59314, 51586 and HL73144.

References

1. Paigen B, Albee D, Holmes PA, Mitchell D. Genetic analysis of murine strains C57BL/6J and C3H/HeJ to confirm the map position of Ath-1, a gene determining atherosclerosis susceptibility. *Biochem Genet* 1987; **25**: 501–511.
2. Piedrahita JA, Zhang SH, Hagaman JR, Oliver PM, Maeda N. Generation of mice carrying a mutant apolipoprotein E gene inactivated by gene targeting in embryonic stem cells. *Proc Natl Acad Sci U S A* 1992; **89**: 4471–4475.
3. Plump AS, Smith JD, Hayek T, et al. Severe hypercholesterolemia and atherosclerosis in apolipoprotein E-deficient mice created by homologous recombination in ES cells. *Cell* 1992; **71**: 343–353.
4. Ishibashi S, Brown MS, Goldstein JL, Gerard RD, Hammer RE, Herz J. Hypercholesterolemia in low density lipoprotein receptor knockout mice and its reversal by adenovirus-mediated gene delivery. *J Clin Invest* 1993; **92**: 883–893.
5. Brewer HB, Jr., Santamarina-Fojo S. New insights into the role of the adenosine triphosphate-binding cassette transporters in high-density lipoprotein metabolism and reverse cholesterol transport. *Am J Cardiol* 2003; **91**: 3E–11E.
6. Christiansen-Weber TA, Voland JR, Wu Y, et al. Functional loss of ABCA1 in mice causes severe placental malformation, aberrant lipid distribution, and kidney glomerulonephritis as well as high-density lipoprotein cholesterol deficiency. *Am J Pathol* 2000; **157**: 1017–10129.
7. Groen AK, Bloks VW, Bandsma RH, Ottenhoff R, Chimini G, Kuipers F. Hepatobiliary cholesterol transport is not impaired in Abca1-null mice lacking HDL. *J Clin Invest* 2001; **108**: 843–850.
8. Aiello RJ, Brees D, Bourassa PA, et al. Increased atherosclerosis in hyperlipidemic mice with inactivation of ABCA1 in macrophages. *Arterioscler Thromb Vasc Biol* 2002; **22**: 630–637.
9. Li H, Reddick RL, Maeda N. Lack of apoA-I is not associated with increased susceptibility to atherosclerosis in mice. *Arterioscler Thromb* 1993; **13**: 1814–1821.
10. Hughes SD, Verstuyft J, Rubin EM. HDL deficiency in genetically engineered mice requires elevated LDL to accelerate atherogenesis. *Arterioscler Thromb Vasc Biol* 1997; **17**: 1725–1729.
11. Nakamuta M, Chang BH, Zsigmond E, et al. Complete phenotypic characterization of apobec-1 knockout mice with a wild-type genetic background and a human apolipoprotein B transgenic background, and restoration of apolipoprotein B mRNA editing by somatic gene transfer of Apobec-1. *J Biol Chem* 1996; **271**: 25981–25988.
12. Nakamuta M, Taniguchi S, Ishida BY, Kobayashi K, Chan L. Phenotype interaction of apobec-1 and CETP, LDLR, and apoE gene expression in mice: role of apoB mRNA editing in lipoprotein phenotype expression. *Arterioscler Thromb Vasc Biol* 1998; **18**: 747–755.

13. Linsel-Nitschke P, Tall AR. HDL as a target in the treatment of atherosclerotic cardiovascular disease. *Nat Rev Drug Discov* 2005; **4**: 193–205.
14. Zhang SH, Reddick RL, Piedrahita JA, Maeda N. Spontaneous hypercholesterolemia and arterial lesions in mice lacking apolipoprotein E. *Science* 1992; **258**: 468–471.
15. Meir KS, Leitersdorf E. Atherosclerosis in the apolipoprotein-E-deficient mouse: a decade of progress. *Arterioscler Thromb Vasc Biol* 2004; **24**: 1006–1014.
16. VanderLaan PA, Reardon CA, Getz GS. Site specificity of atherosclerosis: site-selective responses to atherosclerotic modulators. *Arterioscler Thromb Vasc Biol* 2004; **24**: 12–22.
17. Calara F, Silvestre M, Casanada F, Yuan N, Napoli C, Palinski W. Spontaneous plaque rupture and secondary thrombosis in apolipoprotein E-deficient and LDL receptor-deficient mice. *J Pathol* 2001; **195**: 257–263.
18. Santamarina-Fojo S, Gonzalez-Navarro H, Freeman L, Wagner E, Nong Z. Hepatic lipase, lipoprotein metabolism, and atherogenesis. *Arterioscler Thromb Vasc Biol* 2004; **24**: 1750–1754.
19. Homanics GE, de Silva HV, Osada J, et al. Mild dyslipidemia in mice following targeted inactivation of the hepatic lipase gene. *J Biol Chem* 1995; **270**: 2974–2980.
20. Busch SJ, Barnhart RL, Martin GA, et al. Human hepatic triglyceride lipase expression reduces high density lipoprotein and aortic cholesterol in cholesterol-fed transgenic mice. *J Biol Chem* 1994; **269**: 16376–16382.
21. Mezdour H, Jones R, Dengremont C, Castro G, Maeda N. Hepatic lipase deficiency increases plasma cholesterol but reduces susceptibility to atherosclerosis in apolipoprotein E-deficient mice. *J Biol Chem* 1997; **272**: 13570–13575.
22. Nong Z, Gonzalez-Navarro H, Amar M, et al. Hepatic lipase expression in macrophages contributes to atherosclerosis in apoE-deficient and LCAT-transgenic mice. *J Clin Invest* 2003; **112**: 367–378.
23. Rader DJ, Ikewaki K, Duverger N, et al. Markedly accelerated catabolism of apolipoprotein A-II (ApoA-II) and high density lipoproteins containing ApoA-II in classic lecithin: cholesterol acyltransferase deficiency and fish-eye disease. *J Clin Invest* 1994; **93**: 321–330.
24. Sakai N, Vaisman BL, Koch CA, et al. Targeted disruption of the mouse lecithin:cholesterol acyltransferase (LCAT) gene. Generation of a new animal model for human LCAT deficiency. *J Biol Chem* 1997; **272**: 7506–7510.
25. Lambert G, Sakai N, Vaisman BL, et al. Analysis of glomerulosclerosis and atherosclerosis in lecithin cholesterol acyltransferase-deficient mice. *J Biol Chem* 2001; **276**: 15090–15098.
26. Ishibashi S, Herz J, Maeda N, Goldstein JL, Brown MS. The two-receptor model of lipoprotein clearance: tests of the hypothesis in 'knockout' mice lacking the low density lipoprotein receptor, apolipoprotein E, or both proteins. *Proc Natl Acad Sci USA* 1994; **91**: 4431–4435.
27. Ishibashi S, Goldstein JL, Brown MS, Herz J, Burns DK. Massive xanthomatosis and atherosclerosis in cholesterol-fed low density lipoprotein receptor-negative mice. *J Clin Invest* 1994; **93**: 1885–1893.
28. Linton MF, Atkinson JB, Fazio S. Prevention of atherosclerosis in apolipoprotein E-deficient mice by bone marrow transplantation. *Science* 1995; **267**: 1034–1037.
29. Merkel M, Eckel RH, Goldberg IJ. Lipoprotein lipase: genetics, lipid uptake, and regulation. *J Lipid Res* 2002; **43**: 1997–2006.
30. Weinstock PH, Bisgaier CL, Aalto-Setala K, et al. Severe hypertriglyceridemia, reduced high density lipoprotein, and neonatal death in lipoprotein lipase knockout mice. Mild

hypertriglyceridemia with impaired very low density lipoprotein clearance in heterozygotes. *J Clin Invest* 1995; **96**: 2555–2568.
31. Rigotti A, Miettinen HE, Krieger M. The role of the high-density lipoprotein receptor SR-BI in the lipid metabolism of endocrine and other tissues. *Endocr Rev* 2003; **24**: 357–387.
32. Huszar D, Varban ML, Rinninger F, et al. Increased LDL cholesterol and atherosclerosis in LDL receptor-deficient mice with attenuated expression of scavenger receptor B1. *Arterioscler Thromb Vasc Biol* 2000; **20**: 1068–1073.
33. Trigatti B, Rayburn H, Vinals M, et al. Influence of the high density lipoprotein receptor SR-BI on reproductive and cardiovascular pathophysiology. *Proc Natl Acad Sci U S A* 1999; **96**: 9322–9327.
34. Veniant MM, Withycombe S, Young SG. Lipoprotein size and atherosclerosis susceptibility in Apoe(-/-) and Ldlr(-/-) mice. *Arterioscler Thromb Vasc Biol* 2001; **21**: 1567–1570.
35. Sanan DA, Newland DL, Tao R, et al. Low density lipoprotein receptor-negative mice expressing human apolipoprotein B-100 develop complex atherosclerotic lesions on a chow diet: no accentuation by apolipoprotein(a). *Proc Natl Acad Sci U S A* 1998; **95**: 4544–4549.
36. Thomas CE, Ehrhardt A, Kay MA. Progress and problems with the use of viral vectors for gene therapy. *Nat Rev Genet* 2003; **4**: 346–458.
37. Carter BJ. Adeno-associated virus and the development of adeno-associated virus vectors: a historical perspective. *Mol Ther* 2004; **10**: 981–989.
38. Tenenbaum L, Chtarto A, Lehtonen E, Velu T, Brotchi J, Levivier M. Recombinant AAV-mediated gene delivery to the central nervous system. *J Gene Med* 2004; 6 Suppl 1: S212–222.
39. Nakai H, Fuess S, Storm TA, Muramatsu S, Nara Y, Kay MA. Unrestricted hepatocyte transduction with adeno-associated virus serotype 8 vectors in mice. *J Virol* 2005; **79**: 214–224.
40. Chao H, Sun L, Bruce A, Xiao X, Walsh CE. Expression of human factor VIII by splicing between dimerized AAV vectors. *Mol Ther* 2002; **5**: 716–722.
41. McCarty DM, Fu H, Monahan PE, Toulson CE, Naik P, Samulski RJ. Adeno-associated virus terminal repeat (TR) mutant generates self-complementary vectors to overcome the rate-limiting step to transduction in vivo. *Gene Ther* 2003; **10**: 2112–2118.
42. Thomas CE, Storm TA, Huang Z, Kay MA. Rapid uncoating of vector genomes is the key to efficient liver transduction with pseudotyped adeno-associated virus vectors. *J Virol* 2004; **78**: 3110–3122.
43. Grimm D, Kay MA, Kleinschmidt JA. Helper virus-free, optically controllable, and two-plasmid-based production of adeno-associated virus vectors of serotypes 1 to 6. *Mol Ther* 2003; **7**: 839–850.
44. Bell P, Wang L, Lebherz C, et al. No Evidence for Tumorigenesis of AAV Vectors in a Large-Scale Study in Mice. *Mol Ther* 2005; **12**: 299–306.
45. Amiss TJ, McCarty DM, Skulimowski A, Samulski RJ. Identification and characterization of an adeno-associated virus integration site in CV-1 cells from the African green monkey. *J Virol* 2003; **77**: 1904–1915.
46. Dutheil N, Yoon-Robarts M, Ward P, et al. Characterization of the mouse adeno-associated virus AAVS1 ortholog. *J Virol* 2004; **78**: 8917–8921.
47. Nakai H, Montini E, Fuess S, Storm TA, Grompe M, Kay MA. AAV serotype 2 vectors preferentially integrate into active genes in mice. *Nat Genet* 2003; **34**: 297–302.
48. Lebherz C, Gao G, Louboutin JP, Millar J, Rader D, Wilson JM. Gene therapy with novel adeno-associated virus vectors substantially diminishes atherosclerosis in a murine model of familial hypercholesterolemia. *J Gene Med* 2004; **6**: 663–672.

49. Nemerow GR. Cell receptors involved in adenovirus entry. *Virology* 2000; **274**: 1–4.
50. Dechecchi MC, Melotti P, Bonizzato A, Santacatterina M, Chilosi M, Cabrini G. Heparan sulfate glycosaminoglycans are receptors sufficient to mediate the initial binding of adenovirus types 2 and 5. *J Virol* 2001; **75**: 8772–8780.
51. Gaggar A, Shayakhmetov DM, Lieber A. CD46 is a cellular receptor for group B adenoviruses. *Nat Med* 2003; **9**: 1408–1412.
52. Kochanek S. High-capacity adenoviral vectors for gene transfer and somatic gene therapy. *Hum Gene Ther* 1999; **10**: 2451–2459.
53. Schiedner G, Hertel S, Johnston M, Dries V, van Rooijen N, Kochanek S. Selective depletion or blockade of Kupffer cells leads to enhanced and prolonged hepatic transgene expression using high-capacity adenoviral vectors. *Mol Ther* 2003; **7**: 35–43.
54. Palmer DJ, Ng P. Helper-dependent adenoviral vectors for gene therapy. *Hum Gene Ther* 2005; **16**: 1–16.
55. Nuno-Gonzalez P, Chao H, Oka K. Targeting site-specific chromosome integration. *Acta Biochim Pol* 2005; **52**: 285–2891.
56. Recchia A, Perani L, Sartori D, Olgiati C, Mavilio F. Site-specific integration of functional transgenes into the human genome by adeno/AAV hybrid vectors. *Mol Ther* 2004; **10**: 660–670.
57. Liu F, Song Y, Liu D. Hydrodynamics-based transfection in animals by systemic administration of plasmid DNA. *Gene Ther* 1999; **6**: 1258–1266.
58. Ehrhardt A, Xu H, Huang Z, Engler JA, Kay MA. A direct comparison of two nonviral gene therapy vectors for somatic integration: in vivo evaluation of the bacteriophage integrase phiC31 and the Sleeping Beauty transposase. *Mol Ther* 2005; **11**: 695–706.

22

Hypertension

Daiana Weiss and **W. Robert Taylor**

Cardiology Division of the Department of Medicine, Emory University School of Medicine, Atlanta, GA, USA

Introduction

Hypertension is a major risk factor for cardiovascular disease that leads to stroke, renal insufficiency, coronary artery disease and heart failure. End organ damage from hypertension is extremely common as evidenced by the fact that a history of hypertension is present in approximately 90 per cent of patients with congestive heart failure, two-thirds of patients presenting with stroke and half of all patients with a myocardial infarction.[1] Overall, one out of three adults in the United States is hypertensive with an overall prevalence of almost 60 million individuals.

The development of hypertension is determined by a combination of genetic and environmental factors. Long-standing hypertension is characterised by increased vascular resistance to flow (due to constriction of resistance arteries), enhanced central and peripheral sympathetic output as well as sodium and water retention due to abnormalities in renal function. Although each of these abnormalities have been shown to be associated with hypertension in population studies and to cause hypertension in experimental settings, it is generally accepted that the pathogenesis of hypertension in humans is multifactorial and involves more than one of these mechanisms in a given individual. Various animal models of hypertension have been developed and widely used to study the etiology of hypertension, the pathogenesis of end-organ damage or to develop drugs to treat the disease.[2] Although these animal models have proven to be extremely useful in elucidating the various mechanisms of hypertension, no single model encompasses all aspects of hypertensive disease encountered in humans. Conceptually, a major problem

A Handbook of Mouse Models of Cardiovascular Disease Edited by Qinbo Xu

with all animal models of hypertension is the fact that hypertension is not a distinct disease entity but rather a clinical syndrome with a complex and incompletely understood etiology.

While many different species of been used as models of experimental hypertension, the rat has been the predominant species used in most studies. With the dramatic expansion in the use of transgenic and knockout mice, there has been a shift toward the use of murine models of hypertension. These genetic models are not only helpful in dissecting out the etiology of hypertension but they also lead to insights into the molecular mechanisms of end organ damage. This chapter will review the most commonly used murine models of hypertension and discuss their unique advantages as well as their limitations.

Murine models of hypertension can be divided into three broad, general groups: pharmacological, surgical and genetic models (see Table 22.1). While each of these strategies has the potential to provide valuable experimental results, each model has distinctive limitations in terms of their applicability. In addition, very few genetically engineered mouse models develop spontaneous hypertension.[3] Most require a pharmacological or salt challenge to induce hypertension.

Table 22.1 Mouse models of hypertension

Pharmacologically induced hypertension
Angiotensin II-induced hypertension
Norepinephrine-induced hypertension
L-NAME-induced hypertension
DOCA-salt-induced hypertension
Renal models of hypertension
Two kidney-one clip and one kidney-one clip models of hypertension
Suprarenal artery aortic coarctation
Genetically induced hypertension
Loss of function
B_2 salt-sensitive hypertension
ANP salt-sensitive hypertension
ANPR-A
Norepinephrine
D_{1A}
D_3
NHE1
eNOS
Gain of function
Angiotensinogen
Angiotensinogen (kidney-specific promoter)
Human renin-angiotensinogen

See text for abbreviations used.

Pharmacological models of hypertension

These models are caused by administering a pharmacological agent via a subcutaneous or oral route for relatively short periods of time ranging from days to weeks. Pharmacological models have been widely used because of their simplicity, reproducibility and lower cost.

Angiotensin II-induced hypertension

This is probably currently one of the more widely used pharmacological models of murine hypertension. It is well known that angiotensin II (Ang II) is a critical mediator of hypertension in both humans and various animal models of hypertension. Ang II can be delivered to mice subcutaneously via Alzet® osmotic mini pumps (Durect Corporation, Cupertino, CA USA) for a period of up to 2–4 weeks. Typically, doses of 0.70–1.0 mg/kg per day are used which cause a chronic elevation in plasma Ang II of approximately 80 fold over normal physiological levels.[4,5] This dose typically results in a rapid increase in systolic blood pressure of approximately 40–50 mmHg.[5] Hypertension persists for the duration of treatment and blood pressure normalises 2–3 days after the treatment is stopped. Administration of Ang II for 4–8 weeks in a mice prone to develop atherosclerosis (apolipoprotein E or low-density lipoprotein (LDL) receptor deficient) has been used as a model of accelerated atherosclerosis and aortic aneurysm formation[5,6]

The mechanism by which these animals develop hypertension in response to Ang II was initially thought to be due to the direct vasoconstrictor actions of Ang II on peripheral vasculature. This concept was recently challenged by studies demonstrating that subcutaneous delivery of Ang II leads to accumulation of Ang II in the central nervous system and local activation of superoxide production in subfornical region of brain.[7–9] Brain-specific delivery of an adenovirus overexpressing a superoxide scavenging enzyme or intracranial treatment with an AngII receptor blocker prevented the hypertension but not the cardiac hypertrophy suggesting that in this model the hypertensive response is due to central actions of Ang II, while the cardiac hypertrophy is induced by direct peripheral actions of Ang II.[7–9]

The Ang II model of hypertension can be used as an acute (7–14 days) or chronic infusion (4–8 weeks) to study Ang II-induced hypertension and end-organ damage. After 2 weeks of infusion, animals develop aortic and cardiac hypertrophy as well as cardiac fibrosis. If Ang II is used at intermediate concentrations (0.25–0.5 mg/kg per day to yield a two- to six-fold increase in normal plasma Ang II levels), the animals develop a ‘slow pressor response’ with a blood pressure increase delayed until the second week of infusion.[4] This model has been shown to cause oxidative stress and increased renal vasoconstriction which is at least partially mediated by renal thromboxane activation.[10] Administration of Ang II at very low doses of 0.15 mg/kg per min does not cause hypertension but still provokes a more modest degree of

cardiac and aortic hypertrophy and provides a model to study the non-hypertensive end-organ effects of Ang II.[11]

The technique for implanting the osmotic mini pumps to administer Ang II is relatively simple. After performing light anesthesia (Avertin or ketamine/xylazine administered intraperitoneally) the pumps are inserted in the back of the animals using aseptic technique. An incision is made in the skin using scissors. Using a hemostat, a subcutaneous pouch is created by blunt dissection and the pump is inserted into the pouch. The incision can be closed using non-absorbable sutures that necessitate their removal after healing in 10–14 days. Alternatively, an absorbable suture material can be used, although this approach is more likely to cause difficulties with dehiscence of the surgical incision. The blood pressure increase begins 2–3 days after pump implantation and reaches a plateau at 5–7 days.

The main advantages of the Ang II model of hypertension include, the ease of preparation of the animals, the reproducibility of the time course and magnitude of the hypertensive response and the ability to study disease mechanisms related to the renin–angiotensin system. The major disadvantages of this model are that it is a model that by definition is based on activation of the angiotensin signaling pathways and that the plasma levels of angiotensin II achieved are at the extreme of those seen in renovascular hypertension in humans.

Norepinephrine-induced hypertension

Norepinephrine (noradrenaline) is another agent used in animals to induce hypertension. Similar to the Ang II model, norepinephrine is given via subcutaneously implanted osmotic pumps. Our laboratories have used the dose of 5.6 mg/kg per day. This results in a blood pressure increase 2–3 days after pump implantation that reaches a similar level to that observed with the mice treated with Ang II. Norepinephrine infusion has been used as a model of cardiac hypertrophy or hypertension-induced accelerated atherosclerosis. Although the hypertensive effects are similar to those with Ang II, the magnitude of end-organ damage is generally less than that seen with Ang II infusion.[5] This difference is likely secondary to the non-pressor effects of Ang II.

L-NAME-induced hypertension

Inhibition of nitric oxide synthase (NOS) has been another pharmacological approach used to induce experimental hypertension. Arterial pressure is determined in part by the basal tone of arteries which depends on the balance between vasoconstrictors and vasodilators. One of the principal endogenous vasodilators *in vivo* is nitric oxide, which under normal conditions in the arterial wall is generated primarily by endothelial NOS (eNOS or NOS III). Administration of an inhibitor of eNOS such as N^{ω}-nitro-L-arginine methyl ester (L-NAME) in drinking water (1 mg/ml of water,

approximately equivalent of 100–120 mg/kg per day) effectively inhibits NO production by the endothelium. L-NAME is an L-arginine analog (the substrate of eNOS), which functions as a competitive inhibitor to prevent NO production. L-NAME induces moderate hypertension resulting in a 30–40 mmHg increase over control that occurs progressively over a two week period.[12–14] L-NAME administration for 8 weeks results in hypertension-induced vascular and cardiac hypertrophy and fibrosis. Importantly, eNOS knock out mice exhibit a similar degree of hypertension and end-organ damage, thus confirming the mechanism of this model.[12–14,15–19]

DOCA-salt-induced hypertension

Deoxycorticosterone acetate-salt (DOCA-salt) hypertension is a model of mineralocorticoid-induced hypertension associated with volume overload in which hypertension is generated by plasma volume expansion secondary to sodium retention. The DOCA-salt model is associated with dramatic reductions in plasma renin and Ang II concentrations. Note that some mouse strains (e.g., C57BL/6, C3H and BALB/c) have one renin gene (*Ren-1*^{c}) while others (e.g., 129SvJ and DBA/*2*) have two renin genes (*Ren-1*^{d} and *Ren-2*). A recent report suggests that the presence of the two renin genes does not alter baseline renin levels.[20] However, the *Ren-2* gene is thought to be constitutively expressed thus raising the possibility that plasma renin levels may not be suppressed in the DOCA-salt model when strains of mice are used that have the *Ren-2* gene.

The development of hypertension requires the presence of DOCA and a salt load (induced by a combination of 1 per cent NaCl in drinking water and reduction of renal mass by unilateral nephrectomy). DOCA comes in the form of a pellet that is implanted subcutaneously in the back of the mice by making a small incision in the skin and creating a small pouch for the pellet.[21,22] Pellets are available in a variety of formulations to release a given dose for a specificed time period. Our laboratory typically uses the 25 mg, 60 day release DOCA pellet (Innovative Research of America). This results in a dose of DOCA of approximately 0.02 mg/kg per day. In order to perform a unilateral nephrectomy, after induction of anesthesia with xylazine/ketamine, the abdomen and lateral flank of the mouse are shaved to avoid contamination with hair. Next, an incision is made on the left side below the rib cage and the left kidney is exposed. A hemostat is placed underneath the kidney to clamp of all the vessels connected to the left kidney. A suture is placed underneath the hemostat and all the vessels are ligated. The left kidney is removed together with the hemostat. The skin is closed with non-absorbable suture. The mice are given 1 per cent NaCl in the drinking water for the duration of the study.

The blood pressure usually begins to increase 3–5 days after surgery and the magnitude of the hypertensive response is similar to the one induced by hypertensive concentrations of Ang II. The mice develop not only hypertension but also cardiac and aortic hypertrophy as well as cardiac and renal fibrosis. Although the plasma renin–angiotensin II system is (RAS) reduced in this model, the tissue RAS has a role in the pathogenesis of end-organ damage because type 1 angiotensin II receptor

antagonists (AT1RA) prevent the abnormal cardiac, vascular and renal remodeling induced by DOCA-salt. However, hypertension is unaffected by AT1RA. Since hypertension is driven by volume retention in this model, aldosterone receptor antagonists or diuretics can effectively modulate the degree of the hypertensive response.[21,22]

Hypertension in the DOCA-salt model appears to be mediated in part by oxidative stress with evidence of a reduction in eNOS-derived NO and an increase in superoxide production from uncoupled eNOS and vascular reduced nicotinamide adenine dinucleotide phosphate oxidases.[23] Although this model *per se* is not encountered in human disease, its pathogenic mechanisms simulate to a great extent sodium-induced human hypertension and in particular oxidative stress-induced vascular dysfunction from hypertensive cardiovascular disease. This model of hypertension does exhibit some characteristics of the clinical form of hypertension found in the African American population.[24] This model has been used in other animals to study the effects of sodium overload on cardiovascular disease.[25–27] The DOCA-salt model does have some limitations including the requirement for certain expertise with surgical technique and the use of large amounts of sodium and mineralocorticoid. In addition, these mice may also develop hypokalemia and metabolic alkalosis caused by mineralocorticoid excess which can impact the degree of cardiac fibrosis and hypertrophy.[28]

Renal models of hypertension

Two kidney-one clip and one kidney-one clip models of hypertension

Goldblatt developed these models originally in dogs[29] and subsequently they were replicated in cats, sheep, rabbits, rats and more recently in mice[30]. The models rely on reduction of renal blood flow in one kidney by partial occlusion of the renal artery and preservation of one or both kidneys. Both of these are models of activation of the plasma RAS in acute phase during the first week after surgery. However, in the chronic phase, the mechanism of hypertension is different in the two models. In the two kidney-one clip model, hypertension is maintained by chronic activation of plasma RAS as a result of the under-perfused kidney. However, in the one kidney-one clip model, chronic hypertension is maintained by the increase in plasma volume due to inability of the remnant kidney to excrete the excess salt and water and therefore this is a renin-independent model.[29,30]

Wiesel *et al.* have provided an excellent description of the operative technique in mice in their original paper.[30] U-shaped stainless steel or clips are used ($3 \times 2 \times 1$ mm with a 2 mm long cleft, Exidel SA) to partially occlude the renal artery. The width of the clip opening is 0.12 mm. Large C57Bl6 mice (28-30 grams) and the kidneys are exposed through a small flank incision and externalised with a fine forceps. For clipping, the renal artery of the left kidney is separated by blunt dissection, and a clip is placed at the ostium of the renal artery close to the aorta. Next, a right nephrectomy

is performed by tying two ligatures around the renal vascular pedicle and ureter. The kidney is removed without the adrenal gland. The muscle layer is sutured, and the skin incision is closed with surgical staples. Note that when using mouse strains that have two renin genes, the same caveats described above for the DOCA-salt model apply.

Suprarenal artery aortic coarctation

The aortic coaraction model has also been applied in mice in order to generate a transient, high renin model of hypertension. This surgery for this model is technically difficult in mice in terms of creating the correct degree of aortic coarctation. Generally, younger mice are used in this model to allow the coarctation to develop with growth. Two-month-old mice are placed under general anesthesia and the abdomen is opened using a midline longitudinal incision. The abdominal aorta at the suprarenal level is exposed by gentle dissection of the retroperitoneal peri-aortic adipose and adventitial tissue. The aortic constriction is created by placing a 6-0 silk suture ligature against a 28G needle (for males) or 30G needle (for females) which cause approximately a 1/3 reduction in the luminal diameter of aorta.[31] This procedure creates a pressure gradient of approximately 20 mmHg between supra- and infrarenal aorta which induces an increase in plasma renin activity by the ischemic kidneys. In our experience, any attempt to induce a greater degree of coarctation and subsequently higher blood pressures is associated with an unacceptable degree of mortality. This model has been used to study the role of hypertension induced by endogenous activation of the RAS in the development and progression of atherosclerosis in apolipoprotein E-deficient mice. With this model, the mice develop cardiac hypertrophy and dilation 3–4 weeks after this procedure, which after 8 weeks progresses to cardiomegaly and heart failure in response to the chronic cardiac overload.[31] The use of this model is limited due to the technical difficulty of the model as well as the limited degree of hypertension that can be created. A distinct advantage of the model is the ability to examine aortic tissue above and below the coarctation which have been exposed to the same metabolic milieu but different blood pressures.

Genetic models of hypertension

The study of a gene function *in vivo* is achieved currently by using two approaches: overexpression (transgenic) or deletion of a candidate gene (knockout mouse). Given its critical role in the regulation of blood pressure, the RAS system was one of the first molecular pathways to be targeted for creating genetic hypertension in mice. Subsequently, genetic manipulation of other systems has been shown to cause hypertension in mice through a variety of different mechanisms. It is important to note that some of the 'models' of hypertension were not developed as models of hypertension *per se* but rather

they were developed to test specific hypotheses regarding the functional importance of the gene of interest in regulating blood pressure.

Transgenic mouse models utilising components of the RAS

Transgenic mice which overexpress rat angiotensinogen (rAGT) under the control of its endogenous promoter develop hypertension.[32] These animals exhibit elevated levels of plasma angiotensinogen which is a limiting factor in the RAS cascade leading to the generation of Ang II. Other mouse models have been developed by overexpressing the human renin (hREN) and angiotensinogen (hAGT)[33] and when crossed together exhibit severe hypertension and renal lesions characteristic of chronic elevation of plasma Ang II that are very similar to the Ang II infusion model.[34] Similar results were obtained when the AT1aR was specifically over-expressed in the brain although this model may involve central release of the potent vasoconstrictor hormone vasopressin.[2,35]

eNOS knockout mice

Nitric oxide is a potent vasodilator which is a primary regulatory element of endothelium-dependent control of basal vascular tone. Mice lacking eNOS exhibit moderate spontaneous hypertension,[18,19] which appears to be mediated in part by a persistent activation of plasma renin activity and subsequent increased superoxide production in the vascular wall.[23] Arteries isolated from eNOS knockout mice have impaired relaxation to acetylcholine and display increased wall thickness.[17]

Bradykinin B_2 receptor (BB2R) knockout mice

Bradykinin is an important vasodilator which stimulates release of nitric oxide and prostaglandins from the endothelium and regulates sodium and water excretion at the renal level. Most of the cardiovascular effects of bradykinin are mediated by the type 2 receptor. Mice deficient in BB2R are normotensive but develop hypertension after prolonged exposure to salt loading (3.1 per cent NaCl).[36] A detailed analysis of renal hemodynamics showed that bradykinin is a key vasodilator of renal arteries required to maintain renal perfusion. This appears to occur by decreasing renal vascular resistance in an attempt to compensate for the increase in blood volume that occurs with salt loading.[36]

Atrial natriuretic peptide (ANP) and atrial natriuretic peptide receptor (ANPR) knockout mice

ANP is a hormone released by atria in response to distension that most commonly occurs as a result of increased atrial pressure. Via direct effects on the vasculature, ANP stimulates the release of cyclic GMP which in turn activates guanylate cyclase.

This initiates a signaling cascade involving stimulation of protein kinase G which leads to vasodilatation in a pattern similar to that seen with nitric oxide. ANP also activates renal excretion of sodium after binding to ANPR in the renal tubular cells. Another important function of ANP is to oppose aldosterone secretion and Ang II-mediated effects. Therefore, mice lacking ANP or ANPR have spontaneous mild hypertension and develop severe hypertension upon exposure to a salt load (typically 2 per cent NaCl in the drinking water).[37,38] ANPR knockout mice also develop not only renal abnormalities but also cardiac hypertrophy and sudden death.[39]

Dopamine receptor knockout mice

Dopamine is a critical mediator of sodium transport and renin release in the kidney. Activation of the dopamine receptor D_{1A} (D1AR) prevents sodium reabsorption and induces renin release from the juxtaglomerular apparatus (JGA).[40] Deletion of D1AR causes hypertension most likely by reducing urinary sodium excretion and the resultant intravascular volume expansion.[41] In contrast to $D_{1A}R$, the stimulation of dopamine receptor D_3 inhibits renin release from JGA and induces renal vasodilation.[40] D_3R knockout mice develop mild hypertension (approximately a 20 mmHg increase in arterial blood pressure) and have a modest increase in plasma renin activity. In these mice, the hypertensive response is blocked by Ang II receptor antagonists proving that the mechanism of hypertension in these mice involves enhanced activation of RAS.[42]

Na^+–H^+ exchanger (NHE) transgenic mouse model

The reabsorption of sodium at the renal tubules is achieved by type 1 NHE by co-transporting sodium and hydrogen ions across basal membrane of proximal tubular cells. Therefore NHE regulates indirectly blood pressure by controlling the total body sodium and therefore vascular volume. Mice overexpressing type 1 NHE exhibit significant reduction in urinary excretion of sodium and are normotensive.[43] However, upon stress with a salt-loading diet (2 per cent NaCl), NHE transgenic mice become hypertensive due to increased sodium and intravascular volume expansion.[43]

Thus, there are a variety of mouse genetic models of hypertension. As pointed out above, many of these animals were developed to test hypotheses related to the functional importance of the various genes in the regulation of blood pressure. The strengths of these models lie in the well defined genetic abnormalities. This is distinctly different from many of the rat genetic models of hypertension which involve inbred strains that have altered expression of myriad genes. Conversely, the primary limitation of these models is that by definition they, like many of the pharmacological models, exhibit an alteration in a single gene product which is not reflective of the disease in humans. In addition, care must be taken to evaluate the effects of the background strain on the hemodynamic responses.

Measurement of blood pressure in mice

No discussion of mouse models of hypertension is complete without consideration of the technical challenges of blood pressure measurement in mice. There are basically three types of techniques available for measuring blood pressure in mice: catheter-based methods, telemetry systems and the non-invasive tail cuff technique. These techniques have recently been reviewed.[44]

Catheter-based techniques typically consist of either traditional fluid-filled catheters or transducer tipped catheters. In mice these techniques pose some unique considerations. First, the small size and extremely high heart rates make recording of accurate pressure waveforms very difficult. In fact, the high heart rate of mice essentially limits fluid-filled catheters to measuring only mean blood pressure. In addition, many anesthetic agents in mice significantly impair cardiac function, which limits the utility of this methodology to accurate reflect basal blood pressure.

Alternatively chronic indwelling telemetry units can be used to collect near continuous recordings of blood pressure in conscious, unrestrained mice for extended periods of time. The advantage of this method is the high quality of the recordings and the ability to collect data over extended periods of time. However, there are significant limitations to the use of this system. First, it is extremely expensive in terms of the initial purchase as well as ongoing costs for refurbishing transducers. In addition, in mice the surgery required to implant the telemetry units is quite extensive, which can have a significant physiological impact on blood pressure.

The most commonly used method for measuring blood pressure in mice is the non-invasive tail cuff technique. This methodology employs a tail cuff and a blood flow sensor to obtain assessments of systolic blood pressure. The main advantages of this technique are that it is relatively simple, rapidly performed and it allows the possibility of screening larger number of animals. The disadvantages are that the animals must be acclimated to a passive restraint system, only systolic blood pressures can be obtained and blood pressure is measured over a very short period of time.

Recently, the American Heart Association published a Scientific Statement detailing the advantages and disadvantages of the various techniques for measuring blood pressure in experimental animals.[44] The thrust of this position paper was that telemetry was a superior technique. However, it should be pointed out that this paper was not focused on mice where the technical and surgical issues relevant to the telemetry device can be extremely problematic. Our laboratory has experience with all three of these techniques and in most cases, the tail cuff technique is adequate for measuring blood pressure in mice with the caveat that an automated system is used, repeated measurements are made and that adequate time is allowed for the animals to become acclimated to passive restraint.

Summary

Currently there are numerous models available to study hypertension in mice. These models employ pharmacologic, surgical, genetic and combined approaches. When

designing studies involving mouse models of hypertension, it is critical to be aware of the physiologic mechanism of hypertension relevant to the model, the effects of background strain and the utility of the various modalities to assess the degree of hypertension.

References

1. AHA. Heart Disease and Stroke Statistics – 2005 Update. *Heart and Stroke Facts* 2005; **2005**: 26.
2. Sun ZJ, Zhang ZE. Historic perspectives and recent advances in major animal models of hypertension. *Acta Pharmacol Sin* 2005; **26**(3): 295–301.
3. Cvetkovic B, Sigmund CD. Understanding hypertension through genetic manipulation in mice. *Kidney Int* 2000; **57**(3): 863–874.
4. Kawada N, Imai E, Karber A, et al. A mouse model of angiotensin II slow pressor response: role of oxidative stress. *J Am Soc Nephrol* 2002; **13**(12): 2860–2868.
5. Weiss D, Kools JJ, Taylor WR. Angiotensin II-induced hypertension accelerates the development of atherosclerosis in apoE-deficient mice. *Circulation* 2001; **103**(3): 448–454.
6. Daugherty A, Manning MW, Cassis LA. Angiotensin II promotes atherosclerotic lesions and aneurysms in apolipoprotein E-deficient mice. *J Clin Invest* 2000; **105**(11): 1605–1612.
7. Zimmerman MC, Dunlay RP, Lazartigues E, et al. Requirement for Rac1-dependent NADPH oxidase in the cardiovascular and dipsogenic actions of angiotensin II in the brain. *Circ Res* 2004; **95**(5): 532–539.
8. Zimmerman MC, Lazartigues E, Lang JA, et al. Superoxide mediates the actions of angiotensin II in the central nervous system. *Circ Res* 2002; **91**(11): 1038–1045.
9. Zimmerman MC, Lazartigues E, Sharma RV, et al. Hypertension caused by angiotensin II infusion involves increased superoxide production in the central nervous system. *Circ Res* 2004; **95**(2): 210–216.
10. Kawada N, Dennehy K, Solis G, et al. TP receptors regulate renal hemodynamics during angiotensin II slow pressor response. *Am J Physiol Renal Physiol* 2004; **287**(4): F753–759.
11. Schultz Jel J, Witt SA, Glascock BJ, et al. TGF-beta1 mediates the hypertrophic cardiomyocyte growth induced by angiotensin II. *J Clin Invest* 2002; **109**(6): 787–796.
12. Ribeiro MO, Antunes E, de Nucci G, et al. Chronic inhibition of nitric oxide synthesis. A new model of arterial hypertension. *Hypertension* 1992; **20**(3): 298–303.
13. Kaikita K, Fogo AB, Ma L, et al. Plasminogen activator inhibitor-1 deficiency prevents hypertension and vascular fibrosis in response to long-term nitric oxide synthase inhibition. *Circulation* 2001; **104**(7): 839–844.
14. Baylis C, Mitruka B, Deng A. Chronic blockade of nitric oxide synthesis in the rat produces systemic hypertension and glomerular damage. *J Clin Invest* 1992; **90**(1): 278–281.
15. Knowles JW, Reddick RL, Jennette JC, et al. Enhanced atherosclerosis and kidney dysfunction in eNOS(−/−)Apoe(−/−) mice are ameliorated by enalapril treatment. *J Clin Invest* 2000; **105**(4): 451–458.
16. Rudic RD, Shesely EG, Maeda N, et al. Direct evidence for the importance of endothelium-derived nitric oxide in vascular remodeling. *J Clin Invest* 1998; **101**(4): 731–736.
17. Faraci FM, Sigmund CD, Shesely EG, et al. Responses of carotid artery in mice deficient in expression of the gene for endothelial NO synthase. *Am J Physiol* 1998; **274**(2 Pt 2): H564–570.
18. Shesely EG, Maeda N, Kim HS, et al. Elevated blood pressures in mice lacking endothelial nitric oxide synthase. *Proc Natl Acad Sci U S A* 1996; **93**(23): 13176–13181.

19. Huang PL, Huang Z, Mashimo H, et al. Hypertension in mice lacking the gene for endothelial nitric oxide synthase. *Nature* 1995; **377**(6546): 239–242.
20. Hansen PB, Yang T, Huang Y, et al. Plasma renin in mice with one or two renin genes. *Acta Physiol Scand* 2004; **181**(4): 431–437.
21. Johns C, Gavras I, Handy DE, et al. Models of experimental hypertension in mice. *Hypertension* 1996; **28**(6): 1064–1069.
22. Wang Q, Hummler E, Nussberger J, et al. Blood pressure, cardiac, and renal responses to salt and deoxycorticosterone acetate in mice: role of renin genes. *J Am Soc Nephrol* 2002; **13**(6): 1509–1516.
23. Landmesser U, Dikalov S, Price SR, et al. Oxidation of tetrahydrobiopterin leads to uncoupling of endothelial nitric oxide synthase in hypertension: role of the NADPH oxidase. *J Clin Invest* 2002; **111**: 1201–1209.
24. Taylor AL, Ziesche S, Yancy C, et al. Combination of isosorbide dinitrate and hydralazine in blacks with heart failure. *N Engl J Med* 2004; **351**(20): 2049–2057.
25. Houghton JL, Smith VE, Strogatz DS, et al. Effect of African-American race and hypertensive left ventricular hypertrophy on coronary vascular reactivity and endothelial function. *Hypertension* 1997; **29**(3): 706–714.
26. Kalinowski L, Dobrucki IT, Malinski T. Race-specific differences in endothelial function: predisposition of African Americans to vascular diseases. *Circulation* 2004; **109**(21): 2511–2517.
27. Kalinowski L, Malinski T. Endothelial NADH/NADPH-dependent enzymatic sources of superoxide production: relationship to endothelial dysfunction. *Acta Biochim Pol* 2004; **51**(2): 459–469.
28. Wang Q, Domenighetti AA, Pedrazzini T, et al. Potassium supplementation reduces cardiac and renal hypertrophy independent of blood pressure in DOCA/salt mice. *Hypertension* 2005; **46**(3): 547–554.
29. Goldblatt H LJ, Hanzal RF, Summerville WW. Studies on experimental hypertension: production of persistent elevation of systolic blood pressure by means of renal ischemia. *J Exp Med* 1934; **59**: 347–379.
30. Wiesel P, Mazzolai L, Nussberger J, et al. Two-kidney, one clip and one-kidney, one clip hypertension in mice. *Hypertension* 1997; **29**(4): 1025–1030.
31. Wu JH, Hagaman J, Kim S, et al. Aortic constriction exacerbates atherosclerosis and induces cardiac dysfunction in mice lacking apolipoprotein E. *Arterioscler Thromb Vasc Biol* 2002; **22**(3): 469–475.
32. Ohkubo H, Kawakami H, Kakehi Y, et al. Generation of transgenic mice with elevated blood pressure by introduction of the rat renin and angiotensinogen genes. *Proc Natl Acad Sci U S A* 1990; **87**(13): 5153–5157.
33. Takahashi S, Fukamizu A, Hasegawa T, et al. Expression of the human angiotensinogen gene in transgenic mice and transfected cells. *Biochem Biophys Res Commun* 1991; **180**(2): 1103–1109.
34. Fukamizu A, Sugimura K, Takimoto E, et al. Chimeric renin–angiotensin system demonstrates sustained increase in blood pressure of transgenic mice carrying both human renin and human angiotensinogen genes. *J Biol Chem* 1993; **268**(16): 11617–11621.
35. Lavoie JL, Bianco RA, Sakai K, et al. Transgenic mice for studies of the renin-angiotensin system in hypertension. *Acta Physiol Scand* 2004; **181**(4): 571–577.
36. Saitoh S, Scicli AG, Peterson E, et al. Effect of inhibiting renal kallikrein on prostaglandin E2, water, and sodium excretion. *Hypertension* 1995; **25**(5): 1008–1013.

37. Melo LG, Veress AT, Chong CK, et al. Salt-sensitive hypertension in ANP knockout mice: potential role of abnormal plasma renin activity. *Am J Physiol* 1998; **274**(1 Pt 2): R255–261.
38. Melo LG, Veress AT, Ackermann U, et al. Chronic regulation of arterial blood pressure in ANP transgenic and knockout mice: role of cardiovascular sympathetic tone. *Cardiovasc Res* 1999; **43**(2): 437–444.
39. Oliver PM, Fox JE, Kim R, et al. Hypertension, cardiac hypertrophy, and sudden death in mice lacking natriuretic peptide receptor A. *Proc Natl Acad Sci U S A* 1997; **94**(26): 14730–14735.
40. Jose PA, Raymond JR, Bates MD, et al. The renal dopamine receptors. *J Am Soc Nephrol* 1992; **2**(8): 1265–1278.
41. Albrecht FE, Drago J, Felder RA, et al. Role of the D1A dopamine receptor in the pathogenesis of genetic hypertension. *J Clin Invest* 1996; **97**(10): 2283–2288.
42. Asico LD, Ladines C, Fuchs S, et al. Disruption of the dopamine D3 receptor gene produces renin-dependent hypertension. *J Clin Invest* 1998; **102**(3): 493–498.
43. Kuro-o M, Hanaoka K, Hiroi Y, et al. Salt-sensitive hypertension in transgenic mice overexpressing Na(+)-proton exchanger. *Circ Res* 1995; **76**(1): 148–153.
44. Kurtz TW, Griffin KA, Bidani AK, et al. Recommendations for blood pressure measurement in animals: summary of an AHA scientific statement from the Council on High Blood Pressure Research, Professional and Public Education Subcommittee. *Arterioscler Thromb Vasc Biol* 2005; **25**(3): 478–479.

23

Ischemia-induced Neovascularisation

Ken-ichiro Sasaki, Christopher Heeschen, Alexandra Aicher and **Stefanie Dimmeler**

University of Frankfurt, Frankfurt, Germany

Introduction

The adult vasculature has the ability to remodel itself in response to tissue ischemia. This remodeling attempts to increase blood supply to better serve tissue metabolic demands, because normal tissue function basically depends on adequate supply of oxygen through blood vessels.[1] In humans, a number of clinical conditions exist, in which blood supply is insufficient (e.g., cardiac ischemia resulting from coronary artery disease and intermittent claudication resulting from peripheral arterial disease). Therefore, understanding the mechanisms of neovascularisation following tissue ischemia will finally lead to more effective treatments for these conditions.

Until now, the hind limb ischemia (HLI) animal model has been extensively used and perceived as a model of human peripheral arterial disease for numerous studies in vascular biology. This model is generated by unilateral ligation of the femoral artery to investigate ischemia-induced neovascularisation *in vivo*. Historically, the first HLI animal model was performed in rabbits.[2] During the last decade, most investigators in cardiovascular research switched to a mouse model of hind limb ischemia. Mouse models have gained popularity for a number of reasons including rapid gestation period (21 days), large litter size, and relatively low maintenance costs. In contrast to rabbits and rats, the mouse genome has been extensively characterized and gene-targeted 'knockout' and transgenic mice are attractive tools

A Handbook of Mouse Models of Cardiovascular Disease Edited by Qinbo Xu

to study the role of certain genes on neovascularization *in vivo*.[3] Therefore, the murine HLI model is a useful tool to investigate biological, biochemical, physiological, and pathological processes of ischemia-induced neovascularisation.[4] Eventually, this will lead to new treatment modalities for the management of ischemic disease in man.

In this chapter, we provide a comprehensive description of the techniques required to perform and to analyse the murine HLI model.

Materials and methods

Surgical procedures

The murine hind limb ischemia model is usually performed in 6∼8-week-old mice, which are anesthetised with chloral hydrate (400 mg/kg; Riedel-de Häen/ Sigma-Aldrich) intraperitoneally (i.p.) and medetomidine (0.1 mg/kg; Domitor®, Pfizer) intramuscularly. To remove the fur on the surface of the skin, the medial side of the right hind limb is cleaned either with a commercial depilatory cream or a shaver. The mice are placed in a spine position with the paws taped to the operating table. After disinfection of the skin with 70 % ethanol, a longitudinal skin incision is made using small scissors or a disposable scalpel. Then, the incision should be extended from a point just proximal of the knee to the inguinal ligament (Figure 23.1a). Fatty connective tissue on or around the limb muscle should be carefully removed to generate a severe phenotype of HLI, because adipose tissue may promote the angiogenic recovery after ischemia. In most instances of accidental tissue bleeding, it is usually sufficient to use a piece of gauze or cotton swabs for hemostasis. Magnification by a microscope (e.g., Stemi DV4 SPOT, KL200, Zeiss) should be used to get a detailed view of the surgical site. After a part of the abdominal wall adjacent to the inguinal ligament is lifted with the tip of a delicate mosquito forceps, the handle of the forceps is fixed on the opposite side of the animal using needles. Then, the femoral artery and vein are exposed and freed from connective tissue along their entire length using a curved forceps and cotton swabs. After identifying the deep femoral artery (Figure 23.1b,c) as a descending branch, it is ligated by an electric coagulator (e.g., ERBOTOM ICC50, ERBE). Next, the superficial femoral artery and vein as well as the superficial epigastric arteries are completely excised by electrocoagulation ranging from their proximal origin as a branch of the external iliac artery to the distal bifurcation to form the saphenous and poplital arteries. After confirming successful limb ischemia by checking the severe paleness of the feet, the overlying skin is closed with surgical staples (e.g., BD BBL™ 9 mm AUTOCLIP® Applier, No.427630, Becton Dickinson). The wound is finally disinfected again, and the mice are placed in a clean environment to prevent possible contamination of the surgical site. To reduce postoperative pain, carprofen (5 mg/kg; Rimadyl®, Pfizer) should be injected subcutaneously.

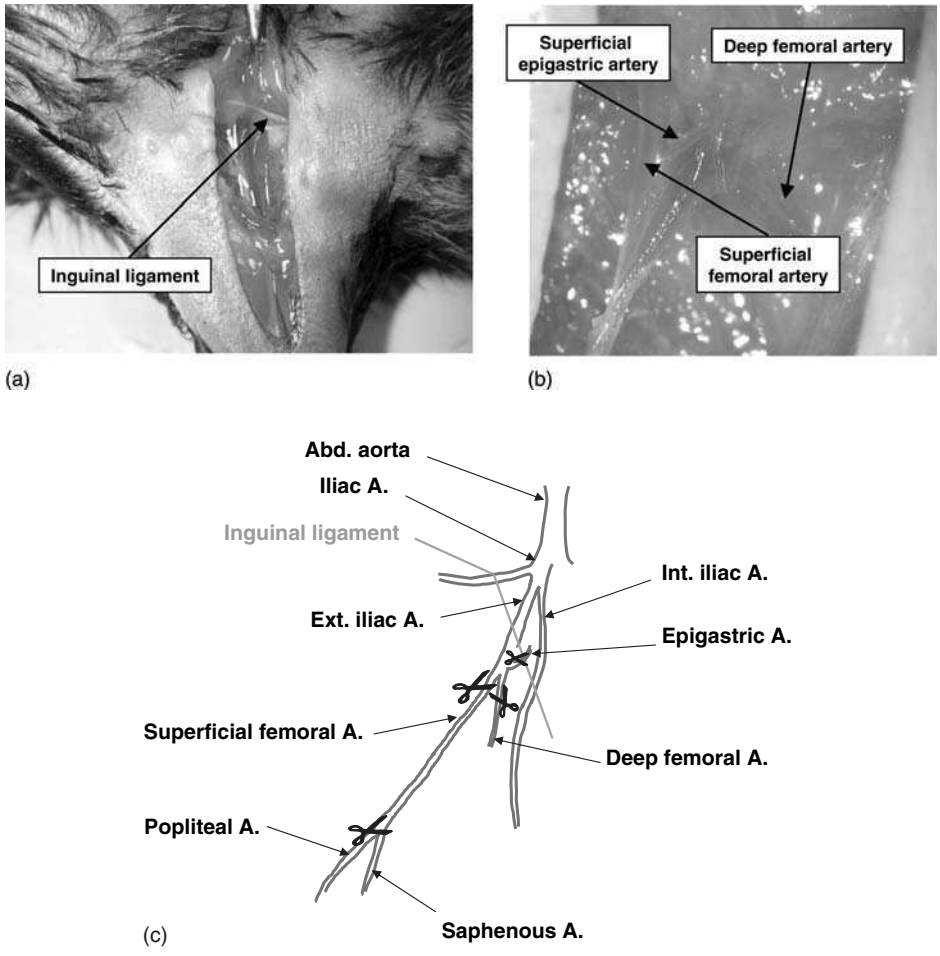

Figure 23.1 Macroscopical (a) and microscopical view (b) of the surgical site. A scheme of the anatomy of arteries in the murine hind limb is given in (c). For a color version of this figure, please see the images supplied on the accompanying CD

Assessment of neovascularisation

Laser doppler perfusion imaging

A Laser Doppler perfusion imager (LDPI) can be used to perform serial and non-invasive blood flow measurements. The laser Doppler perfusion monitoring was proposed for measurements of blood flow in the microcirculation over 20 years ago,[5–7] with the use of spectral broadening (due to the Doppler effect) of laser light scattered in the tissue. This technique relies on the frequency and phase shifts of the incident light beam to detect the velocity of red blood cells, with an algorithm to derive a signal which is called the laser Doppler flux (LDF) from the bandwidth of the Doppler spectrum. This LDF is related to the average velocity and number of red cells

within the tissue volume (although white cells also make a minor contribution) and is not influenced by the geometrical direction of each velocity component (i.e., flows in opposing directions are not inhibiting).[6]

The LDPI system (e.g., moorLDI^{TM}-Mark 2, Moor Instruments Ltd; Figure 23.2a) scans the target tissue with a low-power laser beam, which consists of a visible red laser beam (633 nm) and the low power light from a monochromatic stable laser (e.g. a helium neon gas laser or a single mode near infrared laser diode). Moving blood in the microvasculature causes a Doppler shift of the scattered laser and a color-coded map of blood flow is generated. The stored perfusion values for each pixel are then available for data analysis. Simultaneously, a digital camera records a still image which is similar to the blood flow image in size and aspect. This system is able to map tissue blood flow in areas ranging from 5×5 cm up to 50×50 cm with 256×256 pixel resolution, each pixel being an actual measurement. The frequency-broadened light, together with laser light scattered from static tissue, is photodetected and the resulting photocurrent processed to provide a blood flow measurement.

LDPI is performed to record perfusion of both right and left hind limbs at defined time points following surgery. After anesthesia with chloral hydrate (400 mg/kg i.p.), the excess fur on the area of interest is removed with either depilatory cream or a shaver. To measure blood flow, the animals are placed on a black rubber board to reduce background, followed by fixing all four limbs (fore and hind limbs) with 27G needles (e.g., BD Microlance^{TM} 3, 27G, Becton Dickinson). The black rubber board is then placed on a heating pad (e.g., Heating pad TM22, Beurer) or on a heating chamber at 37°C to minimise temperature variation. Each measurement is continuously obtained over the same defined region of leg and foot with simultaneous records

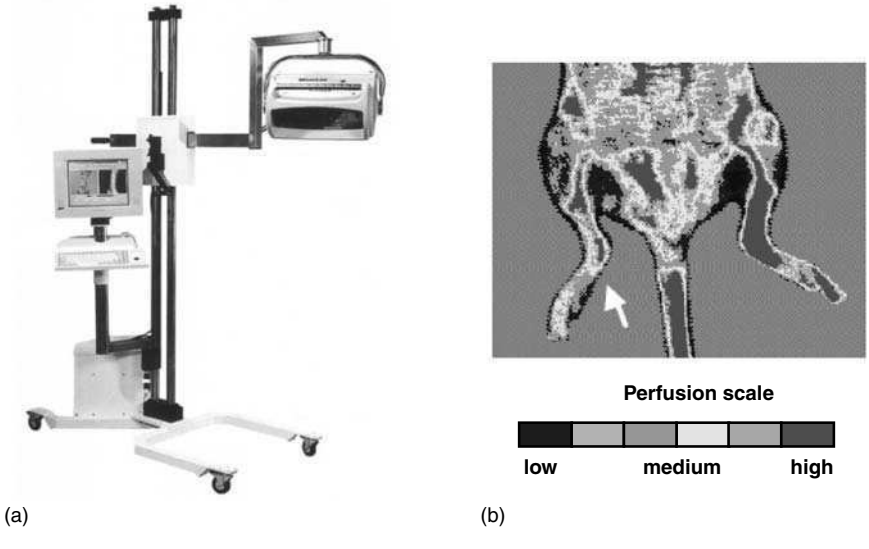

Figure 23.2 The laser Doppler device (a) and a representative laser Doppler scan (b) of a mouse 14 days after induction of hind limb ischemia. The perfusion scale depicts low perfusion as blue color, whereas red color represents high perfusion. For a color version of this figure, please see the images supplied on the accompanying CD

of color coded images for left and right limbs (Figure 23.2b). The latter analyses of blood flow are performed by calculating the mean of LDF on both ischemic and non-ischemic limbs, with the use of computer processing software provided by the manufacturer. To take into account the variables as ambient light and temperature, calculated perfusion of each mouse is further analysed and expressed as a ratio of left to right limb as the 'laser Doppler-derived relative blood flow.'[8–13]

Troubleshooting: one frequently asked question is how to avoid the assessment of the disturbing skin perfusion that is quite often enhanced and interferes with the blood flow underneath. For that purpose, the investigator could consider removing the skin before scanning to uncover the vessels. The drawback of this method is a fast dehydration of the uncovered muscles. Another important technical hint is to remove all staples using a staple remover (e.g., BD BBL^{TM} 9 mm AUTOCLIP^{R} Remover, No.427637, Becton Dickinson) as soon as possible (usually 1 week following surgery), to avoid inflammatory hyperperfusion of the surgical wound. This inflammatory hyperperfusion may lead to overestimation of the tissue perfusion in the ischemic limb. In case of hyperperfusion, this area should be excluded from the calculation of the mean flux of the blood flow in the whole ischemic hind limb. Consistently, in case of limb necrosis or limb loss related to ischemic necrosis, the mean flux of blood flow has to be corrected for the valid number of pixels in the measurement area. For this purpose, the necrotic area is set as zero. On the contrary, hypotension caused by overdose anesthesia induces a systemic hypoperfusion in the whole area of the ischemic/non-ischemic limbs and should be avoided. It is important that the measurements are performed, while sufficient and consistent perfusion is recorded in the tail as well as the non-ischemic limbs of all mice. Another question to which people paid attention is related to artifacts resulting in a gap between the animal's tail and body. Interestingly, these artifacts are generated by unremoved fur and hyperpigmented skin areas (Figure 23.3). Therefore, this problem is not present in light-skinned nude mice, which are well established for the transplantation of xenogenic cells. Finally, the

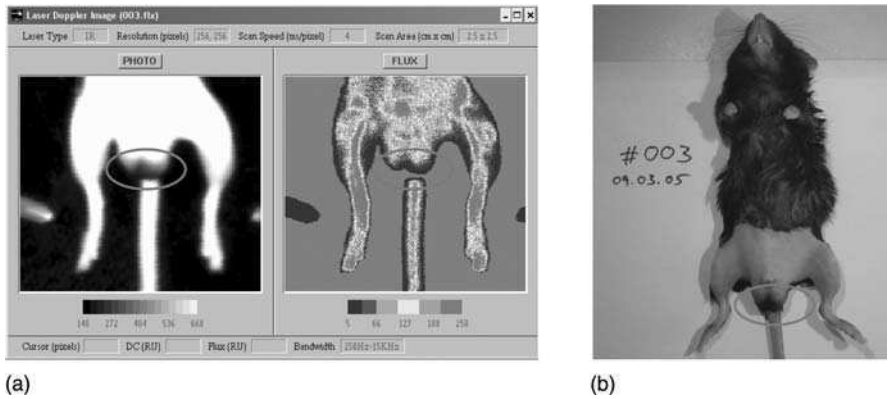

Figure 23.3 Still image taken by a digital camera (a: left panel), laser Doppler scan (a: right panel), and macroscopical view (b) of an untreated C57B1/6J mouse. The red circle marks the hyperpigmented and/or furry skin of the scrotum, which is producing the artifact. For a color version of this figure, please see the images supplied on the accompanying CD

distance between the detector and the measuring site should be identical for all measurements. Recently, Seifalifan *et al.*[14] demonstrated that the LDPI was dependent on the distance between the detector and the tissue but not from tissue oxygenation in the range of 10.7 to 66 kPa. Moreover, the investigator has to pay special attention to the laser Doppler processing software, because it can be difficult to univocally identify the original file representing the actual laser Doppler measurements.

Microsphere assay

The regional blood flow of the skeletal muscles in the hind limbs can also be measured by using stable gold-labeled microspheres at different time points after surgery.[15] After anesthesia with chloral hydrate (400 mg/kg i.p.), medetomidine (0.1 mg/kg i.m), and carprofen (5 mg/kg), the mice are placed in a spine position with paws taped to the operating table. It is important that the fore limbs are not over-stretched, as this can compromise respiration. To obtain sufficient ventilation during open chest intracardial injection, the mice are either intubated or tracheotomised and connected to the respirator (e.g., Mouse Ventilator MINIVENT Type 845, Harvard Apparatus), followed by thoracotomy to expose the heart. To achieve a maximal vasodilatation in the tissue of hind limbs, adenosine (1.5 mg/kg, ADREKAR®, Sanofi Winthrop) is infused via the left ventricle together with a thoroughly mixed suspension of microspheres (0.5×10^6 microspheres in 0.2 ml, 15 μm diameter, e.g., STERIspheres™-Gold, No.C-15H20, BioPAL). Mice have to be kept alive for at least 5 min following infusion to achieve a sufficient systemic circulation of the microspheres. Eventually, the adductor and gastrocnemial muscles are harvested from both the right and left limbs. After the wet weight of each tissue sample has been determined, they are kept in a plastic tube and dried at 70°C over night using a hybridisation oven (e.g., Hybridiser HB-1D, Techne), and sent to the company (e.g., BioPAL; BioPhysics Assay Laboratory)[14] for spectrophotometric analysis to detect the microspheres trapped in the capillaries of the harvested muscles. The achieved values have to be corrected for the corresponding tissue weight and a ratio between ischemic and non-ischemic limbs is calculated.

Histological assessment of neovascularisation

The histological evidence of neovascularisation after tissue ischemia can be determined by measuring the capillary density and the number of conductant vessels in microscopic sections obtained from the ischemic hind limbs.[4,8,10,13] Mice are killed at defined time points following surgery by inhalation of an overdose of isoflurane. Tissue specimens are obtained as transverse sections from the adductor and the semimembranous muscle of ischemic and non-ischemic limbs in each animal. These two muscles are chosen for the histological analysis because they are the major muscles of the medial thigh where neovascularisation is occurring after ligation of the deep femoral artery. Muscle samples are

embedded in OCT compound (e.g., OCT compound 4583, Tissue-Tek^{R}, Sakura) and frozen, while sitting on a grid in prechilled 100 % 2-methylbutane isopentane (No.59075, Fluka/Sigma-Aldrich) in a container floating in a larger dewar container filled with liquid nitrogen. Frozen tissue sections (5–10 µm in thickness) are cut from each specimen on a cryostat (e.g., CM3050S, Leica Microsystems) so that the muscle fibers are oriented in a transverse way. Frozen cross-sections are then air dried for 30 min, and fixed in cold acetone for 2 min. Air drying is performed for another 5 min, and the sections are washed with phosphate-buffered saline (PBS) for 10 min. After encircling the tissues on a dry glass slide (e.g., Menzel-Gläser SuperFrost® Plus, Menzel) with a felt-tip pen for immunohistochemistry (e.g., DAKO pen, No.S2002, Dako) to provide a barrier to liquids, non-specific protein binding is blocked incubation with 5 % bovine serum albumin in PBS for 30 min. Then, immunohistochemical staining for capillary density is performed by the identification of the cell membranes by an antibody for laminin (Abcam) followed by anti-rabbit-Alexa488 (Molecular Probes)[13] and of the vasculature by an antibody for CD31 (PE-labeled; BD Biosciences; Figure 23.4a). To stain conductant vessels, antibodies for smooth muscle α-actin (Cy3-labeled; Dako) are used (Figure 23.4b).[8–12] After the final washing of the stained sections with PBS, aqueous mounting medium (e.g., Fluorescent Mounting Medium, No. S3023, DakoCytomation) is dropped on the tissue, followed by covering with a coverslip (e.g., Cover glasses 24 × 55 mm, NO.1, Paul Marienfeld). Images are examined with a fluorescent microscope.

Capillary density, an index of angiogenesis, is examined by counting the number of capillaries in the tissue sections taken from the ischemic and non-ischemic limbs.

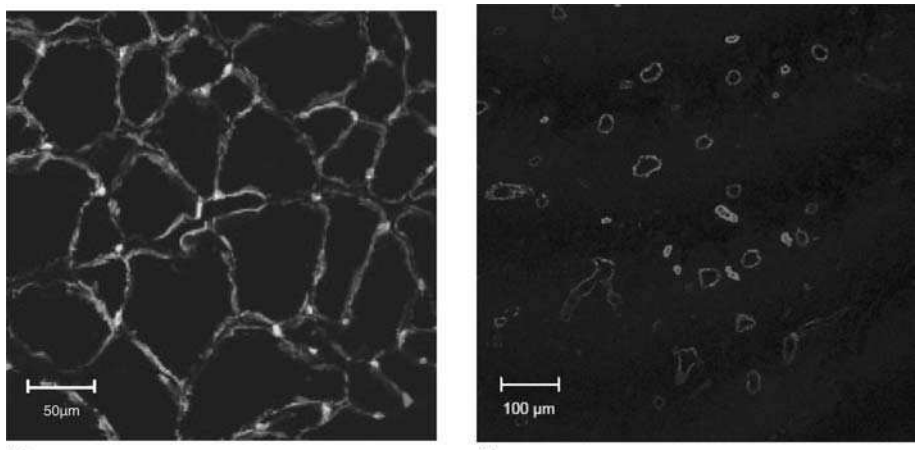

Figure 23.4 Histological analysis of the capillary density, which is obtained from the ratio of the number of capillaries (CD31 staining for endothelial cells; red) and the number of myoctes (staining of the myocte membrane by laminin; green) (a). Conductance vessels are stained by smooth muscle α-actin (red) (b). For a color version of this figure, please see the images supplied on the accompanying CD

Capillaries are counted using a 40× objective in 10 randomly selected fields. To ensure that analysis of capillary density is not overestimated due to muscle atrophy, or underestimated due to interstitial edema, capillary density is expressed as number of capillaries per myocyte. Moreover, conductance vessels identified by staining for smooth muscle α actin are counted separately as small (20–50 μm), medium, (>50–100 μm), and large vessels (>100 μm).

The swimming test as a measurement for functional changes

While LDI measurements detect changes in blood flow in an anesthetised animal without physical stress, we use a swimming test that allows us to examine genetic or pharmacologic effects on the blood flow during physical activity. For this purpose, we used a jet stream swimming pool (Figure 23.5a).[16,17]

In comparison to exercise tests on treadmills, the swimming test offers many advantages. The animals have to be trained for some weeks to get used to run on the treadmill and during that time there are many drop-outs. Moreover, it is another disadvantage that the animals try to escape from running on the treadmills, so that they have to be forced to keep on running by electric shocks, which are painful and do not represent a physiological physical stress. In contrast, the swimming test measures the maximum of a balanced physical activity without pain and appears to be superior to treadmill experiments. In addition, the test focuses on the physical activity of the animals' hindlimbs, which are the target after induction of hindlimb ischemia. To perform the swimming test, mice are dropped into swimming pool with a jet stream generated by a water pump. According to previous experiments by Matsumoto *et al.*,[16] the number of hindlimb kicks but not forelimb was increased by speeding up the current of water. Moreover, the current speeds of water revealed a strong correlation with the workload. Another technical hint is to generate a jet stream of water to prevent the mice from resting at exposed tubings originating from the water pump system. The depth of the water should just allow them to touch the ground if they stretch out completely so that the animals do not panic during exhaustion. To get best results, the water temperature has to be kept at 34°C.[16] The mice have to be trained the week before the final experiment is scheduled in order to learn how to swim. To minimise the variability between good and bad swimmers, some animals will also drop out. For the final experiments, the total time that the mice can keep on swimming without submerging for 5 s is scored. If the goal is to examine the effects of a pharmacologic or cell therapy, the results of the swimming test before and after the onset of the therapy will be determined. Eventually, we compared the LDI and the swimming test blood flow measurements and found a strong correlation between these two experimental set ups (Figure 23.5b). As expected, the LDI blood flow measurements underestimate the genetic or therapeutical changes, because the animals are kept at rest and had to undergo anesthesia for the recording of the LDI measurements. Therefore, the swim test seems to be more useful to detect less pronounced functional changes in blood flow.

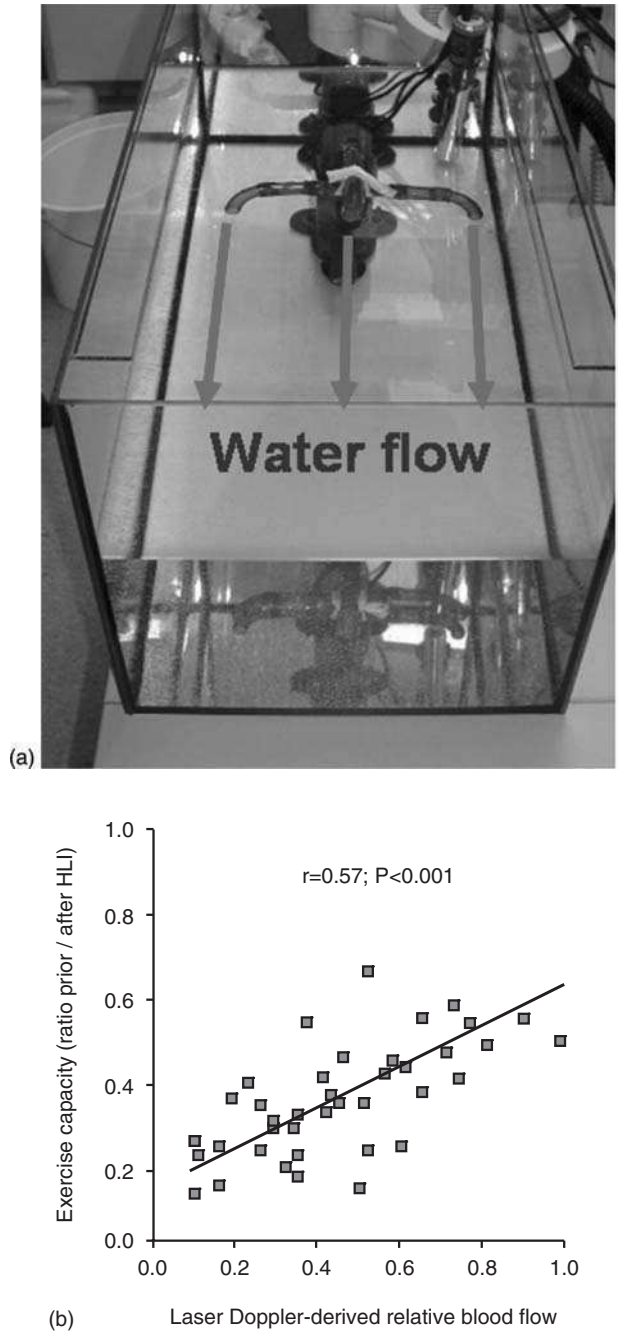

Figure 23.5 (a) A typical swimming pool for the swim test is shown. (b) Correlation between the LDI measurements of anesthesized nude mice 14 days after induction of hindlimb ischemia and the ratio of the time scored before a mouse submerges for 5 s in the swimming test before and 14 days after induction of hindlimb ischemia. For a color version of this figure, please see the images supplied on the accompanying CD

Discussion

At least three distinct processes are involved in postnatal vascular remodeling: these processes have been termed 'angiogenesis', 'vasculogenesis', and 'arteriogenesis', These processes occur in different types of vessels and are regulated by separate stimuli.

Angiogenesis is recognised as the sprouting of pre-existing capillaries, attributed to endothelial cells' migration, proliferation, and tube formation within the ischemic tissue, and thereby contributes to improved oxygen delivery of individual cells.[1] On the other hand, vasculogenesis describes a process involving the mobilisation and recruitment of endothelial progenitor cells (EPCs) from the bone marrow in response to ischemia. These EPCs are capable of incorporation and differentiation into endothelial cells in foci of neovascularisation.[18,19]

Arteriogenesis is referred to the enlargement of pre-existing collateral arterioles, allowing increased blood flow to downstream tissue, serving to restore tissue perfusion when the original pathway for blood flow has been obstructed. For instance, arteriogenesis in the upper thighs of animals with experimental hind limb ischemia increases blood flow to the distal limb. On the other hand, several experimental groups suggested that tissue ischemia does not appear to be an important controller of arteriogenesis in animal models of peripheral vascular disease, because the collateral vessels, which are undergoing remodeling, are typically not surrounded by ischemic tissue.[20,21] However, the increased collateral flow after tissue ischemia actually activates the endothelial cells via several molecular processes, and these cells further upregulate b-fibroblast growth factor, platelet-derwed growth factor-B and transforming growth factor-β 1, thereby inducing the proliferation of smooth muscle cells and vessel enlargement in ischemic tissue.[1] Therefore, the process of arteriogenesis in the model of hind limb ischemia should be assessed histologically by counting the number of conductant vessels attributed by arteriogenesis.[9,11]

Taken together, postnatal neovascularisation is generated not only by the formation of new vessels attributed to angiogenesis and vasculogenesis but also by the enlargement of preexisting collateral vessels. Thus, the model of HLI is a helpful tool to investigate three distinct aspects (angiogenesis, vasculogenesis, and arteriogenesis) contributing to postnatal neovascularisation. In this respect, laser Doppler perfusion imaging provides a non-invasive, reproducible, and beneficial technique to assess the tissue blood flow after induction of hindlimb ischemia.

Application

The presented mouse model turns out to be a adequate means for studying not only the effects of gene targeting on neovascularisation, but also the impact of different types of circulating stem and progenitor cells (e.g., different primary cells, pharmacologically modified cells, gene-modified cells) on postnatal neovascularisation. Therefore, the HLI model is a useful tool to investigate physiological and pathological processes

of neovascularization in vivo, and may lead to new therapeutic strategies for patients with cardiovascular diseases.

References

1. Carmeliet P. Mechanisms of angiogenesis and arteriogenesis. *Nat Med* 2000; **6**: 389–395.
2. Hendricks DL, Pevec WC, Shestak KC, Rosenthal MC, Webster MW, Steed DL. A model of persistent partial hindlimb ischemia in the rabbit. *J Surg Res* 1990; **49**: 453–457.
3. Lin MC, Rockman HA, Chien KR. Heart and lung disease in engineered mice. Nat Med 1995; **1**: 749–751.
4. Couffinhal T, Silver M, Zheng LP, Kearney M, Witzenbichler B, Isner JM. Mouse model of angiogenesis. *Am J Pathol* 1998; **152**: 1667–1679.
5. Stern MD. *In vivo* evaluation of micro-circulation by coherent light scattering. *Nature* 1975; **254**: 56–58.
6. Stern MD, Lappe DL, Bowen PD, et al. Continuous measurement of tissue blood flow by laser-Doppler spectroscopy. *Am J Physiol* 1977; **232**: H441–448.
7. Bonner R, Nossal R. Model for laser Doppler measurements of blood flow in tissue *Appl Opt* 1980; **20**: 097–2107.
8. Chavakis E, Aicher A, Heeschen C,et al. Role of {beta}2-integrins for homing and neovascularisation capacity of endothelial progenitor cells. *J Exp Med* 2005; **201**: 63–72.
9. Heeschen C, Lehmann R, Honold J, et al. Profoundly reduced neovascularisation capacity of bone marrow mononuclear cells derived from patients with chronic ischemic heart disease. *Circulation* 2004; **109**: 1615–1622.
10. Aicher A, Heeschen C, Mildner-Rihm C, et al.Essential role of endothelial nitric oxide synthase for mobilization of stem and progenitor cells. *Nat Med* 2003; **9**: 1370–1376.
11. Heeschen C, Aicher A, Lehmann R, et al. Erythropoietin is a potent physiologic stimulus for endothelial progenitor cell mobilization. *Blood* 2003; **102**: 1340–1346.
12. Heeschen C, Weis M, Aicher A, Dimmeler S, Cooke JP. A novel angiogenic pathway mediated by non-neuronal nicotinic acetylcholine receptors. *J Clin Invest* 2002; **110**: 527–536.
13. Urbich C, Heeschen C, Aicher A, Cathepsin L is required for endothelial progenitor cell-induced neovascularisation. *Nat Med*; 2005 **11**: 206–213.
14. Seifalian A, Saravanamuthu J, Reid W, Winslet M, MacLean A. Validation of laser doppler perfusion imager for assessment of tissue blood flow. *Cancer Detection and Prevention* 1996; **20**: (abstract).
15. Reinhardt CP, Dalhberg S, Tries MA, Marcel R, Leppo JA. Stable labeled microspheres to measure perfusion: validation of a neutron activation assay technique. *Am J Physiol* 2001; **280**: H108–116.
16. Matsumoto K, Ishihara K, Tanaka K, Inoue K, Fushiki T. An adjustable-current swimming pool for the evaluation of endurance capacity of mice. *J Appl Physiol* 1996; **81**: 1843–1849.
17. Luttun A, Tjwa M, Moons L, Revascularisation of ischemic tissues by PlGF treatment, and inhibition of tumor angiogenesis, arthritis and atherosclerosis by anti-Flt1. *Nat Med* 2002; **8**: 831–840.
18. Asahara T, Murohara T, Sullivan A, et al. Isolation of putative progenitor endothelial cells for angiogenesis. *Science* 1997; **275**: 964–967.

19. Takahashi T, Kalka C, Masuda H,et al. Ischemia- and cytokine-induced mobilization of bone marrow-derived endothelial progenitor cells for neovascularisation. *Nat Med* 1999; **5**: 434–438.
20. Hershey JC, Baskin EP, Glass JD, Hartman HA, Gilberto DB, Rogers IT, Cook JJ. Revascularisation in the rabbit hindlimb: dissociation between capillary sprouting and arteriogenesis. *Cardiovasc Res* 2001; **49**: 618–625.
21. Ito WD, Arras M, Scholz D, Winkler B, Htun P, Schaper W. Angiogenesis but not collateral growth is associated with ischemia after femoral artery occlusion. *Am J Physiol Heart Circ Physiol* 1997; **273**: H1255–H1265.

24

Angiogenesis in biomatrices and artificial materials

Pieter Koolwijk and **Victor W.M. van Hinsbergh**

Dept. Tissue Repair, TNO Quality of Life, Gaubius Laboratory, Leiden, and Laboratory for Physiology, Institute for Cardiovascular Research, VU University Medical Center, Amsterdam, the Netherlands

Abstract

Several animal models have been developed to study the mechanisms involved in angiogenesis and to evaluate the efficacy of agents that inhibit or stimulate this process. In addition to investigating neovascularisation in the mouse *in situ*, such as in tumours, the retina, and wound healing, evaluation of agents that support or inhibit angiogenesis can be performed *in vivo* using biomatrices or artificial matrices. The vascularisation of these latter matrices also bears impact on the survival of implanted tissue engineered grafts. The present chapter focuses on a slight modification of the model originally described by Guedez et al (Am J Pathol. 2003;162:1431-1439), in which neovascularisation is evaluated in the mouse in a matrix-containing angioreactor. Three protocols are given and discussed describing (1) the preparation of the angioreactors, (2) their implantation in the flanks of the mouse, and (3) the evaluation of the invaded vessels using 70,000 Da FITC-dextran.

Introduction

Although the vascular system in the adult animal has a clearly defined size and pattern, adaptation of the vascularisation is required in ischemic tissue after wounding or and after tissue damage due to inflammation. New microvessels originate by sprouting from existing ones (angiogenesis), possibly facilitated by intussusception of blood-borne cells (vasculogenesis), and sometimes by elongation of vessels, as occurs in the cyclical thickening of the endometrium. Usually, these

A Handbook of Mouse Models of Cardiovascular Disease Edited by Qinbo Xu

processes together also are indicated as angiogenesis. In addition to growth and healing, angiogenesis occurs in a number of diseases, such cancer, diabetic retinopathy, rheumatoid arthritis and psoriasis. Three lines of interest have contributed to a large interest in influencing angiogenesis. First, the perspective that inhibition of angiogenesis may retard or stop tumor growth has stimulated research and largely contributed to the recognition of many angiogenic growth factors and angiogenesis inhibitors. Second, the generation of many different transgenic mice with over- and underexpression of specific genes has largely contributed to recognising important factors involved in neovascularisation, because frustration of the outgrowth of the vascular bed caused embryonal death due to impaired vascular development. Clinically, the neovascularisation of the endometrium and placenta are considered as cricial processes to guarantee proper implantation of the early embryo and development of the fetus. Third, in the cardiovascular field, stimulation of angiogenesis is desired in areas of ischemia, such as in the border zone of an infarct after acute myocardial infarction, to support survival of cardiomyocytes and maintenance of their function. Furthermore, investigators involved in tissue engineering have realised that the long-term success of transplanted engineered tissue pieces depends on adequate vascularisation.

It is therefore not surprising that a number of animal models have been developed to study the mechanisms involved in angiogenesis and to evaluate the efficacy of agents that inhibit or stimulate this process. Other publications have focused on modulating angiogenesis in animal/mouse models of angiogenesis in tumours,[1–3] cardiovascular healing and collateral formation[4–6] and retinopathy.[7,8] In this chapter we focus on models by which neovascularisation can be evaluated in various biological and artificial matrices. Several techniques have been used, such as the implantation of sponges filled with matrix proteins usually supplemented with growth factors, inhibitors or angiogenesis stimulating cells,[9–11] implanted chambers with a porous membrane which have been filled with the matrix proteins to be tested[12] and small tubes filled with matrix proteins, which were indicated as angioreactors.[13] In this chapter we provide protocols for the preparation, implantation and evaluation of matrigel- or fibrin-filled angioreactors implanted in the flanks of mice.

Materials and methods

The preparation of the angioreactors, their implantation in the sides of mice, and the final evaluation of perfused vessels by assay of fluoroscein isothiocyanate (FITC)-dextrans are given in three subsequent protocols.

They present a slight modification of the model originally described by Guedez *et al.*[13] Figure 24.1 depicts the angioreactor and its location after implantation in the mouse.

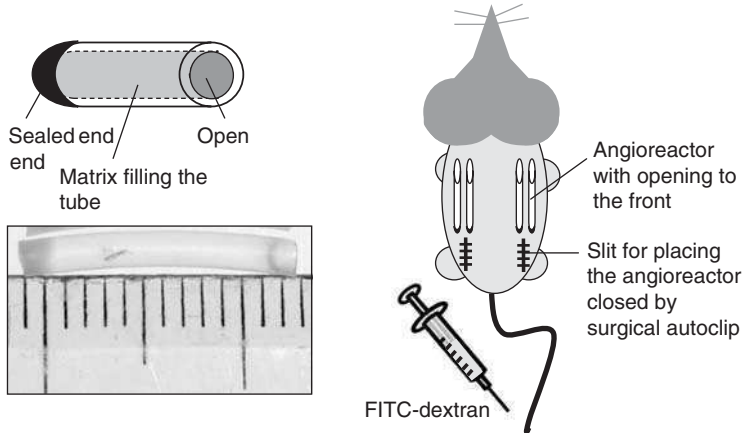

Figure 24.1 Schematic representation of the angioreactor and its position after implantation in the mouse, according to Guedez *et al.*[13] with slight modifications. Top left: The angioreactor is sealed on one side with nail cover (called bottom side) and filled with matrigel or fibrin. It is placed via a slit opening in the side of the mouse (two reactors can be placed per side) with the top side towards the head of the animal. Subsequently, the tissue opening is carefully closed. After 1 or 2 weeks, depending on the matrix used, FITC-dextran is injected via the tail vein and subsequently after 30 min the angioreactor is removed and evaluated for its FITC-dextran content (see also Protocols and Discussion). For a color version of this figure, please see the images supplied on the accompanying CD

Protocol 1. Preparation of the angioreactors

Reagents and equipment

- Laminar-flow hood
- Sterile gloves
- Clean laboratory coat
- Scalpel
- Incubator with 5 % CO_2/95 per cent air atmosphere and humidified
- Polyethylene tubing (inner diameter 1.4 mm; other diameter 1.9 mm, sterilised, Portex Ltd, Hythe, UK)
- Nail polish (colourless, local store)
- Phosphate-buffered saline (PBS)

- Matrigel (Basement membrane matrigel w/o phenol red, growth factor reduced, mouse natural, BD Biosciences Labware, Bedfort, USA) solution (concentration 6 mg/ml, diluted in PBS), stored in small portions of 500 µl at −20°C
- Fibrinogen (Chromogenix AB, Mölndal, Sweden), 2 mg/ml solution in medium M199
- Thrombin (Organon-Teknika, Boxtel, The Netherlands)
- Fibroblast growth factor-2 (FGF-2) (human recombinant, PeproTech, Inc., Rocky Hill, NJ, USA) or vascular enclothelial growth factor (VEGF) (human recombinant, ReliaTech GmbH, Braunschweich, Germany)
- Heparin (Leo Pharma BV, Breda, the Netherlands)
- Syringe + needle (BD micro-fine + U-100 insulin syringe + needle; 0.33 mm (29G) × 12.7 mm; Beckton & Dickinson Biosciences, Bedfort, USA)
- Compounds to be tested, e.g. angiogenesis inhibiting or enhancing agents.

Procedure

1. Matrigel solution stored in small portions at −20°C, is thawed on ice (overnight) to prevent gelation of the material at room temperature.
2. Using a scalpel, sterile polyethene tubing is cut into 1.3 cm length pieces in order to prepare the angioreactors.
3. One end of the angioreactors is sealed with colourless nail polish, and allowed to dry for 24 h at room temperature.
4. Then, the angioreactors are filled with 30 µl of a solution containing matrigel (600 ng/ml), FGF-2 or VEGF (end concentrations of 500 or 1000 ng/ml, respectively), and heparin (end concentration of 50 IU/ml), with or without (depending on the route of administration) the compound(s) to be tested using an insulin syringe at 4°C.
5. Alternatively, fibrin can be used as matrix. For that, the angioreactors are filled with a 2 mg/ml fibrinogen solution supplemented with thrombin (end concentration 0.2 IU/ml), FGF-2 or VEGF (end concentrations of 500 or 1000 ng/ml, respectively), and heparin (end concentration of 50 IU/ml), with or without the agent to be tested compound(s).
6. After filling, the matrigel or fibrin is allowed to gelate under 5 % CO_2/95 per cent air atmosphere, 37°C and 90 per cent humidity for at least 1 h.

7. Prior to the implantation in the flanks of mice, the angioreactors are cut into lengths of 1.0 cm.

Protocol 2. Implantation of the angioreactors

Animals, reagents and equipment

- Mice (10 weeks old, e.g. FVB/N or C57BL6)
- Fentanyl (Janssen-Citag NV, Beerse, Belgium, 0.05 mg/ml)
- Midazolam (Roche Nederland BV, Woerden, the Netherlands, 3 mg/ml)
- Medetomidine (Orion Pharma, Espoo, Finland, 1 mg/ml)
- Shaver
- 70 % ethanol in distilled water
- Scalpel
- Scissors
- Autoclip (BD Biosciences Labware, Bedfort, USA)
- Angioreactor (See protocol 1).

Procedure

1. Mice are anesthetised using a mixture of 30 µl fentanyl (Janssen-Citag NV, Belgium, 0.05 mg/ml), 30 µl midazolam (Roche Nederland BV, Woerden, the Netherlands, 3 mg/ml), 15 µl medetomidine (Orion Pharma, Espoo, Finland, 1 mg/ml) in 75 µl PBS.

2. At the flanks of the mice 1.5 × 1.5 cm of the skin was shaved and sterilised using 70 % ethanol.

3. A small incision is made at each flank and subcutaneously a pocket of 1.5 × 0.5 cm wide is created using a surgical pair of scissors, which would be enough space to fit two angioreactors.

4. Two angioreactors are slid into the pocket with the closed sites of the angioreactors facing in the direction of the incision.

5. Thereafter, the incision is closed using a surgical autoclip. Check whether the wound is closed completely, to prevent one of the angioreactors being able to slip out of the pocket during the study period.

6. Perform this surgical procedure at both flanks.

7. The angioreactors filled with the matrigel matrix are kept in the mice for 10–14 days, whereas the fibrin containing reactors are kept for a period of 5–7 days.

Protocol 3. Determination of blood vessel formation

Reagents and equipment

- PBS
- Dextran-FITC (MW: 70 000, Sigma-Aldrich)
- Syringe with injection needle
- Scalpel
- 0.5 % Triton-X-100 in PBS
- 1 ml sterile pipet or Pipetman P200
- FLUOstar Galaxy microplate reader (BMG Labtechnologies GmbH, Germany).

Procedure

1. After a period of 5–7 (fibrin matrices) or 10–14 days (matrigel matrices) blood vessel formation is determined using dextran-FITC measurement. 30 min prior to killing the animals, 100 µl of a 25 mg/ml dextran-FITC (MW: 70 000, Sigma-Aldrich) PBS solution is injected into the tail-vein of the animals.

2. After 30 min the mice are killed, and the angioreactors are removed from the animal.

3. Inmediately thereafter, the sealed bottom of the angioreactor is removed by a scalpel.

4. Subsequently, the matrix (including the dextran-FITC containing vessels) is removed from the angioreactors and dissolved using 150 µl PBS + 0.5 %

Triton-X-100. When matrigel is used as a matrix this can be done by placing the angioreacters upside down in an eppendorf vial (1.5 ml) for 2–3 h at 4°C. This liquifies the matrigel. If a fibrin matrix is used, the gel is pushed out of the angioreactor by a sterile pipette into an eppendorf vial, after which it is homogenised by moving it back and forward through the pipette.

5. One hundred µl of this solution is added to a 96-well plate and the fluorescence is measured using a FLUOstar Galaxy microplate reader (excitation 485 nm, emission 520 nm, BMG Labtechnologies GmbH, Germany).

Discussion

Materials and supports for angiogenesis studies

Several aspects should be considered when testing a biological or artificial matrix for its ability to support angiogenesis. In particular the solidity and stability of the matrix material determine how such a matrix can be used in the mouse. Some biomaterials are solid and can be implanted directly, e.g. engineered cartilage and bone. Other materials need some kind of support. Fibrinogen or mouse plasma (derived from the same strain as the donor) can be coagulated directly or after mixing it with various collagens, thus providing a fibrinous matrix. However, such matrix has to be implanted in some kind of container. This is not only needed for its coagulation, but also because a fibrinous matrix will lyse during angiogenesis after implantation, and this interferes with the proper assay of the degree of angiogenesis. This problem can be overcome using a nondegradable sponge, in which the fibrin or other matrix protein is gelated.[9–11] A sponge can also absorb wound fluid and thus fill spontaneously with a fibrinous exudate during the implantation procedure. Alternatively a small container is offered to hold the matrix. This can be an angioreactor as described in this chapter (Figure 24.1).

The angioreactor must be in direct contact with tissue or sealed to it with the fibrinous matrix of wound fluid. It is important that after implantation the device does not move within the tissue and is placed in such a way that the animal can move freely. Otherwise the contact of the angioreactor with the tissue becomes disturbed and the ingrowth of new vessels fails. Although the nature of matrigel is such that it can be directly used in an animal, the angioreactor appeared in our hands very valuable for the standaradised evaluation of agents that affect the ingrowth of vascular structures, not least because the agents to be tested could be mixed in the matrix of the angioreactor from which they diffuse only slowly. This enables the investigator to use limited amounts of these agents. Furthermore, the angioreactor prevents deformation of the matrix within the animal, which would make it very difficult to quantify angiogenesis.

As an alternative for the support of such semi-stable matrices by the angioreactor, the matrix can be gelated in a Plexiglass ring covered on both sides with a 13 mm

diameter 30 μm nylon net filter (Millipore Corporation, MA, USA), through which the new vessels can grow.[12]

Evaluation of vascularisation

The FITC-dextran assay in the angioreactor appeared to be a useful method for quantitative analysis. It is advised to take blood samples from the animals just before taking out the angioreactors as a control for the successful injection of the FITC-detran. The FITC-dextran method is convenient, but has two limitations. First non-perfused vessels are not detected. Such vessels do also not contribute to the oxygenation and nutrition of the matrix at the time of evaluation. Second, in specific cases in which the perfused vessel in the matrix leak massively one may get an overestimation of the degree of vascularisation. However, normally the interstitial pressure equilibrates, counteracting further leakage, and within the time period of evaluation the diffusion of the 70 kDa dextran from the vessels into the matrix was very limited.

An attractive alternative is to use TIE2-GFP or TIE2-*LacZ* mice, which express green fluorescent protein (GFP) or β-galactosidase behind the endothelial specific promoter TIE-2. After extraction GFP can be assayed by fuorescence spectrophotometry and β-galactosidase activity assayed by enzymatic reaction. These assays provide quantifications of the total amont of endothelial cells that have invaded the angioreactor.

Estimation of the amount of hemoglobin can also be made as an estimate of the degree of perfused neovascularisation. However, two caveats exist. First, hemoglobin often sticks to the outside of the angioreactor caused by wounding during implantation and dissection. Second, some matrices have the tendency to contract slightly, and one has to verify that no local detachment between the matrix and the angioreactor has occurred that may cause penetration of the wound fluid during the first day after implantation.

Additional information can be obtained by making cross-sections of the invaded matrix. For the determination of the degree of vascularisation such sections should be made in the length direction of the angioreactor preferentially through the middle. Mild fixation e.g. with 0.4 per cent paraformaldehyde is advised. Endothelial cells can be stained with CD34 or CD31, but also other epitopes such as thrombomodulin VEGF receptor-2 (flk-1) and endoglyn have been used.[14–16]

Precautions

Several aspects merit attention. The angioreactor should be inserted in such a way that it does not move freely in the skin pocket. If that is the case, the invasion of new vessels into the angioreactor will be disturbed. Also careful closure of the skin opening with an surgical autoclip is important to avoid the angioreactor squeezing out after the implantation.

Furthermore, after the incubation period the angioreactor has to be removed carefully, so that one prevents part of the matrix material, which in in contact with the tissue, being accidently removed.

Finally, certain matrices prepared from fibrin and collagen may shrink. If such matrices are made immediately before the implantation their shrinking may cause sucking of wound fluid and even blood into the reactor, usually in a thin area between the tube and the matrix.

Application

The assay can be used for the evaluation of growth factors that stimulate angiogenesis. Figure 24.2 shows the stimulatory action of VEGF. It is also a valuable tool to assay agents that inhibit angiogenesis. In the latter case an angiogenesis stimulus VEFG or bFGF is mixed together with the inhibitory compound to be tested. Figure 24.2 also shows the effect of a thrombospondin-1 peptide, which was used as an angiogenesis inhibitor.[17]

The model can also be used to evaluate the effects of gene deficiency or gene overexpression. Depending on the gene this can be done by using various transgenic mice, which determines the effect of the gene alteration on the ingrowing vessels. Alternatively, one can provide matrices prepared from the plasma or tissue of transgenic mice, from which the contribution of specifically altered matrix proteins can be evaluated.

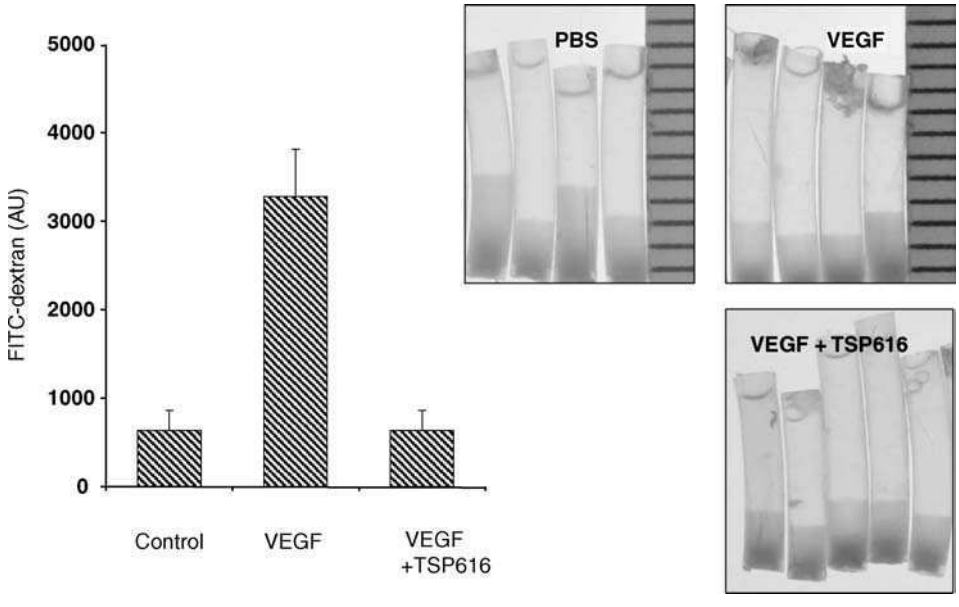

Figure 24.2 Effects of VEGF-A and the thrombospondin (TSP) peptide 616, SPWSSCSVTCGDGVITRIR, described by Iruela-Arispe *et al.*[17] on VEGF-induced *in vivo* angiogenesis in matrigel™. Angiogenesis was induced and measured as GFP expression by the endothelial cells, as described in Materials and Methods, and expressed as the mean ±SEM of the arbitrary units (AU) present in the angioreactors. For a color version of this figure, please see the images supplied on the accompanying CD

Acknowledgments

The study was supported by a grant of the Dutch Program for Tissue Engineering (grants VGT.6747 and BGT.6733).

References

1. Dellian M, Witwer BP, Salehi HA, Yuan F, Jain RK. Quantitation and physiological characterization of angiogenic vessels in mice: effect of basic fibroblast growth factor, vascular endothelial growth factor/vascular permeability factor, and host microenvironment. *Am J Pathol* 1996; **149**: 59–71.
2. Carmeliet P, Jain RK. Angiogenesis in cancer and other diseases. *Nature* 2000; **407**: 249–257.
3. Brown EB, Campbell RB, Tsuzuki Y, Xu L, Carmeliet P, Fukumura D, Jain RK. In vivo measurement of gene expression, angiogenesis and physiological function in tumors using multiphoton laser scanning microscopy. *Nat Med* 2001; **7**: 864–868.
4. Scholz D, Ziegelhoeffer T, Helisch A, Wagner S, Friedrich C, Podzuweit T, Schaper W. Contribution of arteriogenesis and angiogenesis to postocclusive hindlimb perfusion in mice. *J Mol Cell Cardiol* 2002; **34**: 775–787.
5. Couffinhal T, Silver M, Zheng LP, Kearney M, Witzenbichler B, Isner JM. Mouse model of angiogenesis. *Am J Pathol* 1998; **152**: 1667–1679.
6. Chapter 23 in this book.
7. Hammes HP, Brownlee M, Jonczyk A, Sutter A, Preissner KT. Subcutaneous injection of a cyclic peptide antagonist of vitronectin receptor-type integrins inhibits retinal neovascularization. *Nat Med* 1996; **2**: 529–533.
8. Gardiner TA, Gibson DS, de Gooyer TE, de la Cruz VF, McDonald DM, Stitt AW. Inhibition of tumor necrosis factor-alpha improves physiological angiogenesis and reduces pathological neovascularization in ischemic retinopathy. *Am J Pathol* 2005; **166**: 637–644.
9. Andrade SP, Machado RD, Teixeira AS, Belo AV, Tarso AM, Beraldo WT. Sponge-induced angiogenesis in mice and the pharmacological reactivity of the neovasculature quantitated by a fluorimetric method. *Microvasc Res* 1997; **54**: 253–261.
10. Tolsma SS, Volpert OV, Good DJ, Frazier WA, Polverini PJ, Bouck N. Peptides derived from two separate domains of the matrix protein thrombospondin-1 have anti-angiogenic activity. *J Cell Biol* 1993; **122**: 497–511.
11. Lage AP, Andrade SP. Assessment of angiogenesis and tumor growth in conscious mice by a fluorimetric method. *Microvasc Res* 2000; **59**: 278–285.
12. Kragh M, Hjarnaa PJ, Bramm E, Kristjansen PE, Rygaard J, Binderup L. In vivo chamber angiogenesis assay: an optimized Matrigel plug assay for fast assessment of anti-angiogenic activity. *Int J Oncol* 2003; **22**: 305–311.
13. Guedez L, Rivera AM, Salloum R, Miller ML, Diegmueller JJ, Bungay PM, Stetler-Stevenson WG. Quantitative assessment of angiogenic responses by the directed in vivo angiogenesis assay. *Am J Pathol* 2003; **162**: 1431–1439.
14. Baluk P, Morikawa S, Haskell A, Mancuso M, McDonald DM. Abnormalities of basement membrane on blood vessels and endothelial sprouts in tumors. *Am J Pathol* 2003; **163**: 1801–1815.

15. van Amerongen MJ, Molema G, Plantinga J, Moorlag H, van Luyn MJ. Neovascularization and vascular markers in a foreign body reaction to subcutaneously implanted degradable biomaterial in mice. *Angiogenesis* 2002; **5**: 173–180.
16. Young PE, Baumhueter S, Lasky LA. The sialomucin CD34 is expressed on hematopoietic cells and blood vessels during murine development. *Blood* 1995;85:96–105.
17. Iruela-Arispe ML, Lombardo M, Krutzsch HC, Lawler J, Roberts DD. Inhibition of angiogenesis by thrombospondin-1 is mediated by 2 independent regions within the type 1 repeats. *Circulation* 1999; **100**: 1423–1431.

25

Venous thrombosis

Alberto Smith, James Gossage, Matthew Waltham, Bijan Modarai and **Julia Humphries**

Academic Dept of Surgery, Cardiovascular Division, King's College London School of Medicine, at St Thomas' Hospital, London, UK

Abstract

Successful thrombus induction in the veins requires the presence of at least one of a triad of factors (Virchow's triad) - hypercoagulability, endothelial cell disturbance or reduced blood flow. The thrombus produced should have a coralline structure, consisting of layers of fibrin, platelets and associated leukocytes that create a mesh entrapping the main red cell mass. This is different from a clot, which comprises a red cell mass trapped in a loose, disorganised fibrin mesh with platelets and leukocytes distributed randomly throughout. The disparity in the morphology of these structures may therefore give rise to differences in the processes that regulate their formation and resolution. The mouse model described in this chapter produces corraline thrombus in a reliable manner and allows investigation of the mechanisms that regulate both the generation and resolution of venous thrombi.

Key words

thrombus, venous, mouse, model

Background

Deep vein thrombosis (DVT) of the lower limb is a common condition, affecting 1–2 per cent of the population, with an annual incidence of 1 per 1000.[1,2] Between 25 and 75 per cent of patients have residual venous obstruction or reflux after developing a deep vein thrombosis.[3–7] The incidence of long-term complications of venous thrombosis (post-thrombotic syndrome – leg swelling, pain, skin changes and ulceration) can be as high as 50 per cent after 1 year[8] and greater than 70 per cent after 10 years.[9] These conditions are debilitating and cost the NHS over £500 million each year to treat.

A Handbook of Mouse Models of Cardiovascular Disease Edited by Qinbo Xu

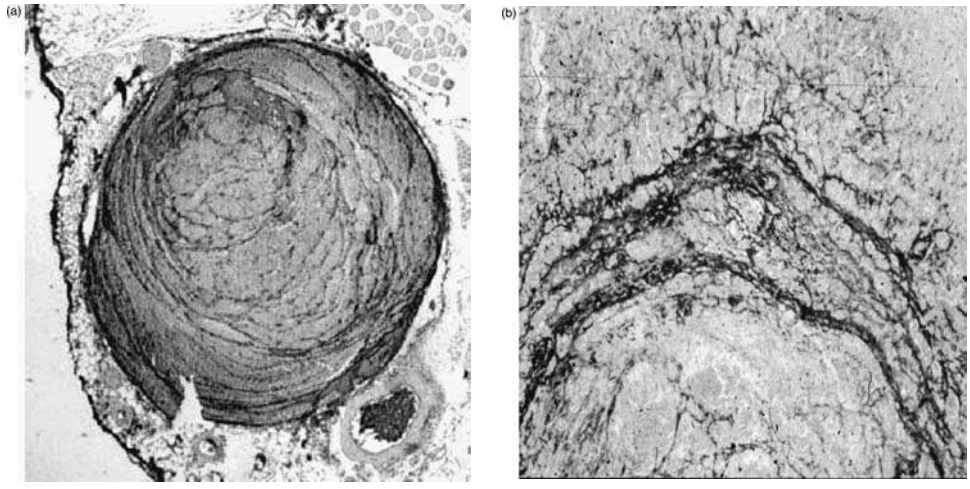

Figure 25.1 Laminar thrombus veins stained with the CD41 platelet marker (black) in (a) mouse and (b) human

A venous thrombus is a semi-solid mass formed from the components of flowing blood and consists of laminations of platelets, fibrin and leukocytes (lines of Zahn) that trap the main red cell mass (Figure 25.1a,b). This is different from a 'clot', which is formed in stationary blood and consists mainly of a red cell mass trapped within a fine fibrin mesh, with leukocytes and platelets distributed randomly throughout (Figure 25.2). These differences suggest that thrombus and clot may develop and resolve through different mechanisms.

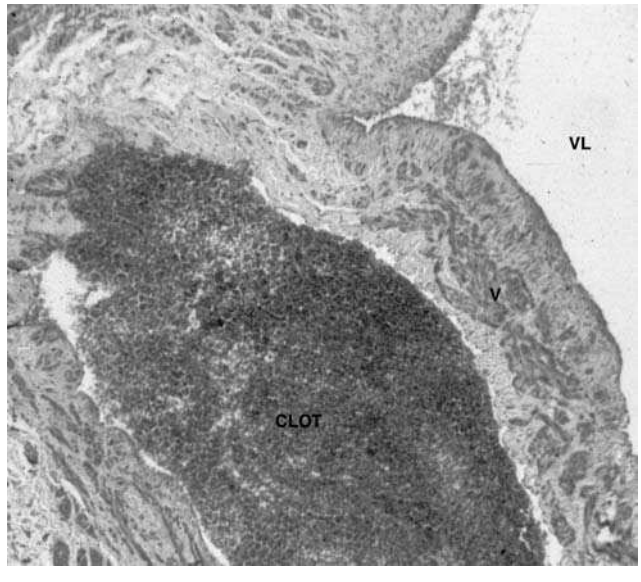

Figure 25.2 Amorphous clot formed in the valve cusp of a human vein. V = valve; VL = vein lumen

In 1856 Virchow put forward three pathological mechanisms he considered responsible for the formation of venous thrombi (Virchow's triad).

1. Alterations in the blood constituents (increased coagulability of the blood)

2. Changes in the endothelial lining of the vessel wall (endothelial disturbance)

3. Stasis or reduced blood flow.

These conditions are still accepted as the major instigators of thrombogenesis in the veins and are the basis for the induction of venous thrombosis in all animal models.

Whatever the cause, it is clear that the thrombus develops as a laminated coralline structure, extending in the bloodstream, bending in the direction of the blood flow. As the thrombus extends across the lumen, it causes turbulent blood flow beyond which more red cells and fibrin deposit. This leads to propagation of the thrombus.

Subsequent natural thrombus resolution occurs by a process of organisation and recanalisation[10–12] that is similar to the events seen during wound healing, including infiltration by inflammatory cells (mainly monocytes), endothelial cells, myofibroblasts and bone-marrow-derived progenitors.[13,14] Recanalising channels develop between the vessel wall and thrombus and also within the body of the thrombus.[11,15] These channels can carry blood and it is speculated that their coalescence into large channels, combined with contraction of the thrombus, is the mechanism by which blood flow is restored through the vein.

The precise mechanisms that lead to the formation and resolution of a venous thrombus are still poorly understood. It is difficult to elucidate these *in vitro*, as culture conditions do not provide the dynamic cellular and molecular environment that exists *in vivo*. It would also be ethically unacceptable to form a thrombus and to study its subsequent resolution in a human vein because of the possibility of the thrombus embolising. Much of what we know about venous thrombosis in man is derived from analysis of blood samples taken from patients with this condition. This can only examine global changes in the coagulation and fibrinolytic systems and is unable to address changes within the microenvironment of the thrombus. The development of animal models that reproduce the conditions leading to venous thrombogenesis in man has improved our understanding of the pathophysiological processes that occur during thrombus formation and its subsequent resolution.

Models of thrombosis

An 'animal model' can be defined as a living organism with an inherited, naturally acquired or induced pathological process, that in one or more respects closely resembles a disorder occurring in man.

Animals used in thrombosis models

An ideal model of venous thrombosis should produce a thrombus similar in structure to that found in man, be reproducible, has a low morbidity and mortality, and be technically easy to perform. The most frequently used species have been the rat and rabbit but, over the past decade, the development of gene knockout and transgenic systems[16] has led to the increased use of mice.[17] The ability to manipulate the mouse genome so that it is possible to investigate the role of individual factors, such as plasminogen activators;[18] or to track the recruitment of specific cells into the thrombus (e.g. bone-marrow-derived progenitors,[19] has provided a powerful tool in the study of thrombus formation and its resolution.

Site and methods of thrombus induction

Although venous thrombi are more common in the lower limbs in humans, it is technically difficult to develop thrombi in the veins of the lower limbs of small animals such as mice. The vena cava has therefore been the site of thrombus development in small rodents because of its size and accessibility.

A variety of methods have been used to induce thrombosis in veins and these have been based on promoting one or more of Virchow's triad of factors.[21] Thrombus has been induced in animal models by producing venous stasis alone or in combination with endothelial damage or hypercoagulability of the blood; however, many of these models have not been characterised to determine whether they resemble the laminated thrombi found in humans.[20–21] Extrapolations from these systems to how human thrombi form and resolve may therefore be difficult. Furthermore, the technical complexity of the methods by which thrombus is induced may lead to a longer 'learning curve', a greater mortality and a diminished reproducibility.

The St Thomas' model

We have developed a model of venous thrombosis in the mouse that is technically simple, highly reproducible (>90 per cent), has a high survival rate (>99 per cent), and induces a corraline thrombus with a morphology resembling that of human venous thrombi.

In this model thrombus formation is induced using a combination of reduced blood flow and endothelial damage (unlike our rat model where thrombus induction occurs simply by reducing caval blood flow alone).[22] This method has been successfully used to induce thrombus in more than seven strains of knockout mice[14,18,23] and more recently in a strain with severe combined immunodeficiency (SCID, unpublished data).

The SCID mouse mutation has proved a useful tool for the development of small animal models as hosts for the *in vivo* analysis of the activity of human

cells in disease.[24] The use of cells of human origin rather than murine cells eliminates the need for donor animals and thereby reduces animal numbers required for study. Human cells are also available in larger numbers and their analysis is facilitated by the widespread availability of human antibodies and assay systems.

Method

The mouse is anaesthetised using isoflurane. The abdomen is shaved and an antiseptic agent applied to the skin. A midline laparotomy is performed with stay sutures placed to expose the abdominal contents. The intestines are retracted with cotton buds and wrapped in gauze soaked in normal saline. The peritoneum is dissected away using blunt dissection, revealing the retroperitoneal structures (Figure 25.3a).

The inferior vena cava is mobilised beneath the level of the left renal vein and the lumbar tributaries identified (Figure 25.3b). A plane is developed behind the vena cava and between any lumbar vessels (Figure 25.3c). On the left side the abdominal aorta is separated from the inferior vena cava using blunt dissection with two pairs of fine forceps. A 2-0 silk tie (Ethicon, UK) is placed behind the vessel just inferior to the left renal vein (Figure 25.3d). A 5-0 prolene suture (Ethicon, UK) is placed longitudinally over the inferior vena cava and the silk suture tied over the top (Figure 25.3e). The prolene is then removed. This procedure creates a stenosis that markedly reduces blood flow (Figure 25.3f). Endothelial

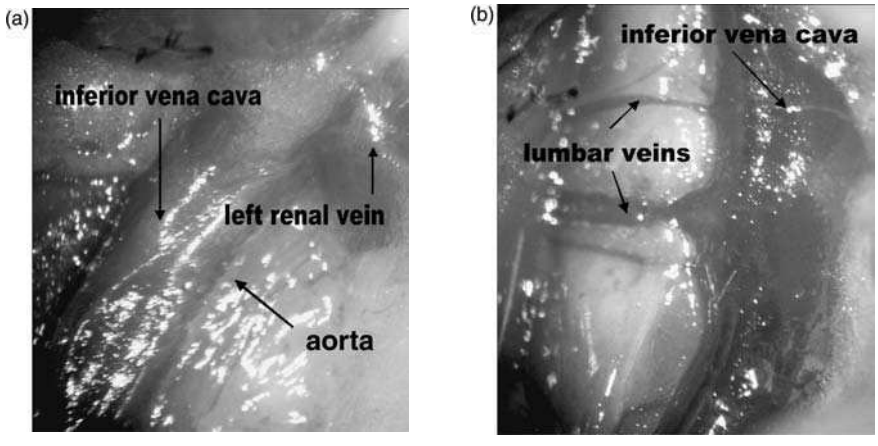

Figure 25.3 Steps taken in the induction of a venous thrombus in the St Thomas's model: (a) anatomy of the mouse IVC and left renal vein; (b) retraction of IVC to reveal posterior lumbar veins; (c) blunt dissection to separate the IVC from surrounding structures; (d) placement of the silk ligature; (e) placement of the prolene suture along the length of the vein and tying of the silk ligature; (f) removal of the prolene suture to allow reduced blood flow; (g) application of a vascular clip to create endothelial damage

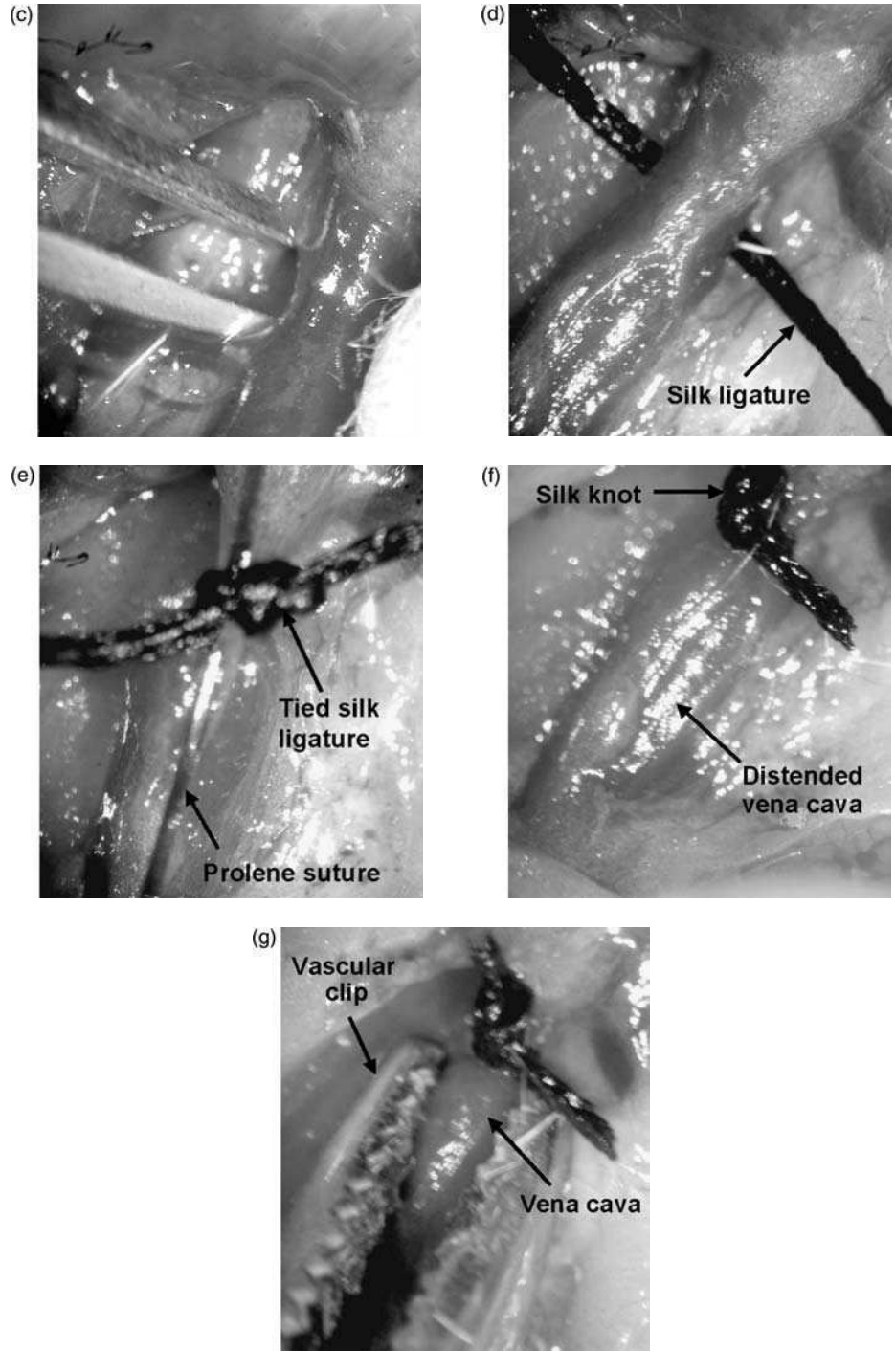

Figure 25.3 (*Continued*)

damage is induced using a neurovascular surgical clip (Braun Medical) applied to the vessel in two separate positions below the renal vein, for twenty seconds at a time (Figure 25.3g). This procedure induces reproducible (>90 per cent) thrombus formation.

The bowel is placed carefully back into the abdominal cavity. The laparotomy is closed using 3-0 monocryl in layers. Subcutaneous buprenorphine (0.01–0.1 mg/kg) and 0.5 ml of saline are immediately administered for postoperative analgesia and to replace intraoperative fluid loss.

Thrombus formation occurs rapidly (usually within 1 hour of tying the ligature, Figure 25.4a–d) in this model as has been shown in humans.[24] The initial thrombus produced consists predominantly of red cells with laminations that contain fibrin, platelets and leukocytes (mainly polymorphonuclear, Figure 25.5). The experimental thrombus resolves through a process of organisation and recanalisation (Figure 25.6) reminiscent of that seen in human venous thrombi and healing wounds. There is a progressive cellular infiltration that consists of inflammatory cells (mainly macrophages, Figure 25.7), myofibroblasts and endothelial cells, which line the vascular channels that form between the vein wall and thrombus and within the main body of the thrombus (Figure 25.6).

The models described are useful for both studying the efficacy of antithrombotic agents and in the analysis of the cellular and molecular mechanisms that regulate resolution, as the experimental thrombi resolve over a period of 4 weeks.

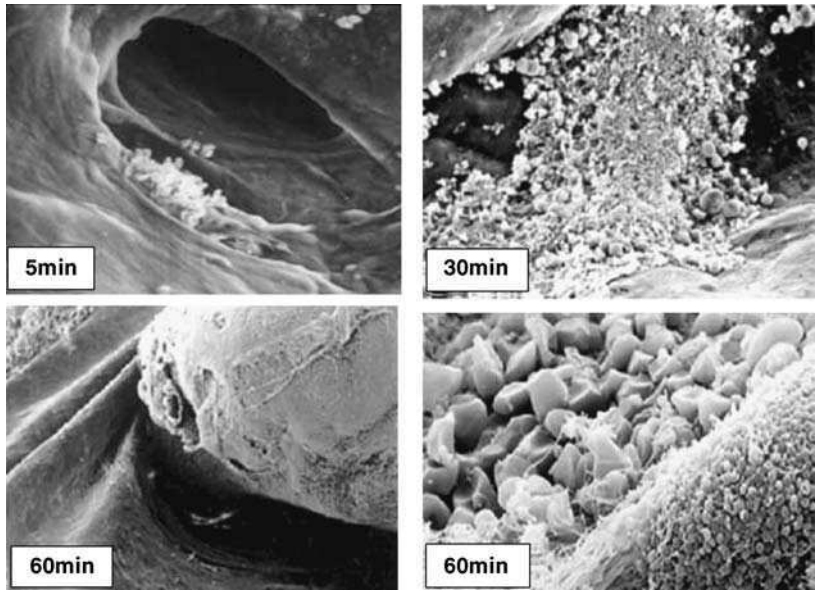

Figure 25.4 Scanning electron micrographs of forming thrombus taken at intervals up to 1 h after placement of the ligature. For a color version of this figure, please see the images supplied on the accompanying CD

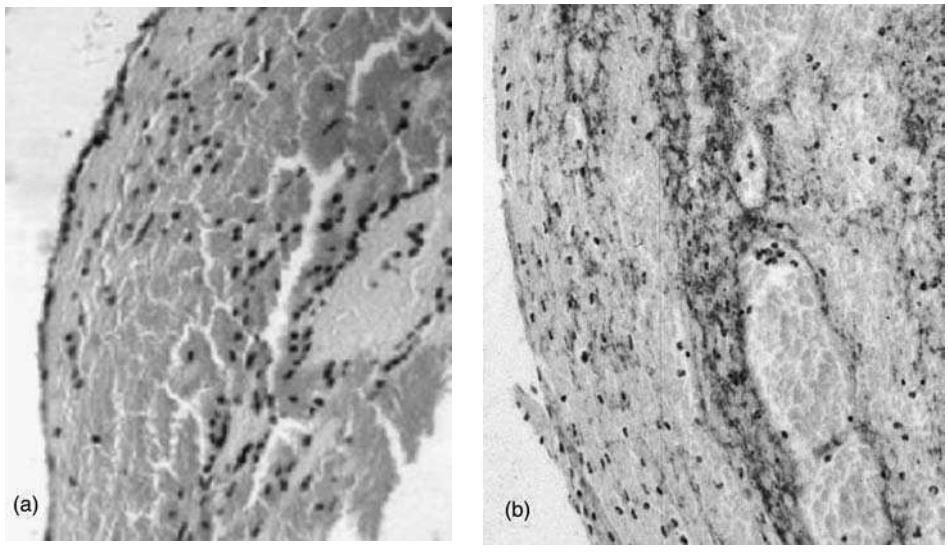

Figure 25.5 Sections taken through (a) 1-day-old thrombus in mouse vein, and (b) human vein. Note the laminations which consist of fibrin, platelets and leukocytes

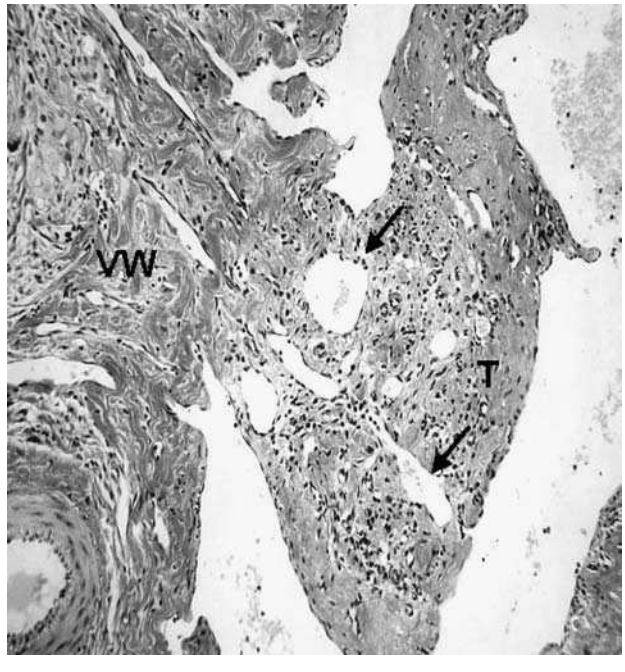

Figure 25.6 Organised 4-week-old thrombus in the mouse vein stained by MSB. Note the large numbers of infiltrating cells and cell-lined vascular channels, some of which contain erythrocytes. VW, vein wall; T, thrombus

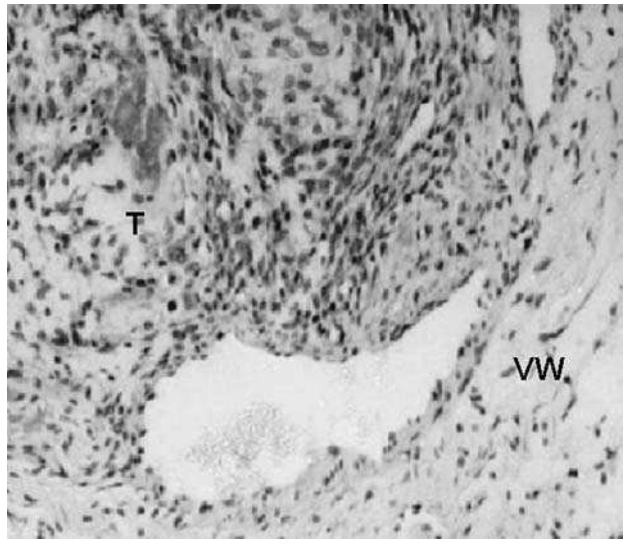

Figure 25.7 Organised thrombus in mouse vein showing infiltration by monocytes. This paraffin section was stained using the anti-mouse macrophage marker, MAC-3. VW, vein wall; T, thrombus. For a color version of this figure, please see the images supplied on the accompanying CD

References

1. Anderson FA Jr, Wheeler HB, Goldberg RJ, et al. A population-based perspective of the hospital incidence and case- fatality rates of deep vein thrombosis and pulmonary embolism. The Worcester DVT Study. *Arch Intern Med* 1991; **151(5)**: 933–938.
2. Heit JA, Silverstein MD, Mohr DN, et al. The epidemiology of venous thromboembolism in the community. *Thromb Haemost* 2001; **86(1)**: 452–463.
3. Heijboer H, Jongbloets LM, Buller HR, Lensing AW, ten Cate JW. Clinical utility of real-time compression ultrasonography for diagnostic management of patients with recurrent venous thrombosis. *Acta Radiol* 1992; **33(4)**: 297–300.
4. Arcelus JI, Caprini JA, Hoffman KN, et al. Laboratory assays and duplex scanning outcomes after symptomatic deep vein thrombosis: preliminary results. *J Vasc Surg* 1996; **23(4)**: 616–621.
5. Killewich LA, Macko RF, Cox K, et al. Regression of proximal deep venous thrombosis is associated with fibrinolytic enhancement. *J Vasc Surg* 1997; **26(5)**: 861–868.
6. Prandoni P, Lensing AW, Prins MR. Long-term outcomes after deep venous thrombosis of the lower extremities. *Vasc Med* 1998; **3(1)**: 57–60.
7. Meissner MH, Caps MT, Zierler BK,et al. Determinants of chronic venous disease after acute deep venous thrombosis. *J Vasc Surg* 1998; **28(5)**: 826–833.
8. Kahn SR, Solymoss S, Lamping DL, Abenhaim L. Long-term outcomes after deep vein thrombosis: postphlebitic syndrome and quality of life. *J Gen Intern Med* 2000; **15(6)**: 425–429.
9. Bauer G. A roentgenological and clinical study of the sequels of thrombosis. *Acta Chir Scand* 1942; **74** (Suppl).

10. Cox JS. The maturation and canalization of thrombi. *Surg Gynecol Obstet* 1963; **116**: 593–599.
11. Sevitt S. The mechanisms of canalisation in deep vein thrombosis. *J Pathol* 1973; **110(2)**: 153–165.
12. Modarai B, Burnand KG, Humphries J, Waltham M, Smith A. The role of neovascularisation in the resolution of venous thrombus. *Thromb Haemost* 2005; **93(5)**: 801–809.
13. McGuinness CL, Humphries J, Waltham M, Burnand KG, Collins M, Smith A. Recruitment of labelled monocytes by experimental venous thrombi. *Thromb Haemost* 2001; **85(6)**: 1018–1024.
14. Modarai B, Burnand KG, Sawyer B, Smith A. Endothelial progenitor cells are recruited into resolving venous thrombi. *Circulation* 2005; **111(20)**: 2645–2653.
15. Waltham M, Burnand KG, Collins M, McGuinness CL, Singh I, Smith A. Vascular endothelial growth factor enhances venous thrombus recanalisation and organisation. *Thromb Haemost* 2003; **89(1)**: 169–176.
16. Carmeliet P, Mulligan RC, Collen D. Transgenic animals as tools for the study of fibrinolysis in vivo. *J Intern Med* 1994; **236(4)**: 455–459.
17. Levi M, Dorffle-Melly J, Johnson GJ, Drouet L, Badimon L. Usefulness and limitations of animal models of venous thrombosis. *Thromb Haemost* 2001; **86(5)**: 1331–1333.
18. Singh I, Burnand KG, Collins M, L et al. Failure of thrombus to resolve in urokinase-type plasminogen activator gene-knockout mice: rescue by normal bone marrow-derived cells. *Circulation* 2003; **107(6)**: 869–875.
19. Virchow RR. Cellular Pathology. *London, Churchill:1860.*
20. Millet J, Vaillot M, Theveniaux J, Brown NL. Experimental venous thrombosis induced by homologous serum in the rat. *Thromb Res* 1996; **81(4)**: 497–502.
21. Xie H, Kim K, Aglyamov SR, et al. Staging deep venous thrombosis using ultrasound elasticity imaging: Animal model. *Ultrasound Med Biol* 2004; **30(10)**: 1385–1396.
22. McGuinness CL, Humphries J, Waltham M, Burnand KG, Collins M, Smith A. Recruitment of labelled monocytes by experimental venous thrombi. *Thromb Haemost* 2001; **85(6):** 1018–1024.
23. Singh I, Smith A, Vanzieleghem B, et al. Antithrombotic effects of controlled inhibition of factor VIII with a partially inhibitory human monoclonal antibody in a murine vena cava thrombosis model. *Blood* 2002; **99(9)**: 3235–3240.
24. McCune JM, Namikawa R, Kaneshima H, Shultz LD, Lieberman M, Weissman IL. The SCID-hu mouse: murine model for the analysis of human hematolymphoid differentiation and function. *Science* 1988; **241(4873)**: 1632–1639.
25. Kakkar V. The diagnosis of deep vein thrombosis using the 125 I fibrinogen test. *Arch Surg* 1972; **104(2)**: 152–159.

26

Virus-induced vasculitis

Philippe Krebs and **Burkhard Ludewig**

Research Department, Kantonal Hospital St Gallen, St Gallen, Switzerland

Keywords

atherosclerosis, dendritic cell, myocarditis, MCMV, vasculitis

Introduction

Vasculitis is characterised by infiltration of lymphocytes and macrophages into the vessel wall. This inflammation can provoke destruction of the media, fibrosis, and proliferation of smooth muscle cells in the intima leading to neointima formation. Importantly, inflammatory changes associated with systemic vasculitides may promote formation of atherosclerotic lesions.[1] The origin of systemic vasculitides most probably relies on infection of the vasculature by pathogens. *Staphylococcus aureus*[2] and human parvovirus B19,[3] for example, have been associated with Wegener's granulomatosis. Furthermore, human parvovirus B19 has also been suggested to be involved in Kawasaki disease,[4] and polyarteritis nodosa.[5] Moreover, many other infectious agents have been proposed to cause vascular pathological changes, often in addition to the main clinical manifestation.[6] For example, cytomegalovirus (CMV) infection is frequently linked with human vasculitides and atherosclerosis. Indeed, CMV antigens or nucleic acids have been found in arterial tissue and in atherosclerotic lesions of human patients with coronary artery disease[7,8] and with inflammatory abdominal aortic aneuryms.[9] Human CMV (HCMV) and to a lesser extent murine CMV (MCMV) have been shown to infect smooth muscle and endothelial cells of the vessel wall.[10] Moreover, CMV infections can induce intimal injury resulting in neointima formation and vasculopathy.[11,12] Therefore, it is likely that chronic persistence of pathogens in the vessel wall, as it is the case in HCMV infection, may lead to a continuously recruitment of effectors of the immune system that may eventually induce an inflammatory milieu able to generate and sustain

A Handbook of Mouse Models of Cardiovascular Disease Edited by Qinbo Xu

autoimmune reactions. Destruction of cells in the vascular wall, either through direct cytolytic activity of the infectious agent or by immune mechanisms directed against the pathogen, may lead to the release of self-antigens and to the subsequent activation of autoimmune responses. However, it is difficult to distinguish between direct pathogen-induced vascular damage and immunopathology triggered by continuous activation of microbe-specific T and B cells. We have recently reported a transgenic mouse model with defined T-cell-mediated cardiovascular immunopathology[13] that permits uncoupling of these two mechanisms. Transgenic SM-LacZ mice express the bacterial βgalactosidase (βgal) protein exclusively in cardiomyocytes of the right heart and in arterial smooth muscle cells.[14] The βgal transgene is immunologically ignored in these mice, despite its widespread expression in the vascular system. Repetitive priming of SM-LacZ mice with dendritic cells (DC) presenting a H-2K^b-restricted peptide derived from βgal (Figure 26.1a) causes acute vascular immunopathology with strong lymphocytic infiltration in lung arteries and aorta (arteritis) as well as in the right heart (myocarditis), that may eventually lead to dilated cardiomyopathy[15] (Figure 26.1b).

Besides providing a valuable tool for studying autoimmune vasculitis and myocarditis, SM-LacZ mice can also be used to shed light on the mechanisms underlying atherosclerosis. To this end, SM-LacZ mice were crossed with hypercholesterolemic apolipoprotein E (ApoE)-deficient mice. ApoE$^{-/-}$ mice spontaneously develop lipid depositions in major arteries[16] and are used as animal models for atherosclerosis. Upon induction of transgene-specific CD8$^+$ T cells by DC immunisation, transgenic ApoE$^{-/-}$ $\times$ SM-LacZ mice display atherosclerotic lesions that are significantly increased by the immune-mediated arterial inflammation.[13] Furthermore, the use of a βgal recombinant MCMV virus (MCMV-LacZ) and SM-LacZ mice (Figure 26.1a) allows study of the role of a persisting viral antigen (βgal transgene) in blood vessels for the development of inflammatory atherosclerotic lesions. Hence, SM-LacZ transgenic mice provide an effective model to study immune-mediated vasculitis and its interplay with cholesterol-induced atherosclerosis.

Materials and methods

Mice

The generation of SM-LacZ[14] and ApoE$^{-/-}$[16] mice have been described elsewhere. Typing of SM-LacZ mice was performed by polymerase chain reaction (PCR) analysis from tail DNA. The following oligonucleotides were used as primers for LacZ PCR; 5′-ATCCTCTGCATGGTCAGGTC-3′ and 5′-CGTGGCCTGATTCA TTCC-3′. PCR conditions were as follows: 3 min 90°C, 30 cycles of 30 s 95°C, 30 s 58°C, 45 s 72°C and eventually 10 min 72°C, with an expected product size of 315 bp. For the typing of ApoE$^{-/-}$ mice, blood was collected in microtainer tubes (BD, # 365951). Serum was separated according to the manufacturer's protocol and diluted 1 : 2 in phosphate-buffered saline (PBS). Serum cholesterol was determined enzymatically with a Hitachi 917 analyser at the Institute for Clinical Chemistry at the Kantonal Hospital, St Gallen. Normal cholesterol levels are 2.4 ± 0.4 mmol and 14.5 ± 3.5 mmol for C57BL/6 and

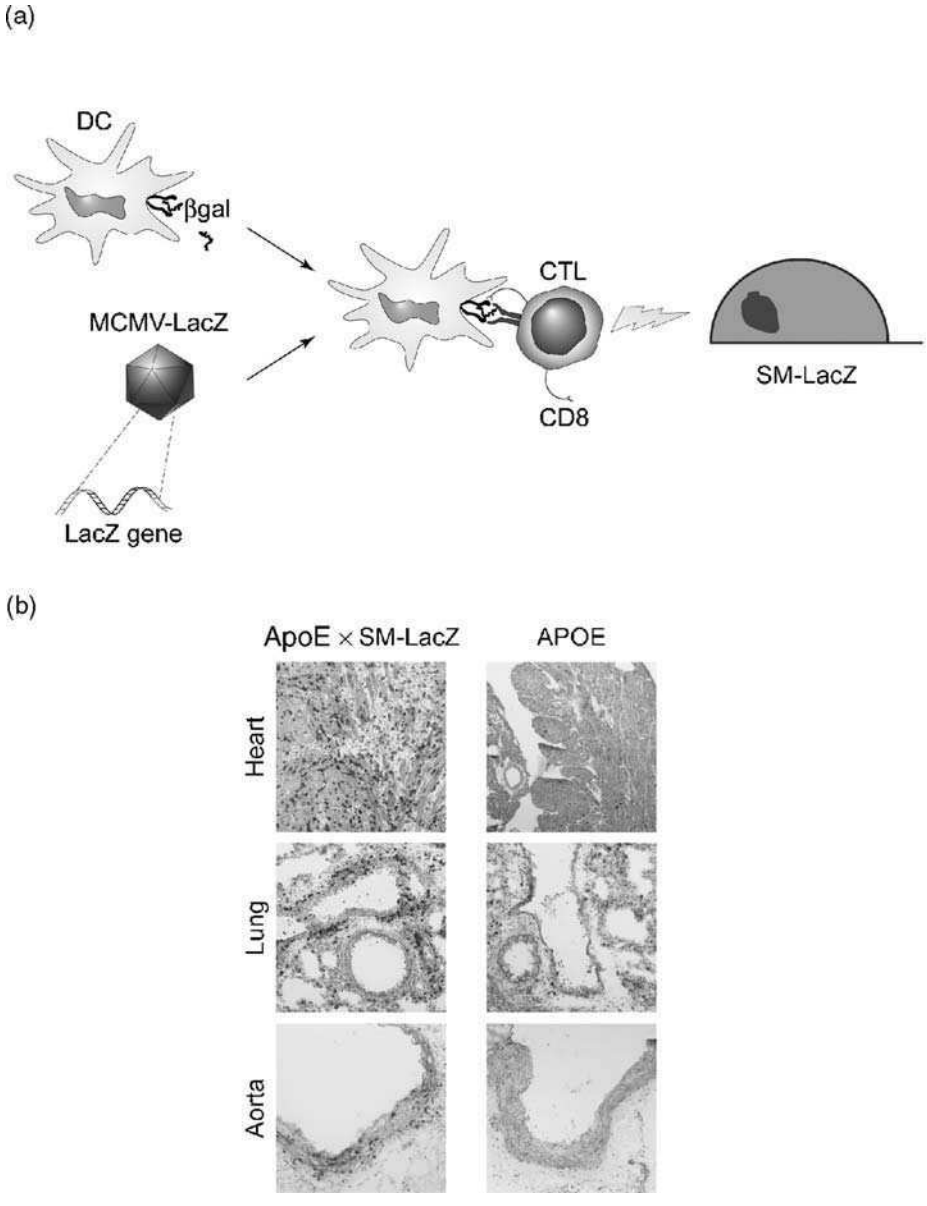

Figure 26.1 $CD8^+$ T cell-induced vasculitis in SM-LacZ transgenic mice. (a) Scheme illustrating how vasculopathy can be induced in SM-LacZ transgenic mice. DC pulsed with βgal 497–504 peptide or antigen-presenting cells infected by recombinant MCMV-LacZ virus present the βgal 497–504 peptide on MHC I molecules to $CD8^+$ T cells. βgal-specific $CD8^+$ T cells are thereby activated and cause damage in peripheral tissue constitutively expressing the transgene (heart, lung arteries, aorta). (b) $ApoE^{-/-} \times$ SM-LacZ and $ApoE^{-/-}$ mice were injected with βgal peptide loaded DC on days 0, 1, 9 and 10. Organs were taken on day 14 and stained with anti-CD8 antibody. For a color version of this figure, please see the images supplied on the accompanying CD

ApoE$^{-/-}$ mice, respectively. To obtain ApoE$^{-/-}$ × SM-LacZ mice, SM-LacZ mice were crossed with ApoE$^{-/-}$, LacZ PCR positive F_1 offspring were intercrossed and LacZ PCR positive F_2 mice with cholesterol values >8 mmol were used for experiments.

Generation of bone-marrow-derived DC and induction of vasculitis in SM-LacZ mice

Bone-marrow-derived DC were prepared as follows. Femurs and tibiae from 6–7-week-old mice were isolated and muscle tissue was removed. Bones were placed into a 60 mm Petri dish containing PBS or balanced salt solution (BSS), washed once with 70 per cent ethanol and twice with PBS or BSS. Both ends of the bones were cut with scissors and the bone-marrow was flushed out into a 50 ml Falcon tube using BSS with a 20 ml syringe and a 21 G needle. The marrow was resuspended well with the syringe. Cells were centrifuged for 5 min at 1200 r.p.m and room temperature (RT), resuspended in 1 ml RPMI (without additives). Thereafter, 1 ml 1.66 per cent NH_4Cl per bone-marrow was added for lysis of erythrocytes. Cells were incubated for 3 min at RT and the 50 ml Falcon tube was subsequently filled with RPMI (without additive) and centrifuged for 5 min at 1000 r.p.m. at RT. Cells were transferred to a 15 ml Falcon tube and washed twice with RPMI (without additives), re-suspended at a concentration of 1×10^6/ml in RPMI containing 5 per cent fetal calf serum (FCS). The medium was supplemented with 1000 U/ml recombinant mouse gcanulocyte-macrophage colony-stimulating factor (GM-CSF) (Sigma, # G0282). Three ml/well of the cell solution were plated in a six-well plate. Cultures were fed on days 2, 4 and 6 by aspirating off 2 ml of the medium and adding fresh medium supplemented with 1500 U/ml GM-CSF. At the day of the injection, DC were pulsed with the H-2K^b-binding βgal peptide 497–504 (Neosystems Laboratoire, Strasbourg, France) at a concentration of 10^{-6} M for 60 min at 37°C with constant shaking. Living DC were purified on Optiprep (Axon Lab AG, Baden, Switzerland, # 111 4542) gradient, in accordance with the manufacturer's protocol and washed three times with BSS. A total of 3×10^5 cells were injected intravenously in a volume of 0.5 ml of BSS. The cytotoxic T lymphocyte (CTL) peak can be recorded on day 6–7 post-immunisation by flow cytometry using βgal-specific major histocompatibility complex (MHC) class I tetramers. Alternatively, peptide-pulsed DC are suitable as stimulators in an enzyme-linked immunospot (ELISPOT) assay (see Figure 26.2a).

Peptide

βgal 497–504 peptide (ICPMYARV)[17] was purchased from Neosystem (Strasbourg, France) and diluted in minimal essential medium (MEM) medium supplemented with 2 per cent FCS at a concentration of 10^{-6} M.

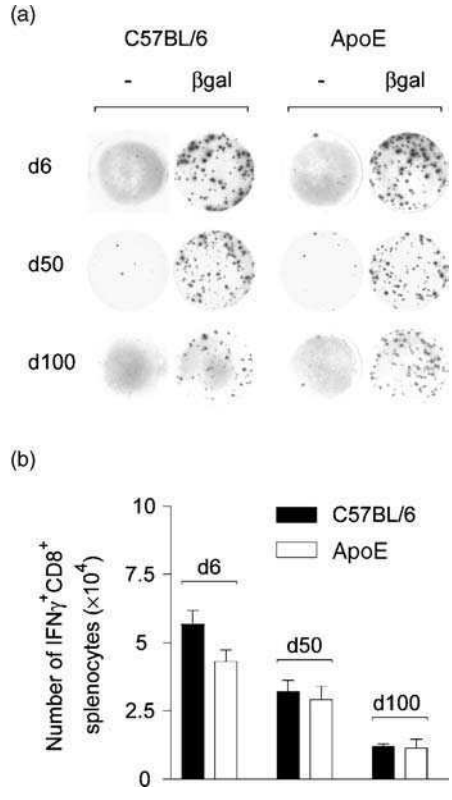

Figure 26.2 IFNγ-ELISPOT data following immunization with MCMV-LacZ. (a) C57BL/6 and ApoE$^{-/-}$ mice were immunized intravenously with 2×10^6 p.f.u. MCMV-LacZ and spleens were harvested on the indicated day post-immunisation and restimulated in the absence or presence of βgal peptide. (b) Total amount of βgal-specific, IFNγ producing CD8$^+$ splenocytes from MCMV-LacZ infected C57BL/6 and ApoE$^{-/-}$ mice ($\pm$ SEM; $n = 3$). Days post-MCMV-LacZ infection are indicated

Immunohistology

Freshly removed organs were immersed in Hanks' balanced salt solution and snap-frozen in liquid nitrogen. Frozen tissue sections were cut in a cryostat and fixed in acetone for 10 min. Sections were incubated with rabbit immunoglobulin G fraction anti-βgal (MPbio/Cappel, # 55976) and anti-mouse monoclonal antibody against CD8$^+$ cells (YTS169), followed by goat anti-rat immunoglobulin (Caltag Labs.) and alkaline phosphatase-labeled donkey anti-goat Ig (Jackson ImmunoResearch Labs.). Nuclei were counter-stained with hemalum.

Expansion and purification of MCMV

Recombinant MCMV expressing the βgal protein under the transcriptional control of the human CMV *ie*1/*ie*2 promoter–enhancer (MCMV-LacZ RM427[18]) was kindly

provided by Prof. E. S. Mocarski (Stanford University, CA). MCMV was propagated and titrated on NIH 3T3 fibroblasts (ECACC, England, # 93061524). MCMV-LacZ was injected intravenously at a dose of 2×10^6 p.f.u.. For preparation of virus stocks and titration, NIH 3T3 cells were expanded in Dulbecco's MEM (DMEM) supplemented with 5 per cent FCS medium. When cells had reached a confluency of 10–50 per cent, medium was removed and an inoculum of 0.01 p.f.u./cell MCMV was added in a minimal volume of DMEM supplemented with 3 per cent FCS. For this step, cells should remain covered by medium. Cells were incubated at 37°C in a 5 per cent CO_2 incubator until the cell layer was completely infected. Complete infection was achieved within 3 to 5 days indicated by extensive cell rounding. Cells were recovered by vigorous pipetting and collected with the supernatant. The mixture of cells and supernatant was transferred into sterile 500 ml centrifuge buckets. Cell and debris were separated from medium by centrifugation at $6400 \times \boldsymbol{g}$ for 20 min at 4°C. Supernatant was decanted into sterile 250 ml buckets. Cell pellets were resuspended in 5 ml cold DMEM 3 per cent FCS medium and dounced 20 times on ice to disrupt cells. The debris were pelleted at $22\,000 \times \boldsymbol{g}$ for 10 min at 4°C and the supernatant of the cell-associated virus was pooled with the free virus collected before. Virus was pelleted from the pooled supernatants by centrifugation at $26\,000\,\boldsymbol{g}$ for $\geq$3 h at 4°C. The virus pellet was resuspended in MEM supplemented with 2 per cent FCS, passed through a 0.45 μm sterile filter (Nalgene, # 194-2545) to deplete virus aggregates, aliquoted and stored at −80°C. One aliquot was thawed and virus titer was determined as described below.

Determination of MCMV titer using plaque-forming assay

This assay can be used either for determination of MCMV titer from stock preparations or to assess MCMV titers in organ homogenates. The day before titration, 24-well tissue culture plates were seeded with NIH 3T3 fibroblasts. Cells should be 60–80 per cent confluent at the day of the titration. Serial $\log_{10}$ dilutions were prepared in DMEM supplemented with 3 per cent FCS (ranging from 10^{-3} to 10^{-10} for viral stocks and starting with a 200-fold dilution for organ homogenates) and 500 μl were added per well. Duplicates of each dilutions were made. Plates were then centrifuged at $800\,\boldsymbol{g}$ for 30 min and incubated for 1 h at 37°C. Medium was eventually removed and about 1 ml of a viscous solution containing 2 × DMEM 10 per cent FCS and 2 per cent methyl-cellulose (1 : 1 solution) was added. Infected cells were then incubated for 4–5 days and, when cytopathicity was clearly visible, cells were fixed and stained with a crystal violet solution (0.1 per cent crystal violet (Sigma, C3886), 10 per cent ethanol, 0.15 M NaCl, 4 per cent formaldehyde) and the number of plaque-forming units (p.f.u.) per ml virus preparation was determined.

Assessing the activation status of βgal-specific $CD8^+$ cells

The activation status of antigen-specific T cells can be evaluated by assessing their capacity to produce the effector cytokine interferon-γ (IFNγ) upon *in vitro* peptide

restimulation. Cytokine production can be measured both with ELISPOT assay and/or with intracellular cytokine (ICS) staining. The former is better suited if the frequency of IFNγ producers in the $CD8^+$ T-cell pool is expected to be <1 per cent.

Spleens were removed at the desired time points, ground in 10 ml BSS through a metal grid using a syringe stopper and re-suspended several times using a 10 ml pipette in order to obtain a single cell suspension. Spleen suspensions were then centrifuged briefly at 1000 r.p.m. to pellet larger debris. Pellets were discarded and cell suspensions were centrifuged for 5 min at 1500 r.p.m. at RT, and the supernatant was aspired.

For ELISPOT analysis, cells were re-suspended in 5 ml BSS, passed through filter units (BD, # 340627, 30 µm cup filcons) to remove cell clusters that may block magnetic-activated cell sorting (MACS) columns and resuspended in 475 µl MACS buffer (PBS with 2 per cent FCS). $CD8^+$ T cells were positively selected by using anti-CD8 beads (# 130-049-401) from Miltenyi (Bergisch-Gladbach, Germany) in accordance with the manufacturer's protocol. MACS-purified $CD8^+$ T cells (5×10^4) and 2×10^4 autologous DC were incubated in the presence or absence of the βgal peptide in 96-well ELISPOT filter plates (Millipore, MAIP N4510, Multi-Screen-IP, # 0848645645) coated with an affinity purified anti-IFNγ capture antibody derived from clone AN18.[19] Purified $CD8^+$ T cells stimulated with phorbol 12-myristate 13-acetate (PMA, 2.5×10^{-7} M, Sigma, # P-8139) and ionomycin (1.25 µg/ml, Sigma, # I0634-1MG) served as positive control. After overnight incubation, IFNγ secretion was revealed using a biotin-conjugated anti-IFNγ detection antibody (XMG-D6-biotin conjugate) and streptavidin-conjugated alkaline phosphatase (Dianova, Hamburg, Germany, # 016-050-084). Reactive spots were visualized with 5-bromo-4-chloro-3-indol-phosphate-toluidine (BCIP, AppliChem, Darmstadt, Germany, # A1117,0005) and nitroblue-tetrazoliumchloride (NBT, AppliChem, Darmstadt, Germany, # A1243,0005) (Figure 26.2a). Spots were counted with an ELISPOT reader from AID and analysed with the software ELISPOT 3.1SR (AID, Strassberg, Germany) (Figure 26.2b).

For ICS, single cell suspensions of 1×10^6 splenocytes were incubated for 5 h at 37°C in 96-well round-bottom plates in 200 µl RPMI culture medium containing 25 U/ml interleukin-2 and 5 µg/ml Brefeldin A (Sigma, # B-7651). Cells were stimulated with PMA (50 ng/ml) and ionomycin (500 ng/ml) as positive control or left untreated a negative control. For analysis of peptide-specific responses, 10^6 cells were stimulated with 10^{-7} M βgal peptide. After stimulation, splenocytes were centrifuged 5 min at 1500 r.p.m. at 4°C in 96-well plates, supernatant was rapidly and carefully flicked off, and following slight mixing on a vortex, cells were washed in 150 µl fluorescence-activated cell sorting (FACS) buffer (PBS, 2 per cent FCS, 20 mM ethylenediamine tetra-acetic acid, 0.1 per cent NaN_3). Splenocytes were then surface-stained with anti-CD8-FITC (clone 53.6.72.4) in FACS buffer for 20 min at 4°C. Following surface staining, cells were washed three times with FACS buffer as described above. Cells were thereafter fixed and permeabilised with Cytofix/Cytoperm™, (BD, # 554722) in accordance with the manufacturer's protocol. Cells were stained intracellularly with anti-IFNγ-FITC (clone AN18)[19] in permeabilisation buffer for 30 min at 4°C. Cells were eventually washed three times with

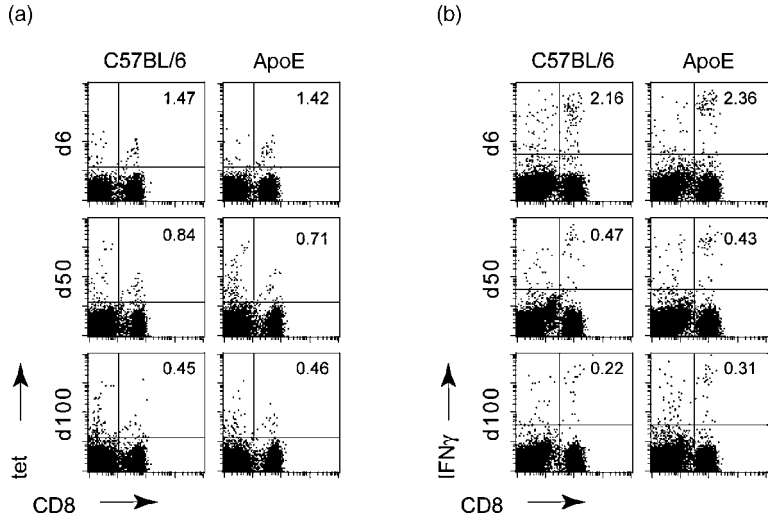

Figure 26.3 Quantification of the percentage of βgal-specific CD8$^+$ T cells following immunisation with MCMV-LacZ. C57BL/6 and ApoE$^{-/-}$ mice were immunised intravenously with 2×10^6 p.f.u. MCMV-LacZ and spleens were harvested on the indicated days post-immunisation. The percent of βgal-specific CD8$^+$ T cells was assessed with MHC I tetramers (a) or by production of IFNγ by intracellular cytokine staining (b). Activation of CTL has been shown to lead to TCR down-regulation[27-30] and may explain the relatively low mean fluorescence intensity of the tetramer positive CD8$^+$ T cells

permeabilisation buffer, and the percentage of IFNγ-producing cells was determined after gating on CD8$^+$ cells using a FACScalibur flow cytometer (BD) (Figure 26.3b).

Tetramer staining

Analysis with MHC tetramers allows to track antigen-specific T cells and to shed light on their dynamics and distribution.[20] T-cell receptors (TCR) of CD8$^+$ T cells bind to their cognate peptide presented in conjunction with MHC class I molecules on the surface of antigen-presenting cells (APC). Since this recognition is specific, it is possible to identify CD8$^+$ T cells by the binding of soluble peptide–MHC complexes attached to fluorochrome groups. Through cooperative interaction with multiple TCR, MHC-tetramers allow better binding to T cells than monomeric peptide–MHC complexes. MHC class I (H-2K^b) monomers complexed with βgal peptide were produced as described[21] and tetramerised by addition of streptavidin-PE (Molecular Probes, Eugene, OR). On the day of analysis, single cell suspensions were prepared from spleen. Aliquots of 5×10^5 cells or three drops of blood were stained using 50 µl of a solution containing tetrameric MHC class I-peptide complexes at 37°C for 10 min followed by staining with anti-CD8-FITC (clone 53.6.72.4) at 4°C for 20 min. Following CD8 and tetramer stain, cells were resuspended in FACS buffer containing

1 µl of the stock solution of the vitality marker 7-AAD (Sigma, # A 9400) per 0.4 ml FACS buffer, incubated at 4°C protected from light for 20 min. Eventually, cells were gated on viable, 7-AAD low leukocytes and analysed with a FACScalibur flow cytometer (BD) (Figure 26.3a).

Discussion

We present here a mouse model to study autoimmune arteritis, myocarditis, as well as immune-mediated acceleration of atherosclerosis. In the SM–LacZ model, both DC immunization and infection with a recombinant MCMV-LacZ virus can be used to induce specific cardiovascular pathology. It has to be stressed here that, despite eliciting a substantial expansion of specific CTL, a single DC injection is usually not sufficient to elicit significant immunopathology. Repeated application of peptide-pulsed DCs was required to achieve full differentiation of effector CTL and to induce the most severe phenotype of this experimental disease – with arteritis, myocarditis and dilated cardiomyopathy. A less frequent administration of βgal peptide-loaded DC triggers a less severe and transient cardiovascular inflammation.[22]

On the other hand, a too strong stimulus may lead to terminal differentiation of CTL, making them short-lived, and induce exhaustive tolerance. Whereas DC immunization induced proliferation of antigen-specific $CD8^+$ T cells in SM-LacZ mice, infection with a recombinant adenovirus applied via the intravenous route resulted in exhaustion and physical deletion of βgal-specific CTL, and consequently absence of immunopathology.[23] Therefore, it appears that the peripheral antigen dose is critical for the efficient induction of βgal-specific $CD8^+$ T cell and subsequent immune-triggered disease in SM-LacZ mice.

Determination of MCMV virus titer by plaque assay can present a certain variance depending on factors such as density and fitness of NIH 3T3 target cells. Furthermore, plaque assay has a limited sensitivity. In case of low virus concentration in cell suspensions of organs that display cytotoxicity when not sufficiently diluted, such as the liver, measurement of virus titers may be inaccurate. Real-time PCR technique has been shown to provide a rapid and reproducible quantitative method for the detection of MCMV.[24] Real-time PCR of MCMV displays several advantages over the plaque assay, such as high sensitivity, detection of viral nucleic acid derived from non-replicating virus as well as precise quantification of CMV DNA copies.

Application

By crossing SM-LacZ mice onto the hypercholesterolemic $ApoE^{-/-}$ background, we were able to assess the influence of elevated serum cholesterol values on the development of immune-mediated arterial inflammation and to evaluate the significance of $CD8^+$ T-cell-mediated arteritis in the chronological process of cholesterol-induced atherosclerosis.[13] We have shown that, in a context of high cholesterol levels in the serum, a specific CTL response can be raised against a vascular antigen. This

immune mediated vascular inflammation accelerated atherosclerosis progression.[13] We are currently using ApoE$^{-/-}$ × SM-LacZ mice infected with a βgal recombinant MCMV to assess the role of a viral antigen persisting in the vasculature on the initiation and progression of atherosclerotic lesions. In this constellation, not only the influence of the MCMV-mediated 'bystander' inflammation can be investigated,[25,26] but also the specific contribution of the adaptive immune system against the 'persistent' vascular antigen can be studied and correlated with the development of atherosclerosis. We have found that, following immunization with MCMV-LacZ, ApoE$^{-/-}$ × SM-LacZ mice displayed significantly elevated atherosclerotic lesions compared to their ApoE$^{-/-}$ counterparts, hence emphasising the role of pathogen-driven inflammatory process in atherogenesis (Krebs *et al*., manuscript in preparation).

References

1. Numano F. Vasa vasoritis, vasculitis and atherosclerosis. *Int J Cardiol* 2000; **75**(Suppl 1): S1-8; discussion S17–19.
2. Popa ER, Stegeman CA, Kallenberg CG, Tervaert JW. *Staphylococcus aureus* and Wegener's granulomatosis. *Arthritis Res* 2002; **4**: 77–79.
3. Nikkari S, Mertsola J, Korvenranta H, Vainionpaa R, Toivanen P. Wegener's granulomatosis and parvovirus B19 infection. *Arthritis Rheum* 1994; **37**: 1707–1708.
4. Nigro G, Zerbini M, Krzysztofiak A, Gentilomi G, Porcaro MA, Mango T, Musiani M. Active or recent parvovirus B19 infection in children with Kawasaki disease. *Lancet* 1994; **343**: 1260–1261.
5. Leruez-Ville M, Lauge A, Morinet F, Guillevin L, Deny P. Polyarteritis nodosa and parvovirus B19. *Lancet* 1994; **344**: 263–264.
6. Mandell BF, Calabrese LH. Infections and systemic vasculitis. *Curr Opin Rheumatol 1998;* **10**: 51–57.
7. Chiu B, Viira E, Tucker W, Fong IW. *Chlamydia pneumoniae*, cytomegalovirus, and herpes simplex virus in atherosclerosis of the carotid artery. *Circulation* 1997; **96**: 2144–2148.
8. Hendrix MG, Salimans MM, van Boven CP, Bruggeman CA. High prevalence of latently present cytomegalovirus in arterial walls of patients suffering from grade III atherosclerosis. *Am J Pathol* 1990; **136**: 23–28.
9. Yonemitsu Y, Nakagawa K, Tanaka S, Mori R, Sugimachi K, Sueishi K. *In situ* detection of frequent and active infection of human cytomegalovirus in inflammatory abdominal aortic aneurysms: possible pathogenic role in sustained chronic inflammatory reaction. *Lab Invest* 1996; **74**: 723–736.
10. Jarvis MA, Nelson JA. Human cytomegalovirus persistence and latency in endothelial cells and macrophages. *Curr Opin Microbiol* 2002; **5**: 403–407.
11. Hamamdzic D, Harley RA, Hazen-Martin D, LeRoy EC. MCMV induces neointima in IFN-gammaR – / – mice: intimal cell apoptosis and persistent proliferation of myofibroblasts. *BMC Musculoskelet Disord* 2001; **2**: 3.
12. Vossen RC, van Dam-Mieras MC, Bruggeman CA. Cytomegalovirus infection and vessel wall pathology. *Intervirology* 1996; **39**: 213–221.
13. Ludewig B, Freigang S, Jaggi M, *et al* Linking immune-mediated arterial inflammation and cholesterol-induced atherosclerosis in a transgenic mouse model. *Proc Natl Acad Sci U S A* 2000; **97**: 12752–12757.

14. Moessler H, Mericskay M, Li Z, Nagl S, Paulin D, Small JV. The SM 22 promoter directs tissue-specific expression in arterial but not in venous or visceral smooth muscle cells in transgenic mice. *Development* 1996; **122**: 2415–2425.
15. Ludewig B, Ochsenbein AF, Odermatt B, Paulin D, Hengartner H, Zinkernagel RM. Immunotherapy with dendritic cells directed against tumor antigens shared with normal host cells results in severe autoimmune disease. *J Exp Med* 2000; **191**: 795–804.
16. Plump AS, Smith JD, Hayek T, Severe hypercholesterolemia and atherosclerosis in apolipoprotein E- deficient mice created by homologous recombination in ES cells. Cell 1992; **71**: 343–353.
17. Oukka M, Cohen-Tannoudji M, Tanaka Y, Babinet C, Kosmatopoulos K. Medullary thymic epithelial cells induce tolerance to intracellular proteins. *J Immunol* 1996; **156**: 968–975.
18. Manning WC, Mocarski ES. Insertional mutagenesis of the murine cytomegalovirus genome: one prominent alpha gene (ie2) is dispensable for growth. *Virology* 1998; **167**: 477–484.
19. Prat M, Gribaudo G, Comoglio PM, Cavallo G, Landolfo S. Monoclonal antibodies against murine gamma interferon. *Proc Natl Acad Sci U S A* 1984; **81**: 4515–4519.
20. Klenerman P, Cerundolo V, Dunbar PR. Tracking T cells with tetramers: new tales from new tools. *Nat Rev Immunol* 2002; **2**: 263–272.
21. Altman JD, Moss PA, Goulder PJ, et al. Phenotypic analysis of antigen-specific T lymphocytes. *Science* 1996; **274**: 94–96.
22. Ludewig B, Junt T, Hengartner H, Zinkernagel RM. Dendritic cells in autoimmune diseases. *Curr Opin Immunol* 2001; **13**: 657–662.
23. Krebs P, Scandella E, Odermatt B, Ludewig B. Rapid functional exhaustion and deletion of CTL following immunization with recombinant adenovirus. *J Immunol* 2005; **174**: 4559–4566.
24. Vliegen I, Herngreen S, Grauls G, Bruggeman C, Stassen F. Improved detection and quantification of mouse cytomegalovirus by real-time PCR. *Virus Res* 2003; **98**: 17–25.
25. Burnett MS, Gaydos CA, Madico GE, Glad SM, Paigen B, Quinn TC, Epstein SE. Atherosclerosis in apoE knockout mice infected with multiple pathogens. *J Infect Dis* 2001; **183**: 226–231.
26. Hsich E, Zhou YF, Paigen B, Johnson TM, Burnett MS, Epstein SE. Cytomegalovirus infection increases development of atherosclerosis in Apolipoprotein-E knockout mice. *Atherosclerosis* 2001; **156**: 23–28.
27. Busch DH, Pilip IM, Vijh S, Pamer EG. Coordinate regulation of complex T cell populations responding to bacterial infection. *Immunity* 1998; **8**: 353–362.
28. Valitutti S, Dessing M, Aktories K, Gallati H, Lanzavecchia A. Sustained signaling leading to T cell activation results from prolonged T cell receptor occupancy. Role of T cell actin cytoskeleton. *J Exp Med* 1995; **181**: 577–584.
29. Valitutti S, Muller S, Cella M, Padovan E, Lanzavecchia A. Serial triggering of many T-cell receptors by a few peptide-MHC complexes. *Nature* 1995; **375**: 148–151.
30. Viola A, Salio M, Tuosto L, Linkert S, Acuto O, Lanzavecchia A. Quantitative contribution of CD4 and CD8 to T cell antigen receptor serial triggering. *J Exp Med* 1997; **186**: 1775–1779.

27

Surgically induced chronic heart failure

Craig A. Lygate and **Stefan Neubauer**

Department of Cardiovascular Medicine, John Radcliffe Hospital University of Oxford, Oxford, U.K.

Abstract

Over recent years mouse models of chronic heart failure have been increasingly used to test the influence of specific gene overexpression, ablation or mutation on LV remodelling and progression to cardiac failure. In this chapter we review the three main surgical models in the mouse: myocardial infarction due to coronary artery ligation (CAL); pressure overload due to transverse aortic constriction (TAC); and volume overload due to aortocaval fistula. Surgical techniques for the CAL and TAC models are described in detail, along with discussion of potential methodological problems, the natural history of disease progression, and methods for establishing the severity of heart failure.

Key Words:

mouse; animal models; hypertrophy; myocardial infarction; heart failure

Introduction

At least 30 different models of heart failure have been developed in more than 11 species using a variety of approaches: naturally occurring, genetic manipulation, administration of cytotoxic agents or surgically induced. Until recently, the rat was the most commonly used species for heart failure models. However, the advent of transgenic and knockout technologies has pushed the mouse to the forefront of heart failure research, and surgically induced models are particularly well suited to answering how specific genetic modifications affect the progression to heart failure. The utility of the mouse as a model of heart failure is evidenced by the similarities between mouse and man in the pathophysiology following myocardial infarction, as summarised in Table 27.1.

There are three main surgical models of heart failure in the mouse: coronary artery ligation (CAL) to induce myocardial infarction; transverse aortic constriction (TAC)

A Handbook of Mouse Models of Cardiovascular Disease Edited by Qinbo Xu

Table 27.1 Characteristics of heart failure observed after CAL in the mouse

Characteristic of heart failure	Observed in mouse model
Hemodynamic profile – impaired systolic and diastolic function and elevated LV EDP	Numerous examples LVEDP only increases significantly in large infarcts
LV hypertrophy	Increased LV/RV weights Myocyte cellular hypertrophy
LV dilatation	Commonly observed
Interstitial fibrosis	Histological collagen staining and increased collagen protein expression
Lung congestion	Occurs only in largest infarcts
Increased natriuretic peptides	LV gene expression of ANP and BNP are both elevated
LV apoptosis	Elevated up to 6 months post-infarct
Renin–angiotensin system	Increased expression of AT_1 receptors Increased LV aldosterone concentration Efficacy of ACE inhibitors, spironolactone and AT-receptor blockers have been demonstrated in the mouse.
Oxidative stress	Increase in reactive oxygen species

LVEDP, left ventricular end-diastolic pressure; RV, right ventricle; ANP, atrial natriuretic peptide; BNP, B-type natriuretic peptide; ACE, angiotensin-converting enzyme; AT_1, angiotensin type I.

to create a model of pressure overload; and aortocaval fistula to create a model of volume overload. In this chapter we will describe in detail the techniques of CAL and TAC as these are by far the most common of the murine models, with only brief reference to aortocaval fistula. A model of pulmonary artery constriction leading to right ventricular hypertrophy and failure has also been described,[1] but is seldom used, and is essentially a combination of thoracotomy and the TAC technique provided below. To our knowledge, there have been no reports of surgically induced mouse models of aortic or mitral regurgitation.

Coronary artery ligation

Ischaemic heart disease is the most common cause of heart failure in man, making coronary artery ligation the most clinically relevant heart failure model available. The technique is a simple adaptation of the rat CAL model that has been in use for over 50 years and which has a good track record of predicting drug efficacy in human heart failure. It remains to be demonstrated whether the mouse equivalent will be as good a predictive model, but drugs that improve rat and human heart failure are also beneficial in the infarcted mouse heart.[2]

CAL in the mouse was first described as early as 1978,[3] but there was little rationale for groups to adopt this technique in the pre-transgenic era. Furthermore, tools for the assessment of *in vivo* cardiac function were inadequate and it took 20 years until such phenotyping tools became available allowing the structural and hemodynamic consequences of chronic myocardial infarction to be studied in the mouse.[4,5]

Permanent occlusion of a coronary artery ultimately results in necrosis of the downstream myocardium. A complex process of wound healing involving inflammatory cell infiltration, collagen degradation and deposition, necrosis and apoptosis results in the production of a mature infarct scar within the first 2 weeks. In the mouse, infarcts are almost always transmural, but unlike in other mammals, occlusion of the LAD can affect much more than the anterior wall. Often the entire apex will be involved and sometimes even significant portions of the posterior wall. This can result in particularly large infarct scars of up to 70 per cent of the left ventricle (LV).[6] However, as with other CAL models, the mouse exhibits a wide range of infarct sizes (10–70 per cent), and experimental groups are usually retrospectively matched for infarct size. This is necessary as LV remodelling, function, and survival in the chronic infarction model are all directly related to infarct size.[7,8] Therefore, even small differences in infarct size between experimental groups could lead to erroneous conclusions as to the effect of a specific intervention. To determine whether an intervention affects infarct size, mice must be killed at early time points and the infarct size measured relative to the area at risk. Mice with infarct sizes below 30 per cent seldom develop any of the hemodynamic or ventricular remodelling changes associated with heart failure and are often excluded from statistical analysis.[9]

However, the development of heart failure is not only dependent on the loss of myocardium to scar tissue, but also the involvement of non-infarcted myocardium in the absence of further acute insult. Processes involved include, hypertrophy and apoptosis of myocytes, widespread interstitial fibrosis and a gradual decline in chronotropic and luscitropic competence. All these characteristics have been observed in the mouse model of CAL (Table 27.1).

Aortic constriction

The second most common surgical model of heart failure in the mouse is the creation of an aortic constriction resulting in pressure overload, mimicking aortic stenosis in man. A ligature is tied around the aorta to create a stenosis of uniform cross-sectional area. The stenosis is most commonly created at the level of the transverse aorta (TAC) resulting in a constriction of 65–70 per cent, and was first described by Rockman *et al.*[10] However, banding of the ascending[11] and descending[12] aorta have also been described. All result in a progressive concentric LV hypertrophy, which is the more rapid and severe the more proximal the stenosis is to the heart. Further details of these techniques as models for LV hypertrophy are provided earlier in this book. However, TAC is also commonly used as a model of chronic heart failure, as over time the persistently elevated afterload results in decompensation and development of congestive heart failure.[13] The advantage of TAC over other banding placements is the combination of a pressure overload severe enough to result in heart failure, while maintaining access for hemodynamic measurements via the right carotid artery. Therefore a detailed description of TAC surgery is included in this chapter.

Volume overload

A model of heart failure due to chronic volume overload has been described in the mouse by surgical creation of an aortocaval shunt.[14,15] While this model has so far not been used widely, one advantage is that it does not require a thoracotomy and so is technically less challenging. An abdominal mid-line incision is made, and the vena cava and abdominal aorta are dissected free and clamped distal to the renal arteries. A needle is used to puncture the aorta and adjacent vena cava. The puncture sites are then repaired with cyanoacrylate glue to create the aortocaval shunt.[14] Alternatively, a 2 mm anastomosis is created using microsurgical techniques.[15] A successful fistula is evidenced by the mixing of arterial and venous blood within the vena cava. Over a one month period, mice develop significant hypertrophy in all four cardiac chambers in the presence of normal arterial blood pressure but elevated central venous pressure. LV end-diastolic pressure, lung weights and natriuretic peptide expression are all elevated indicating the development of congestive heart failure.[14] However, there is little data on the range of values obtained, and it is difficult to judge how standardised the individual response is in this model. As with other heart failure models it is likely to be varied. Indeed Perry *et al*. quantified shunt severity by using an arterial injection of microspheres designed to lodge in the microcirculation, and measuring how many were found in the lungs. This ranged from 1 to 74 per cent of the total microspheres injected, suggesting a large variation in shunt severity.[15]

Only Scheuermann-Freestone *et al*. provide a breakdown of mortality in this model, and it appears to be a major problem limiting its use. They found perioperative mortality in males to be greater than 80 per cent, and in females 42 per cent, probably due to severe heart failure. Furthermore, of the survivors, 12 per cent did not have a patent shunt on visual inspection at 30 days.[14] For these reasons the aortocaval fistula model remains to be further characterised before it can be applied for the systematic comparison of different strains of mice.

Materials and methods

There are common elements to both CAL and TAC surgery, and where possible these will be discussed together. For convenience, examples of appropriate surgical instruments are provided in the text with catalogue numbers (most can be obtained from FST: Fine Science Tools, Heidelberg, Germany).

Set-up: coronary artery ligation and transverse aortic constriction

It is best practice from a scientific and animal welfare viewpoint if infection is eliminated by appropriate aseptic procedure. In our laboratory we use a purpose-built HEPA-filtered laminar air flow system mounted above the operating table, with three sides open for easy access. An extractor fan is incorporated in to the base unit with

vents surrounding the operating area. This not only protects the mouse from pathogens, but also the operator from exposure to allergens and volatile anesthetics. The filtered downdraft is gently heated to minimise heat loss due to wind chill. We also use a homeothermic heating blanket set to 37°C throughout the procedure (Harvard Apparatus). In addition, all instruments are sterilised and the operating area covered in sterile drapes. For cleaning of instruments between mice, a dry-bead sterilizer may be used (e.g. Sterilquartz).

Preoperative preparation: coronary artery ligation and transverse aortic constriction

The ideal mouse body weight for these surgical procedures is ~25 g (20–40 g is suitable). The anesthetic chamber is pre-filled with 4 per cent isoflurane in 100 per cent O_2 (flow rate 2 l/min) to ensure rapid onset of anesthesia. After induction, the mouse is given a 1 mg/kg subcutaneous injection of buprenorphine for analgesia, before being returned to the anesthetic chamber until deeply anesthetised.

For intubation, the mouse is placed supine with the upper incisors restrained by a rubber band. Surgical tape is then placed across the chest and forelimbs to hold the mouse in position. A bright focused light is shone on to the chest and neck area to aid visualisation of the larynx, which appears as a flash of light on each inspiration. The tongue is moved up and to the side and held into position with curved forceps (e.g. FST 13011-12), while with the other hand, the intubation tube is advanced towards the larynx and timed with inspiration to enter the trachea. The mouse is then attached to a respirator (Hugo-Sachs Electronik Mini-Vent from Harvard Apparatus, which comes with appropriate intubation tube – outer diameter 0.9 mm, length 25 mm) and ventilated at 250–300 µl stroke volume and 150 breaths per minute. Successful intubation is evident when the chest rises in synchrony with the pump. The anesthesia is then reduced to 2 per cent isoflurane for the rest of the procedure, with a flow-rate of 500 ml/min via an anesthetic gas reservoir. Care should be taken to prime the anesthetic circuit prior to intubation, as dead space in the line can be considerable, and may result in loss of adequate anesthesia. To prevent permanent eye damage due to dessication, we routinely applying a preparation of liquid tears (e.g. Viscotears liquid gel®, carbomer 2 mg/kg, Novartis).

Surgical protocol

CAL

The mouse is placed in the position shown in Figure 27.1a, supine with the left hind limb taped over onto the right hind limb, and the left fore limb above the head (Blenderm™ 1.25 cm × 4.5 m, 3M). The chest is shaved and a skin disinfectant applied. An occlusive film dressing is placed over the chest (e.g. Tegaderm®

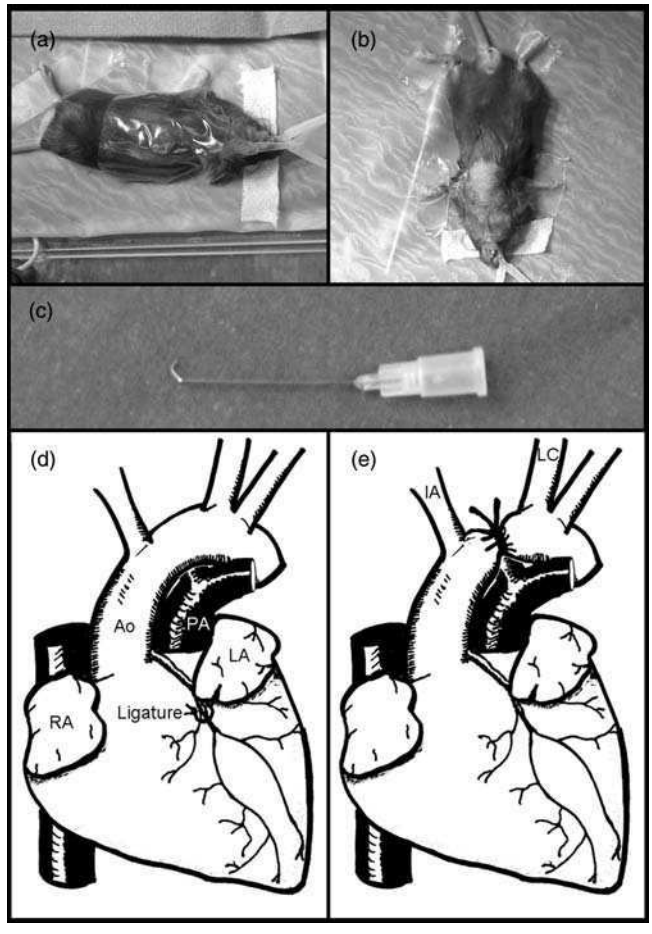

Figure 27.1 Photographs taken from point of view of the operator indicating positioning of mice for surgery. (a) Coronary artery ligation (CAL), hind-limbs are taped together with left fore-limb positioned over the head; (b) transverse aortic constriction (TAC), positioned supine. (c) photograph showing an adapted blunted 27G needle as used during TAC surgery to standardise the degree of stenosis. The banding suture is fed underneath the transverse aorta and tied tight against the adapted needle, which is then promptly removed. Schematic diagrams of the mouse heart are shown indicating the ligature position for CAL at the atrio-ventricular border to produce large infarcts (d) and the positioning of the banding suture between the innominate and left carotid arteries for TAC (e). Ao, Aorta; PA, pulmonary artery; LA, left atria; RA, right atria; IA, innominate artery; LC, left common carotid artery

transparent dressing 1622W, 3M), to prevent fur and dander from entering the wound. An incision ($\sim$1 cm) is made with scissors (FST 14559-11) from just below the left axilla towards the xiphisternum, and the skin is blunt dissected from the underlying pectoralis muscle. The border regions of this muscle are also blunt dissected, and retracted to reveal the rib cage. The position of the heart and lungs can be visualised through the intercostal muscles, allowing a point of incision to be determined that

will not damage either organ. This incision is made with the point of some fine curved forceps (e.g. FST 00649-11), in the space between the fourth and fifth ribs; which is more easily identified as the third intercostal space counting up from the lowest rib with a sternal attachment. The same forceps are then carefully worked underneath the intercostal muscles, prising up small sections to be cut with a pair of mini-Vannas scissors (e.g. FST 15000-08). The left lung is then collapsed with a small square of gauze soaked in saline, the ribs are retracted using mini-Goldstein retractors (FST 17002-02), and the pericardium removed. The left side of the heart is now in full view and the left anterior descending (LAD) coronary artery is identified under a dissecting microscope. To aid identification, the left atrium is lifted to allow visualisation of the LAD from its origin down through the myocardium. The ligature is placed at the atrio-ventricular border, proximal to the main bifurcation (Figure 27.1d), using a 6-0 polyethylene suture (Ethicon, W8712; 7-0 and 8-0 are also suitable). When the suture is tied tight there is a distinct blanching of most of the visible myocardium, if this does not occur, then further sutures are placed to occlude side-branches and increase infarct size.

The retractors and gauze are then removed. While the lung is still collapsed, a suture is placed around the separated ribs (Ethibond Excel 5-0, W6757, Ethicon) and the lung is inflated by temporary occlusion of the expiration line on the ventilator. The rib suture is then pulled tight, and a further suture placed above the heart if necessary. The muscle layers are closed with the same suture material and the skin with 4-0 Vicryl Rapide (W9930, Ethicon). Sham-operated animals are prepared as above, with the exception that no ligature is placed in the heart.

TAC

The mouse is placed in the position shown in Figure 27.1b, supine with head towards the operator. As with CAL surgery, the chest is shaved, applied with disinfectant and covered with an occlusive film dressing. A vertical skin incision is made from the suprasternal notch to the mid-sternum. Curved forceps are used to create a puncture through the muscle layer at the notch (e.g. FST 11051-10), allowing insertion of straight blunt-ended scissors underneath the sternum (e.g. Aesculap BC030R), which is cut in a vertical line as far as the third or fourth rib. Metal clips are used to retract the two halves of the rib-cage, and the thymus is blunt dissected to expose the aortic arch. The transverse portion of the aorta is carefully dissected free of connective tissue by blunt dissection using fine curved forceps (e.g. FST 00649-11). A 7-0 polypropylene monofilament suture (Deklene or silk may be used e.g. Sofsilk 7-0 S-1768, USS EG sutures) is fed underneath the transverse aorta, midway between the innominate and left carotid arteries (Figure 27.1e). The suture is tied tight on to a blunted 27G needle (i.e. 0.4 mm OD adapted as in Figure 27.1c) to standardise diameter of the stenosis, and the needle removed. The rib cage is closed with two to three interrupted sutures (Ethibond Excel 5-0, W6757, Ethicon), and the skin with 4-0 Vicryl Rapide (W9930, Ethicon). Sham animals are prepared in an identical fashion, but without placement of the banding suture. The above technique is similar to the

minimally invasive trans-sternal approach of Hu *et al.*,[16] but alternative access to the aortic arch can be obtained by thoracotomy via the second left intercostal space.[10]

Postoperative care: CAL and TAC

After closing, the wound is disinfected with chlorhexidine spray, the isoflurane anesthesia is turned off, and mechanical ventilation is continued until the mouse regains a gag reflex. Sterile saline is given by subcutaneous injection (0.5 ml) even where there is no blood loss, to allow for reduced fluid intake during the recovery period. On extubation, mice are immediately placed in a heated chamber (37°C) for the first 20 min until fully mobile. They are then transferred to heated cages (32°C) for at least 4 h, before being returned to a normal rack. Typically, five mice are operated on in a morning session, taking about 30 min per mouse from induction to recovery from anesthesia. This allows time during the working day for postoperative surveillance, and remedial action where necessary.

Discussion

Potential pitfalls

Respiratory problems are the most commonly encountered difficulty, and these will become apparent when the mouse takes additional breaths between pump inspirations. A rapid check should be made of the anesthetic circuit, to ensure that adequate anesthesia is still being delivered. However, more often this indicates a problem with mechanical ventilation and not anesthesia. The depth of the intubation tube should be checked. If inserted too far, then the end of the tube can pass the bifurcation of the trachea, thereby ventilating only one side of the lungs. If only the left lung is being ventilated, this will become instantly apparent when the left lung is collapsed during CAL surgery. Milder symptoms may occur if the intubation tube is partially blocked by an accumulation of mucous, or during TAC surgery if the pleura surrounding both lungs are breached. The resulting additional off-pump breaths can often be prevented by increasing the stroke volume and/or stroke frequency on the ventilator, or by providing gentle pressure to the neck to improve the seal between tube and trachea.

Any instruments touching the lung surface will result in bruising, and could cause tearing or punctures. Where lung damage is suspected before closure, it is prudent to test for leaks by filling the chest cavity with preheated sterile saline and looking for air bubbles. If detected, the mouse should be killed, as these mice cannot survive. Damage may also be caused by hyperinflation of the lungs prior to closure, or by trapping a small section of lung when the ribs are splinted together. Often, such problems are only detected after extubation, sometimes several hours afterwards, if the puncture is particularly small. For this reason, mice should be observed up to a 4 h time point postoperatively. The observation of breathing difficulties (e.g. deep gasp breathing involving the diaphragm) should be used as a humane end-point, and the

mouse immediately killed. This is also true of later time-points, when it is the key symptom heralding the onset of acute congestive heart failure. Once mice reach this stage, they will die within hours, and there can be no ethical justification to continue the experiment.

In both CAL and TAC there is a risk of severing the internal mammary artery which runs alongside the sternum, resulting in significant blood loss. This risk can be minimised in CAL by stopping short of the sternum when cutting the intercostal muscles, and in TAC by ensuring a straight cut down the centre of the sternum. The result of rupturing this artery is a large and rapid blood loss which is difficult to stem. However, with good postoperative care, mice usually survive this blood loss. In CAL, warmed saline can be added directly to the chest cavity for absorption, with further saline given subcutaneously (1–2 ml between several injection sites). These animals may take longer to recover from anesthesia and may need supplemental heat for a prolonged period of time (e.g. overnight at 26°C). Another source of blood loss is when the suture needle injures a coronary vessel, or the full thickness of the myocardium is breached. In both these scenarios the best course of action is to quickly tie the suture, to stem any blood loss, and good postoperative care as above.

Due to variations in the branching of the left anterior descending coronary artery, a wide variety of infarct sizes are produced after CAL (10–70 per cent). Partly this is due to the difficulty in directly observing the coronary arteries, as they become embedded in the myocardium a few millimeters from their origin, and the suture is often therefore placed blind. However, even ligating in an identical position every time does not prevent this problem, as there are many variations in arterial branching patterns between individuals. Ahn *et al.* studied branching patterns of mouse coronary circulation in great detail using Latex casts. They describe three main patterns of arterial branching and calculate the frequency that small, medium or large infarct sizes are obtained for a range of suture positions.[17] They suggest a ligature placement with a high probability of producing a consistent infarct size. Unfortunately, such infarcts are consistently small. However, the range of infarct sizes obtained in this model can also be viewed as an advantage, by producing a range of heart failure severity for correlation analysis with other variables.

In TAC, there is also considerable variability in the extent and time course of both LV hypertrophy and congestive heart failure, even when using genetically identical mice. Therefore, it is essential to thoroughly clean all connective tissue from the transverse aorta before constricting, as even very small layers of connective tissue will result in an increased stenosis. Our laboratory has recently described another source of variability in this model. We have found that around 25 per cent of mice develop internalisation of the banding suture through the aortic wall, creating an alternative route for blood flow around the stenosis. This is a gradual process that occurs around 2–6 weeks after surgery, and results in halt or even regression of LV hypertrophy. These mice also fail to develop heart failure.[18] We have described a novel magnetic resonance imaging (MRI) technique to measure the cross-sectional area of the stenotic aorta non-invasively, alternatively, these mice can be excluded from the study by rejecting mice if the pressure gradient across the stenosis is low,[10] or by visual inspection of the band at post mortem. When studying genetically

modified mice, the use of appropriate controls is essential, as strain-dependent differences in hypertrophic response have been described in the TAC model.[19]

Quantifying the extent of injury

It is outwith the remit of this chapter to discuss in detail the numerous techniques available, but whichever model is used, some consideration must be given to quantifying the degree of injury in each individual (Table 27.2). In the CAL model, infarct size has traditionally been measured by histological staining for collagen in the scar tissue, using either Azan Blue or Picro-sirius Red stains.[5,6] The result is

Table 27.2 Phenotyping techniques for murine surgical heart failure models

Methodology	Comments
In vivo non-invasive	
MRI	High resolution cine imaging is gold standard, with greatest accuracy for volume and mass determination. Suitable for longitudinal studies. However, expensive to set-up and relatively time consuming (60–90 min per mouse).
Echocardiography e.g. 2-D, 3-D, M-mode, Doppler-flow	Relatively cheap, quick (5–10 min per mouse) and suitable for longitudinal studies. 2-D and M-mode do not take account of asymmetrical LV after infarction.
ECG	Can be used as a rapid check for adequate infarction size. However, not an accurate determinant of LV hypertrophy in the mouse.
Exercise testing	Clinically relevant measurement, however, stress-response a confounder in forced exercise regimes and variability is large.
In vivo invasive	
LV hemodynamics	High fidelity measurements using microtipped pressure cannula. Closed chest preparation enables pressure–volume loops.
Sonomicrometry	Implantation of miniature piezoelectric crystals in LV wall to obtain stress–strain relationship loops. Open chest and not suitable for infarction model due to scar tissue.
Ex-vivo	
Isolated perfused heart (Langendorff)	Question of what value to set end diastolic pressure. Lower heart rate than *in vivo*, and uses artificial substrate supply.
Myocyte contractility	Ventricular strips or isolated myocytes. Contractility measurements independent of neurohumoral influences or loading conditions.
Histological	
Infarct size	Expressed as percent of total LV circumference e.g. with Azan Blue (healthy myocardium stains red, infarct blue) or Picro-Sirius Red (healthy myocardium stains yellow, infarct red).
Fibrosis	Measure of interstitial fibrosis e.g. with Masson's trichrome stain (collagen stains blue).
Myocyte size	Measure of hypertrophy e.g. with Masson's trichrome stain.

expressed as percent infarct size of total LV circumference. Alternatively, we have recently described non-invasive infarct size determination by both MRI and 3-D echocardiography.[6] However, infarct size measurements only inform about the extent of the original insult, and not the degree of heart failure. For this, *in vivo* techniques are required. Again, MRI and 3-D echocardiography are both excellent for describing global function and LV dilatation, while 2-D echocardiography is less useful for the asymmetrical LV after CAL, but is adequate for the assessment of symmetrical hypertrophy observed in TAC (Figure 27.2). LV catheterisation with a pressure tipped microcannula (e.g. 1.4F Millar Instruments, SPR-671) is

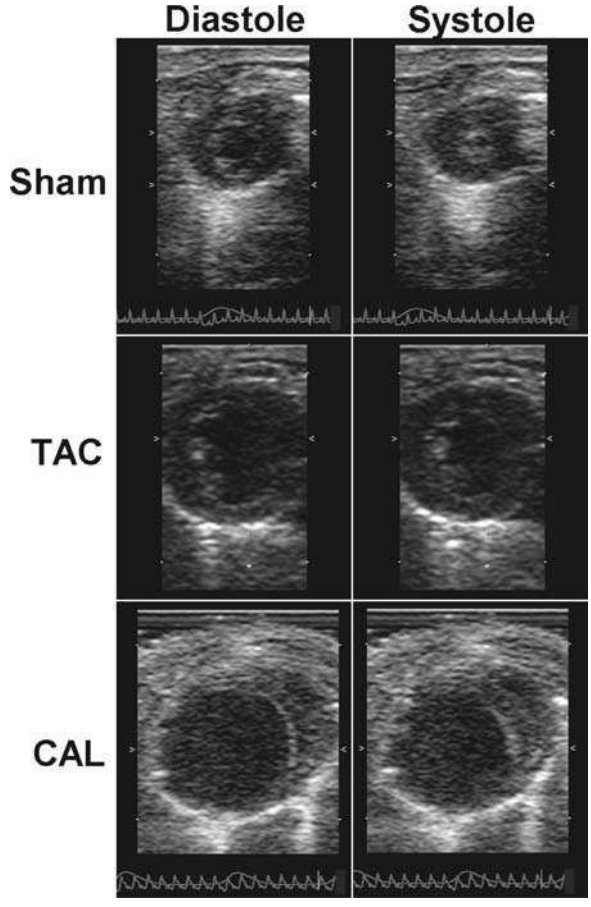

Figure 27.2 Top panels show echocardiograms from sham-operated mice and mice after transverse aortic constriction (TAC) and coronary artery ligation (CAL). All 2-D images are parasternal short-axis views at the level of the papillary muscles, and share the same scale to allow direct comparison. Left hand panels represent end-diastole, right hand panels end-systole. Note the large increase in vessel dimensions in both TAC and CAL images, and the increase in end systolic cross-sectional area indicating that both are in heart failure. A large infarction can be observed in the CAL images, where the myocardial wall is no longer visible as it becomes paper-thin infarct scar

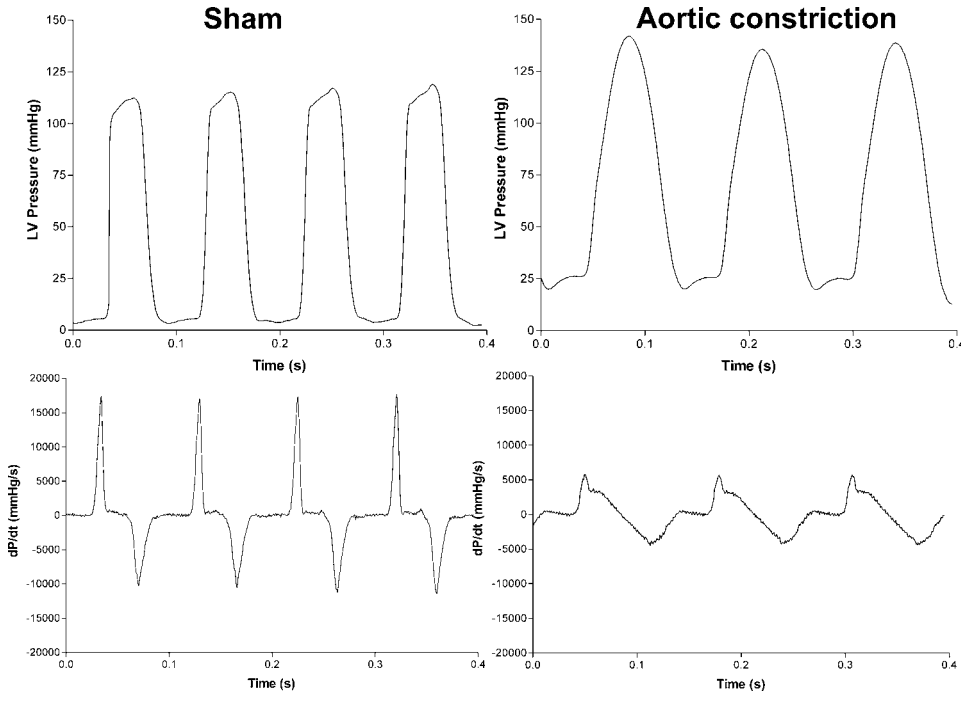

Figure 27.3 Left ventricular hemodynamic traces in a sham-operated mouse and in a mouse with heart failure, 6-weeks after transverse aortic constriction (TAC). Measurements were made in closed-chest spontaneously breathing mice using a Millar microtip pressure cannula and isoflurane anesthesia. The upper panels are LV pressure traces. The elevated end-systolic pressure due to aortic constriction can be clearly observed, as can the increased end-diastolic pressure. The first derivative of LV pressure (dP/dt) is a measure of contractility and is shown in the lower panels. Note the very high baseline contractility in sham mice and the characteristic waveform and impaired contractility after TAC

increasingly used to measure hemodynamic indices in heart failure (Figure 27.3), or the equivalent conductance catheter to analyse pressure–volume loops for load-independent parameters. Organ weights should always be taken as a measure of hypertrophy (LV and RV) and congestion (lungs).

Time course of disease progression

CAL

In the CAL model of post-myocardial infarction heart failure, perisurgical mortality should be low (<5 per cent for an experienced operator). Unlike after CAL in the rat or rabbit, post-ligation arrhythmias are seldom observed in the mouse, and are not a common cause of death. As a consequence, the greatest number of deaths occurs

between day 3 and 7 post-surgery, and is almost invariably due to cardiac rupture. This is easily confirmed at post mortem by the presence of blood in the thorax.

The incidence of cardiac rupture is both strain and sex dependent. In our laboratory, approximately 25 per cent of male C57BL/6 mice, but <5 per cent of females will die of cardiac rupture. Both having testosterone and a lack of estrogen, have been implicated in the pathophysiology.[20] Other groups have published similar values,[20] along with even higher levels up to 59 per cent in males from the 129Sv strain.[21] This is yet another example of why it is critically important to always use an appropriate control strain when studying genetically modified mice. As a consequence it may not be practical or ethical to do an entire study using only male animals in strains with a very high incidence of cardiac rupture.

The most common study period is 4–6 weeks post-surgery, as scar tissue has matured, LV remodelling is usually complete, and mice with the largest infarcts have developed signs of congestion (e.g. elevated RV and lungs weights). Compensation involving hypertrophy of the surviving myocardium and dilatation of the LV cavity mean that, while indices of contractility are severely impaired, cardiac output at rest is often maintained at normal or supranormal values even for very large infarcts.[8,22] However, compensation is incomplete, as mice with large infarcts have an impaired exercise capacity, and maximum cardiac output is impaired.[9] Mice seldom show physical symptoms of heart failure, and in the weeks following surgery appear outwardly normal. However, over a 6 week follow-up, around 5–10 per cent of the infarcted mice will develop acute symptoms such as shortness of breath and will die shortly after of heart failure. Thus, in our hands, overall mortality after CAL in male C57BL/6 is 32 per cent and in females 15 per cent.

TAC

With experience the perisurgical mortality associated with TAC should be less than 5 per cent, with most mice tolerating the procedure well. In the first few days after surgery, systolic function is impaired as the heart works against a suddenly increased afterload, but as LV hypertrophy develops (already measurable at 3 days), systolic function improves back to normal values over the first 2 weeks, i.e. mice show compensated hypertrophy.[23] Over longer time periods, concentric hypertrophy is progressive, increasing for at least the first 11 weeks, by which time heart weight has more than doubled.[13] Two weeks after surgery, systolic function starts to decline and there is LV chamber dilatation and myocardial fibrosis, with around half of the banded mice developing congestion. This decompensation process is also progressive, with more mice developing severe heart failure at later time points.[13] However, there are strong gender differences in disease progression, with female mice exhibiting significantly less hypertrophy at equivalent time-points. In one study, the ratio of heart weight to body weight at two weeks increased by 64 per cent in male mice, but by only 31 per cent in females, and only males had elevated lung weights.[24] It is therefore important to match experimental groups for gender balance when using this model.

Limitations

Many of the limitations of these models are related to the intrinsic differences between mouse and man. Obviously, due to their small size (2000 × smaller myocardial mass than humans) and high heart rate there are technical challenges in performing the surgery and subsequent phenotyping experiments. There are also well-documented differences in murine cardiac physiology (e.g. in electrophysiology, relative abundance of contractile protein isoforms, force–frequency relationship, and in both resting contractility and contractile reserve), and consideration of these should be made when extrapolating from mouse to man.

Another criticism is that surgical models do not reflect the full range of heart failure etiologies observed in man. In the CAL model, infarction is induced suddenly in healthy young animals, and in a single vessel only, compared to myocardial infarction in man which is often a result of multivessel coronary artery disease, complicated by the effects of aging and other underlying pathology. Indeed, Gould *et al*. have proposed the use of mice up to 14 months old, as a greater number of old mice develop true congestive heart failure.[25] However, such an approach has significant cost implications. In the TAC model, a severe pressure overload is induced suddenly with subsequent rapid development of LV hypertrophy, and this may not fully mimic the gradual chronic pressure overload resulting from aortic stenosis or hypertension in man. Furthermore, 'diastolic' heart failure, where systolic function is preserved, is often described in aging human populations, yet there is no surgical model that mimics this condition in the mouse. The closest to this is within the first 2 weeks of TAC, when systolic function is supranormal, but active and passive diastolic function is impaired.[23]

Applications

The principal strength of these surgical techniques is the ability to study genetically modified mice, i.e. the ability to determine the role of single gene products on the development of cardiac rupture, LV remodeling or heart failure, and there are already numerous such studies in the literature, for example Rockman *et al*.[10]

This unique position of mice as the workhorse of genetic modification has resulted in the adoption of mouse models of heart failure by many laboratories. As such, it is increasingly common for these models to replace the rat for the study of basic pathophysiology, to identify potential new treatment targets, and to test the efficacy of new and conventional pharmacological therapy (e.g. Patten *et al.*[2]). New treatment modalities have also been tested in this model such as gene therapy or stem cell regeneration of infarcted myocardium.

Conclusions

Surgical models of heart failure in the mouse are clinically relevant, and develop most of the hallmarks of heart failure previously described in rat and man. Their

application requires an investment in time and funding to develop the necessary technical expertise. However, the potential applications are numerous, and these models are likely to represent the mainstay of heart failure research for many years to come.

References

1. Rockman HA, Ono S, Ross RS, et al. Molecular and physiological alterations in murine ventricular dysfunction. *Proc Natl Acad Sci USA* 1994; **91**(7): 2694–2698.
2. Patten RD, Aronovitz MJ, Einstein M, et al. Effects of angiotensin II receptor blockade versus angiotensin-converting-enzyme inhibition on ventricular remodelling following myocardial infarction in the mouse. *Clin Sci (Lond)* 2003; **104**(2): 109–118.
3. Zolotareva AG, Kogan ME. Production of experimental occlusive myocardial infarction in mice. *Cor Vasa* 1978; **20**(4): 308–314.
4. Patten RD, Aronovitz MJ, Deras-Mejia L, et al. Ventricular remodeling in a mouse model of myocardial infarction. *Am J Physiol* 1998; **274**: H1812–H1820.
5. Lutgens E, Daemen MJ, de Muinck ED, Debets J, Leenders P, Smits JF. Chronic myocardial infarction in the mouse: cardiac structural and functional changes. *Cardiovasc Res* 1999; **41**(3): 586–593.
6. Dawson D, Lygate CA, Saunders J, et al. Quantitative 3-dimensional echocardiography for accurate and rapid cardiac phenotype characterization in mice. *Circulation* 2004; **110**(12):1632–1637.
7. Gao XM, Dart AM, Dewar E, Jennings G, Du XJ. Serial echocardiographic assessment of left ventricular dimensions and function after myocardial infarction in mice. *Cardiovasc Res* 2000; **45**(2): 330–338.
8. Schneider JE, Cassidy PJ, Lygate C, et al. Fast, high-resolution in vivo cine magnetic resonance imaging in normal and failing mouse hearts on a vertical 11.7 T system. *J Magn Reson Imaging* 2003; **18**(6): 691–701.
9. Bayat H, Swaney JS, Ander AN, et al. Progressive heart failure after myocardial infarction in mice. *Basic Res Cardiol* 2002; **97**(3): 206–213.
10. Rockman HA, Ross RS, Harris AN, et al. Segregation of atrial-specific and inducible expression of an atrial natriuretic factor transgene in an in vivo murine model of cardiac hypertrophy. *Proc Natl Acad Sci USA* 1991; **88**(18): 8277–8281.
11. Liao R, Jain M, Cui L, et al. Cardiac-specific overexpression of GLUT1 prevents the development of heart failure attributable to pressure overload in mice. *Circulation* 2002; **106**(16): 2125–2131.
12. Hara M, Ono K, Hwang MW, et al. Evidence for a role of mast cells in the evolution to congestive heart failure. *J Exp Med* 2002; **195**(3): 375–381.
13. Liao Y, Ishikura F, Beppu S, et al. Echocardiographic assessment of LV hypertrophy and function in aortic-banded mice: necropsy validation. *Am J Physiol* 2002; **282**(5): H1703–1708.
14. Scheuermann-Freestone M, Freestone NS, Langenickel T, Hohnel K, Dietz R, Willenbrock R. A new model of congestive heart failure in the mouse due to chronic volume overload. *Eur J Heart Fail* 2001; **3**(5): 535–543.
15. Perry GJ, Mori T, Wei CC, et al. Genetic variation in angiotensin-converting enzyme does not prevent development of cardiac hypertrophy or upregulation of angiotensin II in response to aortocaval fistula. *Circulation* 2001; **103**(7): 1012–1016.

16. Hu P, Zhang D, Swenson L, Chakrabarti G, Abel ED, Litwin SE. Minimally invasive aortic banding in mice: effects of altered cardiomyocyte insulin signaling during pressure overload. *Am J Physiol Heart Circ Physiol* 2003; **285**(3): H1261–1269.
17. Ahn D, Cheng L, Moon C, Spurgeon H, Lakatta EG, Talan MI. Induction of myocardial infarcts of a predictable size and location by branch pattern probability-assisted coronary ligation in C57BL/6 mice. *Am J Physiol Heart Circ Physiol* 2004; **286**(3): H1201–1207.
18. Lygate CA, Schneider JE, Hulbert K, et al. Serial high resolution 3D-MRI after aortic banding in mice: band internalization is a source of variability in the hypertrophic response. *Basic Res Cardiol* 2006; **101**(1): 8–16.
19. Schmitt JP, Semsarian C, Arad M, et al. Consequences of pressure overload on sarcomere protein mutation-induced hypertrophic cardiomyopathy. *Circulation* 2003; **108**(9): 1133–1138.
20. Cavasin MA, Sankey SS, Yu AL, Menon S, Yang XP. Estrogen and testosterone have opposing effects on chronic cardiac remodeling and function in mice with myocardial infarction. *Am J Physiol Heart Circ Physiol* 2003; **284**(5): H1560–1569.
21. Gao XM, Xu Q, Kiriazis H, Dart AM, Du XJ. Mouse model of post-infarct ventricular rupture: time course, strain- and gender-dependency, tensile strength, and histopathology. *Cardiovasc Res* 2005; **65**(2): 469–477.
22. Kanno S, Lerner DL, Schuessler RB, et al. Echocardiographic evaluation of ventricular remodeling in a mouse model of myocardial infarction. *J Am Soc Echo* 2002; **15**(6): 601–609.
23. Takaoka H, Esposito G, Mao L, Suga H, Rockman HA. Heart size-independent analysis of myocardial function in murine pressure overload hypertrophy. *Am J Physiol Heart Circ Physiol* 2002; **282**(6): H2190–197.
24. Skavdahl M, Steenbergen C, Clark J, et al. Estrogen receptor-beta mediates male-female differences in the development of pressure overload hypertrophy. *Am J Physiol Heart Circ Physiol* 2005; **288**(2): H469–476.
25. Gould KE, Taffet GE, Michael LH, et al. Heart failure and greater infarct expansion in middle-aged mice: a relevant model for postinfarction failure. *Am J Physiol Heart Circ Physiol* 2002; **282**(2): H615–6121.

28

Cardiac Electrophysiology

Sander Verheule,[a] Toshiaki Sato[b] and **Jeffrey E. Olgin[c]**

[a]Department of Physiology, Faculty of Medicine, Maastricht University, Maastricht, the Netherlands, [b]Cardio-pulmonary Division, Keio University School of Medicine, Tokyo, Japan and [c]Cardiac Electrophysiology, Division of Cardiology and the Cardiovascular Research Institute, University of California San Francisco, CA, USA

Introduction

In the past decade, the expanding number of transgenic mice with interesting cardiac phenotypes has prompted a rapid development in murine cardiac electrophysiology (EP). This has required a miniaturisation of existing recording techniques. For example, at present detailed epicardial conduction patterns and monophasic action potentials can be recorded in mice. However, many tools for mouse EP are not yet available commercially and have to be designed and built by the researcher.

In this chapter, we provide a detailed description of the research tools we have developed over recent years. Our research on mice has been focused on models of atrial fibrillation (AF), and most of the examples we present here are taken from our studies on the mechanism of AF in mice. Of course, the technical principles described are entirely applicable to studying ventricular electrophysiology.

Is the mouse heart large enough to be useful in studying cardiac arrhythmias? With a heart weight 0.0005 times that of the adult human heart, it was originally thought that the mouse heart would be too small to be able to fibrillate. According to the multiple wavelet theory, fibrillation requires several reentrant wavelets to coexist, where the wavelength of one re-entrant wavelet is the product of the effective refractory period (ERP) and the conduction velocity (CV).[1] In this view, fibrillation can not occur in hearts smaller than a certain 'critical mass', such as the mouse heart.[2,3] However, it has been reported that the mouse ventricle is able to sustain

A Handbook of Mouse Models of Cardiovascular Disease Edited by Qinbo Xu

fibrillation, although its wavelength (15–30 mm) should not allow multiple wavelets to coexist.[4] In our study on mice with selective atrial fibrosis due to overexpression of TGFβ1, the atrial wavelength was around 15 mm.[5] With its length of about 5 mm, these atria could probably not accommodate more than one re-entrant wavelet, if they were a homogeneous substrate. However, the increased interstitial atrial fibrosis in this model makes the atria a structurally heterogeneous substrate. Spach and co-workers have demonstrated that increased interstitial fibrosis and its concomitant decrease in side-to-side electrical coupling can cause slow and heterogeneous conduction during transverse propagation, allowing reentry to occur in relatively small circuits.[6] This would make AF possible in a tissue area much smaller than would be expected based on wavelength or 'critical mass' considerations. So at least as a 'proof of principle', the mouse heart can be a useful model for cardiac arrhythmias.

With respect to the PR interval[7] and many other important physiological parameters,[8] the mouse heart obeys allometric scaling laws. However, there are important differences with larger hearts; for example, the common atrioventricular bundle makes direct contact with the basal side of the interventricular septum, leading to a basoapical activation pattern of the septum.[9] In addition, with a resting heart rate of 550–600 bpm and a Wenckebach frequency of about 750 bpm, the mouse heart has a relatively limited dynamic range, being able to increase its resting rate by only 25–35 per cent.[10] Finally, Bazzett's formula for the rate correction of the QT interval is not useful in mice in its standard form.[11]

As with any study on transgenic mice, some caution must be applied. First, there is considerable strain variability in electrocardiogram (ECG) parameters[12] (for an overview, see the 'cardiovascular' link at www.informatics.jax.org/mgihome/other/mouse_facts3.shtml). Therefore, it is essential to attain sufficient backcrossing before comparing transgenic mice to the wildtype, or to use littermate controls. Second, it is always possible that observations in a transgenic animal model are caused by a defect in embryonic development. For example, some of the earlier observation on conduction defects in adult Cx40 knockout mice[10] may be caused in part by abnormal cardiac morphogenesis early in development.[13] In such cases, an inducible knockout at the adult stage is desirable, as was shown successfully for the case of connexin43.[9]

Anesthesia for adult mice

In all our follow-up studies, we have used urethane for anesthesia. The main advantage of urethane is that it can be used as mono-anesthetic with negligible cardiovascular side effects. In practice, we administer 0.5 ml dose of urethane solution (100 mg/ml urethane in a 0.9 per cent NaCl solution) intraperitoneally (i.e. 2 mg/g for a 25 g mouse) and wait for 5 min. If reflexes have not disappeared at this point, another 0.1–0.2 ml of the solution is injected. In our experience, a bolus injection of urethane will provide a very stable anesthesia for up to 6 h, making it ideally suited for open chest procedures. However, urethane is a suspected carcinogen and the researcher should take care to avoid direct exposure to the solid during

weighing, to the urethane solution during injection and to the blood of urethane-anesthetised animals throughout a procedure. Because of its carcinogenicity, it can only be used in terminal follow-up experiments. As an alternative, inhalation anesthesia with isofluorane can be used for its stability during prolonged surgical procedures. For shorter experiments, such as a normal surface ECG recording or a closed chest study with transesophageal stimulation, avertin or a combination of ketamine and xylazine can be used, with adequate anesthesia lasting 20–40 min after a bolus injection. Avertin has to be freshly made from 2,2,2-tribromoethanol and tertiary amyl alcohol before each experiment, because injection of old avertin solution can cause peritonitis.[14] However, both avertin and ketamine/xylazine can display significant cardiovascular side effects. Pentobarbital has a narrow therapeutic range in mice and higher dosages can cause severe cardiovascular depression. A combination of 0.033 mg/g pentobarbital and 0.033 mg/g ketamine has been used in open chest procedures.[15] A more complete overview of options in mouse anesthesia can be found in elsewhere.[16]

Because of their high surface-to-volume ratio, mice can rapidly become hypothermic, especially during open chest surgery. To maintain proper body temperature during any procedure in anaesthetised mice, animals should be placed on a thermostated operating platform (in our case, a flat rectangular Lucite chamber with a water inlet and outlet), while monitoring core temperature with a rectal probe.

ECG recording and analysis

In anesthetised mice, subcutaneous needle recording electrodes can be used to record ECGs. In the past, we have used both homemade silver wire electrodes (chlorinated by immersion in Chlorox bleach for 30 min) with a sharpened tip. Alternatively, we have used commercially available platinum needle electrodes, which are both thinner and sturdier than silver electrodes, available at Grass Telefactor, West Warwick, RI, USA).

The sampling frequency should be at least 500 Hz for an accurate representation of the QRS morphology. The QRS morphology can be distorted significantly by 50 or 60 Hz notch filters, because part of the frequency spectrum of the mouse ECG is in the 50–60 Hz range. It is therefore advisable to eliminate the need for filtering by proper grounding and shielding, by twisting recording wires for differential amplification and by keeping signal pathways as short as possible.

Figure 28.1a depicts the ECG in a mouse. Most of the characteristic intervals can be measured in a straightforward manner. The P wave duration can be determined accurately by comparing a number of leads and taking the interval between the earliest onset and the latest end of the P wave. Similarly, comparison of a number of leads for the interval between the earliest onset of the Q wave to the J point will provide an accurate estimate of the QRS duration. Because the ventricular action potential in mice does not have a pronounced plateau phase, there is no isoelectric segment between the QRS complex and the T wave. Moreover, because the repolarisation phase is gradual, the amplitude of the Q wave is usually very low.

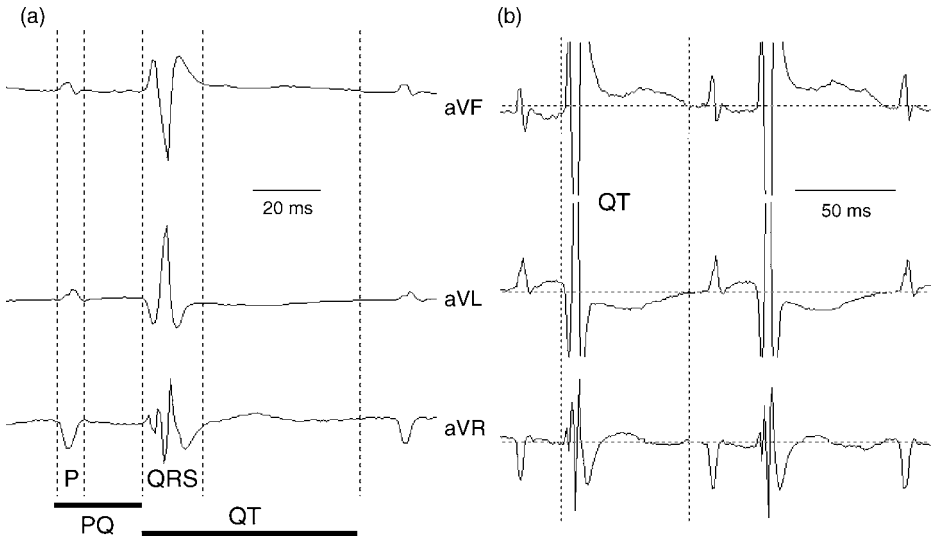

Figure 28.1 Intervals in the mouse ECG. (a) Determination of the characteristic intervals using the unipolar limb leads. (b) The QT interval is more easily determined by expanding the *y*-axis scale

Therefore, the end of the T wave, and thus the QT time, can be difficult to determine. A reasonable estimate can be obtained by expanding the *y*-axis scaling and looking for a consensus point for the end of the T wave in three or more leads (Figure 28.1b). This point in the cardiac cycle corresponds reasonably well with the action potential durations obtained from monophasic action potential recordings.[18]

It is also possible to record mouse EGCs telemetrically using an implanted amplifier/ transmitter (see e.g. Gehrmann and Berul[17], using a system available at DataSciences Intl, St. Paul, MN, USA). This method is ideal to detect the spontaneous and infrequent occurrence of potentially lethal arrhythmias in transgenic mice.

Transesophageal stimulation

As in larger animals, the left atrium can be paced from the esophagus. The diameter and the interelectrode distance are important considerations in choosing the thickness of a transesophageal stimulation electrode. If the catheter is relatively thin, atrial capture is harder to attain. If it is relatively thick, the expansion of esophagus may cause collapse of the trachea and could thereby compromise proper ventilation. The interelectrode distance should be small to minimize the size of the area of the left atrium that is actually captured and to minimize stimulation artifacts. We have used a 4 French quadripolar EP catheter with an interelectrode distance of 1–2 mm. First, the stimulation poles were connected to a differential amplifier, and the catheter was advanced into the esophagus and pulled back while the signal from the electrodes was monitored and compared to the surface ECG. The catheter was placed in the location

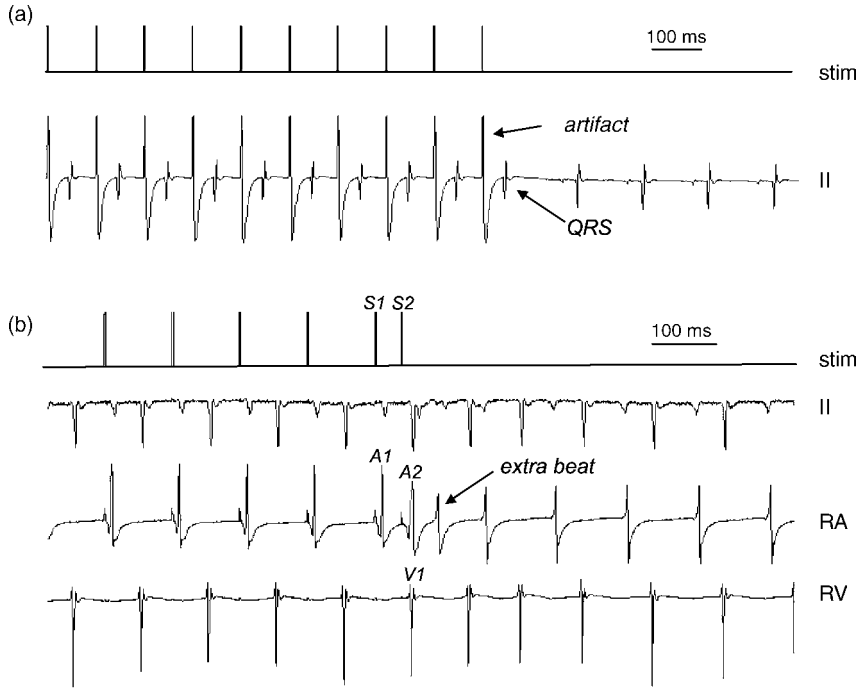

Figure 28.2 Programmed electrical stimulation. (a) Large artifacts are seen on the surface ECG during transesophageal stimulation. Traces show the stimulus output and ECG lead II. (b) Example of right atrial bipolar epicardial pacing in an open chest experiment. The S2 interval of 36 ms, just above the ERP in this animal, evoked an atrial extra beat. Traces show the stimulus output, ECG lead II, and a right atrial and ventricular bipolar electrogram

where the amplitude of the atrial component was maximal. The stimulation electrodes were then connected to the output of a bipolar stimulus isolation unit. During stimulation at a basic cycle length (BCL) of 10–20 ms under the sinus cycle length, the position of the catheter was varied slightly around the original position to find the position with lowest atrial capture threshold. Further programmed electrical stimulation was performed at 1.2–1.5 times threshold at a stimulus duration of 1 ms. Large stimulation artifacts are unavoidable during transesophageal stimulation, obfuscating the P waves on the surface ECG (Figure 28.2a). Therefore, atrial capture has to be assessed by monitoring the QRS complexes visible after the artifacts (at a BCL which allows 1 : 1 conduction to the ventricle). This also means that it is impossible to measure the atrial ERP with transesophageal pacing without a separate (epicardial or endocardial) atrial sensing electrode, because the AV nodal ERP will be higher than the atrial ERP. To record a separate atrial electrogram, an epicardial electrode can be placed in an open chest experiment. As an alternative, the jugular vein allows convenient access to the heart for endocardial recording and pacing in closed-chest mice. Berul and coworkers have developed a miniature endocardial catheter (available as a CIBer mouse EP catheter at NuMed Inc, Hopkinton, NY, USA) which

allows recording and stimulation of the right atrium and ventricle, including recording of His bundle electrograms.[19]

Open chest epicardial measurements

To allow recording from and stimulation of the epicardial surface, the chest has to be opened. Mice were fixed with tape to the thermostated operating platform for stability during these procedures. All surgical procedures are performed using a binocular microscope at 60 × magnification. First, the skin in the neck and the muscle layer surrounding the trachea were opened and a 3-0 silk thread was placed around the exposed trachea. The trachea was then incised just below the vocal cords and a tube was inserted and tied into position. In our case, this tube was connected to a rodent ventilator (C.G. Palmer Ltd.), set to 130 breaths per minute with a tidal volume of 0.5–2 ml, limited to 5 ml water pressure. The pressure limiter consisted of a side branch to the outlet tubing, immersed 5 cm into a water-filled cylinder. This arrangement prevents overinflation of the lungs. Another ventilator system, designed especially for the ventilation rates and volumes of mice, is available at Hugo Sachs/ Harvard Apparatus (March-Hugstetten, Germany). Whatever ventilation system is used, it is essential to minimise the dead volume of the final common inlet/outlet tube inserted in the trachea. With a tidal volume of only 0.2 ml (this and a number of other useful physiological parameters in mice are summarised by Janssen and Smits[8]), a long or thick tube connecting the inlet and outlet to the trachea will cause a rapid increase in pCO_2 and decrease in pO_2 in the inspired air.

In opening the chest, care should be taken to avoid damaging the internal thoracic arteries, which run parallel to the sternum. It is possible to make a midline incision in between these arteries through the sternum and open the chest with a tiny spreader. However, this will not provide much space to work with and access to the atrial epicardial surfaces is poor. Especially when multiple electrodes have to be placed on the heart, it is preferable to make a V-shaped cut from the xyphoid processus towards the front legs. To do this, start by lifting the xyphoid processus with a forceps below the diaphragm and make a small cut into abdominal wall directly underneath. It is helpful at this point to put a tie around the processus and tape this tie to the operating table in front of the head. Looking through the diaphragm, the apex of the left ventricle should be visible. Next, make a small cut into the diaphragm just below the sternum, carefully avoiding the lungs. Then, slowly cut into the chest wall on both sides of the sternum in the direction of the front legs. Damage to the internal thoracic arteries can be easily avoided if sufficient distance is kept from the sternum. After each cut, the tie connected to the xyphoid can be pulled along to open the chest further. When the incision extends all the way to the armpits, the thoracic cage can be folded open completely and the two internal thoracic arteries will be clearly visible. If necessary, these arteries can be tied off with thin sutures (8-0 or 9-0 silk) at the front of the chest. After tying the arteries, the caudal part of opened anterior side of the chest wall can be removed to provide even more space for placing electrodes on the heart. After the chest is opened, it is essential to regularly moisten the heart with a

few drops of physiological saline solution to prevent dehydration. During experiments, the RR interval did not change more than 20 ms and remained stable for up to 5 h. Typical experiments with a complete EP protocol lasted about 2 h.

Epicardial pacing/recording electrodes were made of 0.03 mm fine wire, preferably insulated. The type of wire used for this purpose should have low resistivity. Furthermore, it should be malleable enough to be bent into close proximity to the tissue but stiff enough to be hooked into the tissue. For example, silver wire is unsuitable because of its softness and stainless steel is unsuitable because of its unmalleability. We have successfully used Tungsten wire (California Fine Wire, Grover Beach, CA, USA) and MP35N wire (Fort Wayne Metals, Fort Wayne IN, USA). The advantage of MP35N wire is that it is available after a variable degree of thermal treatment, providing a range of possible tensile strengths. Small lengths of electrode wire were stripped at both ends. One end was soldered into a plug (the individual plugs from an IC (integrated circuit) socket are just the right size). The other end of the electrode was bent to form a small hook.

Fine wire electrodes were held by a small eight-fold manipulator (Figure 28.3a). This manipulator consists of a glass rod, to which eight glass capillaries were tied with silk surgical thread, allowing a rotating movement of the capillaries around the central rod. The capillaries can be made from glass for patch clamp electrodes or hematocrit capillaries and were first bent to varying degrees in a flame. Thin standard electrical wires ran through these capillaries with an IC socket plug at the end. These plugs were kept in place by heat shrink tubing. The plugs of the electrodes were inserted into the plugs of the manipulator, making the electrodes easy to replace.

After opening the pericardial sac in the middle, a pericardial cradle was created by inserting wires with a small hook (similar to the recording electrodes) at one end through the sac and attaching them with tape to the operating platform at the other end. This made the position of the heart more stable and kept the lungs out of the way.

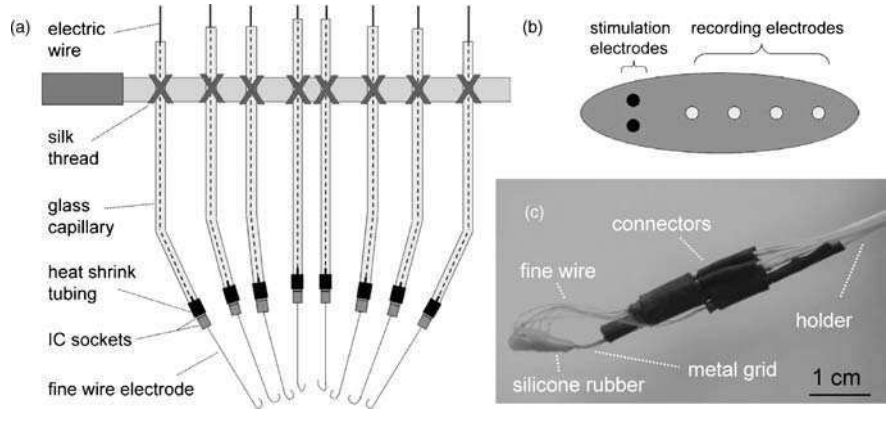

Figure 28.3 Equipment for open-chest measurements. (a) Eight-fold holder for epicardial fine wire electrodes. (b) Schematic of a probe for measuring epicardial conduction velocity. (c) Side view of the probe. For a color version of this figure, please see the images supplied on the accompanying CD

Electrode manipulation and placement was performed using a pair of watchmakers tweezers; a curved tweezer with a 45 degree angle proved to be particularly useful here. Closely spaced pairs of electrodes were attached to the myocardium at the middle of the right atrial appendage, at the right atrium near the atrial septum, at the right ventricular apex and at the middle of the right ventricle for an extensive EP study. A chlorinated silver wire in the right hind leg was used as a common ground. For atrial and ventricular stimulation respectively, the pairs near the atrial septum and the ventricular apex were connected to a TTL (true type logic) triggered bipolar stimulus isolation unit with variable current output. A stimulus amplitude of twice the diastolic capture threshold was used, with a stimulus duration of 2 ms. The pairs not used for stimulation were connected to differential amplifiers for recording.

With programmed electrical stimulation of the atrium (Figure 28.2b), it is possible to record the sinus node recovery time, atrial and AV nodal ERP, AV Wenckebach period, AV 2 : 1 cycle lenght, and inducibility of atrial arrhythmias. Figure 28.4 depicts a number of examples of induced AF episodes in mice, illustrating the variety in complex morphology. Ventricular stimulation yields the ventricular ERP, VA Wenckebach and VA 2:1 cycle lengths and inducibility of ventricular arrhythmias (for details on the applied protocols,[10]). Both in open chest experiments[18] and in perfused mouse hearts,[20] it has proved possible to record ventricular epicardial monophasic action potentials.

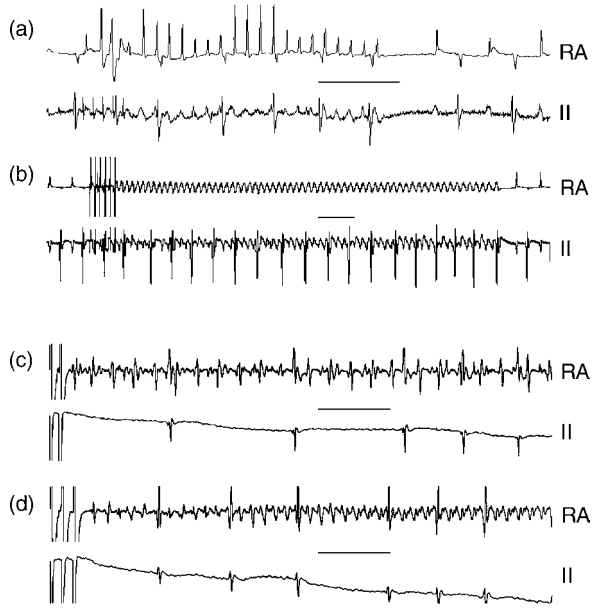

Figure 28.4 Induced AF episodes in mice. (a and b) AF episodes induced by burst pacing on the right atrium in mice lacking the gap junction protein connexin40. (c and d) AF episodes induced by transesophageal burst pacing in mice with atrial fibrosis due to overexpression of TGFβ1. All panels show traces for a right atrial bipolar electrogram and ECG lead II. Calibrations bars represent 200 ms

For direct measurements of the conduction velocity in open chest experiments, we have used a small hand-held probe consisting of two stimulus electrodes for bipolar current stimulation with an interelectrode distance of 0.5 mm, perpendicular to an array of four unipolar recording electrodes with an interelectrode distance of 1 mm (Figure 28.3b,c). Electrodes were made from insulated tungsten fine wire, running through an aluminum grid and stripped at the tip and protruding for approximately 0.1 mm from an embedding silicone rubber matrix. This probe was pressed against the atrial or ventricular epicardial surfaces. The unipolar signals from the probe were sampled at 10 kHz, and differentiated off-line to determine activation times at each recording electrode. These signals, and the signals from the ECG recorder and the differential amplifiers were sampled using a 1401 Plus AD/DA converter (Cambridge Electronic Design Ltd.) connected to a PC. All data sampling, programmed electrical stimulation and off-line analysis in our ECG recordings, transesophageal stimulation and open chest EP experiments were controlled by custom developed software in Spike2 script language (Cambridge Electronic Design Ltd.). This language is specific to the CED 1401 AD/DA converter. To obtain this software for mouse cardiac electrophysiology free of charge, contact us at s.verheule@fys.unimaas.nl.

Studies on Langendorff perfused hearts

Although, in principle, detailed studies of epicardial conduction can be made in open chest studies, we have preferred the more controlled conditions and easier access of Langendorff perfused hearts for this purpose. After rapid excision of the heart, the aorta was canulated for retrograde perfusion at a pressure of 80 cmH_20 with modified Tyrode solution (in mmol/l: NaCl 130, $NaHCO_3$ 24, NaH_2PO_4 1.2, $MgCl_2$ 1, glucose 5.6, KCl 4.0, $CaCl_2$ 1.8, gassed with 95 per cent O_2/5 per cent CO_2). Two chlorinated silver wires were placed in the bath as indifferent and common-ground electrodes. The tissue chamber consisted of an organ bath (preparatory tissue bath #158400-10, Radnoti, Monrovia, CA, USA) with a layer of Kwik-cast rubber (World Precision Instrument, Sarasota, FL, USA) at the bottom, onto which the Langendorff perfused heart could be pinned.

In our study in mice overexpressing transforming growth factor-β1 (TGFβ1),[5] we have recorded atrial conduction patterns during sinus rhythm, epicardial stimulation and AF. To this end, atrial unipolar electrograms were recorded using a 1.2×1.2 mm array of 4×4 unipolar recording electrodes with a pair of stimulation electrodes at the side of the array (Figure 28.5). The electrode array was pressed against the RA or LA surface, covering a large portion of the anterior aspect of the atrial appendage and free wall. This probe can be used for recording in open chest experiments and on Langendorff perfused mouse hearts. The recording electrodes of this probe were Ag3T Teflon coated silver wire (www.sigmundcohn.com). Figure 28.5 shows a 4×4 electrode probe measuring 1.2×1.2 mm, but we have produced probes with more electrodes and/ or a different spatial resolution along the same principles.

To make this type of electrode, we started with a piece of thin nylon mesh (available for example at www.smallparts.com). The holes in the mesh have to be

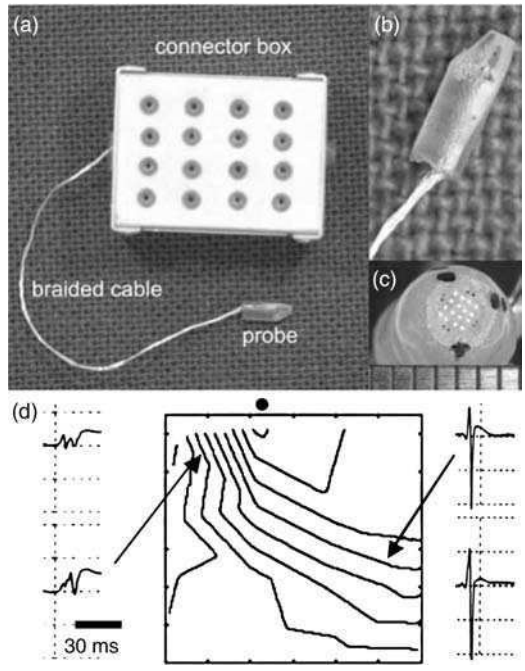

Figure 28.5 Probe for epicardial mapping. (a) The connectors for the stimulation electrodes are on the side of the box. (b) Enlarged side view of the probe. (c) Enlarged frontal view of the surface of the array. The photos show a prototype version without the holding rod mentioned in the text. (d) Activation map of the left atrium of a mouse overexpressing TGFβ1. Insets show the different electrogram morphologies at different sites in the array. For a color version of this figure, please see the images supplied on the accompanying CD

slightly smaller than the diameter of the wire used (Ag3T wire is 0.1143 mm, so we used CMN-105 or CMN-112A mesh (holes of 105 or 112 μm)). A flat metal disk with a hole of about 1 cm diameter cut out in the middle was taped to the top of a metal bowl. The nylon mesh was placed over the hole in the disk and its sides were fixed to the disk with tape (Figure 28.6a). This assembly was placed under a binocular microscope. The distal end of a length of Ag3T wire was inserted through every second hole of the mesh using curved watch-makers forceps and advanced for about 0.5–1 cm. A label with the electrode number was attached to the proximal end of each wire. At the four sides of the array, pairs of electrodes were placed for use as bipolar stimulation pairs (we initially used the same silver wire for this, but switched to Pt3T platinum wire later to reduce corrosion resulting from burst stimulation). After inserting all the electrodes, the wires were straightened somewhat and the piece of nylon mesh was trimmed to a circle, leaving about 2 mm around the inserted electrodes. The wires were then trimmed until they protruded from the mesh about 3 mm.

Another assembly was then used, consisting of a 0.5 ml Eppendorff cuvette (or 1.5 ml, depending on the array size), sitting in a cuvette stand on top of a standard laboratory stand with a diagonal branch (Figure 28.6b). We used a resin that was intended for embedding floral arrangements, but others types will do, as long as they

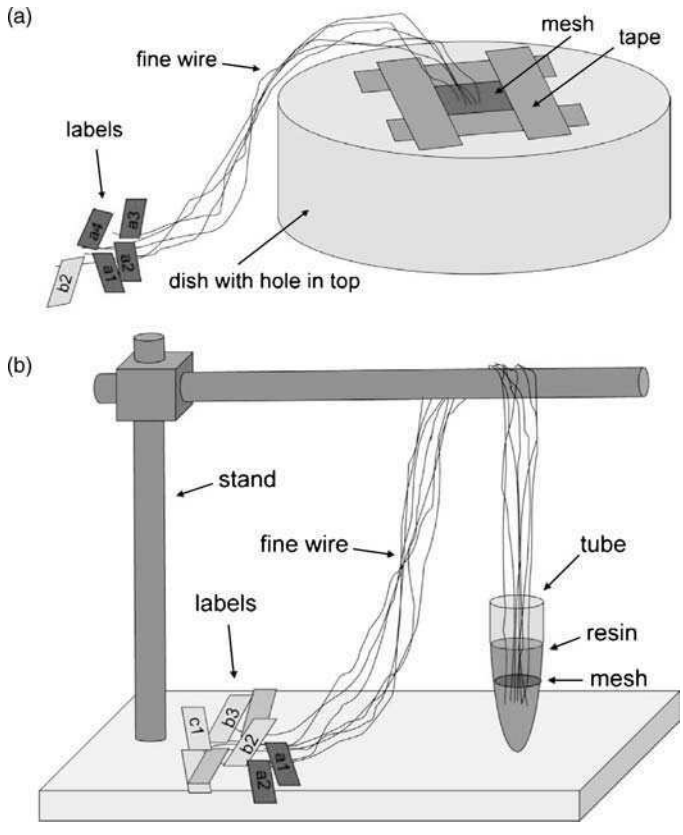

Figure 28.6 Stages during the production of the electrode array shown in Figure 28.5. (a) Insertion of the electrodes in a nylon mesh. (b) Embedding the array in resin. See text for details. For a color version of this figure, please see the images supplied on the accompanying CD

are clear and will harden completely. After mixing the main component and the hardening catalyst in a standard 15 ml centrifuge tube, this container was closed and connected to a vacuum system to get rid of air bubbles. Some of this mixture was then slowly poured into the cuvette. The mesh with wires was then advanced into a cuvette and immersed in the mixture, carefully avoiding the formation/trapping of air bubbles. The circular mesh should be exactly at right angles to the length axis of the cuvette. After this, the cuvette stand was fixed in position and the bundle of long wires at the other end of the mesh was attached to the lab stand. A small stainless steel rod of about 2–3 mm in diameter, held by the clamp, was lowered partially into the cuvette to about 0.5–1 cm from the mesh (not shown in Figure 28.6). This rod will become the holder with which the array can be attached to a manipulator. After hardening, the cuvette was carefully removed (using a scalpel if necessary). Within the resin, the mesh should still be visible. The fine grinding disk on a variable speed Dremel tool (www.dremel.com) was used to slowly grind down the front end of the probe (if the Dremel is used too enthusiastically, the resin will melt). At 3 or 2 mm from the mesh, the spacing between the silver wires will be somewhat irregular.

However, the closer to the mesh, the more regular the array becomes. The trick is to stop grinding just before/just at the level of the mesh. It is better to grind the last little bit with a softer felt polishing disk rather than a harder sandpaper disk.

The bundle of wires at the proximal end of the probe was then disentangled and braided (to make the cabling less vulnerable). The silver wires should be kept as short as is practical at the proximal side (about 10 cm), because the resistivity of these thin wires is not negligible. The braided cable was then fed into a small connector box, where one by one, the labels were removed from individual wires and the wires were soldered onto female tip plugs, which were also organised as a 4×4 array. During recordings, male–male connector cables were used to connect the connector box to the amplifier. Shielding these cables with grounded aluminum foil (or something less primitive) will reduce noise. Our initial probe had a 4x4 electrode configuration, but we have produced 12×12 electrode arrays for the mouse atrium in exactly the same way.

For measurements of atrial conduction, unipolar signals were bandpass-filtered at 0.1–5 kHz using two Iso-DAM8 amplifiers (World Precision Instruments) and sampled at 8 kHz using a 16-channel Gould ACQ-16 data acquisition interface. Commercially available systems capable of handling much high numbers of recording channels are UneMap from the Bioengeneering Institute in Auckland, New Zealand (http://www.bioeng.auckland.ac.nz/projects/unemap/unemap.php?project_id=5) and a system available at Biosemi, Amsterdam, The Netherlands (www.biosemi.com). In general, measuring epicardial conduction in mice requires very high sampling rates. For an interelectrode distance of 0.4 mm and an estimated conduction velocity of 0.6 m/s, the difference in activation time between adjacent electrodes is 0.67 ms, corresponding to a rate of 1.5 kHz. An accurate determination of the conduction pattern would then require a sampling rate of at least 3 kHz.

Atrial conduction was assessed during sinus rhythm and AF and during continuous pacing with one of the bipolar stimulus pairs at a variety of BCLs at a stimulus amplitude of $1.5 \times$ diastolic threshold and a stimulus duration of 1 ms. Activation time points were determined at each of the 16 electrodes as the point of maximal negative dV/dt and activation maps were constructed using custom software. As an example, Figure 28.5D shows an activation map on the left atrium of a mouse with atrial fibrosis due to overexpression of TGFβ1.

In recent years, detailed conduction patterns in the mouse heart have also been recorded successfully using optical mapping. For an overview of this technique, see Efimov *et al.*[21]

Conclusion

In recent years, several mouse models with increased inducibility of atrial tachyarrhythmias have been described. Several studies have reported an increased vulnerability for AF in response to administration of cholinergic agonists in normal mice,[22,23] and in one study, AF could be induced in normal mice without pharmacological intervention.[24] In mice lacking the gap junction protein connexin40, atrial

conduction velocity was decreased and episodes of AF could be evoked by atrial burst pacing.[10,25] In our mice with selective atrial fibrosis due to overexpression of TGFβ1, inducibility of AF was increased.[5] In mice overexpressing Kir2.1, the increase in I_{K1} current was associated with spontaneous AF episodes.[26] Similarly, deletion of KNCE1, an auxiliary subunit for I_{Ks} leads to spontaneous AF episodes.[27] Finally, a growing number of transgenic mice display major atrial enlargement and an associated increase in spontaneous or inducible AF: mice overexpressing junctin,[28] mice with cardiac-specific overexpression of angiotensin-converting enzyme[29], cAMP-response element modulator[30] or tumor necrosis factor alpha.[31] Thus, mouse models are providing a burgeoning contribution to our understanding of the basic mechanism of AF.

References

1. Allessie MA. Atrial electrophysiologic remodeling: another vicious circle? *J Cardiovasc Electrophysiol* 1998; **9**: 1378–1393.
2. Allessie MA, Bonke FI, Schopman FJ. Circus movement in rabbit atrial muscle as a mechanism of tachycardia. III. The 'leading circle' concept: a new model of circus movement in cardiac tissue without the involvement of an anatomical obstacle. *Circ Res* 1977; **41**: 9–18.
3. Winfree AT. Electrical turbulence in three-dimensional heart muscle. *Science* 1994; **266**: 1003–1006.
4. Vaidya D, Morley GE, Samie FH, Jalife J. Reentry and fibrillation in the mouse heart. A challenge to the critical mass hypothesis. *Circ Res* 1999; **85**: 174–181.
5. Verheule S, Sato T, Everett TT, et al. Increased vulnerability to atrial fibrillation in transgenic mice with selective atrial fibrosis caused by overexpression of TGF-beta1. *Circ Res* 2004; **94**: 1458–1465.
6. Spach MS, Boineau JP. Microfibrosis produces electrical load variations due to loss of side-to-side cell connections: a major mechanism of structural heart disease arrhythmias. *Pacing Clin Electrophysiol* 1997; **20**: 397–413.
7. Noujaim SF, Lucca E, Munoz V, Persaud D, Berenfeld O, Meijler FL, Jalife J. From mouse to whale: a universal scaling relation for the PR Interval of the electrocardiogram of mammals. *Circulation* 2004; **110**: 2802–2808.
8. Janssen BJ, Smits JF. Autonomic control of blood pressure in mice: basic physiology and effects of genetic modification. *Am J Physiol Regul Integr Comp Physiol* 2002; **282**: R1545–1564.
9. van Rijen HV, Eckardt D, Degen J, et al. Slow conduction and enhanced anisotropy increase the propensity for ventricular tachyarrhythmias in adult mice with induced deletion of connexin43. *Circulation* 2004; **109**: 1048–1055.
10. Verheule S, van Batenburg CA, Coenjaerts FE, Kirchhoff S, Willecke K, Jongsma HJ. Cardiac conduction abnormalities in mice lacking the gap junction protein connexin40. *J Cardiovasc Electrophysiol* 1999; **10**: 1380–1389.
11. Mitchell GF, Jeron A, Koren G. Measurement of heart rate and Q-T interval in the conscious mouse. *Am J Physiol* 1998; **274**: H747–751.
12. Hoit BD, Kiatchoosakun S, Restivo J, et al. Naturally occurring variation in cardiovascular traits among inbred mouse strains. *Genomics* 2002; **79**: 679–685.

13. Gu H, Smith FC, Taffet SM, Delmar M. High incidence of cardiac malformations in connexin40–deficient mice. *Circ Res* 2003; **93**: 201–206.
14. Desai KH, Sato R, Schauble E, Barsh GS, Kobilka BK, Bernstein D. Cardiovascular indexes in the mouse at rest and with exercise: new tools to study models of cardiac disease. *Am J Physiol* 1997; **272**: H1053–1061.
15. Berul CI, Aronovitz MJ, Wang PJ, Mendelsohn ME. In vivo cardiac electrophysiology studies in the mouse. *Circulation* 1996; **94**: 2641–2648.
16. Rao S, Verkman AS. Analysis of organ physiology in transgenic mice. *Am J Physiol Cell Physiol* 2000; **279**: C1–C18.
17. Gehrmann J, Berul CI. Cardiac electrophysiology in genetically engineered mice. *J Cardiovasc Electrophysiol* 2000; **11**: 354–368.
18. Danik S, Cabo C, Chiello C, Kang S, Wit AL, Coromilas J. Correlation of repolarization of ventricular monophasic action potential with ECG in the murine heart. *Am J Physiol Heart Circ Physiol* 2002; **283**: H372–381.
19. Maguire CT, Bevilacqua LM, Wakimoto H, Gehrmann J, Berul CI. Maturational atrioventricular nodal physiology in the mouse. *J Cardiovasc Electrophysiol* 2000; **11**: 557–564.
20. Knollmann BC, Katchman AN, Franz MR. Monophasic action potential recordings from intact mouse heart: validation, regional heterogeneity, and relation to refractoriness. *J Cardiovasc Electrophysiol* 2001; **12**: 1286–1294.
21. Efimov IR, Nikolski VP, Salama G. Optical imaging of the heart. *Circ Res* 2004; **95**: 21–33.
22. Kovoor P, Wickman K, Maguire CT, Pu W, Gehrmann J, Berul CI, Clapham DE. Evaluation of the role of I(KACh) in atrial fibrillation using a mouse knockout model. *J Am Coll Cardiol* 2001; **37**: 2136–2143.
23. Wakimoto H, Maguire CT, Kovoor P, Hammer PE, Gehrmann J, Triedman JK, Berul CI. Induction of atrial tachycardia and fibrillation in the mouse heart. *Cardiovasc Res* 2001; **50**: 463–473.
24. Schrickel JW, Bielik H, Yang A, et al. Induction of atrial fibrillation in mice by rapid transesophageal atrial pacing. *Basic Res Cardiol* 2002; **97**: 452–460.
25. Hagendorff A, Schumacher B, Kirchhoff S, Luderitz B, Willecke K. Conduction disturbances and increased atrial vulnerability in Connexin40–deficient mice analyzed by transesophageal stimulation. *Circulation* 1999; **99**: 1508–1515.
26. Li J, McLerie M, Lopatin AN. Transgenic upregulation of IK1 in the mouse heart leads to multiple abnormalities of cardiac excitability. *Am J Physiol Heart Circ Physiol* 2004; **287**: H2790–2802.
27. Temple J, Frias P, Rottman J, et al. Atrial fibrillation in KCNE1–null mice. *Circ Res* 2005; **97**: 62–69.
28. Hong CS, Cho MC, Kwak YG, et al. Cardiac remodeling and atrial fibrillation in transgenic mice overexpressing junctin. *FASEB J* 2002; **16**: 1310–1312.
29. Xiao HD, Fuchs S, Campbell DJ, et al. Mice with cardiac-restricted angiotensin-converting enzyme (ACE) have atrial enlargement, cardiac arrhythmia, and sudden death. *Am J Pathol* 2004; **165**: 1019–1032.
30. Muller FU, Lewin G, Baba HA, et al. Heart-directed expression of a human cardiac isoform of cAMP-response element modulator in transgenic mice. *J Biol Chem* 2005; **280**: 6906–6914.
31. Saba S, Janczewski AM, Baker LC, et al. Atrial contractile dysfunction, fibrosis, and arrhythmias in a mouse model of cardiomyopathy secondary to cardiac-specific overexpression of tumor necrosis factor-. *Am J Physiol Heart Circ Physiol* 2005; **289**: H1456–1467.

29

Ligation- and wire injury-induced stenosis

Volkhard Lindner

Center for Molecular Medicine, Maine Medical Center Research Institute, Scarborough, USA

Introduction

Genetic models present a powerful approach to understanding the contribution of specific factors to the development of cardiovascular diseases. This created the need to develop suitable models in the mouse. A lot of attention has been focused on neointima formation and endothelial regeneration following arterial injury. Balloon catheter injury models are well established in the rat[1] and extensive insight into the arterial injury response has been provided by this model. Since there currently is still no good equivalent to the 2F Fogarty embolectomy catheter suitable for mice, my laboratory focused on the development of murine arterial injury models in the early 1990ies. Analogous to the denuding injury of the rat carotid artery we developed a mouse carotid artery injury model using a guide wire tip[2]. Several models that present variations on this wire denudation model have since been reported by others[3,4]. The technical challenges associated with wire denudation models may account for differing results obtained by other investigators. Due to the relatively small size of the mouse arteries uncontrolled thrombus formation and its consequences for lesion development are likely factors contributing to inter-operator variability in denuding injury models. This prompted us to develop the technically very simple model of mouse carotid artery ligation[5]. As this flow cessation model is relatively easy to perform it has the advantage of being relatively free from operator-induced variables. This ligation model was primarily

A Handbook of Mouse Models of Cardiovascular Disease Edited by Qinbo Xu

designed to induce SMC proliferation and neointima formation in a reproducible manner. The ligation model turned out to be a useful model to study intimal lesion formation even though it does not represent a physiological situation. However, the same argument of physiological relevance can be made for denuding injury models, as large scale denudations are not a part of the pathogenesis of cardiovascular diseases in humans. In addition, the ligation model displayed many of the characteristics of constrictive arterial remodeling associated with decreased blood flow. Below a detailed description with emphasis on technical aspects of the wire denudation and the ligation model will be provided.

Materials and Methods

All procedures have to be in compliance with institutional and federal regulations and a veterinarian should be consulted.

For the anesthesia, ketamine (50 mg/ml) and xylazine (20 mg/ml) are mixed with 0.17 ml of xylazine added per 1ml of ketamine. The addition of atropin is optional. To anesthetize a mouse weighing approximately 25 g, 50–70 µl of this mixture are injected intraperitoneally with an insulin syringe (0.5 ml, Becton-Dickinson). To prevent drying of the cornea during anesthesia, an ophthalmic ointment should be applied (e.g. Lacri-Lube, Allergan).

There are many suppliers of surgical instruments that carry the same or similar instruments described below and the catalog number of specific vendors is provided here only as a convenience.

Materials needed:

1. Surgery platform (e.g., Teflon, 13 cm × 15 cm, with stainless steel screws to hold rubber bands for securing the mouse on the platform)

2. Small rubber bands

3. Tape

4. Catheter (i.v.), 24-gauge (Becton-Dickinson)

5. Dissecting microscope (e.g., Stemi 2000, Zeiss, VWR Scientific)

6. Fiberoptic light source (e.g., ACE, EKE with dual gooseneck, Fostec, Auburn, NY)

7. Small hair clipper

8. Betadine solution and 70% ethanol for skin disinfection

9. Gauze (2 × 2 inch)

10. Cotton applicators
11. scalpel
12. 6-0 silk suture (e.g., Deknatel, Queens Village, NY)
13. Microdissecting forceps with curved tip (e.g., Aesculap, FD281)
14. Jeweler's forceps, straight, 4″ (e.g., 160-55, George Tieman & Co., Hauppauge, NY)
15. Microforceps (e.g., Bracken, 10-1942, George Tieman & Co.)
16. Scissors, McPherson-Vannas, straight (e.g., 160-140, George Tieman & Co.)
17. Scissors, Stevens, straight blunt-tipped (e.g., 160-250, George Tieman & Co.)
18. Hemostat, 3″, curved (e.g., 160-751, George Tieman & Co.)
19. Bulldog clamp, Johns Hopkins, 1″ straight (e.g., 160-825, George Tieman & Co.)
20. Bulldog clamp, DeBakey, curved 5″ (e.g., 70-551, George Tieman & Co.)
21. Michel wound clip applying forceps 5″ (e.g., 160-912, George Tieman & Co.)
22. Michel wound clips, 7.5 mm (e.g., 160-898, George Tieman & Co.)
23. Guide wire from angioplasty catheter, 0.014″ (dependent upon vessel size)

Guide-Wire Denudation Model

The flexible tip of a guide wire is cut off from the rest of the wire. The wire tip should be curved, smooth and the coating should not be damaged. The surface of the guide wire can be modified with Epoxy glue if necessary to alter mechanical properties, shape and size of the wire. A trocar can faciliate the insertion of the guide wire into the vessel. A thin-walled Teflon or polyethylene tubing of 2.5 cm length with a bevel cut at the tip may serve this purpose.

Following the induction of anesthesia the mouse is placed with its back on the surgery platform and rubber bands are used to secure the hind legs to the screws mounted on the side of the platform. Another rubber band is used to hold down the head by the upper incisors. A piece of tape is used to keep the front legs clear from the operating field. The skin along the ventral side of the neck is shaved followed by the application of betadine and ethanol disinfectant. A midline incision is made

along the ventral side of the neck (1.5 cm in length). We routinely perform procedures on the left carotid artery since it has no side branches and thus following complete denudation of the common carotid artery re-endothelialization should occur only from the carotid bifurcation and the aortic arch. The left salivary gland is moved laterally by blunt dissection and held away from the carotid bifurcation by the DeBakey clamp. The straight neck muscles are pushed medially while blunt dissection of the of the external carotid artery is performed with the microdissecting forceps with curved tips (Aesculap, FD281). These forceps are very well suited to separate the connective tissue from the vessel and placing the ligatures. The proximal ligature is placed around the external carotid artery just distal of the carotid bifurcation but it is not tied off at this stage. The ends of this ligature are held with a small hemostat and tension is applied in caudal direction to facilitate dissection of the more distal portions of the external carotid artery. The second ligature is placed around the external carotid artery as far distal as possible to isolate the largest segment possible between the two ligatures. The distal ligature is tied into place and tension is applied in cranial direction by attaching the 1.5″ bulldog clamp. A small hole is then cut into the vessel close to the distal ligature while blood flow is blocked by gentle tension on the proximal ligature. With the wire inside the trocar, the tip of the trocar is placed into the hole with the bevel pointing down. Then the wire is advanced until it reaches the proximal ligature, the tension on the proximal ligature is released and the ligature is loosened around the vessel to allow unobstructed advancement of the wire into the common carotid artery. With rotating motion the wire is passed back and forth along the vessel (approximately 2 cm from the hole in the external carotid artery) three times to assure complete denudation. Advancing the wire too far can cause lethal damage to cardiac valves as the wire, once in the aortic arch, has the tendency to move towards the heart upon advancement. Upon removal of the wire from the vessel it is important to verify that blood flow is re-established in the common carotid artery. Pulsation, color of the blood inside the common carotid artery and brisk bleeding from the hole upon removal of the catheter are indications that complete thrombotic occlusion of the common carotid artery has not occurred. The proximal ligature is then tied off, and the skin incision is closed using two wound clips. The recovery of the mouse, preferably on a heating pad, is monitored and postsurgical analgesics are administered in accordance with regulations and institutional operating procedures.

Ligation Model of the Common Carotid Artery

This model is described in the 1997 publication by Kumar and Lindner[5]. Application of this model to a variety of inbred mouse strains has indicated that the remodeling responses are genetically controlled[6]. The surgical procedure is easy to perform and can be completed in less than 5 min from start to finish. This makes this model suitable for studies where large numbers of mice need to be examined.

The dissection for this procedure is carried out as described above for the wire denudation model. The common carotid artery is tied off by placing a ligature just proximal of the carotid bifurcation. Wound closure is performed as described above.

Harvesting of Vessels

Prior to harvesting the vessels subjected to wire denudation, endothelial regrowth in the common carotid artery should be assessed by injection of 50 µl of a 5% Evans blue solution administered via the tail vein. Circulation of the dye for a few minutes is sufficient to stain still denuded segments of the vessel blue while segments with endothelium will remain white. If complete denudation had been achieved at the time of surgery, only a 2–3 mm segment will still be denuded three weeks later. In the presence of incomplete denudation, complete reendothelialization will occur over a substantially shorter period of time. For morphometric analyses this is an important consideration as there is usually no proliferation of SMC or lesion growth in the presence of an endothelium.

For morphometric analyses, perfusion fixation should be performed under physiological pressure with a glutaraldehyde-based fixative. Perfusion fixation via a catheter (24 gauge) placed into the left ventricle is a preferred approach. For good perfusion fixation in the ligation model, a small hole is cut into the common carotid artery just proximal of the ligature prior to fixation. Perfusion fixation with 20 ml of fixative is usually sufficient. The vessels are then excised with the ligature and a piece of the aortic arch still attached. Additional immersion fixation can be performed before processing and embedding of the vessels.

Discussion

A major and very common complication occurring in wire denudation models is unintentional partial or complete vascular occlusion by a fibrin clot. These fibrin clots will get organized by SMC invading from the media. The size of the original clot is likely the single most important parameter influencing neointima development. Evidence for a prior thrombotic event are highly asymmetric neointimal lesions or lesions that completely obliterate the lumen. Since clotting is sometimes not immediately evident, it can lead to misleading results. In our studies using the wire denudation model, we routinely harvest the vessels after injection of Evans blue to determine the extent of reendothelialization. Reendothelialization should occur symmetrically from both ends of the denuded segment. In case of the common carotid artery this would be the aortic arch and the carotid bifurcation. In the mouse carotid artery harvested at 2 weeks after denudation, an Evans blue stained area (approximately 1–2 mm) will be detectable in the central segment of the common carotid artery. These denuded segments are those that should be used for morphometric analyses. Neointimal lesions usually stop growing in denuding injury models as soon as the luminal surface gets reendothelialized. Restricting the

morphometric analysis to denuded segments assures that all measurements are performed on segments of vessels that have not been influenced by the variable of endothelial regeneration. Unfortunately, not many investigators rigorously control for endothelial regeneration and clot-dependent effects on neointima formation. A recent example is the study by Kobayashi et al.[7] where it is apparent that vessels with complete thrombotic occlusions were not excluded from the analysis. Like the rat balloon injury model, proliferation of SMC starts in the media within a few days after denudation and if no reendothelialization occurs, proliferating SMC can be found in the neointima typically within a week. If reendothelialization occurred before SMC could migrate into the intima one will observe medial hypertrophy and hyperplasia since medial SMC proliferation precedes the arrival of SMC in the intima.

One major advantage of the ligation model over other models is that it is hardly ever influenced by variables related to the surgical procedure because it is technically very easy to perform. This fact has made it a very popular model[8–23]. It is understood that this model does not mimic a (patho)physiological situation. It is, nevertheless, a very suitable model to study SMC proliferation. In addition, it displays many aspects of constrictive arterial remodeling associated with reduced blood flow. In nearly all cases, the ligated vessels show no signs of thrombus formation with the exception of a miniscule segment (0.5 mm or less) upstream of the ligature. In the extremely rare instance, that clotting occurred along a longer segment of the vessel, it is usually quite obvious at the time of vessel harvest and these vessels are excluded from the analysis. The carotid artery response to ligation is reproducible and has been characterized along the length of the vessel according to distance from the ligature[24,25]. Since the extent of neointima formation is dependent upon the distance from the ligature, it is crucial that the analysis is performed on sections that are obtained from the same anatomical location with regards to the ligature. For example, the segment with maximal lesion formation will be reproducibly included if sections are obtained at 2, 3, and 4mm distance from the ligature. The technical simplicity of the flow cessation model makes it one of the most suitable models forˆhigh throughput'' screening.

The method of fixation and the type of fixative can have a major impact on the morphometric analysis of sectioned vessels. It is important that the vessels be perfusion fixed at physiological pressure. However, intravascular pressure at the time of perfusion is difficult to assess and with the use of relatively small caliber perfusion catheters a large drop in pressure is likely to occur along the length of the catheter itself. In addition, if fixatives are used that do not contain glutaraldehyde, the vessel will retain some of its elastic properties which will cause the vessel to contract or shrink upon excision. As a consequence, elastic lamellae will appear wrinkled and wavy and this is particularly evident in normal vessels that lack a neointima (compare Figure 29.1a and b). The morphometric anaylsis of sections is facilitated if a histological stain is chosen that highlights the elastic lamellae such as Verhoeff's stain (Figure 29.1). This stain makes it particularly easy to trace the internal and external elastic laminae and thus adds to increased accuracy of the measurements. An artery that has undergone constrictive arterial remodeling will display wavy

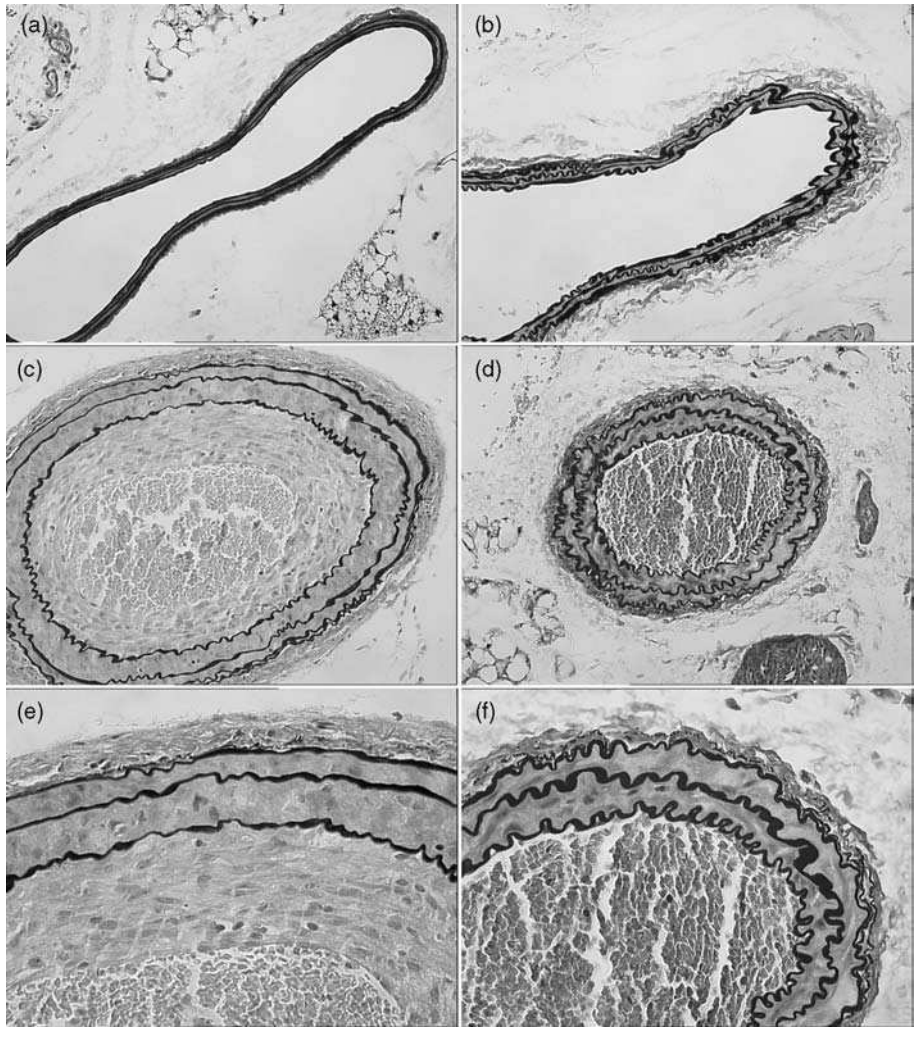

Figure 29.1 Photomicrographs of cross-sectioned mouse common carotid arteries after Verhoeff staining. (a) A normal unmanipulated artery, perfusion fixed with a glutaraldehyde-based fixative shows elastic lamellae in their original in situ length and morphology, while in (b) a similar vessel fixed without glutaraldehyde reveals wavy elastic lamellae. (c) A vessel harvested 3 weeks after carotid artery ligation demonstrates neointima formation and constrictive remodeling and while in (d) only constrictive remodeling and medial hypertrophy is evident at the same time point. (e) is a high power of the vessel shown in c) and (f) is a high power view of the vessel shown in d). Original magnification is 200× for A-D and 400× for e and f. For a color version of this figure, please see the images supplied on the accompanying CD

elastic lamellae even if the vessels were harvested following optimal perfusion fixation (Figure 29.1c-f).

The type of question to be answered by the experiment will determine when the arteries will be harvested for analysis. In the ligation model, an extensive neointimal lesion will form within 2 weeks. The composition of the neointima,

however, will continue to change over the course of several more weeks usually with an increase in extracellular matrix and a decrease in cellularity. SMC proliferation is therefore preferably examined at earlier time points (less than 2 weeks after ligation) and neointimal lesion size preferably at later times (>2 weeks).

Acknowledgments

Support for the investigator's work is provided by a grant from the National Institutes of Health (HL69182). Histology services are made possible by NIH Grant Number P20 RR-18789 from the National Center for Research Resources.

References

1. Clowes AW, Reidy MA, Clowes MM. Kinetics of cellular proliferation after arterial injury. I. Smooth muscle growth in the absence of endothelium. *Lab Invest*. 1983;49: 327–33.
2. Lindner V, Fingerle J, Reidy MA. Mouse model of arterial injury. *Circ Res*. 1993;73:792–6.
3. Roque M, Fallon JT, Badimon JJ, Zhang WX, Taubman MB, Reis ED. Mouse model of femoral artery denudation injury associated with the rapid accumulation of adhesion molecules on the luminal surface and recruitment of neutrophils. *Arterioscler Thromb Vasc Biol*. 2000;20:335–42.
4. Zhou M, Sutliff RL, Paul RJ, Lorenz JN, Hoying JB, Haudenschild CC, Yin M, Coffin JD, Kong L, Kranias EG, Luo W, Boivin GP, Duffy JJ, Pawlowski SA, Doetschman T. Fibroblast growth factor 2 control of vascular tone. *Nat Med*. 1998;4:201–7.
5. Kumar A, Lindner V. Remodeling with neointima formation in the mouse carotid artery after cessation of blood flow. *Arterioscler Thromb Vasc Biol*. 1997;17:2238–44.
6. Harmon KJ, Couper LL, Lindner V. Strain-dependent vascular remodeling phenotypes in inbred mice. *Am J Pathol*. 2000;156:1741–8.
7. Kobayashi K, Yokote K, Fujimoto M, Yamashita K, Sakamoto A, Kitahara M, Kawamura H, Maezawa Y, Asaumi S, Tokuhisa T, Mori S, Saito Y. Targeted Disruption of TGF-{beta}-Smad3 Signaling Leads to Enhanced Neointimal Hyperplasia With Diminished Matrix Deposition in Response to Vascular Injury. *Circ Res*. 2005.
8. Kumar A, Hoover JL, Simmons CA, Lindner V, Shebuski RJ. Remodeling and neointimal formation in the carotid artery of normal and P-selectin-deficient mice. *Circulation*. 1997;96:4333–42.
9. Galis ZS, Johnson C, Godin D, Magid R, Shipley JM, Senior RM, Ivan E. Targeted disruption of the matrix metalloproteinase-9 gene impairs smooth muscle cell migration and geometrical arterial remodeling. *Circ Res*. 2002;91:852–9.
10. Kawasaki T, Dewerchin M, Lijnen HR, Vreys I, Vermylen J, Hoylaerts MF. Mouse carotid artery ligation induces platelet-leukocyte-dependent luminal fibrin, required for neointima development. *Circ Res*. 2001;88:159–66.
11. Morishita T, Tsutsui M, Shimokawa H, Horiuchi M, Tanimoto A, Suda O, Tasaki H, Huang PL, Sasaguri Y, Yanagihara N, Nakashima Y. Vasculoprotective roles of neuronal nitric oxide synthase. *Faseb J*. 2002;16:1994–6.

12. Yogo K, Shimokawa H, Funakoshi H, Kandabashi T, Miyata K, Okamoto S, Egashira K, Huang P, Akaike T, Takeshita A. Different vasculoprotective roles of NO synthase isoforms in vascular lesion formation in mice. *Arterioscler Thromb Vasc Biol*. 2000;20:E96–E100.
13. Hollestelle SC, De Vries MR, Van Keulen JK, Schoneveld AH, Vink A, Strijder CF, Van Middelaar BJ, Pasterkamp G, Quax PH, De Kleijn DP. Toll-like receptor 4 is involved in outward arterial remodeling. *Circulation*. 2004;109:393–8.
14. Murakoshi N, Miyauchi T, Kakinuma Y, Ohuchi T, Goto K, Yanagisawa M, Yamaguchi I. Vascular endothelin-B receptor system in vivo plays a favorable inhibitory role in vascular remodeling after injury revealed by endothelin-B receptor-knockout mice. *Circulation*. 2002;106:1991–8.
15. Sata M, Walsh K. Fas ligand-deficient mice display enhanced leukocyte infiltration and intima hyperplasia in flow-restricted vessels. *J Mol Cell Cardiol*. 2000;32:1395–400.
16. Kuzuya M, Kanda S, Sasaki T, Tamaya-Mori N, Cheng XW, Itoh T, Itohara S, Iguchi A. Deficiency of gelatinase a suppresses smooth muscle cell invasion and development of experimental intimal hyperplasia. *Circulation*. 2003;108:1375–81.
17. Acevedo L, Yu J, Erdjument-Bromage H, Miao RQ, Kim JE, Fulton D, Tempst P, Strittmatter SM, Sessa WC. A new role for Nogo as a regulator of vascular remodeling. *Nat Med*. 2004;10:382–8.
18. Sindermann JR, Smith J, Kobbert C, Plenz G, Skaletz-Rorowski A, Solomon JL, Fan L, March KL. Direct evidence for the importance of p130 in injury response and arterial remodeling following carotid artery ligation. *Cardiovasc Res*. 2002;54:676–83.
19. Kraemer R. Reduced apoptosis and increased lesion development in the flow-restricted carotid artery of p75(NTR)-null mutant mice. *Circ Res*. 2002;91:494–500.
20. de Waard V, Arkenbout EK, Carmeliet P, Lindner V, Pannekoek H. Plasminogen activator inhibitor 1 and vitronectin protect against stenosis in a murine carotid artery ligation model. *Arterioscler Thromb Vasc Biol*. 2002;22:1978–83.
21. Singh R, Pan S, Mueske CS, Witt TA, Kleppe LS, Peterson TE, Caplice NM, Simari RD. Tissue factor pathway inhibitor deficiency enhances neointimal proliferation and formation in a murine model of vascular remodelling. *Thromb Haemost*. 2003;89: 747–51.
22. Schiffers PM, Henrion D, Boulanger CM, Colucci-Guyon E, Langa-Vuves F, van Essen H, Fazzi GE, Levy BI, De Mey JG. Altered flow-induced arterial remodeling in vimentin-deficient mice. *Arterioscler Thromb Vasc Biol*. 2000;20:611–6.
23. Rectenwald JE, Minter RM, Moldawer LL, Abouhamze Z, La Face D, Hutchins E, Huber TS, Seeger JM, Ozaki CK. Interleukin-10 fails to modulate low shear stress-induced neointimal hyperplasia. *J Surg Res*. 2002;102:110–8.
24. Myers DL, Harmon KJ, Lindner V, Liaw L. Alterations of arterial physiology in osteopontin-null mice. *Arterioscler Thromb Vasc Biol*. 2003;23:1021–8.
25. Myers DL, Liaw L. Improved analysis of the vascular response to arterial ligation using a multivariate approach. *Am J Pathol*. 2004;164:43–8.

Index

Note: Figures and Tables are indicated by *italic* page numbers

ABCA1 knockout mice 256–8
abdominal aorta
  cross-sectional measurement 131
  external diameter 71, *72*
  in vivo MRI of atherosclerotic plaques 71, *72*
  weight 131
abdominal aortic aneurysms (AAAs) 125
  quantification in AngII-induced AAA study 129–32
    by incidence of aneurysm formation 129
    by measurements of physical dimensions 130–1
    by non-invasive ultrasound 131–2
    by severity index 129–30
  severity-classification scheme 130
  see also AngII-induced aortic aneurysms
abdominal aortic coarctation, hypertension produced by 279
adeno-associated virus (AAV) 264
  as gene transfer vector 264–5
    disadvantages 264
    production protocols 264–5
adenovirus 265
  as gene transfer vector 97, 265–6
advanced intercross line (AIL), production of 22
advantages of mouse models 20, 287
adventitia
  area defined 106
  stem cells in 122
A/J strain 6
allergic asthma 26
allograft arteriopathy (AA)
  clinical effects 173–4
  compared with conventional atherosclerosis 174
  evaluation scale 180
  intimal lesions 173
  mouse models 175–89
    advantages 175–6
    aortic interposition grafts 175, 183–7
    applications to clinical investigation 187–9
    carotid interposition grafts 182, 183
    ear pinna model 182
    gene knockout strains used 175–6
    heterotopic cardiac transplantation 175, 177–83
    neck model 182
  and perioperative ischemia 180, 188
  pharmacologic interventions 174
allograft rejection
  clinical symptoms 173–4
  control of number and severity of episode 187–8

A Handbook of Mouse Models of Cardiovascular Disease Edited by Qinbo Xu

evaluation of 180–1
immunosuppression affecting 174, 181–2
parenchymal rejection 182
score/scale 180
allograft survival, factors affecting 173
Alzet pumps 127, 226
in aneurysm model 127–8
in hypertension models 275, 276
in hypertrophy model 226
sizes 226
surgery for implantation 128, 227, 276
American Heart Association, on blood pressure measurement 282
analgesia 14
drugs *13*, 14
anatomical similarities (of mouse and human) 159
anesthesia 7–14
drugs 11, *12*, 92, 104
factors affecting choice 7–8
inhalation techniques 11, 148, 178, 222, 339, 353
injection routes 8–9, *8*, *9*, *10*
monitoring 13–14
problems 8
AngII-induced aortic aneurysms 126–33
effect of hyperlipidemia 133
gender effects 127, 133
study methods
acquisition of AAAs 128–9
characterisation of AAAs 132
monitoring during AngII infusion 128
mouse selection 126–7
preparation and implantation of Alzet pumps 127–8
quantification of AAAs 129–32
AngII-induced cardiac hypertrophy 226–7
AngII-induced hypertension 125, 275–6
advantages and disadvantages of model 276
AngII-induced vascular injury, study by pulse wave velocity measurements 251
angiogenesis 296, 299
capillary density as index 293–4
angiogenesis inhibitor(s) 307
angiogenesis studies
evaluation of neovascularisation 304–5, 306
materials and supports 301–3, 305–6
angioplasty
cardiac blood flow restoration by 193
injury inflicted by 90
restenosis after 93
angioreactors, matrix-containing 300, *301*
alterntives 305–6
determination of blood vessel formation 304–5, 306
implantation of *301*, 303–4
precautions 306–7
preparation of 301–3
materials and equipment 301–2
procedure 302–3
requirements 305
angiotensin II
abdominal aortic aneurysms caused by 126, 133
atherosclerosis development affected by 125
hypertension induced by 125, 275–6
ANP knockout mice 280–1
ANPR knockout mice 281
anticoagulants 7
antigen-specific T cells
activation of 324, *325*
assessing activation status 328–30
tracking by tetramer staining 330–1
aortic aneurysms *see* abdominal aortic aneurysms; AngII-induced aortic aneurysms
aortic arch, atherosclerotic plaques in 68
aortic coarctation model of hypertension 279
aortic constriction
cardiac hypertrophy induced by 222–6
in heart failure model 337
see also transverse aortic constriction (TAC)
aortic interposition grafts, murine 175, 183–7
advantages compared with other models 186–7
allograft evaluation 184–5
compared with heterotopic cardiac transplantation 182
disadvantages 187
histology *183*
technical aspects 184
aortic root, size in mouse 68
aortic root lesion area
5-LO/LDLR double knockout mice *27*, 28
quantification method 58–60
area measurements 59
tissue sectioning procedure 58–9
aortic root plaques
ex vivo MRI 75
histological analysis 58–60, 68

aortic stenosis, model for 337
aortic stiffness, determination by pulse wave velocity measurements 245–9
aortocaval fistula model, *see also* arteriovenous fistula model
ApoA1 knockout mice 258
ApoB transgenic mice 263
APOBEC-1 knockout mice 259
APOBEC-1/LDLR double knockout mice 259
ApoE*3-Leiden transgenic mice, neointima formation in 97
ApoE knockout mice 39, 55, 79–80, 256, 259–60, 324
  advantages and disadvantages *61*
  in aneurysm studies 126
  atherosclerotic plaque rupture 79–86
  availability 56, 79–80
  cholesterol levels 256, 259, 324
  collar-induced atherosclerotic lesions 91
  compared with LDL receptor knockout mice 49, *61*
  cross with SM-LacZ transgenic mice 326
  pulse wave velocity measurements 251
ApoE/LDLR double knockout mice 79
ApoE/SR-BI double knockout mice 263
apolipoprotein A1 258
  see also ApoA1
apolipoprotein B mRNA editing catalytic subunit-1 259
  see also APOBEC-1
apolipoprotein B100 (ApoB100) 256, *257*
apolipoprotein E 55, 259
  see also ApoE
arterial allografts and isografts 116–17
arteriogenesis 296
arteriovenous fistula (AVF) model 137–44
  arterial blood pressure measurement 141
  creation of AVF
    anesthesia 138
    microsurgical tools and sutures 139
    mouse preparation 138
    surgical procedure 139–40, *141*
  hemodynamic data 142, *143*
  hemodynamic measurements 141–2
  limitation(s) 144
  structural data 142–3
  tissue harvesting 142
  see also aortocaval fistula model
Artles locus 28
aspirin, venous grafts affected by 121
Ath-1 phenotype 255–6
atherosclerosis 53, 255
  compared with allograft arteriopathy 174
  diet-induced 6, 49, 262
    mouse strains resistant to 6, 33, 256
    mouse strains susceptible to 6, 56, 256, 262
  effect of angiotensin II 125
  magnetic resonance imaging of 68
  resistance to 48
  vascular elasticity affected by 245
atherosclerosis studies
  bone marrow transplantation used 48–50
  environmental factors 57
  gender effects 57
  mouse strains used 6, 56–7, 260
  SM-LacZ transgenic mice used 324, 331
atherosclerosis susceptibility gene, QTL analysis *27*, 28
atherosclerotic lesions
  determination of composition 62–3
    immunocytochemical procedures 63
  development sequence 53–4
  differences between mice and humans 260
  formation of
    in cuff injury-induced stenosis model 91
    role of viral antigens 332
  histological analysis 57–62, 68
    aortic root lesions 58–60, 260
    en face analysis 60–2, 260
  statistical analysis 63–4
atherosclerotic plaque rupture 79
  mouse study 79–87
    diet 81
    genotyping protocol 80–1
    group sizes 85, *86*
    husbandry and selfare 81
    morphological analysis 83
    morphometric analysis 84–5
    strain used 79–80
    study design considerations 85
    termination procedure 81–2
atherosclerotic plaques
  in vivo monitoring 67
  magnetic resonance imaging 67–77
    ex vivo MRI 68–9, 72, *74*, 76
    in vivo MRI 71, *72*
ATP-binding cassette-1 257–8
  see also ABCA1

atrial fibrillation 351–63
  theoretical basis 351–2
atrial natriuretic peptide 280–1
  see also ANP; ANPR
autoimmune vasculitis, study of 324, 331
avertin, side effects 353
Axl, role in flow-induced vascular remodeling 110

B6/129SF2/J strain, in heart preconditioning studies 194
BALB/c strain 6
BALB/cJ strain 6
birds, cardiovascular anatomy 159
blood–brain barrier, permeability, evaluation of 155
blood collection method 7
blood pressure
  measurement in mice 227–9, 282
    catheter-based methods 227–9, 282
    tail cuff technique 282
    telemetry systems 282
  pulse wave velocity affected by 249
  see also hypertension
blood volume (of mouse) 199
bone marrow collection methods 7, 46–7
bone marrow-derived dendritic cells, generation of 326
bone marrow stromal cells, transplantation of 156–7
bone marrow transplantation (BMT)
  analysis of leukocytes after 48
  application in atherosclerosis studies 48–50
  compared with use of transgenic mice 49
  complications 45
  determination of chimerism after 47–8
  genetic modification of stem cells 50
  mouse strain used 46, 47, 262
  role in gene–gene interaction studies 48–9
  techniques 45–7
    isolation of bone marrow cells 46–7
    preparation of acceptor mice 45
    radiation of acceptor mice 46
    transplantation of bone marrow cells 47
brachiocephalic artery
  after dissection *82*
  tissue processing 82–3
brachiocephalic artery plaque rupture
  group sizes for mouse studies 85, *86*
  morphological analysis 83
  morphometric analysis 84–5
brachiocephalic artery plaques
  ex vivo MRI *74*, 75
    automated image analysis 73–5
  histological analysis 68, *74*, 75
bradykinin 280
bradykinin B_2 receptor knockout mice 280
brain microcirculation
  ischemia 155
  monitoring 147, 152–5
breeding of mice 2, 3–4, 20, 57

C3H strain
  as backgound for ApoE knockout mice 56
  in partial ligation study *105*, *108*
C3H/HeJ strain 6
C57 strain, in partial ligation study *105*, *108*
C57BL/6 strain 56
  advantages and disadvantages *61*
  as background for knockout mice 56, 126, 175–6, 256
  cholesterol levels 324
  as graft donors and recipients 178
  susceptibility to atherosclerosis 6, 56, 256
C57BL/6J strain 6
  cross with CAST/Ei strain *27*, 28
  in heart preconditioning studies 194
  susceptibility to hyperlipidemia-induced atherosclerosis 6, 119
  in vein graft studies 119
candidate gene association 20, 25
candidate genes
  functional tests for verification of 26
  vascular remodeling 109
capillary density, as index of angiogenesis 293–4
cardiac enzymes, as index of myocardial infarct size 212
cardiac failure 137, 221
cardiac hypertrophy 221
  see also left ventricular hypertrophy
cardiac hypertrophy models 222–31
  hemodynamic measurements 227–31
  in vivo left ventricular pressure–volume measurements 227–31
  materials and methods
    anesthesia 222
    angiotensin II-induced method 226–7
    animals 222
    suprarenal abdominal aortic constriction method 224–6

tranverse aortic constriction method 223–4
pharmacologically induced hypertrophy 226–7
pressure overload-induced hypertrophy 222–6
cardiac malformations, identification in mouse embryos 160–9
carotid artery
intima–media thickness 28
preparation for vein graft studies 115–16
carotid interposition grafts 182, 183
carotidojugular fistula 137–44
limitations of mouse model 144
see also arteriovenous fistula (AVF) model
CAST/Ei strain, cross with C57BL/6J strain *27*, 28
catheter-based blood pressure measurement methods 227–9, 282
cell therapy, evaluation of 156–7
central aortocaval fistula 137
cerebral ischemia 155
cerebral microcirculation, monitoring 147, 152–5
chemical injury-induced stenosis model 90–1
chimerism, determination after bone marrow transplantation 47–8
cholate-containing diets 55
cholesterol-enriched diet 55, 81
effects
atherosclerotic lesion development 28, 55
cuff injury-induced neointima formation *96*, 97, *98*
cholesterol levels
ApoE knockout mice 256, 259, 324
C57BL/6 mice 324
LDLR knockout mice 256, 261
cholesteryl ester transfer protein (CETP), lacking in mice 256, *257*, 259
ciclosporin 182
Cited2 knockout embryos, cardiac malformations 166, *168*
clot, compared with thrombus 312
commercial breeding institutions 2
services offered 2, 56–7
conditional/inducible transgenic mice, generation of 35
conditional/tissue-specific gene knockout mice, generation of 37, 216
conductance/pressure measurements, *in vivo* assessment of cardiovascular hemodynamics using 227–31
confocal fluorescence microscopy
cerebral microcirculation observations 153–5
dynamic 153–4
static 154–5
tracking of transplanted fluorescent stem cells 156–7
congenic breeding procedure 23
congenic strains 6, 23
generation of 20, 23
use in QTL analysis 22–4
congestive heart failure, factors affecting 273
connexin40 (gap junction protein) *see* Cx40 knockout mice
consomic strains 23
generation of 20
controlled drug release, anti-restenotic compounds 98–100
coronary artery ligation (CAL) model 335, 336–7
characteristics of heart failure *336*
experimental set-up 338–9
injury-quantification techniques *344*, 345–6
limitations 348
postoperative care 342
potential pitfalls 342–4
preoperative preparation 339
surgical procedure 104–5, 111–12, 339–41, *340*
time course of disease progression 346–7
see also partial ligation model
coronary heart disease
consequences 193
genes 160
cranial window in mouse
applications
stroke model 155
tracking transplanted fluorescent stem cells 156–7
measurement methods
laser doppler flowmetry 152–3
laser scanning confocal fluorescence microscopy 153–5
preparation of mice
anesthesia 148
fluorescent labeling of red blood cells 152
implanting closed cranial window 148–51

Cre–LoxP system 37, 49, 216
cuff injury-induced stenosis model 91–8
Cx40 knockout mice, conduction defects 352, 362–3
cyclinE-deficient embryos, cardiac malformations 166, *168*
cytomegalovirus (CMV) infection 323
  see also murine cytomegalovirus (MCMV)

data acquisition sampling rate, pulse wave velocity measurements affected by 249–50
DBA strain, in partial ligation study *105*, *108*
deep vein thrombosis (DVT) 311
dendritic cells
  bone-marrow-derived, generation of 326
  repeat priming of SM-LacZ mice by 324, 326, 331
deoxycorticosterone acetate-salt (DOCA-salt) hypertension model 277–8
  applications 278
  limitations 278
diabetes, susceptibility 28, 50
diet-induced atherosclerosis
  mouse models 6, 49, 255
  resistance in mice 6, 33, 56
diet-induced hyperlipidemia 6, 54–5
dopamine 281
dopamine receptor knockout mice 281
drug-eluting stents, model for 98–100
drug therapy, for vein graft atherosclerosis 121
dynamic imaging, brain microcirculation 153–4
dyslipidemia
  mouse models 255–68
  see also ApoE knockout mice; LDL receptor knockout mice

echocardiography, cardiac function assessed using 212–13, 227
elastin staining 83
electrocardiographic (ECG) measurements
  characteristic intervals (for mice) 353–4
  electrodes 353
  in ischemia–reperfusion model 214
  in surgical heart failure models *344*
  telemetric recording 354
electronic/electrical injury-induced stenosis model 90
electrophysiology 351–63
embryo MRI 160–9
  applications
    environmental effects on development 169
    gentically modified mice 166
    high-throughput genetic screens 166, 169
  cardiac malformations *168*
  data analysis 165
  data reconstruction 164
  hardware 162, 164
  multi-embryo MRI *162*, *165*
    applications 166, 169
  normal cardiac structures 166, *167*
  preparation of embryos 161, *162*
  pros and cons of *ex vivo* MRI 169
embryonal analysis techniques 160
embryonic stem (ES) cells, gene targeting technique using 6, 37, 215
en face analysis of atherosclerotic lesions 60–2, 260, 263
  data presentation 62
  dissection protocol 60
  limitations 62, 68
  stain used 61
end-diastolic pressure–volume relations (EDPVR) 229
end-systolic pressure–volume relations (ESPVR) 229
endothelial denudation, effects in vein grafts 121–2
endothelium 119
eNOS inhibitors 252, 276–7
eNOS knockout mice 277, 280
environmental requirements of mice 3, *4*
epicardial electrophysiological measurements
  Langendorff perfused heart study 359–62
  open chest studies 356–9
episcopic fluorescence image capture (EFIC) 160
European Mouse Mutant Archive (EMMA) 2
euthanasia procedures 14, 71–2, 81–2, 93, 105, 197, 238
Evans Blue stain 197, 210
ex vivo MRI
  advantages 75, 169
  atherosclerotic plaques 68–9, 72, *74*, 76
  correlation with histological analysis 73
  disadvantages 169

mouse congenital heart defects studied by 160–9
resolution limit 75, 169
tissue collection and preparation for 71–2
exercise testing *344*
see also swimming test; treadmill test

F_1 hybrids 5
F_2 intercross mice 5, 21
familial combined hyperlipidemia 39
familial hypercholesterolemia 261
femoral artery excision, hind limb ischemia caused by 288
femoral artery perivascular cuff injury-induced stenosis model 91–8
filter cabinets 4
first generation adenoviral (FGAd) vectors 265
fixation, disadvantages in AngII-induced AAA study 128–9
flow-induced vascular remodeling
complete flow cessation model 103, 108
partial ligation model for 103–12
fluoroscein isothiocyanate (FITC)-dextrans, in angiogenesis studies 304–5, 306
forward genetics 20
FVB strain, in partial ligation study *105*, *108*

gender-specific responses
AngII-induced aortic aneurysms 127, 133
atherosclerotic lesions 57
gene expression profiling 25–6
linked with QTL mapping 26
gene knockin mice 6
advantages compared with transgenic mice 38
generation of 38
in hyperlipidemic research 36, 38
gene knockout mice 6
generation of
conditional/tissue-specific knockout mice 37, 216
conventional knockout mice 37, 215
in hyperlipidemic research 36, 39
limitations 215
gene silencing 26
and bone marrow transplantation 50
gene-targeted mice 6
in hyperlipidemic research 36, 39
see also gene knockin mice; gene knockout mice
gene targeting techniques 6, 37, 215
gene therapy, for vein graft atherosclerosis 121
gene transfer techniques 23, 34–5, 263–6
direct injection of DNA 34–5, 263, 267–8
via vectors 34, 263–6
adeno-associated viral vectors 264–5
adenoviral vectors 265–6, *268*
hybrid vectors 266
gene-to-phenotype strategy 20
genealogy, inbred mouse strains 2
genetic bases for human diseases 19
genetic models of hypertension
ANP and ANPR knockout mice 280–1
BB2R knockout mice 280
dopamine receptor knockout mice 281
eNOS knockout mice 280
Na^+–H^+ exchanger transgenic mouse model 281
RAS-component transgenic mouse models 280
genetic monitoring 3–4
genetical genomics 26
genetics, mouse 5–6, 19–28
genotyping methods 21, 80–1, 324
GFP-expressing marrow stromal cells, tracking after transplantation 156–7
Glagov phenomenon 109
gold-labeled microsphere assay, regional blood flow estimated using 292
graft-versus-host disease (GVHD) 45
growth factors, angiogenesis affected by 307

Harvey, William, use of mice 1
heart allograft model 175, 177–83
advantages and disadvantages 182–3
see also heterotopic cardiac transplantation
heart failure 137, 221
surgically induced 335–49
heart preconditioning 193–4
mouse model 194–9
anesthetic procedure 194
ischemic preconditioning 196
methodological considerations 198–9
mouse strains used 194
myocardial infarction procedure 195–6
open-chest surgical procedure 194–5
pharmacological preconditioning 197
postmortem analysis 197–8
see also ischemic preconditioning
heart pressure overload models 222–6, 335–6, 337–8

heart rates, mouse 198, *230*, 235
heart volume overload models 137, 336, 338
helper-dependent adenoviral (HDAd) vectors 266
  advantages 266
hematopoietic stem cells
  genetic modification of 50
  transplantation of 43–4
hematopoietic system *44*
hemodialysis, arteriovenous fistula used in 144
hemodynamic conditions, role 137
hemodynamic measurements
  arteriovenous fistula model 141–2
  brain microcirculation 152–3
  in hypertrophy model 227–31
  in ischemia–reperfusion model 214–15
  in surgical heart failure model *344*, 345–6
hepatic lipase 260
  see also HL
heterotopic cardiac transplantation, murine 175, 177–83
  advantages compared with other models 182
  allograft evaluation 180–1
  assessment of allograft function 179
  blood flow in donor heart 179
  disadvantages 182–3
  histology *176*
  mice strains used 178
  practice required for operator competence 179
  technical aspects 177–9
high-cholesterol diet *see* cholesterol-enriched diet
high-density lipoprotein (HDL) 54, *257*
  deficiency 258
high-fat diets 28, 55, 81
hind limb ischemia (HLI) mouse model 287–97
  applications 296–7
  assessment of neovascularisation
    histological assessment 292–4
    laser doppler perfusion imaging 289–92
    microsphere assay 292
  surgical procedures 288, *289*
    inflammatory hyperperfusion 291
histological analysis
  arteriogenesis 296
  atherosclerotic lesions 57–62, 68
  cuff-induced neotima formation 94, *96*
  embryo cardiac malformations 160
  heterotopic cardiac transplant *176*
  myocardial infarct size 344–5, *344*
  neovascularisation after tissue ischemia 292–4
  partial ligation model 106
histology
  aortic interposition graft *183*
  thrombus formation *318–19*
historical perspective (use of mice) 1–3
HL knockout mice 260
homing of hematopoietic stem cells to bone marrow 43, 44
homologous recombination 37, 215
Hooke, Robert, use of mice 1
housing conditions (for mice) 3, 4, 57
hybrid mice 5
hydrodynamic systemic injection, gene transfer using 267–8
hypercholesterolemia
  AngII-induced aortic aneurysms and 133
  familial 261
hyperlipidemia
  combined use of gene-targeted and transgenic mouse models 39
  gene-targeted mouse model 36, 39
  induction in mice
    by diet 54–5
    by genetic manipulation 55–6
  pathogenesis 33
  transgenic mouse model 34, 38
  type I 262
  see also dyslipidemia
hyperlipidemia-induced atherosclerosis 53–66
  mouse strains susceptible to 6, 56
hyperlipidemic mice
  atherosclerotic plaque rupture in 79–86
  neointima formation in 91
  see also ApoE knockout mice; LDL receptor knockout mice
hypertension 273–83
  mouse models 274–83
    genetically induced 279–81
    pharmacologically induced *274*, 275–8
    renal models *274*, 278–9
  pathogenesis in humans 273
  prevalence 273
  as risk factor 273
hypertriglyceridemia 38, 262

image analysis software 197, 211, 243
immunosuppression, for allografts 174, 181–2
in vivo confocal microscopy
  cell therapy evaluated using 156–7
  cerebral microcirculation observations 153–5
in vivo left ventricular pressure–volume measurements
  in cardiac hypertrophy models 227–31
  in ischemia–reperfusion models 214–15
in vivo MRI
  atherosclerotic plaque development 71, *72*
  cardiac function assessed using 213–14
  gating to avoid motion artifacts 71
  limitations 76
  preparation of mouse for 70–1
inbred strains (of mice) 5
  generation of 20
individually ventilated cage (IVC) systems 4
inducible transgenic mice, generation of 35
infarcted myocardium, identification of 197
inflammation
  in flow-induced vascular remodeling 108
  in vascular stenosis 97
  vasculitis-associated 323
inhalation anesthesia 11, 148, 178, 222, 339, 353
  advantages 11
injury-induced neointimal hyperplasia 6
intercellular adhesion molecule-1 (ICAM-1) 121
interferon-gamma, effect on allograft arteriopathic lesions 188, 189
intermediate-density lipoproteins (IDL), in lipoprotein metabolism 256, *257*
internal elastic lamina (IEL) *84*, 185
  degradation due to arteriovenous fistula 142–3
  determination of length 84
International Society for Heart and Lung Transplantation, rejection scale 180
interval mapping method 22
intima–media thickening (IMT) 103
intramuscular injection *9*
  drugs *12*
  injection volume range 11
intraperitoneal injection *8*
  drugs 11, *12*, 92, 104, 138, 194
  injection volume range 11
intravenous injection 9, *10*, 11, *11*
  drugs *12*
  gene transfer using 267
  tail vein technique 9, *11*, 267
irradiation, total body 44
ischemia
  cerebral 155
  mouse types used
    conditional knockout mice 216
    knockout mice 215–16
    transgenic mice 216–17
  myocardial 203–4
ischemia-induced neovascularisation mouse model 287–97
ischemia–reperfusion 203–4
  inflammatory response 204–5
ischemia–reperfusion models
  ECG measurements 214
  with ischemic preconditioning 196, 208–9
  Langendorff (*ex vivo*) model 209–10, 241–2
  left ventricular pressure–volume measurements 214–15
  measurement of myocardial infarct size
    by cardiac enzyme concentration 212
    by echocardiography 212–13
    by *in vivo* MRI 213–14
    by scoring of reperfused myocardium 210
    by SPECT 214
    by staining 197–8, 199, 210–11, 242–3
    by transmission microscopy 211–12
  minimally invasive model 206, 208
  open-chest model 194–8, 206, *207*
ischemia without reperfusion 208
ischemic heart disease, heart failure due to 336
ischemic preconditioning 193–4, 208–9
  see also heart preconditioning
isoflurane (inhalation anesthetic), advantages 148, 222, 353
isolated perfused heart model 209–10, 235–44
  see also retrogradely perfused isolated heart model

Jackson Laboratory 2, 56, 215, 256

Kawasaki disease 323
ketamine/xylazine, side effects 353
kidney transplantation, graft half-lives 173

knockin mice *see* gene knockin mice
knockout mice *see* gene knockout mice
Krebs–Henseleit buffer solution 210, *238*

L-NAME-induced hypertension 276–7
Langendorff perfused heart 209–10, 235–7
  advantages of model 244
  atrial fibrillation studies 359–62
  buffer used 210, 237, *238*
  epicardial electrophysiological measurements 359–62
  instrumentation 237, 240–1, 362
  ischemia–reperfusion studies 209–10, 241–2
  preparation and transfer to apparatus 237–9, *240*
  principle of model 235–6
  stimulation/recording electrodes 359–62
  technical data 236–7
  see also retrogradely perfused isolated heart model
laser doppler flowmetry 141, 152–3
laser doppler imaging
  artifacts 291
  hind limb ischemia-induced neovascularisation assessed by 289–92
    compared with swimming test 294, *295*
    skin perfusion interference 291
  perfusion scale *290*
laser scanning confocal fluorescence microscopy
  dynamic 153–4
  static 154–5
LCAT knockout mice 261
LCAT transgenic mice, effect of hepatic lipase deficiency in 260
LDL receptor deficiency, in humans 55–6
LDL receptor knockout mice 39, 48–9, 55–6, 256
  advantages and disadvantages *61*
  in aneurysm studies 126
  availability 56
  cholesterol levels 256, 261
  collar-induced atherosclerotic lesions 91
  compared with ApoE knockout mice 49, *61*
LDL receptor-related protein (LRP) knockout mice 39
LDLR/LRP double knockout mice 28
LDLR/SR-BI double knockout mice 263
lecithin cholesterol acyltransferase 261
  see also LCAT
left anterior descending coronary artery (LAD), occlusion in mouse heart 195, 196, 206–8, 337
left ventricular function, *in vivo* measurements 214–15
left ventricular hypertrophy (LVH) 221
  induction of
    by pharmacological agents 226–7
    by suprarenal abdominal aortic constriction 224–6
    by transverse aortic constriction 223–4
  see also cardiac hypertrophy
leukocytes
  analysis after bone marrow transplantation 48
  in aneurysm formation 126
  in atherosclerotic lesions 63
  role in cardiovascular disease 48
likelihood ratio statistics (LRS) 21
lipid metabolism, neointima formation affected by 98
lipoprotein lipase (LPL) 262
  deficiency in humans 39, 262
  see also LPL knockout mice
lipoprotein metabolism 256, *257*
5-lipoxygenase (5-LO) gene, QTL analysis *27*, 28
liver-directed gene transfer, vectors for 263–6
liver-secreted lipoprotein metabolism 256, *257*
5-LO/LDLR double knockout mice 28
log-of-the-odds-ratio (LOD) scores 21–2
longitudinal studies, atherosclerotic plaque development 67
low density lipoproteins (LDL)
  increased levels 39, 55
  in lipoprotein metabolism 256, *257*
  see also LDL...
LPL knockout mice 39, 262

macrophages, in atherosclerotic lesions 63
magnetic resonance imaging (MRI)
  atherosclerotic plaque evaluation by 67–77
  automated image analysis 73–5
  B_0-field, meaning of term *163*
  cardiac function assessed using 213–14, 227

ex vivo MRI 68–9, 72
advantages and disadvantages 169
mouse embryo MRI 160–9
field of view
in *ex vivo* MRI 72, 164
meaning of term *164*
flip angle, meaning of term *163*
glossary of terms *163–4*
gradient echo sequence, meaning of term *164*
hardware 69, *70*
in vivo MRI 71, *72*
magnetic field gradients, meaning of term *163*
mouse embryo imaging 160–9
see also embryo MRI
mouse imaging 68–9
myocardial infarct measurement by 213–14, *344*, 345
optimising MR images for anaysis 73
RF coils *162*, *163*
spin echo sequence, meaning of term *163*
T_1 relaxation time, meaning of term *163*
T_2 relaxation time, meaning of term *163*
team required 69, 76
zero-filling, meaning of term *164*
see also ex vivo MRI; *in vivo* MRI
Map Manager QTX software 21
marker-assisted selection protocol (MASP) 23
matrix degrading systems 109
matrix metalloproteinases (MMPs) 109, 132, 143, 251
MCMV *see* murine cytomegalovirus
metabolic syndrome, neointima formation affected by 98
methoxyfluorane (inhalation anesthetic), advantages 178
microarray methods 25–6
microconductance/pressure measurements, *in vivo* assessment of cardiovascular hemodynamics using 227–31
microisolator cages 4
microsatellite marker technique 4
microsphere assay, regional blood flow estimated using 292, 338
Miller's/van Gieson method for elastin staining 83
mineralocorticoid-induced hypertension model 277–8
Moens–Korteweg equation 245
morphometric analysis
aortic aneurysm 131
flow-induced vascular remodeling 106, *107*
plaque rupture 84–5
murine cytomegalovirus (MCMV)
determination of titer using plaque assay 328, 331
recombinant MCMV-LacZ
ELISPOT assay following immunization with 326, *327*
expansion of 327–8
purification of 328
myocardial infarction
as area percentage 197–8, 211
factors affecting 273, 336
ischemic preconditioning as protective strategy 193–4, 208–9
measurement of infarct size
by cardiac enzyme concentration 212
by echocardiography 212–13, *344*, *345*
by *in vivo* MRI 213–14, *344*, 345
by scoring of reperfused myocardium 210
by SPECT 214
by tetrazolium staining 197–8, 199, 211, 242–3
by transmission microscopy 211–12
procedure in heart preconditioning mouse model 195–6
myocardial ischemia, effects 204
myocardial ischemia–reperfusion 193–4, 203–6
see also heart preconditioning; ischemia–reperfusion models
myocardial stunning 203, 204
myocarditis 324, 331

N^{ω}-nitro-L-arginine methyl ester 252, 276–7
see also L-NAME
N_2 backcross mice 21
Na^+–H^+ exchanger transgenic mouse model 281
national breeding institutions 2
naturally occurring variations in mouse strains 19–20
neointima formation
in chemical injury-induced stenosis model 90–1
in cuff injury-induced stenosis model 91–2, 94, *96*

effect of hyperlipidemia *96*, 97, *98*
genetic modified factors 97–8
mechanism of induction 94, *95*
in electronic/electrical injury-induced stenosis model 90
in partial ligation model 103, 108–9
vasculitis-provoked 323
neovascularisation
ischemia-induced 287–97, 300
in matrix-containing angioreactors 300–7
NHE transgenic mice 281
NIH image analysis software 197, 243
nitric oxide
cardiac preconditioning triggered by 197
in flow-induced vascular remodeling 143
vascular stiffness affected by 251, 252
as vasodilator 276, 280
nitric oxide synthase inhibitors
hypertension induced by 276–7
vascular stiffness affected by 251–2
norepinephrine-induced cardiac hypertrophy 276
norepinephrine-induced hypertension 276

olfactory bulb glomeruli, dynamic imaging of capillary blood flow 156–7
open chest epicardial electrophysiological measurements 356–9
pacing/recoding electrodes 357, 359
programmed electrical stimulation *355*, 358
surgical procedure 356
optical projection tomography, mouse embryos 160
OPTIMAS image analysis software 211
osmotic infusion minipumps
angiotensin II delivered via 127, 226, 275
norepinephrine delivered via 276
see also Alzet pumps
outbred populations (mice) 5

p53 knockout mice, neointima formation in 121
paclitaxel 99, *100*
palpable heartbeat, as graft criterion 179
partial ligation model 103–12
advantages of mouse model 108–9
animals used 104
applications 108–10
blood flow measurements 108
data analysis 106, *107*
disadvantages in rats and rabbits 103
histological analysis 106
study methods, morphometric analysis 106, *107*
surgical procedure 104–5, 111–12
tissue processing 105–6
see also coronary artery ligation (CAL)
pentobarbital, side effects 353
percutaneous coronary angioplasty
cardiac blood flow restoration by 193
injury inflicted by 90
restenosis after 93
perivascular arterial injury-induced stenosis models 90–8
chemical injury-induced model 90–1
cuff injury-induced model 91–8
electronic/electrical injury-induced model 90
perivascular cuff injury-induced stenosis model 91–8
applications 94–5
effect of hyperlipidemia *96*, 97
materials and methods 92–3
permutation tests 22
pharmacologically induced cardiac hypertrophy 226–7
pharmacologically induced hypertension models 125, *274*, 275–8
AngII-induced 125, 275–6
DOCA-salt-induced 277–8
L-NAME-induced 276–7
norepinephrine-induced 276
phenotype-to-gene strategy 20
photochemical injury-induced stenosis model 90–1
Pitx2c knockout embryos, cardiac malformations 166, *168*
PKCdelta knockout mice, neointima formation in 121
planimetry, myocardial infarct size determination by 197, 211, 243
plaque rupture
morphological analysis 83–4
morphometric analysis 84–5
see also atherosclerotic plaque rupture
plasminogen activators, in ligated carotids 109
pleiotropic effects 28
poly(ε-caprolactone) cuff 99
drug release from 99–100, *100*
on mouse femoral artery 99–100

polymerase chain reaction (PCR)
genotyping by 21, 80–1, 324
real-time technique, detection of MCMV using 331
polymorphic markers 4, 21
pravastatin 86
pressure transducer
left ventricular pressure–volume measurements 215
pulse wave velocity measurements 246
protein kinase C delta 121
Ptdsr knockout embryos 166
pulse wave velocity
definition 245
effect of blood pressure 249
pulse wave velocity measurements 245–52
applications 251–2
data acquisition sampling rate affecting 249–50
factors affecting 249–50
as index of vascular stiffness 245
invasive method 246–7
calculation of pulse wave velocity 247
data analysis 246–7
experimental procedure 246
surgical procedure 246
landmarks on waveforms 250
non-invasive method
advantages 251
animal preparation 247–8
calculation of pulse wave velocity 248, *249*
doppler data acquisition system 248
experimental procedure 248
signal processing 248

QTL analysis 20–1
congenic strains used 22–4
example of use *27*, 28
linked with gene expression profiling 26
number of mice required 21
quantitative trait(s) 20
mapping genes 20–2
quantitative trait locus (QTL) 20
see also QTL analysis

rapamycin 99, *100*, 174, 182
reactive oxygen species
in flow-induced vascular remodeling 143
in ischemia–reperfusion 205
recombinant congenic (RC) strains 6
recombinant inbred (RI) strains 6, 22
generation of 20, 22
red blood cells, fluorescent labeling of 152
renal models of hypertension *274*, 278–9
suprarenal artery aortic coarctation model 279
two kidney–one clip models/one kidney–one clip models 278–9
renin–angiotensin II system (RAS), in hypertension models 277–8, 279
Rep protein 266
restenosis, mouse models 89–102
resting microglial cells, dynamic imaging of 157
retrogradely perfused isolated heart model 235–44
advantages 244
end points studied 242
exclusion criteria 241
ischemia–reperfusion studies 241–2, 242–3
ischemia protocol 241–2
measurement of infarct size 242–3
reperfusion protocol 242
Langendorff system 209–10, 235–7
buffer used 210, 237, *238*
instrumentation 237, 240–1
principle of method 235–6
technical data 236–7
preparation of heart
anesthesia and anticoagulation 237–8
cannulation of aorta 238–9
dissection 238
transfer of heart to Langendorff apparatus 239, *240*
reverse genetics 20
RNA interference (RNAi) 26

St Thomas's venous thrombosis model 314–19
histology of thrombus formation *318–19*
method of thrombus induction 314, 315–17
scanning electron micrographs of thrombus formation *317*
surgical procedure 315–17
salt-induced hypertension, models for 278, 281
saturated fat-rich diet 55, 81
scavenger receptor class B type I 262–3
see also SR-BI

severe combined immunodeficiency (SCID) mice, thrombus induction in 314
single nucleotide polymorphism (SNP) 21, 24
single photon emission computed tomography (SPECT), cardiac imaging by 214
SJL strain, in partial ligation study *105*, *108*
SM-LacZ transgenic mice 324–32
  applications 331–2
  cross with ApoE knockout mice 326, 331
  vasculitis induced in 324, *325*, 326
small interferring RNA (smRNA) 26
smooth muscle cells (SMC)
  in neointima formation 90, 91, 94, *95*, *183*, 185
  in vein graft atherosclerosis 120, 121
smooth muscle-like cells (SMLC), in allograft arteriopathic lesions *183*, 185, *186*, 188
sodium-induced hypertension, models for 278, 281
specific pathogen-free (SPF) status 4
speed congenic approach 6, 23–4
spontaneous hypertension 26
SR-BI knockout mice 262–3
statistical analysis
  aortic aneurysms 129
  atherosclerotic lesions 63–4
stem cells
  embryonic, gene targeting technique using 6, 37
  fluorescent, tracking by *in vivo* confocal microscopy 156–7
  hematopoietic, homing to bone marrow 43, 44
  in vascular adventitia 122
stroke
  factors affecting 273
  mouse model 147, 155
subcutaneous injection *10*
  drugs *12*
  injection volume range 11
sudden deaths 81
suprarenal abdominal aortic constriction, cardiac hypertrophy induced by 224–6
suprarenal artery aortic coarctation model of hypertension 279
suramin, venous grafts affected by 121
surgically induced heart failure models 335–49
  applications 348
  experimental set-up 338–9
  injury-quantification techniques 344–6
  limitations 348
  postoperative care 342
  potential pitfalls 342–4
  preoperative preparation 339
  surgical procedures 339–42
  time course of disease progression 346–7
  see also aortocaval shunt model; coronary artery ligation (CAL) model; transverse aortic constriction (TAC) model
swimming test 294, *295*
  compared with treadmill exercise test 294
  correlation with laser doppler blood flow measurements 294, *295*

tail cuff technique (for bp measurement) 282
tail vein
  catheterisation 152
  hydrodynamic systemic injection 267–8
  intravenous injection 9, *11*, 267
Tangier disease 26, 256, 258
TaqMan analysis, chimerism determined by 47–8
Tet-O system 36
tetrazolium stains, infarct size measurement using 197, 199, 211, 242–3
thrombogenesis, factors affecting 313
thrombolysis, cardiac blood flow restoration by 193
thrombosis
  models 313–14
    animals used 314
  see also venous thrombosis
thrombospondin peptide, angiogenesis affected by 307
thrombus
  compared with clot 312
  induction, sites and methods in animal models 314
  see also venous thrombus
tissue macrophages, role in metabolic disease 50
tranquilizers *12*
transesophageal stimulation 354–6
transgenic mice 6, 216–17
  atrial fibrillation studies 352–63
  compared with bone marrow transplantation method 49
  compared with gene knockin mice 38

diseases studied using 3
generation of
conventional transgenic mouse line 34–5
inducible transgenic mouse line 35
in hyperlipidemic research 34, 38
transmission scanning microscopy, myocardial infarct size 211–12
transplant arteriosclerosis 6
gene knockout mice used 6
transverse aortic constriction (TAC) model
cardiac hypertrophy induced by 223–4
experimental set-up 338–9
as heart failure model 337
injury-quantification techniques 344–6, *344*
limitations 348
potential pitfalls 342–3
preoperative preparation 223, 339
surgical procedure 223–4, *340*, 341–2
time course of disease progression 347
treadmill exercise test, compared with swimming test 294
2,3,5-triphenyltetrazolium chloride (TTC) stain, infarct size measurement using 197, 199, 211, 242–3
tTA–TRE system (for generating inducible transgenic mice) 35
type 1 angiotensin II receptor antagonists (AT1RA) 277–8
type I hyperlipidemia 39, 262

ultrasound, non-invasive, aortic aneurysms detected by 131–2
urethane, as anesthetic 352–3

vascular adventitia 122
vascular elasticity
effect of atherosclerosis 245
see also vascular stiffness
vascular remodeling
flow-induced 103–12, 137
role of nitric oxide 143
role of reactive oxygen species 143
ischemia-induced 287–97
processes involved 296, 299–300
in vein grafts 121
vascular stenosis, injury-induced 90–8
vascular stiffness
determination by pulse wave velocity measurements 245–50
effect of NO synthase inhibitors 251–2
factors affecting 245
physiological impact 250
vasculitis, virus-induced 323–32
vasculogenesis 296, 299
vein bypass graft *118*
vein graft atherosclerosis 113
cell origins 121–2
drug and gene therapies for 121
mouse model for 6, 113–24
pathogenesis 120–1
progenitor cells and 122
vein graft mouse model 6, 113–24
applications 12
materials and methods
anesthesia 115
cuff application 117
end-to-end anastomosis 117
fixation and incision 115
harvesting vessel grafts 118–19
postoperative care 117
preparation of arterial conduits 116–17
preparation of carotid artery 115–16
preparation of vein graft conduits 116
reagents 114
surgical instruments 114–15
problems after surgery 119
venous thrombosis
long-term complications 311
St Thomas's model 314–19
venous thrombus
compared with clot 312
factors affecting formation 313
ventilatory rates, in mice 198, 223, 339
very low density lipoproteins (VLDL)
increased levels 39, 55
in lipoprotein metabolism 256, *257*
viral vectors 97, *99*, 263, 264–6
Virchow's triad 313

Wegener's granulomatosis 323

xanthomatosis 81, 261

Index compiled by Paul Nash